

**Gold Mineralisation in the Lone Star area of the Klondike Gold
District, Yukon, Canada**

Matthew Russell Grimshaw

Submitted in accordance with the requirements for the degree of
Doctorate in Philosophy

THE UNIVERSITY OF LEEDS
INSTITUTE OF APPLIED GEOSCIENCE
SCHOOL OF EARTH AND ENVIRONMENT

MARCH 2018

The candidate confirms that the work submitted is his/her own and that appropriate credit has been given where reference has been made to the work of others.

©2017 The University of Leeds and Matthew Russell Grimshaw

Acknowledgements

Firstly, I would like to thank my two supervisors, Dr Rob Chapman and Dr Graham McLeod, who have not only guided me through this PhD but were also a major part of my undergraduate. Your endless enthusiasm and support has made my time at Leeds incredibly enjoyable. The best experiences have been during the many trips to the Yukon to conduct fieldwork. It is a privilege to study such an interesting subject in such amazing locations with you both. It is probably best to avoid discussing the time we set fire to a truck and the various escapades in the Westminster Hotel.

Professor Jim Mortensen has an infectious enthusiasm for all aspects of the Klondike and has contributed huge amounts to my understanding of the region. Much of the geology and tectonic information presented in this thesis has come from a lifetime of Jims work. I also want to thank Dr Murray Allan who has provided valuable discussions developing the research. Academic guidance and input has also been provided by Dr Dave Banks, Dr Mark Pearce and Dr Tim Liverton. I want to thank the various people at the University of Leeds that have help provide technical and academic guidance.

My research would not be possible without the financial and logistical support provided by Klondike Gold Corporation. The support of Ian Mitchell was crucial in the development of the project. I also want to thank Peter Tallman for his continued support of research and my PhD. Wes Keats and numerous other KG employees made the fieldwork in the Yukon a pleasure.

I wish to express my gratitude to the numerous placer miners in the Eldorado Creek area of the Klondike. Most notably was the Johnson family whose hospitality and insights were incredibly valuable.

I want to thank numerous people for their help in collecting samples, conducting analysis and for providing scientific discussions: Will James, Sean Jefferson, Rob Lowther, Carl Spence-Jones, Rob Dawson and Owen Lokuciejewski Taylor.

My families support during my research has provided me with the belief that gaining a PhD was possible. I dedicate this PhD to Aisling who is the most important person in my life and knows more than anyone what it has taken to complete.

Abstract

The Klondike Gold District (KGD) is located in north-west Yukon and is well known for the extensive placer deposits that were exploited in the Gold Rush of 1896. Intensive exploration in the region led to the discovery of the White Gold District in 2009 and accompanying metallogenic studies identified a regional episode of orogenic mineralisation, which includes that within the KGD (Allan et al., 2013). This period has produced huge amounts of gold from relatively small areas, which lack the large-scale features associated with well-established orogenic gold deposits.

This PhD investigates the largest lode occurrence in the KGD that is located in the Lone Star area and includes the richest placer drainages of the Eldorado and Bonanza creeks. This research project develops a paragenetic evolution for gold bearing quartz veins and a, newly discovered, unit of gold bearing schist to establish a genetic relationship to better understand gold distribution in the Lone Star area.

Textural and mineralogical analysis of gold bearing quartz veins has revealed that gold is paragenetically late and is associated with a volumetrically minor phase of quartz. Detailed petrographic studies have revealed that gold disseminated in a unit of schist along the Lone Star ridge is epigenetic and formed during a period of permeable fluid flow. The gold-bearing quartz veins and gold bearing schist are genetically linked and formed at shallow crustal conditions from a relatively cool hydrothermal fluid.

A tectonic setting proposed by Staples et al. (2016) is consistent with a model whereby metamorphic devolatilisation at depth has generated a fluid which was driven upwards into fractures. This model accounts for the widespread nature of gold occurrences (as indicated by placer activities) with the formation of multiple fluid conduits formed in an extensional environment throughout the period of mineralisation. The associated lack of fluid focusing distinguishes the mineralisation in the region from other economically important orogenic gold deposits globally. Historical exploration in the area has focussed on auriferous veins, and the apparent discrepancy between in situ and placer gold. The identification of the schist as a potential gold source resolves this problem whilst providing a template for studies of other areas where similar discrepancies exist.

Table of Contents

Contents

Chapter 1 Introduction	1
1.1 Aims	2
1.2 Thesis Structure	2
Chapter 2 Current understanding of Orogenic Gold Deposits	5
2.1 Introduction.....	5
2.2 Evolution of classification	7
2.2.1 Empirical deposit classification.....	8
2.2.2 An overarching model for OGDs	9
2.3 Metellogenetic epochs.....	10
2.3.1 Precambrian.....	11
2.3.2 The Boring Billion.....	11
2.3.3 Phanerozoic	12
2.4 The Principles of OGD Formation	13
2.4.1 Metal and Fluid Source	14
2.4.2 Transport.....	20
2.4.3 Trap.....	23
2.5 A critique of the OGD model.....	26
2.5.1 Fluid generation	26
2.5.2 An applicable model for OGDs.....	28
2.6 A summary of OGDs and its application in the LSSA.....	28
Chapter 3 Regional Geology and Metallogeny	30
3.1 Introduction.....	30
3.2 Tectonic evolution of the Yukon Tanana and Slide Mountain Terranes	31
3.2.1 Tectonostratigraphy of the YTT.....	31
3.2.2 Tectonostratigraphy of the Slide Mountain Terrane	34
3.2.3 Klondike Orogeny.....	34
3.2.4 The final accretion onto Laurentia.....	35
3.2.5 Orogen parallel tectonics	36
3.3 Geology of the Klondike Gold District.....	37
3.3.1 Slide Mountain Ocean Assemblage	37
3.3.2 Finlayson Assemblage	37
3.3.3 Klondike Assemblage.....	39

3.3.4	Indian River Formation	40
3.3.5	Carmacks Volcanic group	40
3.3.6	Quartz Feldspar Porphyry	41
3.4	Structural Evolution of the Klondike Gold District	41
3.4.1	Foliation development	41
3.4.2	Post peak metamorphic deformation.....	42
3.4.3	Fault-fold deformation	44
3.4.4	Normal faults.....	45
3.5	Metallogeny	45
3.5.1	Syngenetic Mineralisation	48
3.5.2	Mineralisation related to Magmatic Events.....	49
3.5.3	Orogenic Gold Deposits	50
3.6	Physiography and glaciation.....	59
3.6.1	Physiography	60
3.6.2	Glaciation	60
3.7	Placer Gold.....	61
3.7.1	Placer deposits in the Klondike Gold District.....	62
3.8	Summary	64
Chapter 4 The Lone Star Study Area.....		65
4.1	Introduction.....	65
4.2	Geology of the LSSA	66
4.2.1	Lithologic units	66
4.2.2	Structural geology	71
4.2.3	Geological summary	72
4.3	Gold mineralisation in the LSSA.....	72
4.3.1	Eldorado and Bonanza placer deposits.....	72
4.3.2	In situ mineralisation	75
4.3.3	Placer-Lode Relationships	86
4.4	Discussion and summary	88
Chapter 5 The Mineralogy of Native Gold.....		90
5.1	Introduction.....	90
5.2	The features of native gold and associated processes.....	90
5.2.1	Crystal form and crystallography in native gold.....	92
5.2.2	Morphology and shape of detrital gold	94
5.2.3	Composition of native gold	95
5.2.4	Modification and textural variation of native gold.....	100

5.3	Using gold mineralogy to understand ore deposits and mineral exploration.....	103
5.3.1	Morphological variation and transport distance	103
5.3.2	Compositional studies of native gold.....	105
5.4	Discussion and summary	109
Chapter 6 Methodology and Analysis		111
6.1	Introduction.....	111
6.2	Sample collection	111
6.2.1	Quartz vein material	112
6.2.2	Gold in quartz veins	112
6.2.3	Drill Core	115
6.2.4	Gold particle collection	116
6.3	Sample Preparation.....	118
6.3.1	Liberation of gold from quartz vein	118
6.3.2	Preparation of gold particle mounts.....	119
6.3.3	Polished blocks	121
6.3.4	Polished thin sections	122
6.3.5	Polishing protocol for gold specimens.....	123
6.4	Analytical Procedures.....	124
6.4.1	Electron Microprobe	124
6.4.2	Scanning Electron Microscope.....	125
6.4.3	Micro X-Ray Fluorescence	128
6.4.1	Laser Ablation Induced Coupled Plasm Mass Spectrometry 128	
6.5	Summary	129
Chapter 7 Gold-bearing quartz veins		130
7.1	Field observations	132
7.2	Mineralogy and alteration of gold-bearing veins	134
7.3	Quartz vein paragenesis.....	136
7.3.1	Quartz textures observed hand specimens.....	137
7.3.2	Textural variation of quartz in thin sections	139
7.3.3	Interpretation of quartz deposition.....	144
7.3.4	Trace element variation in quartz	149
7.3.5	Interpretation of hydrothermal conditions	152
7.4	Gold in quartz veins.....	156
7.4.1	Textural and mineralogical relationships of gold	156

7.4.2	Paragenetic summary of gold-bearing quartz veins.	159
7.4.3	The controls on gold deposition in gold-bearing quartz veins 160	
7.4.4	Internal crystallography of gold from veins.....	163
7.4.5	The oxidation and weathering of gold-bearing quartz veins. 166	
7.4.6	Gold composition data from veins.....	170
7.5	A model for the formation of gold-bearing quartz veins	181
Chapter 8 Gold-bearing schist.....		186
8.1	Petrography of Quartz Mica Schist Member.....	187
8.2	QMS Member – Interpretation of textures associated with metamorphism and subsequent hydrothermal alteration.....	191
8.3	Gold in schist.....	193
8.3.1	Visible gold in schist.....	193
8.3.2	Disseminated gold in Quartz Mica Schist Member.....	194
8.3.3	Composition of gold in schist across the LSSA.....	196
8.4	Mineralogical and hydrothermal alteration related to gold mineralisation	197
8.5	Paragenetic summary and model for precipitation of gold in schist. 201	
Chapter 9 Detrital gold		205
9.1.1	Crystallography of detrital gold particles	205
9.1.2	Compositional variation.....	206
9.1.3	Alloy composition of detrital gold.....	208
9.1.4	Mineral associations with detrital gold.....	211
9.1.5	Establishing placer-lode relationships in the LSSA	213
Chapter 10 Discussion		216
10.1	Establishing the relationship between gold-bearing quartz veins and gold disseminated in schist.....	216
10.2	A review of the microchemical signatures of gold in the LSSA.....	217
10.3	A model for gold mineralisation in the LSSA	220
10.4	The significance of the LSSA and its relationship to regional OGD formation	223
10.4.1	A metal and fluid source for OGD formation in the LSSA....	223
10.4.2	A comparison of the LSSA to regional OGDs	225
Chapter 11 Concluding remarks.....		227
11.1	Conclusions.....	227
11.1.1	Gold-bearing quartz veins	227

11.1.2 Gold-bearing schist	227
11.1.3 Gold mineralisation in the Lone Star area	228
11.1.4 Relating mineralisation in the LSSA to OGDs globally	228
11.2 Implications of research.....	229
11.3 Future Work.....	230

List of Tables

Table 2-1: Summary of key features of Orogenic Gold Deposits (Groves et al., 1998).	10
Table 2-2 Factors which influence the solubility of gold as the Au[HS]₂⁻ complex (Phillips, 1993).	16
Table 3-1: Mineral Deposits mentioned in the text.	48
Table 3-2: A summary of the main mineralised occurrences in the KGD excluding those in the Lone Star area	55
Table 4-1: Klondike Star Mineral Corporation results of bulk sampling program.	80
Table 4-2: Estimated grades of eroded schist in the LSSA.	88
Table 5-1: Properties of gold.	91
Table 7-1: Summary of gold-bearing vein features at each locality.	143
Table 7-2: Trace elements were mapped in 12 deposits that vary in type and temperature, from Rusk et al. (2008).	154
Table 7-3: A summary of alloy composition data from samples collected during this study.	176
Table 8-1: Examples of the best intercepts from drilling along the Lone Star Ridge in 2016 and 2017.	194
Table 8-2: Summary of alloy data analysed from gold-bearing schist.	197
Table 9-1: A summary of alloy composition data from samples collected during this study.	210
Table 10-1 Classification of gold types defined by Chapman et al. (2010).	218
Table 10-2: Various aspects of this project that provide evidence of low temperature and shallow vein formation.	222
Table 11-1: A summary of all samples and specimens prepared during this research. PB- polished block, PTS- polished thin section, DPW- double polished wafer, CL- cathodoluminescence, EDS- electron dispersive spectroscopy, LA- laser ablation, EPMA- electron probe micro analyser, XRF- X ray fluorescence, EBSD- electron backscatter diffraction.	253
Table 11-2: Results of trace element content of quartz presented in parts per million for each generation of quartz.	260
Table 11-3: Results of trace element content of quartz presented in parts per million for each generation of quartz.	301

List of Figures

- Figure 2-1: Schematic diagram showing tectonic setting and various deposit types. Orogenic Gold Deposits form in the forearc region of a continental margin at a range of depths (Groves et al., 2003).5**
- Figure 2-2: Crustal continuum model proposed by Groves et al. (1993). Sources of fluid and metal are labelled with metal associations at the deposits (Groves et al., 1998, Goldfarb et al., 2005).6**
- Figure 2-3: A simplistic model, proposed by Wyman et al (2016), outlining the features involved in the minerals system approach for genesis of OGDs.8**
- Figure 2-4: Tectonic distribution of OGDs through time. Boring Billion shaded grey (Cawood and Hawkesworth, 2015).11**
- Figure 2-5: Distribution of orogenic gold with variation in oxygen concentration in the Earth's atmosphere over time (Bierlein et al., 2006, Tomkins, 2013b).13**
- Figure 2-6: Eh- pH diagram demonstrating the stability of different complexes (Stefánsson and Seward, 2004).15**
- Figure 2-7: A schematic model of the features, mineralogy and host rocks associated with reduced intrusion related gold system. Zonation of minerals correspond to distance from the intrusion (Hart et al., 2004).19**
- Figure 2-8: Devolatilisation of a subducting slab may either fertilise the above mantle or, travel up dip along the interface of the slab and overlying wedge (Goldfarb and Groves, 2015). Fluids may interact with deep crustal faults which move upwards to produce deposits.20**
- Figure 2-9:A) Devolatilisation model whereby fluid and gold is generated simultaneously (Phillips, 1993). B) Flow through model where a fluid permeates a gold-bearing rock (Cox, 2005).21**
- Figure 2-10: A – Connectivity of pores through fracturing and increased fluid pressure. Dangling pores must connect to reach the percolation threshold. B- Percolation threshold is a function of fracture density and connectivity. (Phillips, 1993, Craw et al., 2002).22**
- Figure 2-11: Fault valve model showing fault rupture at the brittle-ductile transition. This drives fluid upwards into structures where deposition occurs (Sibson et al., 1988, Groves, 1993).24**
- Figure 3-1: A map showing the extent of the North American Cordillera and outlining the extent of the Yukon Tanana Terrane (YTT) and Slide Mountain Terrane (SMT). The Klondike Gold District (KGD) is the main focus of this study. Modified from Nelson et al. (2013) and Berenak and Mortensen (2011).31**

- Figure 3-2: Schematic tectonostratigraphic overview of the Yukon and Alaska (Colpron et al., 2007). The YTT is on the left and partly synchronous with the SMA on the right.32**
- Figure 3-3: Schematic cross section of the tectonic evolution of the YTT. The colours of units correspond to those outlined in the key of Figure 3-2. A) East dipping subduction resulted in formation of the Finlayson Assemblage. B) Slab roll back resulted in back arc opening and the development of associated volcanism. C) Subduction switching to the west beneath the YTT formed the Klondike Assemblage (Colpron et al., 2007, Nelson et al., 2013). .33**
- Figure 3-4 Schematic cross section of the tectonic evolution of the YTT. D) Closure of Slide Mountain Ocean and obduction of YTT creates Klondike Orogeny. E) Final accretion along Laurentian margin results in rapid uplift and propagation of orogenic wedge (Nelson and Mihalynuk, 1993, Nelson and Colpron, 2007, Nelson et al., 2013). The star represents a period of OGD formation that includes the KGD.....35**
- Figure 3-5: A modified map from MacKenzie et al. (2008). Geological units and thrusts are simplified.....38**
- Figure 3-6: Field image showing a rootless isoclinal F1 fold (Liverton, 2011).42**
- Figure 3-7: Annotated photo, from MacKenzie et al. 2007a, looking south along Bonanza Creek. Thrust fault and units are labelled to mark the imbricated thrust slices.43**
- Figure 3-8: A) Crenulation cleavage well developed in a unit of quartz mica schist recovered from drilling. B) Field image of spaced crenulation cleavage (MacKenzie et al., 2007a)44**
- Figure 3-9: A) Reverse fault. B) Angular kink fold.45**
- Figure -3-10: Histogram of compiled geochronological data for the northern YTT (Allan et al., 2013). Key deformation events summarised by MacKenzie et al. (2008b). Mineralisation events and deposits related to magmatism in black compared to orogenic in white.....46**
- Figure 3-11: Major deposits and belts in north-west Yukon labelled. Colours correspond to ages (Yukon Alaska Metallogeny (Allan et al., 2013).....47**
- Figure 3-12: Orogenic districts within Yukon and Alaska. Golden Saddle and Coffee deposits are the biggest OGDs in the region. The KGD lacks a single large deposit but has numerous orogenic occurrences (Allan et al., 2012, Allan et al., 2013).51**
- Figure 3-13: Map of Klondike District showing mineral occurrences and gold placer streams.52**
- Figure 3-14: Field image of the Sheba vein at King Solomon's Dome ..54**
- Figure 3-15: Figure from Mann et al. (2015) showing the last glacial maximum in the Yukon and Alaska.(Mann et al., 2015).....59**

Figure 3-16: Glacial distribution simplified from Dud-Rodkin (1999). Lake Yukon, KGD and Lone Star are labelled for reference. (Duk-Rodkin, 1999)	61
Figure 3-17: Modified from Allan et al (2013) indicating total lode gold resource for each mineral district plotted against total placer gold production. The Dawson Range is dominated by Cretaceous related porphyry and orogenic mineralisation.....	62
Figure 3-18: KGD with alluvial bench gravels of the White Channel Gravel labelled (Lowther et al., 2014).....	63
Figure 3-19: Evolution of placer formation as illustrated by Lowey (2006). Stage 1- Peneplain formation weathers mineralisation and forms Klondike Plateaus, Stage 2 - Degradation and incision produces the LWCG which is followed by aggradation and UWCG, Stage 3 – Incision to present day drainage	64
Figure 4-1: A- A map of the Yukon Territory. B-Klondike Gold District (KGD) with the LSSA outlined. C- Creeks and drainage of the LSSA labelled.	65
Figure 4-2: A modified geological map after Mortensen (2013) with mineral occurrences, historic mines and placer deposits marked.	68
Figure 4-3: Winchester and Floyd plot of immobile elements from a number of drill hole intersections (Winchester and Floyd, 1977). Pink diamonds represent the Meta-Rhyolite Member and blue squares the Quartz-Mica-Schist Member (Mortensen, 2011).	70
Figure 4-4: A) Spotted alteration of the Quartz Mica Schist. B) Foliation parallel band of sulphides.....	70
Figure 4-5: Liverton (2011) sketch cross section of the Lone Star ridge. More detailed structural features, such as parasitic folds are not illustrated.....	71
Figure 4-6: Map of the LSSA showing alluvial placer deposits (yellow), gold absent streams (blue) and palaeo placer WCG deposits (orange).	74
Figure 4-7: WCG alluvial bench gravel deposits and present day alluvial placers looking north down Eldorado Creek.....	74
Figure 4-8 : Historic mine and gold occurrences that form the basis of this PhD project marked on a google Earth image of the LSSA....	76
Figure 4-9: Ore being extracted from Boulder Lode open cut in 1912. .	78
Figure 4-10: 4- headed stamp mill located on Victoria Gulch. Image taken by T.Liverton in 2007.	78
Figure 4-11: The head of incline at the Boulder Lode mine in 1912.	78
Figure 4-12: Violet mine shaft and trenches in 1907.....	79
Figure 4-13:En echelon vein array in large boulder from the Dysle zone, described by Allan et al. (2013).	81

Figure 4-14: Fibrous quartz at margin of vein with blocky infill from the Nugget Zone (Wolff, 2012).....	82
Figure 4-15: Visible gold from drill core hosted in oxidised pyrite.	83
Figure 4-16: 1 metre interval (69-70m) from drill hole 05LS02 sampled by MacKenzie et al 2007. White lines separate samples that were measured for gold content shown in ppm.....	85
Figure 4-17: Gold is enriched in unit of Quartz Mica Schist that is identified by the elevated P/La compared to Meta Rhyolite.....	86
Figure 5-1: A- Dendrite, 3.5cm wide branching crystal from California; B- Octahedron, 3.7cm high skeletal crystal from Chihuahua, Mexico (Francis, 2004); C- Wire like gold crystals (left is 1.2cm) that are flattened during transport from the 60 Mile River, Yukon Canada (Mauthner, 2004); D- Alluvial gold octahedron from Gold Run Creek that, Yukon, Canada that has been flattened (Mauthner, 2004)	93
Figure 5-2: A 9.94-ounce nugget sectioned and chemically etched to reveal internal crystal structure (Liversidge, 1897).	94
Figure 5-3: Back-scattered electron image of placer gold particles from Klondike Gold District. Lighter greyscale reflects higher Au content (Knight et al., 1999a). A- Evidence of smearing influences gold rim. B- Gold rim impregnates particle.	97
Figure 5-4: Back-scatter electron images showing gold rich heterogeneity on interior of gold grain from nugget in Queensland, Australia (Hough et al., 2009).....	97
Figure 5-5: A and B- Subtle alloy variation from Eureka, Yukon (Chapman et al., 2011). C -Ag (and Hg) rich Au mantling Au-Ag alloy. Violet Mine, Klondike, Yukon, partial Au rich rim surrounds both alloys (Chapman et al., 2010a).....	98
Figure 5-6: Examples of gold inclusions from Casino porphyry, Yukon (Chapman, 2014) A- Gold particle with angular shaped inclusion of Bi telluride. B- Chalcopyrite (Cpy) and a range of other sulphosalts in gold particle.	99
Figure 5-7: Surface cracks of eluvial gold nugget collected from Australia (Hough et al., 2007).....	101
Figure 5-8: Micron scale gold within kaolinite-organic (ka-oc) material from Western Australia (Anand et al., 2016).....	102
Figure 5-9: Nano-particulate gold surrounding gold particle from Australia (Rea et al., 2016).	102
Figure 5-10: Morphology of gold used to inform transport distances from source (Townley et al., 2003).	105
Figure 5-11: A cumulative percentile plot that shows examples of how populations of data can vary.	106
Figure 5-12: An example of mineral inclusions plotted on a ternary diagram from the Black Hills area of the Yukon (Chapman et al., 2011)	108

- Figure 5-13: BSE images of mineral inclusions within gold. A- Galena, Ag telluride and Au-Ag telluride inclusion from Eureka Dome, Yukon . B- Bi-telluride and Bi-Cu- sulphide inclusion from the Indian River area of the Yukon.....108**
- Figure 6-1: Example of quartz textures at Dysle that exhibit wallrock relationships.112**
- Figure 6-2: A cartoon of discordant quartz vein and the potential source of gold highlighted as stars. A- Bulk sampling conducted by KGC crushed wallrock and vein material. Most gold particles liberated but have no context to origin. B- Only quartz vein material crushed to liberated gold to provide a comparison to KGC bulk samples. C- In situ visible gold preserves the textural features.113**
- Figure 6-3: Visible gold collected from Buckland Zone (BZ07).114**
- Figure 6-4: A: An image of the White Channel Gravel (WCG). The bench is approximately 30 metres above the present-day French Gulch stream. Samples of gold were collected at the bedrock contact next to historic mine shafts. B: Flow of water from Eldorado Creek was modified using rocks to provide the correct flow for the Le Trap™ sluice. A slurry of water and gravel was fed slowly into the sluice.117**
- Figure 6-5: Flow chart demonstrating process involved to generate specimens from specific sample types or locations.119**
- Figure 6-6: Image of placer gold arranged according to size prior to mounting.120**
- Figure 6-7: Gold particles are separated according to size and arranged into rows. The particles were mounted on double sided tape before being set in resin.120**
- Figure 6-8: An example of 25mm gold particle mount. Polishing was conducted until the interior of the gold grains was revealed.121**
- Figure 6-9: Visible gold from vein cut down to chip prior to mounting in mould and resin.121**
- Figure 6-10: An example of visible gold mounted in 30mm block that has been polished.....121**
- Figure 6-11: An example of a sample that has been cut to a chip ready for mounting and polishing.122**
- Figure 6-12: Abrasive polishing produces an amorphous damage layer known as the Beilby Layer.....123**
- Figure 6-13: Overview of EBSD analysis. A- Electron beam strikes samples tilted to 70°C. Diffraction. produces cones of electrons which are recorded on a CCD. B- Kikuchi bands recorded on CCD correspond to crystal lattice. C- Automation of the process is used to produce maps of data. Colours correspond to crystal orientation plotted as an inverse pole figure (Z).127**
- Figure 7-1 : Historic mine and gold occurrences that form the basis of this PhD project marked on a google Earth image of the LSSA. .131**

- Figure 7-2: Boulder Lode mine cut excavated to reveal bedrock and veining.133**
- Figure 7-3: Anastomosing quartz veins revealed through exploration trenching at the Nugget Zone.133**
- Figure 7-4: Discordant quartz vein at the Upper Nugget Zone. Quartz veining is sub-vertical and hosted in angular kink folds that are related to D₄.134**
- Figure 7-5: A- Euhedral calcite in the centre of the vein surrounding euhedral quartz crystals at the Nugget Zone. B- Example of pyrite, oxidised to limonite, at the Nugget Zone, which is best developed at vein margins.135**
- Figure 7-6: The extent of pyrite surrounding a quartz vein at the Nugget Zone.136**
- Figure 7-7: A- 13cm euhedral quartz crystal cemented, parallel to vein margin, at the Upper Nugget Zone. B- A 6cm quartz crystal growing into centre of vein at the Gay Gulch Vein. C- 3cm clear crystal of quartz recovered from the centre of a vein in drill core. D- 15cm euhedral quartz crystal from the Boulder Lode Mine.138**
- Figure 7-8:A- Bladed quartz in vug from Upper Nugget. B- 6cm wide vein from Dysle Zone with bladed quartz in vug.138**
- Figure 7-9: A- Cross polarised light image showing a gold-bearing quartz vein from the Dysle Zone (MG15_D09). Green marks the foliation of the Meta Rhyolite Member that is cut by discordant quartz (yellow). B- Cross polarised light image of discordant vein from Dysle Zone (MG21_D09). Green marks foliation that is cut but quartz (yellow). XPL shows some textural variation of vein quartz with minor euhedral quartz at margin; however, the majority is large subhedral quartz that displays undulose extinction. The centre has minor calcite infill.140**
- Figure 7-10: A- A montage of quartz cathodoluminescence (CL) of a whole thin section from Dysle Zone as observed in Figure 7-9b (MG21_D09). CL highlights the textural variation that is not observed with XPL. B- Mottled outline of euhedral quartz cross cut by dark CL. C- Euhedral fragment of quartz cemented and cross cut by bright quartz.141**
- Figure 7-11: CL image of quartz from Nugget Zone (MG61_UN01). Q1- Mottled oscillatory zoned Q2- Dark quartz that fractures the sample and fills Q1. Q3- Fractures and cements all previous generations with fibrous growth. Q4- Minor phase in small fractures.142**
- Figure 7-12: Summary of quartz and calcite textures observed in hydrothermal veins. Many of the textures are typical of epithermal quartz. Textures are separated into rapid deposition from boiling fluid and fluids that precipitated more slowly (Sander and Black, 1988, Dong and Morrison, 1995).145**

- Figure 7-13: Examples of primary inward zoned quartz. A- Tokatea epithermal deposit NZ (Bignall et al., 2004). B- Inward zoned euhedral quartz from low temperature veining at Comstock Lode NV, USA (Rusk, 2012).145**
- Figure 7-14: Example of homogenous CL textures. A- Typical orogenic vein texture from Au vein, Valdez Creek, Alaska. B- Mostly homogenous quartz in orogenic vein from Norseman, Australia (Rusk (2012).146**
- Figure 7-15: Example from quartz vein at Nugget Zone. A- Earliest phase of Q3 is fibrous. B- Q3 develops to zonal quartz around fragments of quartz.....147**
- Figure 7-16: Cathodoluminescence of quartz at Curraghinalt, NI. A- Relationships of quartz generations (Rice et al., 2016). B- Electrum next to Q4 (Wilkinson et al., 1999).148**
- Figure 7-17: Box plots showing the variation in trace elements according to generations of quartz. Block represents inter quartile range between the 75th and 25th percentile, whiskers show range of data, black line is median and black circle is mean.....150**
- Figure 7-18: A- A plot of the sum of monovalent cations (Li+Na+K) and Al in different generations of quartz. B- A plot of Ti and Al for different generations.151**
- Figure 7-19: A- A plot of Al and Ba showing positive correlation. B- Al and Sb showing a linear correlation with Sb elevated in Q3.151**
- Figure 7-20: Percentile box plot of Al content from different generations of quartz. Range in Al corresponds to CL intensity.....152**
- Figure 7-21: Compositions of Al and Ti of deposits in Table 7-2 from Rusk et al. (2008). Al content of quartz in the LSSA is presented but Ti values were too low to include.....154**
- Figure 7-22: A- Drill core from Gay Gulch Vein with centimetre-scale gold in limonite (EC15_10). B- Example of visible gold in limonite from a vein at the Buckland Zone (BZ07).156**
- Figure 7-23: Reflected light image of sample of gold from Buckland Zone (MG26_BZ17). Sectioning of visible gold in quartz revealed the textural relationship of gold, limonite and quartz. T.....157**
- Figure 7-24: A- CL image of limonite (outlined in orange) with gold (outlined in yellow) that is next to fracture filled with Q3 (outlined in blue) (MG21_D7). B- CL image of gold in limonite that is fractured by Q3 (MG28_BZ10).158**
- Figure 7-25: BSE image of gold particle, liberated from veining at Upper Nugget Zone. A-Hyalophane forms around the exterior of gold as an exclusion and is coeval. B-. Fractures in limonite filled with gold and hyalophane.159**
- Figure 7-26: Gold-bearing vein paragenesis for the LSSA.....160**

- Figure 7-27: Schematic sketch of the proposed mechanism of visible gold formation in fractured pyrite. High-strain results in migration of gold from the pyrite lattice into fractures (Huston et al., 1992).161**
- Figure 7-28: Modified from Knipe et al (1993). Initial adsorption of gold and ligand then progresses to chemisorption. Clustering and crystal growth follows.....163**
- Figure 7-29: Orientation map (IPFZ) from EBSD showing straight twin boundaries within gold particle from Buckland Zone (MG26_BZ17 and shown in Figure 7-23).....164**
- Figure 7-30: Recrystallisation diagram of pure gold showing grain size as a result of annealing temperature and deformation (Hough et al., 2007).165**
- Figure 7-31: Oxidised pyrite particles showing volume loss (Hu et al., 2006).167**
- Figure 7-32: BSE image of gold in limonite from Buckland Zone (MG24_BZ07).....167**
- Figure 7-33: A- EDS map of margin of gold and limonite from Upper Nugget Zone (MG53_OLT15_15). Gold crystals occur alongside an unidentified mineral with a lozenge shape that is composed of lead and sulphur. B- Limonite has a spongy box-work texture that is filled with silver telluride, barite and clay (MG21_D07).168**
- Figure 7-34: BSE images of gold in limonite from Nugget Zone (MG68_OLT15_14) . A-The surface of gold in limonite is covered in micro-crystalline pure gold. B- Abraded surface of gold with micro-crystalline gold and clay in embayments and fractures.....168**
- Figure 7-35: BSE image of margin of gold and limonite from Upper Nugget Zone (MG53_OLT15_15). Dissolution of primary gold and precipitation in limonite pseudomorph from Nugget Zone.....169**
- Figure 7-36: BSE images and EDS maps of gold particles. A- Diffuse silver enrichment (darker areas) with small pure gold particles (bright spots) along grain boundaries (Nugget Zone MG53_UNOLT15_15). B-Gold particle showing diffuse silver enrichment along grain boundaries with small gold crystals in spaces of limonite (Nugget Zone MG53_UNOLT15_15). C- Gold with hyalophane along fractures of limonite. Gold rich tracks are represented by green (Au) tracks (Nugget Zone). D- Thin gold rich tracks that cut otherwise homogenous alloy (uniform greyscale) (Buckland Zone -MG52_BKOLT15_29).....171**
- Figure 7-37: EBSD and EDS data of gold particle showing grain boundaries (black), twins (red), Au (green), and Ag (blue). A- Gold particle from Adams Hill alluvial deposit showing silver depleted tracks. B- Gold rich areas on interior of gold particle lack new grain boundaries. Silver depleted area results in slight distortion of straight twin.172**

- Figure 7-38: A- BSE image of MG26_BZ17, with traverse lines marked. B- Silver values recorded along traverses.174**
- Figure 7-39: A-Cumulative percentile plots of silver content of gold particles at each locality. B Percentile box plots of silver variation of gold particles at each locality.177**
- Figure 7-40: A- BSE image of gold particle from vein the Buckland Zone. Chalcopyrite and sphalerite inclusions are labelled within the gold (MG28_BZ10). B- An inclusion of acanthite from the Dysle Zone. A margin of Au, Ag, S suggests exsolution has occurred.....178**
- Figure 7-41: Variation of Ag within different populations of gold collected from the Nugget Zone. The TOTAL curve is the overall signature from the nugget Zone when all particles are combined.....179**
- Figure 7-42: Schematic model of schist units in the LSSA. The development of crenulation cleavage and foliaform veins are cross cut by angular kink folds associated with D4. Quartz veining localises in the D4 fractures.182**
- Figure 7-43: Schematic cartoons for the formation of auriferous veins in the LSSA.....185**
- Figure 8-1: Visible gold in drill core. A- Gold in schist close to metamorphic quartz segregation (05LS16_60.76). B- Gold in pyrite with no association with discordant quartz veins (MG56_05LS16_82.68).186**
- Figure 8-2: Micro XRF scan of gold-bearing schist interval (MG8_05LS27). Banding of mica (red) and quartz-feldspar (blue) has pyrite (yellow) and rutile (green) aligned along foliation.....187**
- Figure 8-3: Micro XRF scan of gold-bearing schist interval (MG45). Dark blue is feldspar, pink is rutile and yellow is pyrite. Light blue and bright green represent alteration (outlined in dashed yellow) of hyalophane and Mg-Fe carbonate minerals along foliation and in micro-veinlets.188**
- Figure 8-4: Cross polarised light images of QMS Member. A- Opaque pyrite aligned along foliation (MG45). B- Fracture cross cutting foliation filled with euhedral feldspar and carbonate minerals (MG45). C- Crenulation cleavage marks spaced D3 cleavage (MG9_05LS27). D- Crenulation is well developed in mica rich intervals (MG8_05LS27).189**
- Figure 8-5: SEM BSE images. A- Small rutile grains aligned with foliation at the core of a euhedral pyrite pseudomorph (MG9_05LS27). B- BSE image of pyrite cluster with rutile inclusions and surrounding hyalophane (MG10_05LS27).189**
- Figure 8-6: A- BSE image of margin of micro-veinlet filled with euhedral hyalophane and carbonate minerals. Ba variation in the hyalophane marks grain boundaries (MG45). B- BSE image of micro veinlet showing Ba variation (greyscale) in hyalophane with barite (brightest phase) at centre (MG45).....190**

- Figure 8-7: Visible gold from drill core (05LS09_36.76) A-Photo of visible gold in core. B- BSE image of gold with pyrite at margin of quartz segregation. Fine grained hyalophane is observed along foliation of mica (MG55_05LS09).....193**
- Figure 8-8: A- BSE image of gold and hyalophane in pyrite pressure shadow and along spaces in foliation (MG59_05LS27). B- BSE image showing gold infilling space between phengite in crenulation hinge (MG45).....195**
- Figure 8-9: EDS maps. A- Gold with hyalophane and Fe carbonate (MG45). B- Gold in fracture of pyrite associated with telluride minerals (MG8_05LS27).196**
- Figure 8-10: A- Micro veinlet with euhedral hyalophane that decreases in barium content towards the centre. Vein is filled with Mg-Fe carbonate, barite, pyrite and petzite (MG45). B- BSE image of fracture in pyrite filled with hyalophane, gold and hessite (MG8_05LS27).....196**
- Figure 8-11: Barite solubility in H₂O solutions at depth from a specific pressure gradient. A- Constant composition curves on the barite saturation surface projected in P,T. B- Barite solubility is shown from a standard geothermal gradient of 30°C/km.....199**
- Figure 8-12: Variations of Te₂ and S₂ fugacity with respect to selected telluride-sulphide-oxide equilibria at 200°C. Yellow highlights the conditions constrained by stability of minerals observed in the LSSA. Fo-forsterite, Po- pyrrhotite, Py- pyrite, Cv- calaverite, Au-gold, PbTe- altaite, PbS- galena, Cpy-chalcopyrite, Bn-bornite, Ag₂Te-altaite, Ag₂S-acanthite.....200**
- Figure 8-13: Paragenetic summary of gold in schist from LSSA.....203**
- Figure 8-14: A schematic summary of gold formation in schist.....204**
- Figure 9-1: Orientation map (IPFZ) of detrital gold particle from Upper Gay Gulch stream, which has a distinctive twin through the centre. The twin has been bent slightly during transport.....206**
- Figure 9-2: BSE image of gold particle rim. Greyscale corresponds to Au content with brighter colours being almost pure gold.....207**
- Figure 9-3: EBSD and EDS data of detrital gold particle showing: grain boundaries (black), twin boundaries (red) and Au (green) and Ag (blue). A- Gold rich rim at margin of gold particle. B- Pure gold at margin separated by grain boundaries.....208**
- Figure 9-4: Cumulative percentile plots demonstrating variation in silver content of each population. A- Gold particles collected from different WCG deposits. B- Gold particles collected from modern drainages.....209**
- Figure 9-5: A: Eldorado Creek gold particle. B: CL image of gold particle in A. Different generations of quartz are labelled with Q3 forming in association with gold.212**

- Figure 9-6: A comparison of the gold-bearing vein localities of Nugget and Buckland Zone with a small first order drainage placer deposit of Oro Grande.214**
- Figure 10-1: Geographic extent of gold types according to the classification in (Chapman et al. 2010)218**
- Figure 10-2: Schematic model of gold-bearing fluids moving upwards through the schist resulting in gold deposition (red stars) at shallow crustal depths. Localisation of fluid into discordant quartz veins results in gold deposition. Diffuse fluid flow along the QMS Member results in the deposition of gold along foliation. Mixing with meteoric fluids occurs, and is followed by deposition of gold, tellurides, and barite.....223**
- Figure 10-3: A schematic model of fluid generation and gold transport responsible for formation of OGDs in the region.225**

Abbreviations

BSE	Backscatter Electron
CL	Cathodoluminescence
CSIRO	Commonwealth Scientific and Industrial Research Organisation
D ₍₁₋₄₎	Deformation events
EBSD	Electron Backscatter Diffraction
EPMA	Electron Probe Micro Analyser
EDS	Energy Dispersive Spectroscopy
f	Fugacity
g/t	Grams per ton
Hz	Hertz
IPF	Inverse Pole Figure
Km	Kilometre
KGC	Klondike Gold Corporation
KGD	Klondike Gold District
KS	Klondike Star
LA-ICP-MS	Laser Ablation Induced Coupled Plasma Mass Spectrometry
LSSA	Lone Star Study Area
LWCG	Lower White Channel Gravel
m	Metre
µm	Micrometre
mm	Millimetre
Ma	Million years
OGD	Orogenic Gold Deposit
ppb	Parts per billion
ppm	Parts per million
S ₍₁₋₄₎	Planar structure
QMS	Quartz Mica Schist Member
Q(1-4)	Quartz phase
SEM	Scanning Electron Microscopy
SMT	Slide Mountain Terrane
UTM	Universal Transe Mercator
UWCG	Upper White Channel Gravel
VMS	Volcanic massive sulphide
wt. %	Weight %
WCG	White Channel Gravel
YTT	Yukon Tanana Terrane

Chapter 1 Introduction

The Klondike Gold District (KGD) is one of world's richest and most productive placer regions, with over 20 million ounces of gold sourced from a geographically compact area (Burke et al., 2005). Bonanza Creek and its tributary Eldorado Creek were spectacularly rich, and the dividing ridge ('Lone Star Ridge'), has been the focus of considerable exploration and small-scale lode mining for over 120 years.

There are several historical occurrences of gold-bearing quartz veins in the KGD, but two new and important discoveries have been made elsewhere in the region over the last ten years (White Gold and the Coffee deposit) (Allan et al., 2013). The associated increase in exploration activity provided the incentive for a study that has provided a regional metallogenic framework. One outcome of the research by Allan et al. (2013) has been the identification of a widespread episode of orogenic gold mineralisation in the Mid-Late Jurassic, which provides a genetic link between the KGD and the recent economically important discoveries.

Exploration for a plausible bedrock source in the Lone Star area, and the region in general, has traditionally focussed on the auriferous, discordant quartz veins which were assumed to be the source of the extensive placer deposits (Tyrrell, 1907). The veins are poorly exposed, are anastomosing or discontinuous themselves, and occur in zones that lack continuity. In short, historical exploration for the source of the gold which contributed to the placer deposits has been unsuccessful. More recently gold has been found disseminated within a unit of schist that crops out along the Lone Star ridge. This discovery raises the possibility that auriferous veins may not be the only potential source of gold. One remit of the current project is to characterise this type of mineralisation and to investigate its relationship to the auriferous veins in the Lone Star Study area (LSSA).

In general, exploration programs are heavily influenced by prevailing deposit models which are essentially generic templates that identify the elements of the 'source- transport- trap' process. The widely cited deposit model describing

orogenic gold deposits (OGDs) is based on studies of established mining districts such as Western Australia and the Canadian Shield (Groves et al., 1998). Currently, there is no distinction made between the genesis of Archean age deposits and smaller, but often richer, Phanerozoic deposits, such as the KGD even though the prevailing tectonic regimes are completely different. The Lone Star area provides an opportunity to develop a deposit model for a small but exceedingly rich orogenic gold system and to evaluate the relevance of that model to other localities worldwide.

1.1 Aims

The overall aims of the PhD project are as follows:

- To establish the paragenesis of gold-bearing quartz veins in the Lone Star area and to identify the main controls on gold deposition.
- To characterise gold mineralisation in the schist in terms of mineralogy, texture and alteration of host rocks.
- To establish any genetic relationships between gold mineralisation hosted in the schist and the quartz veins.
- To evaluate the chemical and mineralogical features of native gold from gold-bearing quartz veins and schist.
- To establish the relationship of placer deposits to known in situ occurrences. New and existing gold particles will be analysed, in order to speculate on the nature of the eroded mineralisation.
- To interpret the outcomes of the present study more broadly in terms of orogenic mineralisation regionally and globally.

1.2 Thesis Structure

The overall structure of the thesis is provided below with a rationale for each chapter:

Chapter 2 – Current understanding of Orogenic Gold Deposits

Bedrock mineralisation at Lone Star is interpreted to be part of a regional period of OGD formation. The current understanding of the processes and principles surrounding this style of deposit classification are reviewed in Chapter 2.

Chapter 3 – Regional Geology and Metallogeny

The KGD is part of the North American Cordillera, which hosts a large number of mineral deposits. The extensive mineral endowment is related to a diverse tectonic history, which is described in Chapter 3. A tectonic framework of the region will provide context for describing the geology, structural evolution and metallogeny of the KGD.

Chapter 4 – The Lone Star Study Area

The regional geology and structures described in Chapter 3 provide a framework in which to discuss the various lithologies in the LSSA. A prolonged history of exploration and mining in the area has resulted in multiple interpretations of the geology and structure with a corresponding array of nomenclature. A description and classification of rocks in the Lone Star is presented, based on observations made during this PhD, which correlate with the regional geology (Chapter 3). This chapter also presents a review of the various mineralised localities and placer deposits in the study area.

Chapter 5 – The Mineralogy of Native Gold

A novel aspect of this study is the deduction of mineralising conditions through consideration of the mineralogy of native gold. Chapter 5 describes the various characteristics of native gold and how they may be utilised in this regard.

Chapter 6 – Methodology and Analysis

Chapter 6 describes the methodologies employed during this study, from sample collection to preparation. Details are provided of the various analytical procedures employed.

Chapter 7 – Gold-bearing quartz veins

This chapter describes various aspects of gold-bearing quartz veins in the LSSA. Field observations at each mineralised locality are presented, which includes; mineralogy, alteration and quartz textures. The chemical and mineralogy of native gold in veins is presented and discussed in relation to quartz textures. The chapter presents a new paragenesis of gold-bearing quartz veins and concludes with a proposed model gold deposition in quartz veins.

Chapter 8- Gold-bearing quartz veins

A petrographic study of mineralised and un-mineralised schist is undertaken to distinguish processes related to gold deposition and metamorphism. A paragenesis for gold mineralisation in the schist is presented which is used to develop a summary of the conditions responsible for gold enrichment

Chapter 9- Detrital Gold

This chapter presents the chemical and mineralogical information gained from detrital gold sample locations in the LSSA. Populations of gold particles provide information on the associations with bedrock sources discussed in Chapter 7 and 8.

Chapter 10 Discussion

Chapter 8 provides a discussion of the various project aims described in section 1.1. The first section combines the observations of gold-bearing quartz veins and gold-bearing schist to investigate whether there is a genetic relationship. The next section provides a critique of the most current deposit model proposed by Chapman et al. (2010a) and concludes with an overarching model for gold mineralisation in the LSSA. The final section discusses the relationship of mineralisation in the LSSA to orogenic gold deposits regionally and globally.

Chapter 9 – Conclusion

A summary of the key findings of the research is presented with an evaluation of project outcomes in relation to the project aims. The implications of the research, and future work is also presented.

Chapter 2 Current understanding of Orogenic Gold Deposits

2.1 Introduction

Gold deposits in metamorphic terranes have undergone a range of classifications over the last 35 years as a result of an increased understanding of plate tectonics and mineralisation processes. The formation of gold-rich deposits occurs at all stages of orogen evolution and contain a diverse range of deposit types (Groves et al., 1998). Deposits related to volcanism in convergent margins or oceanic arcs include epithermal Ag-Au, porphyry Cu-Au and Au rich volcanic massive sulphide deposits (Figure 2-1) (Groves et al., 2003).

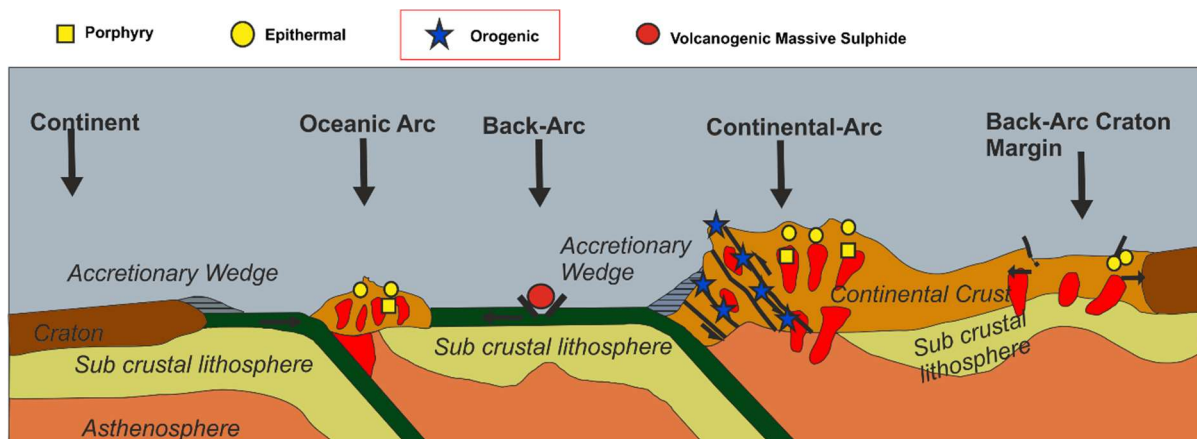


Figure 2-1: Schematic diagram showing tectonic setting and various deposit types. Orogenic Gold Deposits form in the forearc region of a continental margin at a range of depths (Groves et al., 2003).

The remaining group of deposits occur in clusters in metamorphic terranes and are described as being *gold only* due to the sole or dominant product being gold (Phillips and Powell, 2010). Groves et al. (2003) argues that these deposits are the most predominant gold deposit in metamorphic terranes, which include several giant (>250t Au) and numerous world-class (>100t Au) deposits.

Groves et al. (1998) described these as *Orogenic Gold Deposits (OGD)* and provided an overarching model based on a *crustal continuum model* (Figure 2-2). OGDs are classified as epigenetic, structurally-hosted gold deposits, which are gold only, and occur over a range of depths (Groves et al., 1998). They form from 2-15km in a continuum from 180°C at 1kb to 700°C at 5kb (Figure 2-2) (Groves

et al., 1992, Groves, 1993). These vertically extensive deposits form in thermal equilibrium with wall rocks from fluids that are aqueous-carbonic, low salinity and have near neutral pH (Goldfarb et al., 2005). The deposits occur in greenschist facies rocks and are linked to post-peak metamorphism (Groves et al., 1992, Groves, 1993). Mineralising fluids are focussed into crustal scale faults and deposited in second order structures (Groves, 1993).

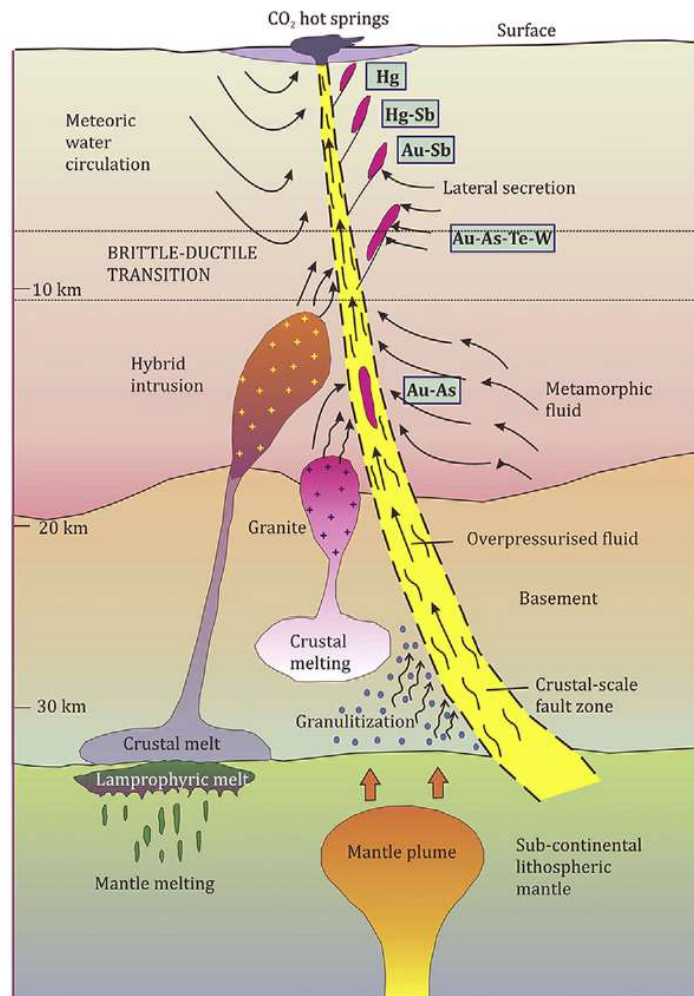


Figure 2-2: Crustal continuum model proposed by Groves et al. (1993). Sources of fluid and metal are labelled with metal associations at the deposits (Groves et al., 1998, Goldfarb et al., 2005).

The model of Groves et al. (1998) was developed through studies of deposits in Western Australia; however, the same characteristics are evident elsewhere, such as the Abitibi gold belt in Canada, West Africa, and other metamorphic terranes globally (Goldfarb et al., 2005). The description of orogenic gold deposits has been broadly applied as a deposit type (Goldfarb et al., 2001, Goldfarb et al., 2005, Bierlein et al., 2006, Goldfarb and Groves, 2015); however,

there is still continued discussion surrounding terminology (Phillips and Powell, 2015) and the fundamental processes governing ore genesis (Goldfarb and Groves, 2015, Groves and Santosh, 2016).

Numerous authors have provided reviews of orogenic deposits which includes; Groves et al (1998); McCuaig and Kerrich (1998); Goldfarb et al. (2005); Phillips and Powell (2013); Goldfarb and Groves (2015). This chapter outlines the accepted principles involved in deposit formation and provides a summary of conflicting theories. A broad understanding of the various aspects of OGDs is necessary to better understand the ore forming processes in the study area for this project.

2.2 Evolution of classification

The classification of ore deposits has evolved as our understanding of plate tectonics, Earth evolution and mineralisation processes has improved. In the 1900s deposit classification was descriptive and avoided ambiguity by relating deposits to rock types or locations (Cox and Singer, 1986). The lumping or splitting of deposits into groups according to their key features, such as age, rock type and depth, led to a variety of deposit descriptions (Cox and Singer, 1986). These descriptions were based on well constrained examples that involve location specific processes. Consequently, the development of an overarching model is challenging but is overcome by an improved understanding of fundamental ore forming processes. The improved understanding of transport and deposition of gold in metamorphic environments provided a classification of deposits according to a *mineral systems approach* which shares many similarities with the oil system (Fyfe and Kerrich, 1976, Wyman et al., 2015a, Wyman et al., 2015b). This is summarised as a source-transport-trap model where dissolution of a metal at a source is transported, and then accumulated at a site of deposition (Fyfe and Kerrich, 1976). Wyman et al. (2016) describes how the size and frequency of OGDs display power law distribution (where one quantity varies as a power of the other) similar to forest fires, Earthquakes and fault size population. The current deposit model is based on large deposits that are rare, therefore anomalous, rather than the more common but smaller deposits. The power law distribution of OGDs can be used to examine aspects of deposit genesis such as, energy source, a fluid reservoir and a threshold

barrier (Figure 2-3) (Wyman et al., 2016). Wyman et al. (2016) describes how gold deposition occurs by overcoming a system threshold, that is triggered by tectonics and typically exhibits power law behaviours (Figure 2-3).

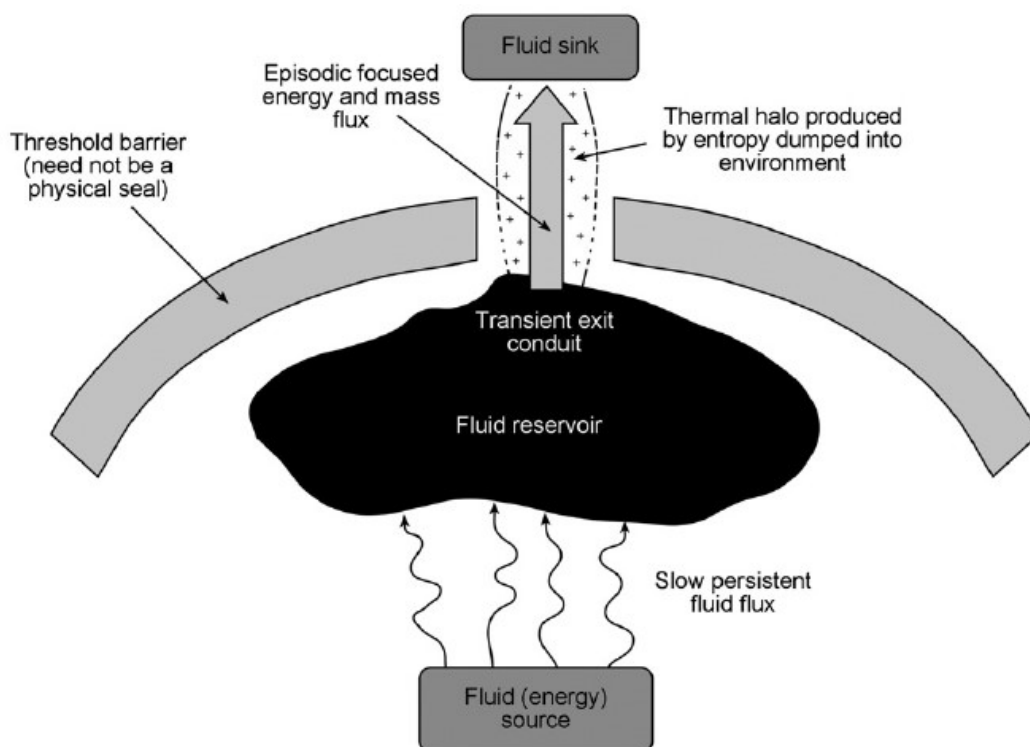


Figure 2-3: A simplistic model, proposed by Wyman et al (2016), outlining the features involved in the minerals system approach for genesis of OGDs.

2.2.1 Empirical deposit classification

Lindgren (1907) was one of the first authors to observe a relationship between ore deposition and its physical environment. This work provided a framework for deposits to be classified according to pressure, temperature and crustal depth (Lindgren, 1933). Formation of mineralisation was assumed to be linked to magmatism and individual deposits were classified as either mesothermal (1.5-3km and 150-300°C) or hypothermal (>3km and >300 °C) (Emmons, 1933, Lindgren, 1933). A number of subdivisions were subsequently proposed (e.g. hypothermal veins, shear zone hosted, mesothermal Au-Pb-Se ores (Bateman and Jensen, 1950)), which culminated in a compilation of gold deposit styles by Boyle in 1979. This review described deposits according to host rocks in an attempt to be objective that had no bias towards interpretation of processes in the name (Boyle, 1979). Fyfe (1978) classified deposits by considering their association with volcanic rocks, sedimentary rocks, and other complex

lithologies, which resulted in names such as: turbidite hosted, slate belt and greenstone hosted gold deposits. In the 1980s the USGS, attempted to produce renewed classifications of deposits that had over 48 separate models (Cox and Singer, 1986). This classification of deposits also incorporated geographical locations in the name such as; Motherlode, Bendigo and Homestake.

In the early 80s Kerrich and Fyfe (1981) developed a simpler classification that considered the origin of fluid and metals. During this time deposit descriptions included lamprophyre, tonalitic magma, oxidised felsic magma and metamorphic (Kerrich, 1983). Nesbitt et al (1991) suggested that meteoric fluids contributed to the formation of gold in some deposits; however, advances in fluid chemistry studies provided evidence that the primary ore fluid responsible for gold transport were either metamorphic or magmatic in origin (Ridley and Diamond, 2000). Deeply circulating meteoric fluids may play an important role in the transport of gold above the ductile zone as proposed in New Zealand by Pitcairn et al. (2006).

2.2.2 An overarching model for OGDs

Previous deposit classifications lacked consistency and included geographical locations, such as Homestake or host rock types, such as Turbidite Hosted. Groves et al. (1992) proposed the *crustal continuum model* (Figure 2-2) which provided a framework to describe deposits in metamorphic terranes. The crustal continuum model permits mineralisation formed at different depths and within different environments in a single evolving system to be described together (Figure 1). A modification of Lindgrens (1933) crustal depth profile forms the basis of the terminology: epizonal (<6km depth and 150°C-400°C), mesozonal (6-12km depth and 300°C-475°C) and hypozonal (>12km depth and >475°C). The classification of gold deposits as mesothermal was prevalent during the 1990s; however, Groves et al. (1998) highlighted that this description corresponded to a specific range of crustal depth and was not universally applicable. These authors proposed the term orogenic gold deposits (OGD) as an overarching label, which is summarised in Table 1 below.

Feature	Orogenic Gold Deposit
Tectonic setting	Forearc or back-arc.
Timing	Post peak metamorphism when fluid is in thermal equilibrium with host rocks.
Host rocks	Greenstones, turbidite, banded iron stones, schist or volcanic rocks.
Alteration	Carbonate minerals, pyritisation, sericite and silicification
Structure	Crustal scale shear zones. Mineralisation concentrated in first-second order structures.
Fluid	H ₂ O - CO ₂ -CH ₄ N ₂ – H ₂ S bearing, low to moderate salinity and near neutral fluids.
Mineralogy	Gold, pyrite ± arsenopyrite, chalcopyrite, galena and sphalerite.

Table 2-1: Summary of key features of Orogenic Gold Deposits (Groves et al., 1998).

2.3 Metallogenetic epochs

The formation of OGDs are linked to crustal subduction and terrane accretion along cratonic margins, which results in continuous orogeny and recycling of fertile crust (Goldfarb et al., 2001, Goldfarb et al., 2005). The distribution and abundance of continental margins is controlled by the configuration of continents that varies throughout Earth history (Figure 2-4) (Cawood and Hawkesworth, 2015). The evolution of the hydrosphere-atmosphere, global heat flow and long term tectonic trends of the Earth have had significant influences on mineralisation processes. Earth evolution has resulted in periods of time that are characterised by more significant occurrences of metal ore mineralisation and can be grouped into metallogenetic epochs (Cawood and Hawkesworth, 2015). Periods of stability that lack mineralisation are important to consider as the tectonic configuration is not favourable for deposit generation. The most important period is the ‘Boring Billion’ between 1600-500ma (Meyer, 1988),

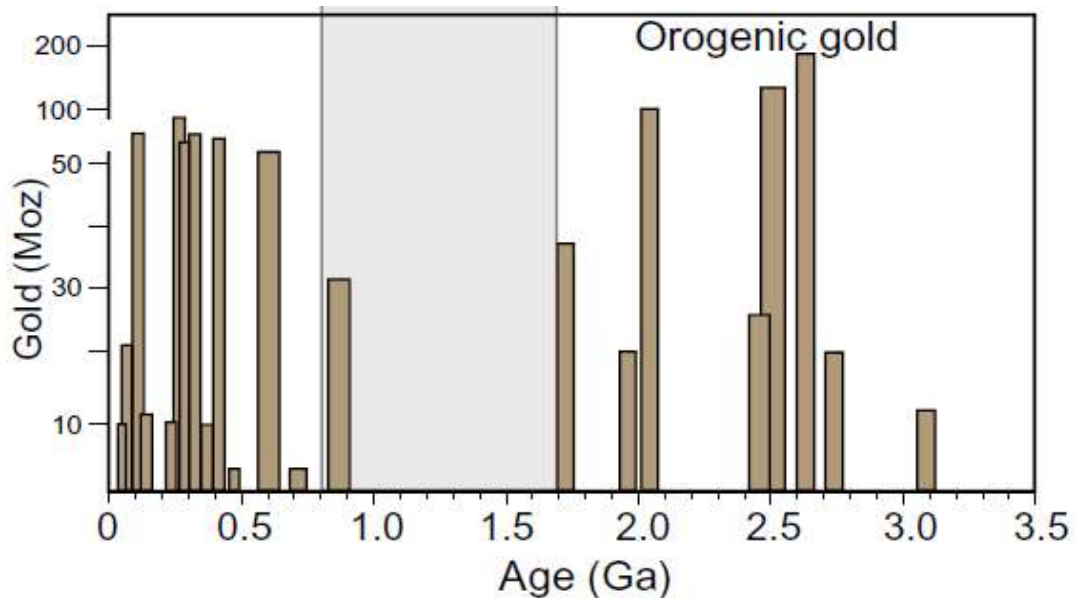


Figure 2-4: Tectonic distribution of OGDs through time. Boring Billion shaded grey (Cawood and Hawkesworth, 2015).

2.3.1 Precambrian

A large proportion of the world's richest OGDs are located in Archean and Precambrian shields around the globe (Hamilton, 1998, Goldfarb et al., 2005, Goldfarb et al., 2010). These are split into two distinct periods of gold formation with the oldest occurring 2900-2550Ma, and the other 2100-1800Ma (Goldfarb et al., 2005). Low levels of erosion in cold cratonic centres has resulted in preservation of deposits in areas such as the Superior Province in Canada, the Zimbabwe craton, and the Yilgarn Craton of Western Australia (Groves, 1993). These gold deposits are typically associated with metamorphosed mafic volcanic rocks, banded iron stone formations, and meta-sediments (Goldfarb et al., 2005). The increased heat flow and faster rate of plate movement in the Archean resulted in the rapid break up and formation of multiple volcanic arcs, resulting in the numerous greenstone belts (Goldfarb et al., 2001). The collision and obduction of these greenstone tectonic terranes resulted in large crustal scale faults which are the host for many of the orogenic deposits (Goldfarb et al., 2001).

2.3.2 The Boring Billion

The 'Boring Billion' is a period of time from 1600-570Ma, first described by Meyer (1988), as a period of tectonic and environmental and evolutionary stability (Figure 2-4). The period is characterised by intracontinental extension of the

Rodinia supercontinent and a lack of continental collision (Cawood and Hawkesworth, 2014). The *Boring Billion* accounts for 20% of Earth's history but the lack of orogeny means that OGDs from this period represent 1% of known production (Cawood and Hawkesworth, 2014, Cawood and Hawkesworth, 2015).

2.3.3 Phanerozoic

Tomkins (2013b) suggests that the Phanerozoic represents the most significant period of time for the formation of economically important orogenic gold deposits. This estimate discounts the Archean Witwatersrand deposit due to it being a palaeo-placer but includes the Muruntau deposit in Uzbekistan, which is still a poorly defined deposit (Bierlein et al., 2006). The onset of continuous crustal growth due to a cooler Earth resulted in the formation of Cordilleran style orogenic belts, such as those that bound the west of North America (Goldfarb et al., 2001). Phanerozoic deposits are typically greenschist-hosted in metamorphic belts dominated by sedimentary sequence (Tomkins, 2013a).

The combined influence of changing tectonic processes and an evolving biosphere influenced the formation of diagenetic pyrite in sedimentary rocks (Tomkins, 2013a). Tomkins (2013b) proposed a link between the oxidation of the oceans that favoured the solubility of gold in deep waters. Bacterial sulphate reduction drove pyrite formation while destabilising gold from solution (Tomkins, 2013a). The uptake of gold into pyrite in sedimentary rocks provides a rich source rock that releases gold during subsequent tectonic collision and metamorphism (Tomkins, 2013a, Finch and Tomkins, 2017). Biogenic processes in the Phanerozoic may explain why OGDs during this metallogenetic epoch are so rich (Figure 2-5) (Gaboury, 2013, Tomkins, 2013a, Tomkins, 2013b).

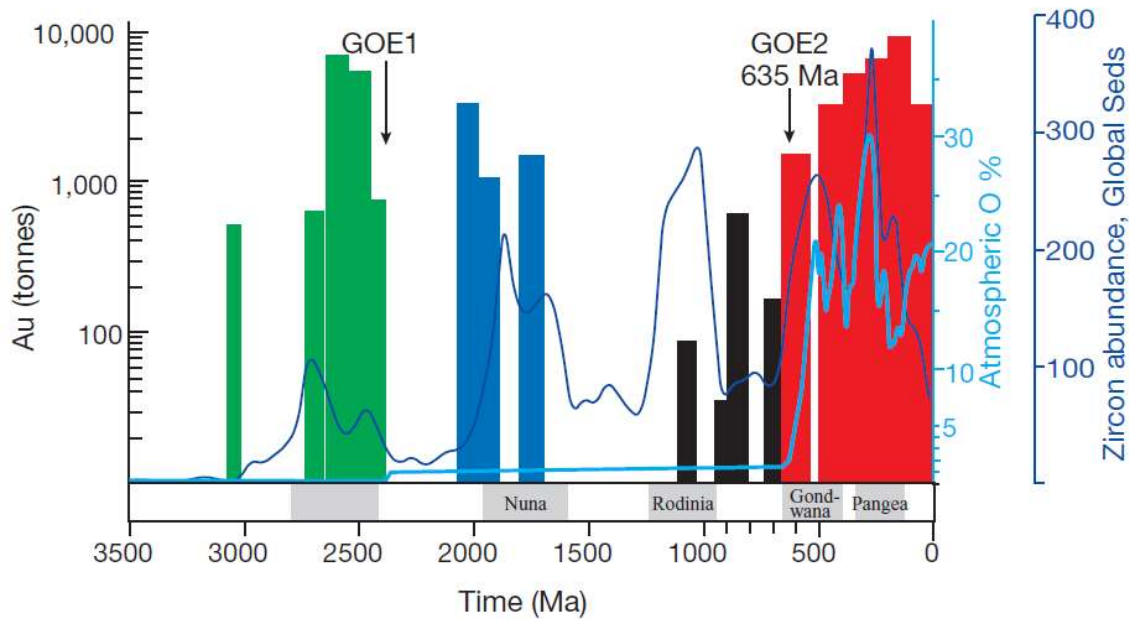


Figure 2-5: Distribution of orogenic gold with variation in oxygen concentration in the Earth's atmosphere over time (Bierlein et al., 2006, Tomkins, 2013b).

The distribution of deposits in the Palaeozoic are a result of the continental collisions arising from the Rodinia breakup and subsequent assembly of Gondwana and Laurentia (Goldfarb et al., 2005). The closure of the Tethys Ocean occurred during the Ordovician to Carboniferous periods and resulted in the formation of OGDs now exposed in the North American Appalachians and through the European Caledonides (Goldfarb et al., 2005). OGDs in the Mesozoic-Cenozoic eras are associated with the world's largest placer deposits including the Sierra Foothills belt, Klondike, Fairbanks, Yana-Kolyma belt, Amur and Otago area (Goldfarb et al., 2010). Goldfarb et al (2001) suggests that the formation of these placer deposits typically requires around 100 million years of exhumation. The lack of major bedrock occurrences younger than the Early Cretaceous is thought to be due to a lack of erosion and exposure (Goldfarb et al., 2001).

2.4 The Principles of OGD Formation

The characteristics of OGDs, described in Table 1, are well established and remain uncontroversial; however, many authors continue to discuss terminology and processes (Phillips and Powell, 2015). This section describes the key aspects of the source-transport-trap model with an aim to provide a comprehensive overview of the current literature.

2.4.1 Metal and Fluid Source

Establishing the origin of gold in hydrothermal systems is very challenging due to the unknown transport distances of the mineralising fluids (Tomkins, 2013b). The dissolution, transport and deposition of gold requires concentration of the element by a factor of 1000-10,000 from its average crustal abundance of 1ppb (Phillips and Powell, 2010, Pokrovski et al., 2014). This value is typically one to two orders of magnitude greater than for base metals such as copper, zinc or lead (Rudnick and Gao 2003). The mobilisation of gold requires transportation in a fluid which may either have an external source or form at the same time as gold dissolution (Phillips and Powell, 2010). The high degree of concentration required means the sources of metal and fluid are likely to be derived from large volumes of rock (Phillips and Powell, 2010). There are two end members: the first invokes a metamorphic origin of fluid during dehydration reactions and the second, proposes a magmatic fluid source formed during fractional crystallisation (Tomkins, 2013b, Goldfarb and Groves, 2015).

2.4.1.1 Dissolution of Gold

Gold is the most noble metal due to its lack of corrosion or reactivity in surface conditions (Williams-Jones et al., 2009). The understanding of gold solubility was driven by alchemy with the discovery of aqua regia (one-part nitric acid and three parts hydrochloric acid) in the 8th century. Metallurgy and geochemistry led to the patenting of the cyanidation process, in the 18th century, which remains the primary process today of extracting gold from ore (Williams-Jones et al., 2009). The transport and concentration of gold into deposits by crustal fluids has been recognised for 500 years, but the first quantitative experiments of gold solubility were conducted by Ogryzlo (1935).

Gold is described as a soft metal according to the Pearson classification (Pearson, 1963) in which metals and their ligands are characterised as either small strongly charged ions (hard) or large, easily polarizable and weakly charged ions (soft). The classification suggests that where there is competition between ions: hard ions will complex with hard ligands, and vice versa (Pearson, 1963, Williams-Jones et al., 2009). At elevated temperatures, those often associated with OGDs, the most significant gold related ligand is the soft hydrogen bisulphide complex which forms under reducing conditions as $\text{Au}(\text{HS})_2^-$

(Equation 1) (Mikucki and Ridley, 1993, Stefánsson and Seward, 2004). The dissolution of gold is primarily controlled by the availability of sulphur in fluids, therefore we can predict that solubility will be influenced by changes in the activity of HS^- and $f\text{O}_2$ and pH as summarised in Table 2-2 and Figure 2-6 (Pokrovski et al., 2014).

Equation 1 (Phillips and Powell, 2010):

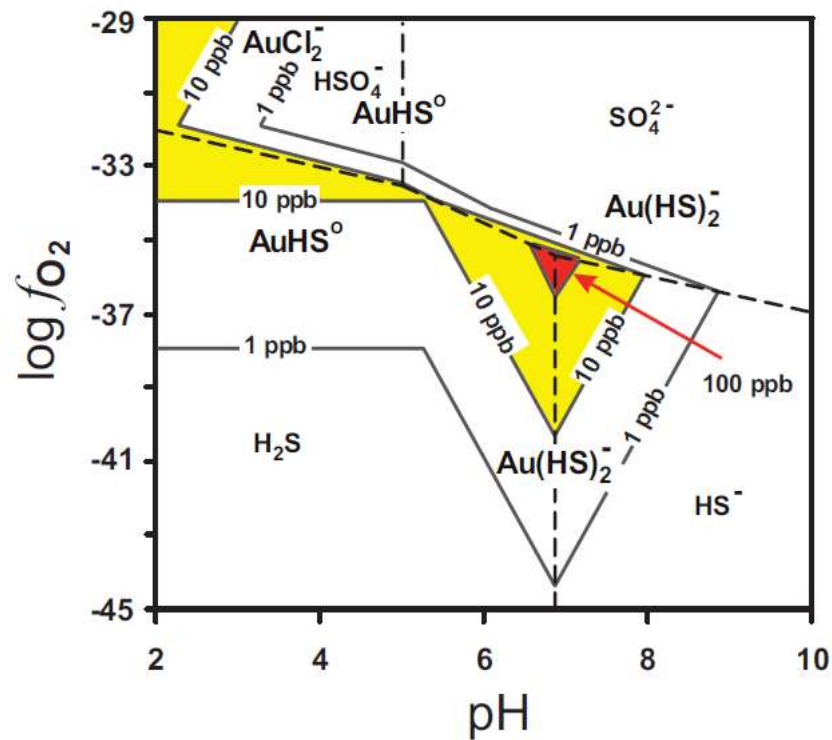
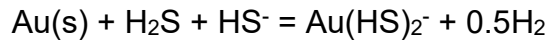


Figure 2-6: Eh- pH diagram demonstrating the stability of different complexes (Stefánsson and Seward, 2004).

Factor	Influence on gold solubility
Total sulphur in solution	Must be high and preferably in equilibrium with pyrite
Sulphur Distribution	Sulphur at a pH where $[H_2S] = [HS^-]$ and where sulphate is less than sulphide.
Redox	Intermediate; fO_2 below the field of sulphate dominance and below hematite, fO_2 above the field of reduced carbon and methane.
Temperature	250-350°C and but may complex up to 450°C
Pressure	Change in pressure is less likely to influence solubility

Table 2-2 Factors which influence the solubility of gold as the $Au[HS]_2^-$ complex (Phillips, 1993).

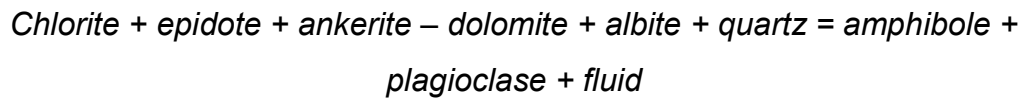
2.4.1.2 Fluid characteristics

The transportation of gold from a source requires large quantities of fluid which are intimately associated with the origin of the metals (Yardley and Cleverley, 2013). A range of techniques have been used to investigate the origin of fluids which include; stable isotopes, radiogenic isotopes, halogens, trace element data and fluid inclusions. The nature of fluids at the deposit (trap) show remarkable consistency across all deposits and are typically aqueous-carbonic ($H_2O-CO_2-H_2S$), low salinity (2-7wt% NaCl) with near neutral pH (Mikucki and Ridley, 1993, Mikucki, 1998, Phillips and Powell, 2010). The composition of the fluid is generally independent of the host rocks, although there is some association of methane with carbonaceous shales (Hu et al., 2016). A review by Groves et al (2015) concludes that extensive evidence eludes to a deeply sourced, over pressured, advecting fluid but the ultimate origin remains ambiguous.

2.4.1.3 Metamorphic fluid

The metamorphic devolatilisation model, as summarised by Phillips and Powell (2010), proposes that hydrated and carbonated greenschist facies rocks are devolatilised during prograde metamorphism across the greenschist-amphibolite facies boundary. The devolatilisation occurs at the mineral grain scale via the reaction in Equation 2 (Phillips and Powell, 2010).

Equation 2 Reactions associated with metamorphism (Phillips, 1993, Phillips and Powell, 2010)



Facies change releases H₂O rich fluid with $X(\text{CO}_2) < 0.1$ and $X(\text{CO}_2) \sim 0.2-0.3$ at temperature ranges of 440-470°C and 500-520 °C respectively (McInnes et al., 2008). The fluid release is accompanied by liberation of sulphur which is important in the solubility and transport of gold (McInnes et al., 2008, Garofalo and Ridley, 2014, Sahoo and Venkatesh, 2015). The original calculations describing devolatilisation were based on Archean mafic rocks which can release 5wt% fluid (Groves et al., 1992, Phillips and Powell, 2010). These calculations may not be applicable to Phanerozoic OGDs that are dominated by metamorphic sequences with a sedimentary or volcanic origin (Yardley and Cleverley, 2013). Pitcairn et al (2006) analysed the Otago Schists of New Zealand to investigate whether un-metamorphosed rocks could release enough metals to form a deposit. The results showed a decrease in chlorite, carbonate and other trace elements (Au, As, Bi, W, Sb and Te) in amphibolite facies rocks compared the equivalent greenschist facies rocks (Pitcairn et al., 2006). Zhong et al. (2015) modelled the release of gold, sulphur and base metals from pelites during fluid generation associated with prograde metamorphism. The results of this study highlighted the importance of muscovite and chlorite dehydration as a release of fluid which is accompanied by the release of sulphur (Zhong et al., 2015). Other authors highlight the importance of the pyrite-pyrrhotite reaction during prograde metamorphism which results in the release of gold and arsenic into solution (Kogan et al., 1994, Tom et al., 1997, Large et al., 2011). The reaction of pyrite to form pyrrhotite (Equation 3) provides a source of reduced sulphur that influences the solubility and transport of gold (Thomas et al., 2011, Finch and Tomkins, 2017). The transition of pyrite-pyrrhotite occurs at 450° to 600 °C under greenschist metamorphic facies and is accompanied by the dehydration of chlorite (Sahoo and Venkatesh, 2015).

Equation 3: Pyrite to pyrrhotite that releases hydrogen bisulphide (Phillips and Powell, 2010)



The metamorphic devolatilisation model is significant as it provides a single source of metal and fluid which are generated simultaneously (Phillips and Powell, 2010).

2.4.1.4 Meteoric fluid

The deep convection of meteoric fluids and their role in OGDs relies primarily on the permeability of the continental crust (Nesbitt et al., 1989, Hagemann et al., 1994). The penetration of meteoric fluids is documented in sedimentary basins and volcanic environments; however, is much more challenging to recognise in orogenic environments. Nesbitt (1988) presents isotopic evidence that meteoric fluids can circulate throughout the brittle portion of the crust and generate precious metal deposits.

The fluids responsible for quartz veins in the Alpine Schist of New Zealand are shown by Jenkin et al. (1994) to have a meteoric origin. Pitcairn et al. (2006) describes a model for OGD formation in Otago of New Zealand in which high topography results in deep penetration of meteoric fluids through the brittle crust. The majority of metals and fluids are shown to be sourced from metamorphic devolatilisation; however, mixing with meteoric fluids is responsible for leaching and remobilisation of gold (Craw and Campbell, 2004, Pitcairn et al., 2006).

2.4.1.5 Magmatic-hydrothermal fluid

Proposals regarding a magmatic origin of gold deposits were prevalent in the first half of the 20th century and were driven by observations of deposits proximity to lamprophyres, small felsic porphyry dykes or sills (Groves et al., 1995). The formation of porphyry and epithermal deposits in orogenic belts have a clear association with subduction related magmatism, are base metal rich and display extensive alteration (Goldfarb et al., 2005). A number of deposits in the Yukon and Alaska share many features with OGDs (such as similar mineralogy, fluid chemistry and structural control); but have a clear relationship with reduced back arc magmatism (Hart, 2007). However, unlike OGDs in metamorphic terranes these occurrences exhibit chemical zoning related to distance from the intrusion (Figure 2-7) (Lang and Baker, 2001). These types of deposits are termed a reduced intrusion related gold systems (RIGS) and their characteristics have been summarised by Hart (2007).

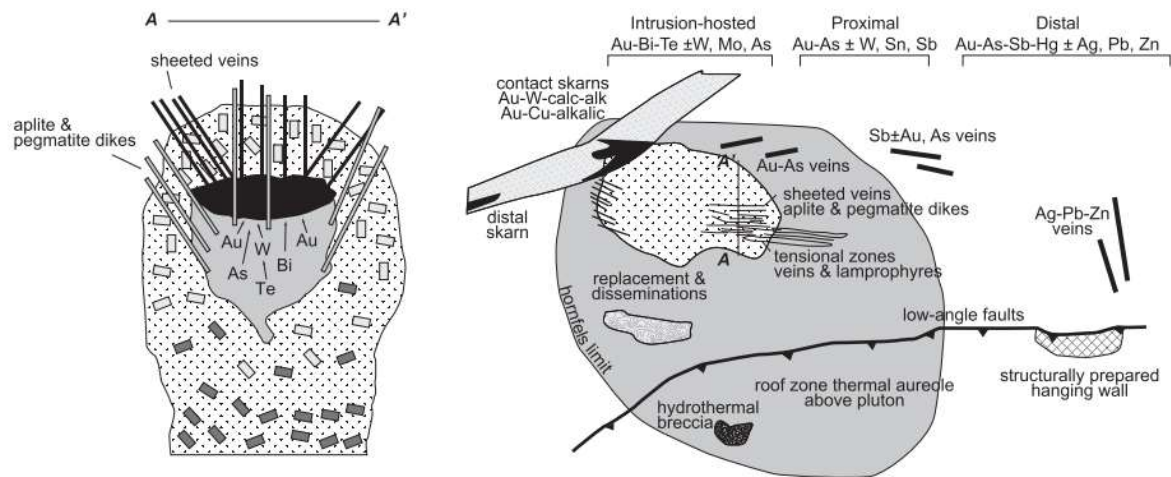


Figure 2-7: A schematic model of the features, mineralogy and host rocks associated with reduced intrusion related gold system. Zonation of minerals correspond to distance from the intrusion (Hart et al., 2004).

A solely magmatic origin for mineralising fluids seems unlikely because many OGDs lack the spatial or temporal association with a magmatic source (Goldfarb and Groves, 2015). However, the evidence from RIGS shows that fluids with similar chemistry to OGDs can form from magmatism (Hart, 2007). Ascribing a solely magmatic or metamorphic origin to mineralising fluids in OGDs seems unlikely due to the potential overlap of fluids from each source. A more probable explanation is that fluids are a mixture and are produced due to both magmatism and metamorphism that occur during orogeny.

2.4.1.6 Sub-crustal fluid

The consistency of fluid chemistry in OGDs has led various authors to suggest the source may be independent of supra crustal rocks and have a common sub crustal origin (Goldfarb et al., 2001, Hronsky et al., 2012, Goldfarb and Groves, 2015). Hronsky et al. (2012) proposes that fluid may be sourced from a heterogeneous, fertile lithospheric mantle which is tapped during tectonic and magmatic events. A gold enriched fertile upper mantle source in accretionary orogens may play an important role in ore genesis in deposits such as porphyries however the link to orogenic mineralisation is less clear (Goldfarb and Groves, 2015, Groves and Santosh, 2016). Groves and Santosh (2016) suggest that the devolatilisation of a subducted slab may be a source for fluids which travel upwards through supracrustal rocks (Figure 2-8). The Jiadong gold deposit, in China, has undergone prograde metamorphism in the Precambrian 2 billion

years before gold mineralisation, which is dated at 130-120Ma (Hronsky et al., 2012, Groves and Santosh, 2016). The supracrustal rocks could not provide fluid for mineralisation and therefore a sub-crustal source of fluid released during devolatilisation of a subducting slab is proposed (Yang et al., 2016).

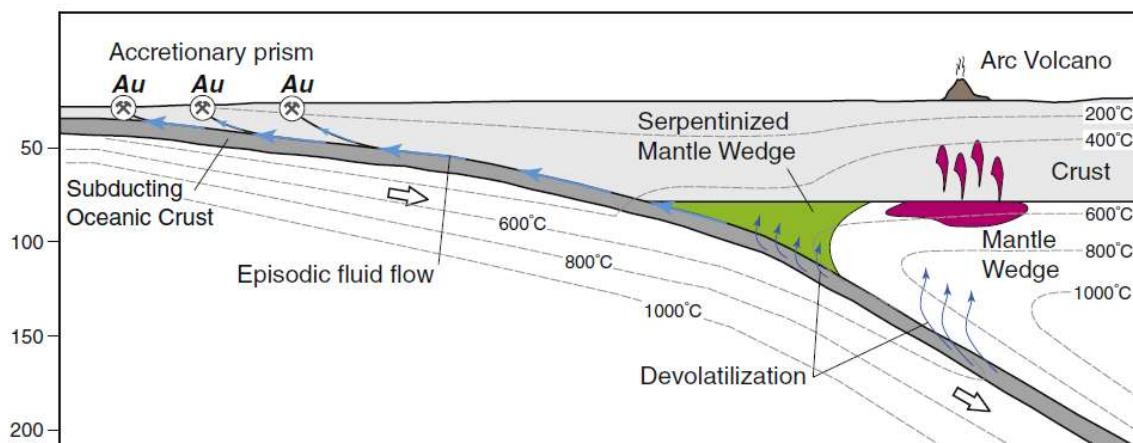


Figure 2-8: Devolatilisation of a subducting slab may either fertilise the above mantle or, travel up dip along the interface of the slab and overlying wedge (Goldfarb and Groves, 2015). Fluids may interact with deep crustal faults which move upwards to produce deposits.

2.4.2 Transport

2.4.2.1 Maintaining Stability

The transport of gold in solution from its source to a site of deposition is key to the formation of an economic deposit. The low concentration of gold in the crust, as described in section 2.4.1, means that fluids must maintain stability as they travel great distances through a large volume of source rock to generate a deposit (Phillips and Powell, 2010). Fluid-wall rock interaction during fluid flow may result in changes in pH and diffuse gold deposition along the pathway as the gold hydrosulphide complex is progressively destabilized (Williams-Jones et al., 2009, Phillips and Powell, 2010). The presence of significant levels of CO₂ buffers the fluid at a pH conducive to gold solubility (McInnes et al., 2008). The fluid must also maintain a favourable redox condition (Figure 2-6) and avoid removal of sulphur from solution through contact with iron-rich rocks (Williams-Jones et al., 2009).

2.4.2.2 Migration from the source

The earliest stages of fluid generation and migration can be divided into two scenarios in which; (1) the fluid and gold are generated simultaneously at a single

source (Figure 2-9a), or, (2) a fluid permeates a volume of gold-bearing rock (Figure 2-9b) (Phillips and Powell, 2010). The first scenario is the most widely accepted and is described in the previous section 2.4.1.3 as the *metamorphic devolatilisation model* (Phillips and Powell, 2010).

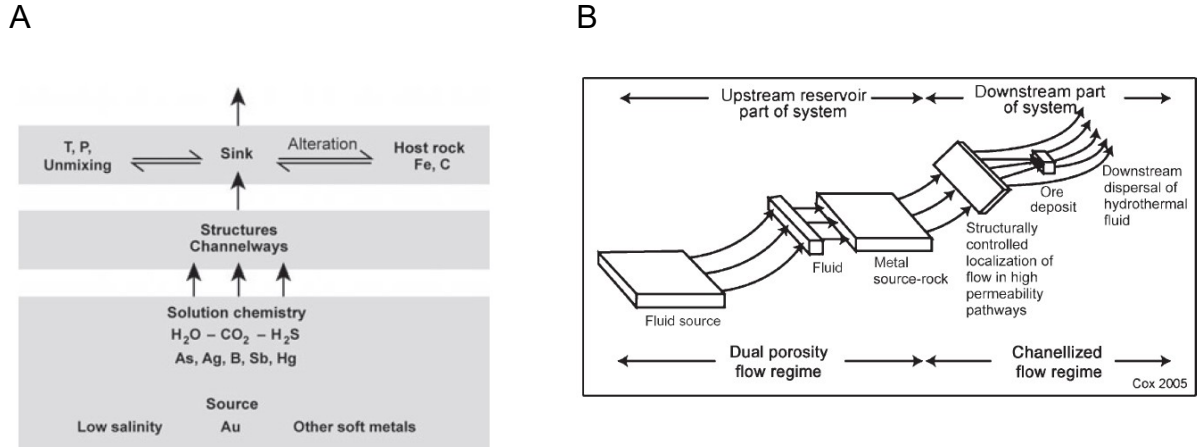


Figure 2-9:A) Devolatilisation model whereby fluid and gold is generated simultaneously (Phillips, 1993).
B) Flow through model where a fluid permeates a gold-bearing rock (Cox, 2005).

In both scenarios the initial movement of fluid is thought to occur at 500-520°C in the aseismic region of the crust (Groves, 1993, Phillips and Powell, 2010). The primary migration of fluid and gold from a source must reconcile processes at the mineral scale under high pressures in ductile, amphibolite facies rocks (Yardley and Cleverley, 2013). Linking the release of fluid from minerals within cubic kilometres of crust to channelized pathways requires permeability (Cox et al., 1991, Cox, 2005). Fluid flow may occur either via intrinsic permeability where pervasive flow of fluid through pores or grain boundaries occurs, or via hydraulic permeability where flow is channelized into cracks (Sibson et al., 1988). Intrinsic permeability is common at shallower levels and is the dominant process in aquifers where connectivity between pores can be maintained (Cox, 1999, Cox, 2005). However, deeper in the crust where rocks are hotter and more ductile fluid flow is likely to occur along fractures and channels (Cox, 2005, Hodkiewicz et al., 2005). An increase in stress creates greater fracture density until pores become connected (Figure 2-10a) (Sibson et al., 1988). This connectivity is known as the percolation threshold and results in episodic release of fluid until mineral precipitation seals the fractures (Figure 2-10b) (Hodkiewicz et al., 2005).

Fluctuations in regional stress as a result of seismicity causes episodic fluid release (Cox, 1999, Hodkiewicz et al., 2005).

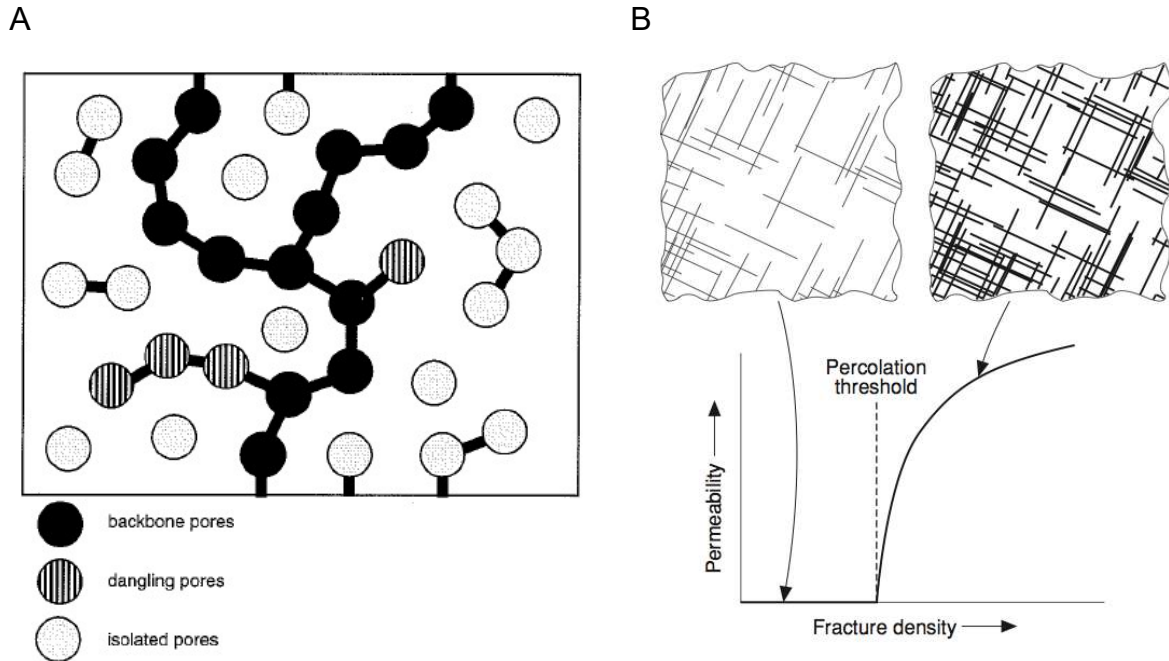


Figure 2-10: A – Connectivity of pores through fracturing and increased fluid pressure. Dangling pores must connect to reach the percolation threshold. **B-** Percolation threshold is a function of fracture density and connectivity. (Phillips, 1993, Craw et al., 2002).

2.4.2.3 Upward migration

The upward migration of fluid may not always be possible due to a lack of pathways and channels (Cox, 2005). Channelization of fluid is important in the formation of deposits as it extracts auriferous fluid from large areas and also minimises the opportunity of wall rock interaction that can result in diffuse deposition of gold (Phillips and Powell, 2010). The brittle-ductile transition is highlighted in the crustal continuum model as a major zone for the formation of faults and fluid pathways (Groves et al., 1992, Groves, 1993). The formation of OGDs often have an association with kilometre scale faults with mineralisation occurring in complex second or third order structures (Cox, 2005). This is well characterised in the Yilgarn Craton in Western Australia which hosts many large deposits that are spatially associated with the Boulder Lefroy shear zone (Groves et al., 1992, Groves, 1993, Goldfarb et al., 2001). Many other regions host gold deposits in association with first order structures such as the Abitibi belt alongside the Porcupine and Larder Lake Cadillac breaks, the Kolar mines of the

Champion Reef System and the Ashanti deposits along the Obuasi-Ashanti shear zone (Goldfarb et al., 2005).

2.4.3 Trap

The 'trap' aspect of OGD formation causes precipitation of gold from solution due to changes in the chemical and physical parameters governing gold transport. The efficient deposition of a large volume of gold from an auriferous fluid is critical to the genesis of an economic OGD. This section discusses the various trapping mechanisms responsible for OGD formation.

2.4.3.1 Faulting

The fault valve model, proposed by Sibson et al. (1977), provides a mechanism for upward migration of fluid and deposition of gold (Figure 2-11). The process involves an increase in frictional forces within the fault, due to a build-up of fluid pressure (Sibson et al., 1988). When the lithostatic pressure is exceeded it results in rupturing and seismicity creating a zone of low shear stress but high fluid pressure (Sibson et al., 1988). The rapid expulsion of fluid upwards, from the ductile to brittle zone, is focussed into subsidiary fractures where mineral precipitation occurs (Sibson et al., 1988, McCuaig and Kerrich, 1998). The deposition of minerals and gold due to a pressure decrease seals permeability in the rupture zone causing stress to build and the process to repeat (Hodkiewicz et al., 2005). Cox et al (2005) highlighted that the frequency of seismic events, as aftershocks, is more significant for the accumulation and deposition of gold than the magnitude of an Earthquake.

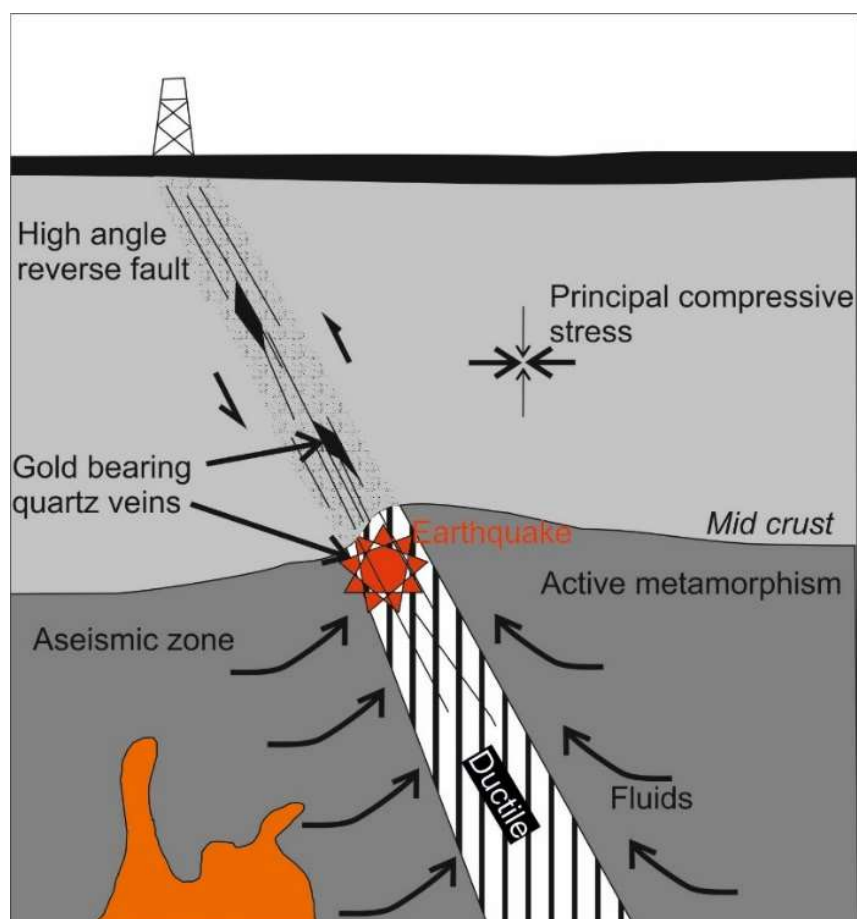


Figure 2-11: Fault valve model showing fault rupture at the brittle-ductile transition. This drives fluid upwards into structures where deposition occurs (Sibson et al., 1988, Groves, 1993).

The *fault-valve-model* relies on decreasing pressure to influence gold deposition whereas Weatherley and Henley (2013) propose a mechanism of flash vaporisation, in which an extreme change in conditions results in the complete deposition of silica and gold. The drop-in pressure acts as a pump which sucks more fluid and gold into the zone until fluid stability is achieved (Weatherley and Henley, 2013).

2.4.3.2 Destabilisation

The deposition of gold is influenced by the opposing parameters that control solubility (Table 2-2); however, the formation of a deposit requires efficient deposition of gold in a localised area. The most significant influences on gold destabilisation from solution are a decrease in $f(\text{O}_2)$ (e.g. towards the stability field of reduced carbon), a decrease in total sulphur and an increase in $f(\text{O}_2)$ towards the hematite stability field (Boyle, 1979, McInnes et al., 2008, Williams-Jones et al., 2009). Changes in pH have a small influence on gold destabilisation

due to the CO₂ content of the fluid buffering the environment. A decrease in temperature during upward migration has a small effect on destabilisation; however, a catastrophic temperature drop due to flashing results in rapid deposition (McInnes et al., 2008, Williams-Jones et al., 2009).

The reduction of a gold-bearing solution can be achieved by an interaction with wall rocks containing reduced carbon (Phillips and Powell, 2010). Black shales or carbonaceous units provide reactive horizons which are observed at Ballarat and Bendigo in Australia (Wilson et al., 2013). The role of carbonaceous rocks is a major influence in the formation of Carlin deposits in Nevada USA (Cline et al., 2005).

Wall rock sulphidation is one of the most significant influences on gold solubility. The formation of pyrite or arsenopyrite removes sulphur from the fluid and causes gold deposition according to the reversal of Equation 1. (Williams-Jones et al., 2009). The process depends upon the presence of Fe in wall rock as represented by equations 4 and 5 below:

Equation 4: Pyrite formation as a result of wall rock sulphidation with silicate
(Phillips and Powell, 2010)



Equation 5 Pyrite formation as a result of wall rock sulphidation with oxide
(Phillips and Powell, 2010)



The interaction of gold-bearing fluid with reducing lithologies, such as iron rich tholeites, banded iron formations and carbonaceous and pelitic sequences, are key to gold deposition (Phillips and Powell, 2010).

The maximum solubility of gold as a bisulphide is shown in Figure 2-6 as function of $f\text{O}_2$ and pH (Williams-Jones et al., 2009). Oxidation of the fluid would result in a large decrease in the solubility and of HS⁻ and consequent deposition of gold (Williams-Jones et al., 2009). This process may occur if an auriferous fluid undergoes oxidation by interaction with hematite bearing rock or mixing with oxygenated meteoric waters (McInnes et al., 2008).

2.5 A critique of the OGD model

The previous section discusses a range of formation principles proposed for the formation of OGDs; however, metamorphic devolatilisation is the most favoured mechanism for the generation of individual deposits. Although this model reconciles many aspects of OGD formation there remains a number of challenges, which will be described in this section.

2.5.1 Fluid generation

The key problem with the proposed metamorphic devolatilisation model is that mineralisation typically postdates peak metamorphism, sometimes up to several million years (Wilson et al., 2013). The standard explanation for such late timing is that the peak metamorphism has occurred and the metamorphic fluid generation is associated with deeper levels (Groves, 1993). Yardley and Cleverley (2013) suggest that the process of prograde metamorphism is too slow to account for the relatively short time scales observed in the formation of OGDs. England and Thompson (1984) estimated average regional heating to be 10-20°C/Ma which is limited by endothermic metamorphic reactions. The metamorphic devolatilisation reactions are thermally limited and cannot explain the release of large quantities of fluid necessary for an ore forming time scale (~1Ma) (Yardley and Cleverley, 2013). A large input of heat from magmatism could drive an appropriate level of dehydration, but in many cases mineralisation is not contemporaneous with such activity. Craw et al (2010) proposed that, an elevated geotherm resulting from rapid uplift can explain the formation of gold mineralisation in Taiwan. The high mountains of Taiwan are currently undergoing exhumation of 2 mm/yr. which creates decompression and normal faulting in a region of tectonic compression (Craw et al., 2010). The resulting elevated geotherm drives devolatilisation and extensional fractures that permit fluid mobility. The drop-in pressure can drive prograde metamorphic reactions although the temperature may be decreasing (Yardley and Cleverley, 2013).

The presence of late orogenic magmatism is noted in a number of orogenic belts, by Yardley and Cleverley (2013), and is proposed as a potential additional source of fluid alongside metamorphism. Yardley and Cleverly (2013) suggest that in some large scale orogenic deposits, such as Sunrise Dam, Western Australia,

fluid mixing of mantle and magmatic fluid may be necessary to produce so much gold and fluid (Yardley and Cleverley, 2013).

Cox et al. (2005) describes the challenges of efficiently releasing fluid from ductile rocks that are at amphibolite facies temperature and pressure. Maintaining permeability via fractures is not possible and a mechanism of porosity waves is proposed by Connolly (1997). The process requires the generation of fluids which propagate as waves through ductile crust until they are channelized into faults (Connolly, 1997, McInnes et al., 2008). An alternative mechanism of fluid release during devolatilisation is proposed by Craw et al. (2010), where rapid uplift generates extensional fractures to drive efficient expulsion of fluid upwards. Pitcairn et al. (2006) describes how high topography during rapid uplift in New Zealand has resulted in convection of deep penetrating meteoric fluids that transport and deposit gold.

Conceptual models for OGDs rely heavily on characterization of fluid parameters gained through fluid inclusion studies and other experimental work (Ridley and Diamond, 2000). However, identifying the fluid phase responsible for gold precipitation in a vein is complicated. Interpreting the fluid chemistry of the bulk of quartz veins may not be representative of the mineralising episode, as veins may be made of multiple growth events, and provide inadequate interpretation. Experimental studies on the transport of gold have focused around the role of bisulphide which places a constraint on the amount of fluid needed to produce a specific amount of gold (Benning and Seward, 1994).

Research conducted by Pearce et al. (2015) provides evidence that a small volume of fluid, which was very rich in gold, is responsible for the Junction Gold Deposit in Western Australia (Pearce et al., 2015). Thermodynamic modelling shows that alternate transport mechanisms would be required and a theory of colloidal transport is postulated (Pearce et al., 2015). The transport of gold as colloids in hydrothermal solution may be possible where chloride and sulphur species are not stable (Saunders, 1990). This mechanism is proposed by Herrington and Wilkinson (1993) and thought to be relevant in veins that formed as a result of rapid pressure drop. The destabilisation results in the initial precipitation of amorphous silica gel that stabilises gold colloid formation (Herrington and Wilkinson, 1993). Subsequent crystallisation of silica to quartz

results in the formation of gold along grain boundaries (Herrington and Wilkinson, 1993). The mechanism of gold transport via colloids is poorly understood but may be an important process in transporting significant amounts of gold that deposit to generate rich deposits.

2.5.2 An applicable model for OGDs

The basis for the original outline of OGDs model proposed by (Groves et al., 1998) is heavily biased towards the world-class deposits in Western Australia, and unfortunately, fails to take account of many other small deposits. Large OGDs are often part of atypical and complex systems, such as St Ives in Western Australia that has multiple stages of enrichment (Meffre et al., 2016). Small occurrences are much simpler, such as orogenic veining in NW Italy (Yardley et al., 1993), and provide an opportunity to investigate the fundamental processes of gold formation in metamorphic terranes. Gold is found in almost all orogenic belts around the globe and is often expressed as placer deposits or sub economic veining. The Victoria Goldfields in Australia has produced around 1375 tonnes of placer gold but only small historic mines have been discovered (Hughes et al., 2004). Examples of using placer deposits to interpret OGD formation include studies by Chapman et al. (2010a) and Chapman and Mortensen (2016), with further detail in Chapter 5. Placer gold can be used as a tool to inform on exploration and mineralisation but is often neglected by exploration and academia.

2.6 A summary of OGDs and its application in the LSSA

This chapter has outlined the current understanding and continuing challenges surrounding the investigation of *OGDs*. The way that deposits have been described has evolved significantly since Lindgren (1907) recognised an association with formation and crustal depth. Boyle (1979) provided a comprehensive overview of gold mineralisation that made significant improvements in summarising the formation of deposits globally. The crustal continuum model and subsequent classification of orogenic gold deposits, by Groves et al. (1992), provided an overarching model which continues to be the favoured description of gold in metamorphic terranes. An increased

understanding of the hydrosphere-atmosphere, global heat flow and long term tectonic trends of the Earth is informing mineralisation processes.

The metamorphic devolatilisation model releases gold and fluid simultaneously. Prograde metamorphism from greenschist-amphibolite facies releases a fluid that is focussed upwards into regional scale faults during crustal uplift or transpression. This model accounts for all aspects of the source-transport trap model required to generate an economic deposit; however, the origin of fluids in OGDs continue to be discussed, with Groves and Goldfarb (2016) recently proposing a sub-crustal origin. The understanding and debate surrounding gold deposits in metamorphic terranes continues to be dominated by the work of Goldfarb and Groves (2016).

Research typically focusses on the largest OGDs and fails to account for many smaller but more widespread deposits. Many of these small OGDs have been linked to the world's largest placer gold deposits (Goldfarb et al., 2001). Determining the processes that govern gold distribution in these deposits can help interpret why large deposits form.

This thesis investigates orogenic mineralisation in the Lone Star area of the KGD that is best known for its extensive placer deposits. Estimates of placer gold production are in excess of 20 million ounces from a compact area (~1200km²), which places the area into a category of 'world-class' (100T Au) (Burke et al., 2005, Bierlein et al., 2006). There are several examples of small orogenic gold-bearing quartz veins and disseminated gold occurrences within the KGD that have undergone historic mining producing a total of 1240 ounces. However, a huge discrepancy remains between the gold recovered from placers and that recovered from bedrock occurrences. Although mineralisation described as being 'orogenic' many of the large scale structural features associated with OGD formation are absent. This project aims to use the extensive placer deposits and in situ mineralisation of the Lone Star area of the KGD to understand ore forming processes. A revised model for OGD in the LSSA and more regionally can then be discussed.

Chapter 3 Regional Geology and Metallogeny

3.1 Introduction

The area of this study is situated in the Klondike Gold District (KGD) in the Northwest Yukon, Canada, which forms part of the North American Cordillera (Figure 3-1). This orogen records 1.8Ga of subduction and accretion onto the North American Craton, also known as Laurentia, and extends from Alaska and Canada southward to the USA and Mexico (Colpron et al., 2007, Nelson and Colpron, 2007). The northern part of the Cordillera spans British Columbia, Yukon and Alaska, and has a number of significant mineral deposits (Allan et al., 2013).

The extensive mineral endowment corresponds to the diversity of tectonic environments and the prolonged evolution of the orogen (Allan et al., 2013). The Cordillera is divided up into tectonostratigraphic terranes, which correspond to regions of similar stratigraphy and tectonic style (Figure 3-1) (Monger et al., 1982). The study area is underlain by the arc-related Yukon-Tanana-Terrane (YTT) and the oceanic-related Slide Mountain Terrane (SMT), which formed in the Palaeozoic (Colpron et al., 2007, Beranek and Mortensen, 2011).

This chapter outlines how the evolution of the tectonic terranes has influenced the regional geology and structure in the KGD. The understanding of tectonic processes has provided a framework in which to understand metallogeny across the North American Cordillera (Allan et al., 2013). In turn, the regional metallogeny provides context to the mineralisation in the KGD and the study area.



Figure 3-1: A map showing the extent of the North American Cordillera and outlining the extent of the Yukon Tanana Terrane (YTT) and Slide Mountain Terrane (SMT). The Klondike Gold District (KGD) is the main focus of this study. Modified from Nelson et al. (2013) and Beranak and Mortensen (2011).

3.2 Tectonic evolution of the Yukon Tanana and Slide Mountain Terranes

3.2.1 Tectonostratigraphy of the YTT

The lithological relationships preserved in the YTT provides evidence for the tectonic evolution and geology that formed the KGD (Nelson et al., 2013). The YTT and SMT can be traced through the north-west Yukon into Alaska and is bound to the north-east by the Tintina fault and the Denali Fault in the south-west (Figure 3-1) (Beranek and Mortensen, 2011, Allan et al., 2012). Figure 3-2 provides a schematic overview of the tectonostratigraphic relationships of assemblages observed in the YTT.

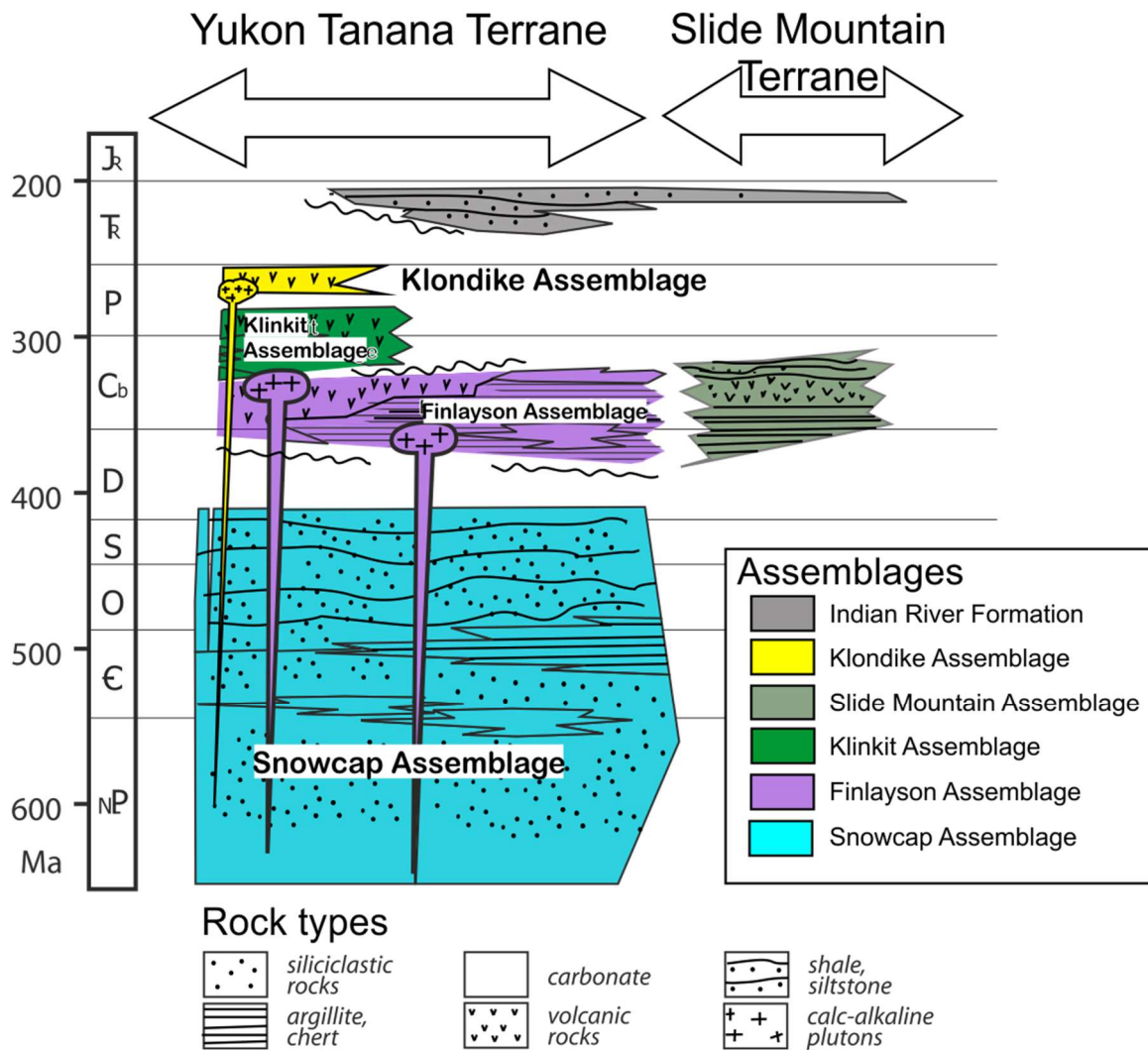


Figure 3-2: Schematic tectonostratigraphic overview of the Yukon and Alaska (Colpron et al., 2007). The YTT is on the left and partly synchronous with the SMA on the right.

The oldest unit in the YTT is the pre- Late-Devonian, *Snowcap Assemblage*, which is composed of metasedimentary and metavolcanic rocks (Piercey and Colpron, 2009, Beranek and Mortensen, 2011). The assemblage represents a continental margin succession with siliciclastic material originating from the west of Laurentia (Piercey and Colpron, 2009). The formation of the Snowcap Assemblage coincided with the breakup of the Rodinia supercontinent in the Pre-Cambrian (790-750Ma) (Piercey and Colpron, 2009).

The Finlayson Assemblage overlies and intrudes the Snowcap Assemblage and is composed of a series of metavolcanic, intrusive and metasedimentary units (Figure 3-2) (Murphy et al., 2006). The lower part of the Finlayson Assemblage, the Middle-Late Devonian, represents an arc sequence which formed during westward migration of Laurentia due to the initiation of east dipping subduction

beneath Laurentia (Figure 3-3A) (Nelson and Colpron, 2007, Nelson et al., 2013).

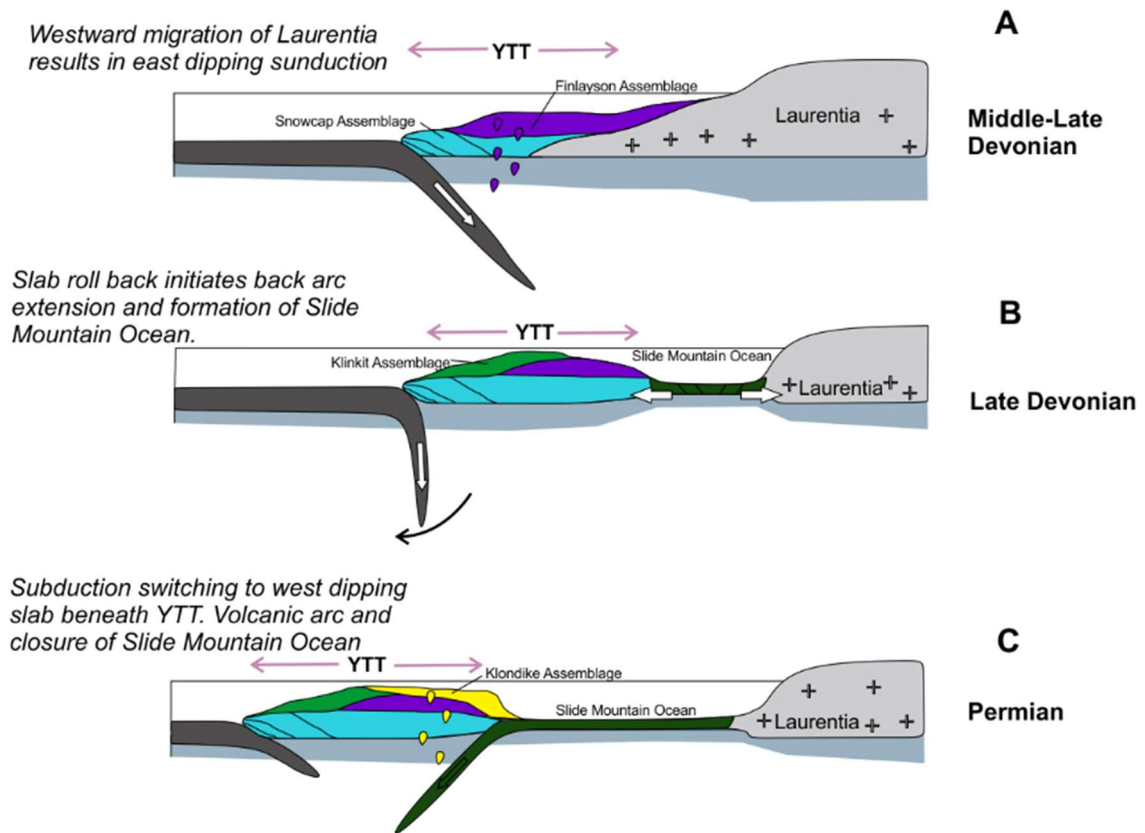


Figure 3-3: Schematic cross section of the tectonic evolution of the YTT. The colours of units correspond to those outlined in the key of Figure 3-2. A) East dipping subduction resulted in formation of the *Finlayson Assemblage*. B) Slab roll back resulted in back arc opening and the development of associated volcanism. C) Subduction switching to the west beneath the YTT formed the *Klondike Assemblage* (Colpron et al., 2007, Nelson et al., 2013).

The upper units of the Finlayson are Early Carboniferous and consist of bimodal volcanics and rocks with a basinal facies (Beranek and Mortensen, 2011). The units correspond to back-arc volcanism and rifting, which resulted from slab roll back and the detachment of the YTT from Laurentia (Figure 3-3B) (Beranek and Mortensen, 2011, Nelson et al., 2013).

The overlying Klinkit Assemblage is a series of metavolcanics and metasedimentary sequences which includes a unit of carbonate (Figure 3-2) (Simard et al., 2003, Beranek and Mortensen, 2011). The Assemblage represents a Late Carboniferous-Early Permian arc sequence which formed as rifting continued and the back-arc basin developed into the Slide Mountain Ocean (Simard et al., 2003, Beranek and Mortensen, 2011).

Beranek and Mortensen (2011), describe the Klondike Assemblage as a series of metavolcanics and plutonic rocks which formed in the Late Permian. This period marks a major change in the geodynamic setting and an end to the long lived east dipping subduction (Nelson and Colpron, 2007). The Klondike Assemblage represents an arc sequence that formed as a result of subduction switching towards the west which consumed the Slide Mountain Ocean (Figure 3-3c) (Nelson et al., 2013).

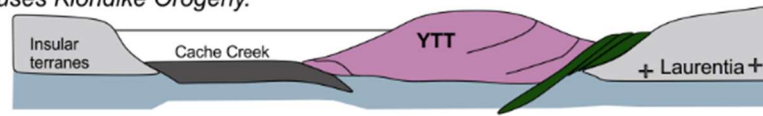
3.2.2 Tectonostratigraphy of the Slide Mountain Terrane

The SMT is composed of a sequence of oceanic related rocks which include greenstones, mafic volcanics and sedimentary material (Plint and Gordon, 1997, Colpron et al., 2007). The rocks formed during oceanic spreading and include ophiolite sequences, ocean floor basalts and deep marine sediments (Plint and Gordon, 1997, Murphy et al., 2006). Slab roll back of the east dipping plate beneath the Laurentian margin in the Late Devonian produced rifting on the YTT and the formation of an arc preserved as the Finlayson Assemblage (Figure 3-3B) (Nelson et al., 2013). The rifting continued from the Late Devonian to the Permian and produced Slide Mountain Ocean, which Beranek and Mortensen (2011) estimated to be 3000km wide at its maximum (Figure 3-3C).

3.2.3 Klondike Orogeny

Beranek and Mortensen (2011) conducted regional U-Pb geochronology which provided crystallisation ages, across the Yukon, of greenschist-amphibolite facies metamorphism between 260 and 252Ma. The metamorphism corresponds to a period of orogeny related to the closure of the Slide Mountain Ocean in the Late Permian-Early Triassic (Figure 3-4D) (Beranek and Mortensen, 2011). The consumption of the SMT beneath the YTT resulted in obduction of both terranes onto the Laurentian margin (Figure 3-4D) (Nelson et al., 2013). This period of mountain building is described by Beranek and Mortensen (2011) as the *Klondike Orogeny* (Figure 4D).

Permo-Triassic collision of YTT onto Laurentia causes Klondike Orogeny.



D

Late Permian -
Triassic

Final accretion of Insular Terranes results in ~15km of uplift and underthrusting of foreland wedge.



E

Jurassic -
Cretaceous

Progressive underthrusting resulted in amphibolite metamorphism at depth while uplift of the upper crust was brittle. This may provide a source for mineralising fluid

Figure 3-4 Schematic cross section of the tectonic evolution of the YTT. D) Closure of Slide Mountain Ocean and obduction of YTT creates Klondike Orogeny. E) Final accretion along Laurentian margin results in rapid uplift and propagation of orogenic wedge (Nelson and Mihalynuk, 1993, Nelson and Colpron, 2007, Nelson et al., 2013). The star represents a period of OGD formation that includes the KGD.

3.2.4 The final accretion onto Laurentia

Westward compression associated with the Klondike Orogeny, in the Early Triassic, continued through the Triassic and Jurassic (Figure 3-4D) (Beranek and Mortensen, 2011). The docking of YTT with Laurentia and closure of Slide Mountain Ocean resulted in subduction to step westward and initiate an east dipping slab beneath the continental margin (Figure 3-4D) (Nelson and Colpron, 2007, Nelson et al., 2013). The subduction of the Cache Creek Ocean (Figure 3-4D) resulted in magmatism in the Late Triassic to Early Jurassic forming some of the largest porphyry deposits in British Columbia (Mount Polley, Copper Mountain and Afton) and developed syenite-granodiorite intrusions in the Dawson Range of the Yukon (Nelson and Mihalynuk, 1993, Nelson et al., 2013).

The final period of accretion onto Laurentia occurred in the Early Jurassic as the closure of the Cache Creek Ocean resulted in the docking of the *Insular Terrane* onto the continental margin (Figure 3-4E) (Nelson and Mihalynuk, 1993). The geodynamic setting which resulted in the accretion of the Insular Terrane is

challenging to reconcile; however, Nelson and Mihalynuk (1993) proposed the 'enclosure model'. This model proposes that the northern part of the arc rotated anti-clockwise, in the Late Triassic, forming a tectonic orocline which enclosed the Cache Creek Ocean and resulted in accretion onto Laurentia (Nelson and Mihalynuk, 1993). The YTT is located at the apex of the tectonic orocline which resulted in extensive uplift of up to 15km between 204-185Ma (Figure 3-4E) (Nelson et al., 2013). The accumulation of sediments in the Whitehorse trough are a result of the rapid erosion associated with uplift in the Early Jurassic (Nelson et al., 2013).

The continued westward compression resulted in the propagation of thrusting along the eastern edge of the YTT at the contact with the Laurentian craton (Figure 3-4E) (Staples et al., 2016). This produced a foreland orogenic wedge, in the Middle-Late Jurassic, which resulted in under thrusting of material to a mid-crustal depth (Figure 3-4E). Staples et al. (2016) suggested that the cold hydrous rocks were emplaced along a ductile shear zone to amphibolite facies. The continued propagation resulted in upward migration of the metamorphosed rocks to brittle upper crustal levels (Staples et al., 2016).

3.2.5 Orogen parallel tectonics

The Mid-Cretaceous marks an end to westward compression, in the YTT, which was dominated by thrusting and orogeny (Bacon et al., 1990, Berman et al., 2007, Evenchick et al., 2007). The movement of the North American plate changed its motion at 110Ma to a west-southwest direction, which resulted in dextral transpression within the North American Cordillera (Monger et al., 1982, Lowey and Hills, 1988, Hart et al., 2004). A renewed period of subduction in the Cretaceous produced a continental arc and associated volcanics, which are observed in the Dawson range of the YTT and host a number of economic porphyry deposits (Allan et al., 2013).

The formation of the Denali and Tintina faults (Figure 3-1), in the Eocene, dissected the YTT and resulted in 300-400km of offset (Evenchick et al., 2007).

3.3 Geology of the Klondike Gold District

The KGD is located in the north-west Yukon and covers an area of around 12,000km². The bedrock geology in the KGD has been studied since the discovery of extensive alluvial deposits in the Klondike Gold Rush, 1896. The first geological map was completed by Bostock in 1905 and this informed studies, by McConnell (1907) and Tyrell (1907), investigating the hard rock source of gold. The region is unglaciated, which has hindered interpretation of regional geology due to deep weathering and limited bedrock exposure (Tempelman-Kluit, 1980, Mortensen, 1990, Chapman et al., 2010a). The most recent geological map of the region was published in MacKenzie et al. 2007b (Figure 3-5); however, more detailed information can be gained from mineral exploration reports. This section combines geological information from academic and exploration work with observations gained during fieldwork. The geology is described old to young and reclassified according to the tectonostratigraphic description outlined in section 3.2.

3.3.1 Slide Mountain Ocean Assemblage

This assemblage consists of massive metabasalt, mettagabbro and chloritic schists which have been metamorphosed to lower greenschist facies (Mortensen, 1990, MacKenzie et al., 2008). Mackenzie et al. (2008) divides this unit into massive greenstone and ultramafic rocks (Figure 3-5) which are exposed along the Klondike River Valley, and elsewhere as lenses, ranging from 1-150m thick.

The rocks represent a serpentinitised ophiolite sequence which is overlain by mafic volcanic and volcanoclastic material (Mortensen, 1990). The origin corresponds to the SMT and the opening of the Slide Mountain Ocean during the Late Palaeozoic (Nelson et al., 2013).

3.3.2 Finlayson Assemblage

This assemblage is metamorphosed to upper greenschist, consists of dark grey, micaceous schist with lenses of psammite and marble (Mortensen et al., 2007, MacKenzie et al., 2008). Mortensen (1990) provided U-Pb ages, from zircons at the base of felsic tuffs, of 358.5±1.1Ma. The units are described as being part of

the Nasina Assemblage by Mackenzie et al. (2008) and are exposed as an upper and lower segment within the KGD (Figure 3-5).

The Nasina Assemblage is age equivalent to the Finlayson Assemblage which forms part of the YTT in the Devonian-Carboniferous (Murphy et al., 2006, MacKenzie et al., 2008). The origin of the rocks corresponds to the upper portion of the Finlayson which formed in a back-arc basin (Nelson et al., 2013).

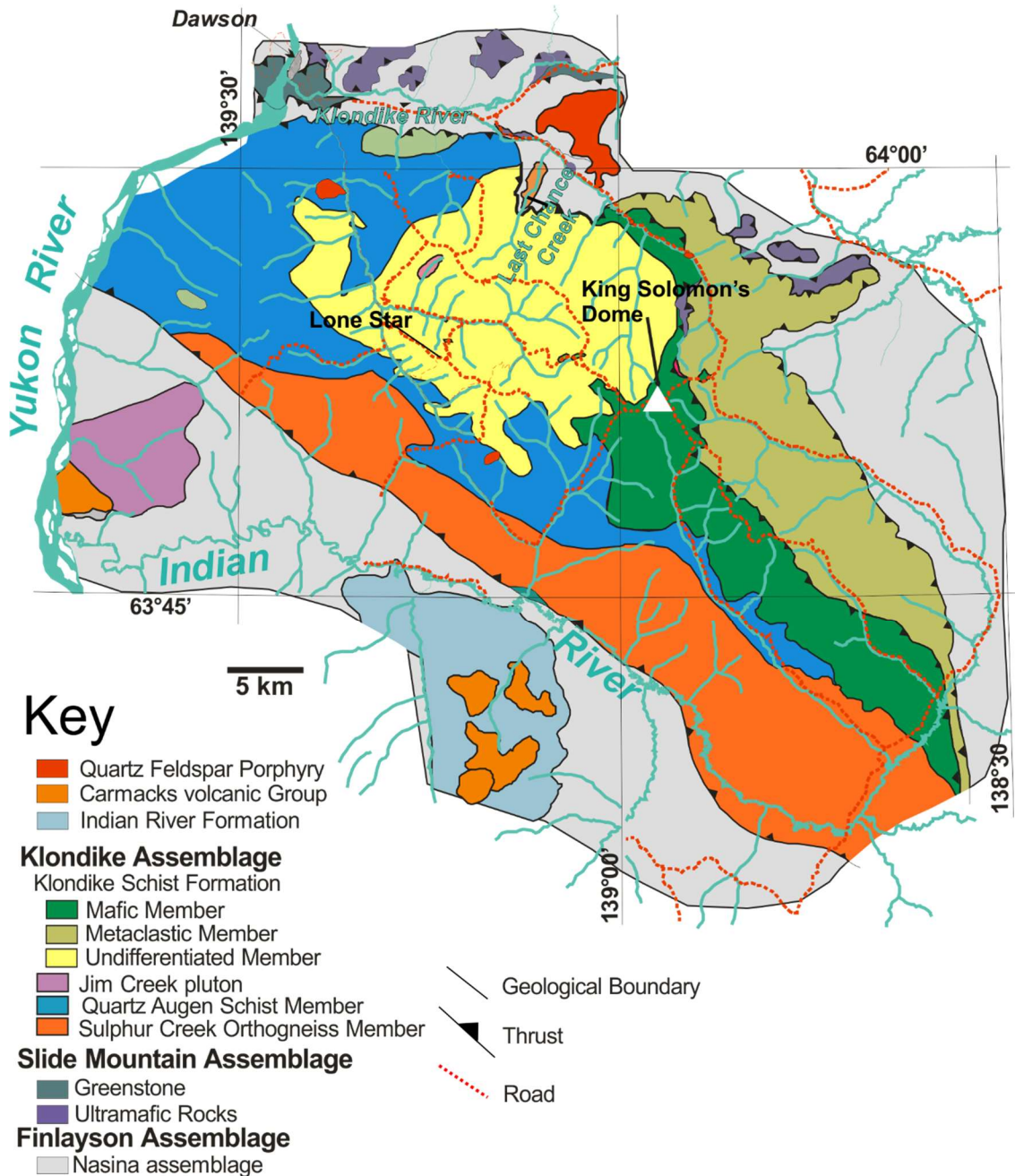


Figure 3-5: A modified map from MacKenzie et al. (2008). Geological units and thrusts are simplified.

3.3.3 Klondike Assemblage

The Klondike Assemblage comprises of a sequence of Late Permian meta plutonic, mafic to felsic metavolcanic and metasedimentary units. The rocks are the uppermost assemblage in the KGD and host all of the known gold-bearing vein occurrences. There are a number of subdivisions within the Assemblage that are described below.

3.3.3.1 Sulphur Creek Orthogneiss Member

The rock is a biotite bearing gneiss that is present in the south and west of the KGD (Figure 3-5) (Beranek and Mortensen, 2011). The upper portions of the unit are characterised by the presence of large (up to 1cm) flattened quartz and feldspar phenocrysts (Mortensen et al., 2007, MacKenzie et al., 2008). Beranek and Mortensen (2011) describe the unit as the Sulphur Creek Orthogneiss which originated as a quartz monzonite and formed at 262.4 ± 2.2 Ma. The upper portion is described as a unit of Quartz Augen schist which has an origin as a quartz-feldspar porphyry (Mortensen et al., 2007).

The Sulphur Creek Orthogneiss formed from the altered plutonic and intrusive rocks that were part of the Klondike Assemblage in the Late Permian (Mortensen, 1990, Mortensen et al., 2007).

3.3.3.2 Klondike Schist Formation

3.3.3.2.1 Undifferentiated Member

The Klondike Schist has a number of subdivisions due to its complex composition which has led to it being classified as a 'undifferentiated member' (Figure 3-5) (Mortensen, 1990, MacKenzie et al., 2008). The member consists of a complex interbeds of mafic, felsic and carbonaceous schist (Mortensen et al., 2007). Fieldwork during this PhD has differentiated the Undifferentiated Member in the LSSA and is described in detail in Chapter 4.

3.3.3.2.2 Metaclastic Member

The rock is distinguished by its tan to medium brown colour, blocky appearance in outcrop and is a quartz-feldspathic and carbonaceous schist. The member is exposed in the east of the Klondike (Figure 3-5) and is described by Mortensen et al (2007) as a metaclastic unit.

The origin of the unit is interpreted to represent the metasedimentary rocks from the seafloor which were subsequently intruded or overlain by volcanic rocks associated with arc sequences (Mortensen et al., 2007). The member forms the base of the Klondike Schist Formation which formed the Klondike Assemblage in the Late Permian of the YTT (Mortensen et al., 2007, MacKenzie et al., 2008).

3.3.3.2.3 Mafic Member

The rock consists of a chloritic schist that is typically medium green and grey chlorite-muscovite-quartz with variable calcite, actinolite and magnetite (Mortensen, 1990, Mortensen et al., 2007). The best exposure of mafic schist is exposed at King Solomon's Dome with local small occurrences of metagabbro which are interpreted as being sourced from mafic to intermediate subvolcanic intrusions (Figure 3-5) (Mortensen, 1990, Mortensen, 2013).

The units have undergone upper greenschist metamorphism, which is observed by abundant segregation veins in the region (MacKenzie et al., 2007b, MacKenzie et al., 2008). The unit corresponds to mafic volcanism associated with the arc sequence in the Late Permian arc sequence of the Klondike Assemblage.

3.3.4 Indian River Formation

The unit comprises of interbedded sandstone, shale, conglomerate and variable amounts of coal that are present in the south of the KGD exposed along the Indian River (Figure 3-5) (Lowey and Hills, 1988). The presence of fossils correlates with the Tantalus Formation, which is Albian (110-112Ma) in age having formed in alluvial-shallow marine facies (Lowey and Hills, 1988, Bond and Chapman, 2006).

The Indian River Formation formed in a forearc basin that extends towards Whitehorse in the south (Lowey and Hills, 1988, Mortensen, 1996).

3.3.5 Carmacks Volcanic group

The Indian River Formation is directly overlain, in the south of the KGD, by a group of intermediate volcanic rocks that have an age of 65-69Ma (Allan et al., 2013). The scattered intrusive and volcanics are correlated with the Carmacks Volcanic Group that is more widespread towards the south-west Yukon (Tafti

and Mortensen, 2003). The middle and lower parts of Last Chance Creek (Figure 3-5) has evidence of coarse clastic sediments and minor felsic tuff which are interpreted to be andesitic in origin (Mortensen et al., 2007, Mortensen, 2013).

3.3.6 Quartz Feldspar Porphyry

A range of small dykes and plugs are present across the KGD which are composed of grey, embayed quartz, euhedral feldspar set in an aphanitic groundmass (Mortensen et al., 2007). The dykes are bimodal in place with mafic compositions that are deeply weathered at the surface (Mortensen et al., 2007). The units are described by Mortensen et al. (2008) as Quartz Feldspar Porphyry and are dated at a $^{40}\text{Ar}/^{39}\text{Ar}$ age of $58.6 \pm 0.7\text{Ma}$ in the Eocene.

3.4 Structural Evolution of the Klondike Gold District

The KGD is underlain by a series of imbricated thrust slices which record a complex structural evolution. There are up to five deformation events observed across the area which correspond to regional tectonic evolution of the YTT (MacKenzie et al., 2008). This section outlines the relationship of small scale and large-scale deformation in the KGD.

3.4.1 Foliation development

The schistose units throughout the KGD are dominated by a pervasive cleavage which is defined by recrystallized, coarse grained metamorphic micas (MacKenzie et al., 2008). This represents a S_2 event that is a composite fabric superimposed over a primary S_1 (MacKenzie et al., 2007b, MacKenzie et al., 2008). The second generation of deformation involved recrystallisation parallel to axial surface of F_1 but is only rarely observed as small rootless isoclinal folds (Figure 3-6) (Liverton, 2011).



Figure 3-6: Field image showing a rootless isoclinal F1 fold (Liverton, 2011).

The development of the pervasive foliation is accompanied by segregation veining that ranges from millimetre to centimetre scale (MacKenzie et al., 2008). The rocks across the KGD are all metamorphosed to greenschist facies which is observed as quartz, chlorite, albite and epidote (MacKenzie et al., 2007b). The deformation of S_1 and S_2 are related to the Klondike Orogeny in the Late Permian-Early Triassic as outlined in section 3.2.1 (Beranek and Mortensen, 2011).

3.4.2 Post peak metamorphic deformation

The KGD is underlain by a series of kilometre scale imbricated thrust slices which were emplaced in the Jurassic (Figure 3-7) (MacKenzie et al., 2007b). The slices are separated by ultramafic rafts that are sheared and vary from 1-150m thick (MacKenzie et al., 2007b).

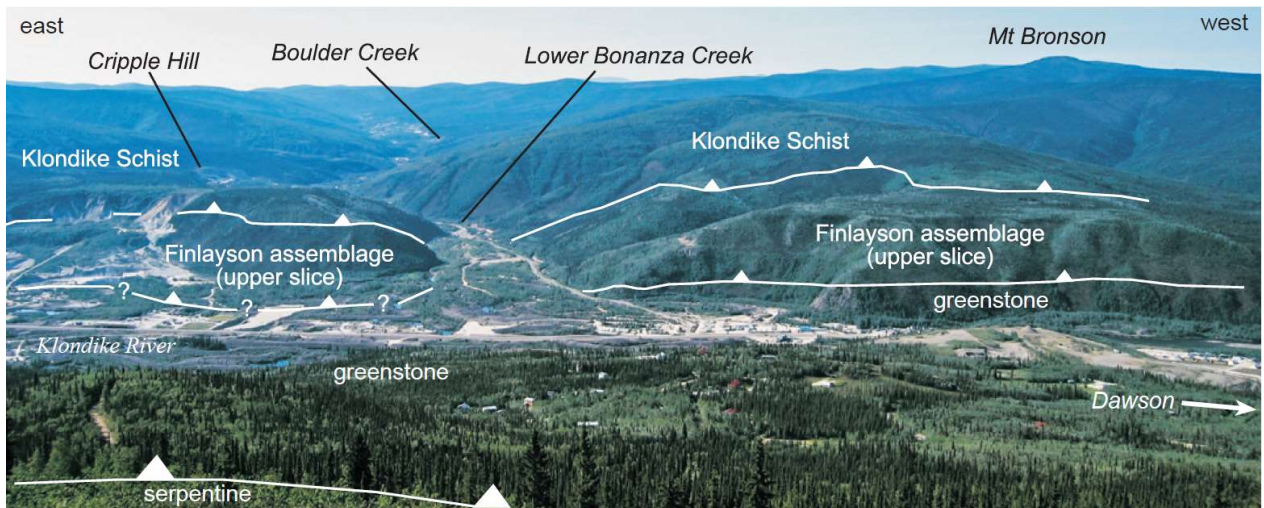


Figure 3-7: Annotated photo, from MacKenzie et al. 2007a, looking south along Bonanza Creek. Thrust fault and units are labelled to mark the imbricated thrust slices.

The thrusting is related to a series of post metamorphic folds which are observed from centimetre to kilometre scale and are synchronous with the development of a spaced crenulation cleavage (Figure 3-8a,b) (MacKenzie et al., 2008). The folding is open and recumbent with crenulation best developed close to hinges where it is perpendicular to the steeply dipping S_2 (Figure 3-8a) (MacKenzie et al., 2008). These structural features are best developed in laminated schistose units and can be phacoidal where deformation is localised around competent units (MacKenzie et al., 2008). The deformation features have a shallow dip to the south-west and are parasitic of larger regional thrusts (MacKenzie et al., 2007b, MacKenzie et al., 2008). The thrusting shows a progression from shearing to faulting and has resulted in large scale thrust imbrication within the KGD (MacKenzie et al., 2007b).

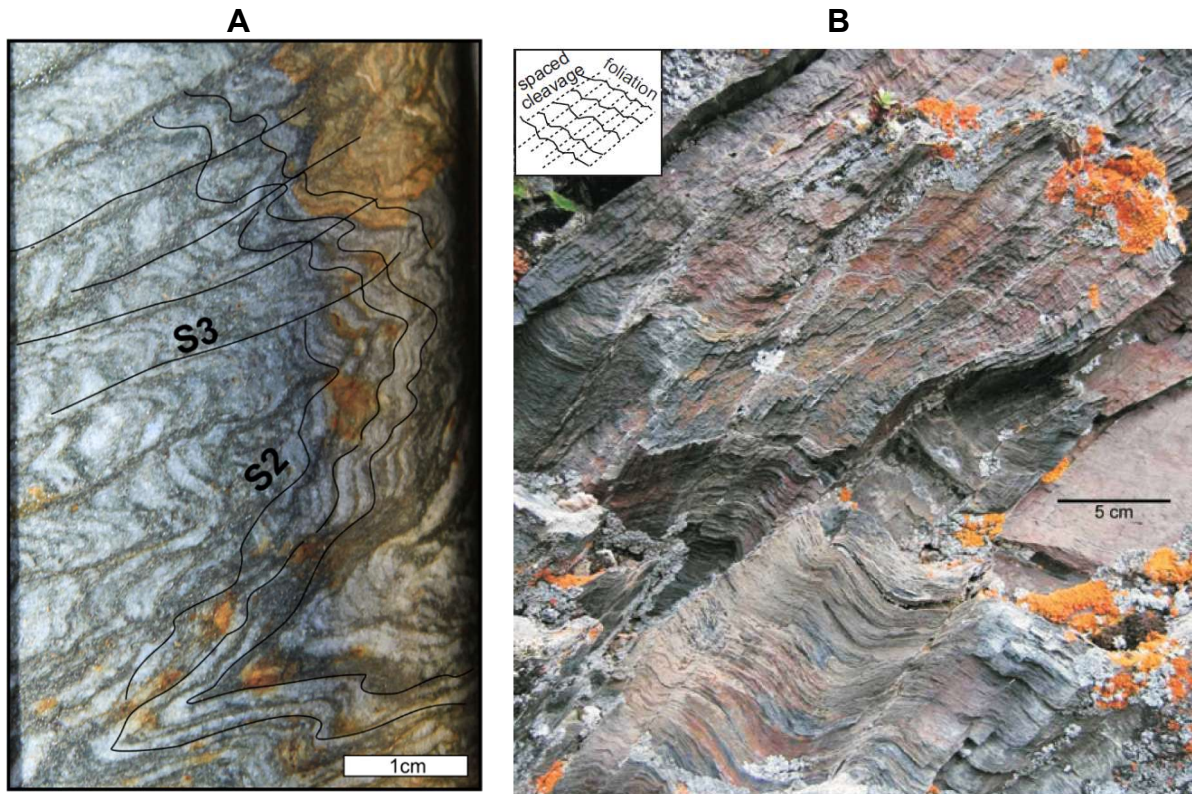


Figure 3-8: A) Crenulation cleavage well developed in a unit of quartz mica schist recovered from drilling. B) Field image of spaced crenulation cleavage (MacKenzie et al., 2007a)

3.4.3 Fault-fold deformation

The structural fabric of rocks in the KGD is mostly shallow dipping; however, the Klondike Schist Formation is cut by two sets of steeply dipping angular kink folds and reverse faults that represent D₄ (Figure 3-9A and B) (MacKenzie et al., 2008). The perpendicular fault-folds strike north-east and north-west, have a width of 1-50cm and occur in zones 10-50m wide (MacKenzie et al., 2008). The angular kink folds are best developed in the structural highest unit of Klondike Schist, which suggests that they formed at relatively shallow levels (MacKenzie et al., 2008). The D₄ progression from kink folding to reverse faulting demonstrates a change from ductile to brittle conditions. The D₄ represents a period of regional exhumation during middle Jurassic orogeny as described in section 3.2.4 (Staples et al., 2016).

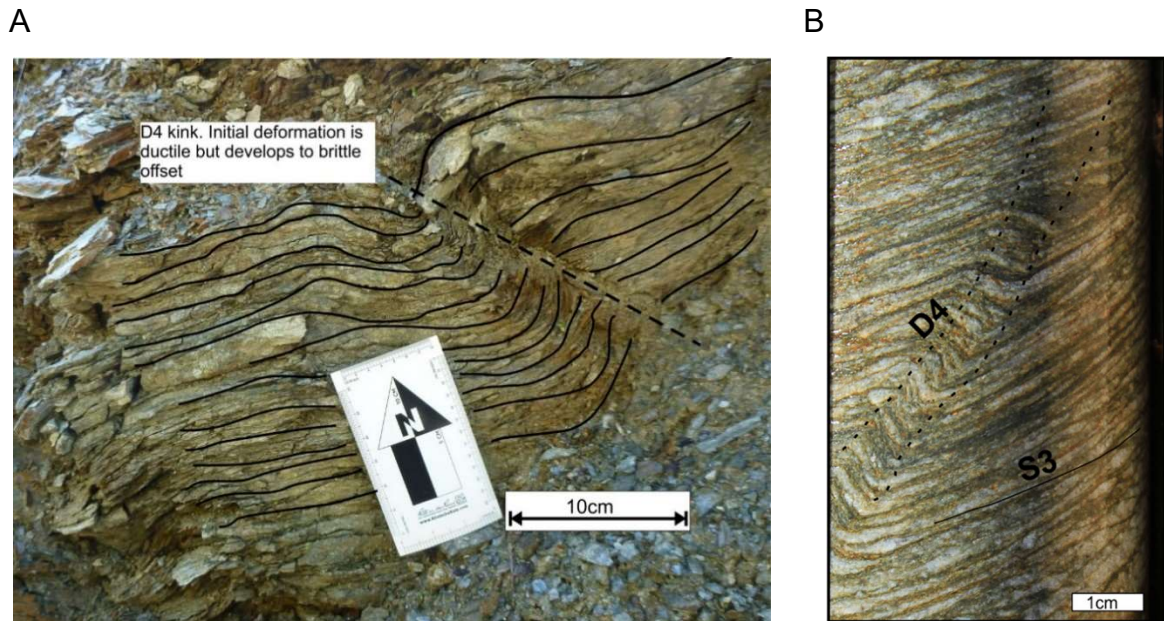


Figure 3-9: A) Reverse fault. B) Angular kink fold.

3.4.4 Normal faults

Normal faulting is observed across the KGD as steeply dipping fractures which typically exploit existing weaknesses (Mortensen et al., 2007). The faults localise in D₄ structures, are filled with gouge and are rarely more than 10s of metres in length (Piercey and Colpron, 2009, Knight et al., 2013). The extensional faulting (D₅) is related to brittle extension in the Cretaceous related to crustal uplift and subsequent relaxation (Knight et al., 2013).

3.5 Metallogeny

A metallogenic framework for the KGD and YTT is described in this section, which relies on the context provided from an understanding of the regional geology, tectonics and structural evolution. Allan et al. (2013) provides a detailed overview of the magmatism and metallogeny of the north-west Yukon and eastern Alaska, which was developed through the interpretation of detailed geochronological data (U-Pb, ⁴⁰Ar/³⁹Ar, ¹⁸⁷Re/¹⁸⁷Os) (Figure -3-10) together with deposit specific contributions from exploration companies. This section describes the key mineralising events across the YTT and how they relate to the KGD.

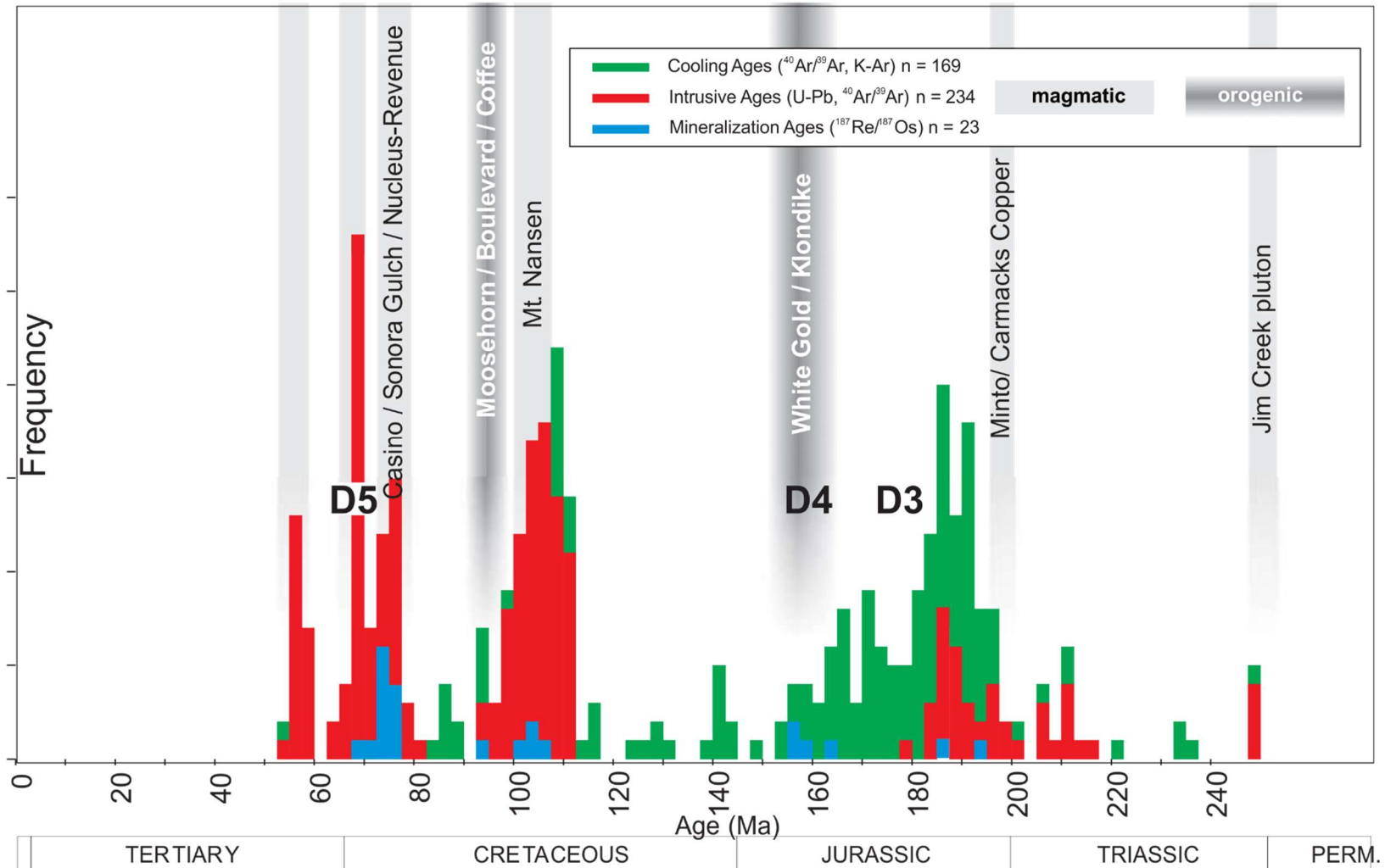


Figure -3-10: Histogram of compiled geochronological data for the northern YTT (Allan et al., 2013). Key deformation events summarised by Mackenzie et al. (2008b). Mineralisation events and deposits related to magmatism in black compared to orogenic in white.

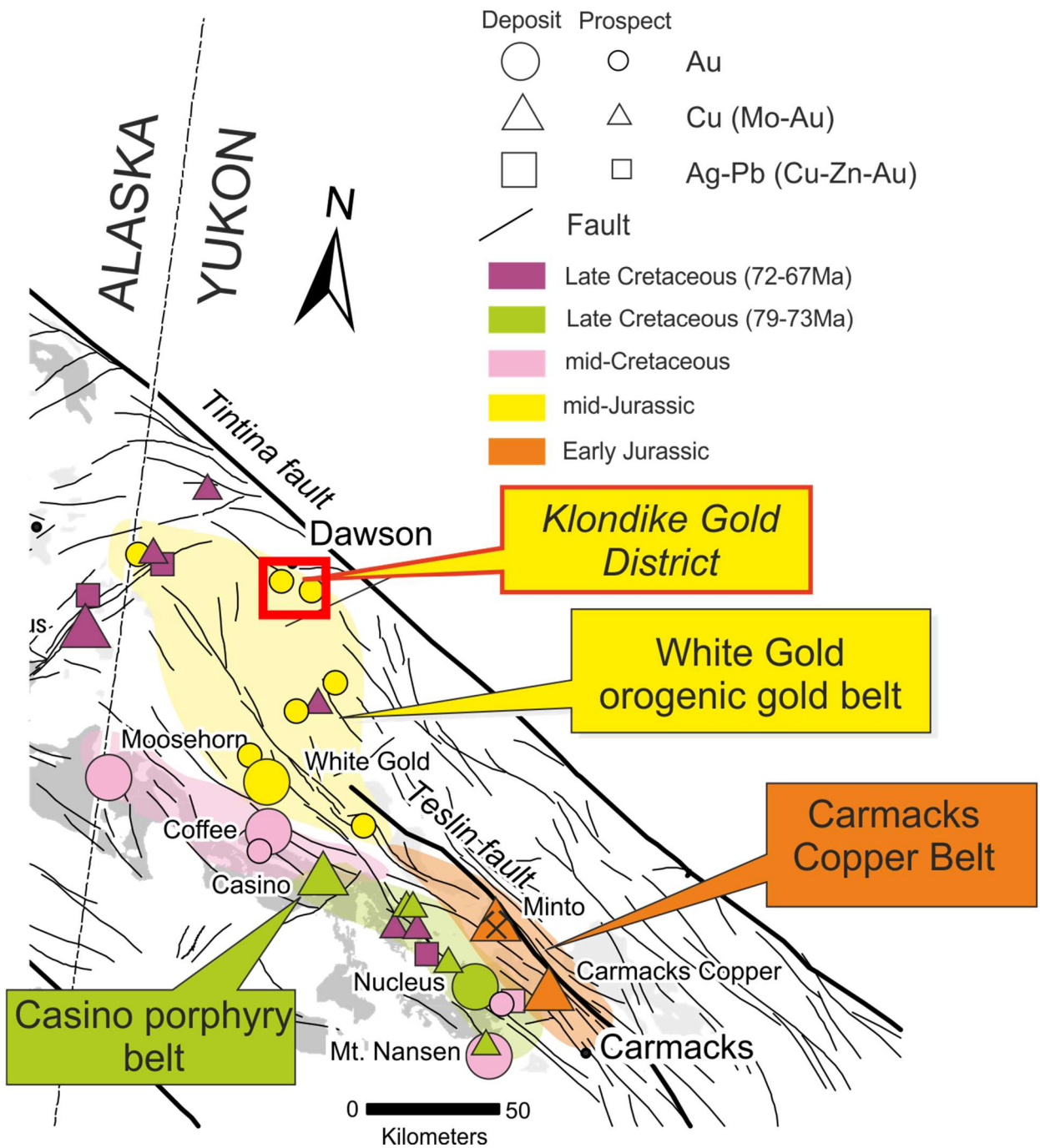


Figure 3-11: Major deposits and belts in north-west Yukon labelled. Colours correspond to ages (Yukon Alaska Metallogeny (Allan et al., 2013))

Table 3-1: Mineral Deposits mentioned in the text.

Deposit	Commodity	Mineralisation style	Tonnage (Mt)	Grade	Reference
Minto	Cu, Au	Intrusion-related	60	1%Cu, 0.4g/t Au	MINFILE 115I 021. Tafti and Mortensen 2003
Carmacks Copper	Cu, Au	Intrusion-related	60	1%Cu, 0.4g/t Au	MINFILE 115I 008. (Tafti and Mortensen 2003)
Mount Nansen and Klaza	Au, Ag	Porphyry-epithermal	0.87	5.3-15 g/t Au, 50-611 g/t Ag	(Chapman et al., 2016)
Casino	Cu, Au, Mo	Porphyry	1,057	0.2% Cu, 0.23 g/t Au, 0.022% Mo	(Casselmann and Brown, 2016)
Revenue	Au, Ag, Cu, Mo	Porphyry	101	0.34 g/t Au, 3.14 g/t Ag, 0.13% Cu, 0.04% Mo	(Allan et al., 2013)
Nucleus	Au, Ag, Cu	Porphyry	90	0.60 g/t Au, 0.94 g/t Ag, 0.65% Cu	(Allan et al., 2013)
Coffee	Au	Orogenic	64.4	1.56g/t Au	(Buitenhuis, 2014)
White Gold-Golden Saddle	Au	Orogenic	13.8	2.93g/t Au	(Bailey, 2013)

3.5.1 Syngenetic Mineralisation

The Devonian-Carboniferous, Finlayson Assemblage (section 3.3.2) is prospective for volcanic massive sulphide (VMS) Cu-Zn-Pb (Au-Ag) mineralisation (Murphy et al., 2006). The upper portion of the Assemblage, described in section 3.3.2 as the Nasina, and has rare narrow, foliation parallel sulphide lenses that are related to minor VMS mineralisation (Murphy et al., 2006, Allan et al., 2013).

Elsewhere there is evidence for small foliation parallel Pb-Zn (Ba) mineralisation that is recorded throughout the KGD (Figure 3-11) (Murphy et al., 2006, MacKenzie et al., 2008). Mortensen et al. (2007) describes how the metal associations, lead isotopes and volcanic setting of the mineralisation are typically features of volcanic-massive-sulphide deposits.

3.5.2 Mineralisation related to Magmatic Events

The formation of a number of arc sequences in the YTT, as described in section 3.2.1, has produced magmatism that has influenced the formation of intrusion related, porphyry and epithermal deposits.

Late Permian magmatism (252-254Ma), related to the Klondike Assemblage and post-metamorphic, crustally derived magmatism, led to the emplacement of the Jim Creek and Teacher Plutons. These host minor intrusion related gold mineralisation (as described in Chapter 2) but no economic deposits have been discovered (Figure -3-10) (Allan et al., 2013).

The study area has no evidence of the Early Jurassic magmatic event (Figure -3-10). However elsewhere, the large Minto mine and the associated Carmacks Copper Belt (Table 3-1) to the south-east comprise economically important mineralisation. (Figure 3-11) (Tafti and Mortensen, 2003). Tafti and Mortensen (2003) proposed that these deposits represent metamorphosed porphyry mineralisation; however, Allan et al. (2013) suggested that the origin is more enigmatic and may be intrusion related gold mineralisation.

Allan et al. (2013) describe three generations of magmatism in the Cretaceous (Figure -3-10), which is a result of renewed arc magmatism related to subduction and crustal transpression (section 3.2.5). The earliest phase of magmatism in the mid Cretaceous (Figure -3-10) is a magnetite-series in the Dawson Range forming the Mount Nansen and Klaza porphyry-epithermal deposit (Figure 3-11 and Table 3-1) (Hart and Langdon, 1997, Chapman et al., 2016). Early Late Cretaceous (Figure -3-10) porphyry Cu-Au mineralisation is distributed along the Big Creek Fault and includes the Casino, Sonora Gulch and Nucleus-Revenue deposits (Figure 3-11 and Table 3-1) (Godwin, 1975, Allan et al., 2013, Casselman and Brown, 2016). This pulse of magmatism formed 79-73Ma (Figure -3-10) and is a small belt with low volumes of magma but rich mineralisation (Allan et al., 2013). The Late Cretaceous (70-67Ma) coincided with the regionally extensive Carmacks Volcanic Group, described in section 3.3.5, which formed porphyry mineralisation in the Sixtymile-Pika area of Alaska (Allan et al., 2013).

3.5.3 Orogenic Gold Deposits

Gold-bearing quartz veins are widely recognised to be the source of the extensive placer gold deposits in the KGD (McConnell, 1907, Tyrrell, 1907, Knight et al., 1994, Knight et al., 1999a). The veins were characterised by Rushton et al. (1993) to be mesothermal, due to their low-salinity-aqueo-carbonic fluid chemistry; however, Allan et al. (2013) ascribe their features to be associated with orogenic gold deposit (OGD) model (described in Chapter 2).

The discovery of gold mineralisation in the White Gold District, Fortymile and Sixtymile (Figure 3-12) are also interpreted to fit the OGD model and are part of two major episodes of mineralisation: Middle Jurassic and Mid Cretaceous. Geochronology (U-Pb, $^{40}\text{Ar}/^{39}\text{Ar}$, $^{187}\text{Re}/^{187}\text{Os}$), summarised in Allan et al. (2013), shows that there is no association with magmatism (Figure -3-10) and that mineralisation coincides with crustal exhumation (Figure -3-10).

Mineralisation in the KGD is described below to provide context to the Lone Star area, that is the study area of this PhD and described in Chapter 4. There are numerous examples of mineralisation across the region related to this period, such as, the Golden Saddle Deposit, in the White Gold District and the Coffee Gold Deposit, in the Dawson Range (Table 3-1). These examples are summarised in the next section.

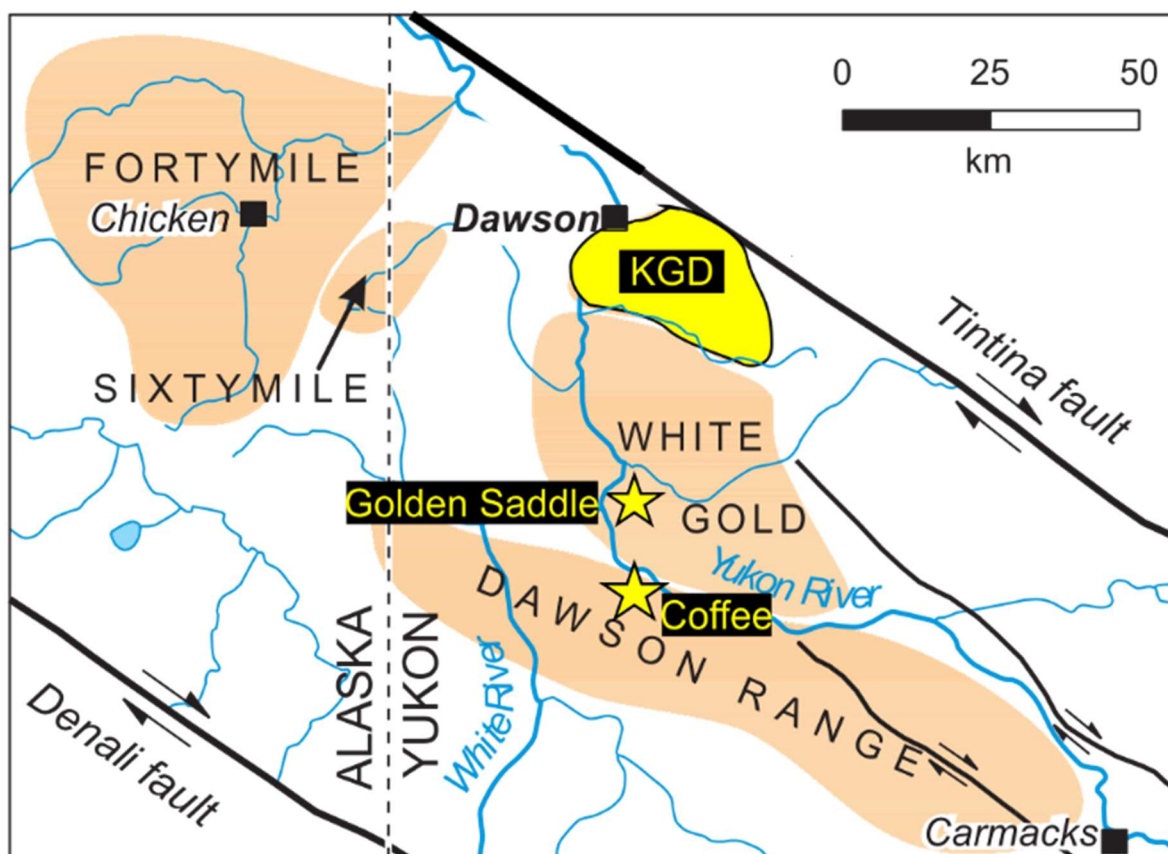


Figure 3-12: Orogenic districts within Yukon and Alaska. Golden Saddle and Coffee deposits are the biggest OGDs in the region. The KGD lacks a single large deposit but has numerous orogenic occurrences (Allan et al., 2012, Allan et al., 2013).

3.5.3.1 Mineralisation in the Klondike Gold District

The KGD is a rich placer district and has produced in excess of 20 Moz of gold from a small geographic area (~1200km²) since its discovery in 1896 (Burke et al., 2005). There are a number of gold-bearing quartz veins across the region that are interpreted to be related to a period of OGD formation in the Mid-Late Jurassic (Allan et al., 2013). The largest occurrence is the Boulder Lode mine that was operational between 1912 and 1914 and has produced almost all of the 1240 ounces of bedrock gold recovered from the KGD (MINFILE 1150 072). The Boulder Lode mine is situated in the Lone Star area (Figure 3-13) which is the study area of this PhD and described in detail in Chapter 4.

Tyrell (1907) and McConnell (1907) recognised that the gold-bearing quartz veins in the KGD represent the source for the extensive alluvial deposits. Developments in analytical procedures meant that chemical characterisation of gold was much easier and larger samples populations could be investigated.

Studies conducted by Knight et al. (1994), Knight et al. (1999b) and Chapman et al. (2010a) used the chemical and mineralogical features of gold to interpret bedrock mineralisation and placer distribution. The application of gold mineralogy to understand mineralisation is a key aspect of this research project and described in Chapter 5.

The huge discrepancy between the 20 Moz of gold in placers versus the small 1240oz of gold from bedrock source has driven interest in the KGD. Although sporadic mineral exploration has been ongoing since the gold rush in 1896, there has been no major economic bedrock discover. More recent exploration has focussed on the Lone Star area which is the focus of this research project and described in detail in Chapter 4.

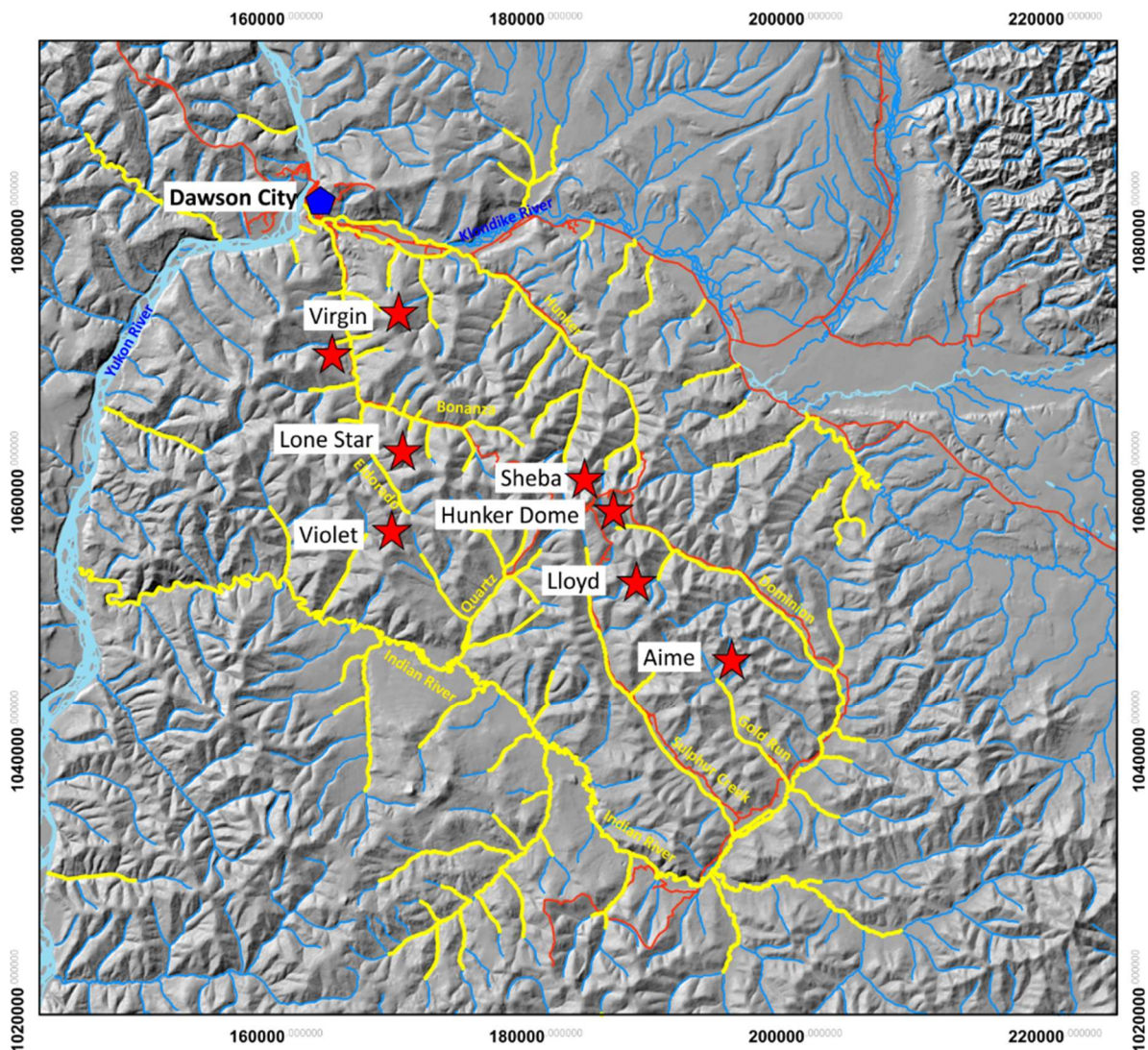


Figure 3-13: Map of Klondike District showing mineral occurrences and gold placer streams.

3.5.3.1.1 Mineralisation

Mineralisation in the KGD is hosted in discordant quartz veins, which are localised in D₄ (section 3.4.3) angular kink folds and reverse faults (section 3.4.3). The majority of gold-bearing veins occur as clusters or swarms that have strikes of 100m. The veins vary from 2cm up to 3m wide and almost entirely composed of subhedral milky white quartz (Rushton et al., 1993). Ribbon banding observed is rare suggesting that most veins in the KGD are a result of a single depositional event. Some quartz banding was observed at the Aime occurrence (Table 3-2 and Figure 3-13), in the south of the KGD, which may be a result of episodic quartz precipitation (Mortensen et al., 2007). Wolff (2011) describes brecciation of quartz veins that is preserved as rafts of wallrock in the centre of veins. Bladed quartz infills vugs at a number of localities, at Violet and in the Lone Star area and is interpreted by Allan et al. (2013), to indicated shallow crustal conditions. The presence of quartz amethyst at Hunker Dome and is described by Rushton et al, (1993) to have formed after the main phase of subhedral quartz deposition.

Veins are composed of ~98% subhedral quartz but have other gangue mineralogy such as barite, carbonate minerals, sheelite, feldspar, muscovite and rare rutile (Friedrich and Hoymann, 1992). Gold in veins occurs with pyrite, in limonite pseudomorphs after pyrite, as microscopic particles or visible gold (Rushton et al., 1993). The sulphide content of quartz veins is generally low with the paragenetically late chalcopyrite, galena, sphalerite and rare sulfosalts recorded across different occurrences (Friedrich and Hoymann, 1992). Gold-bearing quartz veins and their occurrences described in Table 3-2 often have considerable gold grades ranging from 5-150g/t, however they lack consistency. Virgin, Boulder Lode and Violet are the only occurrences to be mined whereas others, like Hunker Dome, only have exploration adits.



Figure 3-14: Field image of the Sheba vein at King Solomon's Dome

The largest and most consistent quartz vein is the Sheba vein (Table 3-2, Figure 3-13 and Figure 3-14) at King Solomon Dome, which is up to 3m thick and can be traced over 2km (Friedrich and Hoymann, 1992). Friedrich and Hoyman (1992) provided a detailed overview of the mineral paragenesis at Sheba and Hunker Dome (Table 3-2) which are hosted in mafic schist. Euhedral pyrite crystals extend up to 2m from the vein replacing magnetite (Friedrich and Hoymann, 1992, Mortensen et al., 2007).

Research by Knight et al. (1994), Knight et al. (1999a) and Chapman et al. (2010a) have used the mineralogical and chemical features of gold to deduce the placer-lode relationships in the KGD. Chapman et al. (2010b) analysed and divided into gold into types according to their Ag alloy composition and further subdivided depending on Hg content and opaque inclusion type. A 'Type 1' gold is defined by low Ag (12-25%) and a variety of inclusions that allow for further sub division. Type 2 gold is defined as being Ag rich (18-55%) and containing Hg values to 9% (3% detection limit). The study also highlighted a Type 3 population of gold which has 10-40% Ag and Hg up to 4% (Chapman et al., 2010b).

Table 3-2: A summary of the main mineralised occurrences in the KGD excluding those in the Lone Star area

Name	Host Rock	Description	Mineralogy	Reference
Lloyd	Mafic Member of Klondike Schist Formation	Extensive strike of quartz vein for 250m with thickness of 0.8-1.5m. Anhedral quartz with vugs.	Pyrite, gold. Some galena	MINFILE 1150 066
Mitchell Sheba	Undifferentiated Member of Klondike Schist Formation	Quartz veins can be traced up to 2km with widths of 1.2-2m. Mostly white quartz with some rutile and pyrite in the centres. Gold occurs at vein margin and extends into pyrite alteration. Sheba vein is 1.5m thick and has 3 stages of mineralisation.	Pyrite, galena, chalcopyrite, azurite, malachite, arsenopyrite and tetrahedrite.	MINFILE 1150 068 (Friedrich and Hoymann, 1992)
Hunker Dome	Mafic Member of Klondike Schist Formation	Veins are hosted in angular reverse faults. Composed of white quartz, galena, ferroan carbonate minerals and pyrite. Gold is found occurring with galena. 4 veins have historic mine shafts.	Galena, sphalerite, pyrite, gold. Sulphosalts and tellurides	MINFILE 1150 067 (Friedrich and Hoymann, 1992)
Oro Fino	Upper Sulphur Creek Orthogneiss	Veins are composed of milky white quartz, ferroan carbonate and trace amounts of pyrite.	Pyrite, galena, arsenopyrite.	MINFILE 11500 128
Violet	Sulphur Creek Orthogneiss	Several quartz-barite veins which are cut by large pegmatite veins. Veins have limonitic box work textures but mostly barren.	Pyrite, galena, chalcopyrite, small visible gold.	MINFILE 1150 073
Virgin	Undifferentiated Member of Klondike Schist Formation	In situ veins are not observed due to historic working. Quartz is subhedral and has evidence of faulting at margins. Gold occurs in fractures of the quartz. Limonite common in vein material	Galena, pyrite and gold	MINFILE 116B 007
AIME	Undifferentiated Member of Klondike Schist Formation with Finlayson lenses.	Vein is 0.5-1m with evidence of slickensides at margin. Wallrock is pyritised and gold-bearing. Quartz veins have evidence of ribbon banding.	Gold, pyrite minor galena.	MINFILE 1150 061 (Rushton et al., 1993)

3.5.3.1.2 Alteration

Wallrock alteration is poorly developed and is not observed in competent lithologies, such as the Sulphur Creek Orthogneiss (section 3.3.3.1); however, more reactive units, such as the Mafic Member of the Klondike Schist Formation (section 3.3.3.2.3), exhibit wallrock sulphidation and carbonate alteration (Allan et al., 2012).

3.5.3.1.3 Age of mineralisation

Dating of the mineralised veins at the Sheba occurrence (Table 3-2) yielded $^{40}\text{Ar}/^{39}\text{Ar}$ ages of 145-143Ma (Allan et al., 2013) but rutile U-Pb ages from Mortensen et al. (2012 unpublished) indicate an age of 160Ma (Hunt and Roddick, 1992). The earlier dates correspond to a period of regional cooling, described by Allan et al. (2013) (Figure -3-10), which is interpreted to represent crustal exhumation (section 3.2.4).

3.5.3.1.4 The origin of fluids

Rushton et al. (1993) conducted a study of fluid inclusions from quartz veins across the KGD. The results provided a range in temperatures and pressures of quartz formation; the south-east showed temperatures of 300-250°C and pressures of 1400-2300 bars and the north-west provided temperatures of 200-310°C and pressures of 300-700 (Rushton et al., 1993). Rushton et al. (1993) describes effervescence of a CO₂ rich phase from quartz samples from central and north-western KGD, which suggests that the fluid and crust were uplifting at the time of emplacement. The results were interpreted by Rushton et al. (1993) to represent a cross section of a mesothermal system that was emplaced during crustal uplift.

A preliminary study of veining in the district, by Allan et al. (2014), investigated the carbon isotope and trace element content of carbonate from alteration, metamorphic veins and marble occurrences. The carbonate associated with alteration is Mg-Fe-Mn and lacks isotopic variation, which suggests a local source (Allan et al., 2014a). Allan et al. (2014) describes that the local origin of carbonate minerals in veins may also indicate a local source for the gold. A comprehensive study of oxygen isotope compositions in quartz was conducted by Rushton et al. (1993). The results provided evidence that vein fluids were

meteoric with a minor metamorphic source (Rushton et al., 1993). Although the research by Rushton et al. (1993) is the most comprehensive investigation of gold-bearing quartz veins in the KGD many of the samples lack paragenetic characterisation and caution must be taken when describing fluids from different veins.

3.5.3.1.5 Overview

A model is proposed by Rushton et al. (1993) in which crustal uplift has produced extensional structures and deep penetration of meteoric fluids. Convection of meteoric fluid through the brittle portion of the crust is thought to interact with metamorphic fluids before being channelled into extensional structures at the surface (Rushton et al., 1993). It is challenging to know whether the mineral occurrences across the KGD are coeval but the overarching conditions governing mineralisation are thought to be the same.

Within the KGD there are areas of very rich placer production that are often adjacent to barren creeks which may imply the existence of small but rich centres of mineralisation (Chapman et al., 2010b). Chapman et al. (2010b) proposed that orogenic mineralisation in the KGD is present as a number of zoned hydrothermal systems.

3.5.3.2 The White Gold District and the Golden Saddle Deposit

The White Gold District is a region to the south of the KGD located near the confluence of the White and Yukon rivers (Figure 3-11). The region is known for its placer production, thought to be 390,000oz historically (LeBarge and Coates, 2007); however, it became of major interest in 2009 when advances in soil geochemistry outlined a number of new hard rock discoveries. The most significant of these discoveries was the Golden Saddle deposit (1.3 Moz Au), which is described below (Allan et al., 2013, Bailey, 2013).

The mineralisation at Golden Saddle (Table 3-1) is hosted in structures that strike north-west and are part of an east-west transpressive zone that is well preserved in Late Permian Orthogneiss (MacKenzie et al., 2010, Allan et al., 2012). Bailey (2013) describes mineralised quartz-feldspar veins which are hosted in D₄ (section 3.4.3) angular kink folds. The gold mineralisation is associated with brecciation of the veins and an intense period of quartz-carbonate-illite alteration

(Allan et al., 2012, Bailey, 2013). The primary minerals associated with gold are tellurides, galena, bismuthite, barite and molybdenite (Bailey, 2013). Pyrite contains inclusions of gold with a simple Au-Ag alloy (type 1) and cross cuts quartz forming in mylonites, stylolites and shears (Bailey, 2013). A second stage of gold is observed in fractures of pyrite that has a more complex alloy of Au-Ag-Hg (type 2) and is paragenetically associated with hessite, barite, galena, molybdenite, chalcopyrite and sulphosalts (Bailey, 2013).

The paragenesis marks a change from ductile to brittle conditions which are interpreted by Bailey (2013) to represent epizonal conditions.

Geochronological techniques were used to inform on the crystallisation ages of rocks and constrain the timing of gold mineralisation in the Golden Saddle deposit (Bailey, 2013). Type 2 gold is associated with molybdenite that provided $^{187}\text{Re}/^{187}\text{Os}$ dates in the Late Jurassic of 160-155Ma (Figure -3-10) (Bailey, 2013). Allan et al. (2013) suggests that mineralisation at Golden Saddle and elsewhere in the White Gold District are comparable to the KGD and formed during a period of crustal exhumation and uplift in the Mid-Late Jurassic (Figure -3-10).

3.5.3.3 Coffee Gold Deposit

The Coffee Gold deposit to the south of the White Gold District (Figure 3-12) is part of a younger phase of mineralisation (Allan et al., 2013). The discovery represents the most significant recent gold discovery in the region and comprises several steeply dipping mineralised zones that have an inferred resource of >4 Moz (Buitenhuis, 2014, MacKenzie et al., 2015). The deposit is hosted in tectonically imbricated rocks that include; the Snowcap Assemblage, Sulphur Creek Orthogneiss and Klondike Schists (MacKenzie et al., 2015). Mineralisation is structurally controlled along the dextral Coffee Creek Fault System and is related to brecciation and extensional fractures (Bailey, 2013, MacKenzie et al., 2015). Gold is hosted in fine-grained arsenopyrite that localises in breccia and biotite bearing host rocks, which include the biotite rich metasedimentary units and the biotite-bearing Cretaceous Coffee Creek granite (MacKenzie et al., 2015). MacKenzie et al. (2015) describe how deposition of gold and arsenopyrite is related to the decomposition and alteration of biotite.

Cross cutting relationships established from veining and the Coffee Creek granite place the timing of mineralisation in the Cretaceous (MacKenzie et al., 2015). MacKenzie et al. (2015) and Allan et al. (2013) suggest that orogenic mineralisation may have occurred after Mid-Cretaceous arc magmatism. Mineralisation at Coffee is concentrated to a localised area compared to the much more extensive Mid-Jurassic period of OGD formation in the KGD and White Gold District.

3.6 Physiography and glaciation

The KGD is part of the 3000 km² area of Beringia which extends from Siberia through Alaska and into Yukon. Hulten (1937) was the first to describe this unglaciated area as a region on the basis of similar arctic and boreal plants, (Figure 3-15). The physiography and sedimentary record for this region records the complex evolution of the palaeo environment across the region. Lowey (2006) and Dud-Rodkin (2001) describe how the palaeo environment has influenced the formation of the KGD and extensive alluvial deposits.

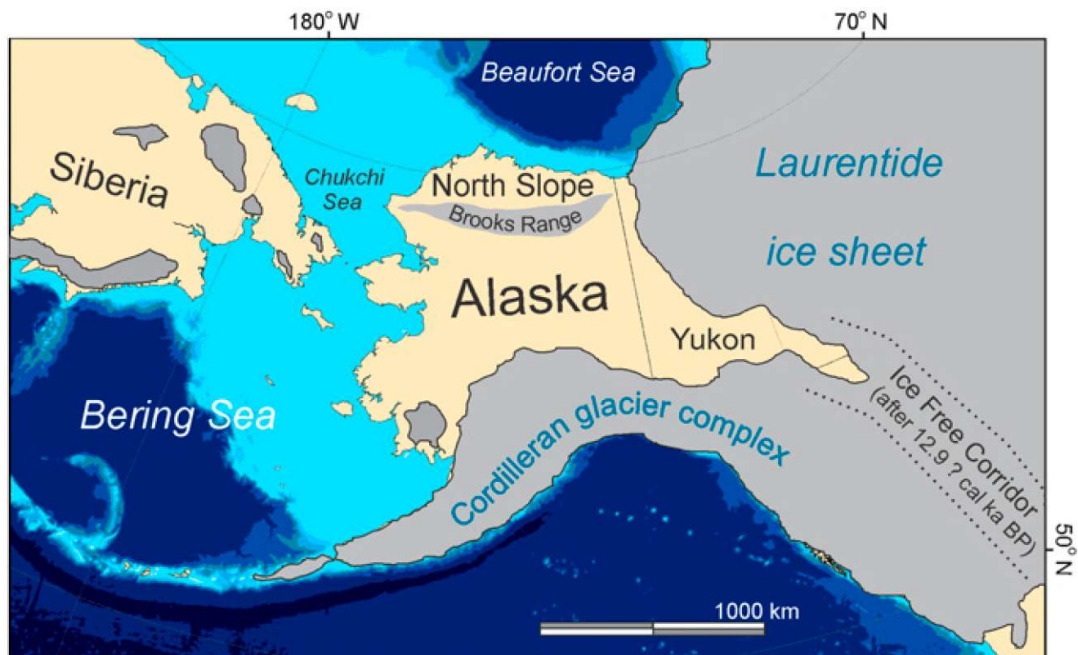


Figure 3-15: Figure from Mann et al. (2015) showing the last glacial maximum in the Yukon and Alaska.

3.6.1 Physiography

The KGD remained relatively unaffected by geological events in the Palaeogene which resulted in the formation of a peneplain (Lowey, 2006). A warm climate during this period resulted in intense chemical weathering and the formation of thick saprolite. These conditions led to the formation of rounded hill tops which were subsequently incised in the Quaternary (Duk-Rodkin et al., 2001). The landscape today is referred to as the Klondike Plateau and is described by Bostock (1948) as a 'maze of deep, narrow valleys, separated by long smooth-topped ridges whose elevations are uniform, and which are remnants of an old uplifted erosion surface'.

3.6.2 Glaciation

Yukon and Alaska are dominated by a continental climate due to a rain shadow formed by the Coast and St Elias mountains. The rapid uplift of the mountains in the Eocene resulted in aridity across the Yukon that was cold enough to support ice sheets but too dry for glacier formation. Dud Rodkin et al. (2001) describes how the cooling climate in the initiation of glaciation and Cordilleran Ice Sheet in the Pleistocene. Glaciation has had a significant influence on the various drainages and Yukon River which initially flowed south. Dud Rodkin (2001) suggests that damming of the Yukon River resulted in the formation of Lake Yukon (Figure 3-16) that eventually reversed flow. Drainage of Lake Yukon to the north incorporated other catchments increasing the total drainage by 20%.

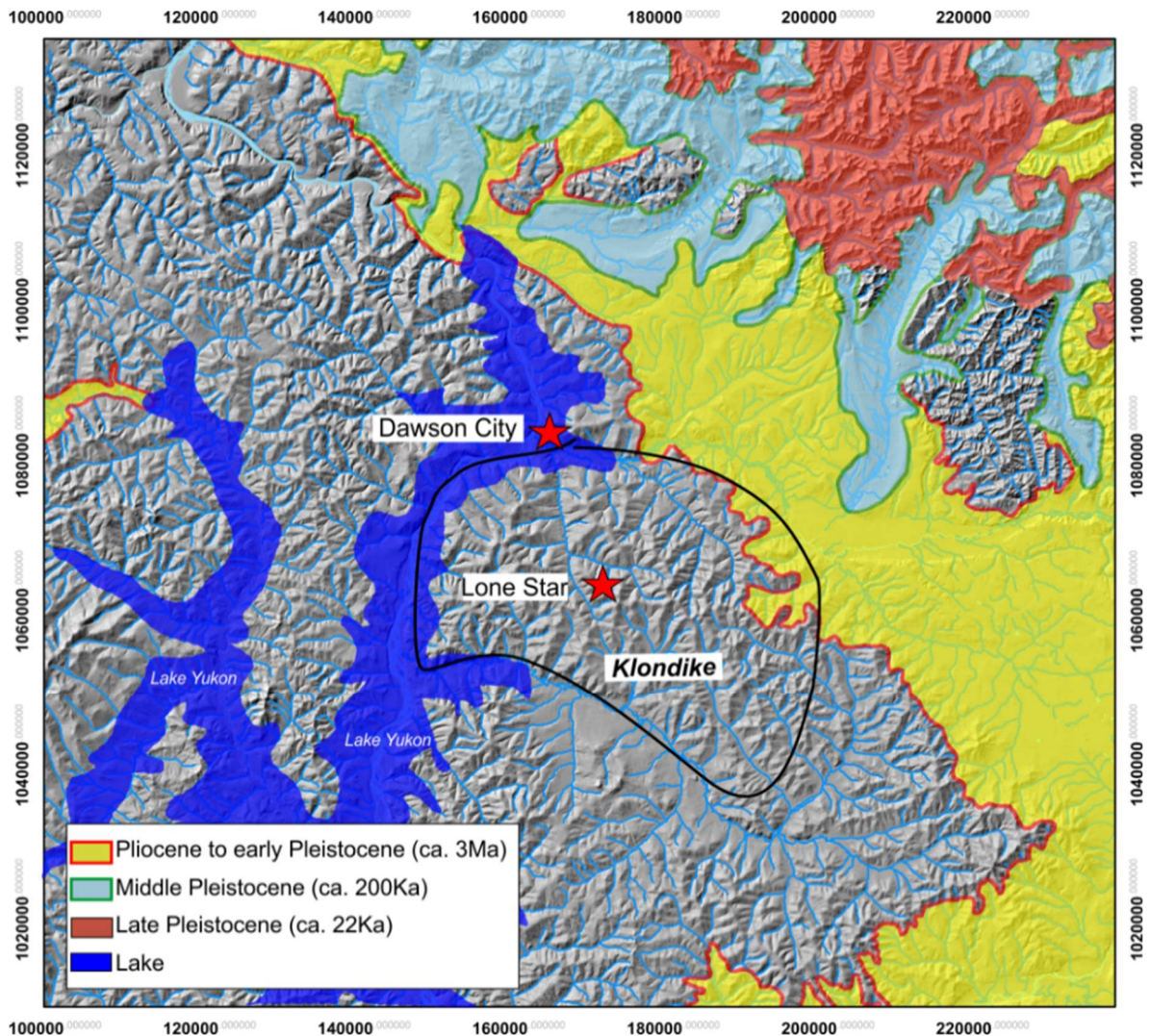


Figure 3-16: Glacial distribution simplified from Dud-Rodkin (1999). Lake Yukon, KGD and Lone Star are labelled for reference.

3.7 Placer Gold

The discovery of gold in the Klondike Gold District (1896) and the subsequent gold rush has resulted in almost continued extraction of gold from a number of established placer mining centres across the north-west Yukon and Alaska. A comparison of lode resource and placer production in the KGD, Fortymile, Sixtymile, Dawson Range and White District is compiled by Allan et al (2013) in Figure 3-17. There is a marked disparity between the lode discoveries and corresponding placer production and vice versa (Allan et al., 2013). The largest areas of placer production include the KGD, Fortymile, Sixtymile and White Gold District, which correspond a period of mid-Jurassic orogenic mineralisation as outlined in section 3.5.3 (Figure 3-12 and Figure 3-17).

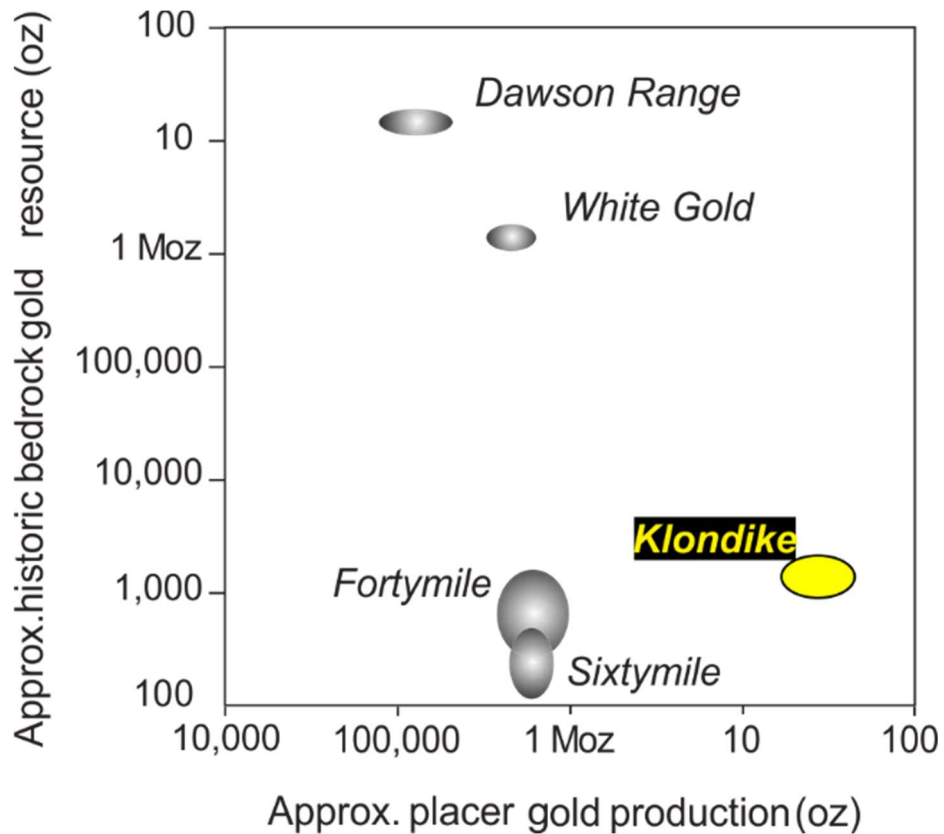


Figure 3-17: Modified from Allan et al (2013) indicating total lode gold resource for each mineral district plotted against total placer gold production. The Dawson Range is dominated by Cretaceous related porphyry and orogenic mineralisation.

3.7.1 Placer deposits in the Klondike Gold District

The current estimates for gold production in the Klondike varies from 12-25 Moz which has been recovered from a relatively localised geographic area of ~1200km² (Chapman et al., 2010a). The KGD continues to produce significant quantities of placer gold from alluvial bench deposits and the current streams (Figure 3-13) with 44,000oz being extracted in 2016.

Supergene enrichment and oxidation of the mineralised veins occurred throughout the Quaternary due to the humid paleoclimate and deep weathering (Figure 3-19) (Duk-Rodkin et al., 2001). Pliocene glaciation and uplift resulted in periods of incision and degradation which has concentrated gold from the weathered veins into rich alluvial deposits (Lowey, 2006). These are exposed today as alluvial bench gravel deposits, known as the *White Channel Gravels* (WCG) and at the bottoms of valleys in the present-day drainage (Figure 3-18) (Westgate et al., 2002, Lowther et al., 2014)

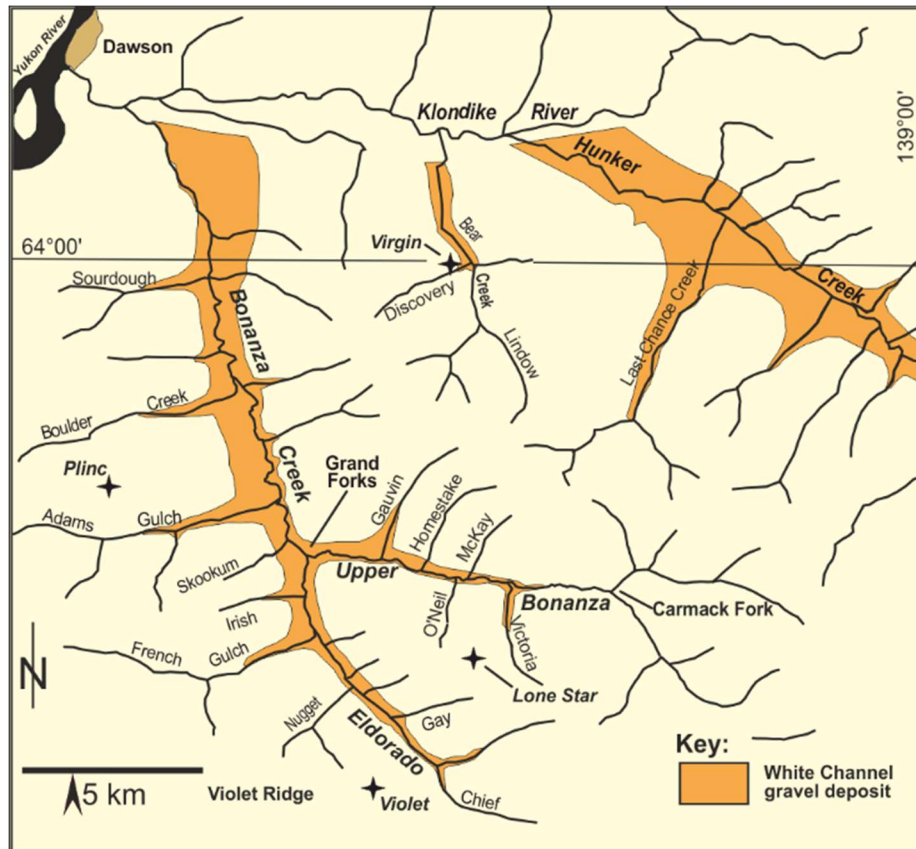


Figure 3-18: KGD with alluvial bench gravels of the White Channel Gravel labelled (Lowther et al., 2014).

The timing of initial incision that formed the bedrock strath beneath the WCGs is still uncertain but Lowey et al (2006) suggest it is limited to the early Pliocene (~5My). The Lower White Channel Gravels (LWCG) have undergone numerous generations of reorganisation and aggradation (Figure 3-19) that resulted in concentration of gold (Lowey, 2006). The gravels' white appearance is due to the high proportion of quartz boulders which resisted intense chemical weathering compared to mica-rich bedrock (section 3.3.3.2) that was altered to clay and washed downstream (Lowey, 2006).

The transition from LWCG to Upper White Channel Gravel is recorded by a thin organic layer described by Lowther et al. (2014) which provides evidence of an end to a warm climate and initiation of periglacial conditions in the Pliocene (3.3Ma) (Westgate et al., 2002, Pound et al., 2015). Palynology has shown that the layer represents lake sediments which may be a precursor to Lake Yukon described in section 3.6.2 (Lowther et al., 2014, Pound et al., 2015). The UWCG have higher rates of aggradation with evidence of ice casts and permafrost (Duk-Rodkin et al., 2001).

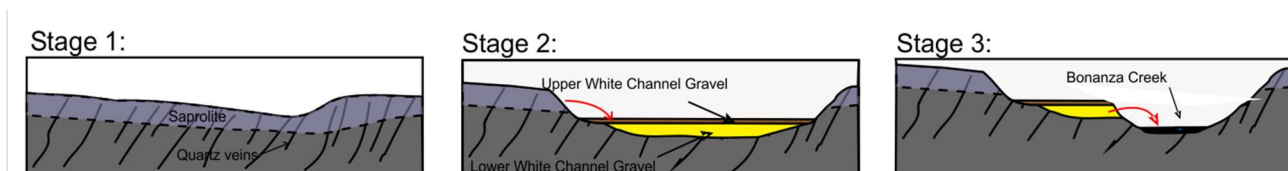


Figure 3-19: Evolution of placer formation as illustrated by Lowey (2006). Stage 1- Peneplain formation weathers mineralisation and forms Klondike Plateaus, Stage 2 - Degradation and incision produces the LWCG which is followed by aggradation and UWCG, Stage 3 – Incision to present day drainage

The incision to the present-day drainage is interpreted to be a result of pre-Reid and Reid glaciation (section 3.6.2 and Figure 3-16) and subsequent decreasing base level (Lowey, 2006). This continued incision resulted in reconcentration of the already very concentrated gold deposits in the WCG (Figure 3-19) (Lowey, 2006).

3.8 Summary

The YTT and SMT are formed from complex tectonic processes that has as a diverse mix of geology. This diversity has led to extensive mineral wealth in the North American Cordillera that, until recently, was poorly understood in the north-west Yukon and eastern Alaska. Allan et al. (2013) has provided a new metallogenic framework for the region that is helping to outline key periods of mineralisation. The KGD is now considered to be related to mineralisation in the White District, Sixtymile and Fortymile during the Mid-Jurassic. The 1.4 Moz Golden Saddle deposit and numerous small veins across the north-west Yukon have contributed large amounts of gold to the placers. A lack of glaciation has resulted in prolonged erosion and concentration of gold into very rich alluvial deposits. The KGD, and Lone Star area in particular, have the richest placer deposits in the region. This highlights the significance of the original bedrock mineralisation LSSA which potentially represented a world class OGD.

Chapter 4 The Lone Star Study Area

4.1 Introduction

The KGD has produced in excess of 20 million ounces (Moz) of gold from placer deposits that are interpreted to originate from orogenic veins across the area (described in Chapter 3). The richest placer creeks in the KGD are the Bonanza and Eldorado creeks have produced an estimated 8 Moz of gold and are separated by the Lone Star ridge (Figure 4-1). The slopes of the ridge and wider drainage have a number of bedrock occurrences, including the Boulder Lode Mine which is responsible for producing almost all of the 1240oz of bedrock gold mined in the KGD (Figure 4-2). The Lone Star area covers 150km² in the southwest of the KGD and forms the study area for this PhD (Figure 4-1C). This chapter provides a description of the geology and mineralisation in the area, which is referred to as the Lone Star Study Area (LSSA). The geology in the LSSA is part of the upper sequence of the Klondike Assemblage, described in Chapter 3. Many of the rocks are described elsewhere in the KGD as Klondike Schist Undifferentiated; however, in the LSSA, fieldwork and mapping during this project has resulted in the differentiation of the geology.

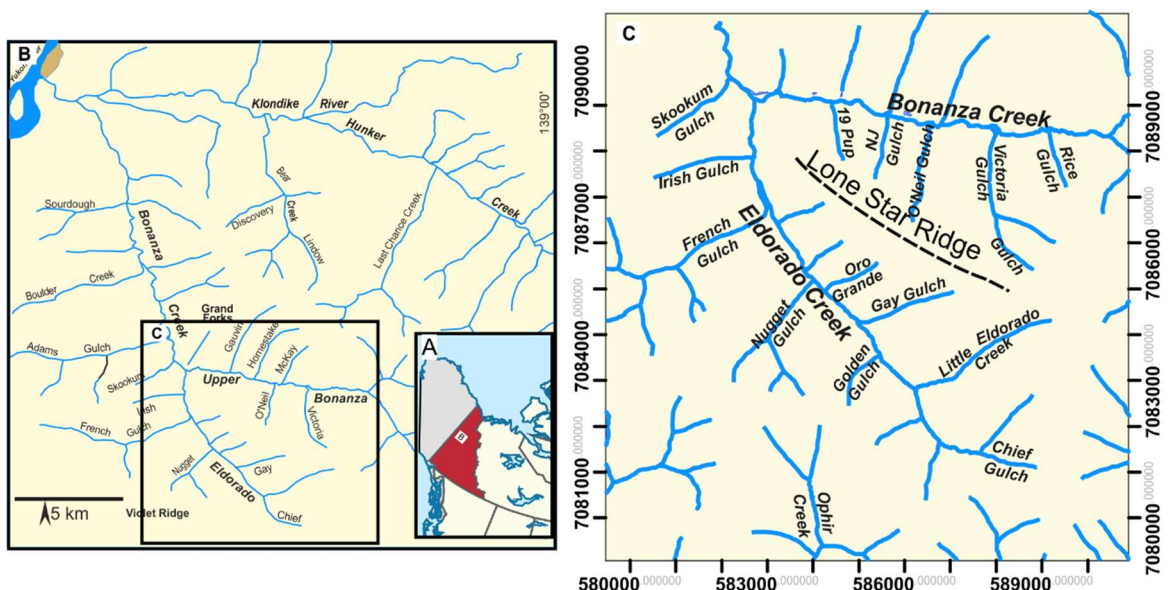


Figure 4-1: A- A map of the Yukon Territory. B-Klondike Gold District (KGD) with the LSSA outlined. C- Creeks and drainage of the LSSA labelled.

The extensive placer deposits are described with relation to the known gold-bearing vein localities in the LSSA. Exploration for a bedrock source responsible for the extensive placer deposits has been ongoing since the discovery of gold on Bonanza Creek in the Great Gold Rush of 1896. Early prospectors focussed on the discovery of gold-bearing veins that typically form in outcrop as clusters of veins from 10m² up to a few 100m² and are referred to as *zones* (Liverton, 2011). The gold-bearing quartz veins have been interpreted to be the only source for the placer deposits (Knight et al., 1994); however, the recent discovery of a unit of gold-bearing schist has provided the potential for an additional source (MacKenzie et al., 2007a).

4.2 Geology of the LSSA

The structural and lithological descriptions outlined in this section draw upon observations collected during PhD fieldwork. Differentiation of the Klondike Schist Undifferentiated formation into mappable units has previously been attempted by successive companies who have acquired the exploration licenses in the LSSA. However, mapping is challenging due to a lack of bedrock exposure, deep weathering and complex lithological boundaries. This led to multiple generations of rock classification that was inconsistent and confusing.

The following section provides a revised summary of the geology in the LSSA and differentiates the rocks according to various 'members'. This provides context to the geology of the PhD area with relation to the region, described in Chapter 3.

4.2.1 Lithologic units

This section provides a description of the various lithologic units in the LSSA and is the most recent and comprehensive description of lithologies. The geology within the LSSA is underlain by the Klondike Schist Assemblage with the upper portion mapped as Klondike Schist Undifferentiated. The rocks are heavily deformed but represent a way up stratigraphy and correspond to the descriptions in Chapter 3.

4.2.1.1 Quartz Augen Schist Member

The Quartz Augen Schist Member is a strongly foliated quartz muscovite schist with abundant deformed quartz and orthoclase augen that are up to 0.8cm in diameter (Mortensen et al., 2007). The rock is described regionally as the upper portion of the Sulphur Creek Orthogneiss Member (Chapter 3.3.3.1); however, it is delineated as a separate unit along the Eldorado Creek valley (Figure 4-2). Mortensen et al. (2007) describes the protolith to be felsic porphyry intrusion that formed during arc volcanism in the Late Permian.

4.2.1.2 Klondike Schist Formation

The following members are further discriminations of the Klondike Schist Formation described in Chapter 3.3.3.2. The regional unit known as the Undifferentiated Member has been mapped in detail in the LSSA with subdivisions described below.

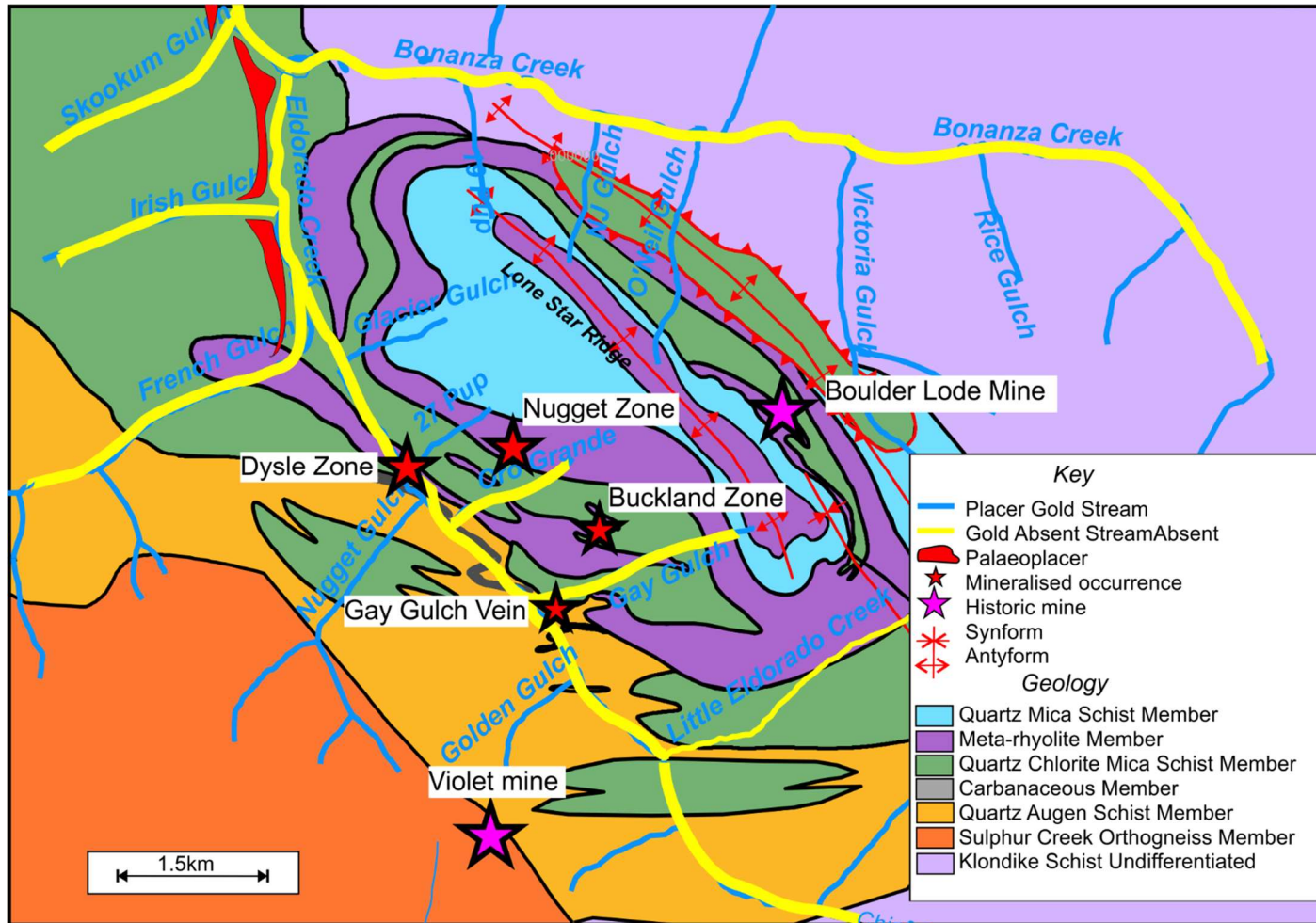
4.2.1.2.1 Chlorite Schist Member

The rock is a green chlorite-rich schist that is strongly foliated with a centimetre scale crenulation cleavage. The rock has a similar composition to the Mafic Member (described in Chapter 3.3.3.2.3); however, is not as coarse grained or as continuous as the unit at King Solomon's Dome. Mortensen (2013) suggested that mafic seafloor volcanic rocks of late Permian age were the protolith for the chlorite schist. The origin of the schist is interpreted by to be from mafic seafloor volcanism in the Late Permian (Mortensen 2016 Pers. Comms).

4.2.1.2.2 Carbonaceous Schist Member

The rock is a fine grained, dark grey, quartz-muscovite schist that is rich in graphite. It varies in thickness from 2-20 metres and has large aggregates of euhedral pyrite (1cm). The rock is heavily sheared and lacks continuity but is easily mapped along the Eldorado Creek (Figure 4-2) due to the persistence of black graphite in regolith. Mortensen et al. (2007) suggested that the schist formed from organic carbon rich clastic material in small basins proximal to volcanic vents on the Late Permian seafloor.

Figure 4-2: A modified geological map after Mortensen (2013) with mineral occurrences, historic mines and placer deposits marked.



4.2.1.2.3 Quartz Chlorite Mica Schist Member

The rock is recognised in outcrop for its blocky appearance and pale green to tan colour. It is composed of quartz, muscovite, minor chlorite and centimetre scale layers of quartz. The unit forms a major portion of the Undifferentiated Member, which originates from volcanic and clastic material on the Late Permian seafloor (Mortensen et al., 2007).

4.2.1.2.4 Meta-Rhyolite Member

The unit is a pale green to yellow foliated rock that has a competent sugary texture. The unit has a distinctive flaggy appearance in weathered outcrop; however, is extremely challenging to distinguish in fresh drill core (Mortensen, 2011). Multi element lithogeochemistry provided elemental data that plotted in a rhyolite field on a Winchester and Floyd diagram (Figure 4-3) (Winchester and Floyd, 1977, Mortensen, 2011). Liverton (2011) defines this rock as a Meta Rhyolite and interprets its origin to be related to Late Permian volcanism.

4.2.1.2.5 Quartz Mica Schist Member

This rock is challenging to distinguish but is the host for disseminated gold mineralisation in the LSSA. The distribution and features of the unit is described in detail in section 4.3.2.7.

The rock displays millimetre to centimetre thick layers of quartz, feldspar and mica that are well foliated. Alteration is developed as spotty chlorite and carbonate minerals with fine grained euhedral pyrite (Figure 4-4A). Lithogeochemical analysis provides elemental data that plots within the dacite/rhyodacite field on a Winchester and Floyd diagram (Figure 4-3) and is interpreted to origin from submarine felsic tuff in the Late-Permian (Chapter 3.5.1) (Mortensen, 2011). Millimetre to centimetre thick bands of barite and fine-grained chalcopyrite, sphalerite and pyrite are found within the QMS member (Figure 4-4B). MacKenzie et al. (2007a) ascribes the sulphide lenses to a volcanogenic massive-sulphide (VMS) origin due to their setting and Pb isotopic compositions (Mortensen et al., 2006).

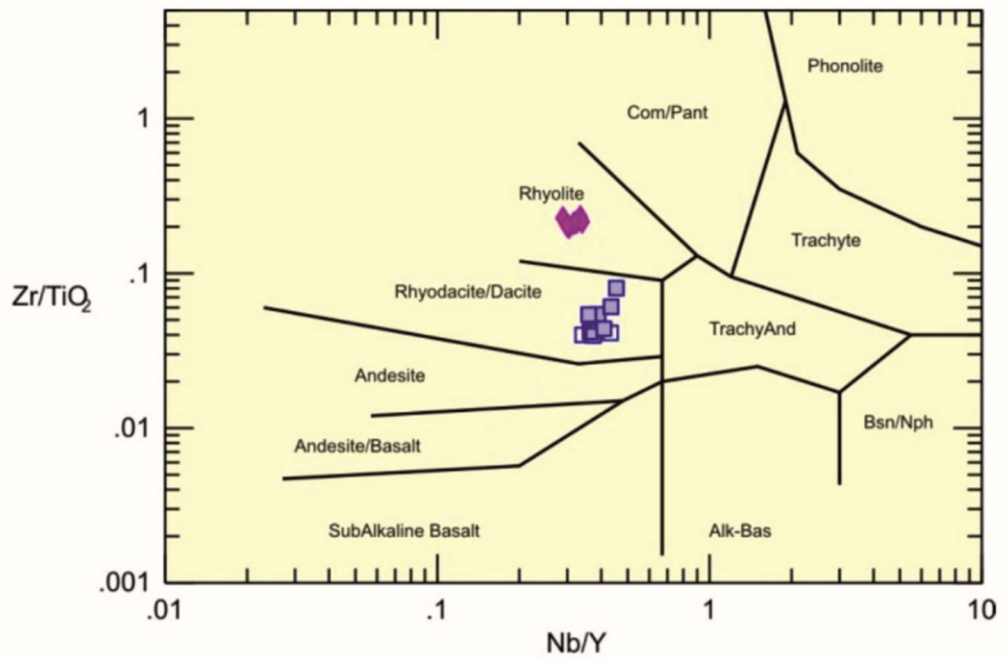


Figure 4-3: Winchester and Floyd plot of immobile elements from a number of drill hole intersections (Winchester and Floyd, 1977). Pink diamonds represent the Meta-Rhyolite Member and blue squares the Quartz-Mica-Schist Member (Mortensen, 2011).

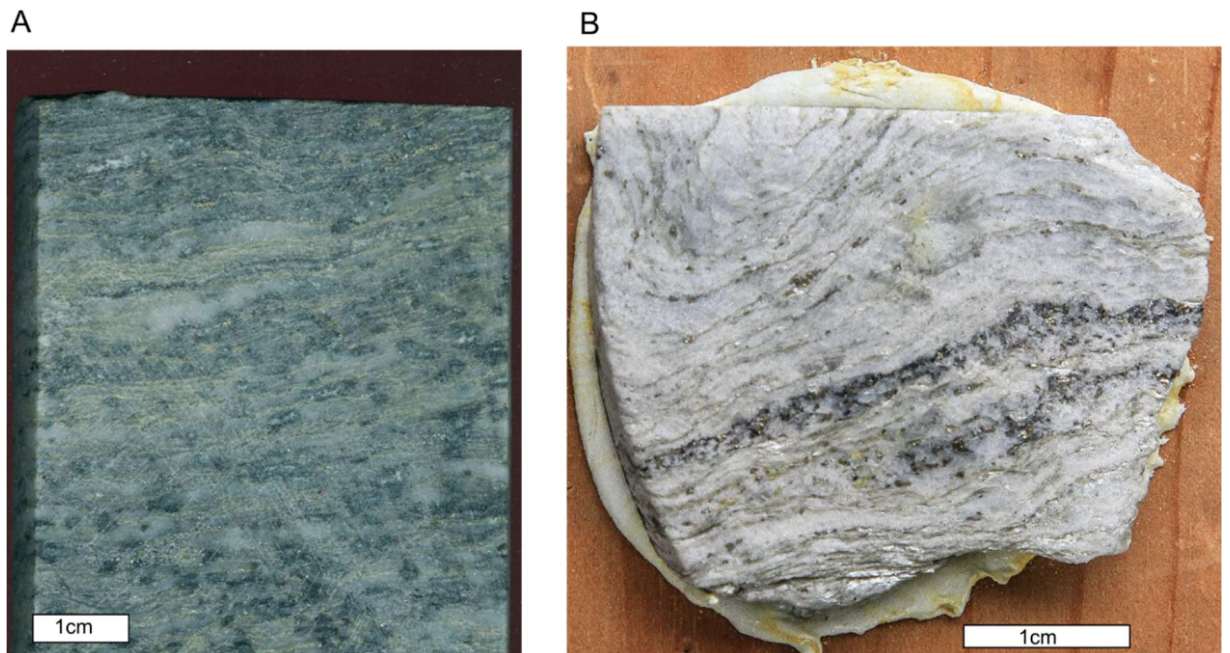


Figure 4-4: A) Spotted alteration of the Quartz Mica Schist. B) Foliation parallel band of sulphides.

4.2.2 Structural geology

The expression of deformation and structural geology in the LSSA relates to the regional features described in Chapter 3.4. The pervasive foliation that is developed in LSSA is part of the S_2 foliation developed across the KGD. Compression from the south-west during the Mid Jurassic (D_3) resulted in the formation of kilometre scale asymmetric folds (Figure 4-5) and a spaced crenulation cleavage (MacKenzie et al., 2007b). Parasitic folding (1-10m) accompanies the regional folds and is best developed in the mica rich lithologies, such as the Quartz Mica Schist and Quartz Chlorite Mica Schist (Liverton, 2011). D_3 progresses from ductile folding towards shearing and results in imbrication of thrust faults (Mortensen et al., 2007).

Liverton (2011) describes the Lone Star Thrust, which is present in outcrop along the north-east side of the Lone Star ridge and in Victoria Gulch (Figure 4-2 and Figure 4-5). Sub vertical (D_4) angular kink faults (described in Chapter 3) and folds are observed across the area (MacKenzie et al., 2008). The D_4 kink faults are extensional features that localise quartz veining and mineralisation (MacKenzie et al., 2008).

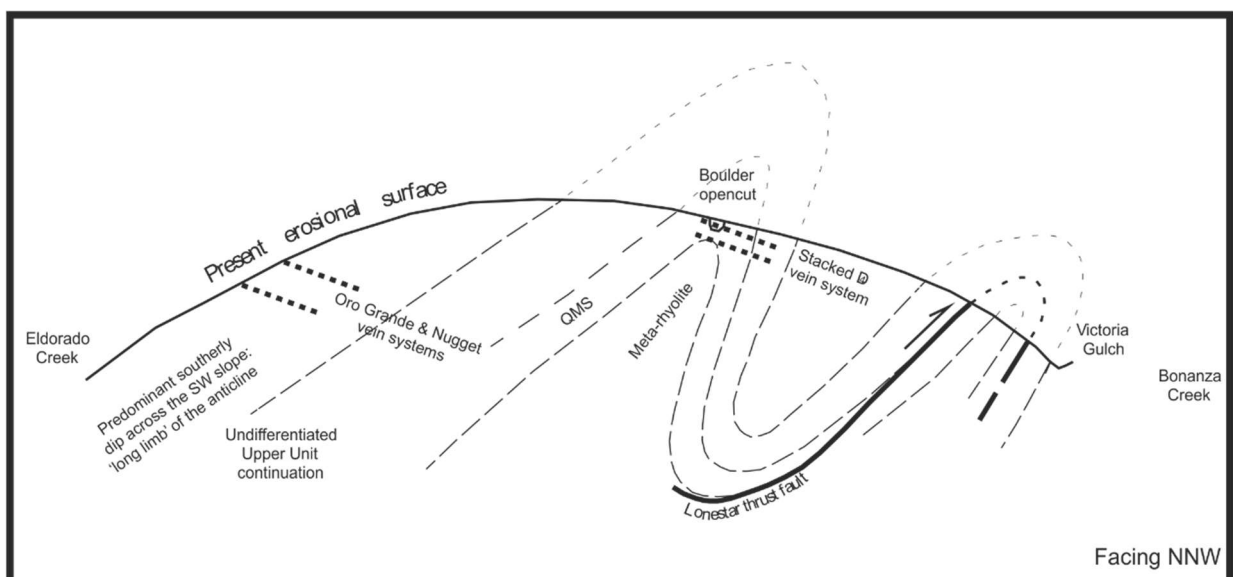


Figure 4-5: Liverton (2011) sketch cross section of the Lone Star ridge. More detailed structural features, such as parasitic folds are not illustrated.

4.2.3 Geological summary

The rocks that form the Klondike Schist Assemblage are interpreted to be a Late Permian volcanic arc sequence, as described in Chapter 3. These rocks are metamorphosed and represent a progression from plutonic rocks in the south-west to intrusive (Sulphur Creek Orthogneiss) and volcanic equivalents (Klondike Schist Formation) in the north-east.

Metamorphism and deformation in the LSSA is part of the same regional structural framework outlined in Chapter 3. Deformation associated with D3 has produced a complex sequence of folding and thrusting (MacKenzie et al., 2007b). Localisation of gold-bearing quartz veins are controlled by D4 angular kink folds that developed in the Mid Jurassic (MacKenzie et al., 2007b).

4.3 Gold mineralisation in the LSSA.

The discovery of placer gold on Bonanza Creek in 1896 sparked the Gold Rush and has led to almost continuous extraction of placer gold. Staking of 'quartz claims' (a parcel of land 1500ft² granted for hard rock mining) occurred almost immediately after the discovery of gold on Bonanza Creek.

This section provides an overview of the numerous placer deposits and bedrock mineralisation which make the LSSA such a rich area for gold.

4.3.1 Eldorado and Bonanza placer deposits

The Eldorado and Bonanza drainages host the richest placer deposits in the KGD producing an estimated 7 Moz of gold. The formation of deposits is discussed in Chapter 3.7.1 and include small first order drainages, valley bottom placers and alluvial bench deposits of the White Channel Gravels (WCG) (Figure 4-6).

The first discovery of gold in the KGD was made on Bonanza Creek, originally known as Rabbit Creek, and sparked the Gold Rush of 1896. It has a general course and direction of north-west and is 27 kilometres long draining a total area of 181 kilometres (Figure 4-6) (LeBarge and Coates, 2007). It has produced an estimated 42,000 ounces of gold from 1966-2004 with a fineness of 809-827 (LeBarge and Coates, 2007). Upper Bonanza has a number of

tributaries that drain the north-east side of the Lone Star Ridge (Figure 4-6). Although there are a number of creeks draining the ridge Victoria Gulch is the only creek to produce placer deposits that have a fineness of 807-820 (LeBarge and Coates, 2007).

Eldorado Creek is the most important tributary of Bonanza Creek and was historically the richest placer creek (~2 Moz) in the KGD. Its course runs in a northerly direction, is 11km long and drains the south-west side of the Lone Star Ridge (Figure 4-6). Production estimates show that 40,0000 ounces was exploited between 1966-2001 which has a fineness of 733-803 (LeBarge and Coates, 2007). French Gulch is a 7.5km long tributary of Eldorado, which runs in an easterly direction and has produced gold with a fineness of 631-750 (Figure 4-6) (LeBarge and Coates, 2007). Irish and Nugget Gulch are the only other productive creeks on the left limit of the Eldorado Creek with numerous creeks having no placer deposits (Figure 4-6). 27 pup, Oro Grande, Gay Gulch, Little Eldorado and Chief Gulch have all produced significant quantities of gold and are first order creeks that drain the SW side of the Lone Star Ridge (Figure 4-6).

There a number of palaeo placer deposits of the WCG, which reach the French Gulch tributary of Eldorado (Figure 4-6 and Figure 4-7). This bench deposit has been mined since the 1960s by J. Archibald, is the richest deposit in the KGD and produced the largest recorded nugget of 8.5 ounces (LeBarge and Coates, 2007). French Hill, Gold Hill, Adams Hill and Chechako are included within this study and are confined to the left limit of the Eldorado and Upper Bonanza (Figure 4-6 and Figure 4-7).

The extraction of placer gold has been almost continuous since the Gold Rush in 1896 and provides valuable information that mineral exploration companies often neglect. These include observations on the gold fineness, size, morphology, associated minerals and underlying bedrock geology. One of the most intriguing observations from compiling historic gold production data is the absence of gold from certain creeks (Figure 4-6).

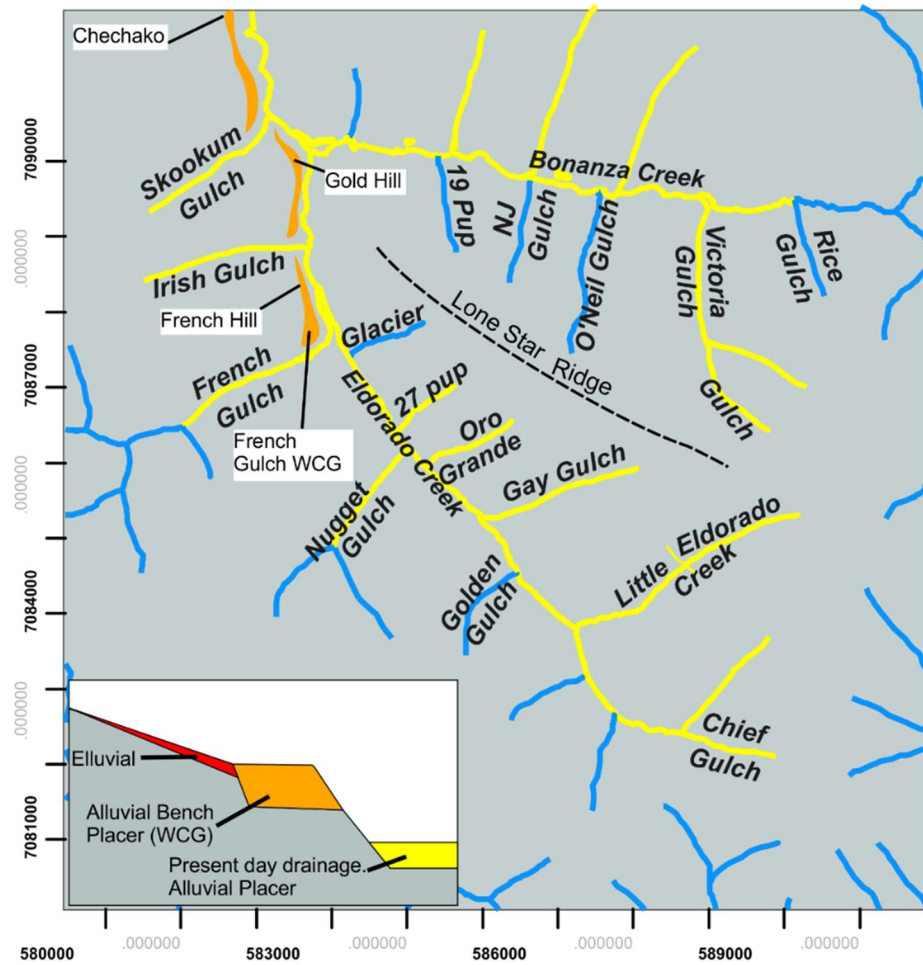


Figure 4-6: Map of the LSSA showing alluvial placer deposits (yellow), gold absent streams (blue) and palaeo placer WCG deposits (orange).

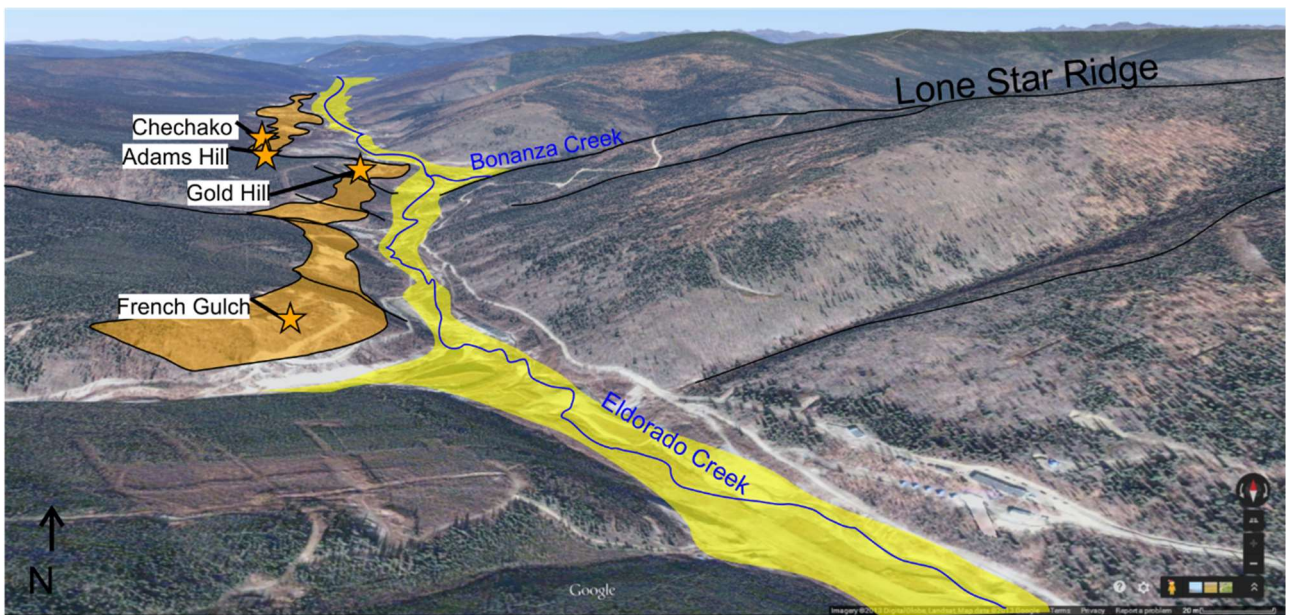


Figure 4-7: WCG alluvial bench gravel deposits and present day alluvial placers looking north down Eldorado Creek

4.3.2 In situ mineralisation

Tyrell (1907) was the first to link gold in placers to gold-bearing quartz veins and resulted in exploration that focussed on the discovery of further veining. Within the KGD the most significant mineralised locality is the Boulder Lode Mine (Figure 4-8) that is centred on the Lone Star Ridge and has produced almost all of the 1450 ounces of gold known to be extracted in the region. The ridge has a number of other mineralised localities that are present as clusters of gold-bearing veins described as zones.

Although much of the exploration and research has focussed on gold-bearing quartz veins, exploration has identified a unit of gold-bearing schist (Tyrell, 1907, MacKenzie et al., 2007a). The presence of gold is localised to the QMS Member (described in section 4.2.1.2.5) along the Lone Star Ridge and may provide an additional source for placers.

This section describes the features of mineralised locations within the LSSA (Figure 4-8). These include, historic gold mines, gold-bearing schist and mineralised zones that represent a cluster of gold-bearing veins.

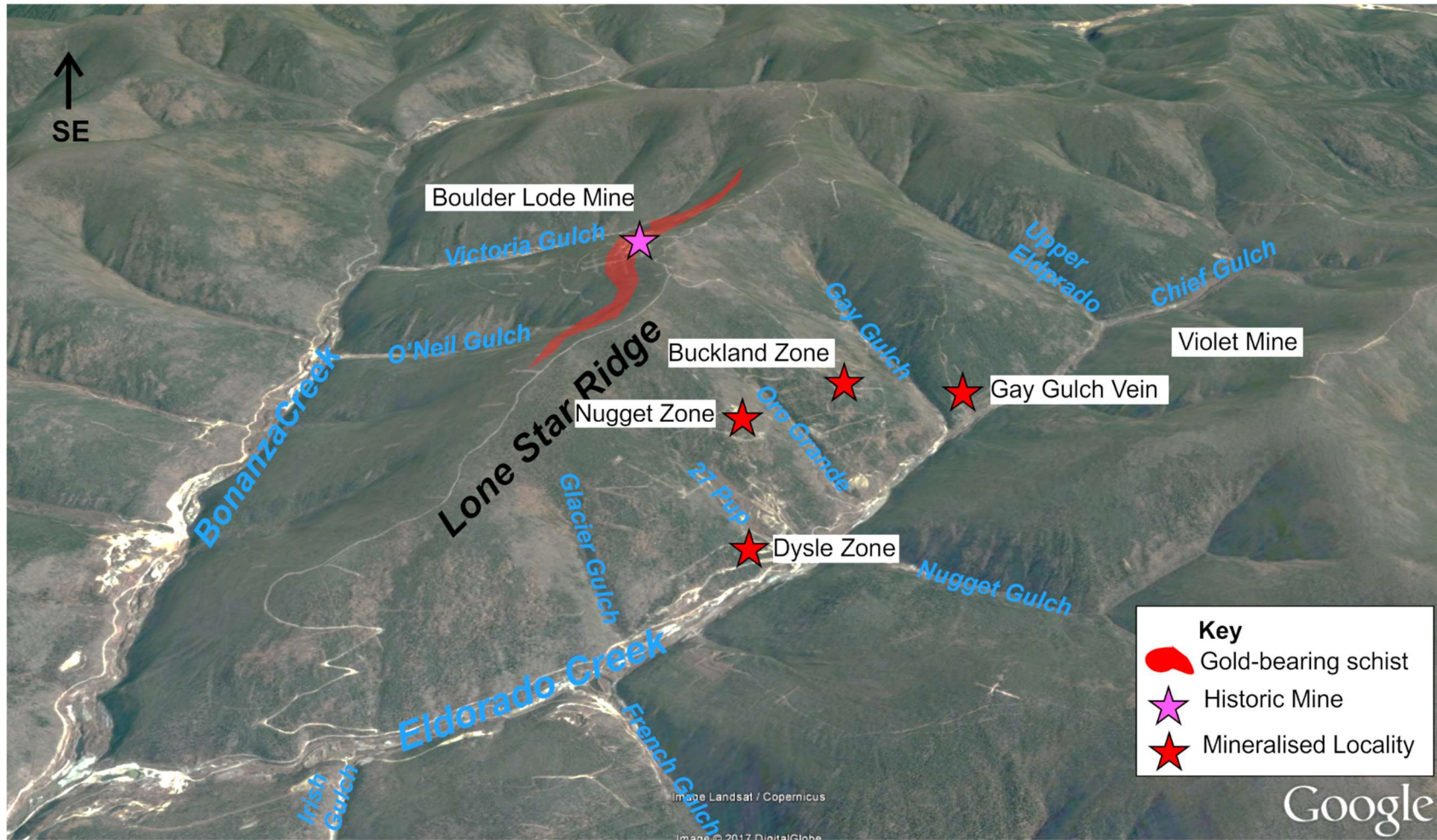


Figure 4-8 : Historic mine and gold occurrences that form the basis of this PhD project marked on a google Earth image of the LSSA.

4.3.2.1 Boulder Lode Mine

The Boulder Lode mine is situated on the north-east side of the Lone Star Ridge at the head of Victoria Gulch (Figure 4-2 and Figure 4-8). The occurrence was originally staked in 1897 by Chute, Corthay and Stewart who shafted the ground in 1903 to exploit the veins visible at the surface (MINFILE). In 1909 the Lone Star Company developed an open cut (Figure 4-9), which was 105m long and 10m deep to exploit mineralisation (MINFILE 115O 072). Shafts were sunk below the cut and were linked with a 225m adit that extracted ore to be processed using a 4-head stamp mill (Figure 4-10) with Wilfley table in Victoria Gulch. A tramway connected the processing in Victoria Gulch to the mine building at Boulder Lode (Figure 4-11) (MINFILE 115O 072). By 1914 an estimated 7650 tons of rock had been mined and is estimated to have produced an average grade of 5.7g/t (Archer Cathro 1979), which at the time was worth \$25,000. Attempts to reopen the mine failed due to financial uncertainty and a lack of investment as a result of the First World War and Great Depression (MINFILE 115O 072). Gold-bearing quartz veins are exposed in the open cut and dip steeply and shallowly to the northeast (Liverton. Pers comm). Oxidation of pyrite in veins permitted gold extraction through simple crushing and gravity separation (MINFILE 115O 072). The nugget effect meant that grade estimation was challenging and drove exploration for additional sources of gold. The historic miners discovered gold in a unit of sulphide rich rock that was below the weathering horizon; however, extraction of gold from fresh pyrite was challenging and resulted in poor recoveries (MINFILE 115O 072).

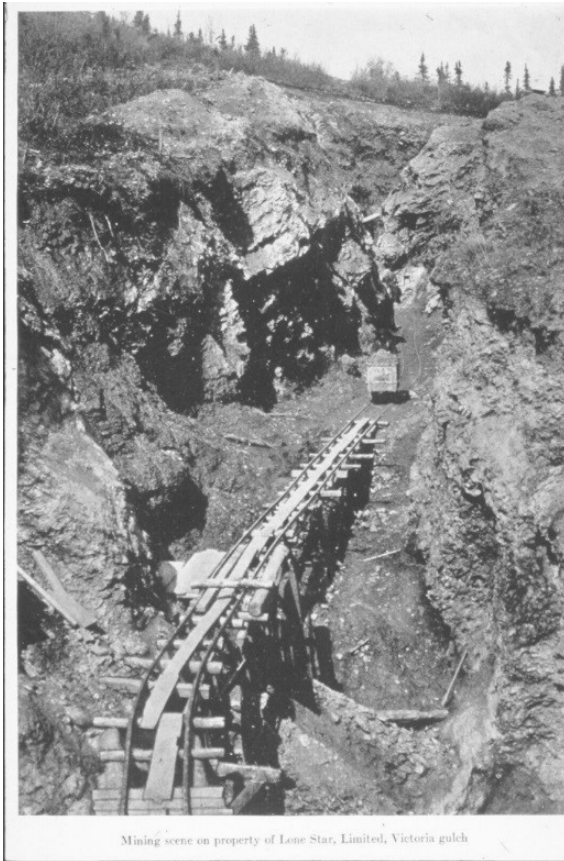


Figure 4-9: Ore being **extracted** from Boulder Lode open cut in 1912.



Figure 4-10: 4- headed stamp mill located on Victoria Gulch. Image taken by T.Liverton in 2007.

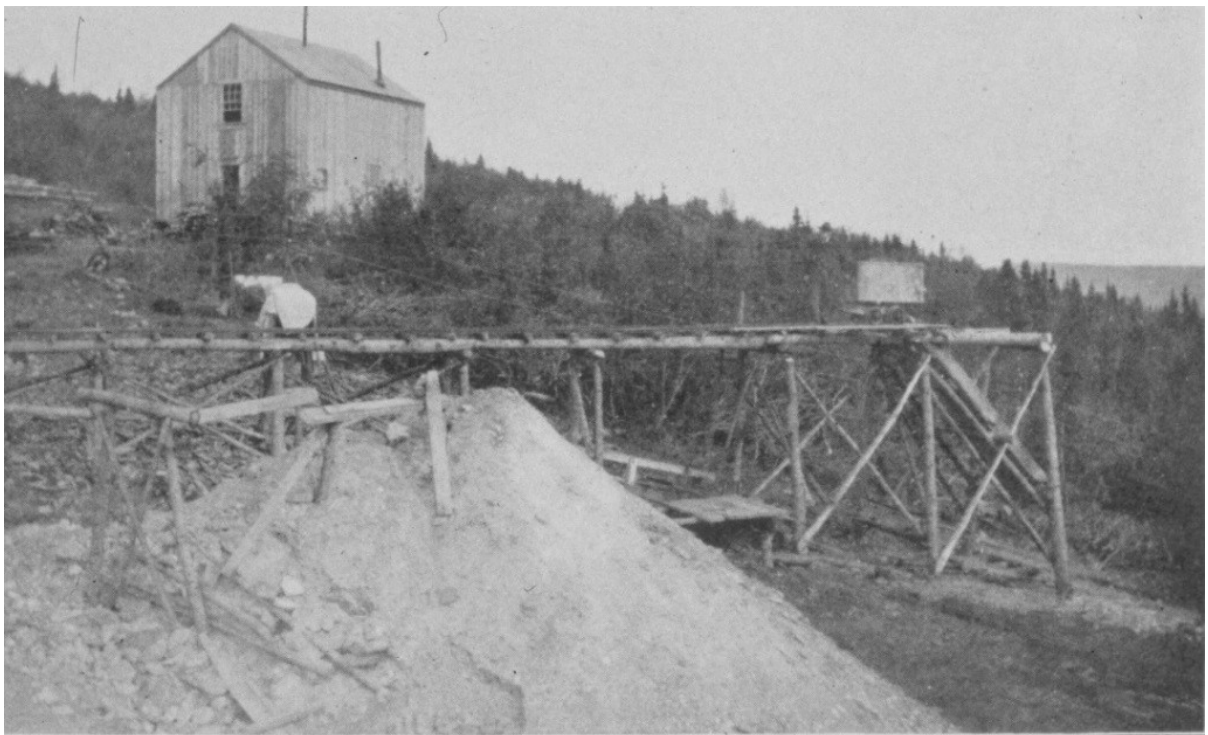


Figure 4-11: The head of incline at the Boulder Lode mine in 1912.

4.3.2.2 Violet Mine

The Violet mine is located in the southwest of the LSSA (Figure 4-8) within the Sulphur Creek Orthogneiss Member (Figure 4-2). The mine was first staked by A.E Bendin, who formed Violet Mining Company in 1907 (MINFILE, 2015). A considerable amount of development was conducted, which included: three shafts (Figure 4-12); 133m of drifting; an open cut mine; and a tramway down to a processing plant on Ophir Creek to the south-west. A lack of work due to low grades led to the claims lapsing and being re-staked in 1947 by Ophir Mining Syndicate, and again in 1981 by Ebony Resources Limited (MINFILE, 2015).

In 1981 and 1982 the Ebony Resources conducted a geophysical survey of the area alongside soil geochemistry. The claims were subsequently transferred to Silvercrest Resources Corporation in 1983 and eventually became part of the Lone Star Property which included Boulder Lode Mine and the Lone Star Ridge.



Figure 4-12: Violet mine shaft and trenches in 1907.

The mineralisation at Violet is hosted in a number of discordant barite-quartz veins (D₄), which cut the Sulphur Creek Orthogneiss Member (Liverton, 2011).

Drilling provided grades from 2.1g/t to 24.7g/t Au over widths of 1-25m. Mortensen et al. (2007) identified a separate set of barren veins composed of orthoclase, biotite, and quartz that are interpreted to be pegmatites. U-Pb crystallisation ages provided preliminary ages of 250Ma and are interpreted, by Mortensen et al. (2007), to have formed in the Late Permian at the same time as the overlying Klondike Schist Formation. The veins have historically been interpreted to be related to mineralisation however, are much earlier than mineralised discordant (D₄) veins.

4.3.2.3 Buckland Zone

The area was first staked in 1898 and is located on the northern slope of Gay Gulch Creek (Figure 4-2 and Figure 4-8) covering an area of ~1km² (MINFILE 1150 077). The zone comprises a series of discordant (D₄) quartz veins that are hosted in Quartz Chlorite Mica Schist (Figure 4-2). The mineralisation is typically coarse nuggety gold (up to 3mm) that has provided grades in grab samples up to 242g/t. A bulk sampling program collected 12,302kg of vein and wallrock material to liberate gold (Table 4-1) and provided an average grade of 0.576g/t for the Buckland Zone (Nelson, 2007).

Table 4-1: Klondike Star Mineral Corporation results of bulk sampling program.

LOCATION	NU OF BULK SAMPLES	WEIGHT (KG)	AU G/T
BOULDER LODGE MINE	8	21,773	0.517
DYSLE ZONE	2	5,176	1.156
BUCKLAND ZONE	2	12,302	0.576
NUGGET ZONE	5	10,253	4.841

4.3.2.4 Dysle Zone

The Dysle Zone is located at the bottom of Glacier Gulch (Figure 4-2 and Figure 4-8) and is a zone of irregular, discordant (D₄) quartz veins hosted in the Meta-Rhyolite Member (Figure 4-2). Vein-wallrock relationships are very sharp with en-echelon vein arrays (Figure 4-13), described by Allan et al.

(2013). Wolff (2012) describes the veins as having coarse grained, elongate crystals of quartz with occasional vugs that are filled with bladed or fine-grained quartz. The results the 2007 bulk sampling program produced an average gold grade of 1.156g/T (Table 4-1).



Figure 4-13:En echelon vein array in large boulder from the Dysle zone, described by Allan et al. (2013).

4.3.2.5 Nugget Zone

The Nugget Zone covers approximately 1km² close to the upper reaches of the Oro Grande Gulch (Figure 4-2) (Liverton, 2011). Kennecott Canada Incorporated conducted exploration in 1994 that provided anomalous gold in soil which was trenched to uncover mineralisation. A total of 10253kg of material from the Nugget Zone was sampled for gold producing a gold grade of 4.g/t (Table 4-1).The veins form a series of shallow-dipping, discordant (D₄) veins that are hosted in Quartz Mica Schist and Quartz Chlorite Mica Schist (Figure 4-2) (Liverton, 2011). Visible gold is present in limonite, oxidised from pyrite, and occurs in the margins of veins. The quartz veins vary in thickness from 0.1-1metre with a variety of textures that are described by Wolff (2012).

He describes quartz vein textures that have a primary phase of elongate quartz growth (Figure 4-14), which is post-dated by brecciation and deposition of fine grained anhedral quartz (Wolff, 2012).

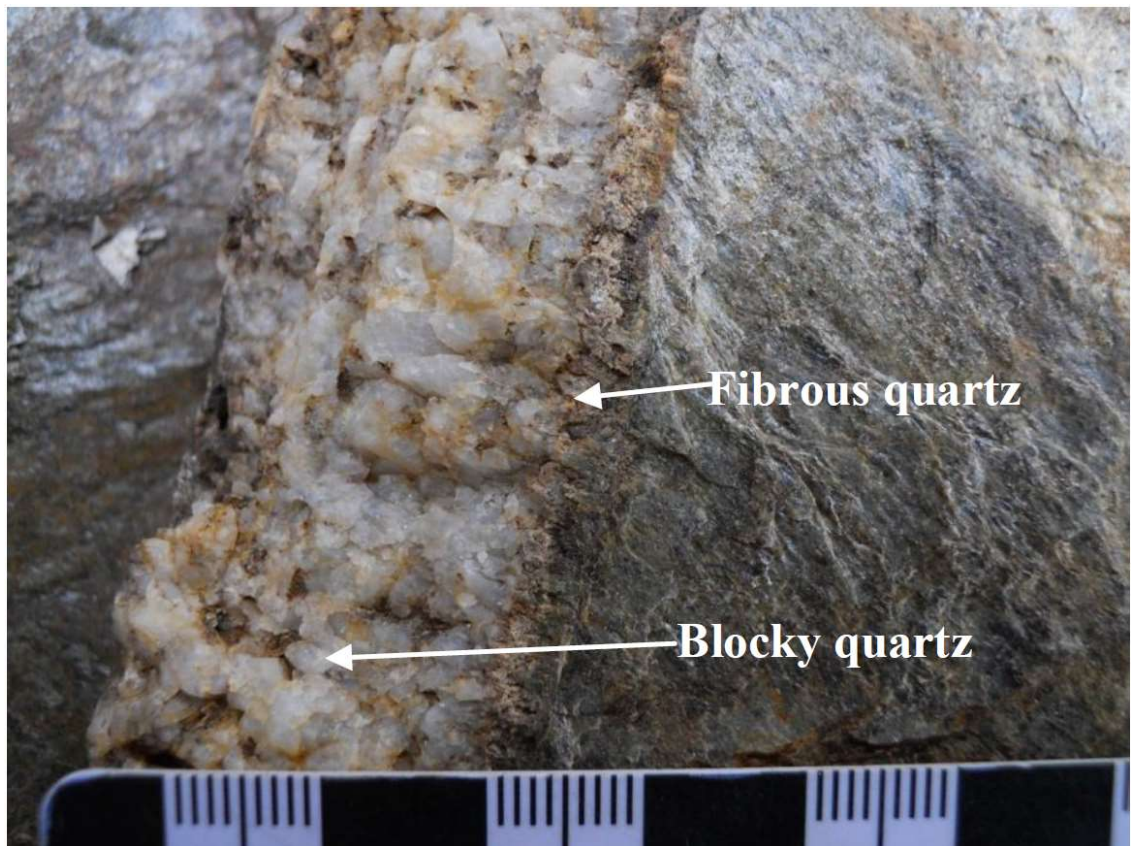


Figure 4-14: Fibrous quartz at margin of vein with blocky infill from the Nugget Zone (Wolff, 2012).

4.3.2.6 Gay Gulch Vein

Veining on the southern slope of Gay Gulch creek, near the confluence with Eldorado Creek (Figure 4-2), was discovered through gold anomalies in soil samples that exceeded 500ppm (Liverton, 2011). Trenching uncovered a series of pyritic discordant (D₄) quartz veins hosted in Quartz Augen Schists (Tallman, 2015). Drilling by Klondike Gold Corporation in 2015 intersected bonanza grades of 420g/t over 0.5m and centimetre scale visible gold (Figure 4-15).

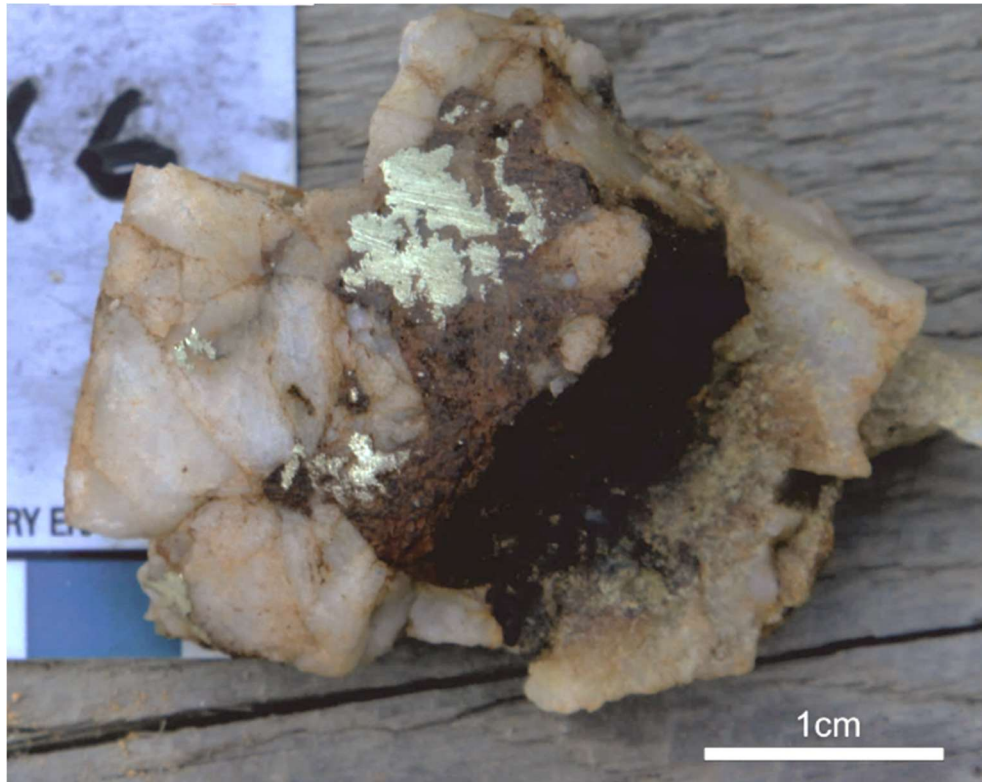


Figure 4-15: Visible gold from drill core hosted in oxidised pyrite.

4.3.2.7 Gold-bearing schist (QMS Member)

Gold in a unit of the QMS Member, (i.e. without quartz veins), has been identified along the Lone Star Ridge proximal to the Boulder Lode mine. Gold in schist is observed elsewhere in the KGD, such as Hunker Dome, but associated with sulphidation in mafic schist around gold-bearing quartz veins (Friedrich and Hoymann, 1992). However, in the LSSA gold is localised in the QMS Member that can be traced 600m along the Lone Star ridge (Figure 4-8) (Knight et al., 1999b). Gold grades of several grams per ton have been recorded and is associated with disseminated, euhedral pyrite and spotty chlorite-carbonate alteration.

Gold in schist was first identified in the early 1900s during the mining of the Boulder Lode (MINFILE 115O 072). Crushing of sulphide rich material using a stamp mill failed to recover adequate and reproducible grades (described in section 4.3.2.1 (MINFILE, 2015). Klondike Gold Corporation and Klondike Star Corporation provided confirmation of the presence of gold in schist during exploration in 2006 and 2007. MacKenzie et al. (2007) sampled a mineralised

interval in detail and discovered that elevated grades were consistent and not a result of the nugget effect (Figure 4-16). The study also highlighted that gold mineralisation associated with quartz veining had elevated elemental arsenic whereas the gold in schist did not (MacKenzie et al., 2007a). This led to a proposal that there were two styles of gold mineralisation: i) gold associated with discordant quartz veins, and ii) gold associated with schist. MacKenzie et al. (2008) suggests that the gold in schist may be syngenetic in origin and formed in association with the small lenses of sulphides, described by as a VMS.

Mortensen (2011) conducted a study using litho-geochemistry to distinguish different lithologies (described in section 4.2.1.2.4). Multi element geochemical analyses was available for 27 drill holes from 2005 that are located proximal to Boulder Lode mine and along the Lone Star ridge.

Gold mineralisation is specifically associated with the Quartz Mica Schist Member, which is identified by its elevated manganese and phosphorous but depletion in lanthanum and thorium (Mortensen, 2011). Mortensen ascribes these elements to be associated with the original lithology rather than any hydrothermal overprint and illustrates the differences by plotting P/La versus depth to interpret different lithologies (Figure 4-17).

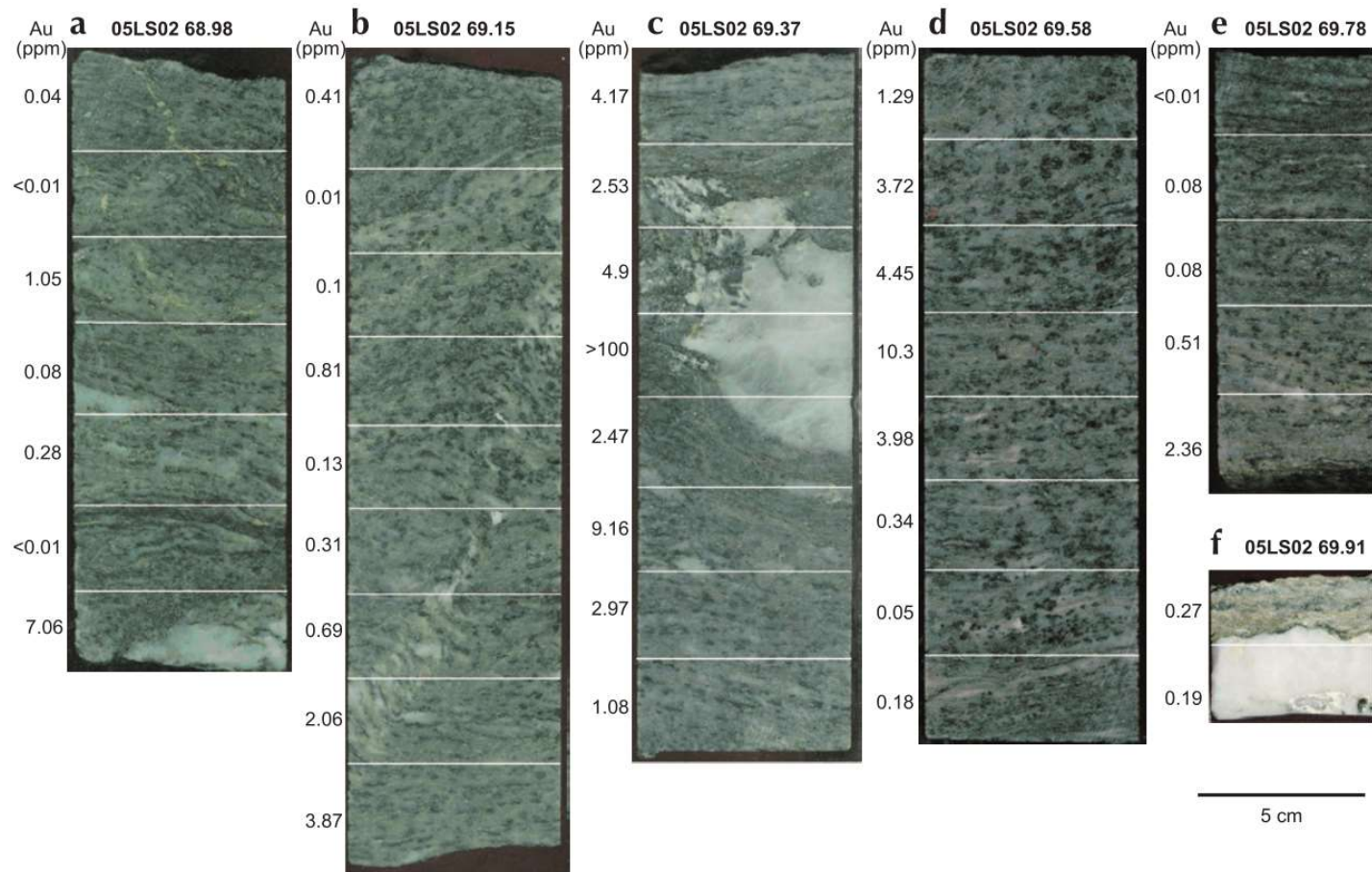


Figure 4-16: 1 metre interval (69-70m) from drill hole 05LS02 sampled by MacKenzie et al 2007. White lines separate samples that were measured for gold content shown in ppm.

Discrimination between the Meta Rhyolite Member and Quartz Mica Schist Member, as described in section 4.2.1.2.4 and 4.2.1.2.5, provides an unbiased method of classifying rock type. The chemo stratigraphic marker horizon shows that the gold-bearing schist (QMS Member) forms a shallow dipping synform bounded by a Meta Rhyolite Member.

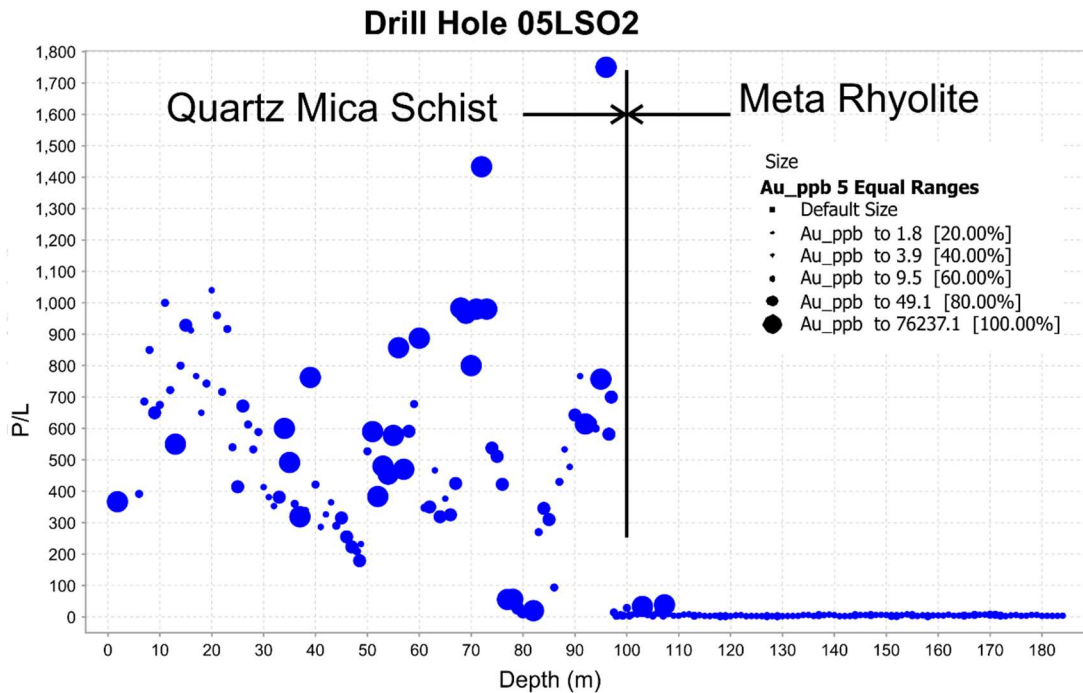


Figure 4-17: Gold is enriched in unit of Quartz Mica Schist that is identified by the elevated P/La compared to Meta Rhyolite.

4.3.3 Placer-Lode Relationships

Exploration over the last century has failed to discover a major bedrock gold resource in the KGD, despite the presence of over 20 million ounces of gold recovered from placer deposits. A lack of glaciation in the KGD has resulted in extensive landscape degradation and the formation of rich placer deposits that have a source constrained by the drainage boundary. The Lone Star area represents an ideal area to establish the relationship between placer gold and a bedrock source due to extensive placers (~7 Moz), numerous bedrock sources (including Boulder Lode mine) and the confined geographic area (180km²).

Chapter 5 describes how the features of native gold mineralogy can be used to understand exploration and mineralisation processes. Establishing a link between placers and lode sources was first discussed by Tyrell (1907) who

identified morphological similarities. Knight et al. (1994) were the first to investigate the chemistry of gold and identified chemical signatures that linked placers with lode source. The results of the research highlight the potential for further un-identified sources of gold in the area (Knight et al., 1994).

A technique of investigating signatures of gold known as *microchemical characterisation* (discussed in Chapter 5) was applied to gold in the LSSA by Chapman et al. (2010a, b). The research identified two types of gold in the LSSA according to the alloy content of the gold (Chapman et al., 2010a). Chapman et al. (2010a, b) further subdivided into sub-types according to the presence of mineral inclusions within the gold (Type 1a-g and Type 2a-b). The distribution of the different types indicated that Type 1 was associated with bedrock sources on the Lone Star ridge with a systematic increase in Ag away and towards the Violet Ridge in the south-west. Chapman et al. (2010a) proposed a single zoned hydrothermal system, which was centred at Lone Star ridge.

The confined geographic area of the LSSA provides an ideal area to investigate variation within a mineralising system. Although other areas in the KGD lack the bedrock sources found in the LSSA the technique of microchemical characterisation to identify placer-lode relationships was shown to be widely applicable.

The composition of gold in bedrock sources is linked to the composition of gold in placers; however, the volume and tonnage of mineralised occurrences fails to account for the amount of gold in placer deposits. A mass balance calculation is tentatively made to estimate the richness of the eroded ore body. Calculations have taken into account the 180km² and estimated the total tonnage of material according a range of schist density and proposed erosion levels. The results show a range from 0.19-0.44g/T for the eroded material that assumes an even distribution across the area. Although this mass balance calculation is crude it suggests that an extremely rich gold deposit may have once existed prior to erosion. It is challenging to reconcile how rich it would have been but raises the question whether there is any further bedrock mineralisation. Chapter 10 provides a renewed theory on sources for the extensive placer gold and revisits the implications for further bedrock mineralisation in the LSSA.

Table 4-2: Estimated grades of eroded schist in the LSSA.

	1km erosion	2km erosion
2.5g/cm ³ Schist	0.44g/T	0.22 g/T
2.9 g/cm ³ Schist	0.38 g/T	0.19 g/T

4.4 Discussion and summary

The understanding of geology and mineralisation in the LSSA has been informed by over a century of mineral exploration and placer mining. Improvements in geological understanding and exploration techniques has led to numerous different interpretations by companies and academics.

The most recent geological interpretation has differentiated the complex relationships of different schist units in the area. These units have undergone multiple episodes of deformation with gold-bearing quartz veins hosted in D₄ angular kink folds.

The ability to trace continuous lithologic boundaries in drill core and outcrop is challenging due to a lack of clear compositional changes and conformable layering. Multiple generations of deformation, a lack of exposure, and deep weathering all make geological mapping extremely challenging for much of the LSSA. Mortensen' 2013 map is a compilation of over 20 years of work in the LSSA and the classifications often have nomenclature that is based on lithogeochemistry rather than lithological features. This makes differentiating the lithologies challenging for those unfamiliar with the area. The map lacks any post-metamorphic features, such as Cretaceous and Eocene volcanics and intrusive units. The map has a bias towards the interpretation of minor schist intervals and may not be reproducible elsewhere due to the difficulty in recognising distinguishable lithological features.

Exploration has been ongoing in the LSSA since the Gold Rush in 1896 with yet no major hard rock discovery. The exploration techniques by early prospectors focussed on shafting and trenching through thick cover to find quartz veins. The prospectors' simple *pick and shovel* exploration strategy led to a number of discoveries across the region, but lacked geological understanding to

differentiate between barren metamorphic quartz (related to D₃) and mineralised discordant quartz veins (related to D₄) (Liverton, 2011).

The mineral localities described in this chapter represent the most significant in the LSSA; however, there are many other small gold-bearing veins within the area that share the same characteristics. Gold-bearing veins occur in zones that lack continuity and have variable grade that produces a significant nugget effect when sampling. The effect of inconsistent gold particle size in samples led to an underestimation of ore reserves and has been a problem for numerous companies in the LSSA. Klondike Star Mineral Corporation undertook a bulk sampling programme between 2005 and 2007 (Table 4-1), that involved the collection of a number of 10-ton vein and host rock samples across the area (Nelson, 2007). Gold was recovered from bulk sample material on site using a ball mill and gravity separation facility (Nelson, 2007). The bulk samples produced reproducible grades compared to sporadic and often inaccurate chip sample results (Liverton, 2011).

The exploration strategies employed by successive companies have been planned according to an assumed model. Gold-bearing quartz veins have been the focus of exploration; however, the presence of a gold-bearing schist provides a low-grade bulk tonnage target. Identification of disseminated gold at the Boulder Lode Mine was first discovered in the early 1900s (described in section 4.3.2.1) but was only extended during drilling by Klondike Star Mineral Corporation in 2007.

The Eldorado and Bonanza creeks represent the richest placer deposits in the KGD and continue to be exploited by local placer miners. These miners have valuable information and knowledge regarding bedrock outcrop and gold mineralogy that is often ignored by exploration companies.

A comprehensive exploration strategy that incorporates the geology, quartz veining, gold in schist, placer deposits and geomorphology of the LSSA is required. The current study will synthesise information from these different sources in order to illuminate the nature and genesis of gold mineralisation at Lone Star.

Chapter 5 The Mineralogy of Native Gold

5.1 Introduction

Gold is an element, metal and mineral, which display a variety of unique properties. In nature, gold occurs as a native metal, forming an alloy with silver, but also with other elements such as copper, palladium mercury and copper (Boyle, 1979). Native gold exhibits a range of distinctive mineralogical features such as: crystal form, shape, size and composition (Hough et al., 2009).

The mineralogical features of gold can be utilised to provide information regarding relationships between placer and lode deposits. This approach is highly relevant to the LSSA where only a limited amount of bedrock sources are identified, whereas the extensive and well constrained placer deposits are documented extensively (Knight et al., 1994, Chapman et al., 2010a). Correlation of mineralogical signatures from hypogene and placer sources has been used by Chapman et al. (2010a) to inform on the hydrothermal conditions responsible for mineralisation in the LSSA. The composition of native gold is intrinsically linked to the environment of formation and can be used to interpret hypogene processes.

This PhD project applies recent advances in studies of gold mineralogy to undertake a coupled micro-textural and geochemical study of the nature of bedrock and vein-hosted lode gold in the LSSA.

This chapter outlines the various mineralogical features developed in native gold and provides a discussion of how these can be interpreted to inform mineral exploration and ore forming processes.

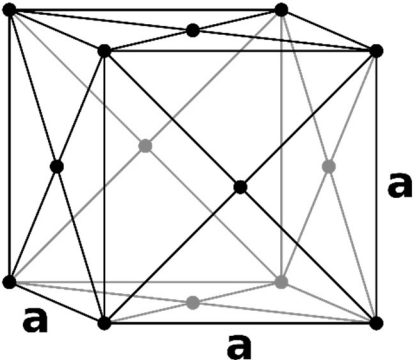
5.2 The features of native gold and associated processes

Gold is a metal that has a distinctive yellow colour, is dense, soft, malleable, ductile and is a good conductor (Table 5-1) (Boyle, 1979, Butt and Hough, 2009). It has a very high melting point (1064°C) and has a face-centred cubic, close packed atomic structure (Table 5-1) (Weinig, 1960, Boyle, 1979). Gold most

commonly forms an alloy with silver but also forms with copper, iron, nickel, platinoids and a number of other elements (Fisher, 1945, Boyle, 1979). Gold's rarity and unique properties make it a valuable commodity that has been coveted for over 5000 years (Butt and Hough, 2009). Metallurgists, minters, goldsmiths and jewellers have applied their understanding of these properties for a variety of purposes (Butt and Hough, 2009).

The natural occurrence of gold displays a variety of properties and features that are described in this section.

Table 5-1: Properties of gold

Symbol	Au (Latin <i>aurum</i>)
Atomic number	79
Atomic mass	196.96655amu
No. neutrons	118
Electrons per shell	2, 8, 18, 32, 18, 1
Abundance	Earth's crust ~1.3ppb Iron meteorite: 1ppm Seawater: 0.0005-0.01ppb
Crystal System	Face-centred Cubic, close packed 
Melting point	1065.43°C
Boiling point	2807
Hardness	Mohs: 2, Vickers HV: 25

5.2.1 Crystal form and crystallography in native gold

Native gold occurs in a variety of habits as; cubes, hexagons, dendrites (Figure 5-1A), wires and octahedra (Figure 5-1B) (Boyle, 1979, Francis, 2004). The variety of crystal forms are a result of the 60° twin law that results in branching crystals or repetition to form wires (Francis, 2004). The various forms of gold can be investigated by characterising the internal crystallography of gold. This technique can illuminate grain growth and formation processes; however, has mostly been neglected with studies focussing on external morphology. One of the first to adopt this approach was, Liversidge (1897), who investigated the interior of gold by sectioning and etching a 9.94-ounce nugget and revealed a polycrystalline texture of large, straight crystals (Figure 5-2) (Liversidge, 1897). The work of Liversidge (1897) was mostly forgotten until Petrovskaya and Fastlovichh (1955) presented the results of a long-term study of detrital gold in Russia where particles had granular or polycrystalline textures. These textures were investigated further by Hough et al. (2007) in 30 gold nuggets ranging from 1g->8kg with an aim to elucidate their origin. The results were combined with quantitative microstructural analysis that revealed the nuggets to all have polycrystalline textures of large grains with straight boundaries separated by 60° twins (Hough et al., 2007). The texture is interpreted by Hough et al. (2007) to be annealing twins because of thermal recrystallisation (Humphreys and Hatherly, 2004b). The annealing process involves the solid-state diffusion of atoms to destroy dislocations and recrystallize in an ordered structure (Humphreys and Hatherly, 2004c, Hough et al., 2007). Hough et al. (2007) described how hand worked, heavily deformed gold anneals at 300°C and suggests that in nature that it may occur in temperatures $>250^\circ\text{C}$.

A



B



C



D



Figure 5-1: A- Dendrite, 3.5cm wide branching crystal from California; B- Octahedron, 3.7cm high skeletal crystal from Chihuahua, Mexico (Francis, 2004); C- Wire like gold crystals (left is 1.2cm) that are flattened during transport from the 60 Mile River, Yukon Canada (Mauthner, 2004); D- Alluvial gold octahedron from Gold Run Creek that, Yukon, Canada that has been flattened (Mauthner, 2004)



Figure 5-2: A 9.94-ounce nugget sectioned and chemically etched to reveal internal crystal structure (Liversidge, 1897).

5.2.2 Morphology and shape of detrital gold

Golds' density and resistance to weathering mean that it is concentrated into rich alluvial and eluvial deposits after liberation from a bedrock source. Additionally, golds' softness and malleability mean that hammering and deformation during transport can alter the primary crystal significantly (Figure 5-1C and D) (Townley et al., 2003). Although morphological change occurs during transport in alluvial and eluvial deposits many of the original features, linked to their bedrock equivalents, are preserved (Liversidge, 1897)

The most common crystal forms of gold in placers are scales, plates and nuggets; however, rare examples of dendrites, wires and hoppers are preserved (Figure 5-1C and D) (Boyle, 1979). The largest masses of gold form nuggets that are defined, by Hough et al. (2007), as gold weighing >1 gram or measuring >4 millimetre. These are typically recovered from alluvial and eluvial deposits, with

the largest example being the Welcome Stranger nugget from Ballarat, Victoria, Australia, which weighed 2217 ounces (Hough et al., 2007).

5.2.3 Composition of native gold

Native gold forms a variety of alloys, most commonly with silver, which are intrinsically linked to their environment of formation. Analysing these compositions has improved due to advances in analytical procedures which are described below.

5.2.3.1 Alloy composition

Gold is almost never found as a pure element, which was recognised as early as 79 A.D. by Pliny the Elder who stated, “in every species of gold there is a proportion of silver, in some one tenth part, in others a ninth”. The association of silver in gold is due to its similar atomic radius and when the alloy content is greater than 20wt% is referred to as electrum (Fisher, 1945, Boyle, 1979).

The ratio of Au in an alloy is referred to as *fineness* ($1000 \times \text{Au}/(\text{Anurag})$) and was first systematically recorded from natural gold by Fisher (1945). Fineness was noted to vary considerably over small areas in placer deposits and with depth or lateral extent in mines (Fisher, 1945). The variation in fineness can be used to inform exploration and mineralisation, which is described in section 5.3. A problem with traditional studies of fineness is that they typically measure processed gold from a mine, which can incorporate Ag from other minerals (Boyle, 1979). The advent of the electron microprobe led to direct analysis of native gold, which provided much more accurate analysis (Antweiler and Sutton Jr, 1970, Lantsev et al., 1971). This technique provides non-destructive and quick analysis of large numbers of gold particles (Lantsev et al., 1971, Boyle, 1979). Quantification of minor alloying elements such as Cu, Pd, Pt and Hg were routinely recorded within populations of native gold (Townley et al., 2003, Chapman et al., 2009, Chapman et al., 2010a, Chapman et al., 2017)

Research has sought to analyse trace proportions of elements in gold and employed the use of LA-ICP-MS. This style of analysis has mostly focussed on tracing the origin of gold bullion for forensic purposes rather than for economic geology (Watling et al., 1994). Outridge et al. (1998) investigated the trace element composition of populations of gold to generate a ‘signature’; however,

their results focussed around development of a methodology rather than the implications. Many studies have investigated the trace element distribution in gold and include Sie et al. (1996), Guerra and Calligaro (2004), Crawford (2007) and Velasquez (2006). The application of using gold alloy composition to interpret hypogene processes is discussed in section 5.3.2.

5.2.3.2 Alloy heterogeneity

Although the majority of native gold particles have homogenous internal alloy compositions a number of particles exhibit compositional heterogeneity. Most commonly this is displayed in the form of varying proportions of Au and Ag.

The presence of gold rich rims, as shown in Figure 5-3, in alluvial particles, was first observed by McConnell (1907) and later described by Boyle (1979). The rims have variable thickness, are almost pure gold and mantle lower fineness gold on the interior (Boyle, 1979). Knight et al. (1999a) report that almost all alluvial gold particles display rims from the KGD, whereas Stumpfl and Clark (1965) observed that rims are absent in alluvial gold particles that are Au-Pt alloys from southeast Borneo. Although gold rich rims are relatively common in alluvial gold they are absent from all lode gold particles (Boyle, 1979).

Various hypotheses are provided to explain heterogeneity in gold particles which are broadly divided into those that favour silver depletion (Petrovskaya and Fastlovichh, 1955, Knight and McTaggart, 1986, Hough et al., 2007) and those that support gold addition (Reith et al., 2010, Rea et al., 2016). The theories responsible for gold addition, outlined in section 5.2.4, develop crystalline gold on the surface of gold particles; however, are mostly responsible for minor volumes of gold. The systematic observations of gold rims in placer and palaeo placers favour a theory of silver loss (McConnell, 1907, Fisher, 1945, Desborough, 1970). Groen et al. (1990) provides the most recent summary of potential processes that could influence the loss of silver and describes a mechanism of self-electro refining. This process involves the dissolution of Au and Ag in oxidising surface waters, leaving the surface of the alloy negatively charged (Groen et al., 1990). Gold reprecipitates by reduction but silver remains in solution and is lost from the surface (Groen et al., 1990).

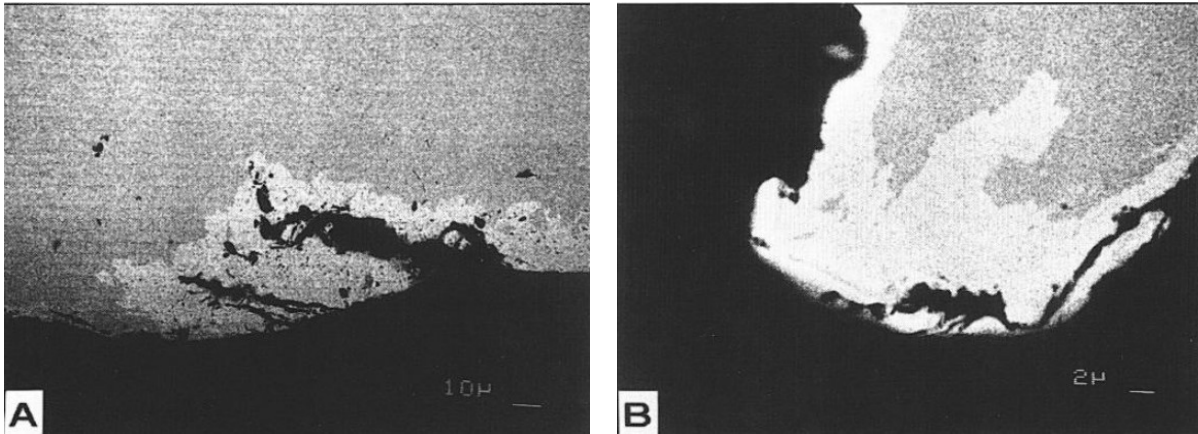


Figure 5-3: Back-scattered electron image of placer gold particles from Klondike Gold District. Lighter greyscale reflects higher Au content (Knight et al., 1999a). **A-** Evidence of smearing influences gold rim. **B-** Gold rim impregnates particle.

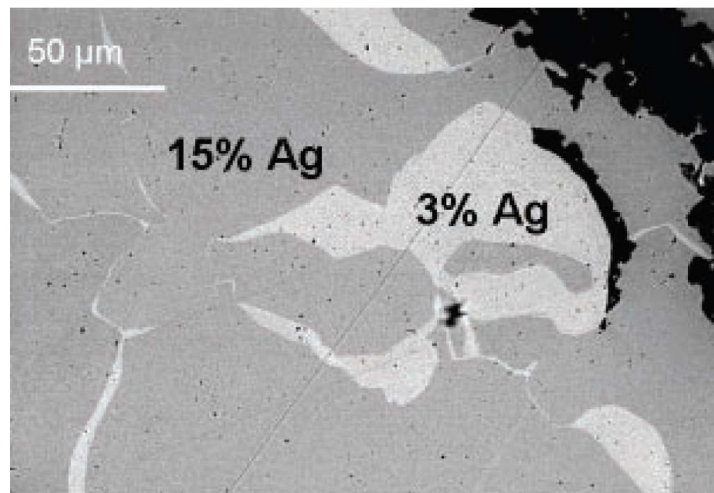


Figure 5-4: Back-scatter electron images showing gold rich heterogeneity on interior of gold grain from nugget in Queensland, Australia (Hough et al., 2009)

Gold rich heterogeneities are also observed on the interior of particles as thin pure gold veinlets (Figure 5-4). They display sharp boundaries with the gold alloy and are cut by the gold rich rims in alluvial gold (Petrovskaya and Fastlovichh, 1955, Knight et al., 1994). Petrovskaya and Fastlovichh (1955) describe the features in gold from Siberia, as pure gold veinlets that have a thickness less than 10 microns. The same features are described from gold in the Cariboo District of British Columbia (Knight and McTaggart, 1986) and the KGD (Knight et al., 1994). Crystallographic data from gold nuggets in Australia, reported by Hough et al. (2007), led to a proposal that the gold rich tracks are developed due to silver depletion along grain boundaries (Knight et al., 1999a, Hough et al., 2007). Hough et al. (2007) proposes that silver depletion is a natural analogue of depletion gilding (Grimwade, 1999), used in metallurgy to enrich the surface

gold by the dissolution of silver from the surface. The formation of gold rich tracks are thought to occur during supergene processes of gold from in situ mineralisation whereas gold rich rims occur in alluvial environments.

Gold also displays rare evidence of more diffuse alloy heterogeneity. Knight et al. (1994) describes rare examples, from the KGD, of low fineness on the interior of gold particles. Chapman et al. (2011) presented further evidence heterogeneous gold that has diffuse boundaries of different alloy content (Figure 5-5).

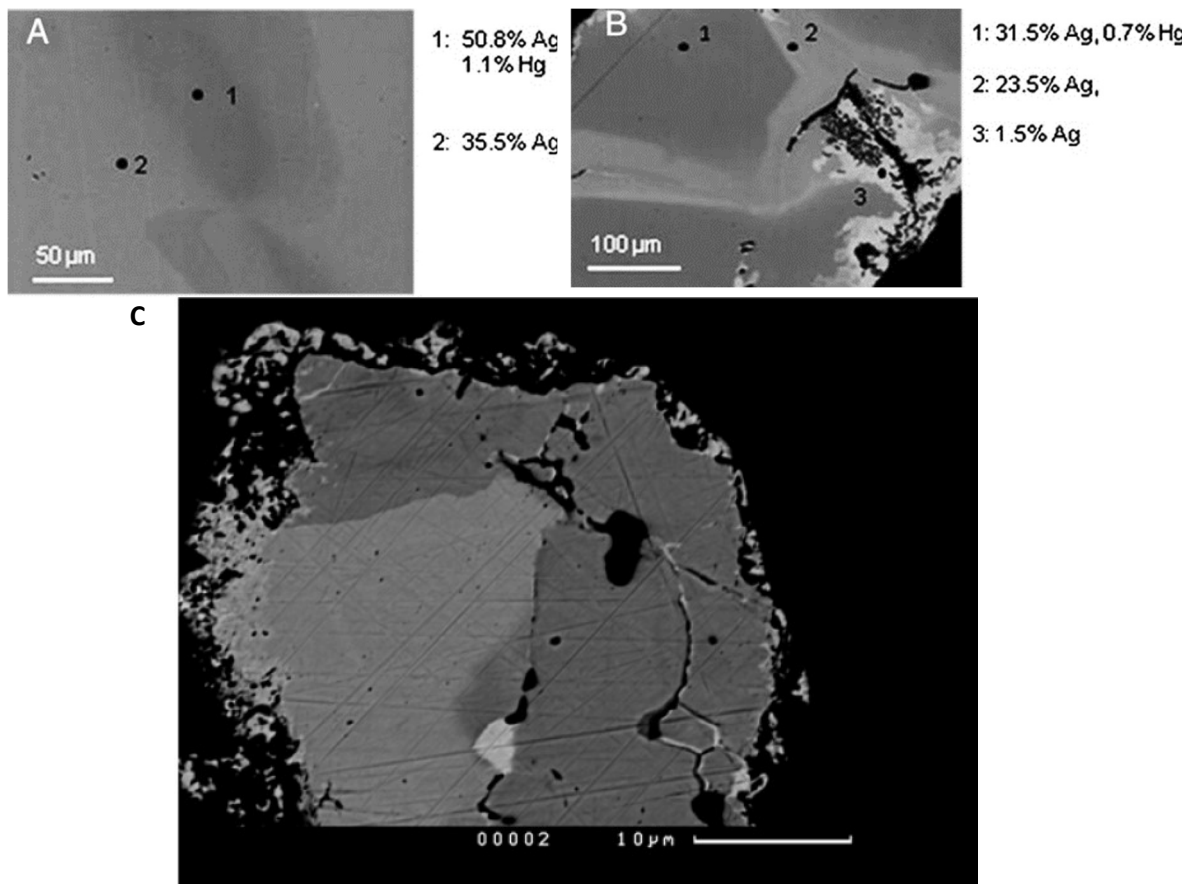


Figure 5-5: A and B- Subtle alloy variation from Eureka, Yukon (Chapman et al., 2011). C -Ag (and Hg) rich Au mantling Au-Ag alloy. Violet Mine, Klondike, Yukon, partial Au rich rim surrounds both alloys (Chapman et al., 2010a)

5.2.3.3 Mineral inclusions

The presence of mineral inclusions within native gold were first used to discriminate between populations of different gold by Desborough et al. (1971). The formation of inclusions in native gold are interpreted to be coeval with gold and therefore provide an indication of the environment of formation (Chapman et al., 2000a). There are a wide variety of inclusions recorded within native gold

such as; gangue minerals, pyrite, magnetite, chalcopyrite, tellurides, galena and many others (e.g. Figure 5-6). Mineral inclusions vary in morphology with some having euhedral or subhedral shape (e.g. Figure 5-6a) whereas others form rounded blebs (e.g. Figure 5-6b).

The systematic recording of mineral inclusions has been combined with alloy composition of native gold to produce a microchemical signature (Leake et al., 1997, Chapman et al., 2000a). Chapman et al. (2000a) and Chapman et al. (2000b) report gold and their associated inclusions from many localities across Great Britain and Ireland to understand regional metallogeny. The technique of recording inclusions has also been investigated in Malaysia (Henney et al., 1994), Zimbabwe (Naden et al., 1994), Ecuador (Potter and Styles, 2003) and the Dawson Range of the Yukon (Chapman 2010a, b, 2014 and 2016). The application of this technique to inform mineral exploration and ore forming processes is described in section 5.3.2.

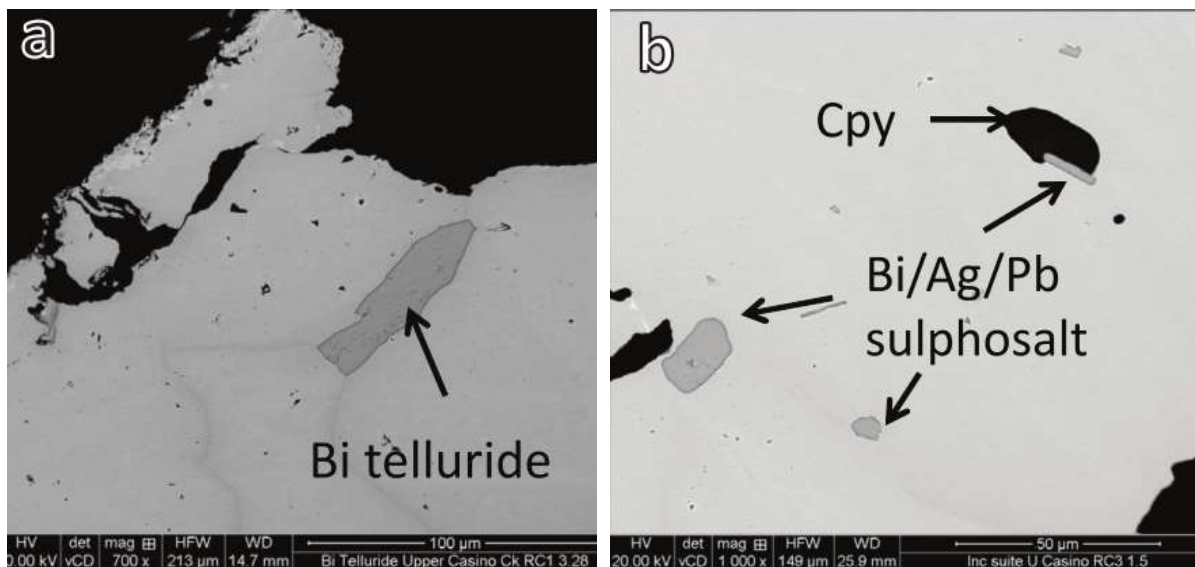


Figure 5-6: Examples of gold inclusions from Casino porphyry, Yukon (Chapman, 2014) **A-** Gold particle with angular shaped inclusion of Bi telluride. **B-** Chalcopyrite (Cpy) and a range of other sulphosalts in gold particle.

The collection of a large population of gold particles is required from each location to build up a representative sample suite (Chapman et al., 2010a). Chapman et al. (2010a) describes that inclusions are recorded in only 5% of gold

particles in the KGD and therefore requires at least 60 particles to produce a robust microchemical signature from each sample location.

5.2.4 Modification and textural variation of native gold

Gold is susceptible to weathering and modification at the Earth's surface that results in various surface features and textures. These features develop in specific environments according to chemical conditions such as those found in laterites. The surface textures of gold particles collected from a laterite in Brazil were investigated by Grimm and Friedrich (1990) who observed pits and vermiform fractures. Elsewhere cracks on the surface of gold nuggets are reported by Cabral et al. (2008) and Hough et al. (2007) (Figure 5-7). These surface features are thought to be a result of weathering, in which Au and Ag is dissolved in supergene environments (Grimm and Friedrich, 1990). Webster and Mann (1984) discusses the importance of chloride, thiosulphate and organically derived complexing agents that may transport gold under surface conditions.

Micron scale gold is observed on the surface of gold particles and in layers of colloform goethite structures infilling cavities that have formed after oxidation of pyrite (Grimm and Friedrich, 1990). Thiosulphate, produced during oxidation of pyrite, complexes both Au and Ag and, is described by Stoffregen (1986), to be responsible for small scale remobilisation and precipitation of the metal.

Another texture present in lateritic profiles, reported by Larizzatti et al. (2008), is dendritic and prismatic gold in the Fazenda Pison area of the Amazon, Brazil. The presence of euhedral gold crystals is recorded by a number of authors in regolith and in cavities of oxidised material (Mann, 1984, McCready et al., 2003, Hough et al., 2008). Similar textures of gold are observed in goethite, kaolinite and cracks in pisoliths from saprolite deposits in Western Australia (Figure 5-8) (Anand et al., 2016).

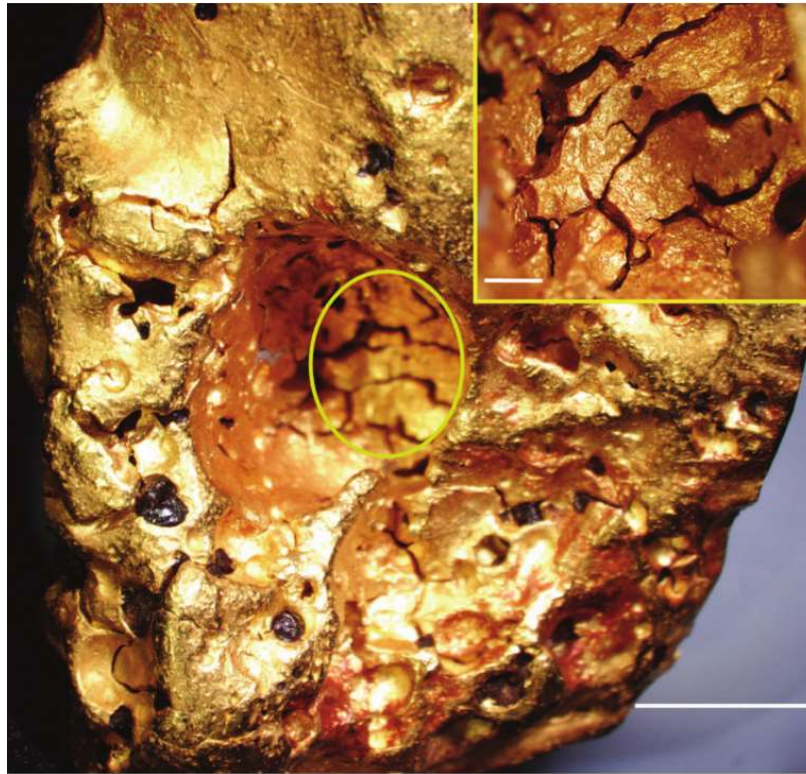


Figure 5-7: Surface cracks of eluvial gold nugget collected from Australia (Hough et al., 2007)

The formation of crystalline gold in the surface environment is described by various authors to be a result of authigenic growth (Clough and Craw, 1989, Krupp and Weiser, 1992, Craw et al., 2017). An example of this process is presented in New Zealand, whereby gold augmentation is thought to generate centimetre scale nuggets (Clough and Craw, 1989, Craw et al., 2015, Craw et al., 2017). The mechanism of *nugget growth* is described by Craw et al (2016) to occur in carbonate-bearing lithologies that generate relatively high pH groundwater.

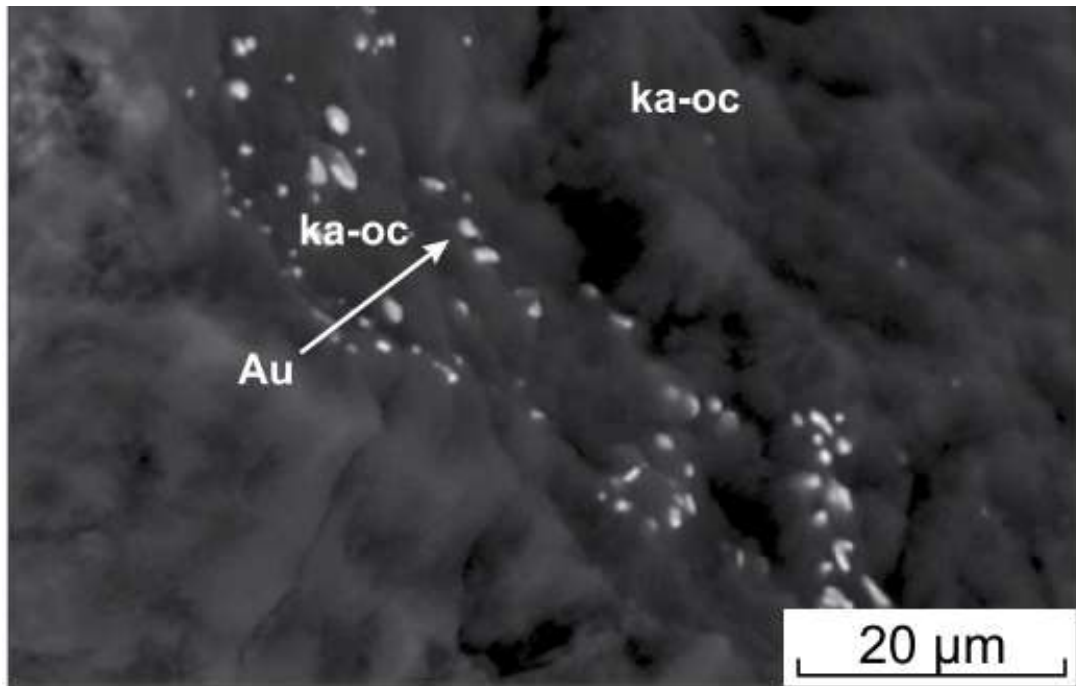


Figure 5-8: Micron scale gold within kaolinite-organic (ka-oc) material from Western Australia (Anand et al., 2016)

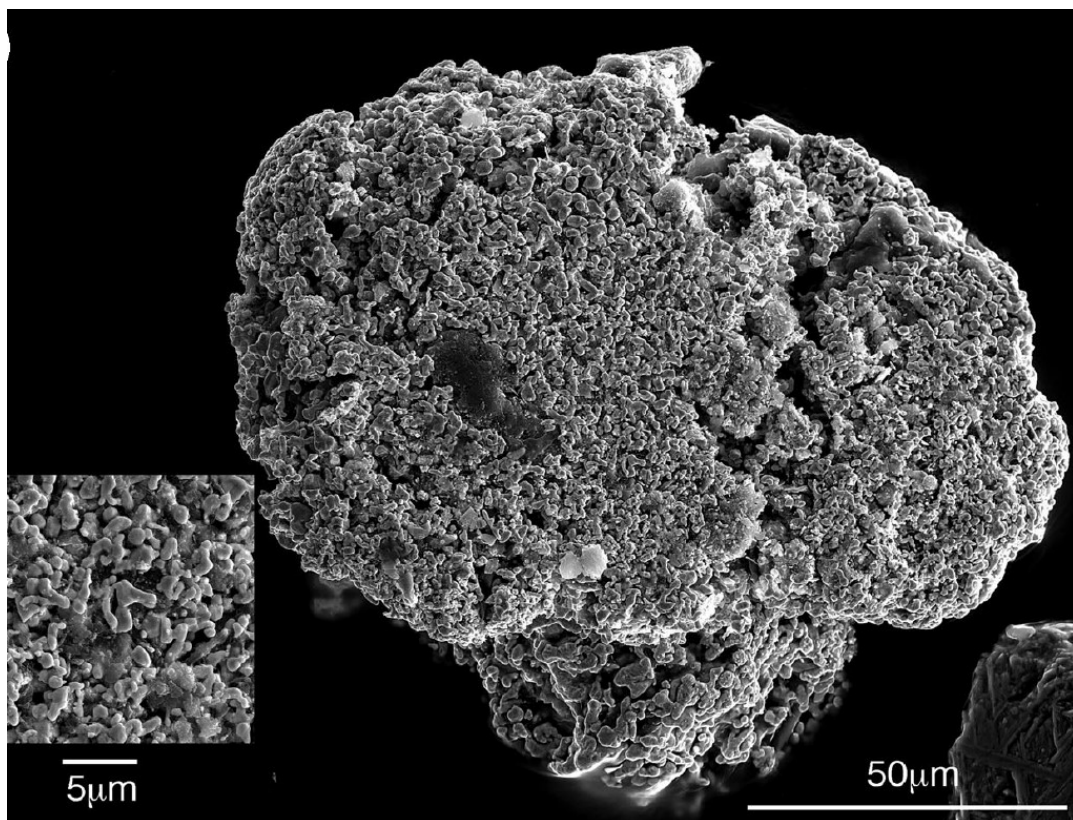


Figure 5-9: Nano-particulate gold surrounding gold particle from Australia (Rea et al., 2016).

Reith et al. (2013) and Rea et al. (2016) provide evidence of nano-particulate gold surrounding gold particles (Figure 5-9). The samples are collected from a variety of eluvial and alluvial environments and comprises of pure Au with crystalline sizes from 0.01-5 μm (Rea et al., 2016). Reith et al. (2010) suggested that gold nanoparticles, formed as biofilms accreted onto pre-existing gold to generate the gold rich rims observed in alluvial deposits.

5.3 Using gold mineralogy to understand ore deposits and mineral exploration.

The previous section has provided a review of the features present in native gold. An understanding of the processes that govern the formation of the mineralogical features is important to understand when identifying hypogene sources.

The presence of gold in streams and soils has been exploited as a resource but its resistance makes it an important indicator mineral for exploration. Establishing a link between placer deposits and hypogene sources has been neglected by geologists over the years. A method of 'prospecting back to source' is complicated by numerous factors, which are discussed in this section.

5.3.1 Morphological variation and transport distance

Establishing a bedrock source for gold in alluvial environments has been employed by prospectors for centuries. The processes are complicated due to the potential of multiple gold sources, erosion of the source and drainage evolution, such as glaciation, that modifies the transport history (Chapman et al., 2000b)

The correlation of placers and lode gold is typically established using a variety of mineralogical features which includes the morphology of native gold. This technique has been applied to deposits around the world and includes; examples from New Guinea (Fisher, 1945), USA (Groen et al., 1990), the UK and Ireland (Leake et al., 1997), Argentina (McCready et al., 2003), Yukon, Canada (Knight et al., 1999b), New Zealand (Youngson and Craw, 1999), Brazil (Grimm and Friedrich, 1990) and Australia (Mann, 1984).

The effect of morphological change of gold in glacial till was discussed by Dilabio (1991) in an attempt to estimate distance to source in dispersion trains. Knight et al. (1999a) were the first author to provide statistics of the physical features of gold by analysing approximately 2700 particles in the Klondike Gold District. Youngson and Craw (2009) assumed that gold particles would become flatter during transport distance due to hammering and analysed particles according to a flatness index. Townley et al. (2003) described general characteristics of gold particles, such as shape, outline, crystal imprints and mineral associations and produced a table of 3 ranges of distance (Figure 5-10).

Quantitative morphological analysis was greatly enhanced by Crawford (2007), who developed a system of recording three dimensional features of gold particles using software. The software incorporated shape and gradient of stream, as a proxy for energy, to produce estimated transport distances (Crawford, 2007). Wrighton (2013) expanded the technique to combine automation of shaped identification with a study of gold compositions across a number of examples in the Yukon of Canada. The determination of shape modification requires an understanding of initial shape, which, as shown in Figure 5-1, can vary considerably (Wrighton, 2013). The technique required further development to understand processes involved with morphological change. Qualitative observations of morphology, such as those by Townley et al. (2003) in Figure 5-10, are the most effective at establishing whether the origin of alluvial gold is local or distal.

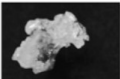
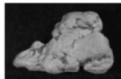
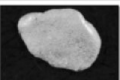
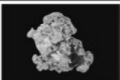
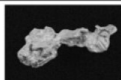
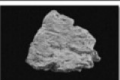
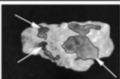
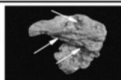
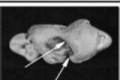
Distance to the source	0-50 m	50-300 m	> 300 m
General shape			
Outline			
Surface			
Primary crystal imprints		Diffuse Evidence	Absent
Associated minerals	Quartz and Fe Oxides 	Fe Oxides 	Limonites 
Flatness index	1-3.6	2.1-6	3.0-7.5

Figure 5-10: Morphology of gold used to inform transport distances from source (Townley et al., 2003).

5.3.2 Compositional studies of native gold

The most effective mechanism of establishing a relationship between placer gold and a hypogene source is through compositional characterisation (Chapman et al., 2000a). This section provides an overview of the method used to characterise native gold and how it is employed to inform hypogene processes.

One of the most common methods for compositional characterisation is gold fineness that first compiled and compared to different deposit types by Fisher (1945). Subsequent studies analysed the composition of alluvial and hypogene gold to inform mineralisation (Badalova and Badalov, 1967, Helgeson and Garrels, 1968, Desborough et al., 1971) and are summarised in detail by Boyle (1979). Morrison et al. (1991) provide a comprehensive overview of fineness data from a range of deposits that modified the classification first outlined by Fisher (1945). Antweiler and Campbell (1977) suggested that gold composition could be used as a vector for mineralisation after noting a systematic increase in Ag with distance from high temperature alteration at the Circle City porphyry in Arizona.

The thermodynamic controls on Au-Ag alloy content were discussed by Gammons and William Jones (1995) in a Au-Ag-S-Cl-H₂O system. The controls of composition are influenced by a number of conditions such as, temperature,

aH^+_{aq} , aHS^-_{aq} , aCl^-_{aq} , Au/Ag in solution and pH. The fundamental controls of Au-Ag composition have been used by Chapman et al. (2010a) and Chapman and Mortensen (2016) to investigate the evolution of orogenic gold systems in the KGD and Cariboo Gold District of British Columbia. Orogenic gold deposits have a narrower range of hydrothermal conditions compared to other styles of mineralisation such as, porphyry and epithermal, which makes interpretation of simple Au-Ag alloy challenging (Chapman et al., 2017).

Alloy data is typically represented as 'cumulative percentile vs. increasing Ag' for each population (Chapman et al., 2000a). The plots allow for direct comparison of populations that may have a different number of particles (Chapman et al., 2000a). The fundamental controls on Au-Ag composition outlined by Gammons and Williams-Jones (1995) suggest that, a single population with a shallow gradient curve (e.g. Figure 5-11), formed under stable mineralising conditions (Chapman et al., 2000a). Steps within a population of gold suggest multiple sources or generations of gold formation whereas a wide range in Ag values suggest temporal variation in conditions (e.g. Figure 5-11) (Chapman et al., 2010a).

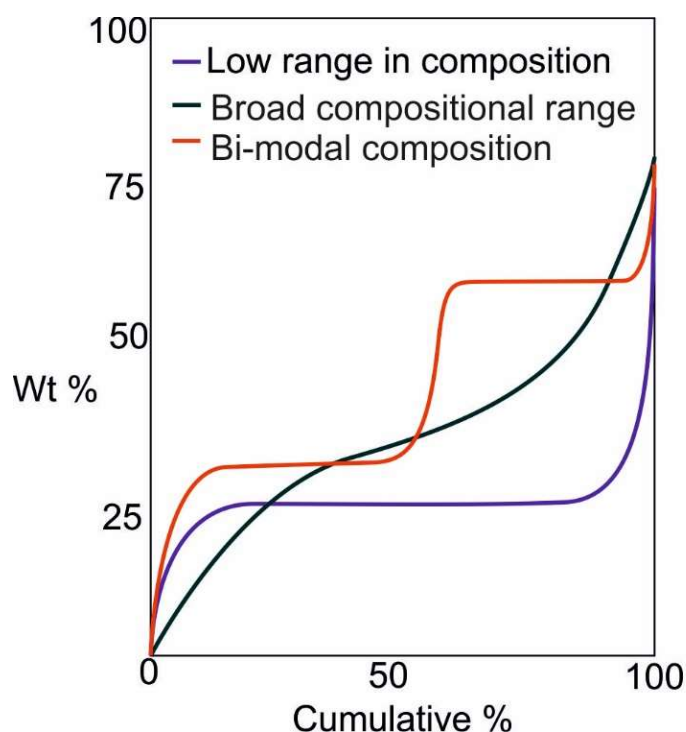


Figure 5-11: A cumulative percentile plot that shows examples of how populations of data can vary.

Although Au-Ag compositions can differentiate populations the identification of minor alloying elements, such as Cu, Pd, Pt or Hg are used as an additional discriminant. The identification of copper within gold alloys was identified from a number of porphyry deposits by Morrison et al. (1991). At Cerro Casals in Chile, Palacios et al. (2001) and Townley et al. (2003) identified variation in copper content of gold alloys associated with alteration and spatial distribution around porphyry mineralisation. The element also forms an alloy constituent in gold from epithermal (Bonev et al., 2002) and orogenic gold deposits (Chapman et al., 2011, Chapman et al., 2016).

Rubin and Kyle (1997) identified Pd in Au-Ag from Grasberg porphyry in Indonesia and used it to investigate gold distribution in placers. Elsewhere Nixon et al. (2004) identified that Pd and lesser amounts of Pt formed as minor alloying elements in Au-Ag particles from alkalic porphyries in British Columbia.

Mercury is commonly investigated as an alloy constituent and forms with gold in orogenic deposits (Chapman et al., 2010a, Chapman et al., 2010b, Chapman and Mortensen, 2016) and with Pd in alkali porphyries in British Columbia (Chapman et al., 2017). Examples of elevated mercury in gold alloys is identified in orogenic gold deposits in the Yukon (Chapman et al., 2010a, Chapman et al., 2010b, Chapman et al., 2011) and in the Cariboo District of British Columbia (Chapman and Mortensen, 2016). Barnes (1997) and Krupp and Seward (1990) discussed the hydrothermal transport of Hg; however, the controls on Au-Ag-Hg formation remain poorly understood (Chapman et al., 2010a)

The application of using mineral inclusions within gold to distinguish the origin of gold was first described by Desborough (1970). The British Geological Survey studied the application of inclusions to inform mineralisation and developed a technique known as 'microchemical characterisation'. The process involves recording the minor alloy composition of gold with any opaque and non-opaque inclusion assemblages within the population to produce a 'microchemical signature' (Leake et al., 1997, Chapman et al., 2000a). The methodology requires large amounts of gold particles to be collected so that groups or types of gold can be identified (Leake et al., 1997). The variety of different inclusions recorded within gold makes it challenging to represent graphically. Inclusions are typically grouped into mineral species (i.e. Sulphides, sulpharsenides and

tellurides) to emphasise relationships or environment of formation (e.g. Figure 5-12).

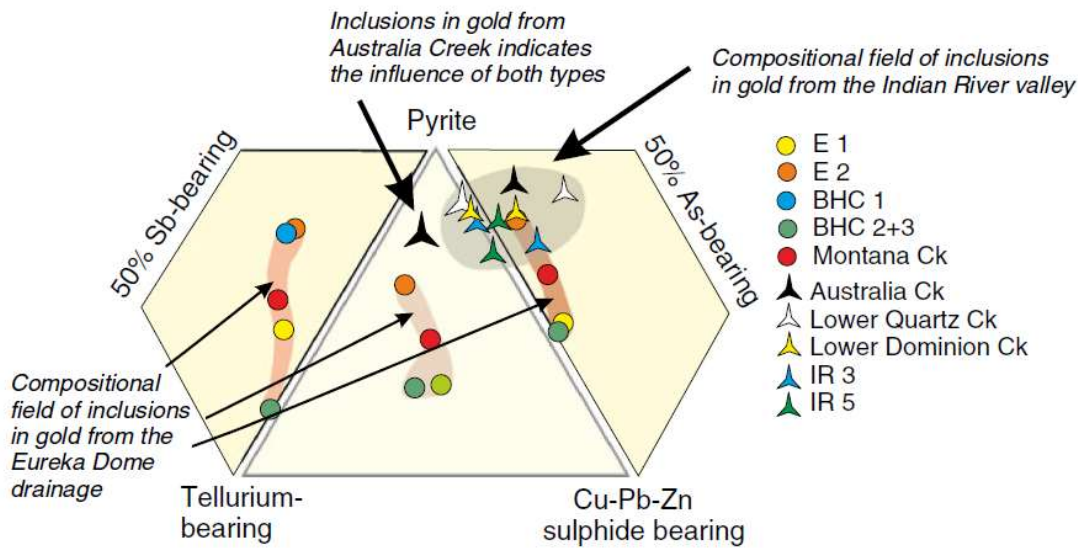


Figure 5-12: An example of mineral inclusions plotted on a ternary diagram from the Black Hills area of the Yukon (Chapman et al., 2011)

The composition of inclusions can also contain multiple, intimately mixed mineral species, such as those in Figure 5-13 from the Yukon (Chapman et al., 2011). These textures suggest exsolution from original mineral after formation due to cooling but provide a valuable indication of the elements present during gold formation (Chapman et al., 2011).

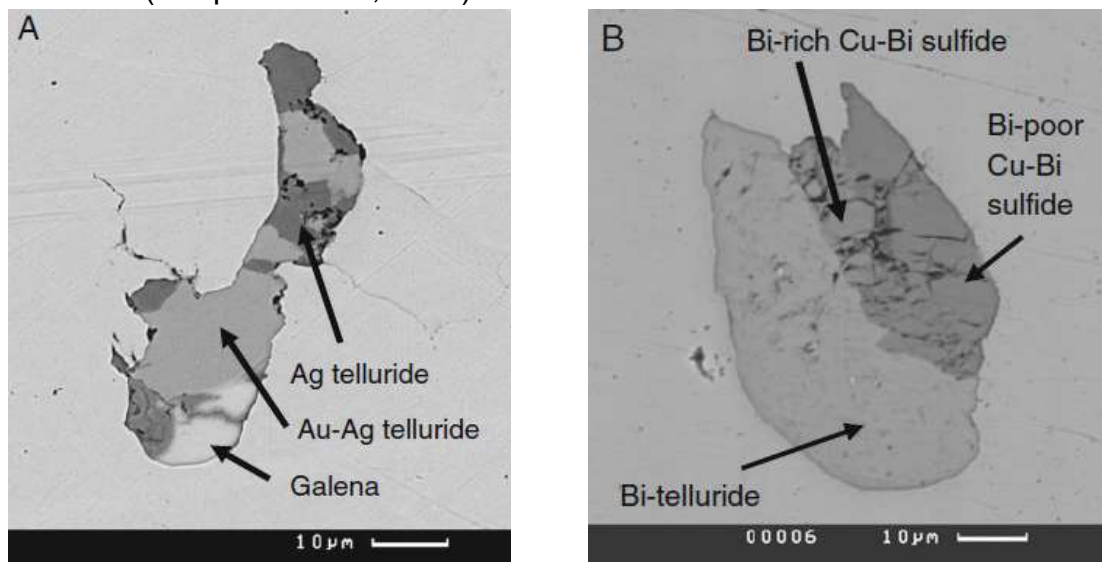


Figure 5-13: BSE images of mineral inclusions within gold. **A-** Galena, Ag telluride and Au-Ag telluride inclusion from Eureka Dome, Yukon . **B-** Bi-telluride and Bi-Cu- sulphide inclusion from the Indian River area of the Yukon

Leake *et al.* (1991) investigated the signature of gold from South Devon by combining observations of palladium bearing mineral inclusions and palladium in gold alloys. Chapman *et al.* (2009) expanded the study to incorporate examples of Au and Pd associations from Australia, Poland, Brazil and the UK. The presence of selenide and telluride inclusions, rather than sulphides, led to the interpretation that conditions during gold formation were oxidising (Chapman *et al.*, 2009). Deposition of gold is interpreted to occur due to reduction of oxidising, low temperature, saline fluids (Leake *et al.*, 1991).

The application of the technique has been repeated to inform mineralisation in Ecuador (Saunders, 1990, Potter and Styles, 2003), Devon UK (Chapman *et al.*, 2009), the Cariboo District, BC and the Yukon, Canada (Chapman *et al.*, 2010a, Chapman *et al.*, 2010b, Chapman *et al.*, 2011, Chapman, 2014, Chapman *et al.*, 2016, Chapman *et al.*, 2017).

More recent research has focussed on the distribution and significance of inclusions within gold related to porphyry environments in British Columbia and the Yukon, (Chapman *et al.*, 2017). The Ag content of alloys varies considerably due to the complex hydrothermal environment but inclusion assemblages have provided an effective mechanism for interpreting mineralising conditions. Calc-alkaline porphyries have a strong Bi-Pb-Te-S signature that are present as Pb-Bi sulphides and tellurides in gold minor Cu alloys (Chapman *et al.*, 2017). The stability of mineral species varies according to alteration stages and transition to epithermal environments (Chapman *et al.*, 2017).

Establishing placer-lode relationships, and interpreting mineralisation processes using the technique of microchemical characterisation, has been shown to be effective on a deposit scale. The technique has also been applied more broadly to studies of regional metallogeny in the Yukon (Chapman *et al.*, 2010b, Allan *et al.*, 2014b) and in Great Britain and Ireland (Chapman *et al.*, 2000b)

5.4 Discussion and summary

The mineralogical features of native gold provide a wealth of information. The preservation of gold in the surface environment due to it being inert, dense and highly malleable mean that crystal form and shape modification have been

investigated in detail. The variety of crystal forms that native gold exhibit makes tracing shape modification challenging. Studying the surface textures of gold has provided valuable information regarding the processes involved in weathering gold. The presence of nanoparticles of gold on particles and in saprolite show that gold complexes and mobilises in the surface environment. However, the volumes of gold involved, which may contribute to authigenic growth, are negligible. The generation of pure rims in alluvial gold particles and gold rich tracks in the supergene environment are dominated by a process of silver loss.

The interior of gold particles preserve primary features that are characterised to interpret the environment of formation. Compositional studies remain the best way of determining the hypogene processes involved in deposition of gold. Developments in analytical processes result in better characterisation of features in native gold and their associations in nature.

Although there are many studies focussed on native gold, there is a lack of information regarding the processes involved in gold crystallisation and generation of large deposits. The application of 'indicator' minerals, such as apatite or magnetite, to inform exploration of porphyry gold and copper deposits, have neglected gold. The persistence of gold in the surface environment and its availability makes it an ideal mineral to investigate ore forming processes.

The LSSA benefits from having extensive placer deposits that have well constrained sources within the Eldorado and Bonanza drainages (Knight et al., 1994). Chapman et al. (2010a) established placer-lode relationships which led to an interpretation that mineralisation was part of a small, gold-rich, orogenic hydrothermal system. Previous research has focussed on defining a microchemical signature (Chapman et al., 2010a) of native gold but lacks characterisation of the features associated with in situ mineralisation. This project provides context to in situ mineralisation and advances the application of chemical and mineralogical studies of native gold by incorporating crystallography. This combined approach to investigate native gold is a novel aspect to this PhD project compared to traditional ore deposit studies.

Chapter 6 Methodology and Analysis

6.1 Introduction

The almost continuous history of placer mining and numerous generations of mineral exploration companies, since the Gold Rush in 1896, has provided over 100 years of research papers and company reports about gold in the LSSA. A number of exploration and academic research projects have informed the approach and methodology of this PhD. A wide variety of samples were already available for study; however, the specific aims of this project (Chapter 1.1) required new samples to be collected.

Sample collection was undertaken independently and alongside Klondike Gold Corporation (KGC) over a total of 13 weeks between 2013 and 2016. The three elements of the sampling program were:

1. Gold and quartz from veining.
2. Gold and schist mineralogy of the mineralised bedrock.
3. Detrital gold collected from alluvial and eluvial settings.

Samples are often prepared by a variety of techniques that can result in numerous specimens from the same sample. This chapter describes the rationale and methodology of collecting, preparing and analysing samples.

6.2 Sample collection

The range of samples, locations and information is summarised in a sample table in the Appendix. Sampling during a number of exploration programs and academic studies has resulted in a variety of different labelling and numbering systems. It is therefore vital that a robust sampling protocol was developed to account for location, year and type of sample. Field samples were generally labelled according to the year of collection, location and number. For example, the first sample collected in 2015 at the Buckland Zone was given the number 15BK01. This section describes the different strategies employed to collect samples across the LSSA

6.2.1 Quartz vein material

A major aim of the project is to characterise the gold-bearing discordant quartz veins in the LSSA. Structural mapping of vein occurrences has been undertaken by KGC that provides a comprehensive overview of the extent of mineralisation. A petrographic study of vein textures was conducted by Wolff (2012), which focussed on the Dysle and Nugget Zone. This study provides detailed descriptions of textures and mineralogy observed at mineral occurrences described in Chapter 4.

Sampling focussed on the collection of vein textures that preserved relationships with wallrock (e.g. Figure 6-1).

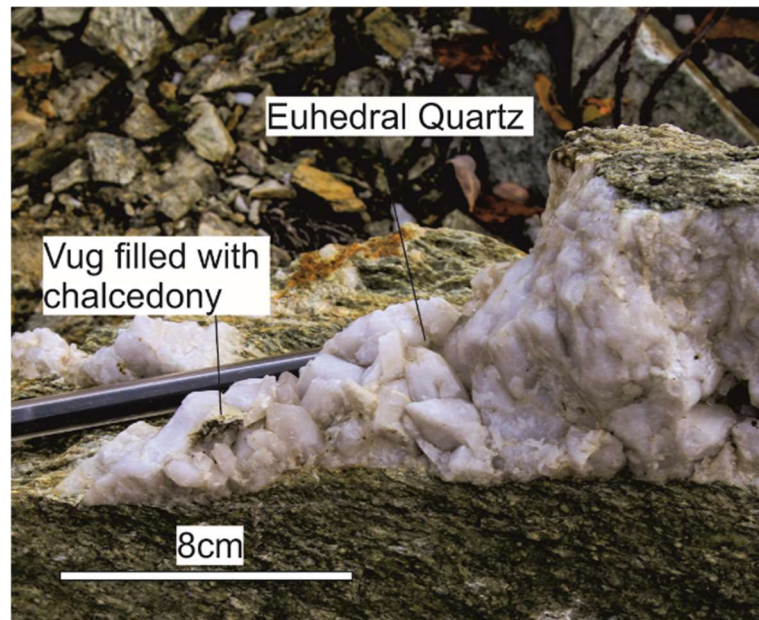


Figure 6-1: Example of quartz textures at Dysle that exhibit wallrock relationships.

6.2.2 Gold in quartz veins

This study aims to characterise the mineralogy of native gold through textural and composition studies. A microchemical signature (defined in Chapter 5) will be developed of gold from bedrock mineral occurrences and provide further detail to the study by Chapman et al. (2010a) that collected 1,163 gold particles from 18 lode sources. Extracting a representative population of gold particles from veins is challenging due to the *nugget affect* that has long been recognised in the LSSA and was first described by MacLean (1914).

Exploration companies have struggled to record consistent grades, which limits the reliability of estimates of ore reserves in the Lone Star area. This reproducibility is a problem for sampling and a range of strategies have been employed to provide a comprehensive study of gold in veins.

The first technique benefitted from existing sample suites of gold liberated from bulk samples (1-10 ton) of vein material, treated in a 10-ton pilot plant operated by Klondike Star Corporation in the Lone Star area from 2005 to 2006 (Nelson, 2007). The grades from this bulk sampling program are provided in Table 4-1. Some samples of gold particles generated in this way have been analysed previously by Chapman et al. (2010a) and were available to the present study.

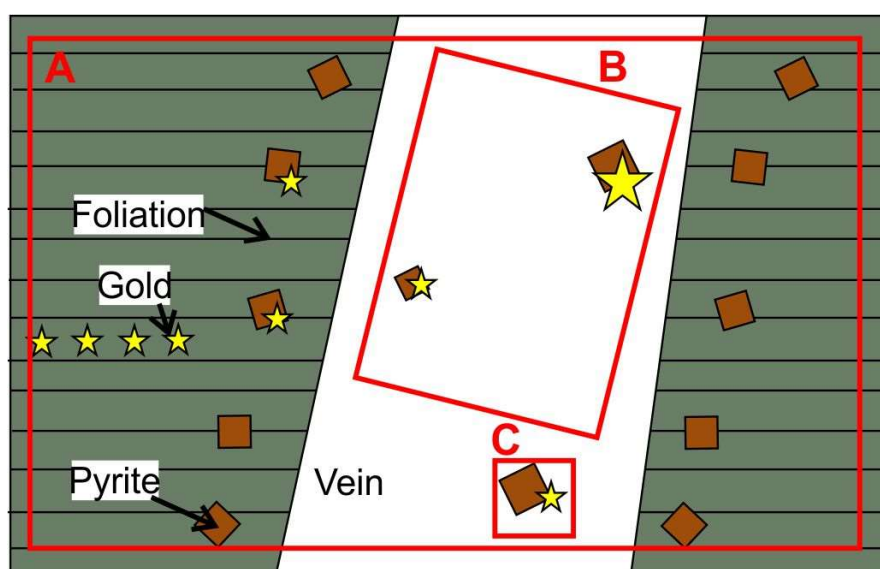


Figure 6-2: A cartoon of discordant quartz vein and the potential source of gold highlighted as stars. **A-** Bulk sampling conducted by KGC crushed wallrock and vein material. Most gold particles liberated but have no context to origin. **B-** Only quartz vein material crushed to liberate gold to provide a comparison to KGC bulk samples. **C-** In situ visible gold preserves the textural features.

The presence of gold in schist at Lone Star raised the possibility that the bulk sampling technique used to liberate gold may incorporate a wall rock constituent (Figure 6-2a). Sampling in 2013 focussed on the collection of vein quartz only (Figure 6-2b) that was subsequently crushed to liberate gold. Selections of vein material were chosen where weathered pyrite and sulphides were evident. Three to four 22 litre buckets were filled with quartz samples from each location and shipped to the University of British Columbia

for processing. The first and second technique of gold liberation assumes that all particles are recovered from the material crushed. However, gold may be too small or present as inclusions within other minerals.

The process resulted in the liberation of 232 gold grains. The crushing of vein material resulted in deformation of gold particles and destroyed the majority of information about in situ mineralisation. Consequently, visible gold was sampled using traditional prospecting at localities where previous exploration by both KGC and KS had indicated grades over 15g/T (Figure 6-2c). Much of the gold collected from samples was found in subhedral milky quartz on oxidised pyrite (e.g. Figure 6-3.). A total of 17 visible gold samples were collected from 5 locations, which provides invaluable textural information for comparison with the populations of gold particles liberated during bulk sampling.



Figure 6-3: Visible gold collected from Buckland Zone (BZ07).

6.2.3 Drill Core

Studying bedrock in the LSSA is challenging due to thick sequences of colluvium and is best exposed through exploration trenches and cuts. However, deep weathering (up to 100m) and surface creep mean that fresh, unaltered lithologies are only observable in drill core. Thirty years of mineral exploration has produced a large amount of drill core, which was available for both inspection and sampling. Examination of drill core permitted characterisation of both unaltered lithologies and mineralised intersections. Mortensen (2011) noted that logging different lithologies in schist is challenging due their similar appearance when unaltered. Inconsistent logging has meant that a large amount of drill core was studied to characterise the different lithologies as described in company reports.

Sampling and investigation of mineralised core focussed on gold-bearing quartz veins and intersections of schist with elevated gold values, identified from assay data and company logs. These intervals were sampled using a diamond core saw to remove visible gold or quartz textures.

MacKenzie et al. (2007a) conducted research into the presence of disseminated gold along the Lone Star Ridge by sampling intervals in drill holes 05LS02 and 05LS09. Their study provided detailed characterisation of a 1m interval that reported average gold grades of 1.2g/t (MacKenzie et al., 2007a). They divided the core into centimetre sections which were sent for multi-element geochemical analysis (MacKenzie et al., 2007a) and these results were used to guide resampling of hole 05LS02 (59-59.5m) at the highest-grade intervals. These samples were compared to others collected from drill hole 05LS27 (69-70m) that was along strike and which had returned comparable grades. The study by MacKenzie et al. (2007) focussed on geochemistry whereas the present study characterised the mineralogy and texture using petrographic techniques.

6.2.4 Gold particle collection

Detailed compositional studies of gold in the Klondike have been undertaken by Knight et al. (1999a) and Chapman et al. (2010a) with a view to elucidating placer-lode relationships (see Chapter 5). Chapman et al. (2010a) investigated 2,777 particles from 27 placer localities and 1163, gold particles from 18 lode sources which are available for the present project. Sampling for this project provided an additional 298 gold grains that focussed on two types of surficial environment: (1) present day drainages close to the source, (2) gold in the alluvial bench gravels of the WCG.

The approach to gold collection varied according to the nature of sample sites, but in general the highest concentrations situated at the base of the sediment were exploited. Sample locations for collection of gold in first order drainages were undertaken in areas of active placer mining, for example gold from Oro Grande Gulch was collected from the base of an excavated placer pit. The basal contact of the WCG and bedrock (Figure 6-4A) provided another ideal sample location.

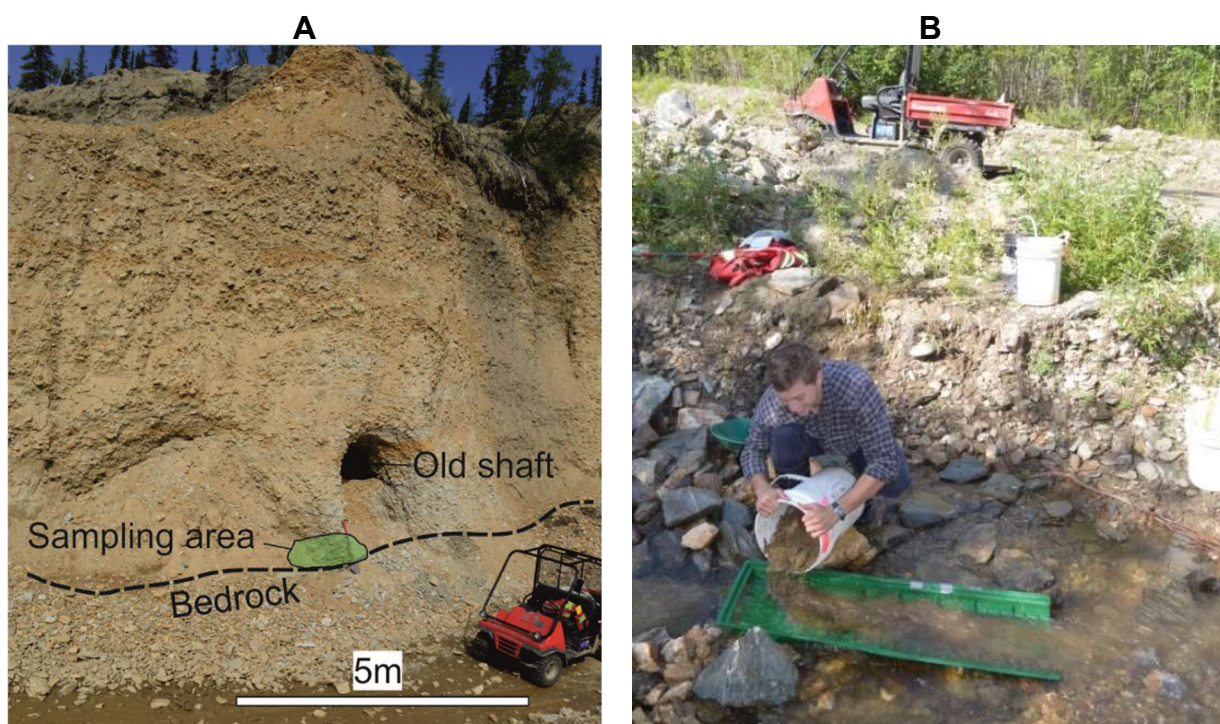


Figure 6-4: A: An image of the White Channel Gravel (WCG). The bench is approximately 30 metres above the present-day French Gulch stream. Samples of gold were collected at the bedrock contact next to historic mine shafts. **B:** Flow of water from Eldorado Creek was modified using rocks to provide the correct flow for the Le Trap™ sluice. A slurry of water and gravel was fed slowly into the sluice.

In most cases, auriferous material was passed through a 1" screen into buckets prior to recovery using a 'Le Trap River Robber' sluice (Figure 6-4b). The use of a portable sluice afforded a far quicker processing option than panning, with no associated loss of recovery (Leake et al., 1997).

The heavy mineral concentrate was further reduced through hand panning to isolate the gold particles. Leake et al. (1997) suggested that around 30 mineral particles are required to produce a robust sample population from each locality. However, Chapman et al. (2010a) highlights a lack of mineral inclusion abundance in the KGD that is vital for distinguishing microchemical signatures. A minimum of 60 particles were collected from each sample location where possible.

6.3 Sample Preparation

The rationale and method of sample collection has been outlined; however, a variety of preparation techniques were required before analysis could be undertaken. The preparation of an individual sample may produce multiple specimens which were labelled separately. For example, the sample 15BK01 was made into a polished block and a thin section which was labelled 15BK01_MG01 and 15BK01_MG02. The methods of preparation are described below and produced specimens of gold particle mounts, polished blocks and polished thin sections (Figure 6-5).

6.3.1 Liberation of gold from quartz vein

Gold-bearing quartz veins unattached to wall rock were transported to the University of British Columbia (UBC) for gold recovery. The samples were comminuted in a two-stage process using a Tm engineering Ltd. Terminator Jaw crusher (material 150-180mm) and a Bico pulveriser disk mill (900rpm) to produce a sand sized feed (74-105 μm). A heavy mineral concentrate was recovered using a Wilfley shaking table and dried under a heat lamp before further separation in heavy liquids to isolate gold particles. The largest particles (5mm x 2mm) recovered had undergone deformation into balls or cylinders during milling.

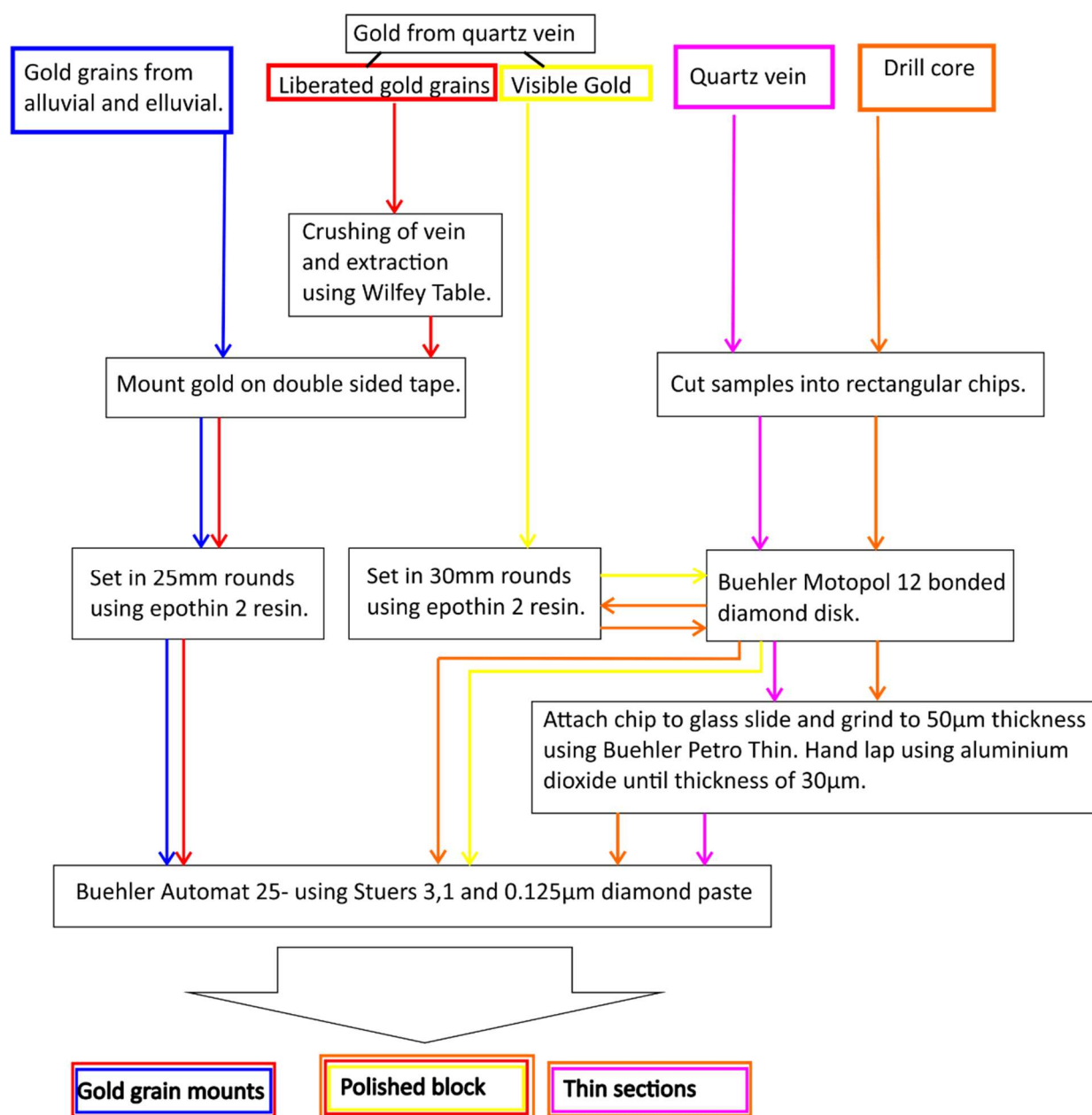


Figure 6-5: Flow chart demonstrating process involved to generate specimens from specific sample types or locations.

6.3.2 Preparation of gold particle mounts

Mounting of gold particles into blocks and polishing is undertaken to reveal their internal characteristics, which is analysed to produce a microchemical signature, as described in Leake et al. (1997). Alluvial, eluvial and liberated vein gold was all prepared via the same procedure.

Gold particles from each sample were dried and separated into groups of roughly similar particle size. These were organised on a rubber eraser with a

scale bar and photographed using an Olympus Zoom Stereo Microscope integrated with Leica Application Suite 10 (LAS) imaging software (Figure 6-6).

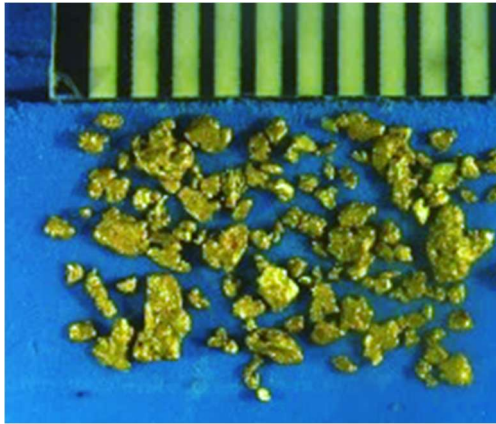


Figure 6-6: Image of placer gold arranged according to size prior to mounting.



Figure 6-7: Gold particles are separated according to size and arranged into rows. The particles were mounted on double sided tape before being set in resin.

The particles were systematically arranged in rows of 5 on double sided adhesive tape fixed to Perspex blocks (e.g Figure 6-7). This was then surrounded by a 25mm diameter mould that was filled with Buehler™ EpoThin 2 epoxy resin at a ratio of 2:1 (resin: hardener) and left to cure for 24 hours, under ambient temperatures. The gold and resin puck were removed from the slide and cleaned with ethanol. Polishing of the puck to expose the gold particles (Figure 6-8) was conducted using Buehler™ Motopol rotating grinding wheel, using 40µm and 10µm diamond-impregnated disks. This operation was undertaken carefully to avoid plucking of the gold particles from their resin host. The samples then were polished further using a Buehler Automat 250 using Struers 3,1 and 0.25µm diamond paste. Times varied from 10-30 minutes with a spinning head of 30 rpm, base of 60rpm and pressure of 2-3lbs.



Figure 6-8: An example of 25mm gold particle mount. Polishing was conducted until the interior of the gold grains was revealed.

6.3.3 Polished blocks

Visible gold, from quartz veins and intervals of drill core, were made into 30mm polished blocks. The internal characteristics of gold were investigated in the same way as the gold particle mounts; however, the textural relationship to quartz and pyrite is preserved.



Figure 6-9: Visible gold from vein cut down to chip prior to mounting in mould and resin.



Figure 6-10: An example of visible gold mounted in 30mm block that has been polished.

Samples were cut to less than 8 cm using a Logitech GTS1 12" diamond saw and reduced further to a size less than 30mm using a Buehler 6" diamond saw (Figure 6-9). A chip capable of fitting into a 30mm cup was prepared with the

gold exposed on the surface. Careful flattening using the Buehler™ Motopol rotating grinding wheel, using 40µm and 10µm diamond-impregnated disks was undertaken prior to positioning within a 30mm puck and addition of Buehler™ EpoThin 2 epoxy resin at a ratio of 2:1 (resin: hardener). The blocks were then polished to reveal the interior of gold (Figure 6-10) using the Buehler Automat 250 using Struers 3,1 and 0.25µm diamond paste. Times varied from 10-30 minutes with a spinning head of 30 rpm, base of 60rpm and pressure of 2-3lbs.

6.3.4 Polished thin sections

Polished thin sections were prepared from samples of quartz vein material, mineralised schist and host rock material. Thin sections were prepared for petrographic analysis to identify in situ mineralogy and textural relationships.



Figure 6-11: An example of a sample that has been cut to a chip ready for mounting and polishing.

The samples were cut down to less than 8 cm using a Logitech GTS1 12" diamond saw and reduced further to a size that could fit on a 48mm x 26mm glass slide using a Buehler™ 6" diamond saw. Careful flattening of the chip was undertaken using the Buehler™ Motopol rotating grinding wheel, using 40µm and 10µm diamond-impregnated disks. The glass slide was prepared by hand lapping in aluminium paste for 10-20 seconds until it was translucent. Buehler™ EpoThin 2 epoxy resin was used to attach the chip to the slide and put under pressure for a few hours on a hot plate. The chip was cut from the glass slide at a thickness of 1mm using a Buehler™ PetroThin Thin-sectioning System. Grinding of the section was achieved by gradually reducing the

thickness in 5 μm increments until the sample was 50 μm thick. Hand lapping using alumina paste was used to achieve an even thickness across the sample until it was around 30 μm micron. The sections were then polished further using the Buehler™ Automat 250 using Struers 3,1 and 0.25 μm diamond paste. Times varied from 10-30 minutes with a spinning head of 30 rpm, base of 60rpm and pressure of 2-3lbs.

6.3.5 Polishing protocol for gold specimens

The internal crystallography of gold particles was investigated through a process of Electron Back Scatter Diffraction, described in the next section, that requires an immaculate fine polish.

Polished blocks and gold particle mounts underwent a process of chemo-mechanical polishing (CMP) where material is etched and removed simultaneously. The process is undertaken by using weighted sample holders on Buehler Vibromat 1 polisher in a solution of colloidal silica in NaOH (SYTON) for 3 hours.

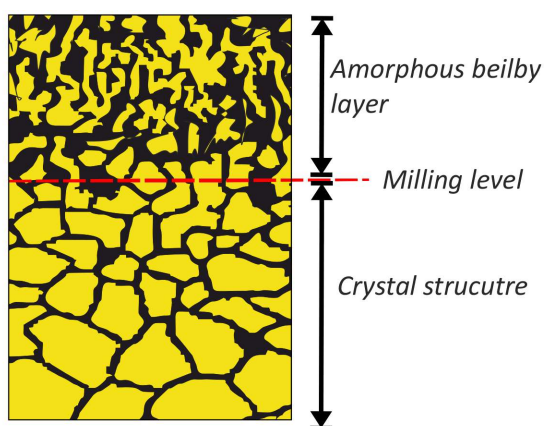


Figure 6-12: Abrasive polishing produces an amorphous damage layer known as the Beilby Layer.

Abrasive polishing techniques, such as CMP, produce an amorphous damage layer known as the *beilby layer* (Figure 6-12) that obscures the crystal structure (Beilby, 1903). Metallurgical techniques of chemical etching or electro-polishing have been used on large gold particles but this process often produces topography and makes EBSD challenging. Halfpenny et al. (2013) outlined a method of using a combined approach of CMP with a broad ion beam polish (BIBP). This technique utilises a wide beam of high-energy ions

to remove a thin layer of the sample without any abrasive damage. A Leica Microsystems EM RES101 instrument with argon gas was used at 2.2mA and 5kV. The incidence of the beam varied from 5-10° tilt and was rotated at 10rpm to gain an even polish across the blocks.

6.4 Analytical Procedures

This section outlines the analytical procedures used to investigate the key research questions outlined in Chapter 6. The procedures are described individually as they are often applied to different types of specimens.

6.4.1 Electron Microprobe

The process of producing a microchemical signature for a population of gold particles firstly requires quantification of an alloy composition. The same process of characterisation was undertaken at the University of Leeds for the gold particle mounts and gold in polished blocks.

Quantitative analysis using a Jeol 8320 automated electron microprobe analyser was used with an excitation voltage of 20kV, a beam current of 40 and 50nA and a peak count time totalling 90 seconds with 30 seconds off peak. The standards used to calibrate before each session was an artificial gold- silver alloy with a composition of 81.5% gold and 18.5% silver, pure copper metal and mercury sulphide. The limits of detection (3σ) varied with each day-long run of the machine and are outlined in the appendix with the data. The results were deemed acceptable if they returned totals between 98-102%.

The element suite of Au, Ag, Hg and Cu used for gold characterisation was informed by the work by Chapman et al. (2010a). Analysis spots within gold particles were chosen in areas that lacked scratches or inclusions. Multiple spots were taken as grids or traverses on some particles or where alloy heterogeneity was present.

6.4.2 Scanning Electron Microscope

A range of SEM based techniques have been employed to investigate the mineralogy, texture and crystallography of specimens collected from the Lone Star area. Analysis was undertaken using a FEI Quanta 650 FEG scanning electron microscope at University of Leeds and a Zeiss Ultrascan at CSIRO's Kensington facility in Perth.

6.4.2.1 Backscatter Electron Detector (BSE) and Energy Dispersive Spectroscopy (EDS)

Back scattered electron (BSE) images and energy dispersive spectroscopy (EDS) is used to gain information on particular element proportions and textures. BSE images provided grayscale images which correspond to mean atomic mass and were used to identify mineral phases. EDS spot analysis provided semi-quantitative information regarding chemical composition of mineral phases, but in most cases, it was possible to deduce the mineral speciation. Mapping of a grid of EDS points was conducted to create compositional maps that show chemical distribution within a sample.

This approach has been applied to thin sections, polished blocks and gold particle mounts. Thin section specimens of mineralised schist were investigated for presence of gold and alteration mineralogy. The textural and mineralogical associations were further investigated using EDS mapping. Gold in polished blocks and particle mounts were investigated for alloy heterogeneity and characterisation of mineral inclusions. Surrounding vein material was also characterised to establish textural relationships.

Mineral phases were interpreted using a FEI Quanta 650 FEG scanning electron microscope. This was operated at 20kV and a spot size of 5. Scanned using BSE and qualitative chemical compositions determined using Oxford Analytical EDS. A Zeiss Ultrascan SEM was used to produce EDS maps while visiting CSIRO's Kensington facility in Perth. A grid of points records spectral information that is interpreted to show compositional variation across a chosen area. The maps were produced using a Bruker Xflash detector at a resolution of 1800x1000 pixels and 20kV. The Bruker Hypermap was recorded and interpreted using ESPIRIT 1.9 software.

6.4.2.2 Cathodoluminescence (CL)

SEM cathodoluminescence (CL) of quartz provides monochromatic images of textures that are unobservable with other techniques (Rusk et al., 2008). Luminescence occurs due to the emission of photons as the surface is bombarded with an electron beam (Götze, 2009, Götze, 2012) and in quartz it has been attributed to a variety of factors including vacant lattice sites, lattice defects, lattice order, mechanical deformation and the presence of impurities (Lehmann et al., 2009, Rusk et al., 2011).

The technique was applied to quartz in polished blocks and thin sections to provide information about crystal growth, trace element content and different generations of quartz that are not observed through standard petrographic or BSE techniques (Götze, 2012).

Analysis was undertaken using the SEM at Leeds, which was fitted with a KE Centaurus panchromatic CL detector. Scanning of the samples was undertaken to locate any textures prior to more detailed investigation. Luminescence was mostly low, so a high voltage of 26kv was used with a large aperture so that the detector could receive enough signal. Count times of 30 seconds provided images with minimal noise. Oxford Instruments Aztec software was used to record images and also produce montages of area. Scan speeds of 30 seconds and 20% overlap were chosen to avoid drift.

6.4.2.3 Electron Backscatter Diffraction (EBSD)

Electron Backscatter Diffraction is a SEM based microstructural-crystallographic technique used to perform quantitative microstructure analysis of crystalline material (Prior et al., 2009). The process is used to investigate a range of materials from metals to most non-organic crystalline materials and is a common technique in Earth science (e.g. Investigating deformation microstructures in quartz). Image capture is facilitated by use of an EBSD detector that has a phosphor screen and CCD camera (Prior et al., 1999). Diffraction is produced when an electron beam strikes a crystalline sample tilted at 70° to normal (Figure 6-13a)(Prior et al., 1999, Prior et al., 2009). The diffracting electrons produce a distinctive pattern which is recorded using the detector. The pattern of diffraction is reliant upon the interaction of

electrons and atomic planes according to the Bragg equation (Prior et al., 1999). The wavelength and angle of the sample is known so the path difference between electrons scattered from adjacent crystal planes is $2d \sin \theta$ (Lloyd, 1987). The scattered electrons produce large angle cones that create a pattern known as Kikuchi bands (Figure 6-13b) (Prior et al., 2009). The internal crystal planes or faces are described using Miller indices indexed to match the Kikuchi bands. The intersections observed on the patterns correspond to a crystal direction that is correlated with a crystal orientation (Figure 6-13c). The automation of this process creates a grid of points across a sample that provides quantitative microstructural data.

This technique has been applied to eluvial, alluvial, liberated vein gold and in situ visible gold. Characterising the crystallography of hypogene and detrital-placer gold particles is intended to investigate modification of shape during transport and deformation.

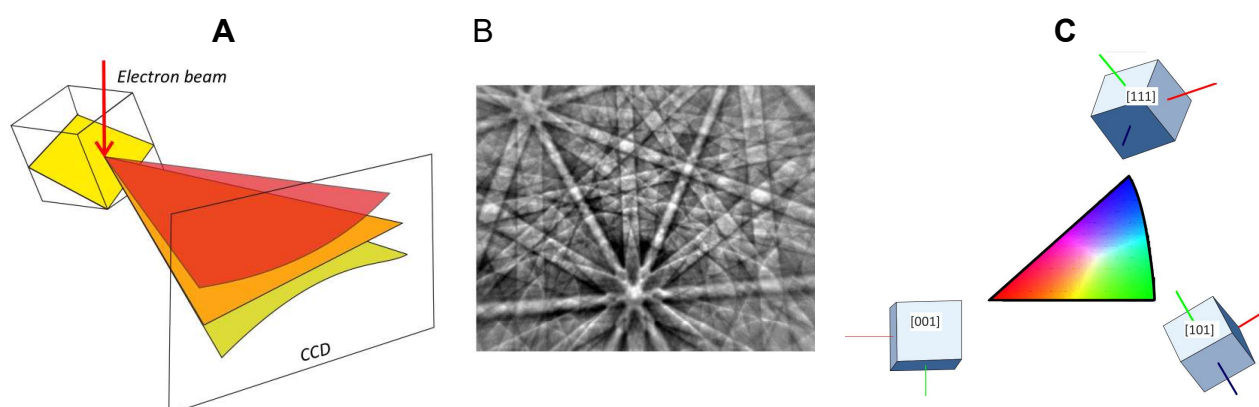


Figure 6-13: Overview of EBSD analysis. **A-** Electron beam strikes samples tilted to 70° . Diffraction, produces cones of electrons which are recorded on a CCD. **B-** Kikuchi bands recorded on CCD correspond to crystal lattice. **C-** Automation of the process is used to produce maps of data. Colours correspond to crystal orientation plotted as an inverse pole figure (Z).

Samples that were polished adequately (described in section 1.3.5) were imaged at CSIRO's Kensington facility in Perth. The orientation data was collected using a Zeiss Ultrascan SEM fitted with a Bruker e⁻ Flash detector and gun. The samples were tilted to 70° with a working distance of 23mm with a scanning voltage of 20kV and aperture of 120 microns. A grid of patterns was produced with a step size from 50nm-1.5 μm with a resolution of 240 x

150 pixel and a scan speed of around 7ms. The data was exported as Channel text files (.ctf) and post processed using Tango module of HKL's Channel 5 software. This provided a range of features reducing noise and plotting all aspects of the data.

6.4.3 Micro X-Ray Fluorescence

Micro X-ray fluorescence mapping provides high-resolution composition and element distribution in whole thin sections. This study used the technique to investigate thin sections of mineralised schist that typically exhibit discrete and diffuse alteration.

Whole thin section characterisation was undertaken while at the CSIRO Kensington facility in Perth using a Bruker M4 Tornado, which was set at 50kV to analyse thin sections at a scan speed of 3mm/s. This produced information on elemental distribution with a resolution of 30 microns. Interpretation of the data was undertaken using Bruker Espirit 1.9 software to create RGB compositional maps.

6.4.1 Laser Ablation Induced Coupled Plasma Mass Spectrometry

Laser Ablation Induced Coupled Plasma Mass Spectrometry (LA-ICP-MS) is an extremely powerful tool in gaining spatially resolved trace element variations in solid material (Allan et al., 2005). It involves a focussed laser beam on the sample surface which generates fine particles that are transported to the ICP via argon gas. The material is ionised in the plasma prior to extraction with the mass spectrometers. LA-ICP-MS was utilised to investigate trace element variation of quartz. The facility at Leeds uses a 193 nm ArF GeoLas Q Plus exciplex laser ablation unit coupled to an Agilent 7500c quadrupole ICP-MS (Allan et al., 2005).

Quartz vein material that had undergone characterisation via CL provided information about different generations of quartz that guided the ablation locations.

Quartz is commonly analysed so the calibration procedure is relatively straight forward. A glass standard SRM 610 from the National Institute of Standards and Technology (NIST) was used as an external calibration standard, which

was ablated for 200 pulses at 5 Hz and $10 \text{ J}\cdot\text{cm}^{-2}$ over a stationary $50 \text{ }\mu\text{m}$ spot.

6.5 Summary

This chapter has provided an overview of the various samples collected during fieldwork. The sample processing and preparation has produced a variety of specimens. The analytical procedures that have produced results that are presented in the next chapters. These form the basis for the discussion of this thesis.

Chapter 7 Gold-bearing quartz veins

A key aim of the research is to illuminate the evolution and history of gold-bearing quartz veins in the LSSA. Previous studies have investigated gold-bearing quartz veins across the KGD and south-central Yukon (described in Chapter 3 and 4), and classify the occurrences as orogenic (Rushton et al., 1993). Rushton et al. (1993) presents an extensive fluid inclusion and stable isotope study of veins in the KGD; however, the interpretations were based on poorly characterised vein samples with little, if any, spatial context. This study aims to generate a paragenesis of gold-bearing quartz veins in the LSSA using a sample suite whose context is well constrained.

Within the LSSA there are numerous mineral occurrences; however, this study focusses on six key localities (described Table 7-1 and shown in Figure 7-1). The key features of veins described in this section are mineralogy, quartz textures, and paragenesis. The results present the best examples of key features that are common at each locality. This chapter presents a discussion of the hypogene processes responsible for gold-bearing quartz vein formation and proposes a new model.

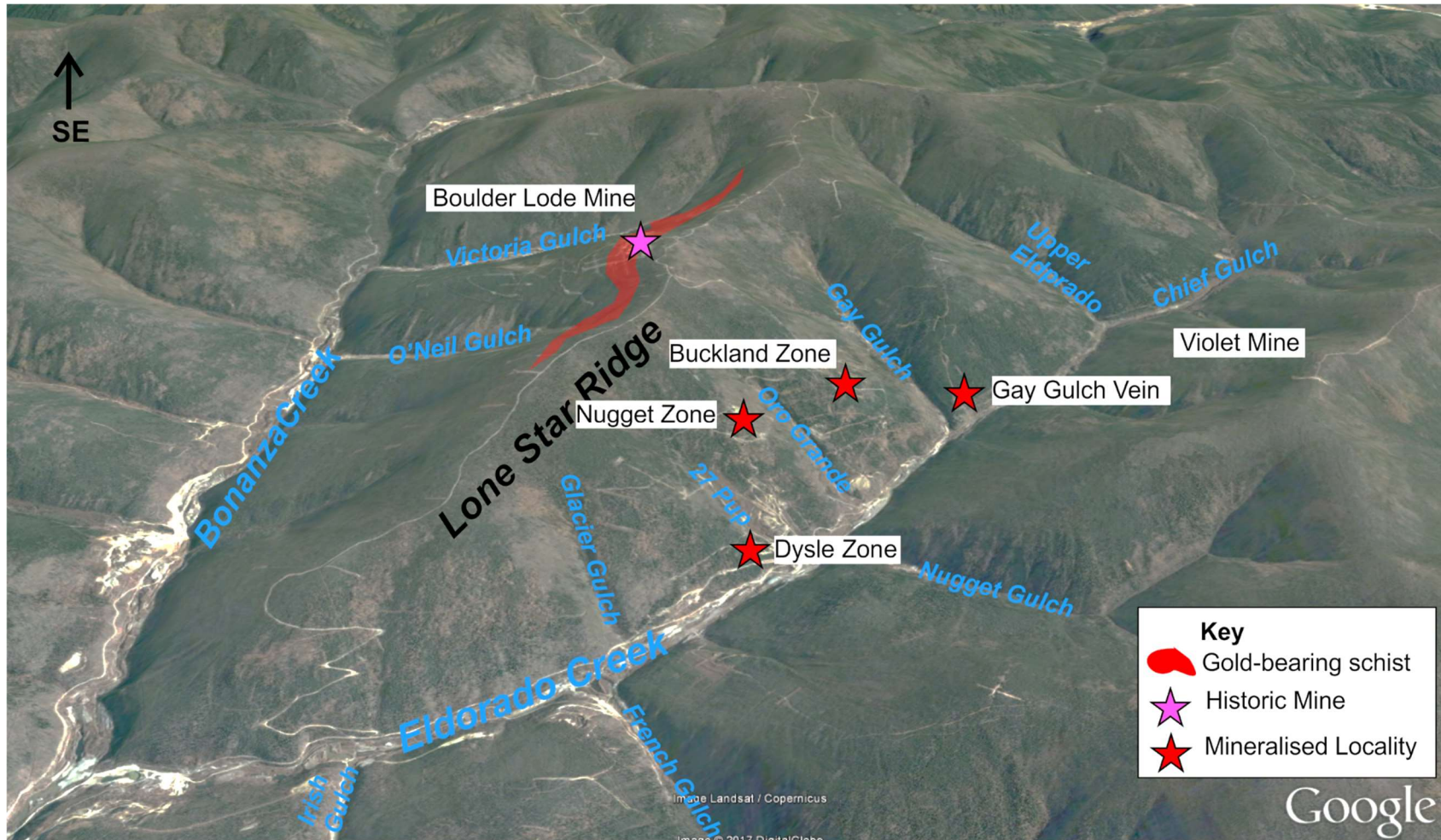


Figure 7-1 : Historic mine and gold occurrences that form the basis of this PhD project marked on a google Earth image of the LSSA.

7.1 Field observations

Gold-bearing quartz veins are only revealed in historic mineral exploration trenches that remove thick overburden and vegetation. Trenching provides an opportunity to observe the structural settings of veins. Deep weathering to >100m means that the lithologies in trenches rarely expose fresh rock.

The Boulder Lode Mine has undergone the most extensive trenching and excavation as it was the original site of open cut mining in the 1900s (Figure 7-2). Dysle, Nugget and Buckland are described as 'zones' where multiple veins are present that typically range in size from 100-200m² (Figure 7-3). Excavation by Klondike Star in 2007 at Nugget Zone, Buckland Zone, Dysle Zone and Violet Mine revealed exposure of quartz veins that are anastomosing and discordant to foliation (Figure 7-4).

The Gay Gulch Vein is the least developed and least studied out of all the gold-bearing vein occurrences considered here. The gold-bearing vein is observed in a trench and drill core, but is not well exposed at surface.

In all mineralised zones and localities gold-bearing quartz veins are localised in angular kink folds associated with D₄ fault-fold deformation. The field observations of mineralised occurrences in the LSSA are the same as other occurrences in the KGD, described in Chapter 3.



Figure 7-2: Boulder Lode mine cut excavated to reveal bedrock and veining.



Figure 7-3: Anastomosing quartz veins revealed through exploration trenching at the Nugget Zone.

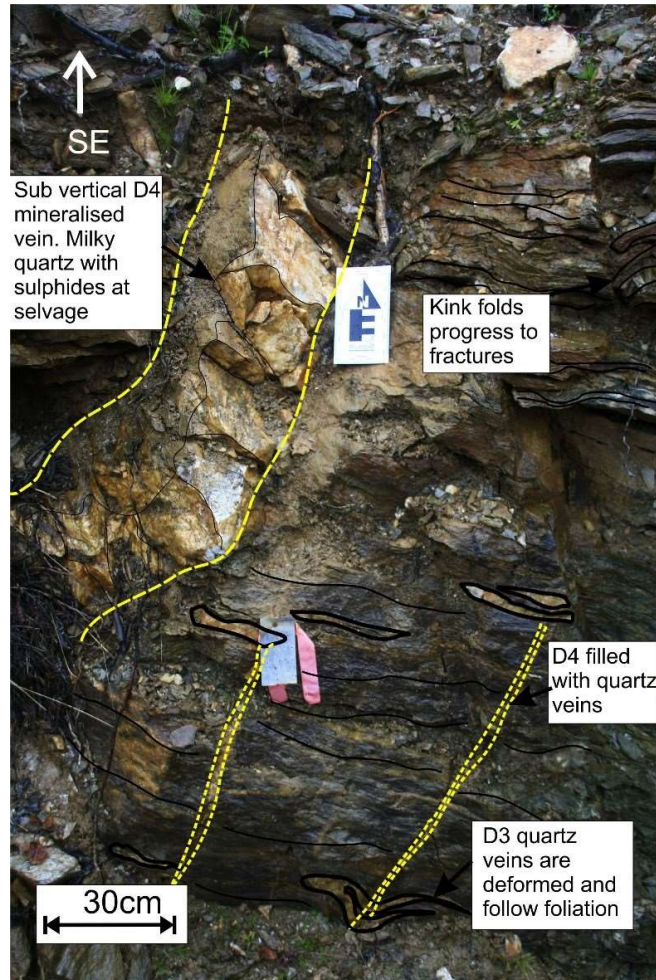


Figure 7-4: Discordant quartz vein at the Upper Nugget Zone. Quartz veining is sub-vertical and hosted in angular kink folds that are related to D₄.

7.2 Mineralogy and alteration of gold-bearing veins

All gold-bearing veins in the study area are dominated by subhedral milky white quartz. The centre of quartz veins are often filled with euhedral calcite crystals up to 2cm in length (Figure 7-5a). Calcite is observed at all localities but best developed in areas where host rocks are more mafic (e.g. Nugget and Buckland zones).

The most common mineral associated with the quartz is brown limonite that occurs as clusters in quartz or at the margin (Figure 7-5b). The limonite presents as pseudomorphs after pyrite, a result of oxidation, and can be up to 1cm in diameter (Figure 7-5b).

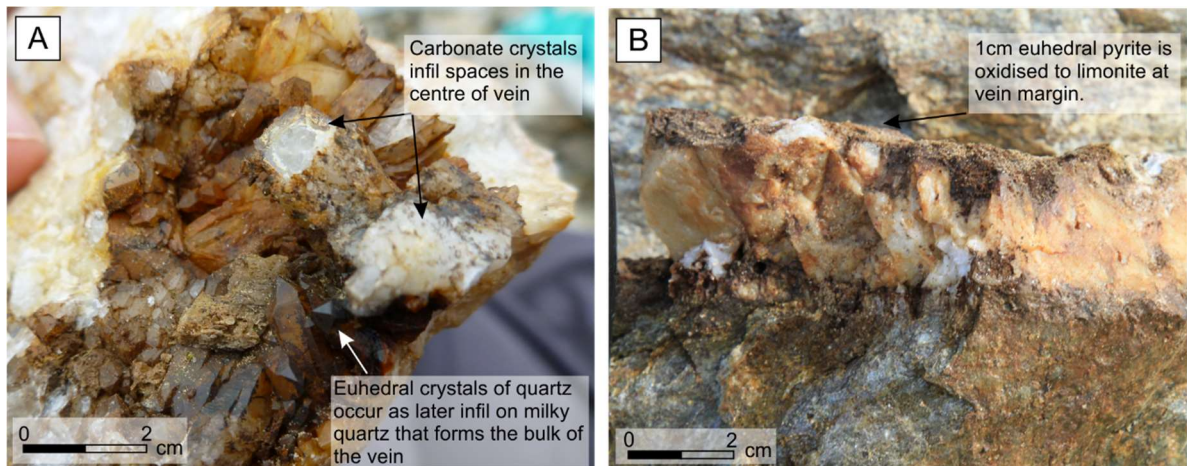


Figure 7-5: **A-** Euhedral calcite in the centre of the vein surrounding euhedral quartz crystals at the Nugget Zone. **B-** Example of pyrite, oxidised to limonite, at the Nugget Zone, which is best developed at vein margins.

The presence or absence of alteration surrounding veining is difficult to recognise due to the intense chemical weathering of bedrock. The heterogeneous, but somewhat similar, lithologies (e.g. QMS Member, QCMS Member, Meta Rhyolite Member), make it difficult to distinguish between compositional variation and alteration.

The presence of carbonate alteration in wall rock is common at all localities, but their origin may be related to metamorphism rather than alteration. Pyrite is present in wall rock as euhedral 1cm grains, and is the easiest alteration style to recognise in the LSSA. It is best developed in chlorite-rich lithologies, such as the Chlorite Quartz Mica Schist Member at the Nugget Zone, where it pervades up to 20cm into wall rock (Figure 7-6).

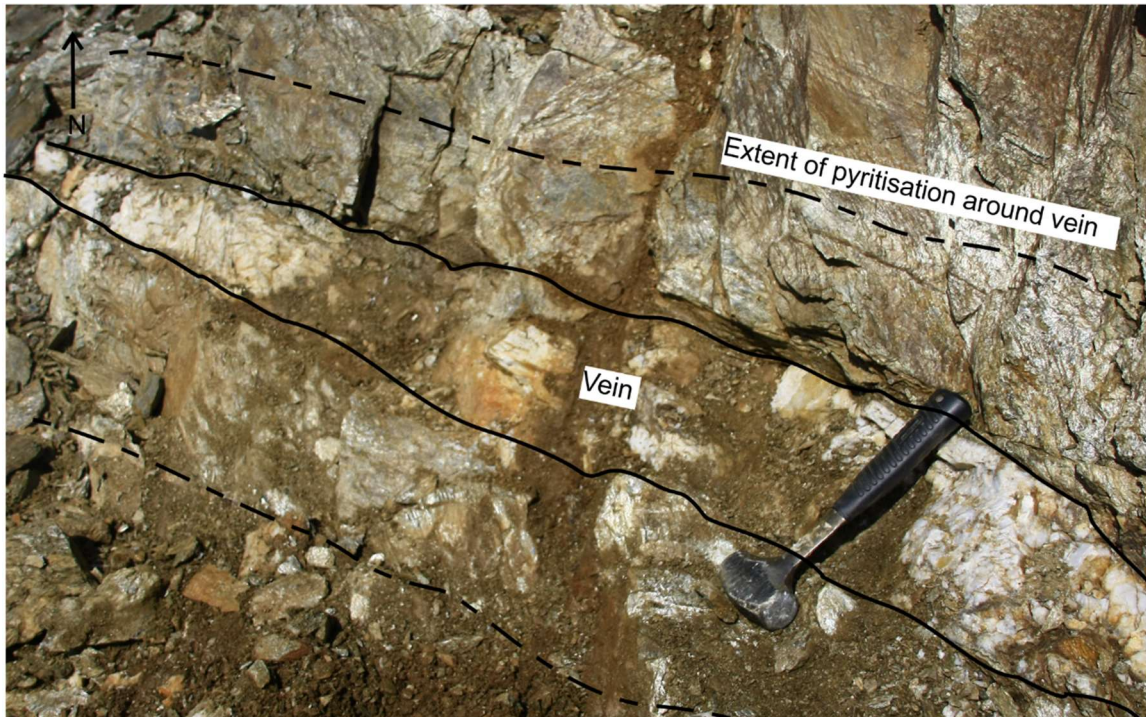


Figure 7-6: The extent of pyrite surrounding a quartz vein at the Nugget Zone.

Galena, chalcopyrite and sphalerite have been observed at Boulder Lode Mine, Nugget Zone, and Dysle Zone, but are very rare and typically form in vugs or close to the centre of the vein (Table 7-1).

The Violet Mine is the only gold-bearing vein occurrence in the LSSA that exhibits significantly different mineralogy. The veins are composed of quartz and barite, and are hosted in the Sulphur Creek Orthogneiss Member. Alteration is present as minor silicification of the wall rock and is easily differentiated from the consistent composition of the unaltered Sulphur Creek Orthogneiss.

7.3 Quartz vein paragenesis

Rushton et al. (1993) studied quartz textures in the discordant gold-bearing quartz veins in the LSSA and described them as being dominated by subhedral quartz. Although this observation hold true for the veins studied in this thesis, various other quartz textures have also been documented. The features described in the following sections are present at each locality, although not always together, and are used to develop a paragenesis of quartz growth.

7.3.1 Quartz textures observed hand specimens

Three distinctive quartz textures have been identified in hand specimens. First is the most easily recognisable, the subhedral quartz; second is the large euhedral crystals that range from millimetres up to 15cm in length (Figure 7-7b, c and d). Epitaxial euhedral quartz crystals are best developed in rocks that have a competent rheology such as the Quartz Augen Schist Member and Meta Rhyolite Member.

Euhedral quartz is preserved in the centres of veins; however, there is evidence of brecciation and fragmentation. Figure 7-7a show a 13cm euhedral crystal in a vein from the Nugget Zone that has been fractured and cemented parallel to the vein margin.

The third texture is observed infrequently, and presents as a minor phase of clear, bladed quartz is present in vugs and cavities of quartz veins. This generation of quartz is best developed at the Dysle Zone and Nugget Zone where it occurs in the centre of veins (Figure 7-8a and b).

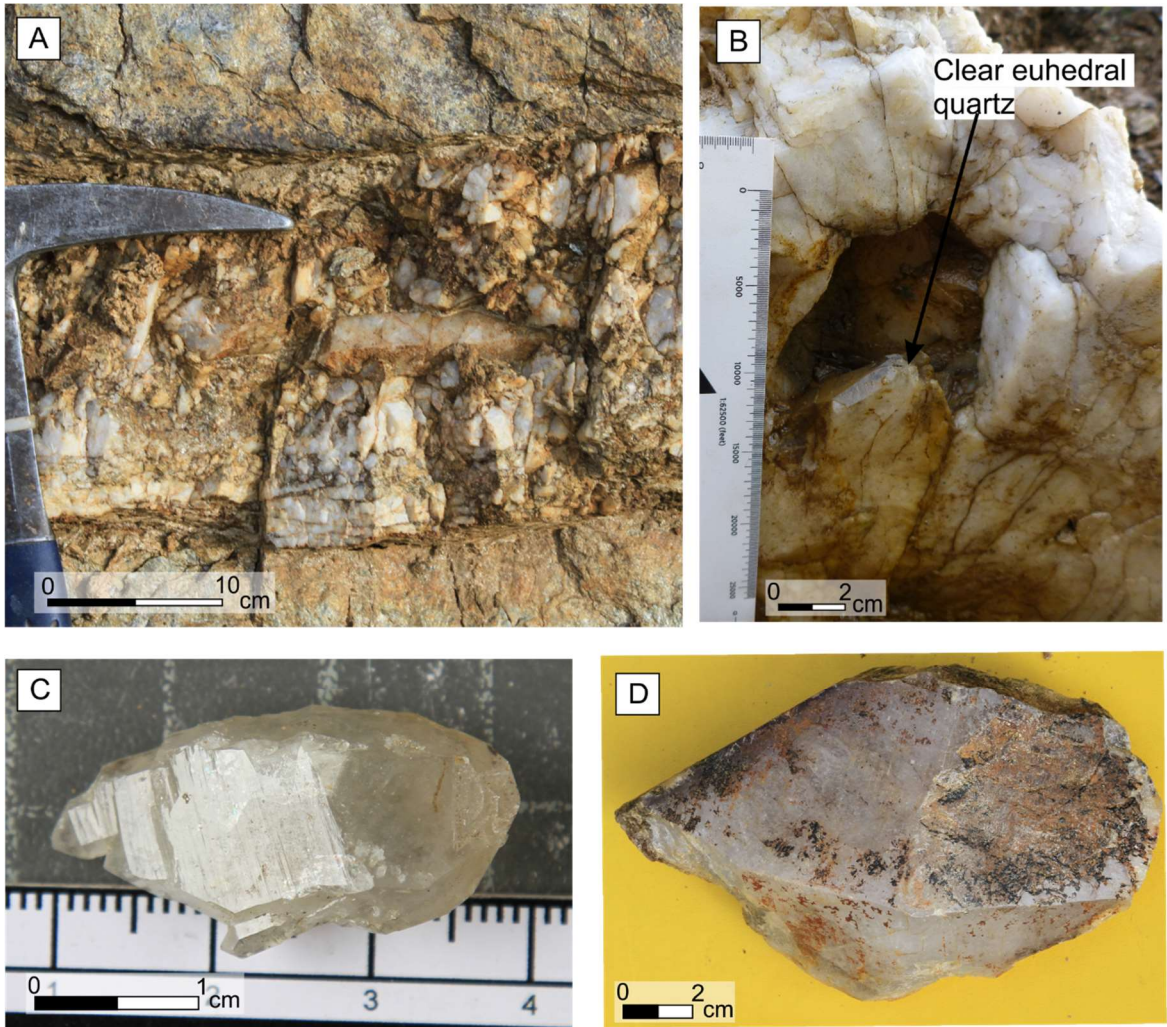


Figure 7-7: A- 13cm euhedral quartz crystal cemented, parallel to vein margin, at the Upper Nugget Zone. B- A 6cm quartz crystal growing into centre of vein at the Gay Gulch Vein. C- 3cm clear crystal of quartz recovered from the centre of a vein in drill core. D- 15cm euhedral quartz crystal from the Boulder Lode Mine.

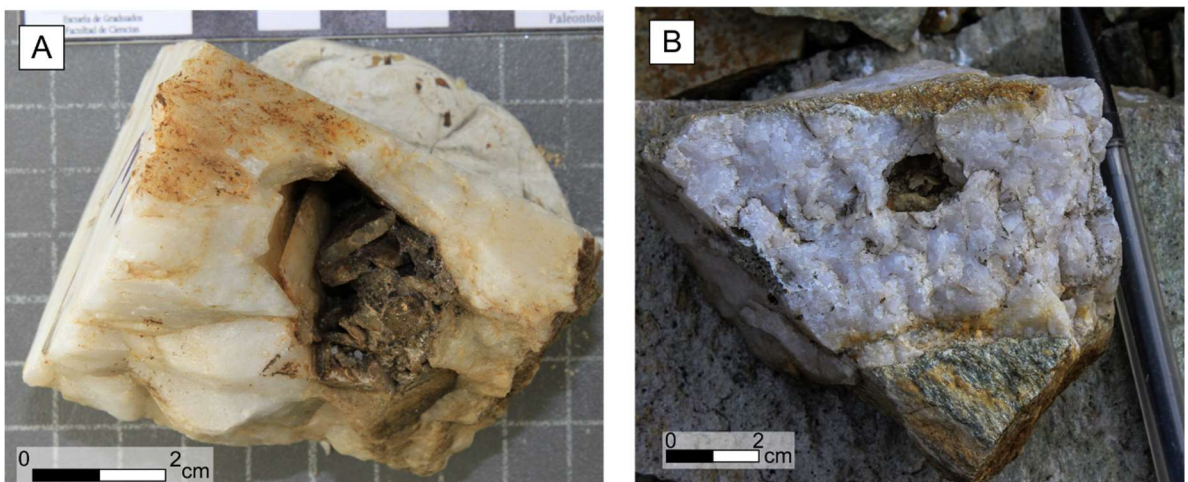


Figure 7-8: A- Bladed quartz in vug from Upper Nugget. B- 6cm wide vein from Dysle Zone with bladed quartz in vug.

7.3.2 Textural variation of quartz in thin sections

The detail of quartz textures in hand specimen are difficult to recognise due to the dominance of subhedral white quartz. Thin sections were made from samples that displayed the textures described in section 7.3.1, and which also demonstrated a good quartz-wall rock relationship.

Gold-bearing quartz veins at the Dysle Zone are hosted in the rheologically competent Meta-Rhyolite Member, which preserves various quartz textures. The thin sections were investigated petrographically using cross-polarised light, and multiple images were combined to generate a montage overview of the section (Figure 7-9a, b).

In all samples analysed the vein-wallrock contact was dominated by large subhedral quartz that has undulose extinction in cross polarised light. Figure 7-9a and b show thin section montages where quartz veining is discordant to the foliation of the host rock. Figure 7-9b shows a quartz vein at the Dysle Zone that has large grains of quartz with smaller crystals of bladed quartz at the centre. Minor calcite is present in the centre of the vein which extends along foliation of the host rock.

Due to the limited textural information provided by transmitted light petrography, the samples were also studied using cathodoluminescence (CL) to provide more detail regarding generations of quartz growth and paragenesis. Figure 7-10a show a CL scan of the thin section displayed in Figure 7-9b. The different shades of greyscale correspond to variations in fluorescence and displays features of quartz textures otherwise not recognised using standard petrographic techniques. This provided an opportunity to define different generations of quartz and establish cross-cutting relationships. A paragenesis was then developed according to the various textural relationships in quartz.

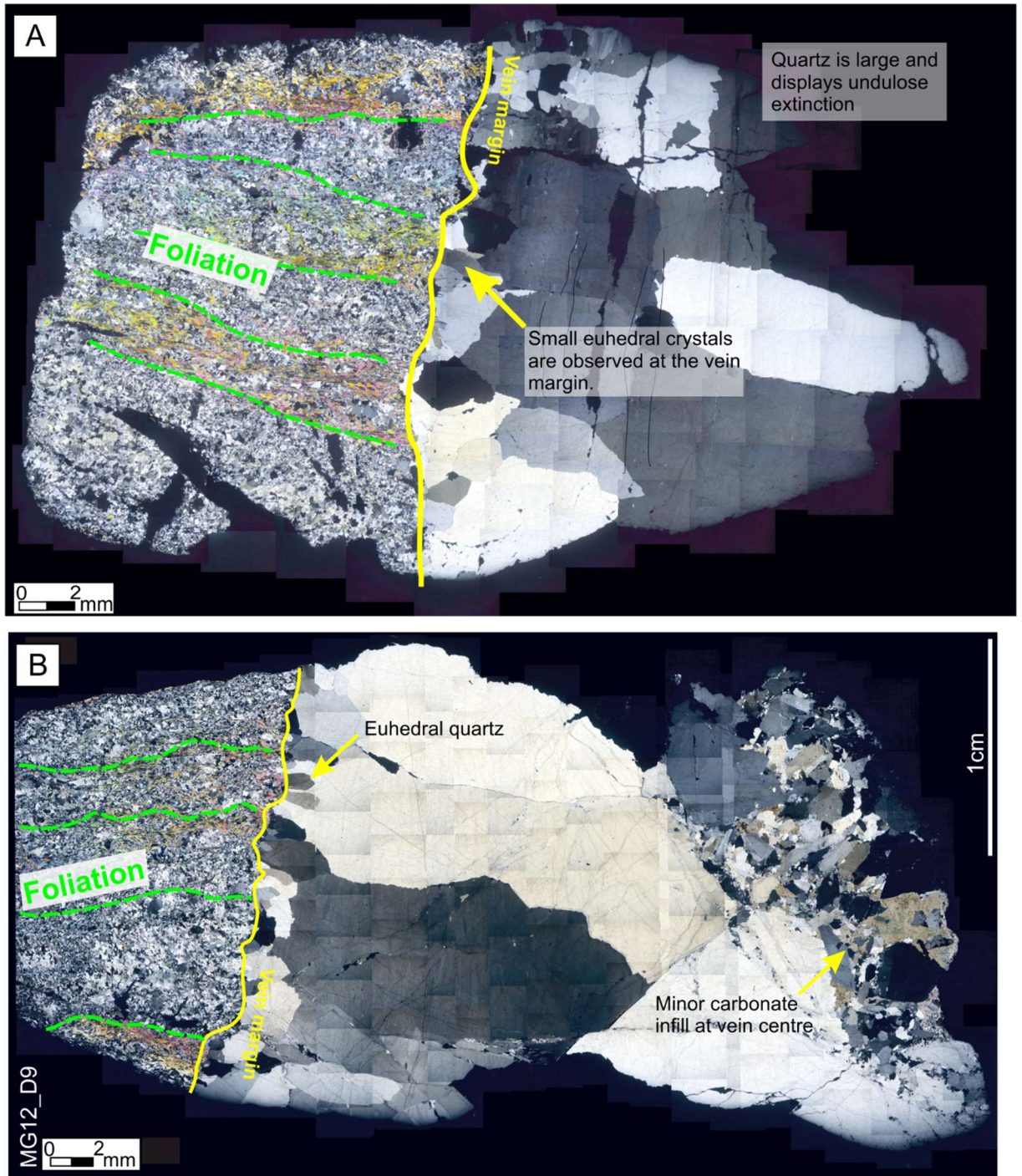


Figure 7-9: A- Cross polarised light image showing a gold-bearing quartz vein from the Dysle Zone (MG15_D09). Green marks the foliation of the Meta Rhyolite Member that is cut by discordant quartz (yellow). B- Cross polarised light image of discordant vein from Dysle Zone (MG21_D09). Green marks foliation that is cut but quartz (yellow). XPL shows some textural variation of vein quartz with minor euhedral quartz at margin; however, the majority is large subhedral quartz that displays undulose extinction. The centre has minor calcite infill.

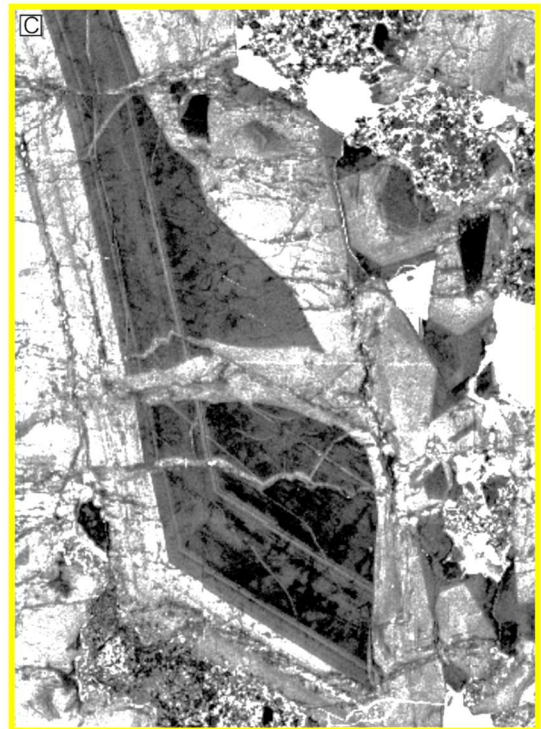
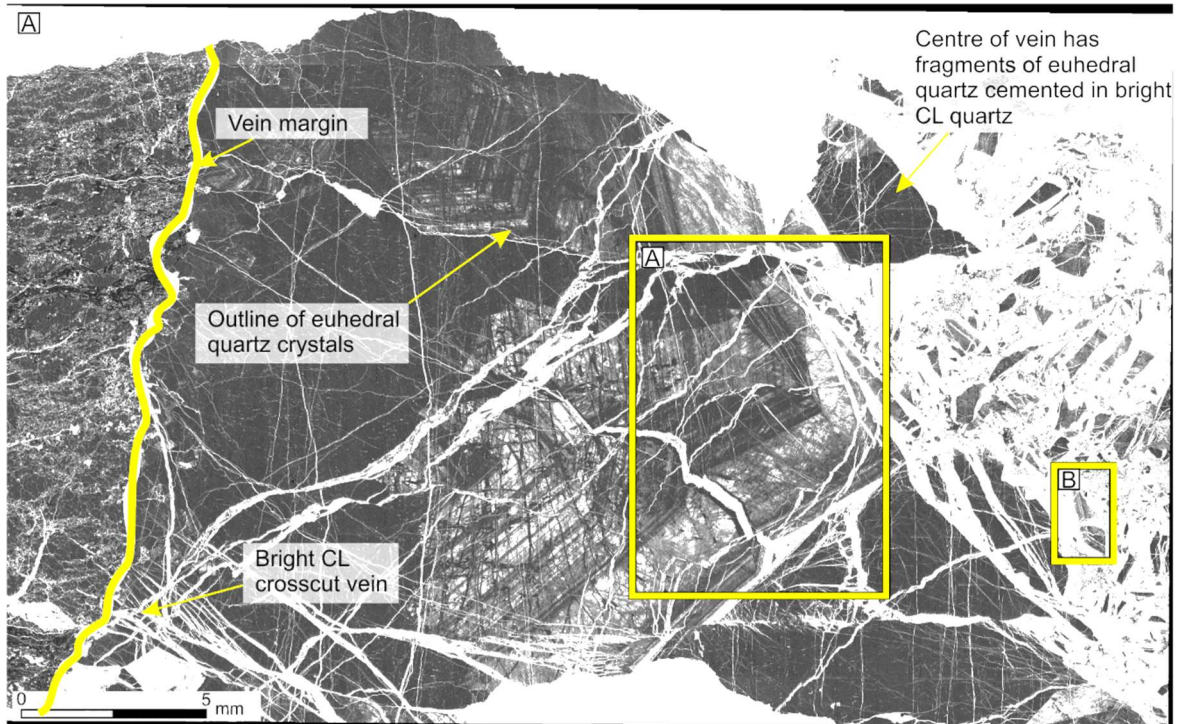


Figure 7-10: **A-** A montage of quartz cathodoluminescence (CL) of a whole thin section from Dysle Zone as observed in Figure 7-9b (MG21_D09). CL highlights the textural variation that is not observed with XPL. **B-** Mottled outline of euhedral quartz cross cut by dark CL. **C-** Euhedral fragment of quartz cemented and cross cut by bright quartz.

A primary phase of quartz (Q1) is identified that has a mottled or 'ghostly' texture and represents a generation of euhedral quartz (Figure 7-10a and b). The most common texture in Figure 7-10a is a dark quartz (black in CL) that has no fluorescence (Q2). This phase of quartz cross-cuts, fractures, and infills the primary phase of mottled (Q1) quartz (Figure 7-10a). The Q2 dark quartz corresponds to the subhedral milky white quartz observed in hand specimens. Very bright CL represents a third generation of quartz growth (Q3), fills fractures up to 500µm in width, and forms less than 10% of total vein quartz (Figure 7-10). Figure 7-10a shows this generation of quartz in the centre of the vein; and this corresponds to the bladed quartz observed in hand specimens. This bright generation of quartz (Q3) cements fragments of Q1 and Q2 and shows initial fibrous growth at the margins, but changes into well-developed oscillatory growth zones (Figure 7-10b). Figure 7-11 below displays another section of vein quartz from the Nugget Zone and illustrates the cross-cutting relationships of Q1, Q2 and Q3. An additional generation of quartz (Q4) is present as very minor fractures that cross-cut Q1-Q3.

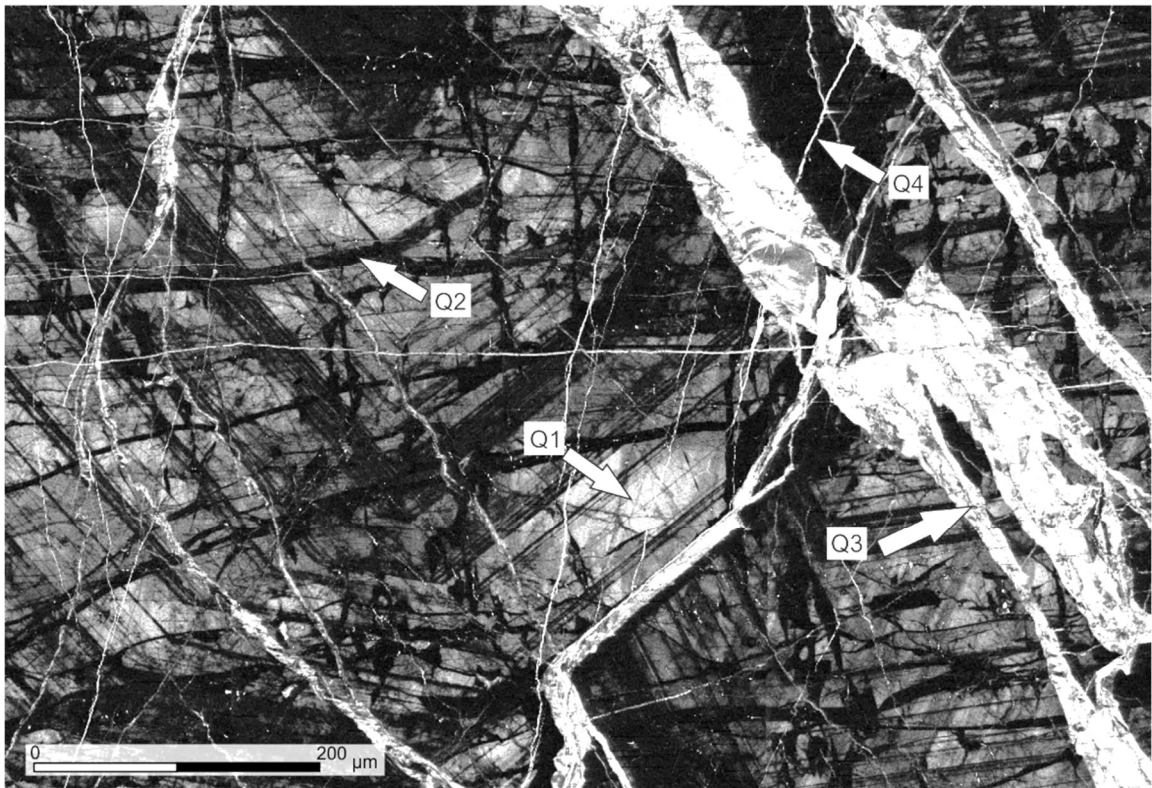


Figure 7-11: CL image of quartz from Nugget Zone (MG61_UN01). **Q1-** Mottled oscillatory zoned **Q2-** Dark quartz that fractures the sample and fills Q1. **Q3-** Fractures and cements all previous generations with fibrous growth. **Q4-** Minor phase in small fractures.

Locality	Host rock	Vein description	Alteration	Minerals	Quartz textures
Dysle Zone	Meta-Rhyolite member	Quartz veins have sharp boundaries with host rocks and vary in width from 1cm up to 20cm.	Minor pyritisation (<1cm into wallrock).	Galena and pyrite.	Euhedral quartz (Q1) with bladed quartz in vugs (Q3).
Nugget Zone	Quartz Chlorite Mica Schist Member	Veins pinch and swell occurring in stacked sets. Upper and Lower zones are identified at Nugget, separated by 100m on the hillside.	Pyritisation up to 20cm from vein. Euhedral carbonate in vein and extending into wallrock.	Rare galena, chalcopyrite and sphalerite in centre of vein. Euhedral calcite in vein centre	Mostly subhedral quartz (Q2) with evidence of brecciated euhedral crystals (Q3).. Bladed quartz in vugs (Q3).
Gay Gulch Vein	Quartz Augen Schist Member	There are numerous small quartz veins but only one is identified to be gold-bearing.	Minor pyritisation	Pyrite and euhedral carbonate minerals	Very large euhedral quartz crystals (Q1).
Buckland Zone	Quartz Chlorite Mica Schist Member	Quartz veins are poorly exposed in trenches. Veining lacks continuity.	Pyritisation up to 2m from vein. Abundant carbonate minerals in wallrock.	Pyrite and euhedral carbonate minerals.	Mostly subhedral milky white quartz (Q2) with some euhedral textures observed (Q1).
Violet Mine	Sulphur Creek Orthogneiss Member	Quartz veining is exposed in large trench. Large pegmatite veins are also present that are cross cut by quartz veins.	Silicification and minor pyritisation	Pyrite and abundant barite	Mostly subhedral milky white quartz (Q2).
Boulder Lode Mine	Quartz Mica Schist and Meta Rhyolite Member	Veins dip steeply or shallowly. A small 2cm quartz vein is rich in limonite and has provided numerous examples of visible gold.	Pyritisation is extensive but wall rock is also pyritic.	Pyrite in veins. Sulphides present as millimetre bands in host rock.	Mostly subhedral milky white quartz (Q2) with example of very large euhedral quartz crystal (Q1).

Table 7-1: Summary of gold-bearing vein features at each locality.

7.3.3 Interpretation of quartz deposition

The textures identified in quartz from the LSSA can be used to understand the physical conditions associated with deposition and mineralisation (Adams, 1920, Sander and Black, 1988, Dong and Morrison, 1995). The investigation of quartz textures using SEM-CL has revealed features that are normally unobservable (Sprunt et al., 1978, Seyedolali et al., 1997, Götze et al., 2001). Quartz veins from the LSSA investigated with CL has led to the identification of cross-cutting relationships that can define the sequence of vein formation, and a clear paragenesis has been developed. Hydrothermal quartz textures show a complex evolution that is a result of multiple stages of fluid flow, quartz deposition, dissolution, fracturing and recrystallisation (Rusk et al., 2011). These features are a result of fluctuating temperature, pressure changes, fluid composition, and rates of quartz growth (Götze, 2009). A summary of typical quartz textures observed globally are compiled by Sander and Black (1988) in Figure 7-12, which separates quartz formed due to boiling from quartz formed under stable hydrothermal conditions. Textures in epithermal quartz are often preserved and has led to the classification by Sander and Black (1998) having a bias towards this style of deposit.

The primary quartz generation in the LSSA (Q1) has a mottled or ghostly appearance but marks the outline of euhedral quartz (Figure 7-11). Q1 is linked to large euhedral quartz crystals found in hand specimen that are up to 15cm in length (Figure 7-7d). The Q1 contains oscillatory zoning of varying thickness and CL intensity (Figure 7-12p). The results suggest that primary quartz (Q1) formed as epitaxial crystals nucleated onto the wallrock, and were deposited under stable hydrothermal conditions. Quartz from epithermal and low temperature veins are described by Götze et al. (2001) and have similar CL textures as those in Q1 in the LSSA (Figure 7-13a and b).

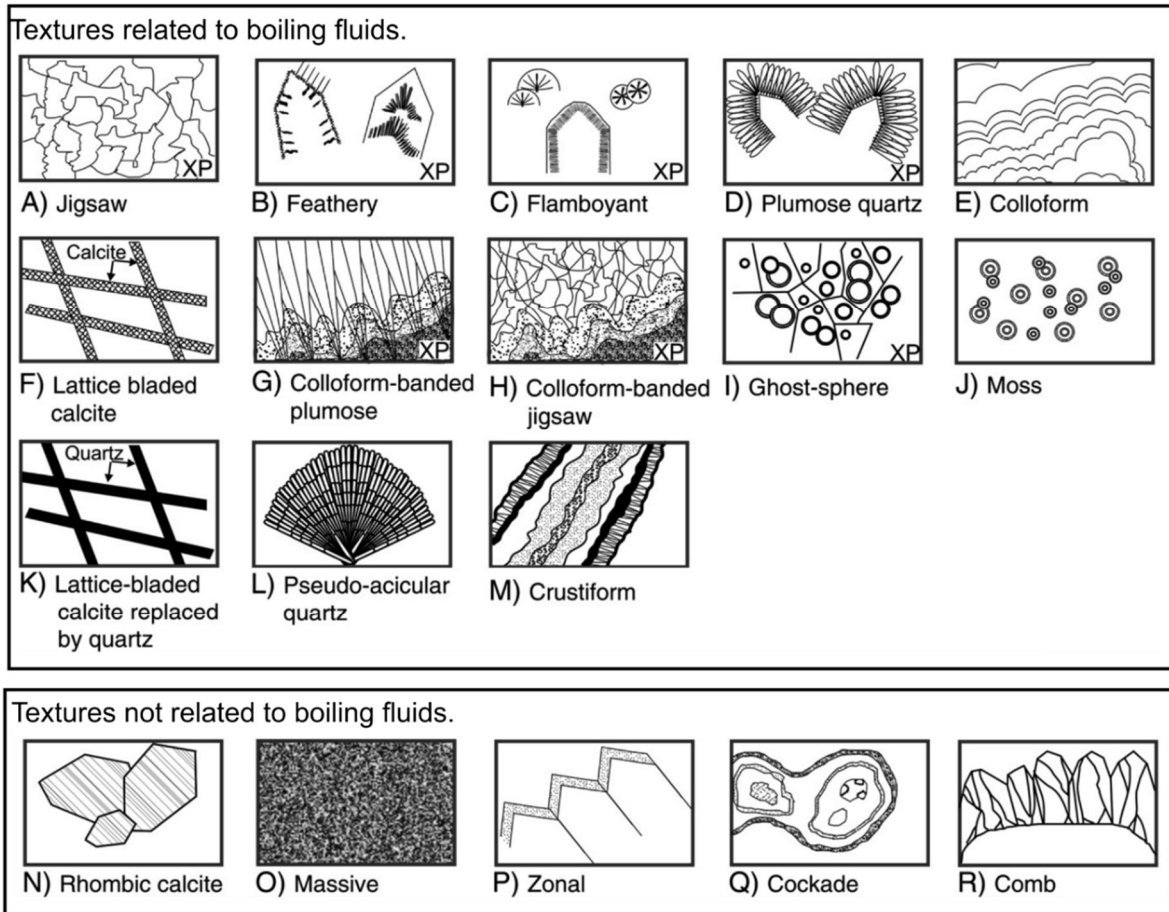


Figure 7-12: Summary of quartz and calcite textures observed in hydrothermal veins. Many of the textures are typical of epithermal quartz. Textures are separated into rapid deposition from boiling fluid and fluids that precipitated more slowly (Sander and Black, 1988, Dong and Morrison, 1995).

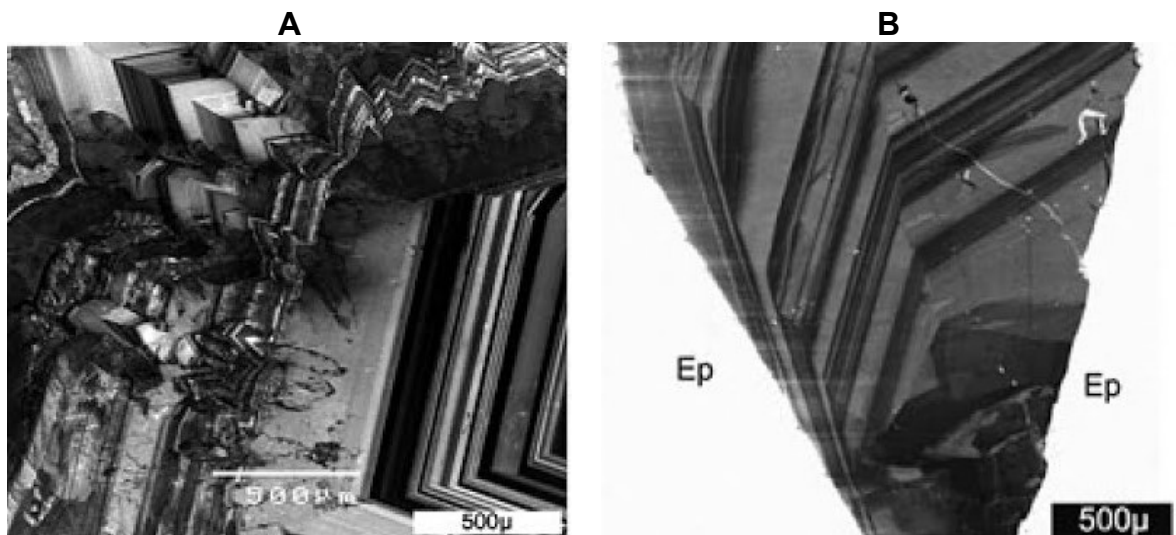


Figure 7-13: Examples of primary inward zoned quartz. **A-** Tokatea epithermal deposit NZ (Bignall et al., 2004). **B-** Inward zoned euhedral quartz from low temperature veining at Comstock Lode NV, USA (Rusk, 2012).

Secondary quartz (Q2) is the most extensive generation of quartz growth in all samples analysed from the LSSA, and is comprised of dark CL that corresponds to white subhedral quartz in hand specimen. Q2 overprints and infills fractures in primary quartz (Q1), resulting in a mottled or ghostly outline of Q1 (Figure 7-10) (Sprunt et al., 1978). The homogenous CL dark quartz of Q2 is a result of annealing, which redistributes lattice defects and trace elements that normally cause luminescence (Götze et al., 2005, Spear and Wark, 2009). The development of homogenous dark CL is described by Rusk (2012), in metamorphic quartz and orogenic veins (Figure 7-14a and b).

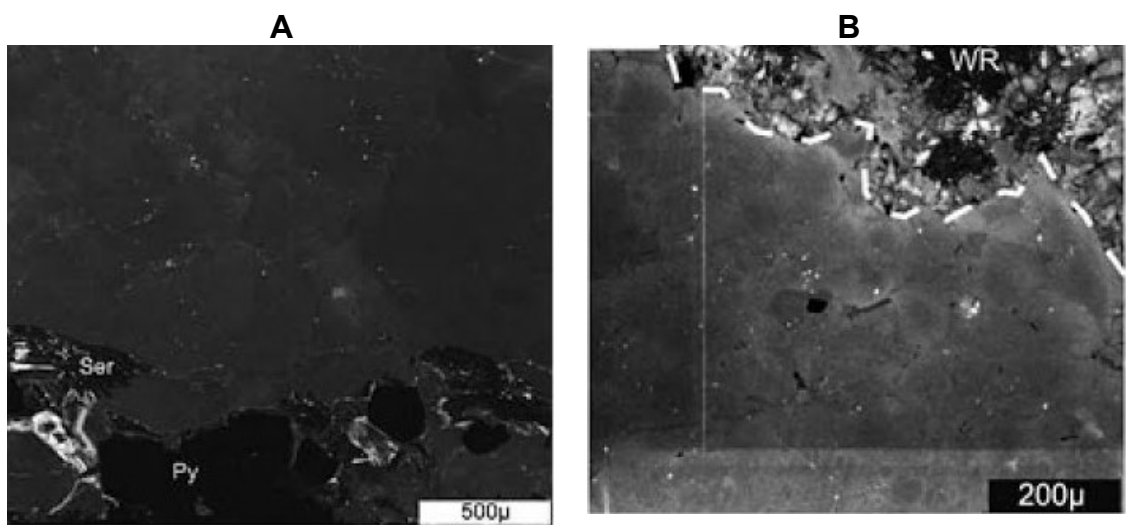


Figure 7-14: Example of homogenous CL textures. **A-** Typical orogenic vein texture from Au vein, Valdez Creek, Alaska. **B-** Mostly homogenous quartz in orogenic vein from Norseman, Australia (Rusk (2012)).

Q2 is fractured, invaded, and cemented by a bright CL generation (Q3), and makes up less than 5% of the total quartz in samples analysed. It is best developed in the centres of veins where it cements fragments of Q1 and Q2 (Figure 7-8a,b and Figure 7-10b). The initial phase of Q3 growth displays plumose or fibrous textures (Figure 7-15a), which progress to zonal growth textures (Figure 7-12). The initial fluid pulse associated with Q3 resulted in hydro-fracturing and brecciation of the earlier Q1 and Q2. The cementation of quartz fragments in vugs provides evidence for an evolution towards to more stable zonal quartz growth (Figure 7-12 and Figure 7-15b) (Sander and Black, 1988, Moncada et al., 2012).

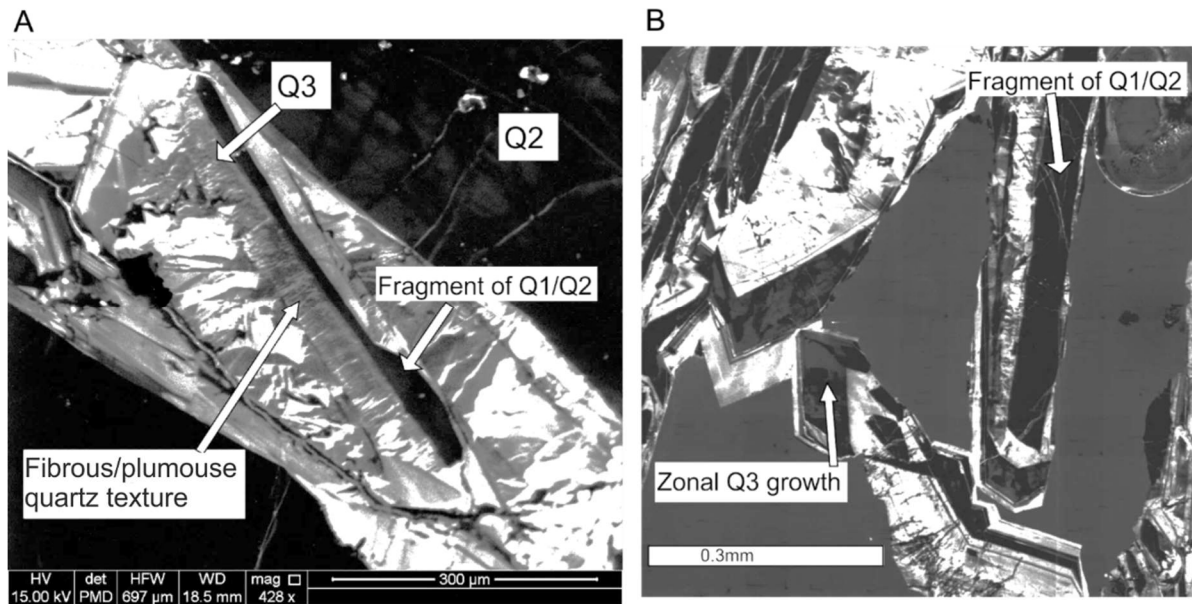


Figure 7-15: Example from quartz vein at Nugget Zone. **A-** Earliest phase of Q3 is fibrous. **B-** Q3 develops to zonal quartz around fragments of quartz.

Q4 is the final generation of quartz to be deposited, and forms less than 2% of total vein volume. It displays very bright CL and occupies fractures that are often also filled with ankerite and calcite (Figure 7-11).

A similar study of vein textures has been conducted on vein-hosted gold mineralisation at Curraghinalt, Northern Ireland (Wilkinson et al., 1999, Rice et al., 2016). Research identified four stages of quartz generation like that in the LSSA. Early euhedral quartz is associated with a pre-mineralisation stage of vein development that forms around 40-60% of vein quartz (Figure 7-16) and is similar to Q1 in the LSSA (Parnell et al., 2000). The most abundant generation of quartz at Curraghinalt is a phase of CL dark quartz referred to as Q2 (Figure 7-16). The Q2 is similar to the CL dark quartz in the LSSA and brecciates Q1 to produce a mottled appearance (Wilkinson et al., 1999). Paragenetic studies conducted by Parnell et al. (2000) suggest that Q2 is synchronous with the main episode of gold deposition in pyrite (Wilkinson et al., 1999). A Q3 is present in small volumes in areas of intense mineralisation forming bright CL and displaying zonal growth (Figure 7-16) (Parnell et al., 2000).

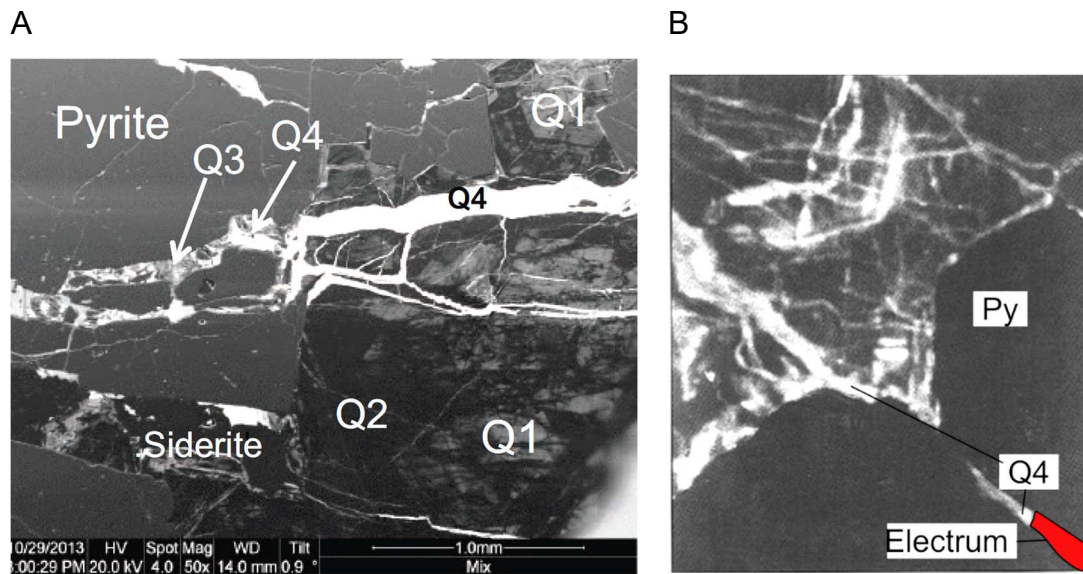


Figure 7-16: Cathodoluminescence of quartz at Curraghinalt, NI. **A-** Relationships of quartz generations (Rice et al., 2016). **B-** Electrum next to Q4 (Wilkinson et al., 1999).

A minor phase of Q4 (>5%) is observed in fractures (Figure 7-16) and displays bright CL with oscillatory zoned textures overgrowing Q3 and Q2 (Parnell et al., 2000). Q4 displays similar textures as Q3 in the LSSA and is associated with a late stage of electrum that occurs along fractures of pyrite (Figure 7-16b).

Wilkinson et al. (1999) present the results of fluid inclusion analysis, at Curraghinalt, of the gold-bearing Q2 and suggests that the original hydrothermal fluid was ~330°C with a moderate salinity. These authors also analysed fluids associated with Q4 that formed gold in fractures of pyrite. The fluids are interpreted to form from a saline fluid that had a lower temperature of 120°C (Wilkinson et al., 1999). Wilkinson et al. (1999) proposes that Q4 fluids are low temperature basinal brines, which remobilised gold within veins. Geochronological Re-Os dating of molybdenite in minor shears, conducted by Rice et al. (2016), has provided a new interpretation of mineralising events from Curraghinalt. The research suggests that late stage mineralisation was earlier, but the authors agree with Wilkinson et al. (1999) that Q4 was formed by a low temperature system at shallow crustal depths. The CL quartz textures revealed at Curraghinalt are comparable to those in the LSSA.

7.3.4 Trace element variation in quartz

Trace element analysis of quartz using LA-ICPMS was undertaken on Q1, Q2 and Q3 to determine differences in element concentrations. Q4 was excluded due to difficulty in finding enough quartz to ablate. A total of 80 ablation points of 25µm diameter were made. The results are presented in table A.2 in the appendix, and as percentile box plots in Figure 7-17.

Numerous trace elements were included in the analysis; however, the majority are close to or below the limit of detection. Figure 7-17 shows aluminium having the greatest variation in concentration between generations of quartz. Aluminium in Q1 ranges from 53 to 1743ppm, Q2 from 5ppm-2424ppm and Q3 from 72-2434ppm.

Fluid inclusion analysis of quartz is commonly undertaken to interpret the pressure, temperature and composition of the hydrothermal fluid responsible for different generations of quartz. A preliminary investigation was conducted to identify fluid inclusion assemblages in numerous vein quartz samples. The quartz has a complex mix of inclusions that were challenging to assign to the established quartz paragenesis due to the abundance of small (<2 µm) secondary inclusions. The largest inclusions identified were up to 15µm but were challenging to assign to a specific quartz generation. The results highlighted the importance to develop a robust paragenesis of the quartz that is required prior to any fluid inclusion studies. Although fluid inclusion analysis would provide valuable information, this PhD project chose to focus on developing a widely applicable paragenesis from quartz veins across the area. The incorporation of elements concentrated within fluid inclusions in quartz may produce elevated concentrations during elemental analysis. Figure 7-18a shows Al plotted against Na, K and Li, which are concentrated in fluid inclusions, and shows no correlation with any of the quartz generations.

The Al/Ti ratio of all quartz generations ranges from 100-230, and when plotted against each other in Figure 7-18b also shows no correlated elevation with any of the quartz generations. Figure 7-19a and b show the relationship of both Ba and Sb with Al, and there is a clear positive correlation. The barium

content does not vary systematically between quartz generations; however, notably, Sb is elevated in Q3 (Figure 7-19).

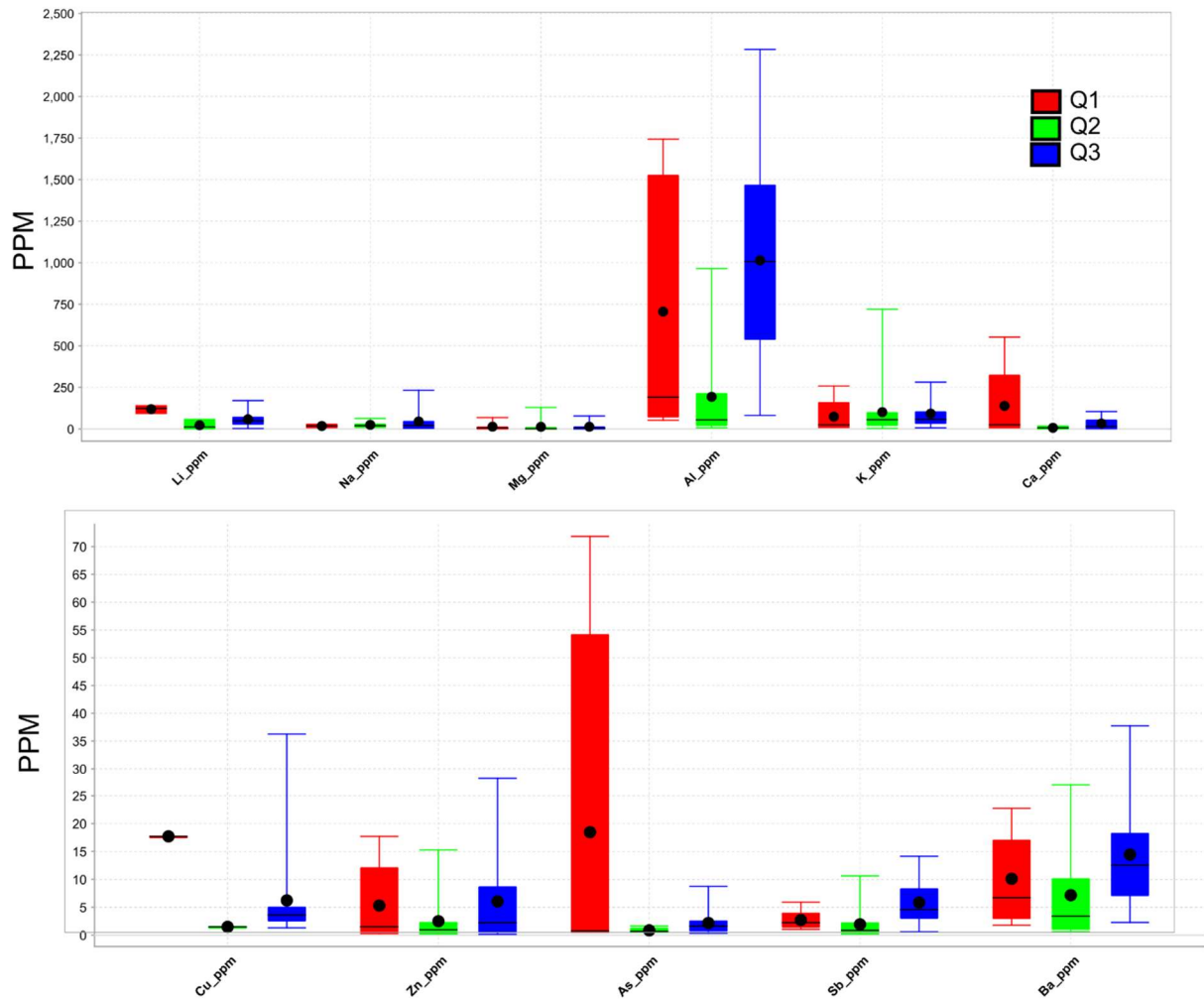


Figure 7-17: Box plots showing the variation in trace elements according to generations of quartz. Block represents inter quartile range between the 75th and 25th percentile, whiskers show range of data, black line is median and black circle is mean.

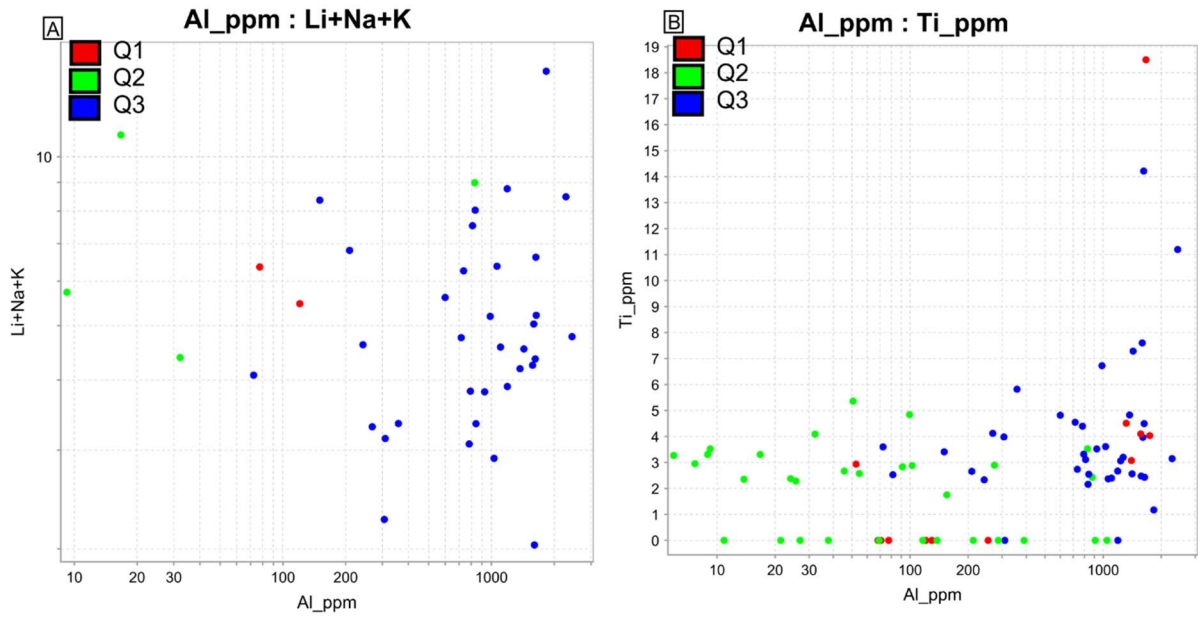


Figure 7-18: A- A plot of the sum of monovalent cations (Li+Na+K) and Al in different generations of quartz. B- A plot of Ti and Al for different generations.

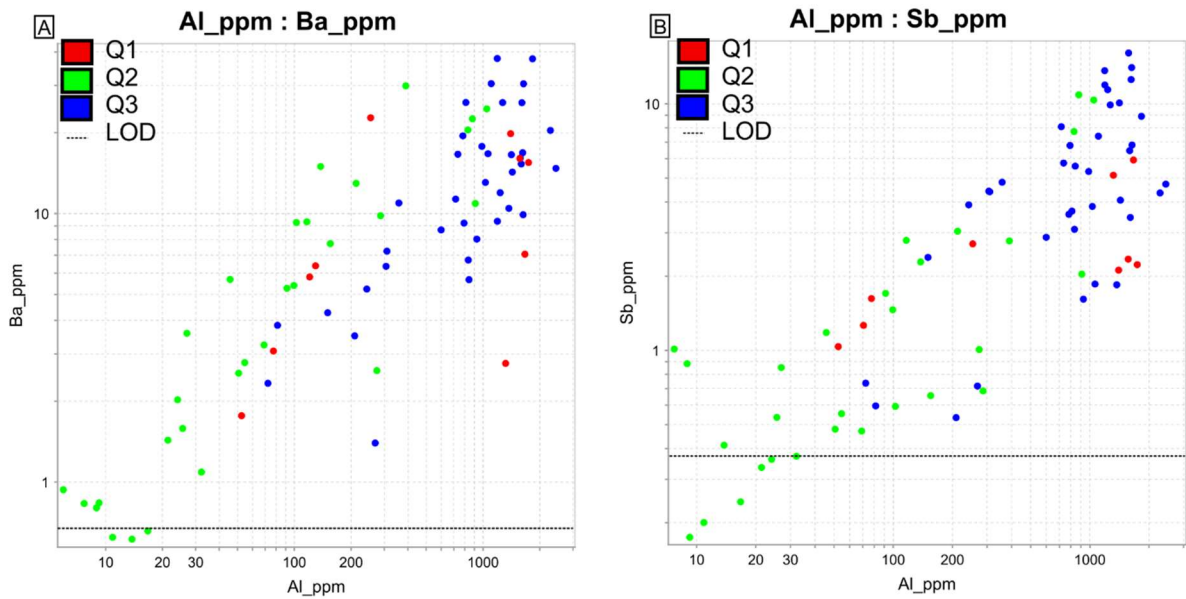


Figure 7-19: A- A plot of Al and Ba showing positive correlation. B- Al and Sb showing a linear correlation with Sb elevated in Q3.

7.3.5 Interpretation of hydrothermal conditions

This section aims to establish the hydrothermal conditions associated with each generation of quartz through the interpretation of CL textures and trace elements concentrations.

The trace element concentrations in quartz are interpreted to influence CL intensity (Rusk et al., 2008). However, lattice defects in quartz also influence CL and make it challenging to reconcile trace element distribution (Rusk, 2012).

Aluminium is the most consistently elevated element in quartz from the LSSA, and shows a correlation with CL intensity (Figure 7-17 and Figure 7-20). The Q3 shows a range of textures in CL that is reflected in the CL intensity. This may be due to the variation of Al which is shown in Figure 7-20 to be the greatest of any generation. Q1 has a mottled and ‘ghostly’ CL response with narrow range of Al, whereas Q2 displays dark CL and has the lowest Al range.

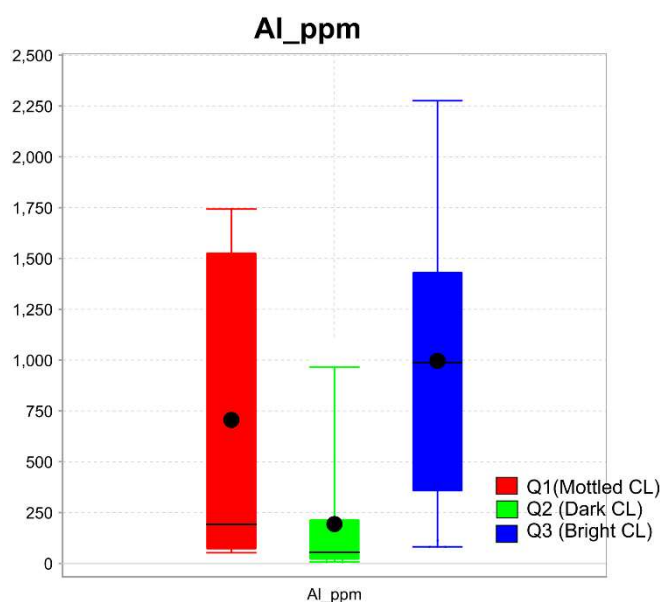


Figure 7-20: Percentile box plot of Al content from different generations of quartz. Range in Al corresponds to CL intensity.

One control on concentration of trace elements, and thus CL intensity, is the rate of crystal growth, with rapid crystal growth favouring higher concentrations of impurities and lattice defects. Elevated aluminium in quartz occurs when Al couples with monovalent cations, such as Na⁺, K⁺ and Li⁺

(Figure 7-18) to substitute for Si^{4+} . This process is more prevalent at lower temperatures where annealing and diffusion of Al^{3+} through quartz is limited (Rusk et al., 2008).

The development of growth zonation textures, identified by varying CL intensities (Figure 7-15) in Q1 and Q3, is thought to be a result of fluctuating conditions during quartz growth. Rusk et al. (2008) proposes that the high aluminium content, corresponding to bright zones, is influenced by the pH of the hydrothermal fluid. Bright CL quartz that has elevated aluminium, such as Q3, may originate from acidic fluids that can transport greater quantities of the element (by a factor of six) compared to neutral fluids (Rusk et al., 2008). This process may influence CL intensity in Q3 in the LSSA, however, there is no evidence for varying pH. Textural evidence indicating rapid growth has likely preserved lattice defects, which results in bright CL.

Another element commonly used to understand the temperature of quartz precipitation is titanium. The work of Wark and Watson (2006) demonstrated that temperatures of $>600^{\circ}\text{C}$ resulted in preservation of titanium in quartz, essentially as a function of temperature (The TitanQ geothermometer). The Ti concentration in quartz from the LSSA is low, with an average concentration of 2.5ppm, and shows no correlation with Al. These results agree with those of Wolff (2012), who attempted to use titanium in quartz as a geothermometer across the KGD. This thesis is in agreement with Wolff (2012) who concluded that the titanium content of quartz is too low for accurate consideration as a geothermometer.

A comparison of the CL textures and trace element content of quartz in the LSSA is made with the work of Rusk et al. (2008), who studied 12 ore deposits ranging in temperature from $100\text{-}700^{\circ}\text{C}$ (Table 7-1). These authors characterise deposits as either low or high temperature and suggest that quartz with 1000s of ppm aluminium are low temperature ($< 350^{\circ}\text{C}$). The data from the LSSA is plotted with other deposits in Figure 7-21, and shows a similar aluminium range to low temperature deposits; however, there are no OGDs included in the work of Rusk et al. (2008) for comparison. The titanium values from the LSSA could not be included in Figure 7-21 because they are

too low and suggests that the quartz is not related to high temperature fluids (Rusk et al., 2008).

Deposit	Deposit type	Vein formation temperature (°C)
Magmont, MO	Mississippi Valley type	~100
McLaughlin, CA ^s	Epithermal Au-Sb-Hg	~200
Jerrit Canyon, NV	Carlin-type Au	~200
Creede, CO ^s	epithermal Ag	~250
Red Dog, AK	Shale-hosted Zn	~250
Comstock Lode, NV	Epithermal Au-Ag	~250
Butte Main Stage, MT	Epithermal base metal	~300
Los Pelambres, Chile	Porphyry Cu-Mo	~500–700
Butte, MT	Porphyry Cu-Mo	~500–700
El Teniente, Chile	Porphyry Cu-Mo	~500–700
Grasberg, Indonesia	Porphyry Cu-Au	~500–700
El Salvador, Chile	Porphyry Cu	~500–700

Table 7-2: Trace elements were mapped in 12 deposits that vary in type and temperature, from Rusk et al. (2008)

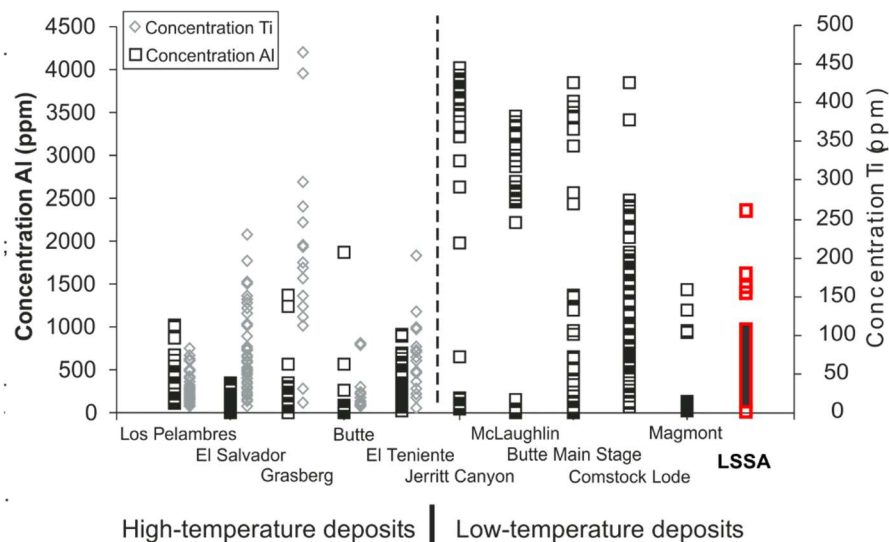


Figure 7-21: Compositions of Al and Ti of deposits in Table 7-2 from Rusk et al. (2008). Al content of quartz in the LSSA is presented but Ti values were too low to include.

A subsequent study by Rusk (2012) analysed elemental data from a further 30 deposits and identified relationships between aluminium and titanium. Although the study presents numerous deposits, the conclusions of Rusk (2012) are challenging to justify fully due to a lack of information on which deposits were studied. Rusk (2012) identified a linear relationship between the elements Al and Ti, which had a Al/Ti ratio between 1-10 in porphyry deposits. These authors compared the Al/Ti ratio of porphyry deposits to that

of epithermals which range from 100-10,000. Rusk (2012) states that orogenic deposits have Al/Ti ratios somewhere between porphyry and epithermal deposits, typically between 10 and 100. Presenting data as a ratio accounts for low Ti levels and is applied to the LSSA. The results show Al/Ti ratios between 100 and 250, which according to Rusk (2012), is intermediate between epithermal and orogenic. Although this result conforms with textural observations in CL from the LSSA, that suggest formation at shallow crustal levels, the classification of deposit types solely on Al/Ti ratio is not very reliable. Chapter 2 discussed the problems in defining OGDs and it is therefore important to analyse which deposits have been included in the 'orogenic' dataset of Rusk (2012) when interpreting quartz compositions.

Figure 7-19a and b show that barium and antimony are enriched in Q3 and have a positive relationship with aluminium. Both elements are commonly elevated in low temperature hydrothermal veins, such as epithermal or epizonal orogenic mineralisation (Groves et al., 1998, Cooke and Simmons, 2000).

The trace element data in quartz has revealed few trends. The large zonal growth textures and euhedral crystals in Q1 are interpreted to represent precipitation in open space under stable hydrothermal conditions. The dark CL associated with Q2 has no significant trace element relationships and makes the environment of formation challenging to reconcile. However, examples of dark CL elsewhere suggest that metamorphism or a metamorphic fluid is responsible (Rusk, 2012).

The most significant relationship found here is the correlation of aluminium and CL intensity identified in Q3. The CL analysis of Q3 revealed fibrous quartz textures and hydro-fracturing typical of boiling fluids, which evolve to more stable zonal growth. The textures are interpreted to represent formation at hydrostatic pressures at shallow crustal levels. Fast quartz growth from low temperature fluids has probably trapped aluminium in the lattice resulting in the increased CL intensity we see in Q3. The combined observations of quartz textures and trace element data has led to an interpretation that Q3 formed

from low temperature fluids at shallow depths, which is typical of epizonal orogenic environments (Groves et al., 1998).

Although trace element analysis has provided some quantitative data on quartz generations in the LSSA it cannot be considered in isolation. Textural data from CL remains the most useful mechanism for interpreting the paragenesis and conditions during mineralisation.

7.4 Gold in quartz veins

7.4.1 Textural and mineralogical relationships of gold

In situ samples of gold were collected (as described in Chapter 6) to investigate the relationship of gold to the surrounding mineralogy and quartz textures, with a view to establishing the paragenesis of the auriferous veins. Visible gold ranges from sub-millimetre up to 3cm in diameter and is typically found in association with limonite and subhedral quartz (Figure 7-22a,b).



Figure 7-22: A- Drill core from Gay Gulch Vein with centimetre-scale gold in limonite (EC15_10). B- Example of visible gold in limonite from a vein at the Buckland Zone (BZ07).

Textural relationships between gold, limonite and quartz were investigated using reflected light petrography with suitable polished blocks (e.g. Figure 7-23).

Gold is present on the surface of limonite, and within fractures (Figure 7-23). The deposition of gold is interpreted to have formed when limonite was pyrite

as it forms in fractures rather than space generated through weathering (Figure 7-23).

The textural relationship between quartz, gold and limonite were investigated using the same CL technique as described in section 7.3.2. Gold and limonite do not fluoresce; however, were compared to BSE images. Quartz surrounding limonite is mostly Q2 which is tentatively interpreted, in section 7.3.3, to be associated with metamorphic quartz. Although the origin of pyrite cannot categorically be related to Q2 it seems likely that the euhedral pyrite grains formed at the same time as metamorphic quartz in veins across the LSSA.

The technique was also applied to quartz in fractures of limonite that coincide with gold. Figure 7-24a and b are CL images that show the presence of gold in fractures with distinctive Q3 CL textures. This provides a genetic relationship between Q3 and gold.

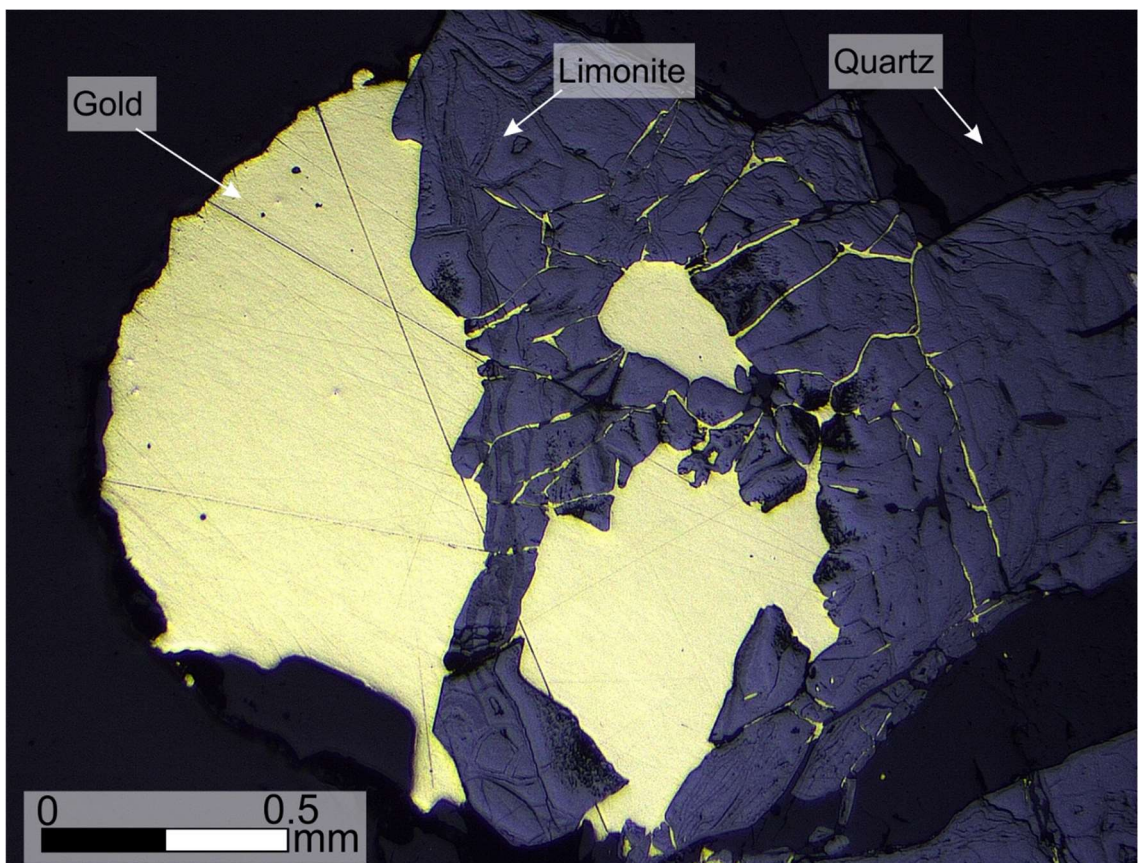
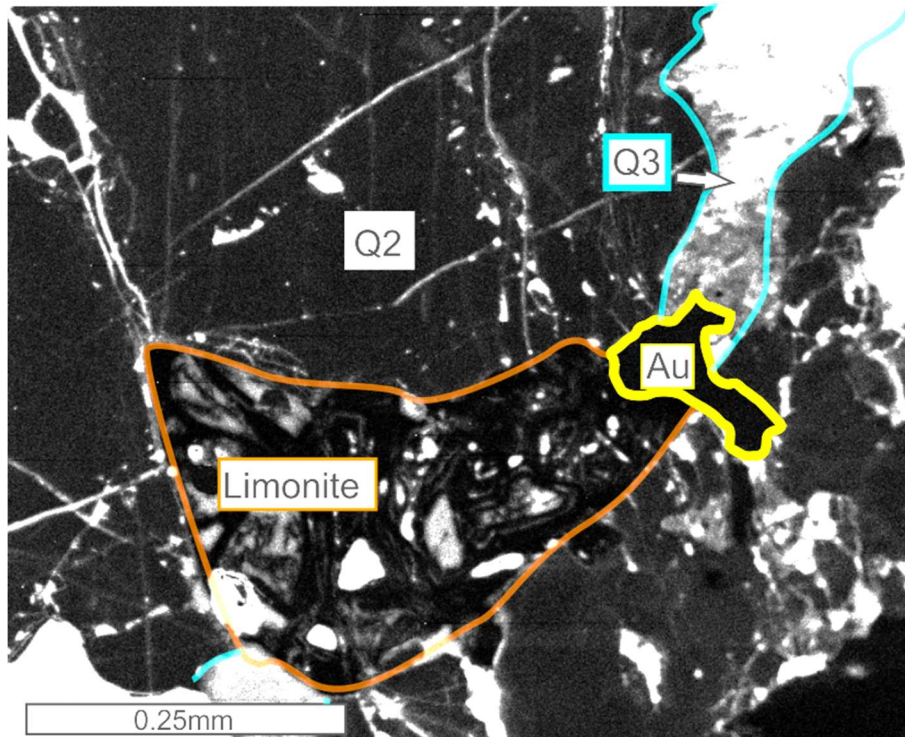


Figure 7-23: Reflected light image of sample of gold from Buckland Zone (MG26_BZ17). Sectioning of visible gold in quartz revealed the textural relationship of gold, limonite and quartz. T

A



B

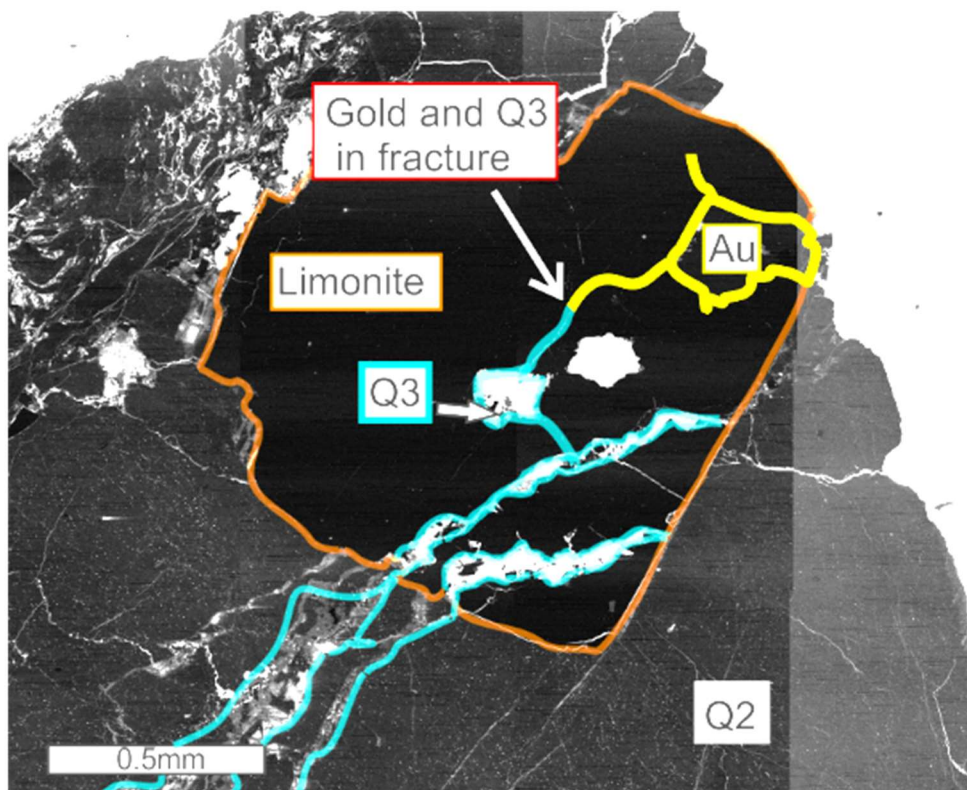


Figure 7-24: A- CL image of limonite (outlined in orange) with gold (outlined in yellow) that is next to fracture filled with Q3 (outlined in blue) (MG21_D7). B- CL image of gold in limonite that is fractured by Q3 (MG28_BZ10).

At the Nugget Zone, a barium rich potassium feldspar is observed along the same fractures of limonite that hosts Q3 and gold (Figure 7-25 b). This mineral is hyalophane and typically exhibits Ba content between 2-16% which is oscillatory zoned. Elsewhere hyalophane is found as ‘exclusions’ on the exterior of gold with sharp crystal edges indicating that it is coeval rather than post-dating the gold (Figure 7-25a). Hyalophane is discussed in further detail in Chapter 8 and is a key mineral associated with gold precipitation in the LSSA.

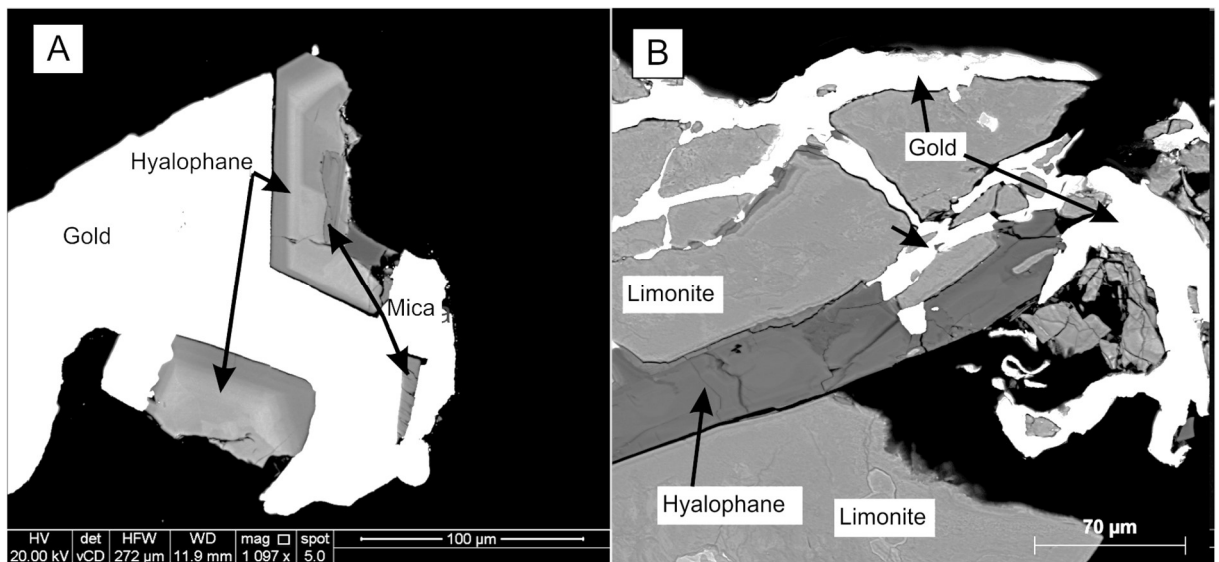


Figure 7-25: BSE image of gold particle, liberated from veining at Upper Nugget Zone. **A-**Hyalophane forms around the exterior of gold as an exclusion and is coeval. **B-** Fractures in limonite filled with gold and hyalophane.

7.4.2 Paragenetic summary of gold-bearing quartz veins.

The results of this study have revealed a much more detailed paragenesis in for the gold-bearing quartz veins of the LSSA than previously proposed by Rushton et al. (1993). The formation of epitaxial quartz crystals is preserved as euhedral quartz in veins, which display a mottled appearance in CL. This generation of quartz is defined as Q1 and is best developed in veins that are hosted in brittle lithologies (Figure 7-26). The Q1 is fractured and subsequently filled by an extensive subhedral milky white quartz generation referred to as Q2 (Figure 7-26). The Q2 phase appears black in CL and may

be associated with alteration related to deposition of pyrite in veins. Q3 cross cuts both previous generations resulting from brecciation of fragments of the original vein material and subsequent cementation with Q3 itself (Figure 7-26). Textural evidence within Q3 suggests the initial quartz phase was fibrous but progressed to oscillatory zonation (Figure 7-26). Q3 also formed along fractures in pyrite, and was deposited in association with hyalophane and gold. Gold particles almost always form on the surface and along fractures within pyrite suggesting that it is coeval with Q3. A minor phase of quartz associated with Mg-Fe carbonate minerals that is characterised as Q4 and forms in minor cross-cutting fractures in the veins.

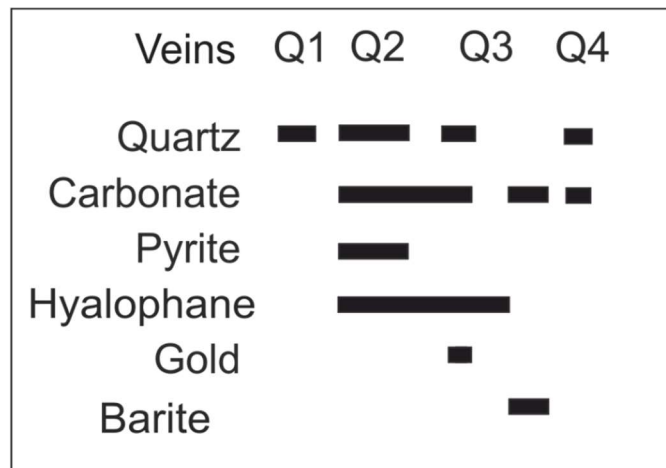


Figure 7-26: Gold-bearing vein paragenesis for the LSSA.

7.4.3 The controls on gold deposition in gold-bearing quartz veins

Textural and mineralogical studies have identified that gold in veins across the LSSA are related to deposition of Q3 and hyalophane. This section provides a discussion of the various controls on gold deposition that are typical of OGDs (Chapter 2.4.3.2).

Rushton et al. (1993) suggested that gold deposition in the LSSA is most likely due to sulphidation reactions and is coeval with pyrite formation. This study has provided a new paragenesis where pyrite predates gold deposition and is tentatively linked to deposition of Q2. Although later than pyrite, deposition of gold has been demonstrated here to have an association with pyrite due to its formation on the surface and along brittle fractures in pyrite altered to limonite.

The presence of large particles of gold along the same fractures is likely to be responsible for the a nugget effect, which has influenced sampling protocol and data interpretation during this PhD.

One potential model for the formation of visible gold found in the LSSA is related to fracturing and recrystallisation of auriferous pyrite. Deformation of the pyrite mobilises sub-micron gold along grain boundaries as a result of solution creep, which causes gold to concentrate into fractures (Figure 7-27). Huston et al. (1992) presents this model for a VMS deposit in Eastern Australia where there is evidence of gold forming in pyrite fractures (Figure 7-27). The same mechanism of formation is proposed by Cepedal et al. (2008) and Vikentyev (2015); however, the amount of gold deposited by this mechanism is limited by the amount of gold dissolved in the pyrite lattice. This mechanism seems highly unlikely to be occurring in the LSSA mainly due to the size of the visible gold compared to the host pyrite (Figure 7-23). The model also fails to account for the presence of alloying elements, which would need to also be hosted within the original pyrite.

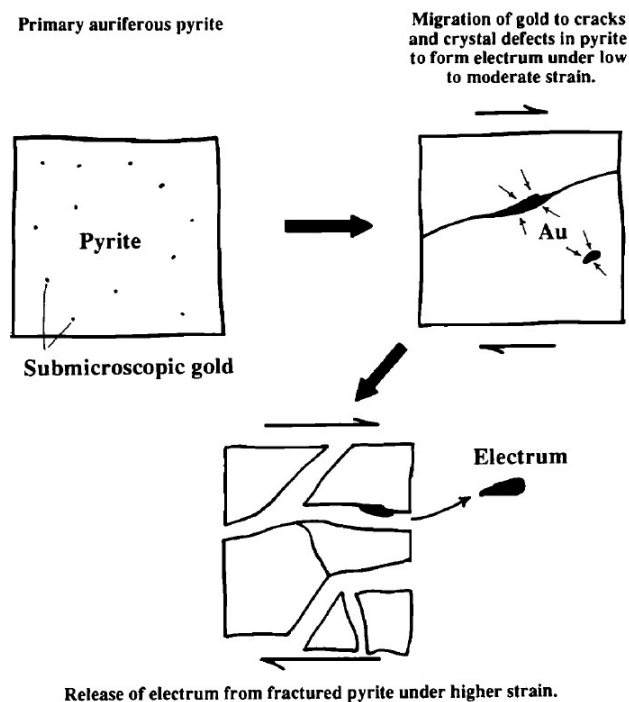


Figure 7-27: Schematic sketch of the proposed mechanism of visible gold formation in fractured pyrite. High-strain results in migration of gold from the pyrite lattice into fractures (Huston et al., 1992).

An alternate mechanism for the formation of visible gold in brittle fractures of pyrite must be found. Gold is associated with the volumetrically minor Q3 that may originate from a silica poor fluid or from an extremely enriched gold-bearing fluid.

A new model is proposed where brittle fracturing of quartz veins (hydrofracturing) provides accommodation space for gold deposition. The transport of fluid up fractures in discordant quartz veins results in depressurisation and precipitation of Q3 and precipitation of gold.

One mechanism for the generation of large visible gold is to have deposition from a very rich gold-bearing fluid. Gold chloride or bisulphide complexes are limited to 10ppb of gold in solution which means an alternate transportation mechanism is required (Stefansson and Seward, 2004). One theory involves the formation and transportation of gold colloids (up to 1 μ m) (Herrington and Wilkinson, 1993). Destabilisation of gold complexes, during depressurisation, can result in the formation of gold colloids. Herrington and Wilkinson (1993) provide evidence of colloidal gold transport and deposition in mesothermal veins; however, they infer crystallisation of gold occurs rapidly due to flashing of hydrothermal fluids.

An alternate mechanism for formation of large visible gold in the LSSA is proposed, where pyrite surfaces influence the nucleation of gold. The relationship of gold and sulphide surfaces was investigated by Jean and Bancroft (1985) who showed that accumulation of Au(III) and Au(I) on sulphide surfaces occurs via adsorption at low temperatures. Starling et al. (1989) investigated similar processes at high temperatures and found that gold concentrated at crystal edges or defects in pyrite. The initial localisation of gold occurs due to weak Van Der Waals forces (Figure 7-28) (Knipe et al., 1992). The establishment of a nucleation site results in subsequent reduction-driven chemical adsorption (Equation 6) (Starling et al., 1989). The electronic characteristics of the nucleation site are transmitted through the newly deposited gold and provide a reactive surface for further deposition and growth of gold.



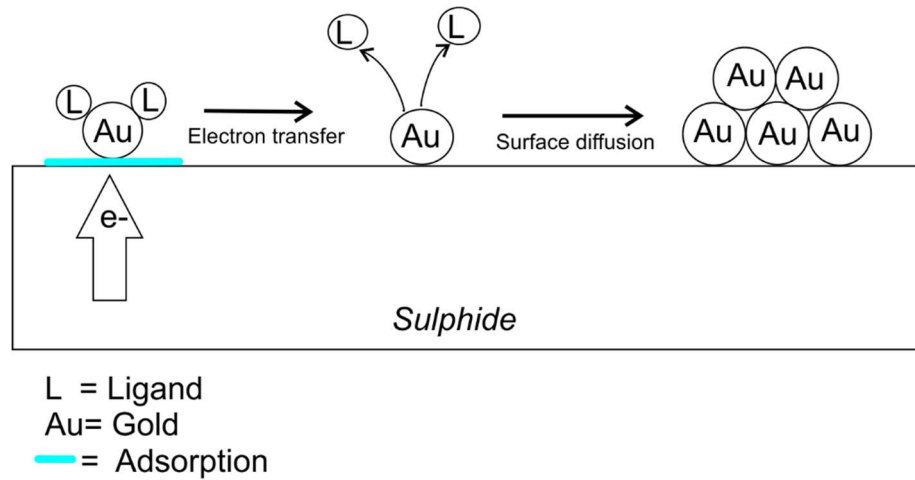


Figure 7-28: Modified from Knipe et al (1993). Initial adsorption of gold and ligand then progresses to chemisorption. Clustering and crystal growth follows.

Sulphides have been shown to behave as semiconductors where conductivity is between a metal and an insulator (Möller and Kersten, 1994). Chemical heterogeneity within the sulphide produces either 'N-type', in which electrons are added resulting in a negative charge, or 'P-type', in which electrons are removed resulting in a positive charge. Gold deposition from a negatively charged gold bisulphide (Equation 6) on the anode (n-type) was far exceeded by the cathode deposition (p-type).

This PhD project proposes a similar mechanism of gold deposition on sulphide surfaces in the LSSA, where a fluid was focussed along fractures in Q1, Q2 and pyrite, and deposited with Q3 quartz. Fluid flow along fractures in discordant quartz veins resulted in depressurisation and destabilisation of gold complexes in the fluid. Nucleation of gold occurs where fractures intersect pyrite particles. Epitaxial gold growth develops once a film of gold is established (Möller and Kersten, 1994). Alternate nucleation sites may be possible; however, pyrite surfaces provide an ideal location for 'nuggety' gold to accumulate (Figure 7-23).

7.4.4 Internal crystallography of gold from veins

The internal crystallography of gold particles was investigated to establish whether gold exhibits evidence for epitaxial growth from sulphide surfaces, as suggested in the previous section. The specimens were polished to remove the surface damage, caused by mechanical polishing (the Beilby layer), to

reveal the crystal structure. EBSD analysis was conducted to determine the variation in the crystallographic orientation of gold. The results are presented as inverse pole figures (IPF) that are colour coded according to crystal orientation (as discussed in Chapter 6.4.2.3). Grain boundaries were defined by a change in orientation $>10^\circ$, and twin boundaries in gold that correspond to a 60° change (111).

Figure 7-29 shows an orientation map of the same gold samples previously illustrated in Figure 7-23. The map shows that gold has straight grain boundaries that are 60° twins. These twins separate $\approx 500\text{-}1000\mu\text{m}$ grains that exhibit low levels of internal lattice mis-orientation. Six samples of visible gold have been investigated in this way and all display very similar characteristics.

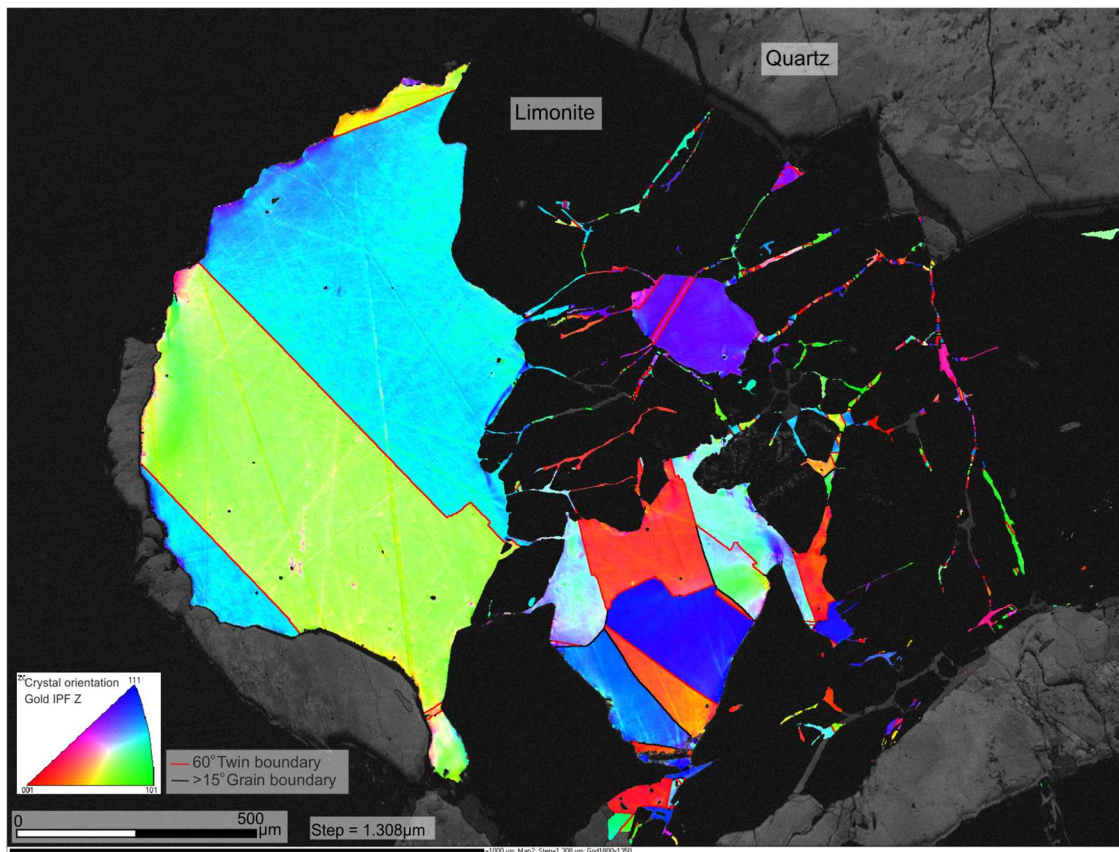


Figure 7-29: Orientation map (IPFZ) from EBSD showing straight twin boundaries within gold particle from Buckland Zone (MG26_BZ17 and shown in Figure 7-23).

The polycrystalline textures are similar to those described by Hough et al. (2007) in gold nuggets from Western Australia. The large twins are interpreted to have formed as a result of annealing during thermal recrystallisation (Humphreys and Hatherly, 2004a, Hough et al., 2007). Annealing occurs as a

result of deformation and heating, which annihilates dislocation and lattice defects via the recrystallisation (Ott and Schindler, 2001). The process involves the solid state diffusion of atoms through the lattice to form new crystals in an ordered structure (Humphreys and Hatherly, 2004a). Hough et al. (2009) describe how the resulting crystal size is dependent upon temperature and deformation as shown in Figure 7-30.

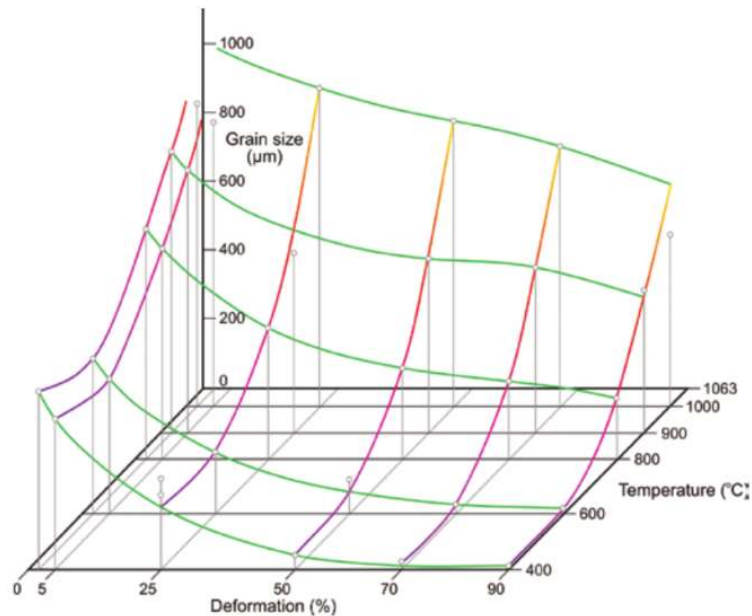


Figure 7-30: Recrystallisation diagram of pure gold showing grain size as a result of annealing temperature and deformation (Hough et al., 2007).

This process of annealing can occur at temperatures of 80°C in pure gold, but with alloys containing only 5% Ag, this increases to 250°C, and with base metal contents of 0.1-0.5 wt.%, recrystallisation occurs at >250 °C (Ott and Schindler, 2001).

The evidence from all visible gold analysed shows that internal grain sizes are large (up to 0.5mm in diameter) and have undergone complete annealing. The straight twin boundaries and lack of internal mis-orientation show that the gold has not undergone deformation and has annealed during thermal recrystallisation. This process, unfortunately, has likely overprinted any primary crystal features associated with epitaxial growth of gold on pyrite surfaces, but does indicate that the veins must have undergone some heating post deposition of the gold.

Whilst the internal crystal structure provides no evidence for nature of growth on pyrite, the size and morphology of the overall particles can provide information on crystallisation processes. The majority of crystal studies (e.g. Humphreys and Hatherly (2004b)) focus on crystal growth from a melt and do not address natural solid-liquid interactions. The kinetics of crystal growth are dependent on nucleation and saturation of an element in the fluid (Sunagawa, 1981, Humphreys and Hatherly, 2004a). Dendritic gold forms when gold is substantially out of equilibrium with the surroundings (Sunagawa, 1981). A lack of stable crystal growth results in branching of crystals controlled by twin relationships (Sunagawa, 1981, Lofton and Sigmund, 2005). The presence of dendritic forms indicate rapid deposition and crystallisation.

The crystal form and shape observed from particles collected from most gold-bearing veins lack dendritic forms and have more likely grown over a period of stable hydrothermal conditions. Mauthner (2004) describes rare examples of detrital dendritic gold from Eldorado Creek suggesting that rapid deposition of gold has occurred within the LSSA, albeit very rarely, and not due to the same processes inferred here for the deposition of the majority of gold present in the veins.

7.4.5 The oxidation and weathering of gold-bearing quartz veins.

Weathering to a depth of around 100m is common across the KGD and has resulted in the oxidation of pyrite in every sample investigated at the surface. This reaction results in the formation of various hydrated iron (III) oxide-hydroxides collectively referred to as limonite. Oxidation results in volume loss creating a distinctive colloform texture (e.g. Figure 7-31). The oxidation textures generate a box-work pattern, which is controlled by the original cubic crystal structure of pyrite (Hu et al., 2006).

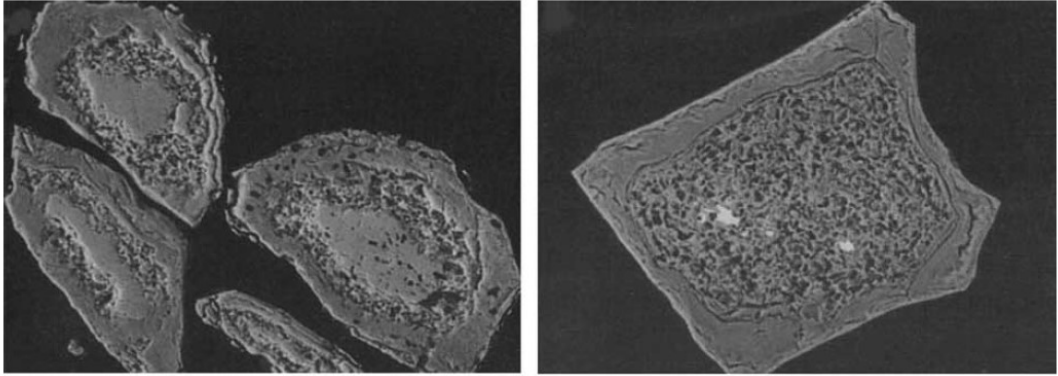


Figure 7-31: Oxidised pyrite particles showing volume loss (Hu et al., 2006).

Samples in the LSSA contain micro-crystalline fine-grained gold, 1-2 μm , within the colloform texture of limonite proximal to the cross cutting gold (Figure 7-32 and Figure 7-35). Figure 7-33b shows a sample of gold from the Dysle Zone where unoxidised pyrite is at the centre of colloform textured limonite (Figure 7-33b). The spaces surrounding the limonite are filled with minor amounts of barite, clay, and occasionally silver telluride (Figure 7-33b). Small crystals of gold were also observed on the surface of larger gold particles from in situ mineralisation (e.g Figure 7-34).

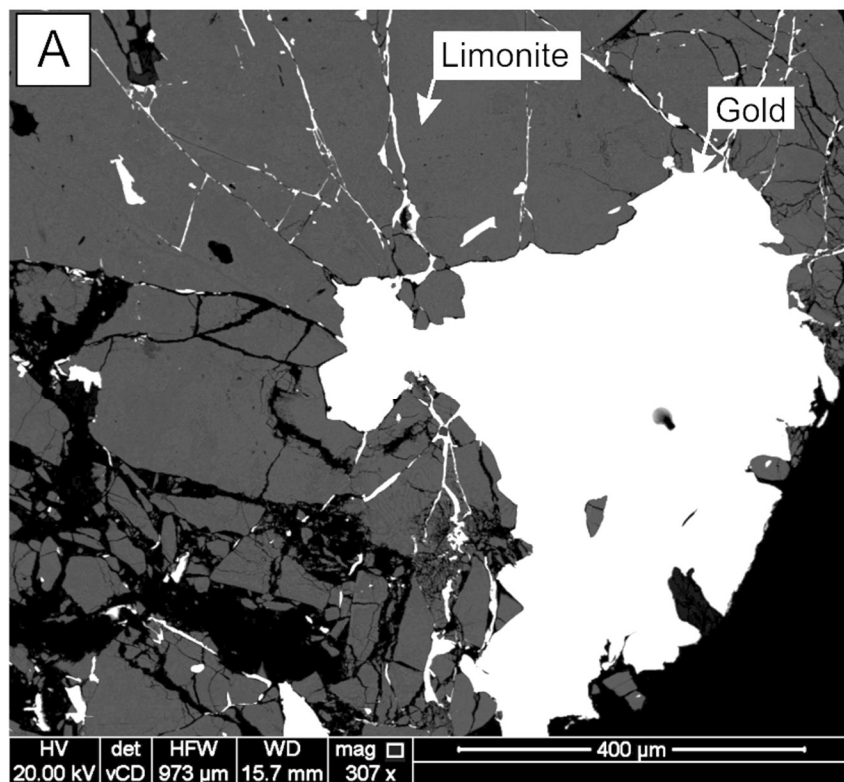


Figure 7-32: BSE image of gold in limonite from Buckland Zone (MG24_BZ07).

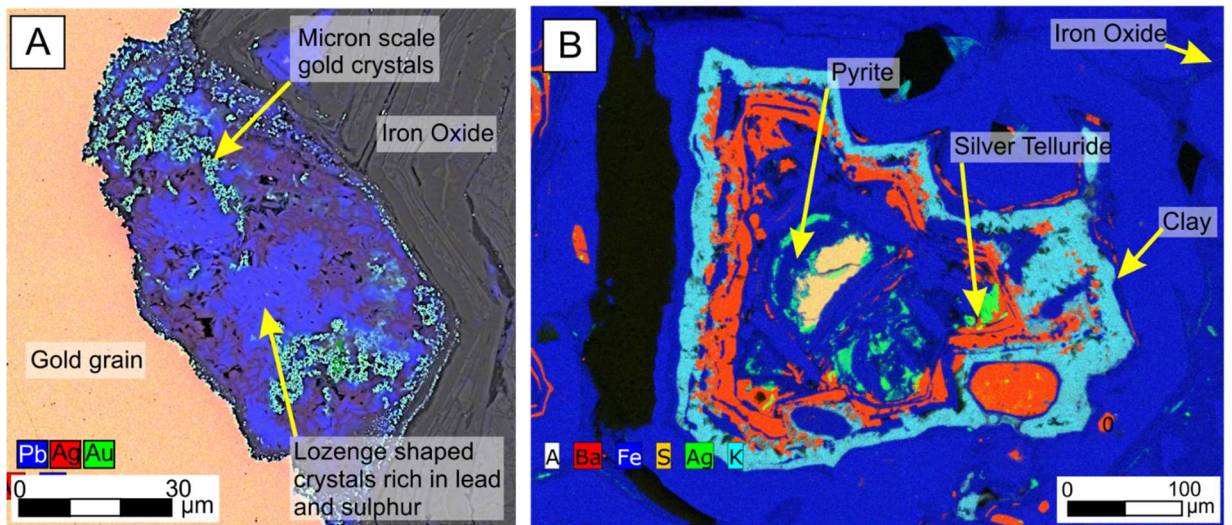


Figure 7-33: A- EDS map of margin of gold and limonite from Upper Nugget Zone (MG53_OLT15_15). Gold crystals occur alongside an unidentified mineral with a lozenge shape that is composed of lead and sulphur. B- Limonite has a spongy box-work texture that is filled with silver telluride, barite and clay (MG21_D07).

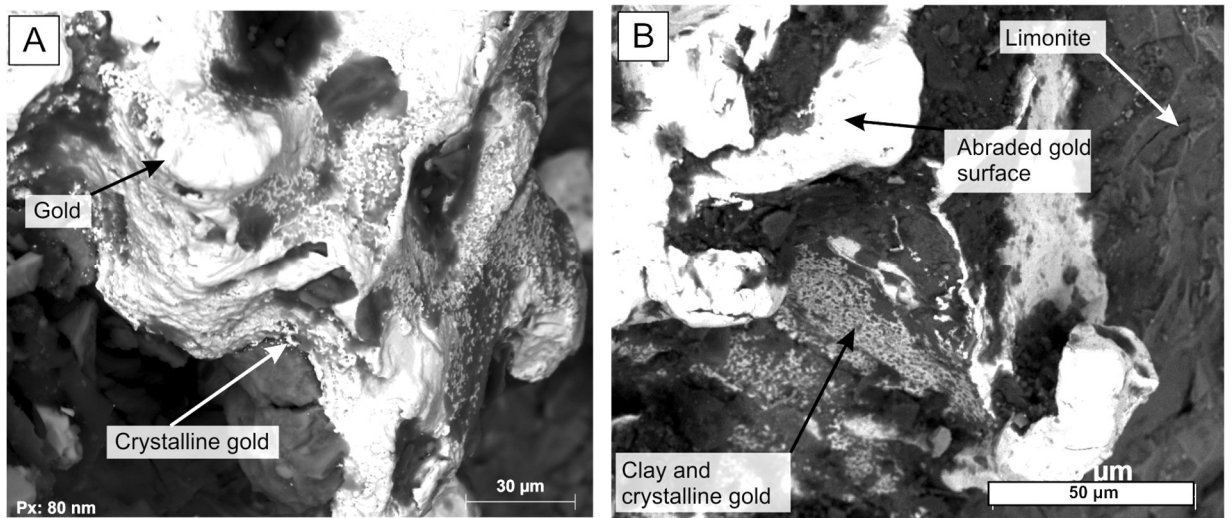


Figure 7-34: BSE images of gold in limonite from Nugget Zone (MG68_OLT15_14). A-The surface of gold in limonite is covered in micro-crystalline pure gold. B- Abraded surface of gold with micro-crystalline gold and clay in embayments and fractures.

This fine-grained gold is interpreted to originate from supergene processes, in which hypogene gold is locally remobilised. An example is shown in Figure 7-35 in which dissolution of gold from a large particle is coupled with local (20 μ m) deposition of micro-crystalline gold in limonite.

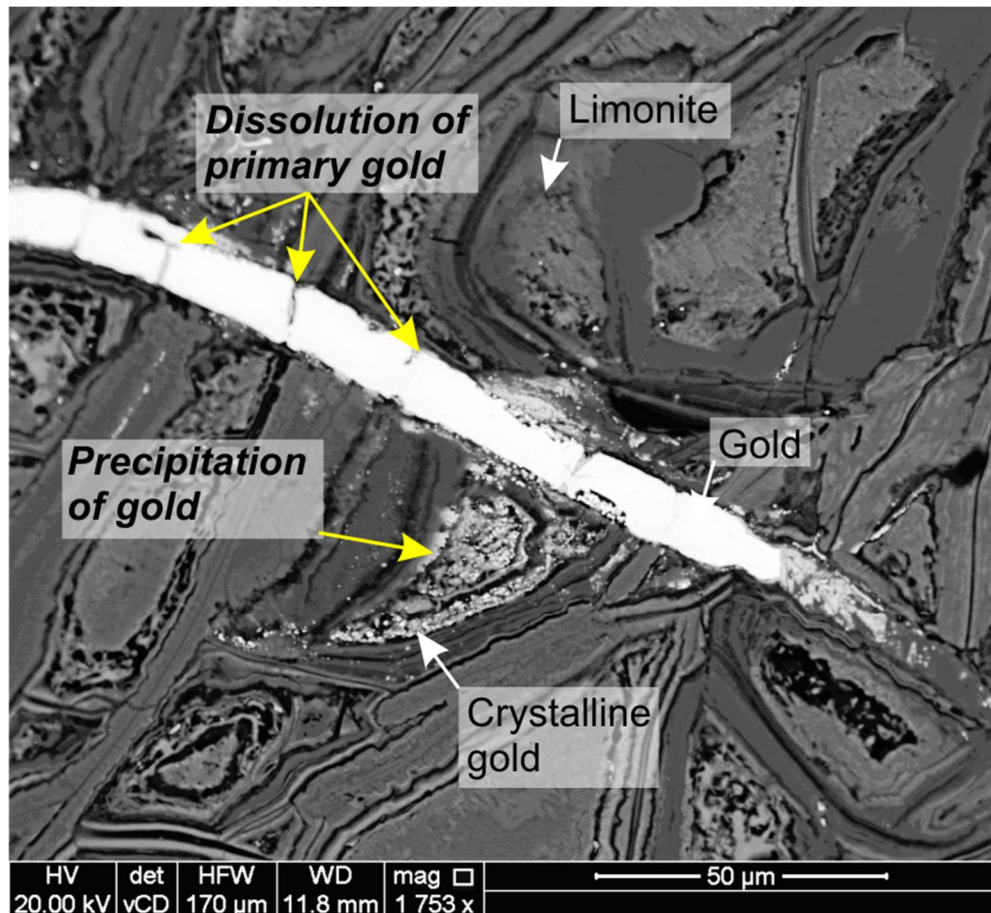
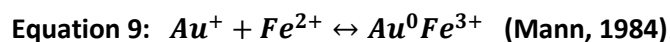
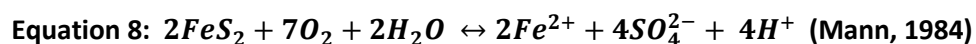


Figure 7-35: BSE image of margin of gold and limonite from Upper Nugget Zone (MG53_OLT15_15). Dissolution of primary gold and precipitation in limonite pseudomorph from Nugget Zone.

Mobilisation of gold occurs with thiosulphate (Equation 7), which is produced during oxidation of pyrite (Stoffregen, 1986). Thiosulphate is highly unstable under surface conditions and is converted to sulphate resulting in precipitation of gold. Stoffregen (1986) describes the role of thiosulphate as an important mechanism in the oxidation of primary gold ores at Summitville in Colorado.



An alternate mechanism of gold transport is linked to the circulation of oxidising groundwater (Mann, 1984). The coupled reactions of Equation 8 and Equation 9 result in the mobilisation and deposition of gold in limonite (Mann, 1984).



Mann (1984) and Möller and Kersten (1994), present this hypothesis to explain gold in limonite in samples from Western Australia.

7.4.6 Gold composition data from veins

Gold alloy compositions (Au, Ag, Cu, Hg) of visible gold specimens were analysed by EMPA. Trace element analysis of gold particles collected from Nugget Zone, Buckland Zone and Boulder Lode Mine was undertaken via LA-ICP-MS. This provided a lower detection limit and further suite of elements than the standard technique of EPMA.

7.4.6.1 Alloy Heterogeneity in gold from veins

The degree of alloy heterogeneity (see examples in Chapter 5) was evaluated by inspection of greyscale images generated in BSE. Alloy heterogeneity was identified in less than 5% of all particles studied and manifested either as diffuse silver enrichment (Figure 7-36a and b) or narrow gold rich tracks (Figure 7-36c and d). Figure 7-36a and b show gold particles that have diffuse silver enrichment that is controlled by the location of grain boundaries. The formation of gold rich tracks typically have a maximum width of 15µm and have sharp boundaries as shown in Figure 7-36C and D.

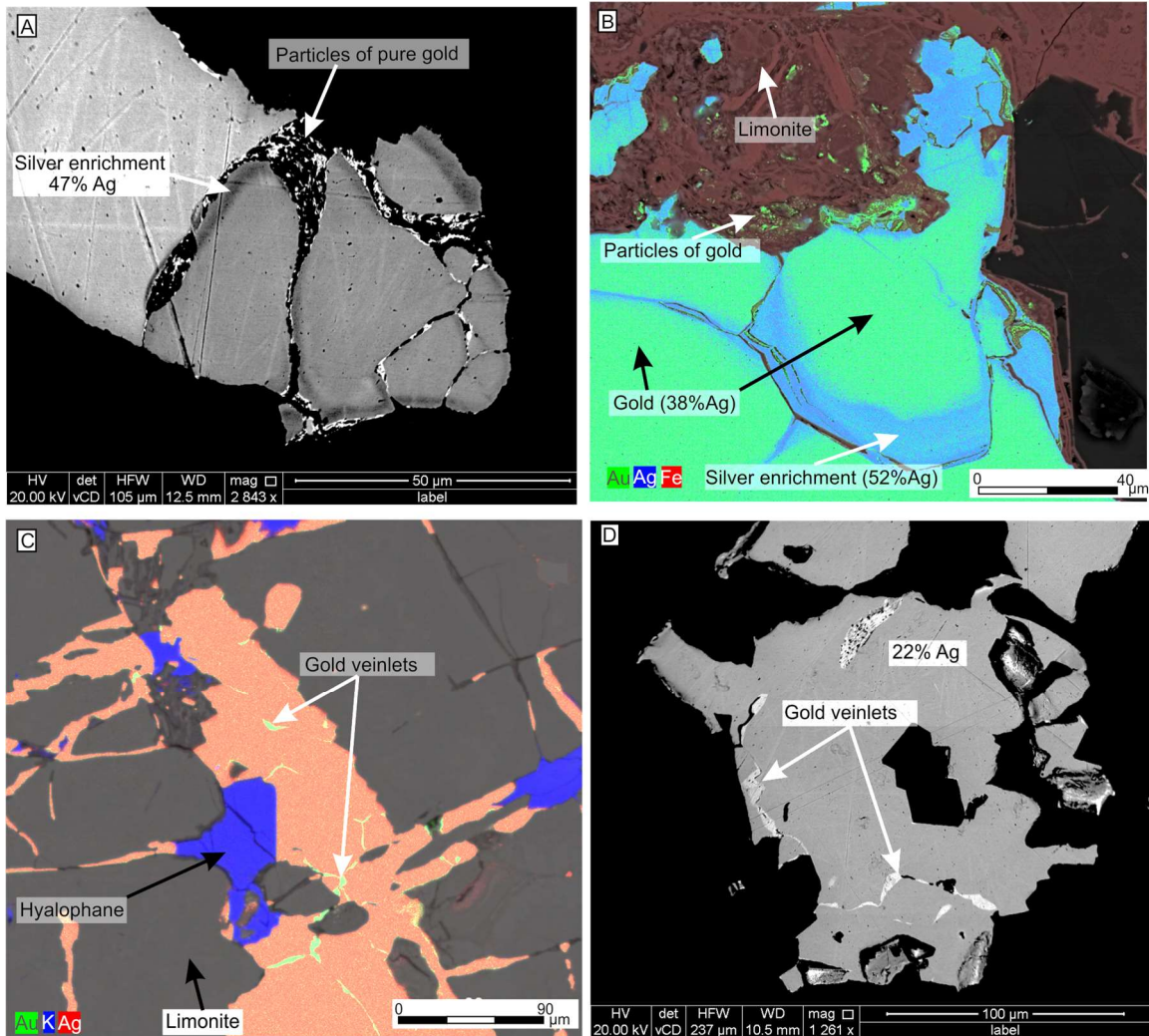


Figure 7-36: BSE images and EDS maps of gold particles. **A-** Diffuse silver enrichment (darker areas) with small pure gold particles (bright spots) along grain boundaries (Nugget Zone MG53_UNOLT15_15). **B-** Gold particle showing diffuse silver enrichment along grain boundaries with small gold crystals in spaces of limonite (Nugget Zone MG53_UNOLT15_15). **C-** Gold with hyalophane along fractures of limonite. Gold rich tracks are represented by green (Au) tracks (Nugget Zone). **D-** Thin gold rich tracks that cut otherwise homogenous alloy (uniform greyscale) (Buckland Zone -MG52_BKOLT15_29).

The gold rich tracks were investigated using a combined approach with EDS and EBSD. Figure 7-37a presents the results of analysis on the interior of a gold particle, which shows gold rich tracks (green) have formed along grain boundaries. The margins of the gold rich areas are not delineated by the generation of a new grain boundary, cross cuts twin boundaries (red) and lack crystal mis-orientation.

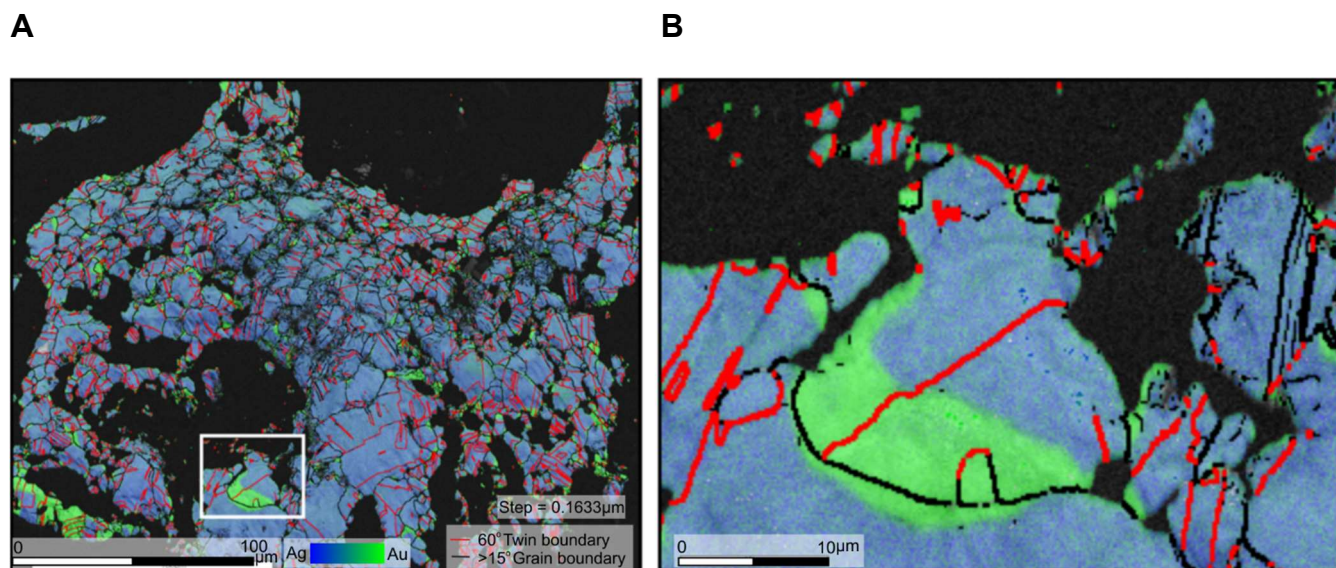


Figure 7-37: EBSD and EDS data of gold particle showing grain boundaries (black), twins (red), Au (green), and Ag (blue). **A-** Gold particle from Adams Hill alluvial deposit showing silver depleted tracks. **B-** Gold rich areas on interior of gold particle lack new grain boundaries. Silver depleted area results in slight distortion of straight twin.

There are two potential theories for the origin of gold rich tracks; the first involves a second phase of gold deposition related to hypogene processes, and the second involves the in-situ loss of silver due to weathering processes. The tracks lack new grain boundaries and therefore are unlikely to be related to a second phase of gold deposition. The tracks are interpreted to have formed by silver depletion where dissolution of silver occurs along grain boundaries. This is a natural analogue to depletion gilding used in metallurgy (Grimwade, 1999) in which the surface of gold is enriched by removal of silver. Hough et al. (2007) present crystallographic data of gold rich tracks in gold nuggets from Australia. These authors link the formation of gold rich tracks to silver depletion in the supergene environment. Fluid mobilisation of gold in the supergene environment effects the exterior of hypogene particles (section 7.4.5) and is interpreted to permeate along internal grain boundaries. Gold rich tracks are a genetic feature described in various examples of gold around the globe (e.g. British Columbia, Yukon and Siberia) (Boyle, 1969).

Grimm and Friedrich (1990) present an example of how weathering effects gold from the Gentio do Ouro region of Brazil. Gold in colluvium exhibits a range of features, described in section 7.4.5, similar to those in the LSSA that are linked to changing weathering processes (Grimm and Friedrich, 1990).

The presence of gold in limonite pseudomorphs after pyrite is described by Grimm and Friedrich (1990) to be a result of very local transport and deposition from primary gold particles. Fluctuating climatic conditions in the region resulted in the circulation of oxidising groundwater's (Grimm and Friedrich, 1990). The infiltration of these fluids along fractures and grain boundaries in primary gold particles led to dissolution of silver from the gold leaving behind pure gold tracks (Grimm and Friedrich, 1990).

Craw et al. (2017) propose that micro-crystalline gold can form centimetre scale nuggets in the supergene environment. The crystallography of supergene nuggets would reveal oscillatory growth of small grains; however; gold particles in the LSSA (section 7.4.4) show large annealing twins that form at high temperatures greater than the supergene conditions. There is no evidence that supergene nuggets are forming in the LSSA.

The results of this present study suggest that processes of gold dissolution and precipitation in the surface environment are occurring. However, the extent to which the mass of placer gold has been increased by such processes is negligible. Nevertheless, it is important to distinguish between primary features observed in gold particles and those forming because of weathering so that hypogene processes can be investigated.

7.4.6.2 Gold alloy composition data from veins

Alloy composition was investigated by conducting EMPA traverses across gold particles. Figure 7-38 presents the variation in silver content associated with five traverses on a gold particle from the Buckland Zone, which appeared homogenous when viewed in BSE. On this basis only two analyses are required to establish the silver content of a visually homogenous particle.

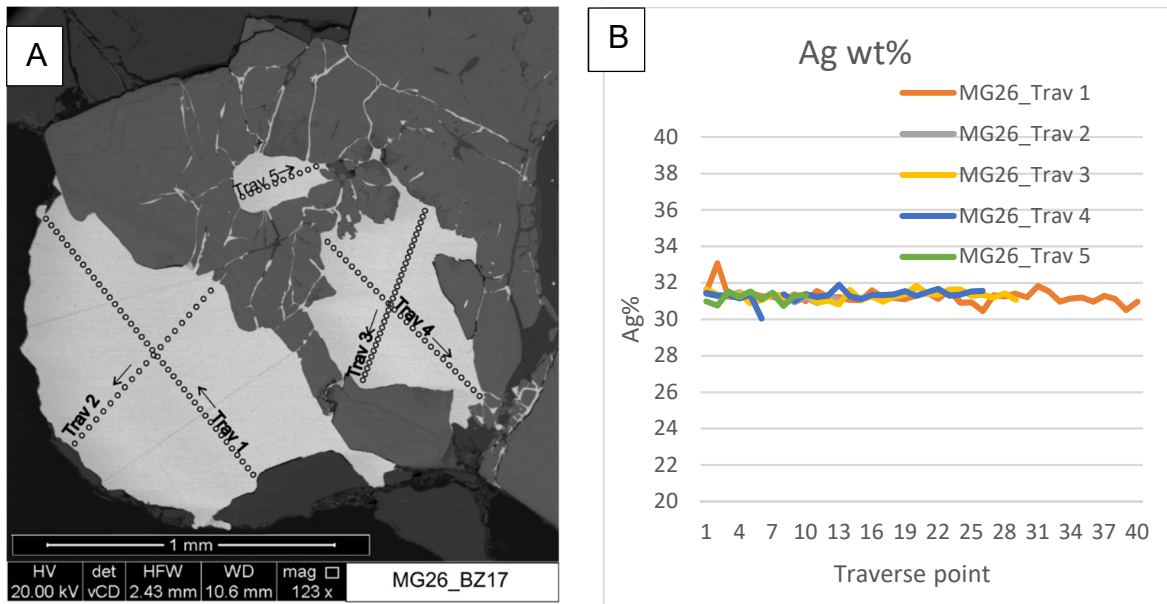


Figure 7-38: A- BSE image of MG26_BZ17, with traverse lines marked. B- Silver values recorded along traverses.

Alloy compositions of over 300 gold particles were determined using EPMA at the University of Leeds. Table 7-3 shows the range of silver contents of samples from different localities. Chapman et al. (2010a) noted that Cu contents of Au alloy were very close to detection limits and concluded that this element did not provide a useful discriminant. The results of the present study confirm this, with recorded values straddling the limit of detection, even in cases where large proportions of a population contain detectable Cu (e.g. Boulder Lode Mine) (Appendix A1.4). Consequently, the accuracy of Cu content of alloys is not reliable and are not considered further. Chapman et al. (2010a) also noted the large variation in the Hg contents of gold particles with location over the LSSA. Table 7-3 presents Hg data that shows some occurrences where a small proportion of particles recorded an alloy composition above the limit of detection.

Figure 7-39a illustrates the silver contents of the gold populations studied here in terms of cumulative percentile plots (as discussed in Chapter 5), to illustrate variations in the composition at each lode occurrence locality. Figure 7-39b plots the same data as percentile box plots in order of increasing silver content per location.

Gold particles from the Nugget Zone and Buckland Zone display a broad range of silver values that are very similar in Figure 7-39a. The mean silver

value of gold at the Nugget Zone is 24.5% and 23.5% at Buckland Zone with an interquartile range of 8.2% (Figure 7-39B). The silver values of gold from the Dysle Zone and Violet Mine are elevated compared to the other locations (Figure 7-39A,B). The silver values have the same interquartile range of 3.5% and are between 26 and 29% silver (Figure 7-39A and B). The samples of gold collected at the Boulder Lode Mine show the least variation in silver (Figure 7-39B) but come from the smallest geographical area. The average value of silver is 15wt% at Boulder Lode Mine with some outliers that are closer to average silver values from the Nugget and Buckland zones (Figure 7-39A and B).

Table 7-3: A summary of alloy composition data from samples collected during this study

Locality	No of particles		Probe data			Mineral Inclusions
	Crushed vein	In situ	Ag% range	Hg % range	%>LOD	
Buckland Zone	25	8	18.1-31.3	0-1.1	87.5	Py, Cpy, Sph, Cal, Kspar
Boulder Lode Mine	24		15.5-24.5	0.1-0.2	87.5	Py, Cpy, Dol, Cal
Dysle Zone	36	1	24.1-31.4	0.1-0.3	9.9	Py, Sph, Ga, Ac
Gay Gulch Vein		1	26.4	ND	0	
Nugget Zone	223	4	14.3-38.5	0-0.3	94.5	Cpy, Py, Asp, Pn, Po, Xenotime, Dol, Rt, Cal, Kspar, Stbn
Violet Mine	18		24.4-42.1	0.3-3.8	100	Py, Ac

Py- pyrite, Cpy- chalcopyrite, Dol-dolomite, Cal- calcite, Sph- sphalerite, Ga-galena, Asp- arsenopyrite, Pn- pentlandite, Po- pyrrhotite, Rt- rutile, Kspar- orthoclase, Stbn- stibnite, Ac- Acanthite

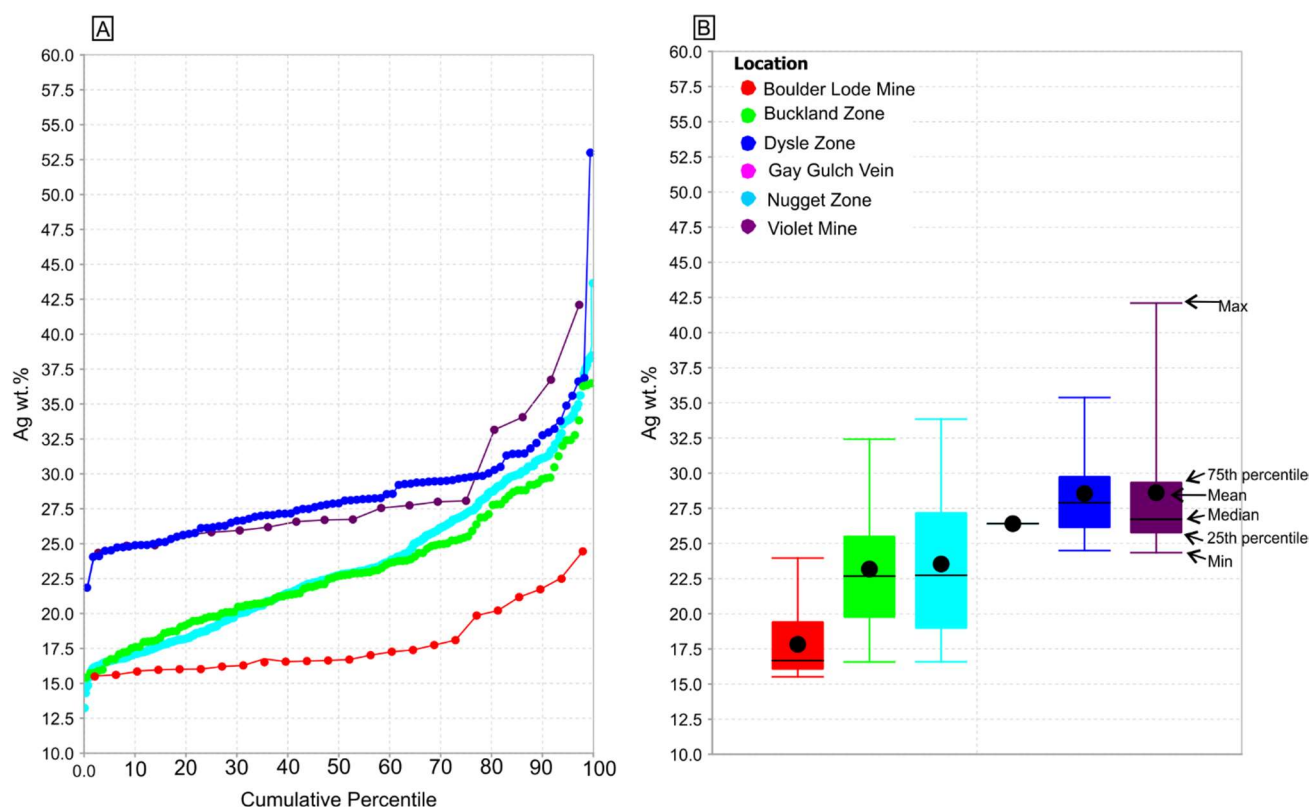


Figure 7-39: A-Cumulative percentile plots of silver content of gold particles at each locality. B Percentile box plots of silver variation of gold particles at each locality.

7.4.6.3 Mineral inclusion assemblages of vein gold

Mineral inclusions within polished gold sections were identified using the SEM. The general scarcity of inclusions reported by Chapman et al. (2010) influenced approaches to gold grain collection, as large populations (50-70 particles) are required to gain a useful inclusion assemblage.

Figure 7-40a show an example of different minerals present as inclusions in an in situ sample from the Buckland Zone. A summary of inclusions identified at each gold-bearing vein locality are included in Table 7-3.

Gold particles from the Boulder Lode Mine have the highest abundance of mineral inclusions and are dominated by base metal sulphides such as galena, sphalerite and chalcopyrite. Sulphides make up the majority of mineral inclusions in gold from the Nugget Zone and Buckland Zone (Figure 7-40A) but are only present in less than 5% of all particles analysed. Gold particles from the Dysle Zone have a low abundance of inclusions, with pyrite being the

most common. There was also a single example of an acanthite (Ag_2S) inclusion, shown in Figure 7-40b. The Violet Mine is defined by its lack of inclusions, with only a few examples of pyrite observed.

The dataset of mineral inclusions discussed in Chapman et al. (2010a) was available for comparison with the observations of this study. These authors describe examples of a variety of other rare inclusions such as sulfosalts and tellurides.

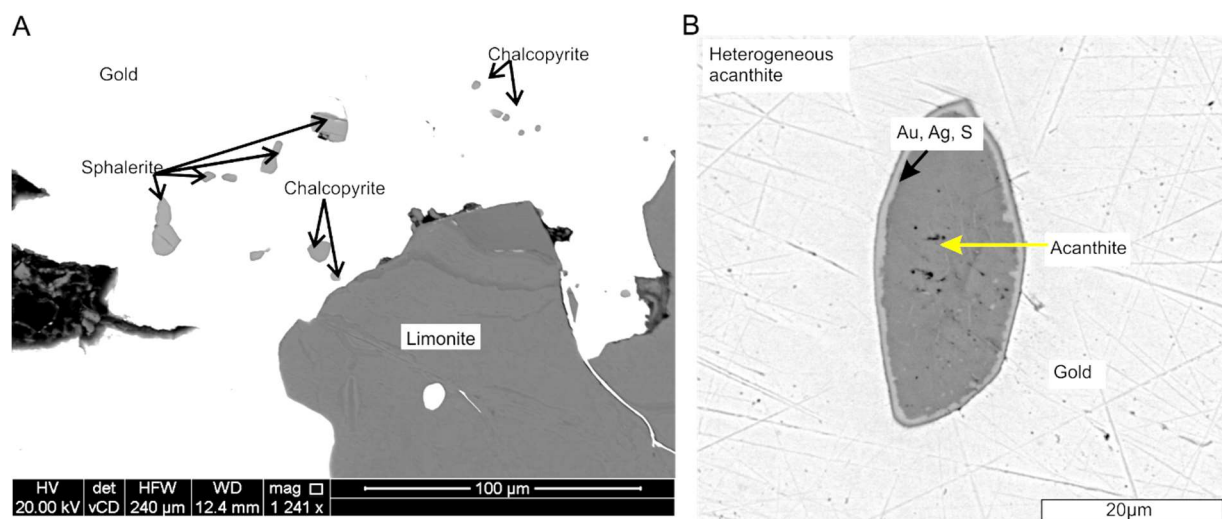


Figure 7-40: A- BSE image of gold particle from vein the Buckland Zone. Chalcopyrite and sphalerite inclusions are labelled within the gold (MG28_BZ10). B- An inclusion of acanthite from the Dysle Zone. A margin of Au, Ag, S suggests exsolution has occurred.

7.4.6.4 Hypogene processes interpreted from analysis of native gold in the LSSA.

Restricted silver variation within a population, such as at Dysle Zone and Boulder Lode Mine (Figure 7-39a), is interpreted to represent gold precipitation under stable mineralising conditions (Gammons and Williams-Jones, 1995). In comparison, silver with a wide variation, like Nugget and Buckland zones, indicates formation from multiple events or varying conditions.

The spread of silver content of gold particles from Nugget Zone was investigated in further detail by plotting samples from different veins within the zone. Gold particles collected from bulk samples, 10-20m apart within the 200m² area of the Nugget Zone, either have small variation (Nugget zone 1 and 2) or large variation (Nugget Zone 3). Silver content of gold particles within

the veins varies on a metre scale within the same area, which may be explained by numerous episodes of gold mineralisation or local fluctuations of composition.

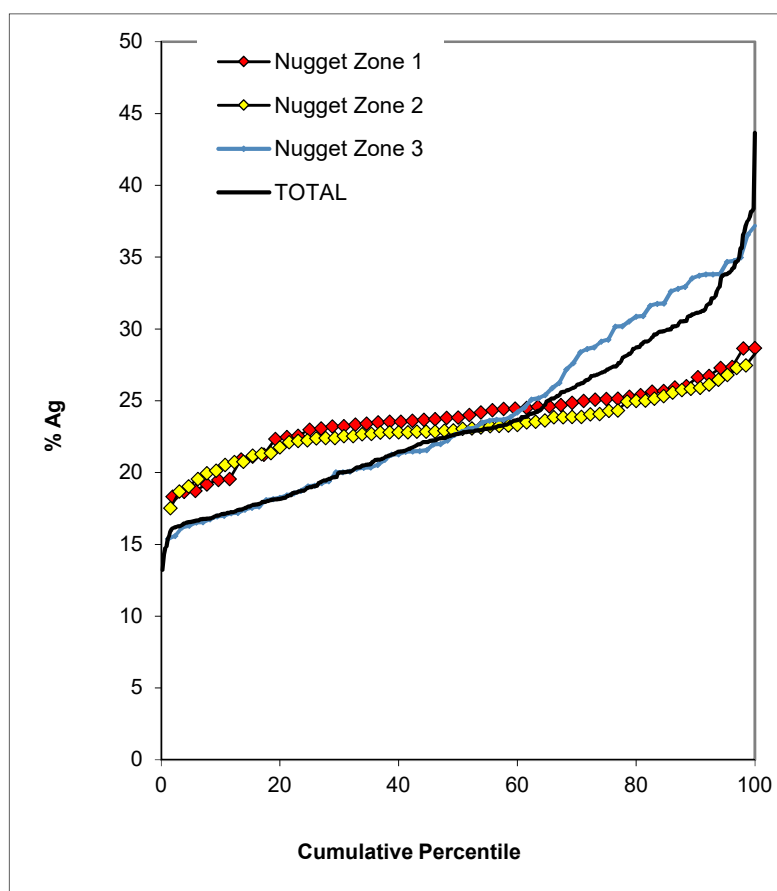


Figure 7-41: Variation of Ag within different populations of gold collected from the Nugget Zone. The TOTAL curve is the overall signature from the nugget Zone when all particles are combined.

The composition of hydrothermal fluids responsible for gold deposition in the LSSA are interpreted by Rushton et al. (1993) to be low salinity and near neutral pH with gold transported as a bisulphide complex. The constraints on Au/Ag ratios of gold are described, by Gammons and Williams-Jones (1995), in a system comprising Au-Ag-S-Cl-H₂O. The ratio of gold and silver is controlled by fluid parameters outlined in Equation 10 (Huston et al., 1992).

$$\text{Equation 10: } \log \left(\frac{a_{\text{Ag}}}{a_{\text{Au}}} \right) = \log K_6 + \log \left(\frac{a_{\text{AgCl}_2^-}}{a_{\text{Au(HS)}_2^-}} \right) - 2\text{pH} + \log a_{\text{Cl}^-} + 2 \log a_{\text{H}_2\text{S}}$$

The interpretation of conditions responsible for gold formation and alloy content rely on temperature, Au/Ag_(aq), pH, *a*Cl⁻ and *a*Hs₂. Gammons and

Williams-Jones (1995) point out that any Au/Ag alloy ratio is possible, depending on the prevailing conditions of gold deposition.

The variety of gold particle alloys on a metre scale, like those at the Nugget Zone, has led to an interpretation that the controls on gold are primarily influenced by the local environment of precipitation rather than the hydrothermal fluid.

Further evidence for the major role the local environment of crystallisation has on gold precipitation in the LSSA is found in the mineral inclusion assemblages of gold. For example, at the Boulder Lode Mine gold particles exhibit a distinctive base metal association (Table 7-3). This signature is interpreted to reflect the fact that the QMS member hosts the veining, and this unit is known to have small lenses of sulphides throughout.

The composition of inclusions in gold can also provide information on the conditions associated with the gold precipitation. The phase relationship of acanthite and the surrounding gold is investigated in a sample from the Dysle Zone. Barton (1980) provides the phase relationships of Au-Ag-S sulphides in terms of temperature and Au/Ag composition. Au-Ag-S forms homogenous minerals, such as utenbogaardite (Ag_3AuS_2), at temperatures above 170°C and shows higher proportions of Au with increased temperatures (Barton, 1980). Cooling below 170°C results in exsolution of Au and acanthite (Ag_2S) (Barton, 1980). The proportions of Au/Ag within sulphide inclusions can be compared to the surrounding Au/Ag alloy to estimate the original temperature of precipitation.

Acanthite (Ag_2S) in the LSSA (Figure 7-40b) exhibits minor enrichment of Au at the margin. The presence of uyttenbogaardite (Ag_3AuS_2) at the edge is interpreted to represent exsolution from the Au-Ag-S system during cooling through 170°C (Barton, 1980). The minor amounts of Au present at the margin of the inclusion suggests that the temperature of formation wasn't much higher than 170°C .

The deposition of gold from a fluid will affect the ratio of Au/Ag remaining in solution and affects the composition of subsequent gold formation regardless of all other chemical parameters (Gammons and Williams-Jones, 1995). This

should result in compositional zonation corresponding to the growth of gold; however, the majority of particles in the LSSA are homogenous.

One theory proposed here is that gold particles formed in equilibrium with a hydrothermal solution that produced the same Au/Ag alloy content. An alternate theory for the origin of homogenous alloy compositions is that annealing has caused homogenisation of a heterogeneous particle. The homogenisation of Au/Ag in gold particles is unlikely under Earth surface conditions due to low diffusion rates of Ag at low temperatures (Czamanske et al., 1973). However, crystallographic evidence in section 7.4.4 has shown that gold particles have undergone complete annealing at temperatures which favour increased rates of diffusion (Czamanske et al., 1973, Gammons and Williams-Jones, 1995). Minor silver enrichment in gold particles (Figure 7-36) is interpreted to have formed from a secondary phase of gold precipitation at lower temperatures, which have not undergone complete homogenisation.

The chemical and mineralogical information of gold gained from gold-bearing quartz veins across the LSSA has provided evidence on the controls of gold precipitation. The evidence suggests that the precipitation of gold from a hydrothermal fluid is primarily influenced by the local environment in each vein. Precipitation occurs due to chemo-adsorption on pyrite, with the composition being influenced by conditions present at the time of initial gold deposition. Mineral inclusion assemblages in gold show metal signatures similar to surrounding host rocks, and is evidence for significant fluid-rock interaction. Further evidence from mineral inclusions, such as acanthite, has suggested that gold is precipitating at low temperatures (>200°C).

7.5 A model for the formation of gold-bearing quartz veins

This section provides a model accounting for the various features of gold-bearing quartz veins in the LSSA. There a number of aspects that have influenced gold mineralisation in the veins across the area which are discussed below.

The first aspect of mineralisation to consider is the localisation of veining in angular kink folds (Figure 7-42). The kink folds are associated with D₄ and shows a progression from ductile folding to brittle reverse faults.

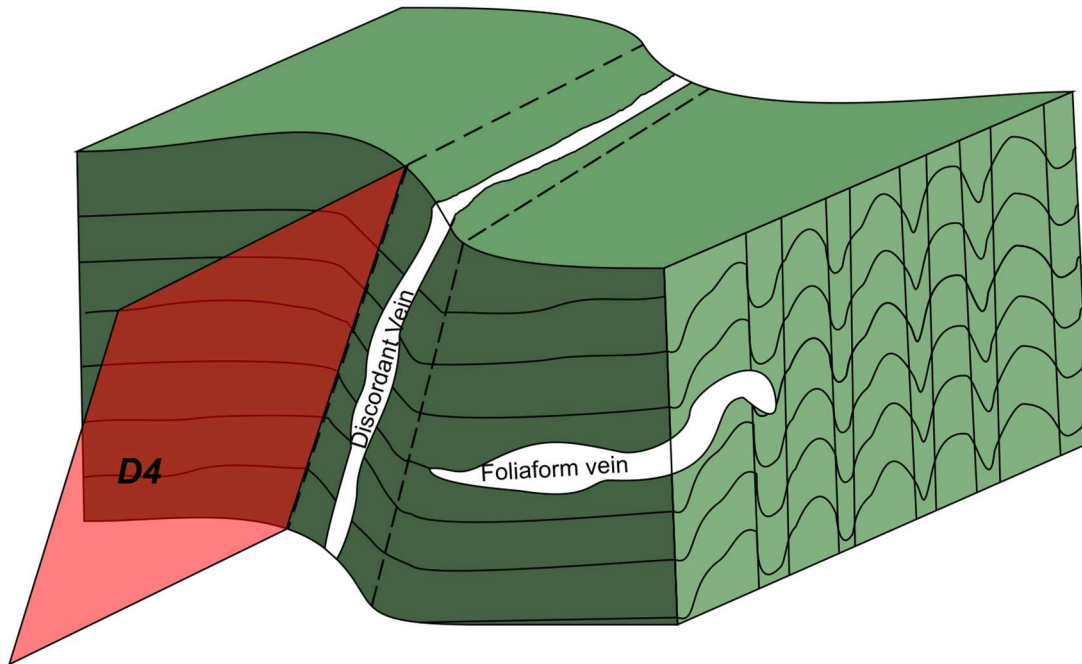


Figure 7-42: Schematic model of schist units in the LSSA. The development of crenulation cleavage and foliaform veins are cross cut by angular kink folds associated with D₄. Quartz veining localises in the D₄ fractures.

The faulting provides a pathway for hydrothermal fluid flow and the deposition of primary quartz (Q₁), which is interpreted to form at hydrostatic pressures under stable hydrothermal conditions, resulting in the generation of large euhedral quartz crystals (Figure 7-43a).

A second generation of fluid fractures Q₁ and results in the deposition of subhedral quartz in hand specimen quartz (Q₂). The Q₂ is typically black in CL and clearly fractures the Q₁ (Figure 7-43b). The hydrothermal conditions responsible for deposition of Q₂ are challenging to reconcile due to the lack of features visible in this generation of quartz when viewed in CL or in transmitted light; however, dark CL is linked to a metamorphic origin in a number of examples described by Rusk et al. (2008), and so is interpreted to be so here. Q₂ surrounds euhedral pyrite that is considered coeval. Pyrite lacks the cross cutting relationships normally used to establish a paragenesis,

but is interpreted to have been deposited by the same metamorphic fluid associated with Q2.

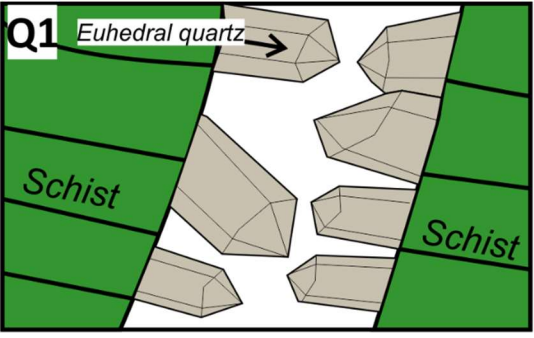
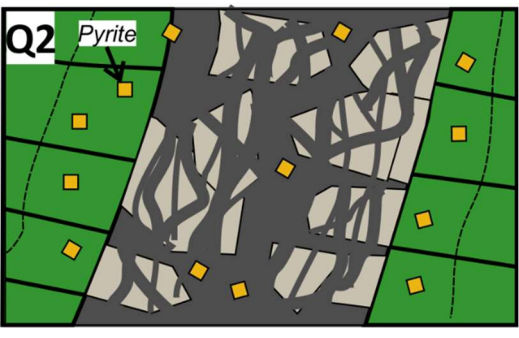
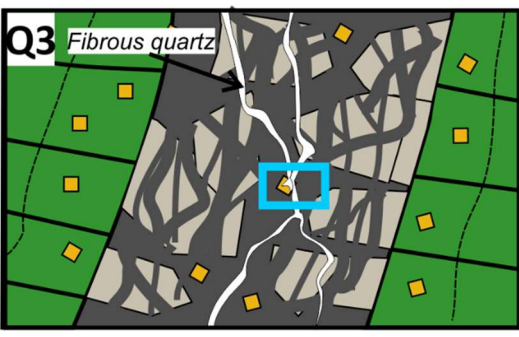
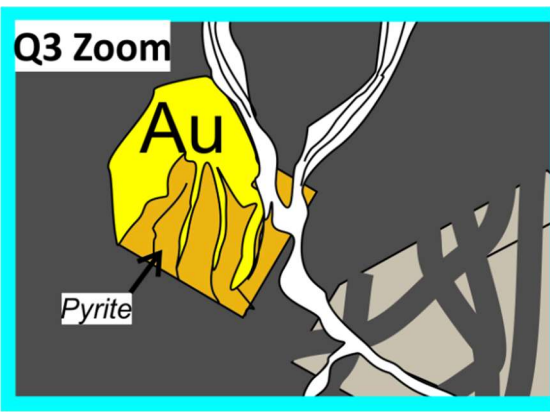
The third phase of veining (Q3) is related to brecciation and fracturing of the previous phases of quartz, (Figure 7-43c). The CL analysis of Q3 displays fibrous textures, which are thought to form as a result of rapid deposition and boiling. Bladed quartz at the centre of veins are a result of hydro-fracturing where Q3 cements fragments of Q1 and Q2. Depressurisation of hydrothermal fluid during vertical flow causes rapid deposition of Q3, typically associated with hydrostatic pressures.

Pyrite, coeval with Q2, is fractured where it coincides with the pathways and fractures associated with Q3 (Figure 7-43d). Depressurisation of gold-bearing fluid results in destabilisation of gold complexes causing gold deposition on and along fractures of pyrite. Chemo-adsorption of gold onto sulphide surfaces is proposed to be the primary mechanism for nucleation and crystal growth of gold in the auriferous quartz veins of the LSSA. This mechanism of gold deposition accounts for the nuggety nature of gold in veins across the LSSA. Gold is associated with a volumetrically minor phase of quartz (Q3) when compared to the total volume of quartz in the veins (volumetrically dominated by Q1 and Q2), and requires a high concentration of gold in a small volume of fluid. The transport of gold as colloids rather than as bisulphide complexes is a potential mechanism to account for the richness but is challenging to reconcile.

A study of gold compositions from gold-bearing quartz veins in the LSSA has revealed that metal contents of gold particles are heavily influenced by the local environment of deposition. Gold particles have metal contents similar to local lithologies, which indicates hydrothermal fluids have undergone considerable fluid-rock interaction. The formation of Q3 at hydrostatic pressures, coupled with evidence of low temperature mineral inclusions (e.g. acanthite) within gold particles, has led to an interpretation that gold mineralisation is associated with epizonal orogenic gold deposits (Groves et al., 1998).

Q4 comprises less than 1% of total vein volume and is associated with ankerite and clay minerals. This phase of vein generation is thought to be related to a late fluid phase potentially linked to groundwater circulation. The origin of the fluids is challenging to elucidate, but a mixed origin of metamorphic fluids and meteoric waters is likely, as previously suggested by Rushton et al. (1993).

Figure 7-43: Schematic cartoons for the formation of auriferous veins in the LSSA

<p>A</p>  <p>Q1 Euhedral quartz</p> <p>Schist</p> <p>Schist</p>	<ul style="list-style-type: none"> • Angular kink folds develop into faults due to a change from ductile-brittle conditions during crustal uplift. • Epitaxial quartz develops in faults to produce veins (Q1).
<p>B</p>  <p>Q2 Pyrite</p>	<ul style="list-style-type: none"> • Subhedral milky white quartz is linked to Q2. • Q2 is typical of metamorphic quartz. • Pyrite formation is linked to Q2.
<p>C</p>  <p>Q3 Fibrous quartz</p>	<ul style="list-style-type: none"> • Q3 fractures all previous quartz generations. • Quartz textures exhibit zonal growth that suggests stable hydrothermal conditions.
<p>D – Zoom of C</p>  <p>Q3 Zoom</p> <p>Au</p> <p>Pyrite</p>	<ul style="list-style-type: none"> • Gold deposition occurs with hyalophane and Q3 along pyrite fractures. • Gold precipitation results from adsorption on sulphide surfaces. • Q4 is minor (>1% quartz) and not related to mineralisation.

Chapter 8 Gold-bearing schist

This section investigates the petrography, mineralogy and textures of host rocks in the LSSA that are gold-bearing, but have no association with alteration or mineralisation related to the discordant gold-bearing veins described in the previous chapter. There are two types of gold mineralisation in the various schists in the LSSA. The first comprises sporadic visible gold within schist that forms with pyrite grains and quartz segregations (Figure 8-1). The second gold type consists of finely disseminated particles within a specific lithostratigraphic unit -the Quartz Mica Schist Member, which is present predominantly along the Lone Star Ridge. This type of gold in schist has been investigated by MacKenzie et al. (2007a), who conducted a study of the geochemistry associated with the gold (described in Chapter 4).

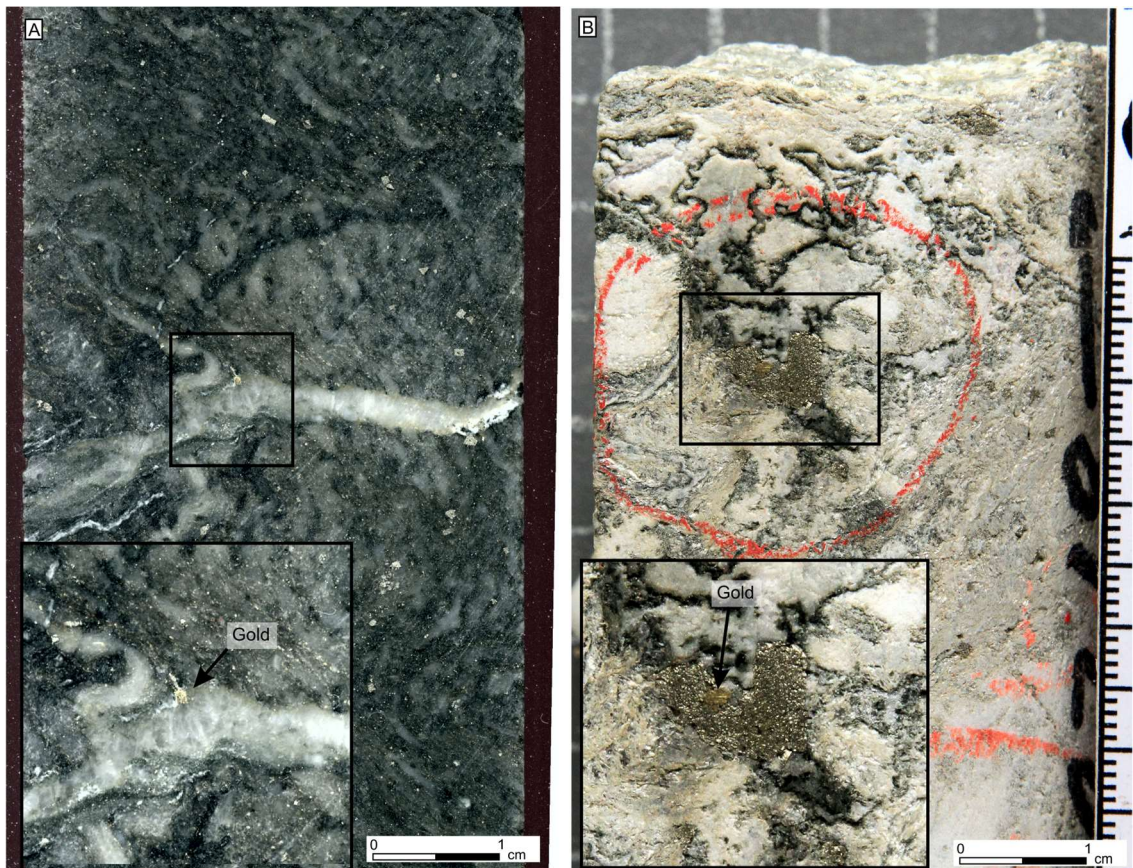


Figure 8-1: Visible gold in drill core. **A-** Gold in schist close to metamorphic quartz segregation (05LS16_60.76). **B-** Gold in pyrite with no association with discordant quartz veins (MG56_05LS16_82.68).

8.1 Petrography of Quartz Mica Schist Member

Disseminated gold is hosted in the Quartz Mica Schist Member of the Klondike Schist Formation, and forms a number of mineralised intervals along the Lone Star Ridge. The distribution of elements within the mineralised and un-mineralised schist was investigated by mapping thin sections with a Tornado XRF (described in chapter 7). The rock is composed of millimetre to centimetre scale bands of quartz, phengitic mica, and plagioclase feldspar (Figure 8-2).

Carbonate alteration is as ankerite along foliation and as spots that are up to 4mm in size (Figure 8-3). Figure 8-3 shows an elemental map of a thin section that displays elevated Ba and Ca in minerals related to alteration along foliation and in micro-veinlets.

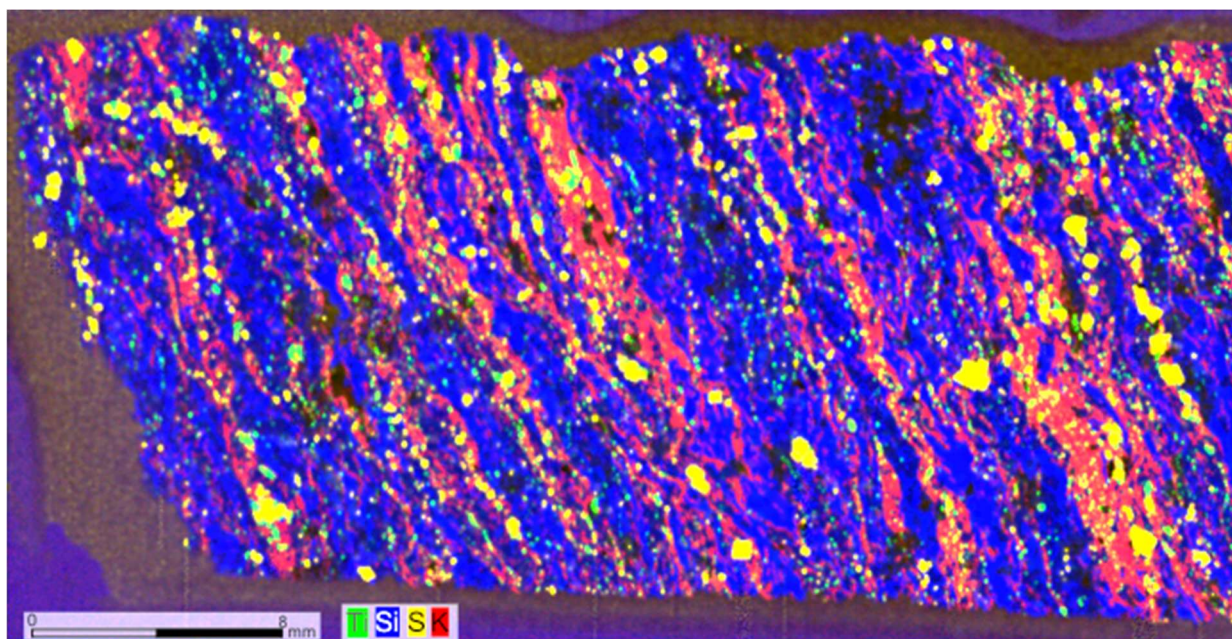


Figure 8-2: Micro XRF scan of gold-bearing schist interval (MG8_05LS27). Banding of mica (red) and quartz-feldspar (blue) has pyrite (yellow) and rutile (green) aligned along foliation.

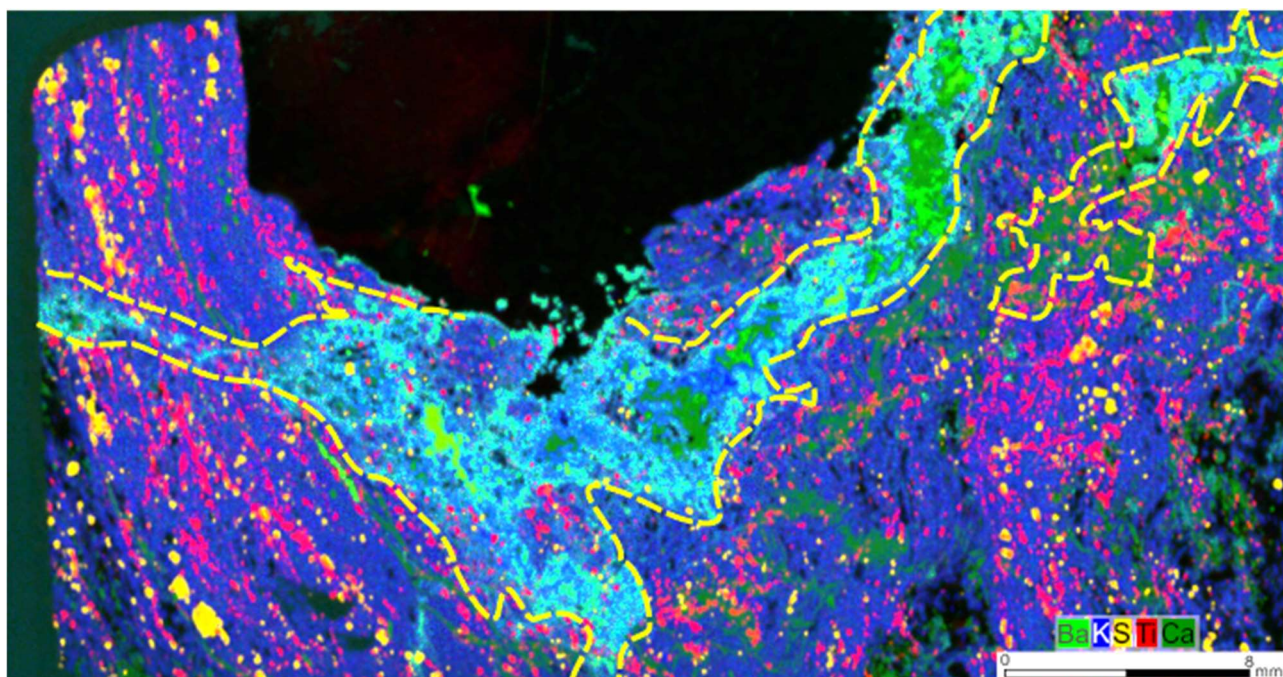


Figure 8-3: Micro XRF scan of gold-bearing schist interval (MG45). Dark blue is feldspar, pink is rutile and yellow is pyrite. Light blue and bright green represent alteration (outlined in dashed yellow) of hyalophane and Mg-Fe carbonate minerals along foliation and in micro-veinlets.

The element maps in Figure 8-2 and Figure 8-3 permitted a more focussed investigation of the thin sections by optical microscopy. Euhedral and subhedral pyrite are aligned along foliation of the quartz, mica and feldspar (Figure 8-4a).

The micro veinlets and fractures that cross cut the schist contain euhedral feldspar crystals that are zoned (Figure 8-4b). The centre of these fractures are filled with Mg-Fe carbonate and rarely, euhedral pyrite. Domains in the schist that have more mica have a strong crenulation cleavage, with evidence of calcite infilling space between mica (Figure 8-4c and d).

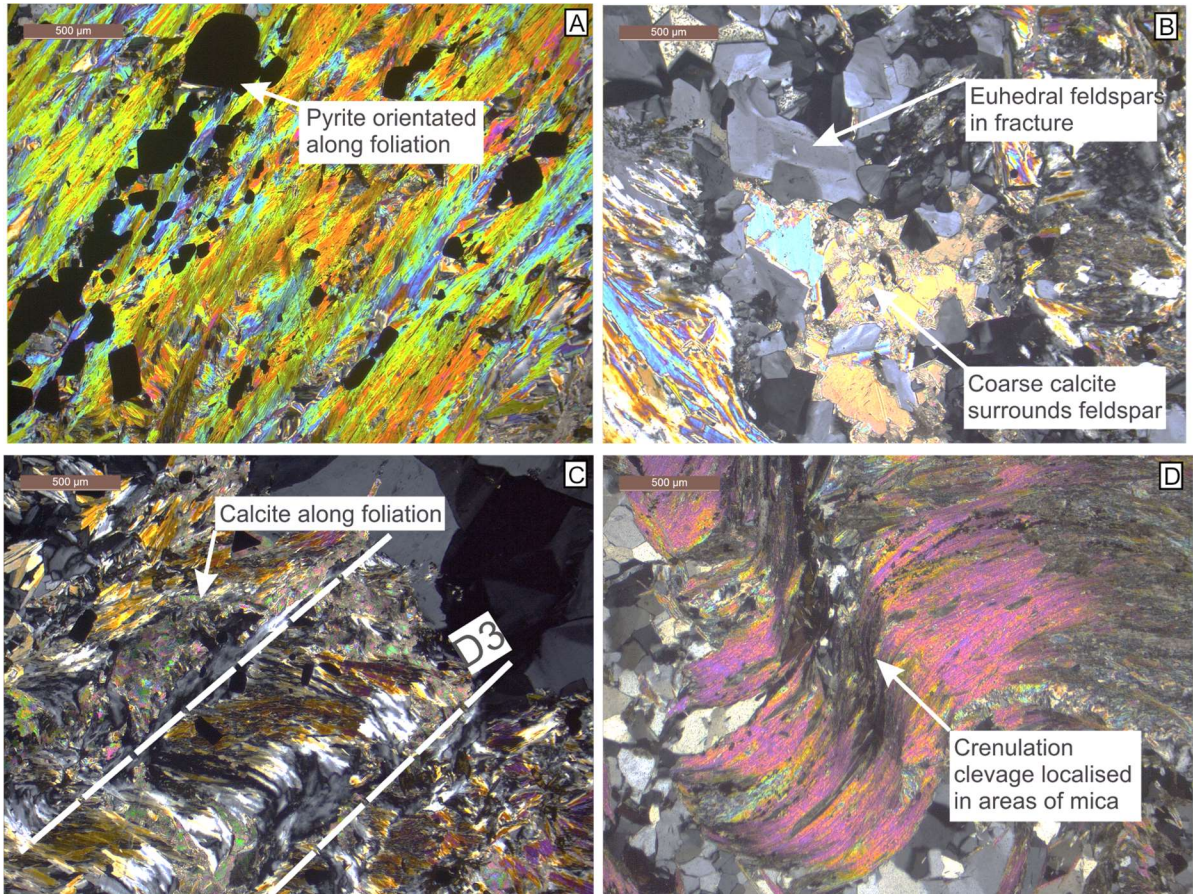


Figure 8-4: Cross polarised light images of QMS Member. **A-** Opaque pyrite aligned along foliation (MG45). **B-** Fracture cross cutting foliation filled with euhedral feldspar and carbonate minerals (MG45). **C-** Crenulation cleavage marks spaced D3 cleavage (MG9_05LS27). **D-** Crenulation is well developed in mica rich intervals (MG8_05LS27).

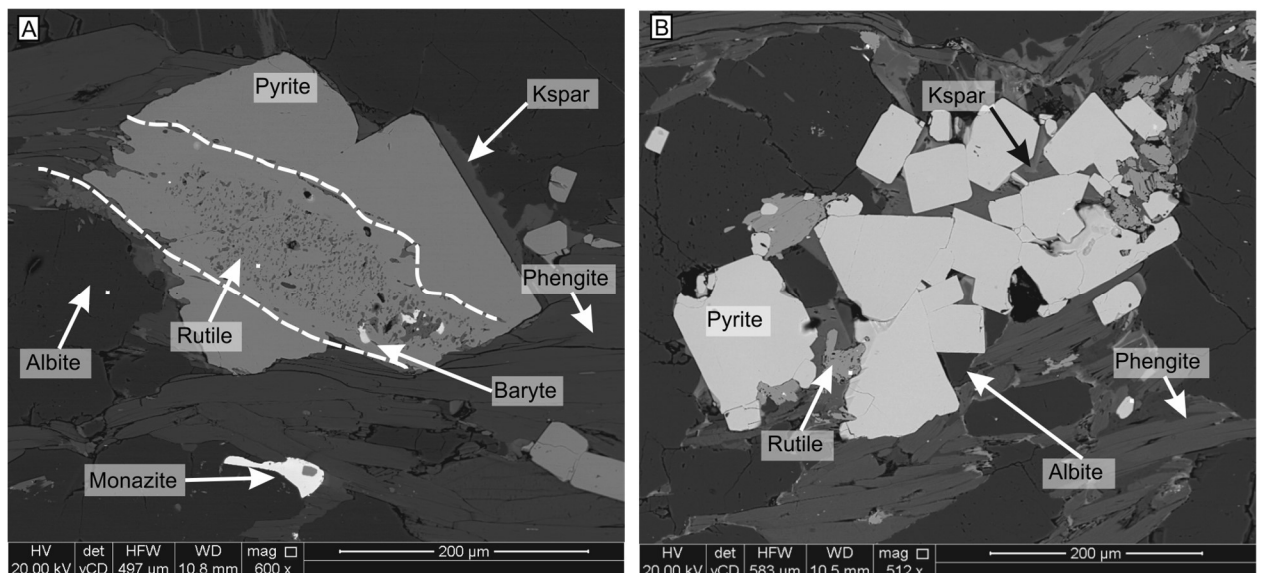


Figure 8-5: SEM BSE images. **A-** Small rutile grains aligned with foliation at the core of a euhedral pyrite pseudomorph (MG9_05LS27). **B-** BSE image of pyrite cluster with rutile inclusions and surrounding hyalophane (MG10_05LS27).

Figure 8-5a shows a BSE image of pyrite in the schist that has abundant rutile inclusions and potassium feldspar around the edges. Mica is phengitic with Fe enrichment around the edge, which is a result of retrograde degradation of biotite. Zonation within euhedral potassium feldspar at the centre of micro veinlets was identified using BSE, and is a result of varying barium content (Figure 8-6). The feldspar is hyalophane, which was also identified in the gold-bearing veins described in section 7.4.1. The barium content was analysed using EDS and varied from 0.5% (dark areas) up to 10.5% (bright area). Barium content corresponds to oscillatory growth zonation within the feldspars, and shows an overall decrease of Ba outwards from core to rim. The centre of the veinlets are filled with Fe-Mg carbonate together with pyrite and barite.

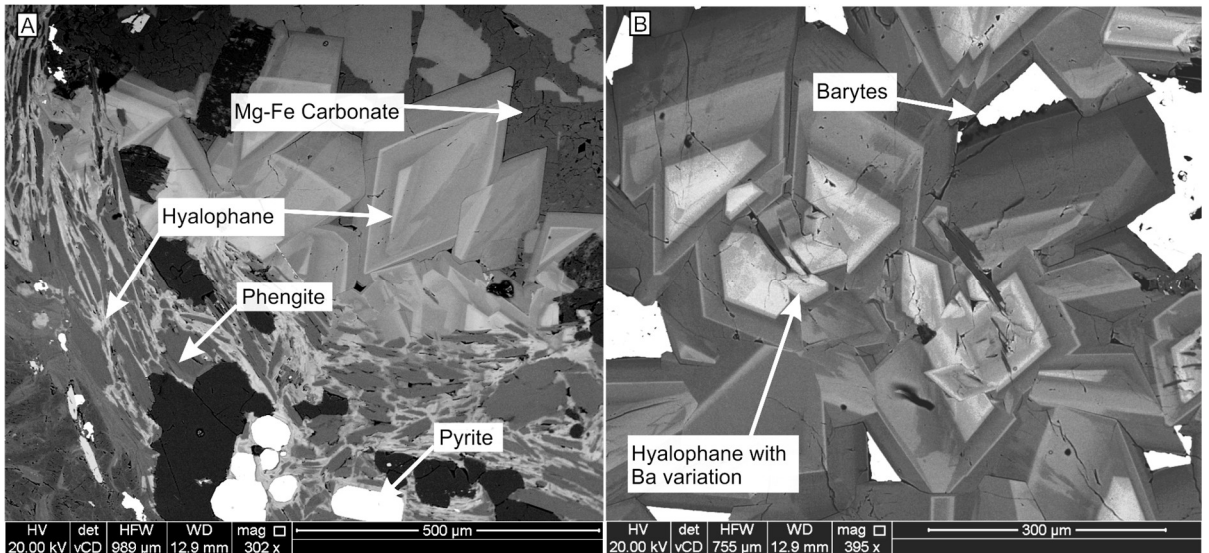


Figure 8-6: **A-** BSE image of margin of micro-veinlet filled with euhedral hyalophane and carbonate minerals. Ba variation in the hyalophane marks grain boundaries (MG45). **B-** BSE image of micro veinlet showing Ba variation (greyscale) in hyalophane with barite (brightest phase) at centre (MG45).

8.2 QMS Member – Interpretation of textures associated with metamorphism and subsequent hydrothermal alteration.

This section discusses the features presented in the previous section with an aim to distinguish alteration (which is related to mineralisation) from features associated with metamorphism.

The compositional banding in the QMS Member represents a penetrative S_2 fabric that is overprinted by a spaced crenulation cleavage best developed in mica rich intervals (Figure 8-4). The presence of Fe in phengitic micas is interpreted to represent retrograde reactions from biotite at greenschist facies (Fyfe, 1978).

Observations from drill core logging show that euhedral and subhedral pyrite in the QMS Member coincides with elevated gold values. Section 8.1 and Figure 8-5 show that pyrite is aligned along foliation and has abundant inclusions of rutile that mark the outline of a unknown remnant crystal. Prograde metamorphism has resulted in pseudomorphs of rutile and pyrite after ilmenite ($FeTiO_3$). Titanium from the ilmenite is immobile and forms small grains of rutile, while sulphur couples with iron to form pyrite. Angiboust and Harlov (2017) provide examples of ilmenite ($FeTiO_3$) breaking down to rutile and titanite, with minor pyrite, under a range of experimental conditions (0.7-1.6GPa, 450-650°C), which correspond to the metamorphic conditions expected within the LSSA prior to mineralisation.

Gold in schist is associated with a diffuse and poorly developed phase of alteration recognisable through detailed petrographic studies. Barium bearing potassium feldspar (hyalophane) occurs in association with gold in visible gold and in every case observed in disseminated gold from the QMS Member every case. Thin section analysis has found that hyalophane is present along foliation of micas and is most evident in micro veinlets where it forms epitaxial euhedral crystals.

Gold also occurs in association with Fe-Mg carbonate; however, its' widespread presence is not always strictly associated with gold

mineralisation. Chlorite and ankerite form distinctive spots of alteration within gold-bearing schist and are seen to cross-cut the primary metamorphic textures. It seems likely that they postdate metamorphism and are related to hydrothermal fluid flow within the schist. A genetic link between carbonate minerals and gold mineralisation is not as clear as the gold-hyalophane relationship. Allan et al. (2014a) compared the stable isotopes of C and O from carbonate from host rocks, metamorphic segregation veins and gold-bearing veins in the KGD. These authors showed that carbonate minerals had a broadly similar signature, which suggests that carbonate is locally sourced. This agrees with the petrographic observations from the LSSA, where it is challenging to recognise whether carbonate minerals are related to metamorphism or alteration during gold mineralisation.

8.3 Gold in schist

This section describes the features associated with gold mineralisation in the LSSA that are not related to gold-bearing quartz veins. Firstly, visible gold that is found sporadically in host rocks across the LSSA is described. Secondly, disseminated gold mineralisation in the QMS Member is characterised. Gold in the QMS Member is much easier to investigate due to its presence along 1600m of strike on the Lone Star ridge.

8.3.1 Visible gold in schist

Four examples of visible gold in schist from drill core have been observed; however, only one sample was made available for analysis from Klondike Gold Corporation (Figure 8-1 and Figure 8-7). The gold is found on and within euhedral pyrite with the largest example of gold being 4mm across. Figure 8-7 shows an example of gold from drill hole 05LS09 that has no alteration other than the presence of hyalophane and carbonate minerals along the foliation of mica proximal to gold. The presence of visible gold in schist across the LSSA is rare and shows no association with a specific lithology.

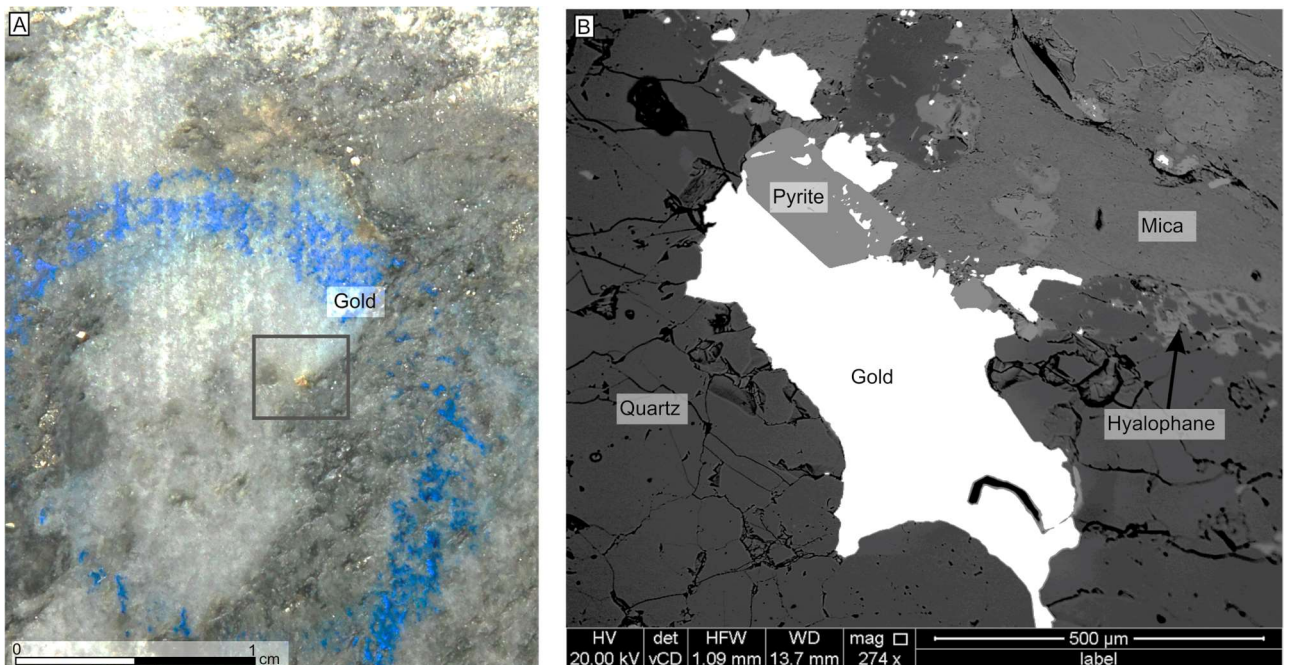


Figure 8-7: Visible gold from drill core (05LS09_36.76) **A-**Photo of visible gold in core. **B-** BSE image of gold with pyrite at margin of quartz segregation. Fine grained hyalophane is observed along foliation of mica (MG55_05LS09).

8.3.2 Disseminated gold in Quartz Mica Schist Member

Drilling along Lone Star Ridge has identified elevated gold grades associated with a specific interval of Quartz Mica Schist Member (described in Chapter 4 and examples shown in Table 8-1). Klondike Gold Corporation announced drill results confirming mineralisation along the Lone Star Ridge that has 1600m of strike and ranges from 10-40m wide (Table 8-1). Samples of drill core which exhibit consistent and elevated gold were selected for mineralogical and textural characterisation. The samples chosen for this study were collected from drill holes approximately 200-300m NE along the ridge from Boulder Lode Mine (Appendix A.1). Core from hole 05LS02 has undergone previous investigation by MacKenzie et al. (2007a) and this material was available for further investigation in this study. Samples of core were selected for thin section preparation on the basis of relatively high gold assays.

Table 8-1: Examples of the best intercepts from drilling along the Lone Star Ridge in 2016 and 2017.

HOLE	INTERVAL (M)	GRADE OF AU (G/T)
LS16-58	37	2.4
LS16-58	7.05	6.6
LS16-58	3.6	9.4
LS16-59	27.7	1.2
LS16-59	7.3	2.3
LS17-81	40.9	2.4
LS17-58	41.1	2.1

A sample taken from the interval 69.50-69.58m had an average grade of 4.4g/t, and two thin sections (MG45 and MG46) were prepared. The second sample is from the drill hole 05LS27, collected at the interval 59.00 to 59.50m, with a grade of 6.6g/t (MG8 and MG10). Resampling of the interval 69-70m in

2012 provided a sample with a grade of 13.3g/t and confirmed that the results were reliable.

Gold was identified as 5-75µm diameter particles forming in crenulation hinges of mica and in around the edges of pyrite (Figure 8-8a and b). The deposition of gold is primarily linked to a drop in pressure when a hydrothermal fluid reaches pockets of space in the schist. Hyalophane and Fe-Mg carbonates are concentrated in similar settings and show an intimate association with gold (Figure 8-9a). Hydrothermal alteration is known to form in brittle fractures as micro-veinlets and as diffuse flow along foliation. The evidence for brittle fractures and deposition of gold in spaces in the schist indicate hydrostatic pressures at shallow crustal levels.

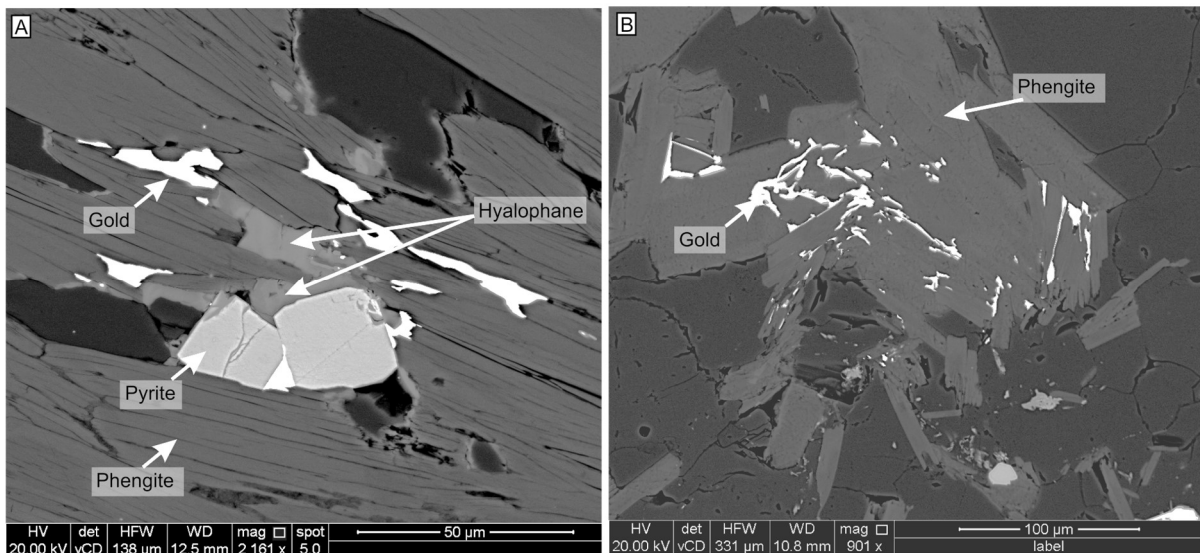


Figure 8-8: A- BSE image of gold and hyalophane in pyrite pressure shadow and along spaces in foliation (MG59_05LS27). B- BSE image showing gold infilling space between phengite in crenulation hinge (MG45).

Elsewhere gold is present as small particles along fractures of pyrite and has a distinctive suite of minerals associated with it: greenockite (CdS); altaite (PbTe); hessite (Ag₂Te); petzite (Ag₃AuTe₂); galena (PbS); and chalcopyrite (CuFeS₂) (Figure 8-9b). Petzite was observed at the centre of a hyalophane micro veinlet with pyrite, barite and Mg-Fe carbonate (Figure 8-10a). Figure 8-10b shows an examples of gold forming as an inclusion within hessite found in a fracture of pyrite that also includes hyalophane.

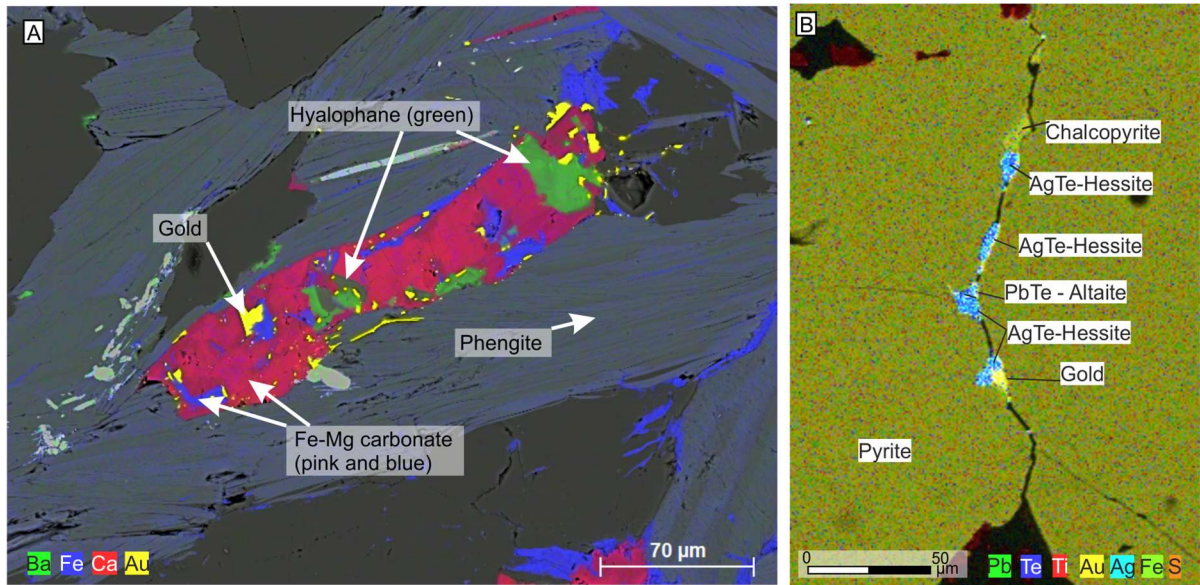


Figure 8-9: EDS maps. **A-** Gold with hyalophane and Fe carbonate (MG45). **B-** Gold in fracture of pyrite associated with telluride minerals (MG8_05LS27).

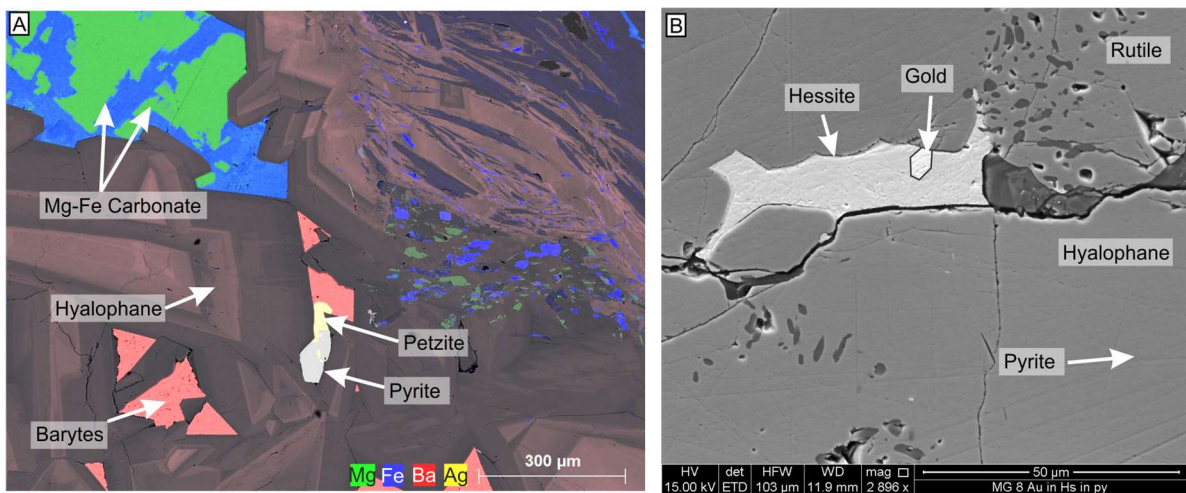


Figure 8-10: **A-** Micro veinlet with euhedral hyalophane that decreases in barium content towards the centre. Vein is filled with Mg-Fe carbonate, barite, pyrite and petzite (MG45). **B-** BSE image of fracture in pyrite filled with hyalophane, gold and hessite (MG8_05LS27).

8.3.3 Composition of gold in schist across the LSSA

The only particle of visible gold in schist available for analysis (MG55), from drill hole 04LS09_36.76m (Figure 8-7), contained 16.14% Ag (Table 8-2). There were numerous examples of gold particles disseminated through the Quartz Mica Schist Member. Unfortunately, most of these were too small to analyse by EPMA. The data gained from analysis of the five largest particles is presented in Table 8-2.

		Ag WT%	Hg WT%	%>LOD Hg
Disseminated	MG45a	13.61	0.2077	100
Disseminated	MG45b	13.70	0.2302	100
Disseminated	MG10	16.16	0.4950	100
Disseminated	MG46	12.91	0.1836	100
Disseminated	MG8	15.29	0.1183	100
Visible Gold	MG55	16.14	0	0

Table 8-2: Summary of alloy data analysed from gold-bearing schist.

8.4 Mineralogical and hydrothermal alteration related to gold mineralisation

Hyalophane is present in the same textural settings as gold and has a close association with mineralisation in all samples analysed. Barium in feldspars range from trace amounts in orthoclase (KAlSi_3O_8) to complete substitution of K for Ba in celsian ($\text{BaAlSi}_3\text{O}_8$); hyalophane is defined as intermediate in composition with 10-50% Ba ($\text{Ca}_{10}\text{-Ca}_{50}$) (Gay and Roy, 1968). The mineral is best developed in small micro veinlets (0.5mm wide) as epitaxial euhedral crystals that display oscillatory growth zonation (Figure 8-6). Growth zones correspond to different levels of Ba, which generally decrease towards the edge of crystals (Figure 8-6). The transportation and deposition of gold in schist is linked to the same fluid that formed hyalophane, and coincides with periods of low Ba growth zones in hyalophane. The hydrothermal processes that control hyalophane compositions are influenced by the solubility, transport and deposition of Ba^{2+} (Essene et al., 2005). The complex zonation displayed in hyalophane is a result of either fluctuating levels of Ba^{2+} in the fluid, or the removal of Ba^{2+} due to interaction with sulphate (Essene et al., 2005).

One potential source for Ba in fluids is from the dissolution of barite in the surrounding rocks of the QMS Member (Chapter 4). The dissolution of barite in hydrothermal fluids occurs over a narrow range of temperature and pressure due to its extreme chemical stability. Maximum solubility occurs at hydrostatic pressures between 100 and 500bars and at temperatures of 100-

200°C (Figure 8-11) (Blount, 1977). Although dissolution of barite may provide a source of Ba in fluids, the chemical stability of the mineral makes other sources more probable. The levels of Ba in hyalophane in the LSSA are relatively low and wouldn't require large quantities of the element to be transported in a fluid. Various trace elements, including Ba, are known to be remobilised during metamorphic dehydration reactions, as discussed in Chapter 2.4.1.3. Ba is also liberated and remobilised during weathering of alkali feldspars, which may then be recycled and concentrated in surface derived fluids (Nesbitt and Markovics, 1980).

Coeval deposition of hyalophane and gold means that the fluids responsible for mobilisation of Ba^{2+} were the same as those for gold transport. Complex compositional zonation of barium in hyalophane is linked to the varying fluid conditions. Fluctuating fluid temperatures may affect the amount of Ba^{2+} able to be dissolved in to the fluids. An alternate mechanism of Ba^{2+} concentration variation is the removal from fluid due to interactions with sulphate (SO_4^{2-}). A common source of sulphate is from meteoric water, which could mix with hydrothermal fluids and produce barite ($BaSO_4$). Fluid mixing and formation of barite may subsequently produce low barium hyalophane as seen here (Figure 8-10a).

Essene et al. (2005) describe the formation of hyalophane in low temperature igneous and metamorphic environments (<200°C). Hyalophane most commonly occurs in epithermal gold deposits where it precipitates from fluids as a result of boiling and pH change (Cooke and Simmons, 2000, Simmons et al., 2005). The empirical evidence provided by the presence and nature of hyalophane in these rocks indicates that the hydrothermal fluid was relatively cool and formed at shallow depths.

Additional evidence of shallow depths is present due to the brittle fracturing of the schist that has resulted in the formation of micro cracks and open porosity within the QMS Member. Hydrostatic pressures would dominate and allow diffuse fluid flow along the schist with gold forming in areas of low pressure, such as crenulation hinges or pressure shadows of pyrite.

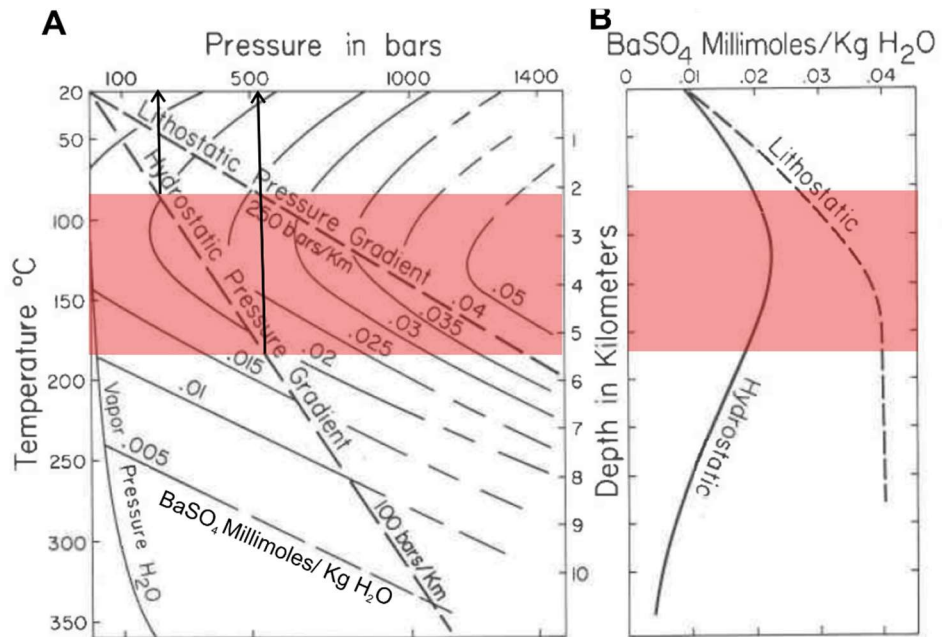


Figure 8-11: Barite solubility in H₂O solutions at depth from a specific pressure gradient. **A-** Constant composition curves on the barite saturation surface projected in *P, T*. **B-** Barite solubility is shown from a standard geothermal gradient of 30°C/km.

A minor phase of gold in the QMS Member, compared to gold found in pore space, forms with telluride-bearing minerals and barite along pyrite grain boundaries and in the centre of micro veinlets which cross-cut the primary metamorphic textures. The minerals found in the schist are: altaite (PbTe), hessite (Ag₂Te), petzite (Ag₃AuTe₂), greenockite (CdS), chalcopyrite (CuFeS₂) and native gold. The temperature of fluids can be used to interpret the fTe_2/fS_2 parameters associated with the formation of the minerals (Figure 8-12) (Afifi et al., 1988). The presence of telluride-bearing minerals, rather than sulphides, (e.g. altaite rather than galena) indicates that a high fTe_2 value was present, as shown in Figure 8-12 (Afifi et al., 1988). Tellurium has very low solubility in aqueous fluids (H₂Te_(aq)) and is therefore thought to have been transported as a vapour (Te_(g)) and precipitated on interaction with surface fluids (Cooke and McPhail, 2001). The identification of epizonal conditions suggests that depressurisation of fluids occurred, which may result in phase separation and the generation of a vapour phase containing Te. The deposition of barite occurs with telluride minerals and provides further evidence that mixing of meteoric and hydrothermal fluids is likely to have occurred.

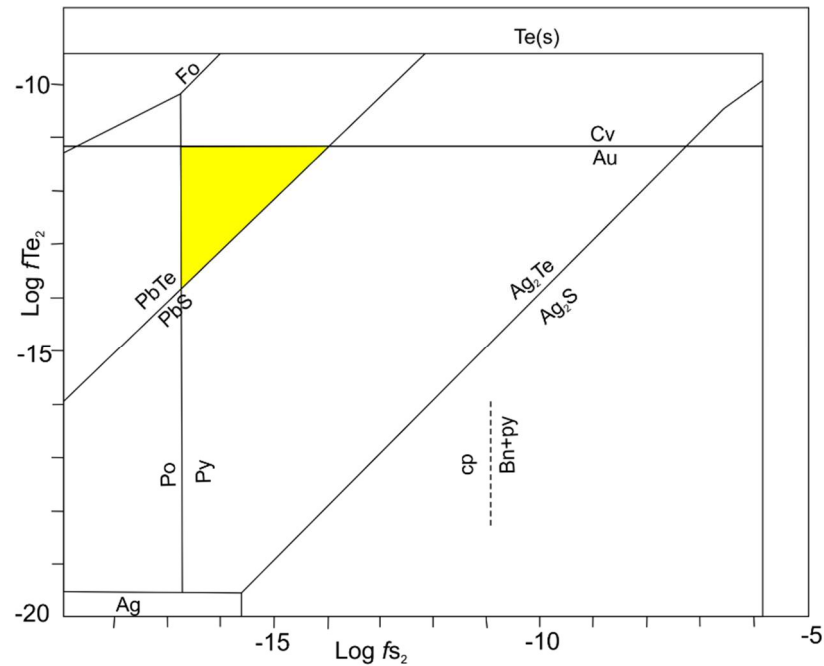


Figure 8-12: Variations of Te_2 and S_2 fugacity with respect to selected telluride-sulphide-oxide equilibria at 200°C . Yellow highlights the conditions constrained by stability of minerals observed in the LSSA. Fo-forsterite, Po- pyrrhotite, Py- pyrite, Cv- calaverite, Au- gold, PbTe- altaite, PbS- galena, Cpy-chalcopyrite, Bn-bornite, Ag_2Te - altaite, Ag_2S -acanthite.

The Haile gold mine in South Carolina of the USA displays similar alteration assemblages as those in the QMS Member in the LSSA. Gold mineralisation has formed in strata-bound pyritic horizons in a series of Precambrian-Cambrian volcanic rocks of the Carolina slate belt (Hardy, 1989). Hydrothermal potassium feldspar and telluride minerals are associated with gold along pyrite fractures (Berry et al., 2016). The mineralisation at Haile may be related to either syngenetic exhalites, orogenesis, or late stage fluids (Berry et al., 2016). Berry et al. (2016) conclude that Haile is an epithermal gold deposit, which lacks many of the structural and textural features in the classification by Cooke and Simmons (2000). The mineralogy and alteration at the Haile mine are very similar to those in the LSSA and both originate from low temperature hydrothermal fluids at shallow depths.

8.5 Paragenetic summary and model for precipitation of gold in schist.

Robust characterisation of gold mineralisation in the schist has been somewhat hampered by the lack of samples. This PhD study is confined to examples of gold in two samples of schist and may not necessarily be representative throughout the whole mineralised unit. However, drilling conducted by Klondike Gold Corporation (examples in Table 8-2) has identified that disseminated mineralisation within the Quartz Mica Schist Member extends 1600m along strike at the Lone Star Ridge. Mineralisation is challenging to recognise when logging due to a lack of typical alteration features associated with gold deposition. Recognising which minerals are associated with gold deposition has only been possible through petrographic and micro-textural studies.

Visible gold in schist is challenging to quantify due to lack of samples and the fact it exhibits a pronounced nugget effect. The gold disseminated in the Quartz Mica Schist Member is much more extensive and provides consistently elevated grades along strike. This type of mineralisation is much easier to sample, and has the capacity to be an exploration target.

The paragenesis of mineralisation can be broken down into four stages. The first stage is related to regional metamorphism of the volcanic protolith to greenschist facies, with evidence of retrograde reactions characterised by biotite changing to phengite (Figure 8-14a). This latter part of stage 1 is associated with the formation of a pyrite pseudomorphs around grains of rutile, and after ilmenite (Figure 8-5 and Figure 8-13). A source of sulphur, thought to originate from metamorphic fluids, reacted with destabilised ilmenite, resulting in the formation of pyrite with a core of rutile grains (Figure 8-14a).

Stage 2 is related to gold deposited in spaces between mica sheets, such as crenulation hinges, or around pyrite grains (Figure 8-13). Hyalophane and Ca-Fe carbonate (Figure 8-8) display a close association with gold and appear coeval (stage 2-3). Brittle fractures and space along foliations has provided a pathway for gold-bearing fluids to permeate (Figure 8-14b). Disseminated gold mineralisation of the schist is bound by the rheologically competent Meta

Rhyolite Member that generates a competency contrast ideal for focussing fluid into the QMS Member. Localisation of gold in the QMS Member is thought to be primarily linked to the porosity and permeability of the rock compared to others in the LSSA.

Depressurisation of fluids results in gold precipitating in areas of low pressure such as crenulation hinges or pressure shadows around pyrite (Figure 8-14b). The controls on the generation of large visible gold particles within schist is difficult to establish due to the small sample set. Both types of gold are accompanied by the presence of hyalophane in foliation or micro veinlets and therefore are interpreted to be sourced from similar fluid compositions.

Euhedral hyalophane forms in micro veinlets that show zonal textures indicative of successive episodes of stable fluid (e.g. not boiling). Hyalophane is present elsewhere in the schist as euhedral crystals in micro veinlets (Figure 8-10). The previous section discusses the various sources of Ba in hydrothermal fluids, which are responsible for the formation of hyalophane. This study has concluded that the concentration of Ba in a fluid is easily reconciled, and a more important consideration is the reason for its uptake in feldspar. Ba most commonly precipitates due to interaction with sulphate to form barite (BaSO_4). The uptake of Ba into feldspars to form hyalophane is rarely observed in general and may suggest a lack of available sulphate. The compositional zoning of Ba in hyalophane is interpreted to represent the episodic interaction between the primary hydrothermal fluid with an external sulphate rich fluid. One potential source for a sulphate rich fluid is meteoric water (discussed in section 8.4) as being an important fluid source in the LSSA for the gold-bearing quartz veins (Rushton et al. 1993).

Stage 3 is represented by deposition of gold along fractures of pyrite (Figure 8-13), where it is associated with greenockite, galena, chalcopyrite, and tellurium-bearing minerals such as altaite and hessite (Figure 8-9 and Figure 8-14c). The presence of telluride minerals suggests that hydrothermal fluid was low temperature with a high $f\text{Te}_2$.

Stage 4 is represented by deposition of Fe-Mg carbonate, barite, pyrite and petzite, found at the centre of micro veinlets (Figure 8-10). The precipitation

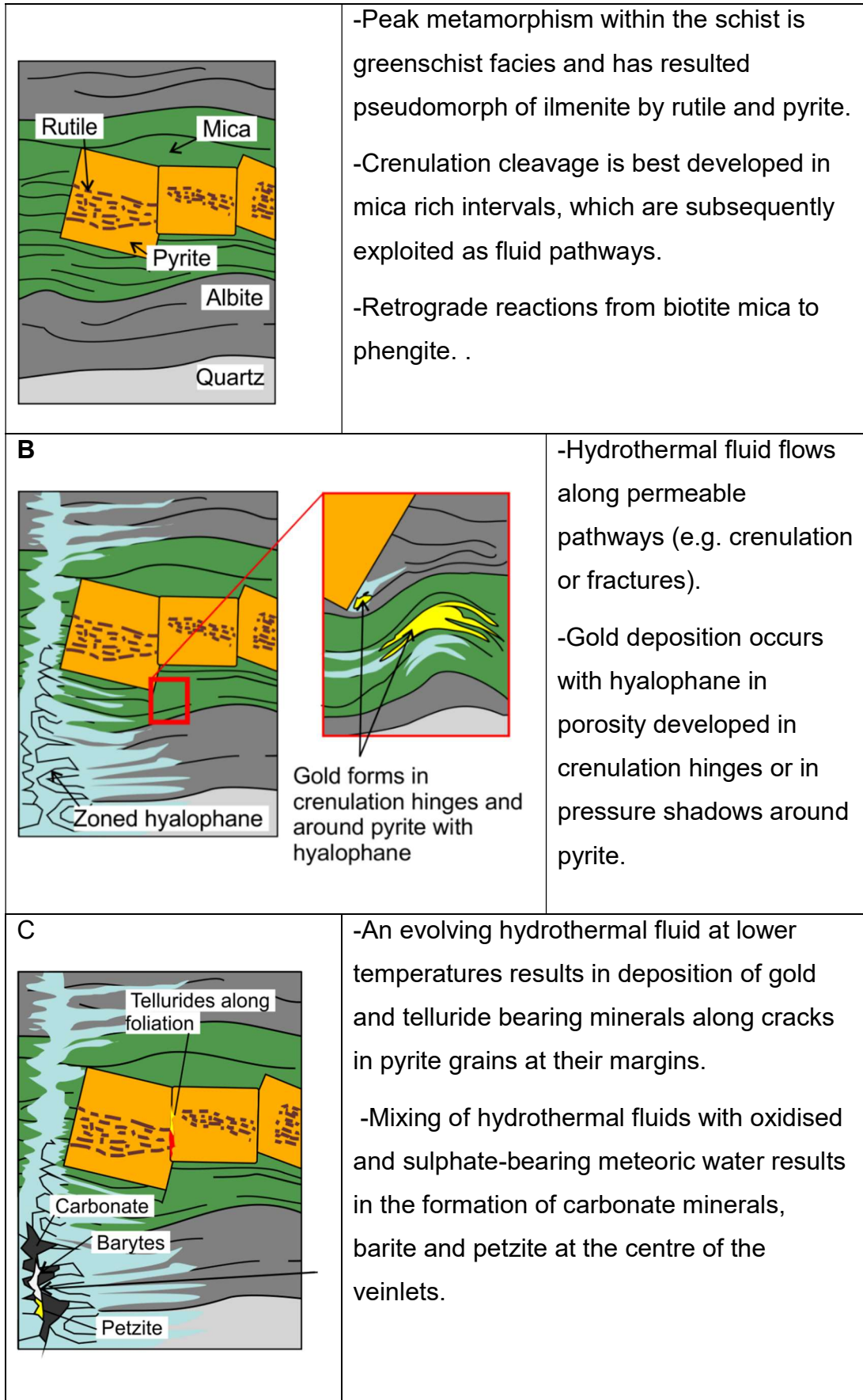


Figure 8-14: A schematic summary of gold formation in schist.

Chapter 9 Detrital gold

The extensive placer deposits of detrital gold in the LSSA provide a source of gold that is investigated here to inform on the relationships with bedrock gold sources. The chemical and mineralogical features of detrital gold from a number of localities were analysed in this thesis.

Detrital gold analysed in this study (298 particles) was collected from a number of sources such as; eluvial soil, first order drainages, present day valley bottoms, and alluvial bench gravel deposits of the WCG (described in Chapter 4.3.1 and shown in Figure 4-6). The project has also benefited from detrital gold samples collected by Crawford (2007) and Chapman et al. (2010a), with analyses and data included from unpublished undergraduate theses by R. Dawson and S. Jefferson (Jefferson, 2013, Dawson, 2017).

9.1.1 Crystallography of detrital gold particles

The approach to studying the crystallography of detrital gold particles is the same as that employed for in situ material, described in Chapter 7.4.4, chiefly, using EBSD.

Every particle analysed displayed large internal grains that are separated by 60° twin boundaries. The textures are similar to those observed in particles of in situ gold collected from gold-bearing quartz veins, described in section 7.4.4.

Compared to particles collected from gold-bearing veins, detrital gold particles often display slight deformation of the straight twins (Figure 9-1). The bending of twins is interpreted to be a result of physical deformation during transport of particle. Hammering of the exterior of the gold during transport has resulted in the recrystallization of gold to small (10 micron) grains that rim the particle.

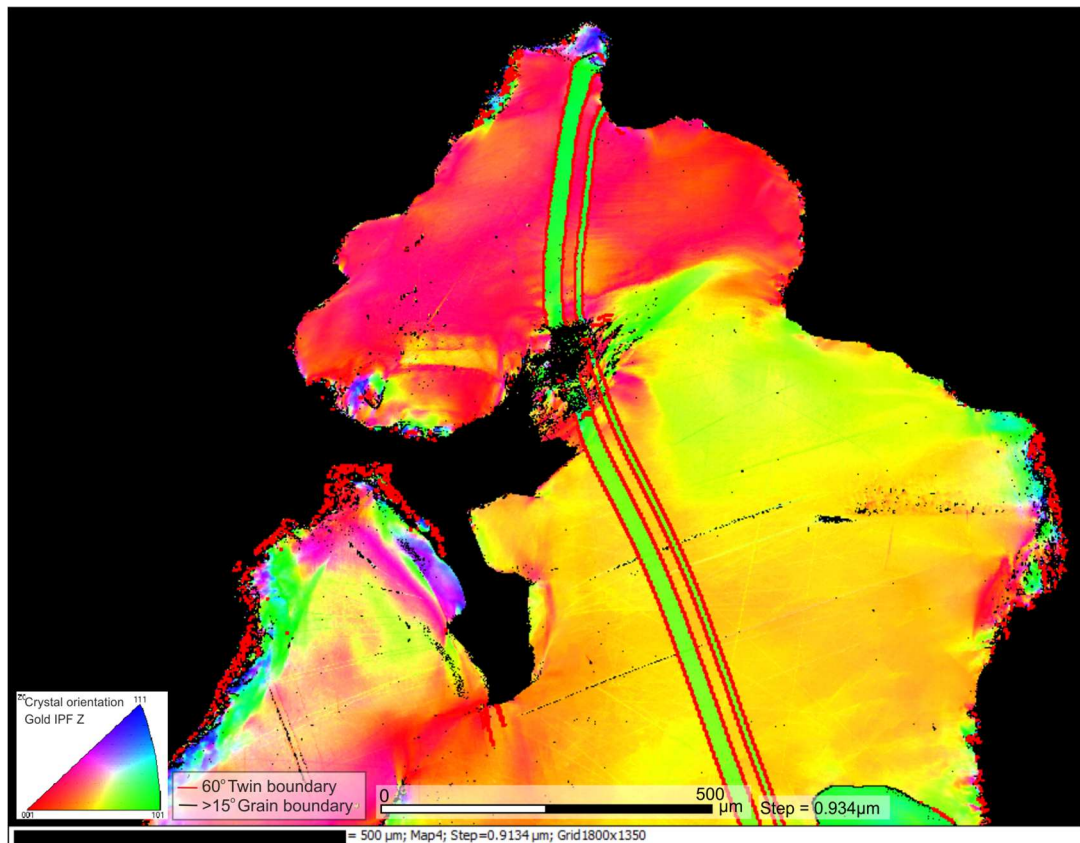


Figure 9-1: Orientation map (IPFZ) of detrital gold particle from Upper Gay Gulch stream, which has a distinctive twin through the centre. The twin has been bent slightly during transport.

9.1.2 Compositional variation

Identification of alloy heterogeneity using BSE was undertaken prior to quantification of the alloy composition. This study revealed that less than 5% of all particles exhibited internal alloy heterogeneity. The gold rich tracks described in section 7.4.6.1 were investigated using a combined approach of EDS and EBSD analysis. The gold-rich tracks are interpreted to be related to weathering of gold in situ, and prior to liberation from a hypogene source.

Almost all particles recovered from the present-day valley bottom placers and WCG deposits display a gold rich rim (Figure 9-2). The best developed rims have formed in gold particles that were originally silver rich. These grains were investigated using a combination of EDS and EBSD.

Figure 9-3 shows how the almost pure gold rims (green) are associated with the formation of new grain boundaries (black lines). The new grains lack a preferred orientation and occur in embayments around the centre of the

particle. These types of rims are confined to detrital gold from alluvial environments and are not observed in particles collected from gold-bearing quartz veins.

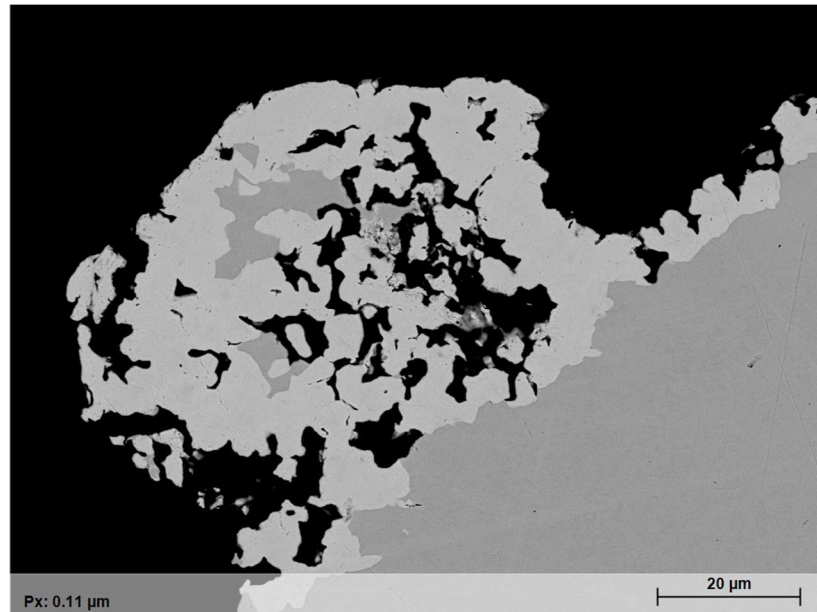


Figure 9-2: BSE image of gold particle rim. Greyscale corresponds to Au content with brighter colours being almost pure gold.

Gold rich rim formation in alluvial gold, discussed in section 5.2.3.2, is primarily controlled by the loss of silver through a process of self-electro refining (Groen et al. 1990). Groen et al. (1990) describe how dissolution of Au and Ag in oxidising surface waters leaves the surface of the alloy negatively charged (Groen et al., 1990). Gold re-precipitates by reduction, but silver remains in solution and is lost from the surface (Groen et al., 1990).

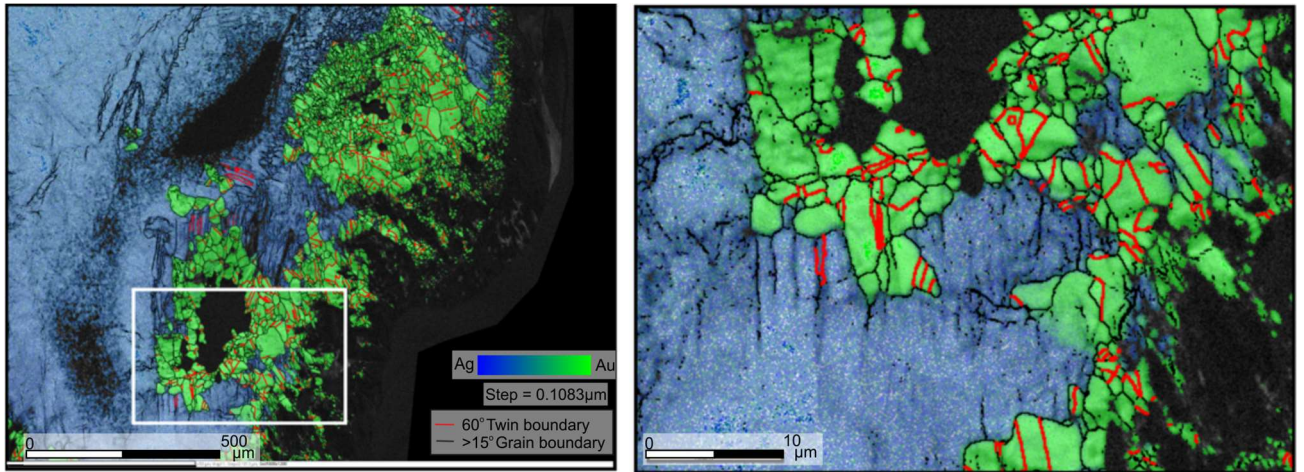


Figure 9-3: EBSD and EDS data of detrital gold particle showing: grain boundaries (black), twin boundaries (red) and Au (green) and Ag (blue). **A-** Gold rich rim at margin of gold particle. **B-** Pure gold at margin separated by grain boundaries.

9.1.3 Alloy composition of detrital gold

The results of alloy data collected from WCG deposits (Figure 4-6) and two valley bottom placers are provided in Table 9-1. The silver values of gold particles from all WCG samples are higher than the bedrock equivalents, presented in Figure 7-39 and Chapter 7.1.4.6. The silver values from Adams Hill WCG has a 25th percentile at 31% and 75th percentile of 45%, which is a much higher interquartile range compared to other deposits (Figure 9-4). All WCG deposits, with the exception of Adams Hill WCG, show similar ranges in silver values, as shown in Figure 9-4a.

Oro Grande is a small creek on the SW side of the Lone Star Ridge that drains the Nugget Zone. Gay Gulch is much larger and drains the Buckland Zone, intersects multiple different lithologies and has been extensively mined for its placer gold. The silver values from Oro Grande and Gay Gulch have a range of 14-58%, but the interquartile range (7th percentile -25th percentile) is low

The gold from Adams Hill and French Gulch WCG have elevated mercury content (Table 9-1:). Adams Hill WCG has a maximum value of 6.5wt% mercury compared to the modern drainages where the values are less than 0.3wt%.

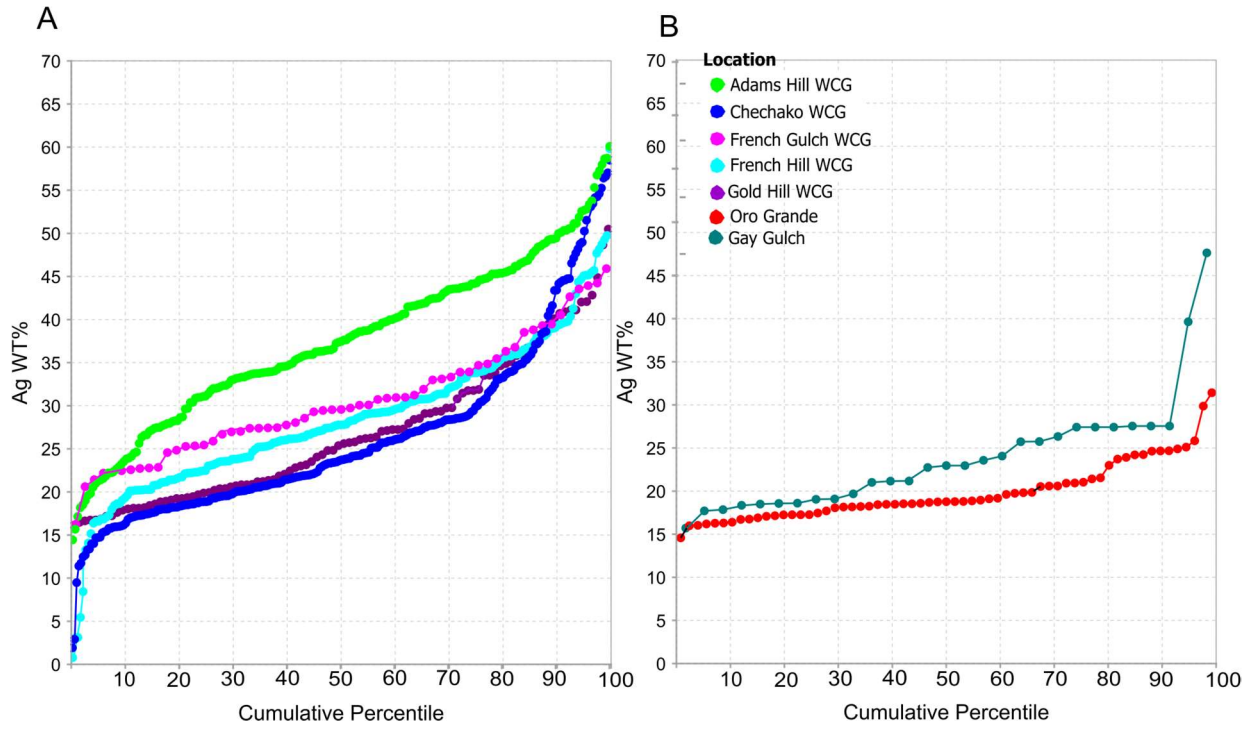


Figure 9-4: Cumulative percentile plots demonstrating variation in silver content of each population. **A-** Gold particles collected from different WCG deposits. **B-** Gold particles collected from modern drainages.

Table 9-1: A summary of alloy composition data from samples collected during this study

Locality	No. Grains	Ag% range	Hg% range	% > LOD Hg	Inclusions
<i>Adams Hill WCG</i>	211	14.5-60	0-6.5	82.	Py, Cpy, Tet, Carb
<i>Chechako WCG</i>	253	1.9-59	0-2.5	26.5	Py, Po, Sph, Ac, Gn, Tet, Carb
<i>French Gulch WCG</i>	59	16.3-45.9	0.5-4.6	98	Py, Gn, Sph, Asp, Cv, Hs, Carb
<i>French Hill WCG</i>	207	1-59.9	0-3.3	42	Py, Gn, Sph, Asp, Cv, Hs, Carb
<i>Gold Hill WCG</i>	101	16.1-50.5	0-3.7	31	Py, Gn, Cpy, Gn, Cv, Hs, Carb
<i>Oro Grande</i>	81	15.7-47.5	0 -0.3	75	Py, Cpy, Carb
<i>Gay Gulch</i>	228	14.5-36.7	0-0.3	3.5	Hs, Py, Gn, Carb

Py- pyrite, **Cpy-** chalcopyrite, **Dol-**dolomite, **Cal-** calcite, **Sph-** sphalerite, **Ga-**galena, **Asp-** arsenopyrite, **Po-** pyrrhotite, **Carb-** Carbonate minerals, **Ac-** Acanthite, **Cv-** Covelite, **Hs-** Hessite.

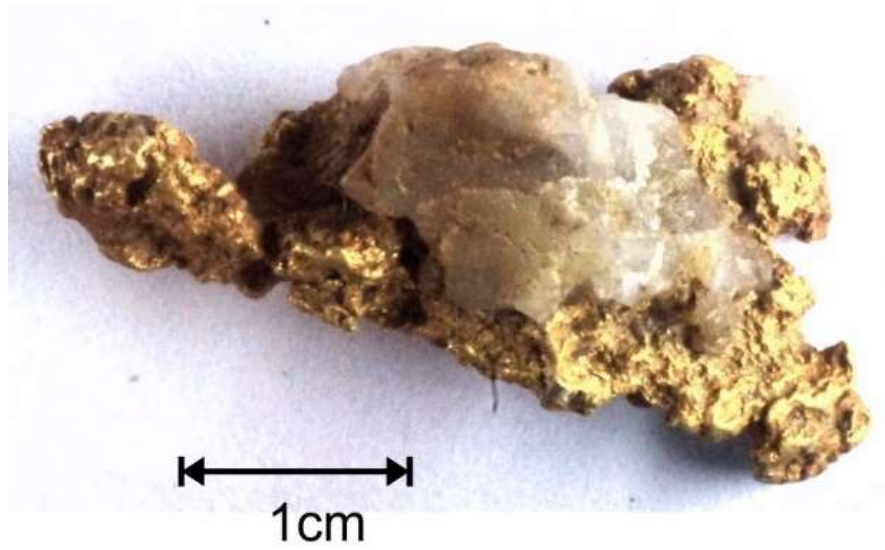
9.1.4 Mineral associations with detrital gold

The mineral inclusions within gold particles collected from each placer locality are described in Table 9-1. The scarcity of inclusions in gold from veins discussed in section 7.4.6.3 also applies to the placer populations from the WCG and modern drainages. This meant that 60+ particles were required from each sample location to generate a robust population and representative set of inclusions.

Gold particles from the modern-day placers of Gay Gulch and Oro Grande are noted for the presence of sulphide mineral inclusions. The variety of inclusions recorded in gold from the WCG is much greater. A distinctive association of WCG gold with telluride mineral inclusions is noted, which is not the case for the present-day gold placers. The larger variety of inclusions from the WCG deposits is interpreted to be due to the increased size of sample populations.

Detrital particles lack the context of surrounding minerals that in situ gold from hypogene sources provide. However, the preservation of minerals as inclusions on detrital gold provides evidence of primary mineral associations. A number of large gold particles associated with quartz, up to 1cm in diameter, were recovered from the confluence of Little Eldorado and Eldorado Creek. The samples were sectioned to investigate the relationship of quartz and gold. CL analysis revealed a variety of quartz textures that correspond to those identified in the paragenesis for gold-bearing veins in section 7.4.1. Figure 9-5 shows gold surrounded by bright Q3, which is interpreted to represent evidence of coeval gold and Q3 deposition. This is direct evidence that these large detrital gold-on-quartz particles must originate from a similar gold-bearing quartz vein to those already known in the LSSA. It also provides further evidence that the relatively small volume of quartz generated in the Q3 event, presumably from a small volume fluid, can also be responsible for deposition of large gold particles.

A



B

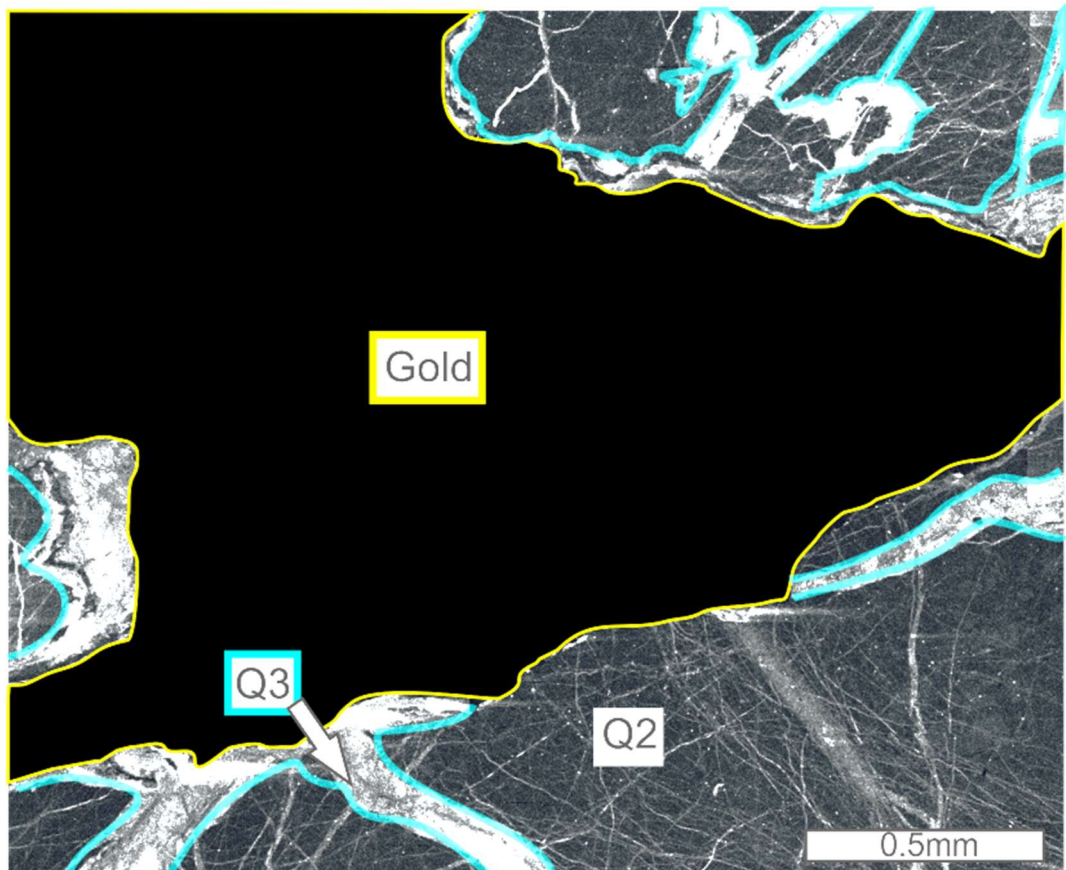


Figure 9-5: A: Eldorado Creek gold particle. B: CL image of gold particle in A. Different generations of quartz are labelled with Q3 forming in association with gold.

9.1.5 Establishing placer-lode relationships in the LSSA

The diversity of bedrock gold signatures discussed in Chapter 7 provides a framework in which to compare the gold from the abundant placer deposits within the LSSA. Tyrrell (1907) was the first to establish that placer gold originated from bedrock veins; however it was Knight et al. (1999a) who first used gold composition to investigate placer-lode relationships. These authors identified a type of gold in placers, that was higher fineness and not accounted for in bedrock deposits, which led to an interpretation that there may be an undiscovered additional source. Chapman et al. (2010a) provided a more detailed critique of placer-lode relationships, incorporating opaque mineral inclusions with gold alloy compositions to produce a 'microchemical signature' (Chapter 5). These authors included gold particles collected not only from the main known drainage placers, but also from the headwaters of drainages to provide enhanced spatial characterisation of local gold mineralisation, and thus to highlight possible exploration targets. This project aims to refine the placer-lode relationships discussed by Chapman et al. (2010a) and investigate whether the potential influence of the gold-bearing schist (Chapter 8) as an additional source.

The recovery of gold from headwaters of first order drainages can be constrained within the catchment due to a lack of glaciation. Bedrock occurrences in the Oro Grande drainage include the gold-bearing quartz veins of Nugget and Buckland Zone. The alloy composition of placer gold from Oro Grande, shown in Figure 9-4b, broadly overlaps with the other bedrock sources within the area. This suggests that the gold is sourced from the same veins; however, the previous section described how gold within each vein locality displayed considerable variation in composition. Therefore, silver alloy compositions are unreliable in isolation when attempting to determine a specific placer-lode relationship. The microchemical signature of gold in Oro Grande Gulch shows mineral inclusions of pyrite and chalcopyrite, which correspond to the Chapman et al. (2010a) Types 1a and 1b described in Table 10-1 (Chapman et al., 2010a). Overall, the gold particles from the Oro Grande gulch probably display a diversity of chemical signatures that correspond to

the diversity of bedrock mineralisation presented in section 7.1.4.6 and shown in Figure 9-6.

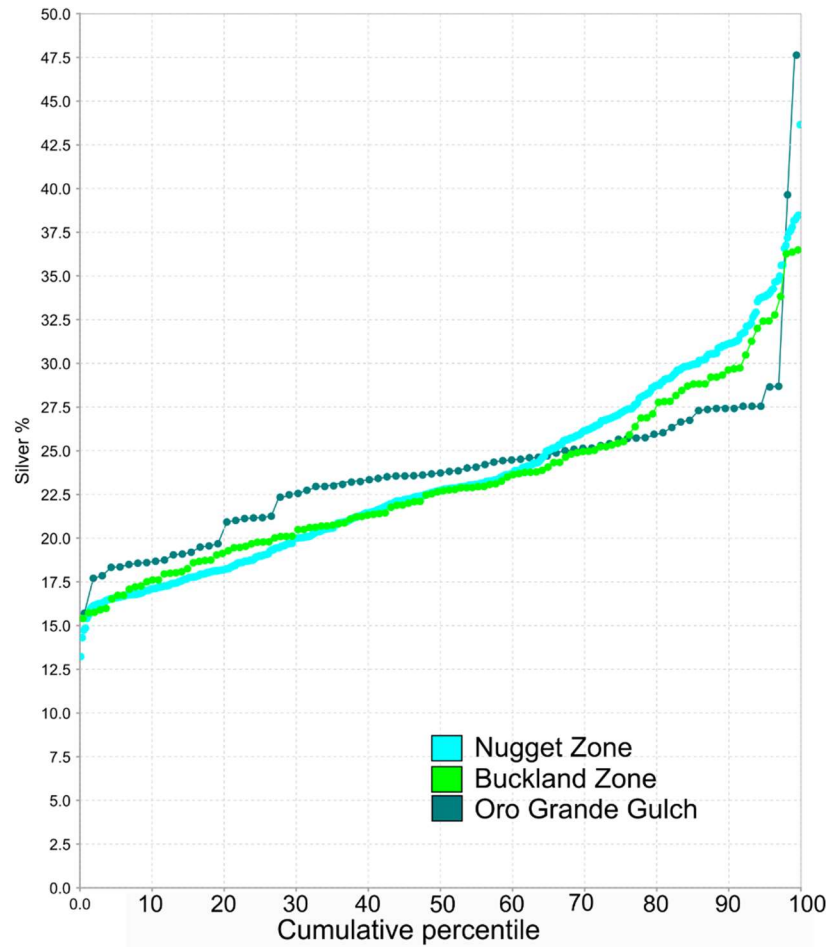


Figure 9-6: A comparison of the gold-bearing vein localities of Nugget and Buckland Zone with a small first order drainage placer deposit of Oro Grande.

The internal crystallography and microchemical signature of gold particles from Gay Gulch were combined with observations reported by Chapman et al. (2010a). Gold particles revealed polycrystalline textures that are typical of those found in hypogene samples (section 9.1.1), and provide evidence that the particles are detrital in origin and did not form in-situ via nugget grown (discussed in section 5.2.4). The minor deformation of a twin boundary in Figure 9-1 is a result of shape modification during alluvial transport and suggests short transport distances. The microchemical signature of gold from Gay Gulch was investigated by Chapman et al. (2010a) who identified a variety of gold compositions that correspond to Types 1b, 1c and 1e (Table 10-1). This study suggests that a range of gold signatures are a result of gold

precipitation in a variety of different lithologies that are present in the relatively large (~5km²) catchment of Gay Gulch. The variety of gold signatures provide further evidence, discussed in section 7.5, that gold alloy compositions are primarily controlled by the local environment of deposition.

The majority of detrital gold particles considered in this study have come from the extensive WCG deposits that form along the NW side of the LSSA. The data presented in Figure 9-4 and Table 9-1 show alloy signatures that are slightly elevated in silver compared to gold particles in bedrock veins, which may represent an alternate source. Mineral inclusions within the WCG deposits are mostly sulphides, but telluride bearing minerals also occur. Adams Creeks is an exception displaying a much higher silver content and larger range of inclusions, this suggests the gold originates from a separate source of bedrock mineralisation from those characterised along the Lone Star Ridge.

The microchemical signature of gold in the WCG deposits corresponds with Type 1f gold which has an alloy composition of 13-29% Ag, along with telluride and sulphide inclusions (Chapman et al. 2010a). This project has established that telluride-bearing minerals accompany paragenetically late mineralisation in the QMS Member. In section 8.5, it was established that gold identified as being disseminated in schist was likely formed in a shallow environment from relatively cool fluids (section 8.5). Type 1f is the primary gold type found in Bonanza Creek, which very likely originates from the erosion and liberation of gold from the QMS Member, which is present along the Lone Star Ridge.

The WCG has formed due to extensive degradation and erosion of a paleo landscape, which has resulted in concentration of gold into rich placers. The results of this study indicate that formation of gold with tellurides was at relatively shallow levels that were subsequently eroded and concentrated into the placers.

Chapter 10 Discussion

This chapter provides a summary of the previous 3 chapters to develop an overarching model for gold mineralisation in the LSSA.

10.1 Establishing the relationship between gold-bearing quartz veins and gold disseminated in schist.

Gold mineralisation in quartz veins and schist have been discussed separately in Chapters 7 and 8 with a model of formation proposed for each. Previous research by MacKenzie et al. (2007a), suggested that the gold-bearing schist was syngenetic in origin, associated with VMS mineralisation, and had no relation to veining. This study has shown that the formation of gold in schist is epigenetic, which means that its relationship to gold-bearing quartz veins must be reconsidered.

The distribution of visible gold in veins, and its textural relationship to a specific generation of quartz growth (Q3,) have provided evidence that the influx of gold is paragenetically late. The model for gold deposition provided in section 7.5 proposes that gold-bearing fluids exploited the pre-existing sub-vertical quartz veins as a vertical pathway and deposited gold where fractures existed in earlier formed quartz and pyrite. Although veins are an ideal pathway, they are not continuous and the various mineralised localities across the LSSA lack evidence at the surface for connectivity. In contrast, evidence within the gold-bearing QMS Member (Chapter 8) suggests a diffuse fluid flow along fractures and foliation.

Alteration associated with gold mineralisation was investigated by MacKenzie et al. (2007b) who studied assay data from drilling. Gold-bearing quartz veins had a crude association with arsenic, whereas gold-bearing schist had no evidence for elevated arsenic (MacKenzie et al., 2007a). Mineralogical investigations during this study have shown hyalophane to be the most distinctive mineral that is always found in association with gold in the schist.

Although the mineral has elevated barium it is unlikely that whole rock geochemistry would be able to identify it as a pathfinder due to the presence of barite in un-mineralised host rocks.

This study has found no evidence that arsenic is associated with Q3, the quartz generation gold is deposited with in the veins, and instead must rely on other mineral associations. Figure 7-25 shows hyalophane from a gold-bearing quartz vein at the Nugget Zone and an example of zoned euhedral hyalophane with a particle of gold. The evidence of hyalophane forming along fractures of pyrite which also host gold and Q3, indicates that it is coeval with the deposition of gold. The fluid responsible for gold in veins and gold in schist both transported Ba^{2+} , which indicates that the process of formation must have been similar. The textural evidence from the quartz vein paragenesis, coupled with the conditions under which hyalophane is known to form (section 8.5), suggest that gold deposition occurred at relatively shallow levels from low temperature hydrothermal fluids.

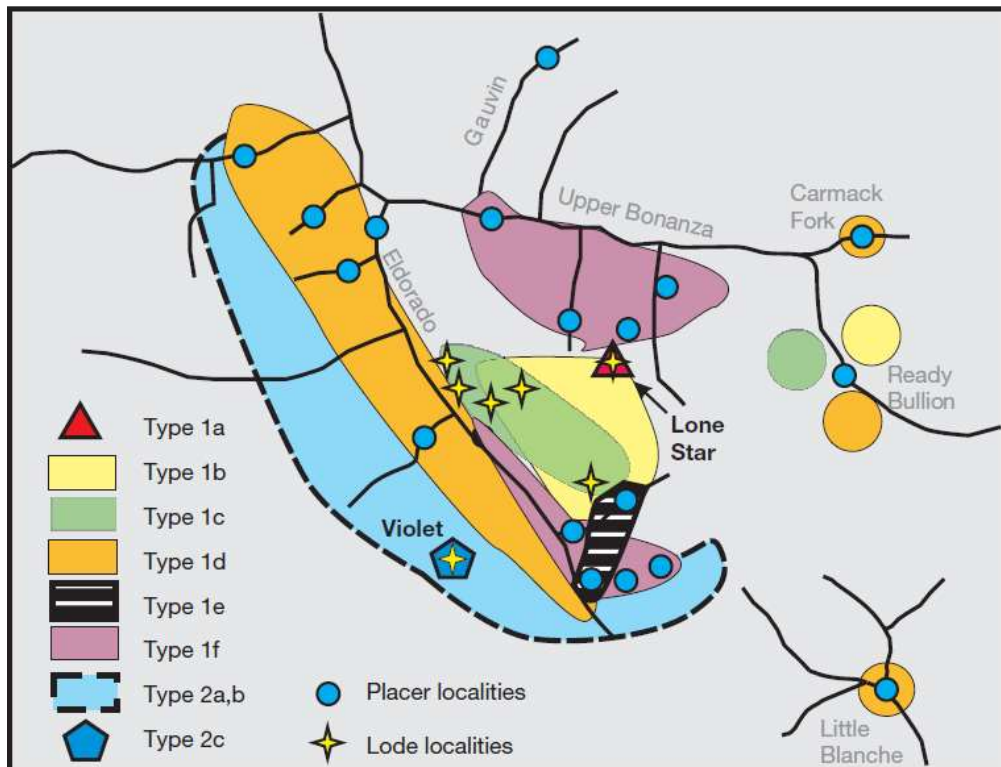
This is the first-time evidence has ever been presented for a genetic link between gold in veins and the gold disseminated in schist. It is challenging to reconcile whether the fluids responsible for gold deposition in both settings are indeed the same, or part of a single hydrothermal event; however, the micro-environment of deposition is remarkably similar, given all the evidence presented here. These observations and conclusions provide the basis in which to develop an overarching model for mineralisation in the LSSA.

10.2 A review of the microchemical signatures of gold in the LSSA

The model by Chapman et al. (2010a) proposed the systematic increase of Ag in gold in successive populations away from the Lone Star Ridge may be due to lateral and temporal zonation within a single hydrothermal system. According to Chapman et al. (2010a) gold deposition at the Violet Mine was cooler and had a lower Au/Ag_{aq} (Type 2) compared to the centre at the Lone Star ridge (Type 1).

Table 10-1 Classification of gold types defined by Chapman et al. (2010).

TYPE	AREA	AG (%)	HG (%)	INCLUSION SUITE
1A	Boulder Lode Mine/ Lone Star Ridge	12-17	<LOD	Base metal sulphides, pyrite and minor sulfosalts
1B	Boulder Lode Mine/ Lone Star Ridge	21-326	<LOD	Base metal sulphides, pyrite and minor sulfosalts
1C	Veronika Vein	30-32	<LOD	Base metal sulphides and pyrite
1D	Dysle Zone	25-30	<LOD	Base metal sulphides, pyrite, and argentite
1E	Lone Star Ridge	15-25	<LOD	Pyrite
1F	Lone Star Ridge	13-29	<LOD	Base metal sulphides, pyrite, minor sulfosalts and minor tellurides.
2A	Violet Mine	18-35	0.2-1.4	Uncommon
2B	Violet Mine	35-55	1.2-9.1	Uncommon
2C	Violet Mine	3-10	0-1.5	Uncommon

**Figure 10-1: Geographic extent of gold types according to the classification in (Chapman et al. 2010)**

This PhD has found evidence that the controls on gold deposition are very local. Evidence of diffuse fluid flow within the QMS Member (section 8.5) shows that there was significant fluid-rock interaction that has provided a local enrichment of metals. The alloy composition of gold is influenced by the amount of fluid focussing and interaction with surrounding rocks, rather than the composition of the original hydrothermal fluid as proposed by Chapman et al. (2010a). The variation of silver composition of gold from the Nugget Zone and Buckland Zone (Type 1b,c) reflects the diverse parameters responsible for gold deposition (section 7.4.6.4). Figure 10-1 shows the distribution of gold Types 1a-1e along the Lone Star Ridge according to Chapman et al. (2010a). This area is adjacent to and/or underlain by the rheologically incompetent Quartz Mica Schist and Quartz Chlorite Mica Schist Members resulting in more diffuse fluid flow through softer rocks. In comparison, gold at the Dysle Zone and Violet Mine (Type 1f and 2) are underlain by the rheologically competent Sulphur Creek Orthogneiss and Quartz Augen Schist Member, that readily fracture and enable efficient fluid flow. This results in limited fluid-rock interaction and led to a lower variation in metal signatures. The gold has a confined environment of deposition compared to deposits along the Lone Star ridge, which are hosted in less competent, more mica-rich, and softer lithologies. Chapman et al. (2010a) ascribe the majority of gold in the Eldorado Creek to be associated with Types 1b and 1c, which are typical of the Nugget and Buckland Zones. The classification of gold types, according to Chapman et al. (2010a) relies on the concept that a gold signature is generated at a specific location. However, this research has shown that gold compositions in the LSSA are largely controlled by their local environment of deposition, which means that signatures can vary considerably on a small scale.

This study agrees with Chapman et al. (2010a) regarding their assertion that the gold-bearing fluids were relatively low temperature and have precipitated gold at shallow crustal levels. The controls on gold alloys presented by Chapman et al. (2010a) are broadly applicable; however, a single hydrothermal system seems unlikely due to the local influences on gold precipitation.

This study proposes a model where gold is transported by multiple metamorphic fluids generated during a period of crustal uplift. Interaction of metamorphic fluids with meteoric fluids results are circulated at shallow crustal levels. Conditions during mineralisation evolved, due to cooling and mixing, and were influenced by changes in the local environment of gold precipitation, rather than the primary fluid content. Wall and host rock composition and rheology influence the amount of fluid focusing and gold content of mineralised localities in the LSSA.

10.3 A model for gold mineralisation in the LSSA

Separate models for gold emplacement in veins and in schist were discussed and shown to be genetically linked. This section presents an overarching model for gold mineralisation in the LSSA, and attempts to provide context with respect to the regional metallogeny.

Peak metamorphism of the rocks in the LSSA are from the biotite zone of the greenschist facies. This has resulted in the recrystallisation of micas to biotite, breakdown of ilmenite and development of an S_2 foliation (section 8.2). Rocks of similar metamorphic and deformation characteristics are observed across the Yukon, and are associated with the Permo-Triassic Klondike Orogeny (section 3.2), when the YTT collided with the North American margin (Beranek and Mortensen, 2011).

D_3 deformation in the LSSA is related to a regional episode of orogeny in the Early Jurassic, caused by the final accretion of the Insular Terrane to the continental margin (section 3.2.4). The rocks of the LSSA underwent ductile deformation that resulted in the formation of a crenulation cleavage and folding before progressing to thrusting. Tectonic uplift in the mid-late Jurassic caused rocks to undergo a transition from ductile to brittle conditions (section 3.2.4) (Allan et al, 2013). The associated deformation, defined as D_4 , shows a progression from ductile to brittle conditions, and is, developed in the LSSA as angular kink folds that progress to reverse faults (section 3.4).

Extension of the D_4 structures during post-orogenic relaxation resulted in the localisation of fluid into them and the formation of euhedral quartz crystals in

a first generation of vein quartz formation named Q1 (section 7.5 and Figure 7-43a). Zonal quartz growth in Q1 indicates that episodic fluid flow has occurred under stable hydrothermal conditions (Table 10-2). A second generation of quartz deposition (Q2) is thought to originate from hydrofracturing of Q1 by metamorphic fluids that are coeval with pyrite formation (Figure 7-43b). The fluid is interpreted to be a result of dehydration reactions related to continental uplift across the Yukon.

Continued uplift through brittle conditions in the Late Jurassic (~165Ma) is linked to the development of orogenic mineralisation across the Yukon and Alaska, which was discussed in Chapter 3 section 3.5.3 (Allan et al. 2013). The features observed in the LSSA are similar to those elsewhere, and are interpreted to be genetically related.

Gold-bearing quartz veins in the LSSA show that gold is associated with a third phase of quartz deposition (Q3). Pre-existing sub-vertical quartz veins have provided an ideal pathway for gold-bearing fluids. The Q3 textures indicate multiple pulses of fluid that hydrofracture the previous generations of quartz, which is apparent by the initial fibrous quartz, related to rapid deposition, and then later zonal growth, related to stable hydrothermal conditions. Q3 fractures cross cut pyrite and are filled with quartz, hyalophane and gold (Figure 7-43c). Gold deposition in these settings is linked to chemo-adsorption of gold onto pyrite that results in the generation of large particles and nuggets. Gold in quartz veins has been shown to be intimately associated with hyalophane, which is also a key mineral associated with gold in the QMS Member, which is present predominantly along the Lone Star Ridge. In contrast to the quartz veins, fluid flow in the schist seems to be much more diffuse. This has resulted in localisation of gold in pressure shadows of pyrite, in the hinges of crenulation cleavages defined by phengite micas, and along micro-veinlets which cross-cut the foliations

Fluid sources are difficult to reconcile, but are thought to be related to a mixed metamorphic and meteoric origin (section 7.1.5). Previous research by Rushton et al. (1990) provided some evidence for a mixed fluid source, but lacked the crucial paragenetic context provided in this PhD project. Gold

hosted in brittle structures (D₄ veins) suggest that mineralisation occurred under hydrostatic pressures and at shallow depths, which would favour circulation of meteoric fluids. Further evidence of fluid mixing, discussed in section 7.5, is provided by the presence of telluride bearing minerals and the oscillatory zoning of Ba in hyalophane (Table 10-2 and Figure 10-2). The various auriferous vein occurrences in the LSSA lack evidence of large scale connectivity. The channelisation of hydrothermal fluids into veins or schist results in numerous separate pathways in which fluid evolution is influenced by the local environment, especially the host-lithologies.

Deep weathering and extensive oxidation of the rocks in the LSSA are a result of a prolonged period of degradation and lack of glaciation, producing the saprolite and regolith. Multiple periods of uplift have resulted in repeated incision of the weathered bedrock by rivers and streams, and the subsequent deposition, remobilisation, and aggradation of fluvial and alluvial sediment has concentrated detrital gold into the rich placer deposits of the WCG. Subsequent periods of degradation, incision, and remobilisation has produced the extremely rich placer deposits in the modern drainages of the LSSA.

Table 10-2: Various aspects of this project that provide evidence of low temperature and shallow vein formation.

Aspect of project	Key observation	Implication
Quartz texture	Q3 forms fibrous and zonal growth textures which are typical of boiling and stable growth respectively	Hydrostatic pressure at shallow depth
Quartz composition	High Al content of Q3 is an indicator it formed at low temperature and hasn't annealed.	Low temperature fluid.
Mineralogy of schist	Tellurides indicate high f_{Te_2} . Barite deposition suggests interaction with surface waters.	Low temperature fluid and interaction with surface water
Gold mineralogy	Mineral inclusions of acanthite indicate temperatures <200°C.	Low temperature fluid.

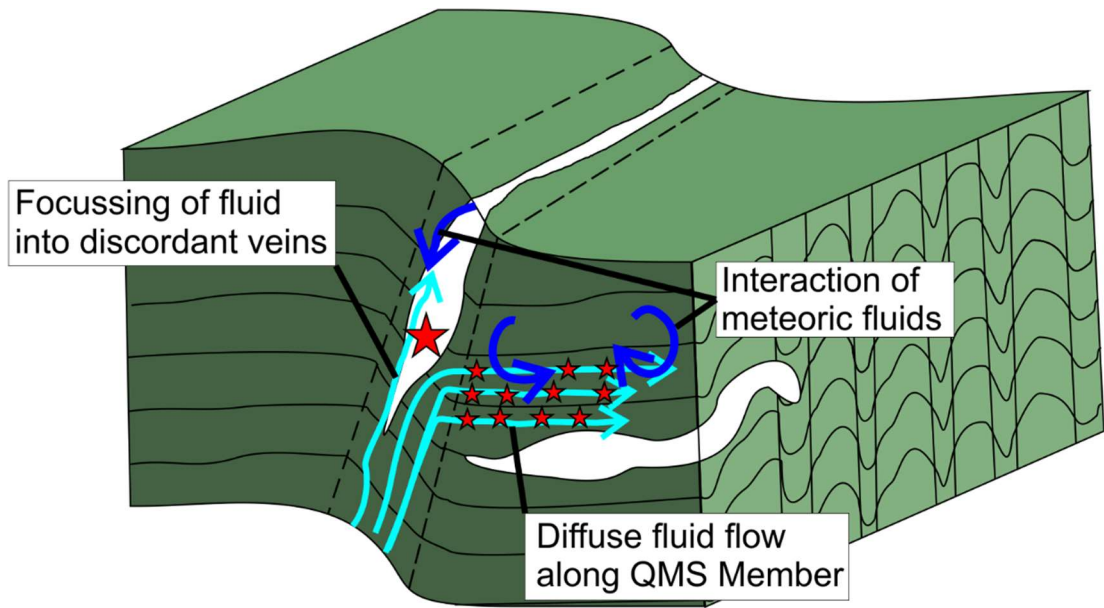


Figure 10-2: Schematic model of gold-bearing fluids moving upwards through the schist resulting in gold deposition (red stars) at shallow crustal depths. Localisation of fluid into discordant quartz veins results in gold deposition. Diffuse fluid flow along the QMS Member results in the deposition of gold along foliation. Mixing with meteoric fluids occurs, and is followed by deposition of gold, tellurides, and barite.

10.4 The significance of the LSSA and its relationship to regional OGD formation

The mineralisation in the LSSA is interpreted to be part of a regional episode of OGD formation, described by Allan et al. (2013) in Chapter 3. This project has provided a refined model for gold deposition in the LSSA and discusses the conditions controlling gold formation. The various aspects of mineralisation in the LSSA are discussed in this section and compared to the current accepted models of OGD formation, as provided in Chapter 2. This provides a framework in which to discuss regional OGD formation in the Yukon, and globally.

10.4.1 A metal and fluid source for OGD formation in the LSSA

Various characteristics of the gold mineralisation in the LSSA provide evidence that gold formed at shallow crustal levels from a cooling hydrothermal fluid (Table 10-2 and Figure 10-2). These features correspond to the epizonal classification, described by Groves et al. (1998), who state

epizonal gold forms from fluids with temperature of 150-300°C, pressures of 500-1500bar, and depths <6km. The origin of hydrothermal fluids from deeper crustal levels are interpreted to be generated through metamorphic devolatilisation (Staples et al., 2016). The tectonic configuration in the Mid Jurassic involved westward compression and the formation of an east-dipping slab beneath the YTT. Staples et al. (2016) suggested that cold hydrous material, such as the Finlayson Assemblage, was emplaced to a mid-crustal depth relatively quickly. Under-thrusting of the rocks into a hot crust resulted in dehydration reactions and expulsion of fluids (Figure 10-3). Uplift of the overlying rocks resulted in extensional faulting and the generation of fluid pathways (Figure 10-3). Progressive NE movement of the YTT resulted in the under-thrusting of the Finlayson Assemblage that subsequently dehydrated and generated pulses of hydrothermal fluid (Figure 10-3). A potential source of metals could be generated from the Finlayson Assemblage that is known host base metal deposits, discussed in section 3.5.1. Additionally, high gold content in the LSSA may be due to the already elevated metal content of the volcanic rocks in the Klondike Schist Assemblage (e.g. base metal content of QMS Member and Finlayson Assemblage, discussed in (section 3.5.1). Mobilisation of these metals may be controlled by the circulation of meteoric fluids. Extensional conditions are thought to provide pathways for deep penetration of meteoric fluids that mix with metamorphic fluids (Rushton et al. 1993).

Mid-late Jurassic

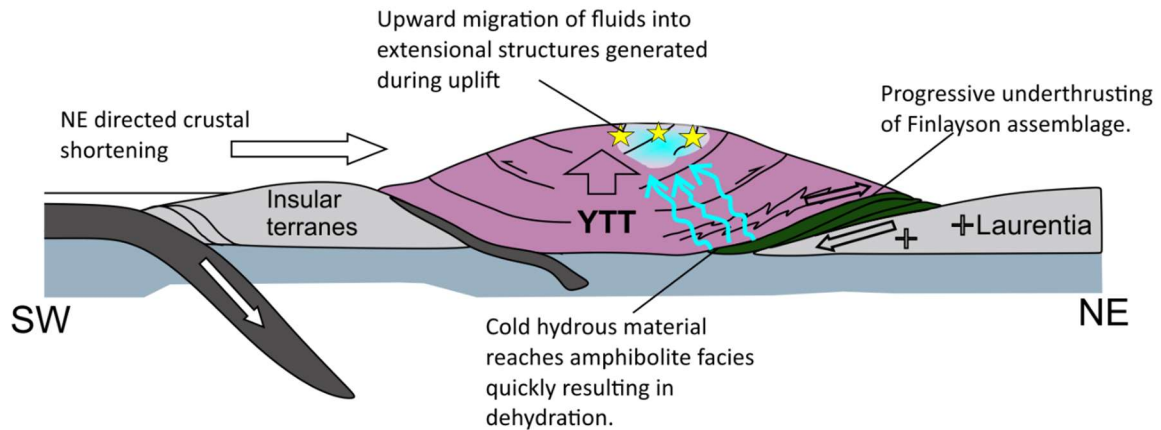


Figure 10-3: A schematic model of fluid generation and gold transport responsible for formation of OGDs in the region.

10.4.2 A comparison of the LSSA to regional OGDs

This section compares the epizonal OGD model at LSSA to other deposits in the region that are related to Mid-Jurassic mineralisation.

Bailey (2013) describes the different processes involved in gold deposition at the Golden Saddle deposit in the White Gold District. Mineralised veins record a progression from ductile-brittle conditions with latter stages, described by Bailey (2013) as epizonal. Gold deposition is linked to a drop in fluid pressure during progressive faulting. The competent meta-intrusive rocks in the area localise fluid into structures that exhibit crack seal textures. This mechanism is described in Chapter 2 as the fault valve model, which is related to seismic activity. The generation of lithology-specific metal associations across the region provides evidence for local metal sources. The conditions of ore formation at Golden Saddle are interpreted to be similar to those at LSSA; however, rheologically competent lithologies at Golden Saddle have resulted in better preserved fluid pathways (Allan et al., 2013).

The presence of gold-bearing quartz veins across the KGD are described by Allan et al. (2013) to be part of the same phase of Mid-Jurassic OGD formation. The controls of gold precipitation at Hunker Dome are interpreted to be a result of sulphidation reactions (Chapter 3) (Rushton et al., 1993). Friedrich and Hoymann (1992) describes three stages of mineralisation at the

Hunker Dome area. Gold deposition was initiated by unmixing of an aqueous-carbonic solution as a result of a drop in pressure and temperature (Friedrich and Hoymann, 1992). This resulted in the formation of sulphides and the precipitation of gold. The successive mineralising events are interpreted by Friedrich and Hoymann (1992) to represent cooler hydrothermal fluids. The evidence of mineralisation at Hunker Dome suggests a progression to cooler and shallower conditions, which are reflected by the observations at LSSA and at Golden Saddle.

The epizonal characteristics of gold mineralisation in the LSSA are evident in orogenic veins across the region. Focussing of gold-bearing fluids into extensional fractures during brittle deformation is further evidence that OGD formation occurred during crustal uplift. The variation in metal signatures between deposits is thought to be a result of local lithological enrichment. A model of episodic fluid generation at depth, described in section 10.4.1, can result in the generation of different mineralised areas within the region. The fluids are unlikely to be connected on a regional scale and gold precipitation is heavily influenced by the local environment of deposition, especially the host lithologies.

Chapter 11 Concluding remarks

This chapter summarises the main findings of the research conducted in this PhD project and considers future research that would develop the current outcomes.

11.1 Conclusions

This section presents the conclusions of the research that correspond to the different aspects of the research outlined in section 1.1

11.1.1 Gold-bearing quartz veins

Textural and mineralogical studies have provided a new paragenesis for the auriferous quartz veining which is related to an evolving hydrothermal system. Gold mineralisation is associated with a volumetrically minor phase of quartz deposited late in vein paragenesis. Epizonal conditions resulted in brittle fracturing and focussing of fluid into the discordant quartz veins. Precipitation of gold is primarily controlled by the depressurisation of fluid which results in the destabilisation of gold complexes, and subsequent nucleation of native gold on pyrite within the late-stage quartz deposited in fractures within the earlier generations of vein quartz.

11.1.2 Gold-bearing schist

The generation of gold disseminated within schist is epigenetic and not syngenetic in origin. Gold is associated with the diffuse flow of hydrothermal fluid in micro-cracks and foliations within the QMS Member. Gold deposition is facilitated by and exploits spaces within the schist, such as crenulation hinges in the micas and pressure shadows of pyrite. A minor phase of gold and telluride-bearing minerals is present very late in the paragenesis and is interpreted to represent hydrothermal fluids mixing with meteoric waters.

11.1.3 Gold mineralisation in the Lone Star area

Gold-bearing quartz veins and gold-bearing schist display similar mineralogical and textural features, which indicate that they are genetically linked. The local micro-environment of deposition influences the chemical and mineralogical features of gold, which is influenced by the metal signature of surrounding lithologies. This research confirms that the variety of gold signatures identified in the extensive placer deposits corresponds to bedrock gold mineralisation in the LSSA.

Gold mineralisation has formed from a relatively cool hydrothermal fluid emplaced at shallow crustal levels, which is typical of epizonal OGDs. Metamorphic devolatilisation at depth has resulted in the formation of fluids that were driven upwards during crustal uplift. Decompression has resulted in extensional faults that enabled meteoric fluid to infiltrate and mix with metamorphic fluids.

Gold mineralisation during the Mid-Late Jurassic is observed elsewhere in the Yukon (e.g. White Gold District), and displays many of the same epizonal features of the LSSA. Crustal uplift has resulted in the production of gold-bearing fluids that form metal signatures and features associated with the local and micro environment of deposition. The impressive combined placer and bedrock gold production shows that the original deposit prior to erosion in the LSSA represented an anomalously rich example of epizonal orogenic mineralisation in the region.

11.1.4 Relating mineralisation in the LSSA to OGDs globally

The epizonal features of mineralisation in the LSSA must be considered in relation to OGDs globally. The source of gold-bearing fluids is interpreted to originate from metamorphic devolatilisation, a common process proposed for OGDs globally (Goldfarb and Groves, 2015). The transport of fluid and metals in the LSSA, and more widely in the Yukon, is the most challenging feature of mineralisation to reconcile with deposits globally. OGDs in Western Australia and Abitibi in Canada are related to large crustal scale faults, which focus fluid during transpression (Goldfarb and Groves, 2015). Crustal uplift in the Yukon during the Mid-Late Jurassic has resulted in an evolution from ductile to brittle

conditions which provides numerous pathways for the upward migration of fluid. The localisation of gold-bearing fluids into fractures at shallow crustal levels has resulted in the formation of characteristic epizonal mineralisation. Mineralisation in the region and at the LSSA shares many features with OGDs globally, but lacks the crustal scale focussing that generates world-class deposits (discussed in Chapter 2).

11.2 Implications of research

The outcomes of this research provide a number of implications that are relevant for ongoing mineral exploration at the LSSA and OGD models globally.

- **A new vein paragenesis:** Mineral exploration within the LSSA had previously focussed on identifying discordant quartz veins. This project has identified that these veins are merely a host for a volumetrically minor generation of gold-bearing quartz (Q3).
- **New exploration targets in the LSSA:** The identification that gold disseminated in schist is epigenetic has raised the potential that favourable lithologies may be present elsewhere within the area. The gold-bearing schist represents a significant resource within the LSSA compared to the gold-bearing quartz veins. Exploration has historically struggled to develop resources from the sporadic gold-bearing quartz veins that exhibit a pronounced nugget affect. Disseminated mineralisation provides a bulk tonnage target that can be enhanced by high-grade gold veins.
- **Mineralisation prior to erosion in the LSSA:** The particle size of gold within the schist and in gold-bearing quartz is often very small (5-20µm). Gold particles of this size are not retained efficiently in placer lags, particularly if the fluvial system is degrading. Consequently, it appears certain that estimates of the original gold inventory of the source (estimates presented in Table 4-2), based on recovered placer gold, are a very large underestimation of the true magnitude.

- **Exploration targets regionally:** Mineral exploration in the Yukon has focussed on gold-bearing veins, and the apparent discrepancy between in situ and placer gold. The identification of epizonal mineralisation in schist raises the potential for a potential gold source in areas where similar discrepancies exist globally.
- **OGDs models:** The generation of small, but exceedingly rich, epizonal orogenic gold systems in the Yukon has shown that the large-scale features associated with OGD models are not necessary for gold mineralisation in orogenic settings. The controls on gold formation in some Phanerozoic OGDs, such as the Yukon, are not the same as those proposed by Groves. et. al. (1998).

11.3 Future Work

The current project has identified several areas that would benefit from future study.

- **Detailed fluid inclusion analysis:** There needs to be a better understanding of Q3, and detailed fluid inclusion analysis will provide quantitative results on the conditions of fluid associated with gold bearing quartz.
- **Detailed paragenetic characterisation of quartz:** This can be done using CL and must be undertaken to determine which phase of quartz certain fluid inclusion assemblages relate to.
- **Studies of regional OGDs:** A comparison of gold-bearing quartz veins could be expanded from the LSSA to other deposits within the KGD, and regionally to veins in the White Gold District. The characterisation of vein textures from these deposits may provide a model of vein evolution that is regionally applicable.
- **Gold bearing schist:** The investigation of gold in the QMS Member has been based on a small sample set. Expanding the same analytical protocol to gold bearing schist along strike of the QMS Member around the Lone Star Ridge would provide a more refined understanding of mineralogical distribution.

Bibliography

- ADAMS, S. F. 1920. *A microscopic study of vein quartz*, Stanford University.
- AFIFI, A. M., KELLY, W. C. & ESSENE, E. J. 1988. Phase relations among tellurides, sulfides, and oxides; I, Thermochemical data and calculated equilibria. *Economic Geology*, 83, 377-394.
- ALLAN, M. M., YARDLEY, B. W. D., FORBES, L. J., SHMULOVICH, K. I., BANKS, D. A. & SHEPHERD, T. J. 2005. Validation of LA-ICP-MS fluid inclusion analysis with synthetic fluid inclusions. *American Mineralogist*, 90, 1767-1775.
- ALLAN, M. M., HART, C. J. & MORTENSEN, J. K. 2012. Yukon Gold Project Final Technical Report. University of British Columbia: Mineral Deposit Research Unit
- ALLAN, M. M., MORTENSEN, J. K., HART, C. J. R., BAILEY, L., SANCHEZ, M. G., CIOLKIEWICZ, W. & CREASER, R. A. 2013. Magmatic and Metallogenic Framework of West-Central Yukon and Eastern Alaska. *Society of Economic Geology Special Publication* 111-168.
- ALLAN, M. M., MORTENSEN, J. K. & COOK, N. 2014a. Preliminary stable isotope and geochemical investigation of carbonate in the Klondike district. *Yukon Exploration and Geology* 2013, 1-20
- ALLAN, M. M., MORTENSEN, J. K., SANCHEZ, M. G., HART, C. J., MCKENZIE, G. G., CIOLKIEWICZ, W., WRIGHTON, T., CHAPMAN, R. J., CREASER, R. A. & JENKINS, S. E. 2014b. *Metallogeny of western Yukon and eastern Alaska*. Mineral Deposit Research Unit: University of British Columbia.
- ANAND, R., LINTERN, M., HOUGH, R., NOBLE, R., VERRALL, M., SALAMA, W., BALKAU, J. & RADFORD, N. 2016. The dynamics of gold in regolith change with differing environmental conditions over time. *Geology*.
- ANGIBOUST, S. & HARLOV, D. 2017. Ilmenite breakdown and rutile-titanite stability in metagranitoids: Natural observations and experimental results. Mineralogical Society of America.
- ANTWEILER, J. & SUTTON JR, A. 1970. Spectrochemical analyses of native gold samples. *US Geological Survey Report USGS-GD-70-003*. Commerce National Technical Information Service. Springfield. Va.; US Geological Survey.; US Dept.
- BACON, C. R., FOSTER, H. L. & SMITH, J. G. 1990. Rhyolitic calderas of the Yukon-Tanana Terrane, east central Alaska: Volcanic remnants of a Mid-Cretaceous magmatic arc. *Journal of Geophysical Research*, 95, 21451-21461.

- BADALOVA, R. & BADALOV, S. 1967. The standard of gold from hypogene ore deposits and occurrences of Uzbekistan; Akad. Nauk SSSR, Dokl., v. 173, no. 4. *Acad. Sci. USSR, Dokl., Earth Sci. Sec.*, 173, 194-197.
- BAILEY, L. 2013. *Late Jurassic Fault-Hosted Gold Mineralization of the Golden Saddle Deposit, White Gold District, Yukon Territory*. Master of Science, University of British Columbia.
- BARNES, H. L. 1997. *Geochemistry of hydrothermal ore deposits*, John Wiley & Sons.
- BARTON, M. D. 1980. The Ag-Au-S system. *Economic Geology*, 75, 303-316.
- BATEMAN, A. M. & JENSEN, M. L. 1950. *Economic mineral deposits*, Wiley New York.
- BEILBY, G. T. 1903. Surface Flow in Crystalline Solids under Mechanical Disturbance. *Proceedings of the Royal Society of London*, 72, 218-225.
- BENNING, L. & SEWARD, T. 1994. Hydrosulphide complexes of gold (I) at high pressures and temperatures: equilibrium and kinetic problems. *Mineral. Mag. A*, 58, 75-76.
- BERANEK, L. P. & MORTENSEN, J. K. 2011. The timing and provenance record of the Late Permian Klondike orogeny in northwestern Canada and arc-continent collision along western North America. *Tectonics*, 30, TC5017.
- BERMAN, R., RYAN, J., GORDEY, S. & VILLENEUVE, M. 2007. Permian to Cretaceous polymetamorphic evolution of the Stewart River region, Yukon-Tanana terrane, Yukon, Canada: P-T evolution linked with in situ SHRIMP monazite geochronology. *Journal of Metamorphic Geology*, 25, 803-827.
- BERRY, J. M., MOBLEY, R. M., GILLON, K. A., YOGODZINSKI, G. M. & BATES, C. C. 2016. A Neoproterozoic epithermal gold deposit—The Haile gold mine, South Carolina, USA. *Field Guides*, 42, 1-8.
- BIERLEIN, F. P., GROVES, D. I., GOLDFARB, R. J. & DUBÉ, B. 2006. Lithospheric controls on the formation of provinces hosting giant orogenic gold deposits. *Mineralium Deposita*, 40, 874-886.
- BIGNALL, G., SEKINE, K. & TSUCHIYA, N. 2004. Fluid-rock interaction processes in the Te Kopia geothermal field (New Zealand) revealed by SEM-CL imaging. *Geothermics*, 33, 615-635.
- BLOUNT, C. 1977. Barite solubilities and thermodynamic quantities up to 300/sup 0/C and 1400 bars. *Am. Mineral.:(United States)*, 62.
- BOND, D. P. & CHAPMAN, R. J. 2006. Evaluation of the origins of gold hosted by the conglomerates of the Indian River formation, Yukon, using a combined sedimentological and mineralogical approach. *Yukon Exploration and Geology*, 93-103.

- BONEV, I. K., KERESTEDJIAN, T., ATANASSOVA, R. & ANDREW, C. J. 2002. Morphogenesis and composition of native gold in the Chelopech volcanic-hosted Au–Cu epithermal deposit, Srednogorie zone, Bulgaria. *Mineralium Deposita*, 37, 614-629.
- BOYLE, R. W. 1979. *The geochemistry of gold and its deposits: together with a chapter on geochemical prospecting for the element*, Geological Survey of Canada Ottawa.
- BUITENHUIS, E. 2014. *The Latte Gold Zone, Kaminak's Coffee Gold Project, Yukon, Canada: Geology, Geochemistry, and Metallogeny*. Master of Science University of Western Ontario.
- BURKE, M., HART, C. J. R. & LEWIS, L. L. 2005. Models for epigenetic gold exploration in the northern Cordilleran Orogen, Yukon, Canada. *In*: MAO, J. & BIERLEIN, F. P. (eds.) *Mineral Deposit Research: Meeting the Global Challenge: Proceedings of the Eighth Biennial SGA Meeting Beijing, China, 18–21 August 2005*. Berlin, Heidelberg: Springer Berlin Heidelberg.
- BUTT, C. R. M. & HOUGH, R. M. 2009. Why Gold is Valuable. *Elements*, 5, 277-280.
- CABRAL, A. R., SUH, C. E., KWITKO-RIBEIRO, R. & ROCHA FILHO, O. G. 2008. Brittle microstructures in gold nuggets: A descriptive study using backscattered electron imaging. *Ore Geology Reviews*, 33, 212-220.
- CASSELMAN, S. & BROWN, H. 2016. Casino porphyry copper-gold-molybdenum deposit, central Yukon. *Yukon Exploration & Geology*, 61-74.
- CAWOOD, P. A. & HAWKESWORTH, C. J. 2014. Earth's middle age. *Geology*, 42, 503-506.
- CAWOOD, P. A. & HAWKESWORTH, C. J. 2015. Temporal relations between mineral deposits and global tectonic cycles. *Geological Society, London, Special Publications*, 393, 9-21.
- CEPEDAL, A., FUERTES-FUENTE, M., MARTIN-IZARD, A., GONZÁLEZ-NISTAL, S. & BARRERO, M. 2008. GOLD-BEARING As-RICH PYRITE AND ARSENOPYRITE FROM THE EL VALLE GOLD DEPOSIT, ASTURIAS, NORTHWESTERN SPAIN. *The Canadian Mineralogist*, 46, 233-247.
- CHAPMAN, R. J., LEAKE, R. & MOLES, N. 2000a. The use of microchemical analysis of alluvial gold grains in mineral exploration: experiences in Britain and Ireland. *Journal of Geochemical Exploration*, 71, 241-268.
- CHAPMAN, R. J., LEAKE, R. C., MOLES, N. R., EARLS, G., COOPER, C., HARRINGTON, K. & BERZINS, R. 2000b. The Application of Microchemical Analysis of Alluvial Gold Grains to the Understanding of Complex Local

and Regional Gold Mineralization: A Case Study in the Irish and Scottish Caledonides. *Economic Geology*, 95, 1753-1773.

CHAPMAN, R. J., LEAKE, R. C., BOND, D. P. G., STEDRA, V. & FAIRGRIEVE, B. 2009. Chemical and Mineralogical Signatures of Gold Formed in Oxidizing Chloride Hydrothermal Systems and their Significance within Populations of Placer Gold Grains Collected during Reconnaissance. *Economic Geology*, 104, 563-585.

CHAPMAN, R. J., MORTENSEN, J. K., CRAWFORD, E. C. & LEBARGE, W. 2010a. Microchemical Studies of Placer and Lode Gold in the Klondike District, Yukon, Canada: 1. Evidence for a Small, Gold-Rich, Orogenic Hydrothermal System in the Bonanza and Eldorado Creek Area. *Economic Geology*, 105, 1369-1392.

CHAPMAN, R. J., MORTENSEN, J. K., CRAWFORD, E. C. & LEBARGE, W. P. 2010b. Microchemical Studies of Placer and Lode Gold in the Klondike District, Yukon, Canada: 2. Constraints on the Nature and Location of Regional Lode Sources. *Economic Geology*, 105, 1393-1410.

CHAPMAN, R. J., MORTENSEN, J. K. & LEBARGE, W. P. 2011. Styles of lode gold mineralization contributing to the placers of the Indian River and Black Hills Creek, Yukon Territory, Canada as deduced from microchemical characterization of placer gold grains. *Mineralium Deposita*, 46, 881-903.

CHAPMAN, R. J., ALLAN, M.M., GRIMSHAW, M.R., MORTENSEN, J.K., WRIGHTON, T.M., AND CASSELMAN, S. 2014. Pathfinder signatures in placer gold derived from Au-bearing porphyries. *Yukon Exploration and Geology* 2013, 21-31.

CHAPMAN, R. J. & MORTENSEN, J. K. 2016. Characterization of Gold Mineralization in the Northern Cariboo Gold District, British Columbia, Canada, Through Integration of Compositional Studies of Lode and Detrital Gold with Historical Placer Production: A Template for Evaluation of Orogenic Gold Districts. *Economic Geology*, 111, 1321-1345.

CHAPMAN, R. J., COOK, M., GRIMSHAW, M. & MYLES, S. 2016. Placer-lode gold relationships in the Nansen placer district, Yukon. *Yukon Exploration and Geology*, 63-78.

CHAPMAN, R. J., MILEHAM, T., ALLAN, M. & MORTENSEN, J. 2017. A distinctive Pd-Hg signature in detrital gold derived from alkalic Cu-Au porphyry systems. *Ore Geology Reviews*, 83, 84-102.

CLINE, J. S., HOFSTRA, A. H., MUNTEAN, J. L., TOSDAL, R. M. & HICKEY, K. A. 2005. Carlin-type gold deposits in Nevada: Critical geologic characteristics and viable models. *Economic Geology 100th anniversary volume*, 100, 451-484.

- CLOUGH, D. M. & CRAW, D. 1989. Authigenic gold-marcasite association; evidence for nugget growth by chemical accretion in fluvial gravels, Southland, New Zealand. *Economic Geology*, 84, 953-958.
- COLPRON, M., NELSON, J. L. & MURPHY, D. C. 2007. Northern Cordillera terranes and their interactions through time. *GSA Today*.
- CONNOLLY, J. 1997. Devolatilization-generated fluid pressure and deformation-propagated fluid flow during prograde regional metamorphism. *Journal of Geophysical Research: Solid Earth (1978–2012)*, 102, 18149-18173.
- COOKE, D. R. & SIMMONS, S. F. 2000. Characteristics and genesis of epithermal gold deposits. *Reviews in Economic Geology*, 13, 221-244.
- COOKE, D. R. & MCPHAIL, D. C. 2001. Epithermal Au-Ag-Te Mineralization, Acupan, Baguio District, Philippines: Numerical Simulations of Mineral Deposition. *Economic Geology*, 96, 109-131.
- COX, D. P. & SINGER, D. A. 1986. *Mineral deposit models*, US Government Printing Office.
- COX, S., WALL, V., ETHERIDGE, M. & POTTER, T. 1991. Deformational and metamorphic processes in the formation of mesothermal vein-hosted gold deposits—examples from the Lachlan Fold Belt in central Victoria, Australia. *Ore Geology Reviews*, 6, 391-423.
- COX, S. F. 1999. Deformational controls on the dynamics of fluid flow in mesothermal gold systems. *Geological Society, London, Special Publications*, 155, 123-140.
- COX, S. F. 2005. Coupling between Deformation, Fluid Pressures, and Fluid Flow in Ore-Producing Hydrothermal Systems at Depth in the Crust. *Economic Geology*, 100th Anniversary Volume, 30-75.
- CRAW, D., KOONS, P. O., HORTON, T. & CHAMBERLAIN, C. P. 2002. Tectonically driven fluid flow and gold mineralisation in active collisional orogenic belts: comparison between New Zealand and western Himalaya. *Tectonophysics*, 348, 135-153.
- CRAW, D. & CAMPBELL, J. R. 2004. Tectonic and structural setting for active mesothermal gold vein systems, Southern Alps, New Zealand. *Journal of Structural Geology*, 26, 995-1005.
- CRAW, D., UPTON, P., YU, B.-S., HORTON, T. & CHEN, Y.-G. 2010. Young orogenic gold mineralisation in active collisional mountains, Taiwan. *Mineralium Deposita*, 45, 631-646.
- CRAW, D., MACKENZIE, D. & GRIEVE, P. 2015. Supergene gold mobility in orogenic gold deposits, Otago Schist, New Zealand. *New Zealand Journal of Geology and Geophysics*, 58, 123-136.

- CRAW, D., HESSON, M. & KERR, G. 2017. Morphological evolution of gold nuggets in proximal sedimentary environments, southern New Zealand. *Ore Geology Reviews*, 80, 784-799.
- CRAWFORD, E. 2007. Klondike Placer Gold: New Tool for Examining Morphology, Composition and Crystallinity
- CZAMANSKE, G. K., DESBOROUGH, G. A. & GOFF, F. E. 1973. Annealing History Limits for Inhomogeneous, Native Gold Grains as Determined from Au-Ag Diffusion Rates. *Economic Geology*, 68, 1275-1288.
- DAWSON, R. 2017. *Determining the host of gold mineralisation from bulk vein samples in the Lone Star area of the Klondike, Yukon, Canada using mineral exclusion and trace element analysis*. Mgeol, Bsc, University of Leeds.
- DESBOROUGH, G., HEIDEL, R., RAYMOND, W. & TRIPP, J. 1971. Primary distribution of silver and copper in native gold from six deposits in the Western United States. *Mineralium deposita*, 6, 321-334.
- DESBOROUGH, G. A. 1970. Silver depletion indicated by microanalysis of gold from placer occurrences, western United States. *Economic Geology*, 65, 304-311.
- DILABIO, R. Classification and interpretation of the shapes and surface textures of gold grains from till. Gisements alluviaux d'or (Alluvial Gold Placers/Yacimientos aluviales de oro), 1991. 297-313.
- DONG, G. & MORRISON, G. 1995. Adularia in epithermal veins, Queensland: morphology, structural state and origin. *Mineralium Deposita*, 30, 11-19.
- DUK-RODKIN, A. 1999. *Glacial limits map of Yukon Territory*, 1:1000000. Open File 3694, Indian and Northern Affairs Canada Geoscience Geological Survey of Canada.
- DUK-RODKIN, A., BARENDREGT, R. W., WHITE, J. M. & SINGHROY, V. H. 2001. Geologic evolution of the Yukon River: Implications for placer gold *Quaternary International*, 82, 5-31.
- EMMONS, W. 1933. On the mechanism of the deposition of certain metalliferous lode systems associated with granitic batholiths. *Ore deposits of the western States: New York, American Institute of Mining and Metallurgical Engineers*, 327-349.
- ESSENE, E. J., CLAFLIN, C. L., GIORGETTI, G., MATA, P. M., PEACOR, D. R., ÁRKAI, P. & RATHMELL, M. A. 2005. Two-, three- and four-feldspar assemblages with hyalophane and celsian: implications for phase equilibria in $\text{BaAl}_2\text{Si}_2\text{O}_8$ - $\text{CaAl}_2\text{Si}_2\text{O}_8$ - $\text{NaAlSi}_3\text{O}_8$ - KAlSi_3O_8 . *European Journal of Mineralogy*, 17, 515-535.

- EVENCHICK, C. A., MCMECHAN, M. E., MCNICOLL, V. J. & CARR, S. D. 2007. A synthesis of the Jurassic–Cretaceous tectonic evolution of the central and southeastern Canadian Cordillera: Exploring links across the orogen. *Geological Society of America Special Papers*, 433, 117-145.**
- FINCH, E. G. & TOMKINS, A. G. 2017. Pyrite-Pyrrhotite Stability in a Metamorphic Aureole: Implications for Orogenic Gold Genesis. *Economic Geology*, 112, 661.**
- FISHER, N. H. 1945. The fineness of gold with special reference to the Morobe goldfield, New Guinea; Part 2. *Economic Geology*, 40, 537-563.**
- FRANCIS, C. A. 2004. Gold Crystals A Primer. *Rocks & Minerals*, 79, 24-29.**
- FRIEDRICH, G. & HOYMANN, K. H. 1992. Gold and sulphide mineralization in the Hunker Creek area, Yukon Territory, Canada. *Indian & Northern Affairs Canada/Department of Indian & Northern Development: Exploration & Geological Services Division*.**
- FYFE, W. S. & KERRICH, R. 1976. Geochemical prospecting: extensive versus intensive factors. *Journal of Geochemical Exploration*, 6, 177-192.**
- FYFE, W. S. 1978. *Fluids In The Earth's Crust: Their Significance In Metamorphic, Tectonic And Chemical Transport Process*, Elsevier.**
- GABOURY, D. 2013. Does gold in orogenic deposits come from pyrite in deeply buried carbon-rich sediments?: Insight from volatiles in fluid inclusions. *Geology*, 41, 1207-1210.**
- GAMMONS, C. H. & WILLIAMS-JONES, A. E. 1995. Hydrothermal geochemistry of electrum; thermodynamic constraints. *Economic Geology*, 90, 420-432.**
- GAROFALO, P. S. & RIDLEY, J. R. 2014. Gold-transporting hydrothermal fluids in the Earth's crust: an introduction. *Geological Society, London, Special Publications*, 402.**
- GAY, P. & ROY, N. 1968. The mineralogy of the potassium-barium feldspar series; III, Subsolidus relationships. *Mineralogical Magazine*, 36, 914-932.**
- GODWIN, C. I. 1975. Alternative interpretations for the Casino Complex and Klotassin batholith in the Yukon crystalline terrane. *Canadian Journal of Earth Sciences*, 12, 1910-1916.**
- GOLDFARB, R. J., GROVES, D. I. & GARDOLL, S. 2001. Orogenic gold and geologic time: a global synthesis. *Ore Geology Reviews*, 18, 1-75.**
- GOLDFARB, R. J., BAKER, T., DUBE, B., GROVES, D. I., HART, C. J. & GOSSELIN, P. 2005. Distribution, character, and genesis of gold deposits in metamorphic terranes. *Economic Geology 100th Anniversary Volume*, 407-450.**

- GOLDFARB, R. J., BRADLEY, D. & LEACH, D. L. 2010. Secular Variation in Economic Geology. *Economic Geology*, 105, 459.
- GOLDFARB, R. J. & GROVES, D. I. 2015. Orogenic gold: Common or evolving fluid and metal sources through time. *Lithos*, 233, 2-26.
- GÖTZE, J., PLÖTZE, M. & HABERMANN, D. 2001. Origin, spectral characteristics and practical applications of the cathodoluminescence (CL) of quartz – a review. *Mineralogy and Petrology*, 71, 225-250.
- GÖTZE, J., PLÖTZE, M. & TRAUTMANN, T. 2005. Structure and luminescence characteristics of quartz from pegmatites. *American Mineralogist*.
- GÖTZE, J. 2009. Chemistry, textures and physical properties of quartz – geological interpretation and technical application. *Mineralogical Magazine*, 73, 645-671.
- GÖTZE, J. 2012. Application of cathodoluminescence microscopy and spectroscopy in geosciences. *Microscopy and Microanalysis*, 18, 1270-1284.
- GRIMM, B. & FRIEDRICH, G. 1990. Weathering effects on supergene gold in soils of a semiarid environment, Gentio do Ouro, Brazil. *Chemical Geology*, 84, 70-73.
- GRIMWADE, M. 1999. The surface enrichment of carat gold alloys–Depletion gilding. *Gold Technology*, 26, 16-23.
- GROEN, J. C., CRAIG, J. R. & RIMSTIDT, J. D. 1990. Gold-rich rim formation on electrum grains in placers. *The Canadian Mineralogist*, 28, 207-228.
- GROVES, D., BARLEY, M., BARNICOAT, A., CASSIDY, K., FARE, R., HAGEMANN, S., HO, S., HRONSKY, J., MIKUCKI, E. & MUELLER, A. 1992. Sub-greenschist to granulite-hosted Archaean lode-gold deposits of the Yilgarn Craton: a depositional continuum from deep-sourced hydrothermal fluids in crustal-scale plumbing systems. *Geology Department (Key Centre) and University Extension, The University of Western Australia Publication*, 22, 325-337.
- GROVES, D., RIDLEY, J., BLOEM, E., GEBRE-MARIAM, M., HAGEMANN, S., HRONSKY, J., KNIGHT, J., MCNAUGHTON, N., OJALA, J. & VIELREICHER, R. 1995. Lode-gold deposits of the Yilgarn block: products of Late Archaean crustal-scale overpressured hydrothermal systems. *Geological Society, London, Special Publications*, 95, 155-172.
- GROVES, D. I. 1993. The crustal continuum model for late-Archaean lode-gold deposits of the Yilgarn Block, Western Australia. *Mineralium Deposita*, 28, 366-374.
- GROVES, D. I., GOLDFARB, R. J., GEBRE-MARIAM, M., HAGEMANN, S. & ROBERT, F. 1998. Orogenic gold deposits: a proposed classification in

the context of their crustal distribution and relationship to other gold deposit types. *Ore geology reviews*, 13, 7-27.

- GROVES, D. I., GOLDFARB, R. J., ROBERT, F. & HART, C. J. 2003. Gold deposits in metamorphic belts: overview of current understanding, outstanding problems, future research, and exploration significance. *Economic Geology*, 98, 1-29.
- GROVES, D. I. & SANTOSH, M. 2016. The giant Jiaodong gold province: The key to a unified model for orogenic gold deposits? *Geoscience Frontiers*, 7, 409-417.
- GUERRA, M. F. & CALLIGARO, T. 2004. Gold traces to trace gold. *Journal of Archaeological Science*, 31, 1199-1208.
- HAGEMANN, S. G., GEBRE-MARIAM, M. & GROVES, D. I. 1994. Surface-water influx in shallow-level Archean lode-gold deposits in Western, Australia. *Geology*, 22, 1067-1070.
- HALFPENNY, A., HOUGH, R. M. & VERRALL, M. 2013. Preparation of Samples with Both Hard and Soft Phases for Electron Backscatter Diffraction: Examples from Gold Mineralization. *Microscopy and Microanalysis*, 19, 1007-1018.
- HAMILTON, W. B. 1998. Archean magmatism and deformation were not products of plate tectonics. *Precambrian Research*, 91, 143-179.
- HARDY, L. S. 1989. Hydrothermal potassium feldspar at the Haile gold mine, South Carolina. *Economic Geology*, 84, 2307-2310.
- HART, C. J. & LANGDON, M. 1997. Geology and mineral deposits of the Mount Nansen camp, Yukon. *Yukon Exploration and Geology*, 129-138.
- HART, C. J. 2007. Reduced intrusion-related gold systems. *Mineral Deposits of Canada: A synthesis of Major deposit types, district metallogeny, the Evolution of geological provinces, and exploration methods: Geological Association of Canada, Mineral Deposits Division, Special Publication*, 95-112.
- HART, C. J. R., GOLDFARB, R. J., LEWIS, L. L. & MAIR, J. L. 2004. The Northern Cordilleran Mid-Cretaceous Plutonic Province: Ilmenite/Magnetite-series Granitoids and Intrusion-related Mineralisation. *Resource Geology*, 54, 253-280.
- HELGESON, H. C. & GARRELS, R. M. 1968. Hydrothermal transport and deposition of gold. *Economic Geology*, 63, 622-635.
- HENNEY, P., SYLES, M., BLAND, D. & WETTON, P. 1994. Characterization of gold from the Lubuk Mandi area. *Terengganu, Malaysia: British Geological Survey Technical Report WC/94/21*.

- HERRINGTON, R. J. & WILKINSON, J. J. 1993. Colloidal gold and silica in mesothermal vein systems. *Geology*, 21, 539-542.
- HODKIEWICZ, P., WEINBERG, R., GARDOLL, S. & GROVES, D. 2005. Complexity gradients in the Yilgarn Craton: fundamental controls on crustal-scale fluid flow and the formation of world-class orogenic-gold deposits. *Australian Journal of Earth Sciences*, 52, 831-841.
- HOUGH, R. M., BUTT, C. R. M., REDDY, S. M. & VERRALL, M. 2007. Gold nuggets: supergene or hypogene? *Australian Journal of Earth Sciences*, 54, 959-964.
- HOUGH, R. M., NOBLE, R. R. P., HITCHEN, G. J., HART, R., REDDY, S. M., SAUNDERS, M., CLODE, P., VAUGHAN, D., LOWE, J., GRAY, D. J., ANAND, R. R., BUTT, C. R. M. & VERRALL, M. 2008. Naturally occurring gold nanoparticles and nanoplates. *Geology*, 36, 571-574.
- HOUGH, R. M., BUTT, C. R. M. & FISCHER-BÜHNER, J. 2009. The Crystallography, Metallography and Composition of Gold. *Elements*, 5, 297-302.
- HRONSKY, J. M., GROVES, D. I., LOUCKS, R. R. & BEGG, G. C. 2012. A unified model for gold mineralisation in accretionary orogens and implications for regional-scale exploration targeting methods. *Mineralium Deposita*, 47, 339-358.
- HU, G., DAM-JOHANSEN, K., WEDEL, S. & HANSEN, J. P. 2006. Decomposition and oxidation of pyrite. *Progress in Energy and Combustion Science*, 32, 295-314.
- HU, S.-Y., EVANS, K., CRAW, D., REMPEL, K. & GRICE, K. 2016. Resolving the role of carbonaceous material in gold precipitation in metasediment-hosted orogenic gold deposits. *Geology*.
- HUGHES, M. J., PHILLIPS, G. N. & CAREY, S. P. 2004. Giant placers of the Victorian gold province. *Society of Economic Geologists Newsletter*, 1-18.
- HUMPHREYS, F. J. & HATHERLY, M. 2004a. Chapter 12 - Recrystallization Textures. In: HATHERLY, F. J. H. (ed.) *Recrystallization and Related Annealing Phenomena (Second Edition)*. Oxford: Elsevier.
- HUMPHREYS, F. J. & HATHERLY, M. 2004b. Chapter 9 - Recrystallization of Two-Phase Alloys. In: HATHERLY, F. J. H. (ed.) *Recrystallization and Related Annealing Phenomena (Second Edition)*. Oxford: Elsevier.
- HUMPHREYS, F. J. & HATHERLY, M. 2004c. Chapter 13 - Hot Deformation and Dynamic Restoration. In: HATHERLY, F. J. H. (ed.) *Recrystallization and Related Annealing Phenomena (Second Edition)*. Oxford: Elsevier.

- HUNT, P. A. & RODDICK, J. C. 1992. A compilation of K-Ar ages, report 21. *Radiogenic age and isotopic studies*. Geological Survey of Canada.
- HUSTON, D. L., BOTTRILL, R. S., CREELMAN, R. A., ZAW, K., RAMSDEN, T. R., RAND, S. W., GEMMELL, J. B., JABLONSKI, W., SIE, S. & LARGE, R. R. 1992. Geologic and geochemical controls on the mineralogy and grain size of gold-bearing phases, eastern Australian volcanic-hosted massive sulfide deposits. *Economic Geology*, 87, 542-563.
- JEAN, G. E. & BANCROFT, M. G. 1985. An XPS and SEM study of gold deposition at low temperatures on sulphide mineral surfaces: Concentration of gold by adsorption/reduction. *Geochimica et Cosmochimica Acta*, 49, 979-987.
- JEFFERSON, S. 2013. *A Refined Model for the Orogenic Hydrothermal System in the Eldorado*. Masters of Geology Masters University of Leeds.
- JENKIN, G. R. T., CRAW, D. & FALLICK, A. E. 1994. Stable isotopic and fluid inclusion evidence for meteoric fluid penetration into an active mountain belt; Alpine Schist, New Zealand. *Journal of Metamorphic Geology*, 12, 429-444.
- KERRICH, R. 1983. *Geochemistry of gold deposits in the Abitibi greenstone belt*, Canadian Institute of Mining and Metallurgy.
- KNIGHT, E., SCHNEIDER, D. & RYAN, J. 2013. Thermochronology of the Yukon-Tanana Terrane, West-Central Yukon: Evidence for Jurassic Extension and Exhumation in the Northern Canadian Cordillera. *The Journal of Geology*, 121, 371-400.
- KNIGHT, J. & MCTAGGART, K. 1986. The composition of placer and lode gold from the Fraser River drainage area, southwestern British Columbia. *Canadian Geology Journal of the CIM*, 1, 21-30.
- KNIGHT, J. B., MORTENSEN, J. K. & MORISON, S. 1994. *Shape and composition of lode and placer gold from the Klondike District, Yukon, Canada*, Indian and Northern Affairs Canada, Exploration and Geological Services Division, Yukon Region.
- KNIGHT, J. B., MORISON, S. & MORTENSEN, J. 1999a. The relationship between placer gold particle shape, rimming, and distance of fluvial transport as exemplified by gold from the Klondike District, Yukon Territory, Canada. *Economic Geology*, 94, 635-648.
- KNIGHT, J. B., MORTENSEN, J. K. & MORISON, S. R. 1999b. Lode and placer gold composition in the Klondike District, Yukon Territory, Canada; implications for the nature and genesis of Klondike placer and lode gold deposits. *Economic Geology*, 94, 649-664.
- KNIFE, S., FOSTER, R. & STANLEY, C. 1992. Role of sulphide surfaces in sorption of precious metals from hydrothermal fluids[site-specific

nucleation of gold on pyrite]. *Institution of Mining and Metallurgy Transactions. Section B. Applied Earth Science*, 101.

- KOGAN, V. V., HINDS, M. W. & RAMENDIK, G. I. 1994. The direct determination of trace metals in gold and silver materials by laser ablation inductively coupled plasma mass spectrometry without matrix matched standards. *Spectrochimica Acta Part B: Atomic Spectroscopy*, 49, 333-343.
- KRUPP, R. E. & SEWARD, T. M. 1990. Transport and deposition of metals in the Rotokawa geothermal system, New Zealand. *Mineralium Deposita*, 25, 73-81.
- KRUPP, R. E. & WEISER, T. 1992. On the stability of gold-silver alloys in the weathering environment. *Mineralium Deposita*, 27, 268-275.
- LANG, J. R. & BAKER, T. 2001. Intrusion-related gold systems: the present level of understanding. *Mineralium Deposita*, 36, 477-489.
- LANTSEV, I. P., NIKOLAEVA, L. A., BADALOVA, R. & DENIOSOVAM, L. K. Distribution of trace elements in native gold from different deposits. Tr. Trsent. Nauch. Issled. Gornorazvedd., 1971. 130-137.
- LARGE, R. R., BULL, S. W. & MASLENNIKOV, V. V. 2011. A carbonaceous sedimentary source-rock model for Carlin-type and orogenic gold deposits. *Economic Geology*, 106, 331-358.
- LARIZZATTI, J., OLIVEIRA, S. M. B. D. & BUTT, C. 2008. Morphology and composition of gold in a lateritic profile, Fazenda Pison "Garimpo", Amazon, Brazil. *Journal of South American Earth Sciences*, 25, 359-376.
- LEAKE, R., BLAND, D., STYLES, M. & CAMERON, D. 1991. Internal structure of Au-Pd-Pt grains from south Devon, England, in relation to low-temperature transport and deposition. *TRANSACTIONS OF THE INSTITUTION OF MINING AND METALLURGY SECTION B-APPLIED EARTH SCIENCE*, 100, B159-B178.
- LEAKE, R., CHAPMAN, R., BLAND, D., CONDLIFFE, E. & STYLES, M. 1997. Microchemical characterization of gold from Scotland: *Institution of Mining and Metallurgy Transactions*, v. 106, sec. B.
- LEBARGE, W. & COATES, J. 2007. Yukon Placer Database 2007-geology and mining activity of placer occurrences. *Yukon Geological Survey, CD-ROM*.
- LEHMANN, K., BERGER, A., GÖTTE, T., RAMSEYER, K. & WIEDENBECK, M. 2009. Growth related zonations in authigenic and hydrothermal quartz characterized by SIMS-, EPMA-, SEM-CL- and SEM-CC-imaging. *Mineralogical Magazine*, 73, 633-643.
- LINDGREN, W. 1933. Mineral deposits , 930 p. *New York and London, McGraw-HillBook Co.*

- LIVERSIDGE, A. 1897. CV.—The crystalline structure of gold and platinum nuggets and gold ingots. *Journal of the Chemical Society, Transactions*, 71, 1125-1131.
- LIVERTON, T. 2011. NI 43-101 Technical Report -Geology and Summary Report of the Lone Star Claim Group (Klondike Goldfield), Yukon Territory. Lonestar Gold Inc.
- LLOYD, G. E. 1987. Atomic number and crystallographic contrast images with the SEM: a review of backscattered electron techniques. *Mineralogical Magazine*, 51, 3-19.
- LOFTON, C. & SIGMUND, W. 2005. Mechanisms Controlling Crystal Habits of Gold and Silver Colloids. *Advanced Functional Materials*, 15, 1197-1208.
- LOWEY, G. & HILLS, L. 1988. Lithofacies, petrography and environments of deposition, Tantalus Formation (Lower Cretaceous) Indian River area, west-central Yukon. *Bulletin of Canadian Petroleum Geology*, 36, 296-310.
- LOWEY, G. W. 2006. The origin and evolution of the Klondike goldfields, Yukon, Canada. *Ore Geology Reviews*, 28, 431-450.
- LOWTHER, R. J., PEAKALL, J., CHAPMAN, R. J. & POUND, M. 2014. A four stage evolution of the White Channel gravel: Implications for stratigraphy and palaeoclimates. *Yukon Exploration & Geology*, 2013, pp. 109-118.
- MACKENZIE, D., CRAW, D., MORTENSEN, J. K. & LIVERTON, T. 2007a. Disseminated gold mineralization associated with orogenic veins in the Klondike Schist, Yukon. *Yukon Exploration and Geology*, 215-224.
- MACKENZIE, D., CRAW, D. & MORTENSEN, J. 2007b. Thrust slices and associated deformation in the Klondike goldfields, Yukon. *Yukon exploration and geology*, 199-213.
- MACKENZIE, D. J., CRAW, D. & MORTENSEN, J. 2008. Structural controls on orogenic gold mineralisation in the Klondike goldfield, Canada. *Mineralium Deposita*, 43, 435-448.
- MACKENZIE, D., CRAW, D., COOLEY, M. & FLEMING, A. 2010. Lithogeochemical localisation of disseminated gold in the White River area, Yukon, Canada. *Mineralium Deposita*, 45, 683-705.
- MACKENZIE, D., CRAW, D. & FINNIGAN, C. 2015. Lithologically controlled invisible gold, Yukon, Canada. *Mineralium Deposita*, 50, 141-157.
- MACLEAN, T. 1914. *Lode Mining in Yukon: Investigation of Quartz Deposits in the Klondike Division*, Ottawa, Government Printing Bureau.
- MANN, A. W. 1984. Mobility of gold and silver in lateritic weathering profiles; some observations from Western Australia. *Economic Geology*, 79, 38-49.

- MANN, D. H., GROVES, P., REANIER, R. E., GAGLIOTI, B. V., KUNZ, M. L. & SHAPIRO, B. 2015. Life and extinction of megafauna in the ice-age Arctic. *Proceedings of the National Academy of Sciences*, 112, 14301-14306.
- MAUTHNER, M. 2004. Morphology of Gold Crystals from the Yukon Territory, Canada. *Rocks & Minerals*, 79, 100-109.
- MCCONNELL, R. G. 1907. *Report on gold values in the Klondike high level gravels*, Government printing bureau.
- MCCREADY, A. J., PARNELL, J. & CASTRO, L. 2003. Crystalline Placer Gold from the Rio Neuquén, Argentina: Implications for the Gold Budget in Placer Gold Formation. *Economic Geology*, 98, 623-633.
- MCCUAIG, C. T. & KERRICH, R. 1998. P—T—t—deformation—fluid characteristics of lode gold deposits: evidence from alteration systematics. *Ore Geology Reviews*, 12, 381-453.
- MCINNES, M., GREENOUGH, J. D., FRYER, B. J. & WELLS, R. 2008. Trace elements in native gold by solution ICP-MS and their use in mineral exploration: A British Columbia example. *Applied Geochemistry*, 23, 1076-1085.
- MEFFRE, S., LARGE, R. R., STEADMAN, J. A., GREGORY, D. D., STEPANOV, A. S., KAMENETSKY, V. S., EHRIG, K. & SCOTT, R. J. 2016. Multi-stage enrichment processes for large gold-bearing ore deposits. *Ore Geology Reviews*, 76, 268-279.
- MEYER, C. 1988. Ore deposits as guides to geologic history of the Earth. *Annual Review of Earth and Planetary Sciences*, 16, 147-171.
- MIKUCKI, E. J. & RIDLEY, J. R. 1993. The hydrothermal fluid of Archæan lode-gold deposits at different metamorphic grades: compositional constraints from ore and wallrock alteration assemblages. *Mineralium Deposita*, 28, 469-481.
- MIKUCKI, E. J. 1998. Hydrothermal transport and depositional processes in Archean lode-gold systems: A review. *Ore Geology Reviews*, 13, 307-321.
- MINFILE, Y. 2015. Yukon MINFILE—A database of mineral occurrences: Yukon Geological Survey.
- MÖLLER, P. & KERSTEN, G. 1994. Electrochemical accumulation of visible gold on pyrite and arsenopyrite surfaces. *Mineralium Deposita*, 29, 404-413.
- MONCADA, D., MUTCHLER, S., NIETO, A., REYNOLDS, T. J., RIMSTIDT, J. D. & BODNAR, R. J. 2012. Mineral textures and fluid inclusion petrography of the epithermal Ag–Au deposits at Guanajuato, Mexico: Application to exploration. *Journal of Geochemical Exploration*, 114, 20-35.

- MONGER, J. W. H., PRICE, R. A. & TEMPELMAN-KLUIT, D. J. 1982. Tectonic accretion and the origin of the two major metamorphic and plutonic belts in the Canadian Cordillera. *Geology*, 10, 70-75.
- MORRISON, G. W., ROSE, W. J. & JAIRETH, S. 1991. Geological and geochemical controls on the silver content (fineness) of gold in gold-silver deposits. *Ore Geology Reviews*, 6, 333-364.
- MORTENSEN, J. 1990. Geology and U-Pb geochronology of the Klondike District, west-central Yukon Territory. *Canadian Journal of Earth Sciences*, 27, 903-914.
- MORTENSEN, J. K. 1996. *Geological compilation maps of the northern Stewart River map area, Klondike and Sixtymile Districts (115N/15, 16; 1150/13, 14; and parts of 1150/15, 16)*. Exploration and Geological Services Division, Yukon Region, Indian and Northern Affairs Canada.
- MORTENSEN, J. K., DUSEL-BACON, C., HUNT, J. & GABITES, J. 2006. Lead isotopic constraints on the metallogeny of middle and late Paleozoic syngenetic base metal occurrences in the Yukon-Tanana and Slide Mountain/Seventymile terranes and adjacent portions of the North American miogeocline. *Paleozoic evolution and metallogeny of pericratonic terranes at the ancient Pacific margin of North America, Canadian and Alaskan Cordillera*. Edited by M. Colpron and JL Nelson. *Geological Association of Canada, Special Paper*, 45, 261-279.
- MORTENSEN, J. K., MACKENZIE, D. & CRAW, D. 2007. Regional Geological and Related Studies of the Klondike Gold District. *Klondike Star Internal Report*.
- MORTENSEN, J. K. 2011. Lithogeochemical studies of Gold-Bearing Felsic Shist Units in the Boulder Lode Area, Lone Star Ridge. *Report prepared for Lonestar Gold, Inc.* .
- MORTENSEN, J. K. Klondike District Field Trip Guidebook, . Dawson Rocks Field Conference, 2013.
- MURPHY, D. C., MORTENSEN, J. K., PIERCEY, S. J., ORCHARD, M. J. & GEHRELS, G. E. 2006. Mid-Paleozoic to early Mesozoic tectonostratigraphic evolution of Yukon-Tanana and Slide Mountain terranes and affiliated overlap assemblages, Finlayson Lake massive sulphide district, southeastern Yukon. *Paleozoic evolution and metallogeny of pericratonic terranes at the ancient Pacific margin of North America, Canadian and Alaskan Cordillera: Geological Association of Canada Special Paper*, 45, 75-105.
- NADEN, J., STYLES, M. & HENNEY, P. 1994. Characterisation of gold from Zimbabwe: part 1. bedrock gold. *British Geological Survey Technical Report WC/94/51*.

- NELSON, D. A. 2007. Klondike Star Mineral Corporation Bulk Sampling Program. 2.2.94 (*Internal report*)
- NELSON, J. & MIHALYNUK, M. 1993. Cache Creek ocean: Closure or enclosure? *Geology*, 21, 173-176.
- NELSON, J. L. & COLPRON, M. 2007. Tectonics and metallogeny of the British Columbia, Yukon and Alaskan Cordillera, 1.8 Ga to the present. *Mineral deposits of Canada: a synthesis of major deposit-types, district metallogeny, the evolution of geological provinces, and exploration methods: Geological Association of Canada, Mineral Deposits Division, Special Publication*, 5, 755-791.
- NELSON, J. L., COLPRON, M. & ISRAEL, S. 2013. The Cordillera of British Columbia, Yukon, and Alaska: Tectonics and Metallogeny. *Society of Economic Geology, Special Publication*, 53-109.
- NESBITT, B. E. 1988. Gold deposit continuum: A genetic model for lode Au mineralization in the continental crust. *Geology*, 16, 1044-1048.
- NESBITT, B. E., MUEHLENBACHS, K. & MUROWCHICK, J. B. 1989. Genetic implications of stable isotope characteristics of mesothermal Au deposits and related Sb and Hg deposits in the Canadian Cordillera. *Economic Geology*, 84, 1489-1506.
- NESBITT, H. W. & MARKOVICS, G. 1980. Chemical processes affecting alkalis and alkaline earths during continental weathering. *Geochimica et Cosmochimica Acta*, 44, 1659-1666.
- NIXON, G., CABRI, L., LAFLAMME, G., SYLVESTER, P. & TUBRETT, M. 2004. Platinum group elements in alkali Cu-Au porphyries. British Columbia Geological Survey. *Geofile*, 2004-2006.
- OGRYZLO, S. P. 1935. Hydrothermal experiments with gold. *Economic Geology*, 30, 400-424.
- OTT, D. & SCHINDLER, U. 2001. Metallography of gold and gold alloys. *Gold Technology*, 33, 6-11.
- OUTRIDGE, P. M., DOHERTY, W. & GREGOIRE, D. C. 1998. Determination of trace elemental signatures in placer gold by laser ablation-inductively coupled plasma-mass spectrometry as a potential aid for gold exploration. *Journal of Geochemical Exploration*, 60, 229-240.
- PALACIOS, C., HÉRAIL, G., TOWNLEY, B., MAKSAEV, V., SEPÚLVEDA, F., DE PARSEVAL, P., RIVAS, P., LAHSEN, A. & PARADA, M. A. 2001. The composition of gold in the Cerro Casale gold-rich porphyry deposit, Maricunga belt, northern Chile. *The Canadian Mineralogist*, 39, 907-915.
- PARNELL, J., EARLS, G., WILKINSON, J. J., HUTTON, D. H. W., BOYCE, A. J., FALLICK, A. E., ELLAM, R. M., GLEESON, S. A., MOLES, N. R., CAREY, P.

- F., LEGG, I. & CAREY, P. F. 2000. Regional Fluid Flow and Gold Mineralization in the Dalradian of the Sperrin Mountains, Northern Ireland. *Economic Geology*, 95, 1389-1416.
- PEARCE, M. A., WHITE, A. J. R., FISHER, L. A., HOUGH, R. M. & CLEVERLEY, J. S. 2015. Gold deposition caused by carbonation of biotite during late-stage fluid flow. *Lithos*, 239, 114-127.
- PEARSON, R. G. 1963. Hard and Soft Acids and Bases. *Journal of the American Chemical Society*, 85, 3533-3539.
- PETROVSKAYA, N. & FASTLOVICHH, A. 1955. *Changes in inner structure of native gold buried in palcers.*
- PHILLIPS, G. N. 1993. Metamorphic fluids and gold. *MINERALOGICAL MAGAZINE-LONDON*-, 57, 365-365.
- PHILLIPS, G. N. & POWELL, R. 2010. Formation of gold deposits: a metamorphic devolatilization model. *Journal of Metamorphic Geology*, 28, 689-718.
- PHILLIPS, G. N. & POWELL, R. 2015. A practical classification of gold deposits, with a theoretical basis. *Ore Geology Reviews*, 65, Part 3, 568-573.
- PIERCEY, S. J. & COLPRON, M. 2009. Composition and provenance of the Snowcap assemblage, basement to the Yukon-Tanana terrane, northern Cordillera: Implications for Cordilleran crustal growth. *Geosphere*, 5, 439-464.
- PITCAIRN, I. K., TEAGLE, D. A. H., CRAW, D., OLIVO, G. R., KERRICH, R. & BREWER, T. S. 2006. Sources of Metals and Fluids in Orogenic Gold Deposits: Insights from the Otago and Alpine Schists, New Zealand. *Economic Geology*, 101, 1525-1546.
- PLINT, H. E. & GORDON, T. M. 1997. The Slide Mountain Terrane and the structural evolution of the Finlayson Lake Fault Zone, southeastern Yukon. *Canadian Journal of Earth Sciences*, 34, 105.
- POKROVSKI, G. S., AKINFIEV, N. N., BORISOVA, A. Y., ZOTOV, A. V. & KOUZMANOV, K. 2014. Gold speciation and transport in geological fluids: insights from experiments and physical-chemical modelling. *Geological Society, London, Special Publications*, 402.
- POTTER, M. & STYLES, M. 2003. Gold characterisation as a guide to bedrock sources for the Estero Hondo alluvial gold mine, western Ecuador. *Applied Earth Science*, 112, 297-304.
- POUND, M. J., LOWTHER, R. I., PEAKALL, J., CHAPMAN, R. J. & SALZMANN, U. 2015. Palynological evidence for a warmer boreal climate in the Late Pliocene of the Yukon Territory, Canada. *Palynology*, 39, 91-102.
- PRIOR, D. J., BOYLE, A. P., BRENKER, F., CHEADLE, M. C., DAY, A., LOPEZ, G., PERUZZO, L., POTTS, G. J., REDDY, S. & SPIESS, R. 1999. The application

- of electron backscatter diffraction and orientation contrast imaging in the SEM to textural problems in rocks. *American Mineralogist*, 84, 1741-1759.
- PRIOR, D. J., MARIANI, E. & WHEELER, J. 2009. EBSD in the earth sciences: applications, common practice, and challenges. *Electron backscatter diffraction in materials science*. Springer.
- REA, M. A., ZAMMIT, C. M. & REITH, F. 2016. Bacterial biofilms on gold grains—implications for geomicrobial transformations of gold. *FEMS microbiology ecology*, 92, fiw082.
- REITH, F., FAIRBROTHER, L., NOLZE, G., WILHELMI, O., CLODE, P. L., GREGG, A., PARSONS, J. E., WAKELIN, S. A., PRING, A., HOUGH, R., SOUTHAM, G. & BRUGGER, J. 2010. Nanoparticle factories: Biofilms hold the key to gold dispersion and nugget formation. *Geology*, 38, 843-846.
- REITH, F., BRUGGER, J., ZAMMIT, C., NIES, D. & SOUTHAM, G. 2013. Geobiological Cycling of Gold: From Fundamental Process Understanding to Exploration Solutions. *Minerals*, 3, 367.
- RICE, C. M., MARK, D. F., SELBY, D., NEILSON, J. E. & DAVIDHEISER-KROLL, B. 2016. Age and Geologic Setting of Quartz Vein-Hosted Gold Mineralization at Curraghinalt, Northern Ireland: Implications for Genesis and Classification. *Economic Geology*, 111, 127-150.
- RIDLEY, J. R. & DIAMOND, L. W. Fluid chemistry of orogenic lode gold deposits and implications for genetic models. *Gold in, 2000*. 141-162.
- RUBIN, J. N. & KYLE, J. R. 1997. Precious metal mineralogy in porphyry-, skarn-, and replacement-type ore deposits of the Ertsberg (Gunung Bijih) District, Irian Jaya, Indonesia. *Economic Geology*, 92, 535-550.
- RUSHTON, R. W., NESBITT, B. E., MUEHLENBACHS, K. & MORTENSEN, J. K. 1993. A fluid inclusion and stable isotope study of Au quartz veins in the Klondike District, Yukon Territory, Canada; a section through a mesothermal vein system. *Economic Geology*, 88, 647-678.
- RUSK, B., KOENIG, A. & LOWERS, H. 2011. Visualizing trace element distribution in quartz using cathodoluminescence, electron microprobe, and laser ablation-inductively coupled plasma-mass spectrometry. *American Mineralogist*, 96, 703-708.
- RUSK, B. 2012. Cathodoluminescent textures and trace elements in hydrothermal quartz. *Quartz: Deposits, Mineralogy and Analytics*. Springer.
- RUSK, B. G., LOWERS, H. A. & REED, M. H. 2008. Trace elements in hydrothermal quartz: Relationships to cathodoluminescent textures and insights into vein formation. *Geology*, 36, 547-550.

- SAHOO, P. R. & VENKATESH, A. S. 2015. Constraints of mineralogical characterization of gold ore: Implication for genesis, controls and evolution of gold from Kundarkocha gold deposit, eastern India. *Journal of Asian Earth Sciences*, 97, Part A, 136-149.
- SANDER, M. V. & BLACK, J. E. 1988. Crystallization and recrystallization of growth-zoned vein quartz crystals from epithermal systems; implications for fluid inclusion studies. *Economic Geology*, 83, 1052-1060.
- SAUNDERS, J. A. 1990. Colloidal transport of gold and silica in epithermal precious-metal systems: Evidence from the Sleeper deposit, Nevada. *Geology*, 18, 757-760.
- SEYEDOLALI, A., KRINSLEY, D. H., BOGGS, S., O'HARA, P. F., DYPVIK, H. & GOLES, G. G. 1997. Provenance interpretation of quartz by scanning electron microscope–cathodoluminescence fabric analysis. *Geology*, 25, 787-790.
- SIBSON, R. H., ROBERT, F. & POULSEN, K. H. 1988. High-angle reverse faults, fluid-pressure cycling, and mesothermal gold-quartz deposits. *Geology*, 16, 551-555.
- SIE, S. H., MURAO, S. & SUTER, G. F. 1996. Trace element distribution in native gold. *Nuclear Instruments and Methods in Physics Research Section B: Beam Interactions with Materials and Atoms*, 109–110, 633-638.
- SIMARD, R.-L., DOSTAL, J. & ROOTS, C. F. 2003. Development of late Paleozoic volcanic arcs in the Canadian Cordillera: an example from the Klinkit Group, northern British Columbia and southern Yukon. *Canadian Journal of Earth Sciences*, 40, 907-924.
- SIMMONS, S. F., WHITE, N. C. & JOHN, D. A. 2005. Geological characteristics of epithermal precious and base metal deposits. *Economic Geology 100th anniversary volume*, 29, 485-522.
- SPEAR, F. S. & WARK, D. A. 2009. Cathodoluminescence imaging and titanium thermometry in metamorphic quartz. *Journal of Metamorphic Geology*, 27, 187-205.
- SPRUNT, E. S., DENGLER, L. A. & SLOAN, D. 1978. Effects of metamorphism on quartz cathodoluminescence. *Geology*, 6, 305-308.
- STAPLES, R. D., GIBSON, H. D., COLPRON, M. & RYAN, J. J. 2016. An orogenic wedge model for diachronous deformation, metamorphism, and exhumation in the hinterland of the northern Canadian Cordillera. *Lithosphere*, 8, 165-184.
- STARLING, A., GILLIGAN, J. M., CARTER, A. H. C., FOSTER, R. P. & SAUNDERS, R. A. 1989. High-temperature hydrothermal precipitation of precious metals on the surface of pyrite. *Nature*, 340, 298-300.

- STEFÁNSSON, A. & SEWARD, T. M. 2004. Gold(I) complexing in aqueous sulphide solutions to 500°C at 500 bar. *Geochimica et Cosmochimica Acta*, 68, 4121-4143.
- STOFFREGEN, R. 1986. Observations on the behavior of gold during supergene oxidation at Summitville, Colorado, USA, and implications for electrum stability in the weathering environment. *Applied Geochemistry*, 1, 549-558.
- STUMPFL, E. & CLARK, A. 1965. Electron-probe microanalysis of gold-platinoid concentrates from southeast Borneo. *Transactions of the Institution of Mining and Metallurgy*, 74, 933-946.
- SUNAGAWA, I. 1981. Characteristics of crystal-growth in nature as seen from the morphology of mineral crystals. *Bulletin de minéralogie*, 104, 81-87.
- TAFTI, R. & MORTENSEN, J. K. 2003. Early Jurassic porphyry (?) copper (-gold) deposits at Minto and Williams Creek, Carmacks copper belt, western Yukon. *Yukon exploration and geology*, 289-303.
- TALLMAN, P. 2015. *Klondike Gold Reports Remaining 2015 Drill Results; Intersects 75.6 g/t Au over 2.8m at Gay Gulch* [Online]. <http://www.klondikegoldcorp.com>.
- TEMPELMAN-KLUIT, D. J. 1980. Evolution of physiography and drainage in southern Yukon. *Canadian Journal of Earth Sciences*, 17, 1189-1203.
- THOMAS, H. V., LARGE, R. R., BULL, S. W., MASLENNIKOV, V., BERRY, R. F., FRASER, R., FROUD, S. & MOYE, R. 2011. Pyrite and Pyrrhotite Textures and Composition in Sediments, Laminated Quartz Veins, and Reefs at Bendigo Gold Mine, Australia: Insights for Ore Genesis. *Economic Geology*, 106, 1-31.
- TOM, E. M., MARK, E. B. & JOAQUIN, R. 1997. Trace Element Analysis of Natural Gold by Laser Ablation ICP-MS: A Combined External/Internal Standardisation Approach. *Geostandards Newsletter*, 21, 271-278.
- TOMKINS, A. G. 2013a. A Biogeochemical Influence on the Secular Distribution of Orogenic Gold. *Economic Geology*, 108, 193-197.
- TOMKINS, A. G. 2013b. On the source of orogenic gold. *Geology*, 41, 1255-1256.
- TOWNLEY, B. K., HÉRAIL, G., MAKSAEV, V., PALACIOS, C., DE PARSEVAL, P., SEPULVEDA, F., ORELLANA, R., RIVAS, P. & ULLOA, C. 2003. Gold grain morphology and composition as an exploration tool: application to gold exploration in covered areas. *Geochemistry: Exploration, environment, analysis*, 3, 29-38.
- TYRRELL, J. B. 1907. Concentration of gold in the Klondike. *Economic Geology*, 2, 343-349.

- VELASQUEZ, A. 2006. Trace element analysis of native gold by laser ablation ICP-MS: A case study in greenstone-hosted quartz-carbonate vein ore deposits, Timmins, Ontario.
- VIKENTYEV, I. V. 2015. Invisible and microscopic gold in pyrite: Methods and new data for massive sulfide ores of the Urals. *Geology of Ore Deposits*, 57, 237-265.
- WARK, D. A. & WATSON, E. B. 2006. TitaniQ: a titanium-in-quartz geothermometer. *Contributions to Mineralogy and Petrology*, 152, 743-754.
- WATLING, R. J., HERBERT, H. K., DELEV, D. & ABELL, I. D. 1994. Gold fingerprinting by laser ablation inductively coupled plasma mass spectrometry. *Spectrochimica Acta Part B: Atomic Spectroscopy*, 49, 205-219.
- WEATHERLEY, D. K. & HENLEY, R. W. 2013. Flash vaporization during earthquakes evidenced by gold deposits. *Nature Geosci*, 6, 294-298.
- WEBSTER, J. & MANN, A. 1984. The influence of climate, geomorphology and primary geology on the supergene migration of gold and silver. *Journal of Geochemical Exploration*, 22, 21-42.
- WEINIG, A. J. 1960. Gold forms in ore. *Mines Magazine*.
- WESTGATE, J., SANDHU, A., PREECE, S. & FROESE, D. 2002. Age of the gold-bearing White Channel gravel, Klondike district, Yukon. *Yukon exploration and geology*, 241-250.
- WILKINSON, J. J., BOYCE, A. J., EARLS, G. & FALLICK, A. E. 1999. Gold remobilization by low-temperature brines; evidence from the Curraghinalt gold deposit, Northern Ireland. *Economic Geology*, 94, 289-296.
- WILLIAMS-JONES, A. E., BOWELL, R. J. & MIGDISOV, A. A. 2009. Gold in Solution. *Elements*, 5, 281-287.
- WILSON, C. J. L., SCHAUBS, P. M. & LEADER, L. D. 2013. Mineral Precipitation in the Quartz Reefs of the Bendigo Gold Deposit, Victoria, Australia. *Economic Geology*, 108, 259-278.
- WINCHESTER, J. & FLOYD, P. 1977. Geochemical discrimination of different magma series and their differentiation products using immobile elements. *Chemical geology*, 20, 325-343.
- WOLFF, G. W. R. 2012. *Microstructures and Trace Element Signatures of Orogenic Quartz Veins in the Klondike District, Yukon Territory, Canada*. BSc (Hons), University of British Columbia.
- WRIGHTON, T. 2013. *Placer Gold Microchemical Characterization And Shape Analysis Applied As An Exploration Tool In Western Yukon*. Masters of Science, University of British Columbia.

- WYMAN, D., HOLLINGS, P. & CASSIDY, K. 2015a. Tribute to Rob Kerrich. *Lithos*, 233, 1.
- WYMAN, D. A., HOLLINGS, P. & CONCEIÇÃO, R. V. 2015b. Geochemistry and radiogenic isotope characteristics of xenoliths in Archean diamondiferous lamprophyres: Implications for the Superior Province cratonic keel. *Lithos*, 233, 111-130.
- WYMAN, D. A., CASSIDY, K. F. & HOLLINGS, P. 2016. Orogenic gold and the mineral systems approach: Resolving fact, fiction and fantasy. *Ore Geology Reviews*, 78, 322-335.
- YANG, L.-Q., DENG, J., WANG, Z.-L., GUO, L.-N., LI, R.-H., GROVES, D. I., DANYUSHEVSKY, L. V., ZHANG, C., ZHENG, X.-L. & ZHAO, H. 2016. Relationships Between Gold and Pyrite at the Xincheng Gold Deposit, Jiaodong Peninsula, China: Implications for Gold Source and Deposition in a Brittle Epizonal Environment. *Economic Geology*, 111, 105-126.
- YARDLEY, B. W. & CLEVERLEY, J. S. 2013. The role of metamorphic fluids in the formation of ore deposits. *Geological Society, London, Special Publications*, 393, SP393. 5.
- YARDLEY, B. W. D., BANKS, D. A., BOTTRELL, S. H. & DIAMOND, L. 1993. Post-metamorphic gold-quartz veins from NW Italy: the composition and origin of the ore fluid. *Mineralogical Magazine*, 57, 407-422.
- YOUNGSON, J. H. & CRAW, D. 1999. Variation in placer style, gold morphology, and gold particle behavior down gravel bed-load rivers; an example from the Shotover/Arrow-Kawarau-Clutha River system, Otago, New Zealand. *Economic Geology*, 94, 615-633.
- ZHONG, R., BRUGGER, J., TOMKINS, A. G., CHEN, Y. & LI, W. 2015. Fate of gold and base metals during metamorphic devolatilization of a pelite. *Geochimica et Cosmochimica Acta*, 171, 338-352.

Appendix A

A.1 Table of samples and specimens

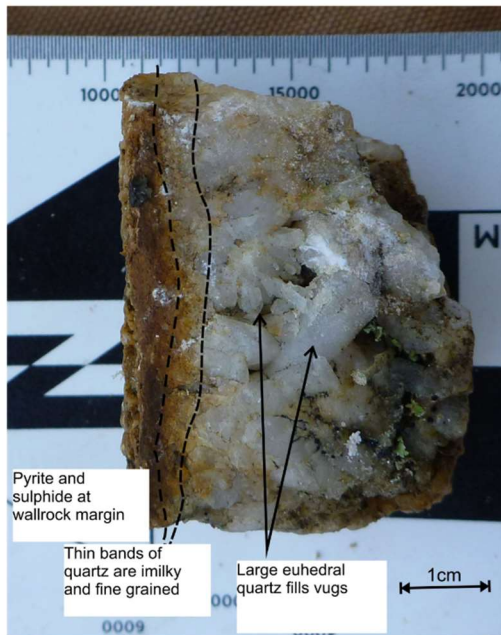
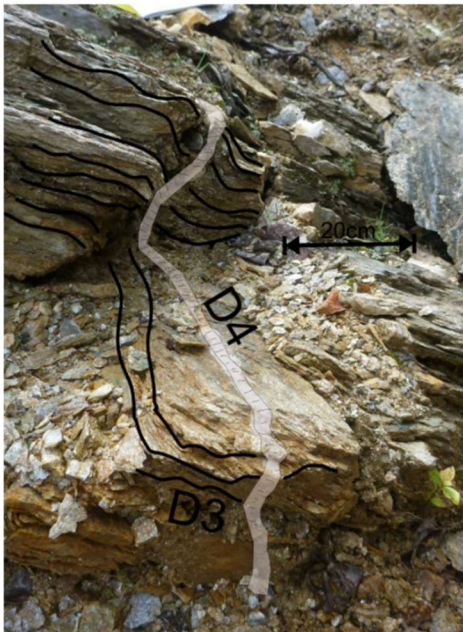
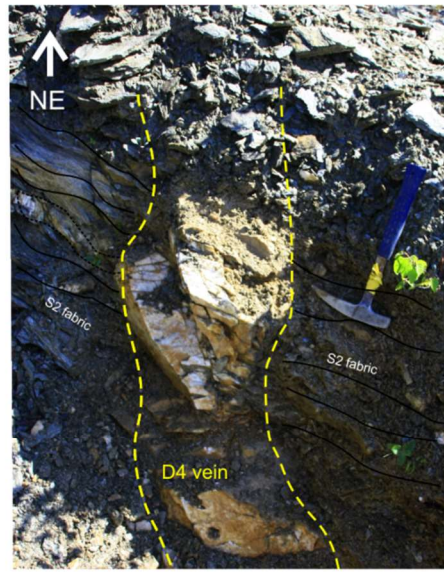
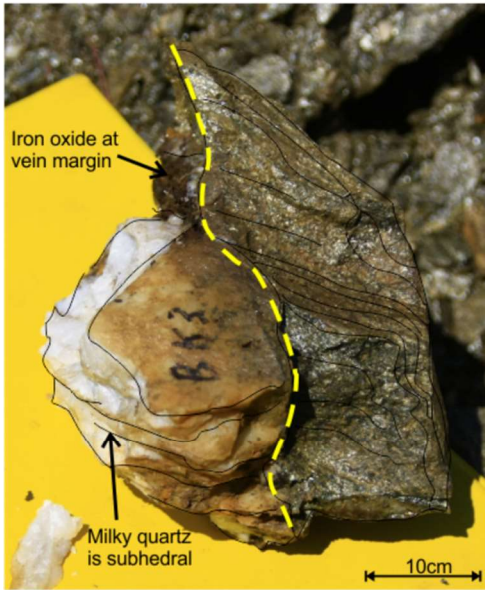
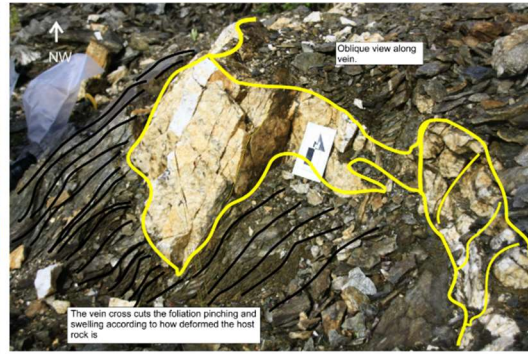
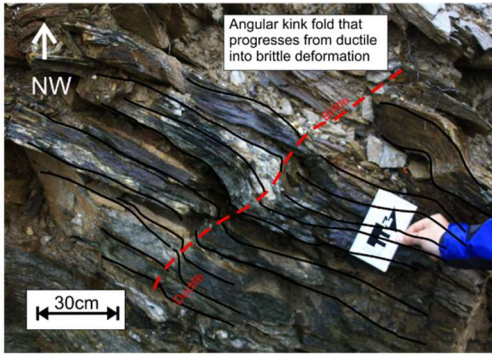
Table 11-1: A summary of all samples and specimens prepared during this research. PB- polished block, PTS- polished thin section, DPW- double polished wafer, CL- cathodoluminescence, EDS- electron dispersive spectroscopy, LA- laser ablation, EPMA- electron probe micro analyser, XRF- X ray fluorescence, EBSD- electron backscatter diffraction.

Location	Sample Number	Grid Reference	Description	Specimens	Type	Analysis
Dysle Zone	14D3	583931 7085562	Visible gold found in vug of quartz	MG23	PB	
	14D4	583931 7085562	Large euhedral galena in the centre of quartz	MG33	PB	CL, EDS, LA
	14D7	583944 7085554	Gold within oxidised pyrite proximal to the wallrock	MG21	PB	CL, EDS, EPMA
	14D8	583933 7085560		MG1	Chip	
	14D9	583912 7085573	Quartz vein cross cutting host rock. Small euhedral quartz	MG12	PTS	CL, EDS, FIA
				MG15	PTS	CL, EDS
15D01		Bladed quartz textures	MG60	DPW	CL, EDS, FIA	
Gay Gulch Vein	14GG8	585243 7084142	Euhedral quartz grain	MG4	PTS	Pet
Violet Mine	14V13	584644 7082095		MG5	Chip	
	14V12	584644 7082095	Pyrite rich part of a vein where pegmatite cross cuts quartz	MG36	PTS	

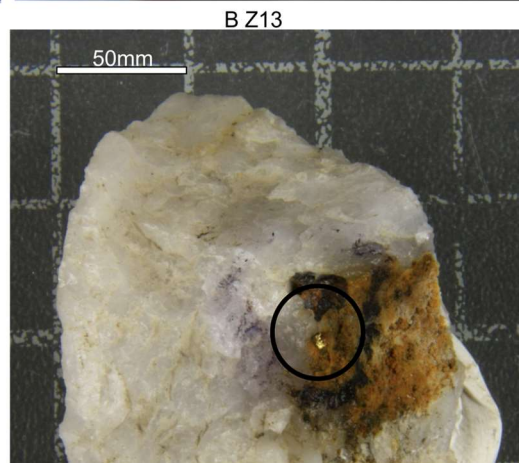
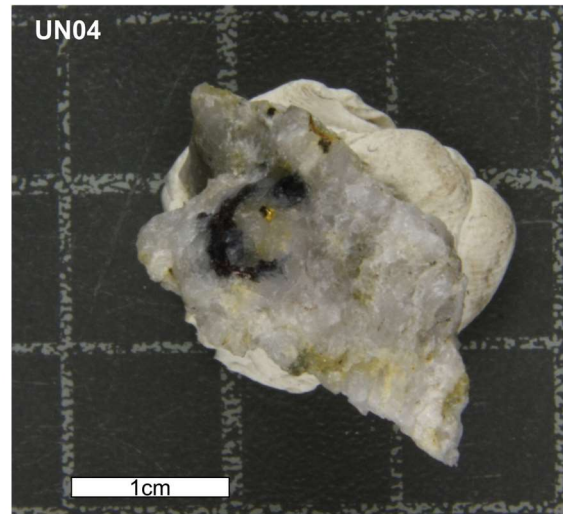
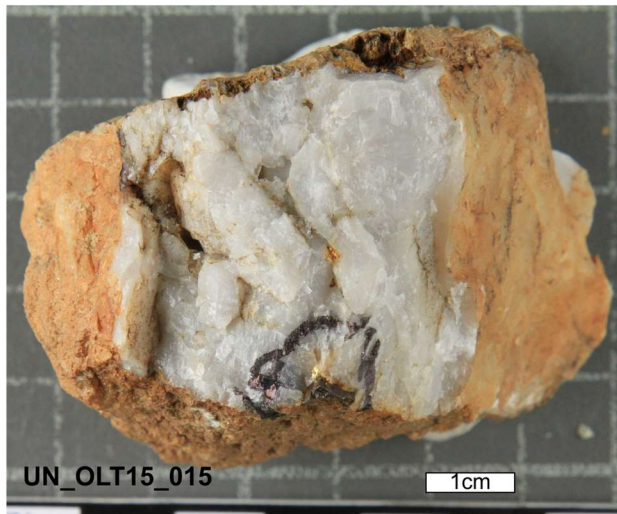
Location	Sample Number	Grid Reference	Description	Specimens	Type	Analysis
Nugget Zone	14UN6	584974 7085674	Sampled from in situ vein that cross cuts an earlier D3 metamorphic quartz vein	MG6	PTS	CL, EDS
	14UN3	584977 7085678	Large visible gold in quartz proximal to the wallrock	MG22	PB	CL, EDS, EPMA
	14UN11	584990 7085674	Sample displays well developed crenulation with multiple generations of quartz growth.	MG14	Chip	
				MG38	PTS	
	14UN8	585021 7085655	Gold in quartz but is a cluster of small particles	MG16	DPW	CL, FIA, EDS
				MG29	PB	RL, EDS, EPMA
	14UN13	584990 7085674	Large particle of gold on pyrite at edge of vein proximal to wallrock	MG17	DPW	CL, FIA, EDS
				MG27	PB	RL, EDS, EPMA
	14UN5	584974 7085674	Gold grain at wallrock margin which is pyrite rich	MG39	PTS	CL, EDS
	15UN01	584977 7085678	Bladed quartz texture	MG61b	DPW	CL, FIA, EDS
OLT15_15	584798 7085578	Gold in pyrite found in quartz	MG53	PB	CL, EPMA, FIA, EDS	
			MG64	DPW	CL, EPMA, FIA	
Nugget Zone	14LN7	584784 7085558	Small piece of visible gold on quartz proximal to the margin	MG25	PB	EDS, EPMA
	14LN6	584782 7085548	Sample of vein with milky quartz and large euhedral calcite in the centre	MG30	PTS	EDS, XRF
Buckland Zone	14BZ10	585626 7084826	Large euhedral pyrite oxidised to limonite. Gold is within the pyrite and proximal to vein margin	MG18	DPW	FIA
				MG28	PB	CL, EDS, EPMA
	14BZ18	585624 7084837	Large piece of euhedral calcite	MG37	Chip	
	14BZ17	585624 7084837	Large gold grain at the wallrock contact. Margin of vein not sharp and rafts of rock can be found within quartz	MG26	PB	EDS, EPMA

Location	Sample Number	Grid Reference	Description	Specimens	Type	Analysis
	BZ16	585624 7084819	Gold grain at vein margin within euhedral pyrite that is oxidised	MG20	PB	EDS, EPMA
	BZ7	585619 7084849	Fibrous quartz grain with gold hosted within euhedral pyrite	MG24	PB	CL, EDS, EPMA
	OLT15_024	585631 7084819	Gold in quartz	MG51	PB	EDS, EPMA
	OLT15_26	585623 7084823	Gold in quartz	MG50	PB	CL, RL, SEM, EPMA
	OLT15_27	585626 7084829	Gold is FREE and in quartz	MG54	PB	CL, EPMA, EDS
	OLT15_29	585970 7084736	Gold in pyrite in quartz	MG52	PB	CL, EPMA, EDS
Boulder Lode Mine	15LS01	587008 7086173	A large crystal of clear quartz found in pit	MG66	DPW	CL, EDS, FIA
Drill core	05LS09		Gold in core 36.76m-76.46m	MG55	PB	EDS,EPMA
	05LS16		Gold in core 73.15m	MG56	PB	EDS,EPMA, CL
	EC15_10		Gold in vein from core 25m	MG57	PB	CL, EPMA, EDS
	05LS02		59.00-59.50M Gold in section	MG7	PTS	EDS
				MG8	PTS	EDS, EPMA, XRF
				MG9	PTS	EDS
				MG10	PTS	EDS, EPMA, XRF
	05LS27		Depth of 69-70M 129,130	MG45	PTS	EDS, EPMA, XRF
			TS 131,132	MG46	PTS	EDS, EPMA,XRF
12LS03	587505 7085896	K186 Sulphide lenses within schist	MG44	PTS	EDS	

A.2 Field samples



A.3 Visible gold in hand specimen

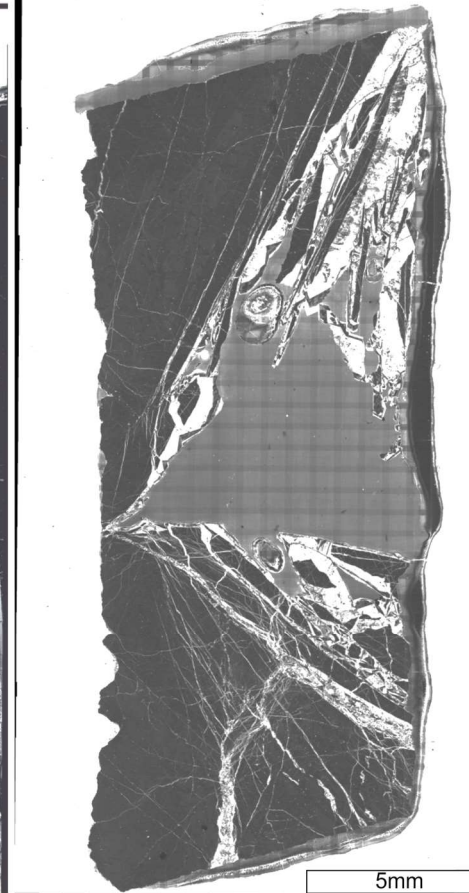


A.4 Cathodoluminescence montage of thin sections

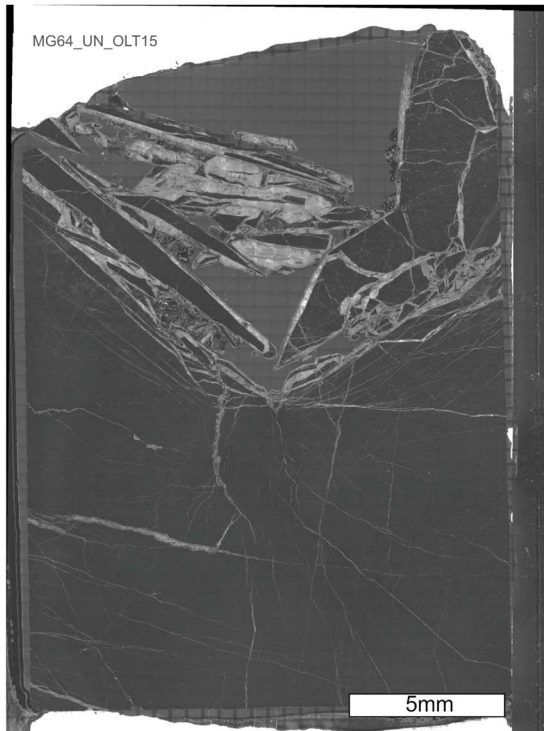
MG 60 15D01



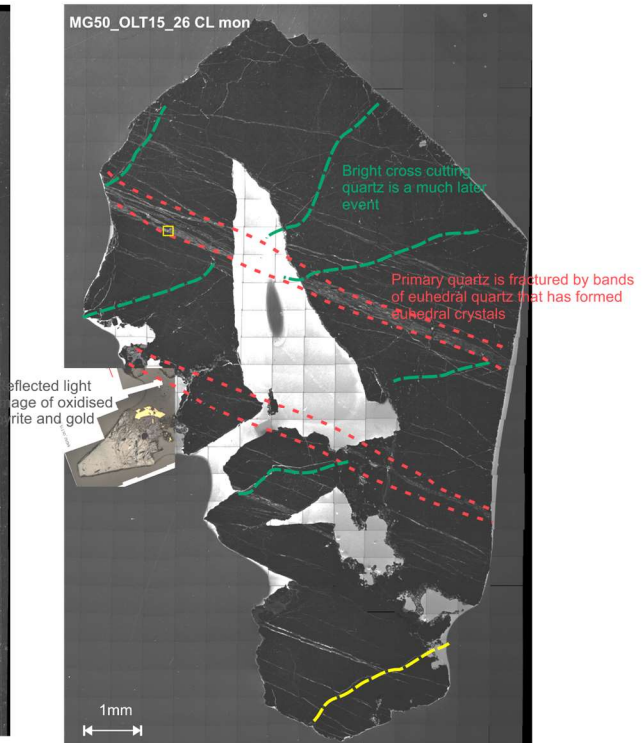
MG 61 15UN01



MG64_UN_OLT15



MG50_OLT15_26 CL mon

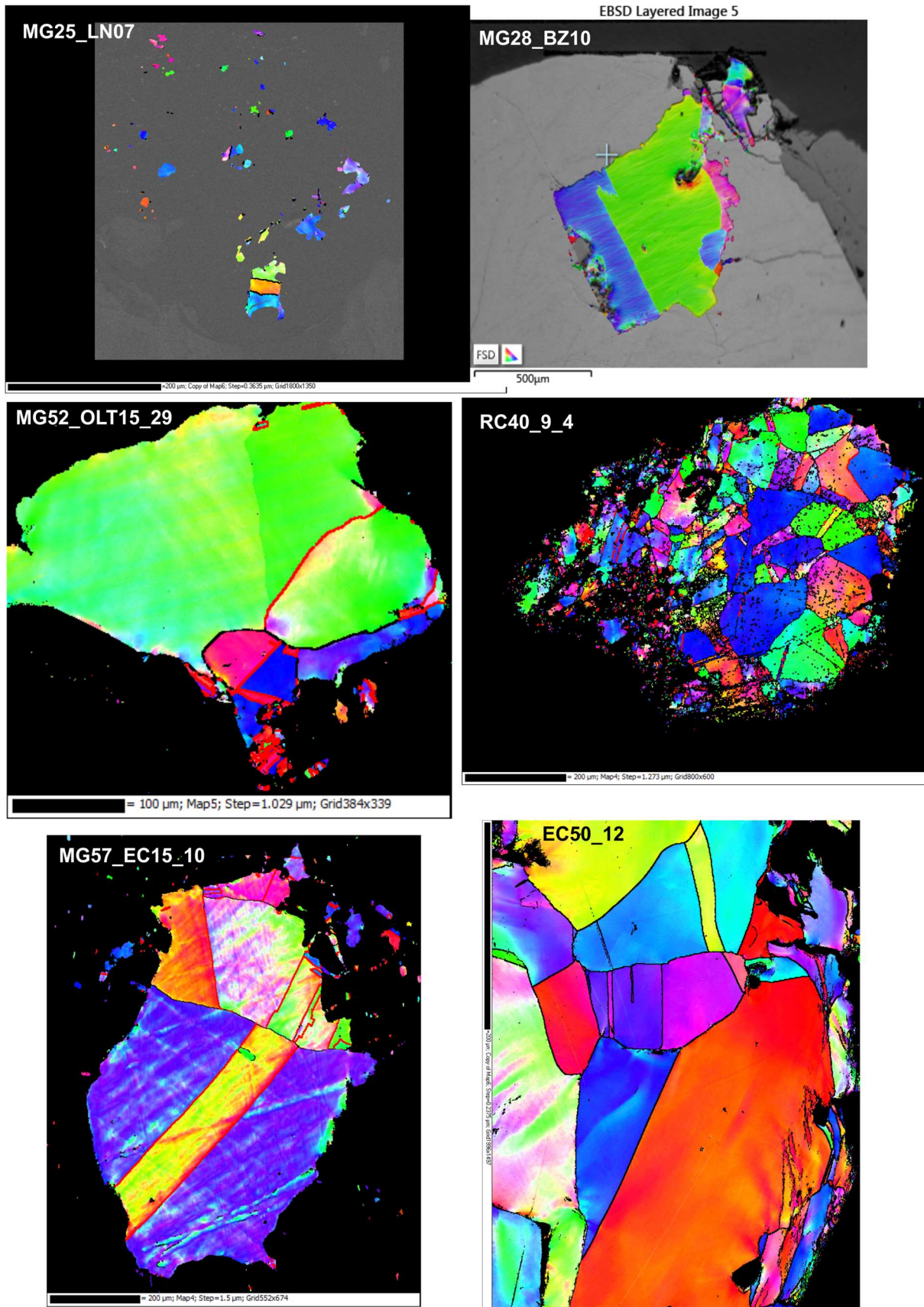


A.6 Trace element data from LA-ICP-MS

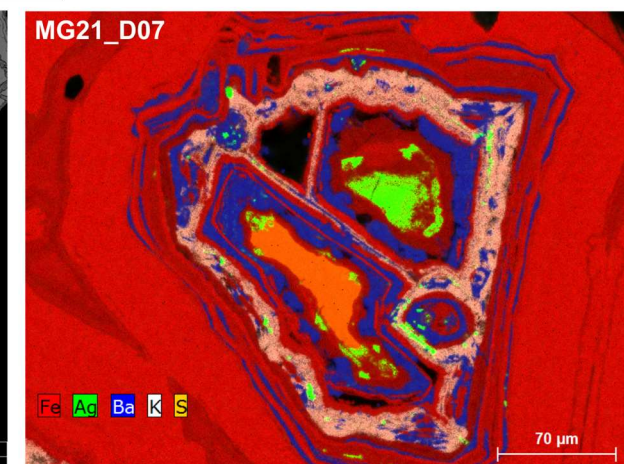
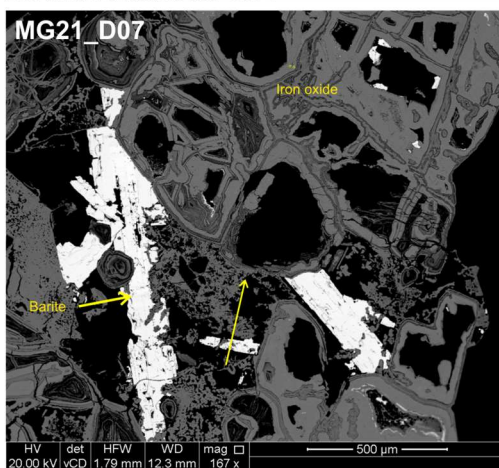
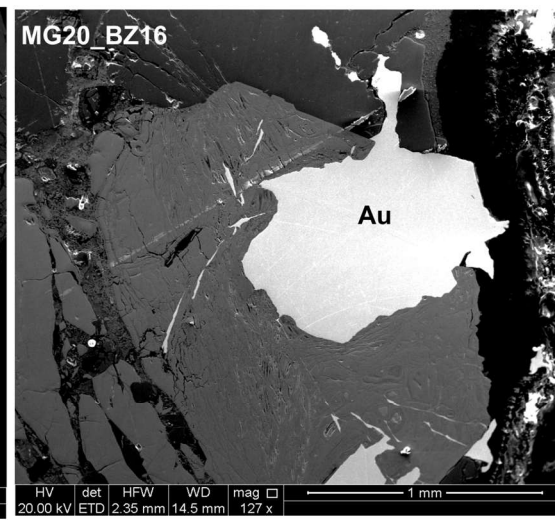
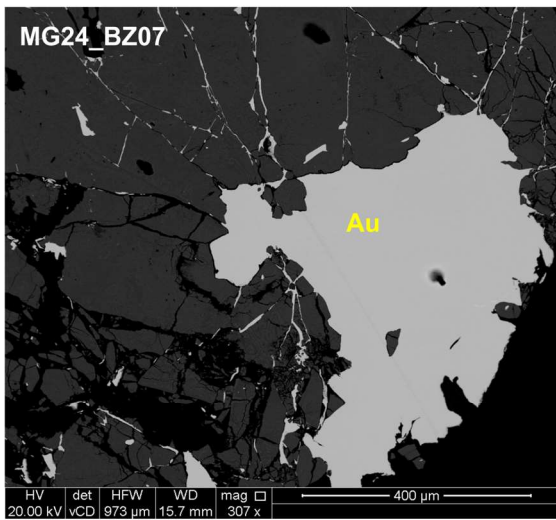
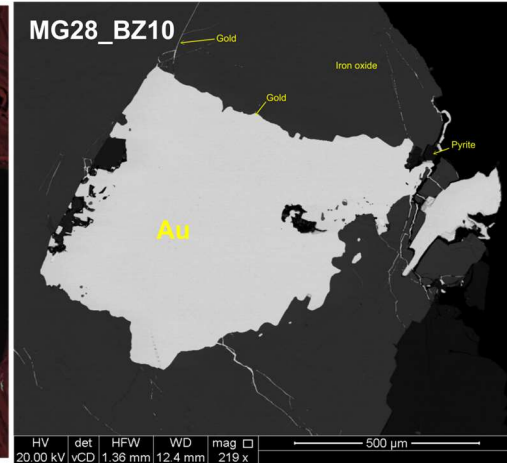
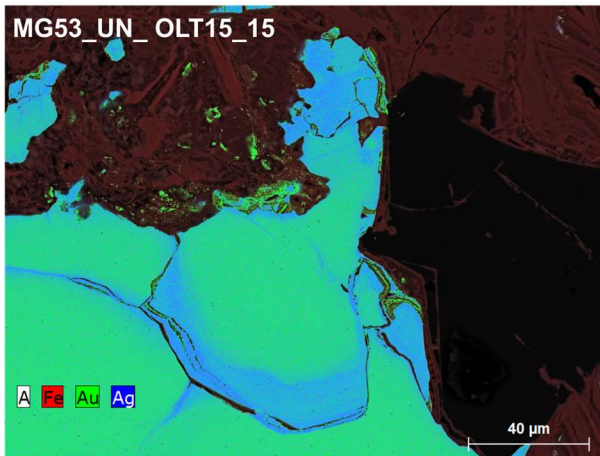
		Li7	Na23	Mg24	Al27	K39	Ca40	Ti47	Mn55	Fe56	Cu63	Zn66	As75	Sr88	Sn118	Sb121	Te125	Ba137	La139	Pb208	Bi209
Q1	Average	118.97	17.86	13.62	705.76	73.98	138.85	3.10	1.61	608.87	17.71	5.30	18.46	2.16	0.70	2.71	5.29	10.10	1.79	90.07	4.49
Q2	Average	22.27	24.65	12.57	193.31	101.21	6.82	1.85	0.59	18.92	1.48	2.49	0.85	0.82	0.08	1.93		7.17	9.46	172.03	1.56
Q3	Average	57.09	138.77	12.78	996.31	109.01	32.05	3.93	4.40	1808.24	7.12	6.83	2.14	3.07	0.16	5.93	5.02	18.12	9.84	107.61	42.75
Q1	Min	93.63	8.38	1.35	52.53	9.46	7.03	0.00	0.30	1.33	17.71	0.29	0.50	0.12	0.09	1.04	5.29	1.77	0.83	0.79	0.01
	Max	139.30	27.34	68.67	1743.15	258.29	552.08	18.50	5.45	4054.06	17.71	17.71	71.85	5.96	2.83	5.92	5.29	22.75	4.92	410.81	15.35
	Range	45.67	18.96	67.32	1690.62	248.83	545.05	18.50	5.15	4052.73	0.00	17.43	71.35	5.85	2.75	4.88	0.00	20.99	4.09	410.02	15.34
	St Dev	20.13	13.41	22.54	745.36	96.03	233.5	5.21	2.20	1519.48		7.37	35.5	2.47	1.20	1.69		7.70	1.56	135.54	6.05
Q2	Min	1.02	9.98	0.18	5.96	3.53	0.72	0.00	0.39	0.25	1.48	0.20	0.50	0.04	0.04	0.17	0.00	0.61	0.19	0.03	0.01
	Max	189.24	3321.66	83.01	2434.31	762.01	215.49	14.21	34.08	46406.3	36.27	32.76	10.27	13.31	0.57	16.09	16.79	157.92	28.81	3596.51	643.55
	Range	188.23	3311.68	82.83	2428.35	758.47	214.76	14.21	33.69	46406.12	34.79	32.56	9.776	13.27	0.52	15.91	16.79	157.31	28.62	3596.48	643.54
	St Dev	23.97	17.22	32.89	299.21	169.88	5.55	1.70	0.23	38.23		4.56	0.44	1.02	0.04	2.83		8.04	16.16	657.16	3.05
Q3	Min	2.73	3.26	0.49	72.43	4.20	1.16	0.00	0.35	0.20	1.30	0.10	0.30	0.08	0.05	0.53	0.97	1.40	0.03	0.02	0.01
	Max	189.24	3321.66	83.01	2434.31	762.01	215.49	14.21	34.08	46406.37	36.27	32.76	10.27	13.31	0.57	16.09	16.79	157.92	28.81	2492.96	643.55
	Range	186.51	3318.39	82.52	2361.88	757.81	214.32	14.21	33.73	46406.17	34.97	32.66	9.976	13.23	0.51	15.55	15.82	156.52	28.78	2492.94	643.55
	St Dev	48.50	562.46	20.38	602.97	161.42	41.51	2.64	7.39	7771.76	9.29	9.36	2.19	2.57	0.15	4.07	4.98	24.78	9.73	439.88	147.67

Table 11-2: Results of trace element content of quartz presented in parts per million for each generation of quartz.

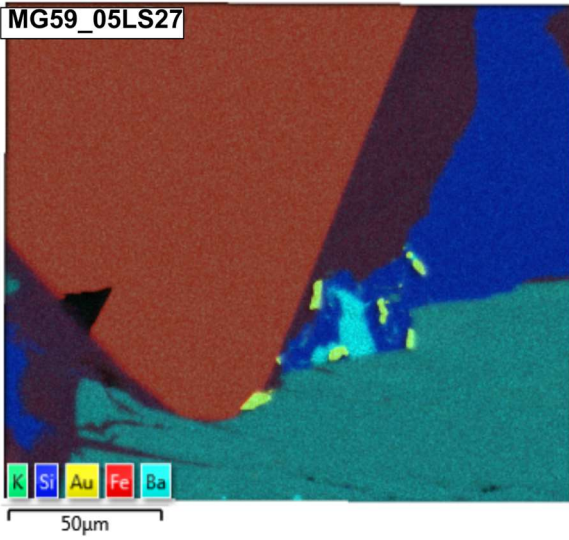
A.7 Electron Backscatter Diffraction



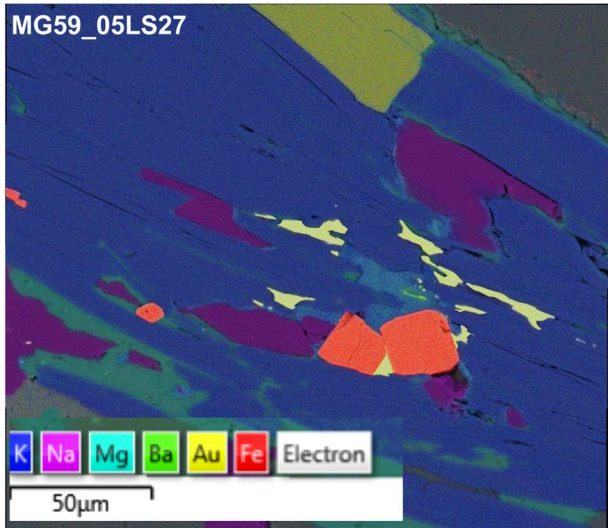
A.8 Scanning Electron Microscopy BSE images and EDS maps



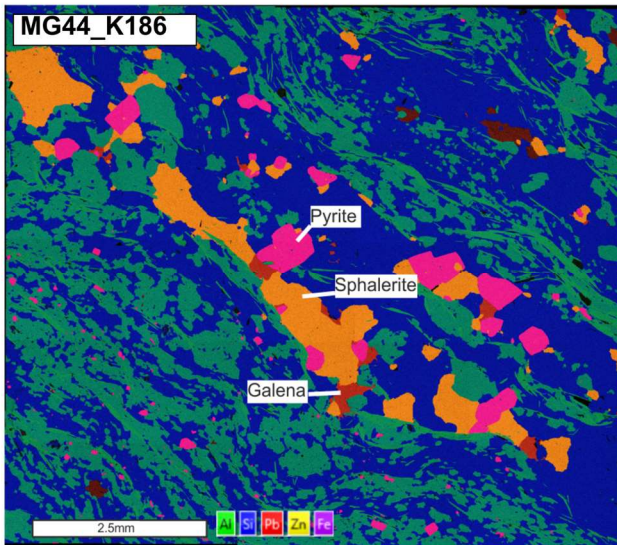
MG59_05LS27



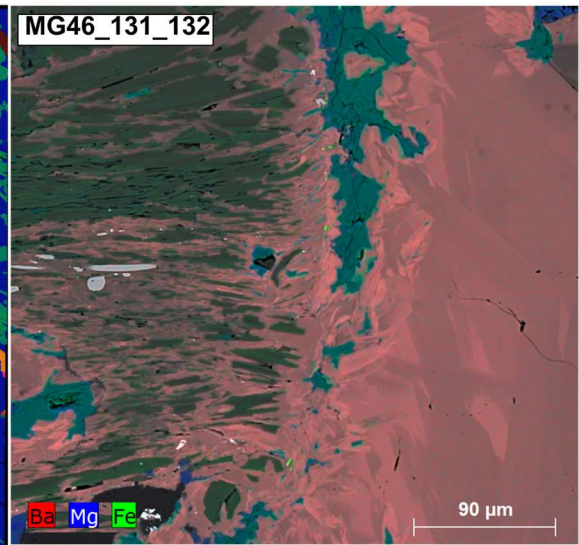
MG59_05LS27



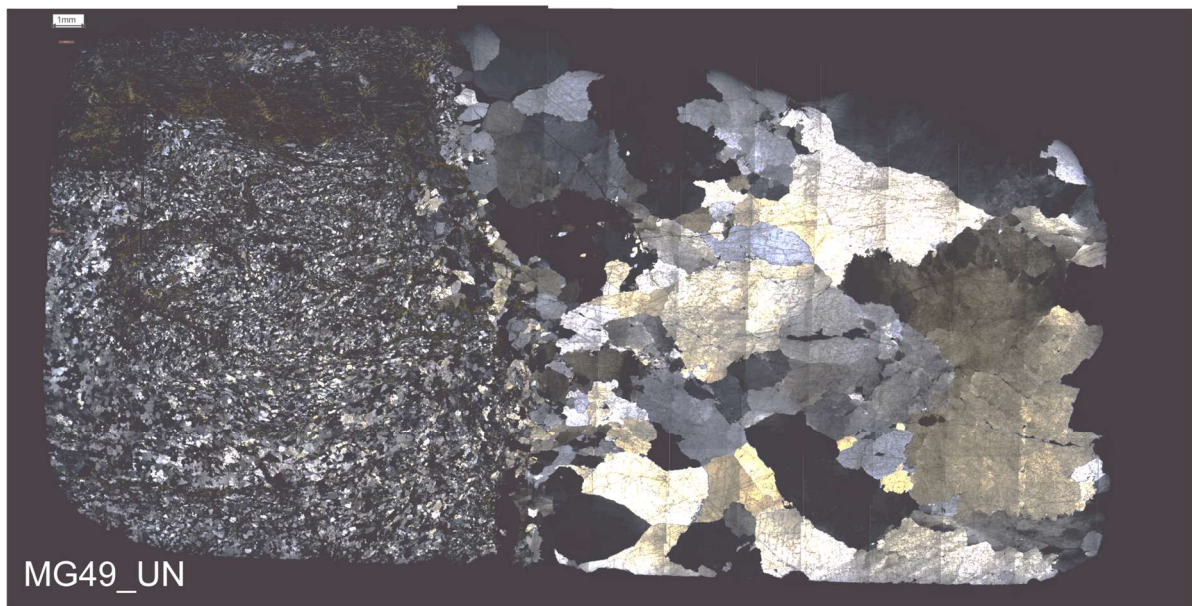
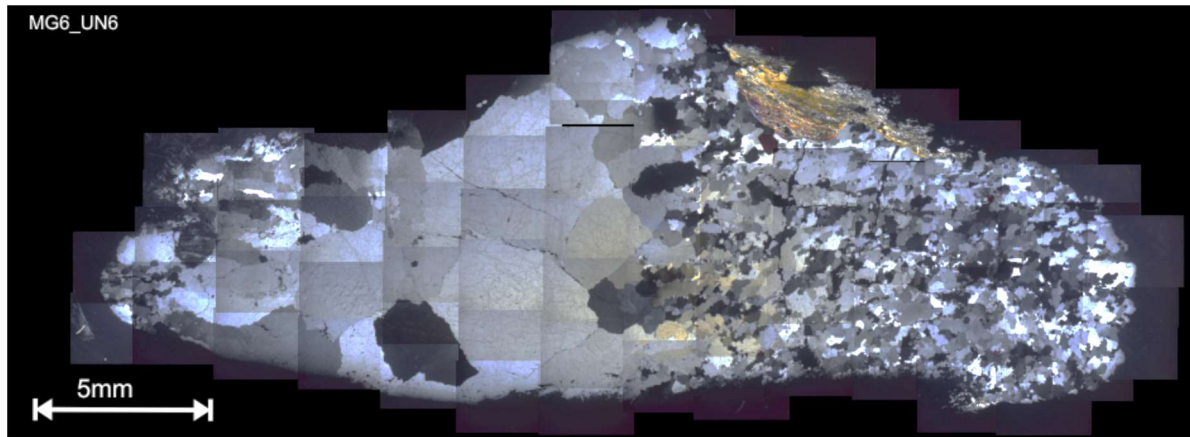
MG44_K186



MG46_131_132

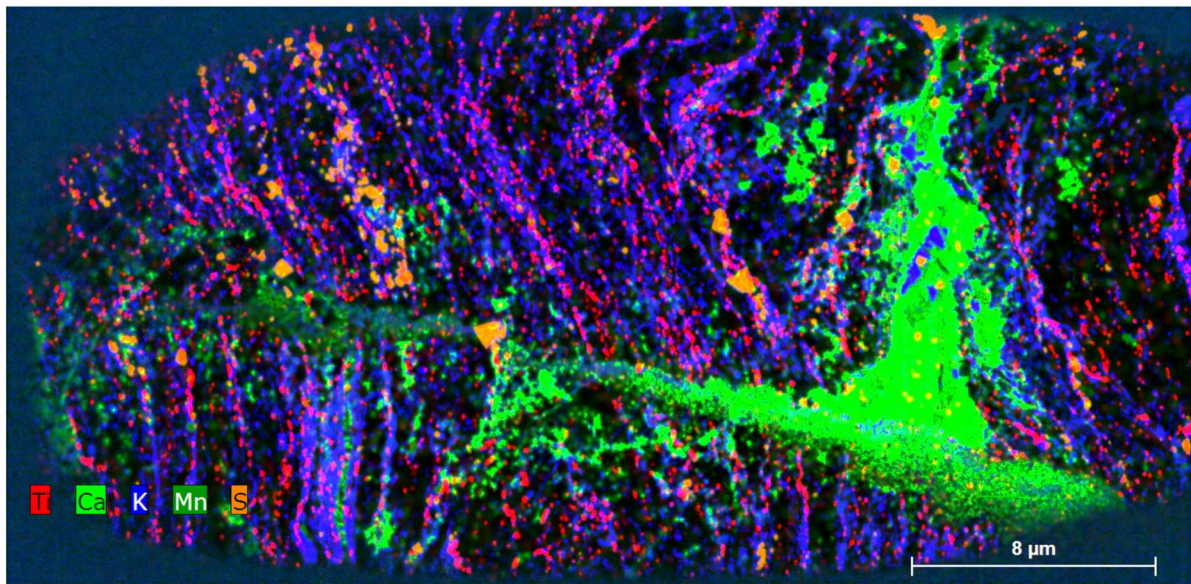


A.9 Petrographic montages

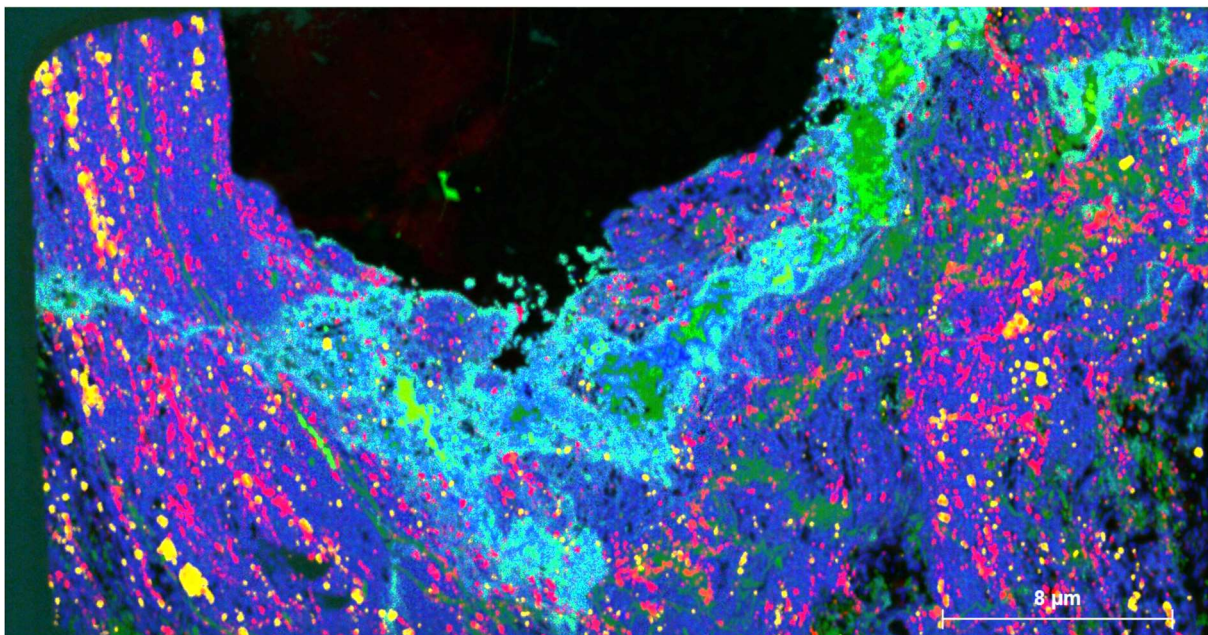


A.10 Tornado XRF element maps and annotated sections

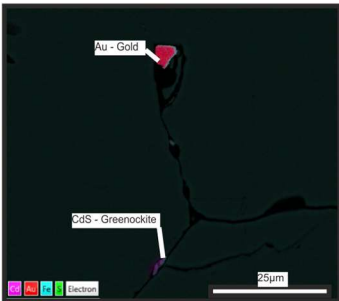
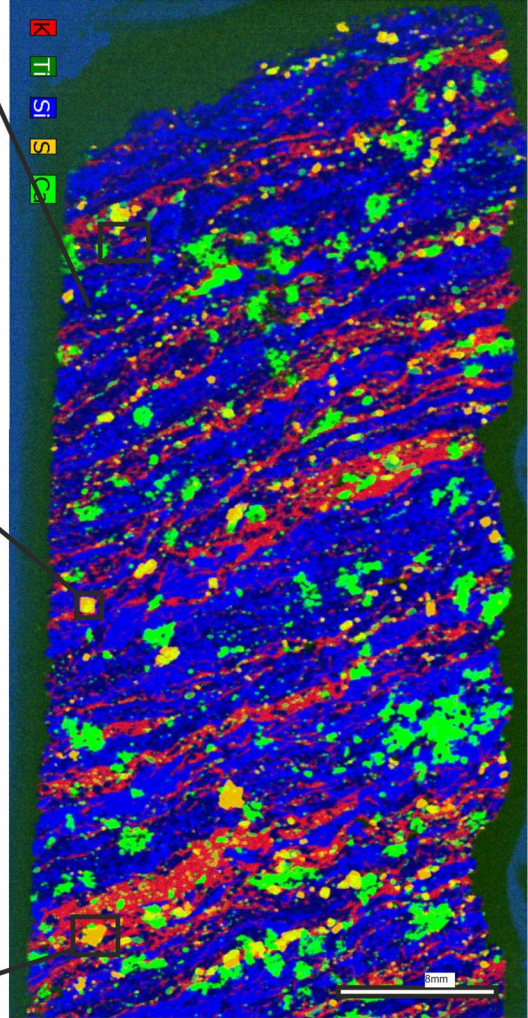
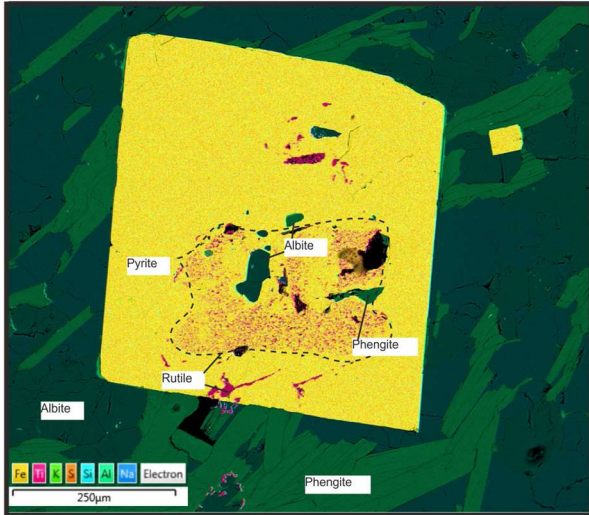
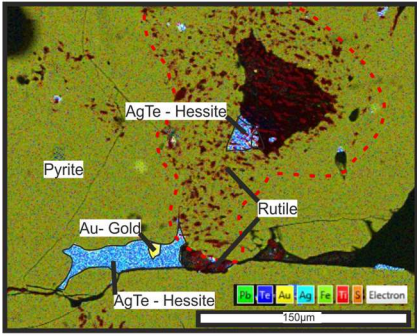
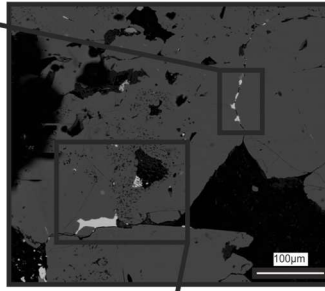
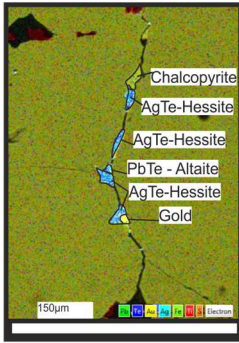
MG 10 05LS27



MG8_05LS27-1B



MG8_05LS27-1B



A.11 Electron Microprobe Data from EPMA

Occurrence	Sample Type	Block and ID	Grain ID	Wt.% (Au)	Wt.% (Ag)	Wt.% (Fe)	Wt. % (Hg)	Wt.% (Cu)	Probe Total
Nugget Zone	Bulk	WRS 1665 D	A	70.59	28.82		0.00	0.00	99.41
Nugget Zone	Bulk	WRS 1665 D	B	77.47	21.76		0.08	0.00	99.31
Nugget Zone	Bulk	WRS 1665 D	C	73.72	25.91		0.00	0.02	99.65
Nugget Zone	Bulk	WRS 1665 D	D	74.52	23.88		0.00	0.02	98.43
Nugget Zone	Bulk	WRS 1665 D	E	71.97	26.89		0.00	0.00	98.86
Nugget Zone	Bulk	WRS 1665 D	F	76.30	22.90		0.03	0.03	99.26
Nugget Zone	Bulk	WRS 1665 D	G	80.99	18.74		0.00	0.03	99.76
Nugget Zone	Bulk	WRS 1665 D	H	76.17	22.09		0.00	0.02	98.27
Nugget Zone	Bulk	WRS 1665 D	I	67.08	32.43		0.01	0.00	99.51
Nugget Zone	Bulk	WRS 1665 D	J	83.07	15.72		0.03	0.04	98.87
Nugget Zone	Bulk	WRS 1665 D	K	82.37	16.73		0.00	0.05	99.15
Nugget Zone	Bulk	WRS 1665 D	L	83.16	15.40		0.00	0.00	98.57
Nugget Zone	Bulk	WRS 1665 D	M	72.32	27.11		0.00	0.00	99.43
Nugget Zone	Bulk	WRS 1665 D	N	69.98	29.33		0.00	0.01	99.32
Nugget Zone	Bulk	WRS 1665 D	O	72.98	26.87		0.00	0.02	99.88
Nugget Zone	Bulk	WRS 1665 D	P	78.04	22.46		0.00	0.00	100.50
Nugget Zone	Bulk	WRS 1665 D	Q	66.67	32.77		0.13	0.02	99.59
Nugget Zone	Bulk	WRS 1665 D	R	69.38	29.74		0.00	0.00	99.12
Nugget Zone	Bulk	WRS 1665 D	S	83.25	15.98		0.00	0.03	99.26
Nugget Zone	Bulk	WRS 1665 D	T	64.46	33.82		0.02	0.02	98.32
Nugget Zone	Bulk	WRS 1665 D	U	76.34	23.50		0.04	0.02	99.89
Nugget Zone	Bulk	WRS 1665 D	V	80.90	18.67		0.00	0.04	99.60
Nugget Zone	Bulk	WRS 1665 D	W	70.55	28.82		0.00	0.03	99.40
Nugget Zone	Bulk	WRS 1665 D	X	75.45	25.23		0.00	0.00	100.69
Nugget Zone	Bulk	WRS 1665 D	Y	82.38	17.50		0.01	0.02	99.92
Nugget Zone	Bulk	WRS 1665 D	Z	82.83	16.52		0.00	0.01	99.37
Nugget Zone	Bulk	WRS 1665 D	A1	76.42	22.76		0.18	0.01	99.36
Nugget Zone	Bulk	WRS 1665 D	B1	75.06	24.95		0.00	0.00	100.01
Nugget Zone	Bulk	WRS 1665 D	C1	73.18	25.33		0.00	0.00	98.51
Nugget Zone	Bulk	WRS 1665 D	D1	67.27	32.00		0.00	0.03	99.30
Nugget Zone	Bulk	WRS 1665 D	E1	70.44	29.21		0.00	0.01	99.67

Occurrence	Sample Type	Block and ID	Grain ID	Wt.% (Au)	Wt.% (Ag)	Wt.% (Fe)	Wt. % (Hg)	Wt.% (Cu)	Probe Total
Nugget Zone	Bulk	WRS 1665 D	F1	70.48	28.82		0.07	0.01	99.37
Nugget Zone	Bulk	WRS 1665 D	G1	71.94	27.83		0.04	0.00	99.80
Nugget Zone	Bulk	WRS 1665 D	H1	69.28	29.62		0.00	0.02	98.92
Nugget Zone	Bulk	WRS 1665 D	I1	76.98	22.10		0.00	0.02	99.10
Nugget Zone	Bulk	WRS 1665 D	J1	83.53	15.90		0.00	0.01	99.44
Nugget Zone	Bulk	WRS 1665 D	K1	71.33	27.82		0.08	0.00	99.22
Nugget Zone	Bulk	WRS 1665 D	L1	79.51	20.10		0.00	0.00	99.61
Nugget Zone	Bulk	WRS 1665 D	M1	70.82	28.16		0.00	0.02	99.00
Nugget Zone	Bulk	WRS 1665 D	N1	66.80	32.41		0.00	0.00	99.21
Nugget Zone	Bulk	WRS 1665 D	O1	68.20	30.48		0.03	0.02	98.72
Nugget Zone	Bulk	WRS 1665 D	P1	76.13	23.69		0.00	0.01	99.82
Nugget Zone	Bulk	WRS 1665 D	Q1	73.77	25.52		0.01	0.00	99.30
Nugget Zone	Bulk	WRS 1665 D	R1	76.03	22.95		0.00	0.02	99.00
Nugget Zone	Bulk	WRS 1665 D	S1	76.52	22.89		0.00	0.00	99.41
Nugget Zone	Bulk	WRS 1665 D	T1	80.06	19.68		0.00	0.00	99.74
Buckland Zone	Bulk	WRS 1665 D	A	82.52	17.20		0.06	0.00	99.78
Buckland Zone	Bulk	WRS 1665 D	B	77.91	21.57		0.00	0.00	99.48
Buckland Zone	Bulk	WRS 1665 D	C	72.14	27.19		0.04	0.02	99.39
Buckland Zone	Bulk	WRS 1665 D	D	79.57	20.02		0.00	0.00	99.59
Buckland Zone	Bulk	WRS 1665 D	E	71.57	28.73		0.00	0.00	100.30
Buckland Zone	Bulk	WRS 1665 D	F	77.84	21.45		0.00	0.03	99.32
Buckland Zone	Bulk	WRS 1665 D	G	81.74	18.15		0.00	0.03	99.93
Buckland Zone	Bulk	WRS 1665 D	H	80.75	19.05		0.00	0.02	99.81
Buckland Zone	Bulk	WRS 1665 D	I	76.18	22.64		0.00	0.00	98.81
Buckland Zone	Bulk	WRS 1665 D	J	82.48	17.65		0.00	0.02	100.15
Buckland Zone	Bulk	WRS 1665 D	K	83.26	16.31		0.02	0.00	99.59
Buckland Zone	Bulk	WRS 1665 D	L	80.47	19.10		0.00	0.00	99.58
Buckland Zone	Bulk	WRS 1665 D	M	82.39	17.19		0.00	0.06	99.64
Buckland Zone	Bulk	WRS 1665 D	N	80.90	18.74		0.00	0.00	99.63
Buckland Zone	Bulk	WRS 1665 D	O	82.24	16.54		0.00	0.00	98.78
Buckland Zone	Bulk	WRS 1665 D	P	77.85	21.25		0.00	0.01	99.10
Buckland Zone	Bulk	WRS 1665 D	Q	76.46	23.69		0.00	0.04	100.19
Buckland Zone	Bulk	WRS 1665 D	R	81.52	18.25		0.00	0.01	99.78
Buckland Zone	Bulk	WRS 1665 D	S	75.20	24.54		0.00	0.00	99.74

Occurrence	Sample Type	Block and ID	Grain ID	Wt.% (Au)	Wt.% (Ag)	Wt.% (Fe)	Wt. % (Hg)	Wt.% (Cu)	Probe Total
Buckland Zone	Bulk	WRS 1665 D	T	61.50	36.58		0.44	0.02	98.54
Buckland Zone	Bulk	WRS 1665 D	U	84.02	15.60		0.00	0.03	99.65
Buckland Zone	Bulk	WRS 1665 D	V	79.21	20.37		0.04	0.00	99.63
Buckland Zone	Bulk	WRS 1665 D	W	75.72	23.87		0.00	0.01	99.60
Buckland Zone	Bulk	WRS 1665 D	X	78.16	21.97		0.00	0.01	100.14
Buckland Zone	Bulk	WRS 1665 D	Y	79.29	20.08		0.00	0.03	99.39
Buckland Zone	Bulk	WRS 1665 D	Z	76.03	23.61		0.00	0.02	99.67
Buckland Zone	Bulk	WRS 1665 D	A1	78.75	21.51		0.00	0.01	100.27
Buckland Zone	Bulk	WRS 1665 D	B1	78.10	21.27		0.00	0.00	99.38
Buckland Zone	Bulk	WRS 1665 D	C1	79.03	20.82		0.08	0.02	99.95
Buckland Zone	Bulk	WRS 1665 D	D1	62.26	36.36		0.73	0.00	99.35
Buckland Zone	Bulk	WRS 1665 D	E1	78.85	20.01		0.00	0.00	98.86
Buckland Zone	Bulk	WRS 1665 D	F1	73.21	26.38		0.00	0.00	99.59
Buckland Zone	Bulk	WRS 1665 D	G1	83.81	16.73		0.00	0.03	100.57
Buckland Zone	Bulk	WRS 1665 D	H1	82.27	17.08		0.00	0.01	99.35
Buckland Zone	Bulk	WRS 1665 D	I1	78.33	21.44		0.08	0.00	99.85
Buckland Zone	Bulk	WRS 1665 D	J1	80.06	19.53		0.03	0.02	99.63
Buckland Zone	Bulk	WRS 1665 D	K1	80.52	17.96		0.00	0.00	98.48
Buckland Zone	Bulk	WRS 1665 D	L1	70.39	28.45		0.00	0.00	98.83
Buckland Zone	Bulk	WRS 1665 D	M1	77.33	22.78		0.00	0.02	100.12
Buckland Zone	Bulk	WRS 1665 D	N1	76.50	21.88		0.00	0.01	98.39
Buckland Zone	Bulk	WRS 1665 D	O1	76.95	22.65		0.00	0.02	99.62
Buckland Zone	Bulk	WRS 1665 D	P1	80.41	19.79		0.00	0.00	100.21
Buckland Zone	Bulk	WRS 1665 D	Q1	61.98	36.27		0.71	0.00	98.95
Buckland Zone	Bulk	WRS 1665 D	R1	79.62	19.78		0.02	0.00	99.42
Buckland Zone	Bulk	WRS 1665 D	S1	81.13	19.47		0.00	0.00	100.60
Buckland Zone	Bulk	WRS 1665 D	T1	79.35	20.74		0.00	0.04	100.12
Buckland Zone	Bulk	WRS 1665 D	U1	80.28	19.46		0.00	0.01	99.74
Buckland Zone	Bulk	WRS 1665 D	V1	78.15	22.00		0.00	0.03	100.18
Buckland Zone	Bulk	WRS 1665 D	W1	82.36	17.61		0.13	0.02	100.12
Buckland Zone	Bulk	WRS 1665 D	X1	79.78	19.13		0.00	0.00	98.91
Buckland Zone	Bulk	WRS 1665 D	Y1	70.18	29.21		0.00	0.04	99.43
Buckland Zone	Bulk	WRS 1665 D	Z1	76.57	23.77		0.00	0.01	100.35
Buckland Zone	Bulk	WRS 1665 D	A2	79.75	20.70		0.00	0.01	100.46

Occurrence	Sample Type	Block and ID	Grain ID	Wt.% (Au)	Wt.% (Ag)	Wt.% (Fe)	Wt. % (Hg)	Wt.% (Cu)	Probe Total
Buckland Zone	Bulk	WRS 1665 D	B2	76.59	22.71		0.00	0.02	99.33
Buckland Zone	Bulk	WRS 1665 D	C2	80.81	18.59		0.00	0.00	99.40
Buckland Zone	Bulk	WRS 1665 D	D2	77.28	22.88		0.04	0.00	100.20
Buckland Zone	Bulk	WRS 1665 D	E2	81.93	17.99		0.00	0.03	99.96
Buckland Zone	Bulk	WRS 1665 D	F2	76.62	23.26		0.00	0.01	99.89
Buckland Zone	Bulk	WRS 1665 D	G2	78.29	21.32		0.00	0.01	99.62
Buckland Zone	Bulk	WRS 1665 D	H2	74.49	24.89		0.02	0.02	99.41
Buckland Zone	Bulk	WRS 1665 D	I2	81.03	19.04		0.00	0.02	100.09
Buckland Zone	Bulk	WRS 1665 D	J2	79.41	20.11		0.00	0.00	99.52
Buckland Zone	Bulk	WRS 1665 D	K2	79.04	20.61		0.00	0.00	99.64
Buckland Zone	Bulk	WRS 1665 D	L2	82.27	17.21		0.00	0.00	99.49
Buckland Zone	Bulk	WRS 1665 D	M2	77.92	22.54		0.07	0.02	100.54
Buckland Zone	Bulk	WRS 1665 D	N2	69.34	29.69		0.00	0.01	99.03
Buckland Zone	Bulk	WRS 1665 D	O2	75.32	24.81		0.00	0.01	100.15
Nugget Zone	Bulk	WRS 1665 B	A	64.97	34.68		0.09	0.00	99.75
Nugget Zone	Bulk	WRS 1665 B	B	74.83	25.08		0.00	0.00	99.91
Nugget Zone	Bulk	WRS 1665 B	C	64.26	34.75		0.00	0.00	99.01
Nugget Zone	Bulk	WRS 1665 B	D	80.13	19.26		0.03	0.00	99.42
Nugget Zone	Bulk	WRS 1665 B	E	80.68	18.55		0.00	0.01	99.24
Nugget Zone	Bulk	WRS 1665 B	F	76.10	21.99		0.00	0.01	98.10
Nugget Zone	Bulk	WRS 1665 B	G	76.94	23.13		0.00	0.00	100.07
Nugget Zone	Bulk	WRS 1665 B	H	70.55	29.12		0.00	0.02	99.68
Nugget Zone	Bulk	WRS 1665 B	I	66.44	32.80		0.09	0.00	99.34
Nugget Zone	Bulk	WRS 1665 B	J	65.54	33.71		0.00	0.00	99.25
Nugget Zone	Bulk	WRS 1665 B	K	82.31	18.09		0.00	0.03	100.43
Nugget Zone	Bulk	WRS 1665 B	L	80.15	19.41		0.08	0.01	99.65
Nugget Zone	Bulk	WRS 1665 B	M	77.08	22.83		0.00	0.00	99.91
Nugget Zone	Bulk	WRS 1665 B	N	64.87	34.99		0.00	0.00	99.86
Nugget Zone	Bulk	WRS 1665 B	O	66.76	31.75		0.00	0.02	98.54
Nugget Zone	Bulk	WRS 1665 B	P	69.68	28.60		0.05	0.03	98.37
Nugget Zone	Bulk	WRS 1665 B	Q	70.02	30.19		0.00	0.00	100.21
Nugget Zone	Bulk	WRS 1665 B	R	66.34	33.80		0.06	0.00	100.21
Nugget Zone	Bulk	WRS 1665 B	S	76.22	23.07		0.00	0.00	99.29
Nugget Zone	Bulk	WRS 1665 B	T	83.15	16.20		0.02	0.01	99.39

Occurrence	Sample Type	Block and ID	Grain ID	Wt.% (Au)	Wt.% (Ag)	Wt.% (Fe)	Wt. % (Hg)	Wt.% (Cu)	Probe Total
Nugget Zone	Bulk	WRS 1665 B	U	83.86	15.40		0.00	0.01	99.27
Nugget Zone	Bulk	WRS 1665 B	V	73.26	26.26		0.02	0.02	99.55
Nugget Zone	Bulk	WRS 1665 B	W	78.51	20.90		0.00	0.03	99.44
Nugget Zone	Bulk	WRS 1665 B	X	77.48	22.23		0.00	0.00	99.71
Buckland Zone	Bulk	WRS 1665 B	A	76.24	23.79		0.00	0.00	100.03
Buckland Zone	Bulk	WRS 1665 B	B	76.65	22.95		0.00	0.00	99.60
Buckland Zone	Bulk	WRS 1665 B	C	78.83	21.22		0.00	0.00	100.05
Buckland Zone	Bulk	WRS 1665 B	D	79.19	20.62		0.08	0.00	99.89
Buckland Zone	Bulk	WRS 1665 B	E	77.47	21.36		0.00	0.01	98.83
Buckland Zone	Bulk	WRS 1665 B	F	78.32	21.89		0.00	0.02	100.24
Buckland Zone	Bulk	WRS 1665 B	G	82.83	17.61		0.00	0.01	100.45
Buckland Zone	Bulk	WRS 1665 B	H	75.55	24.33		0.02	0.02	99.92
Buckland Zone	Bulk	WRS 1665 B	I	79.12	20.88		0.00	0.01	100.01
Buckland Zone	Bulk	WRS 1665 B	J	73.66	25.43		0.03	0.03	99.15
Buckland Zone	Bulk	WRS 1665 B	K	75.09	24.33		0.00	0.03	99.45
Buckland Zone	Bulk	WRS 1665 B	L	81.80	18.72		0.03	0.02	100.57
Buckland Zone	Bulk	WRS 1665 B	M	63.42	17.26		0.06	0.00	80.75
Buckland Zone	Bulk	WRS 1665 B	N	76.03	23.63		0.00	0.02	99.68
Buckland Zone	Bulk	WRS 1665 B	O	78.57	21.40		0.00	0.01	99.98
Buckland Zone	Bulk	WRS 1665 B	P	76.37	23.08		0.00	0.01	99.46
Buckland Zone	Bulk	WRS 1665 B	Q	78.99	20.09		0.00	0.00	99.08
Buckland Zone	Bulk	WRS 1665 B	R	81.66	18.25		0.00	0.00	99.92
Buckland Zone	Bulk	WRS 1665 B	S	70.03	28.70		0.00	0.01	98.73
Buckland Zone	Bulk	WRS 1665 B	T	80.38	18.02		0.01	0.01	98.42
Buckland Zone	Bulk	WRS 1665 B	U	79.59	19.28		0.00	0.00	98.87
Buckland Zone	Bulk	WRS 1665 B	V	76.85	23.11		0.03	0.01	99.99
Buckland Zone	Bulk	WRS 1665 B	W	78.60	21.24		0.00	0.00	99.84
Buckland Zone	Bulk	WRS 1665 B	X	61.97	36.49		0.85	0.00	99.31
Buckland Zone	Bulk	WRS 1665 B	Y	78.06	21.09		0.00	0.02	99.17
Buckland Zone	Bulk	WRS 1665 B	Z	74.53	24.97		0.00	0.00	99.51
Buckland Zone	Bulk	WRS 1665 B	A1	85.31	15.76		0.00	0.04	101.11
Buckland Zone	Bulk	WRS 1665 B	B1	79.35	20.49		0.03	0.00	99.87
Buckland Zone	Bulk	WRS 1665 B	C1	80.05	19.76		0.00	0.01	99.82
Nugget Zone	Bulk	WRS 1572 B	A	76.792	23.86	0	0	0.006	100.66

Occurrence	Sample Type	Block and ID	Grain ID	Wt.% (Au)	Wt.% (Ag)	Wt.% (Fe)	Wt. % (Hg)	Wt.% (Cu)	Probe Total
Nugget Zone	Bulk	WRS 1572 B	B	76.492	24.965	0.009	0	0	101.47
Nugget Zone	Bulk	WRS 1572 B	C	74.264	26.807	0.011	0	0.001	101.08
Nugget Zone	Bulk	WRS 1572 B	D	77.375	23.876	0.004	0	0.031	101.29
Nugget Zone	Bulk	WRS 1572 B	E	74.23	27.47	0.037	0	0.004	101.74
Nugget Zone	Bulk	WRS 1572 B	F	76.061	24.34	0	0	0.017	100.42
Nugget Zone	Bulk	WRS 1572 B	G	79.237	20.151	0.001	0	0	99.39
Nugget Zone	Bulk	WRS 1572 B	H	76.657	23.639	0.018	0	0.007	100.32
Nugget Zone	Bulk	WRS 1572 B	I	74.256	26.143	0.027	0	0.005	100.43
Nugget Zone	Bulk	WRS 1572 B	J	77.981	22.708	0.015	0	0.012	100.72
Nugget Zone	Bulk	WRS 1572 B	K	80.073	19.965	0.02	0.027	0.002	100.09
Nugget Zone	Bulk	WRS 1572 B	L	77.165	23.074	0	0.152	0.004	100.40
Nugget Zone	Bulk	WRS 1572 B	M	76.537	23.514	0.015	0	0.005	100.07
Nugget Zone	Bulk	WRS 1572 B	N	78.561	21.357	0.055	0	0.011	99.98
Nugget Zone	Bulk	WRS 1572 B	O	76.456	22.809	0.001	0	0.013	99.28
Nugget Zone	Bulk	WRS 1572 B	P	77.395	22.865	0.015	0	0	100.28
Nugget Zone	Bulk	WRS 1572 B	Q	76.528	22.917	0	0	0.002	99.45
Nugget Zone	Bulk	WRS 1572 B	R	76.422	23.336	0.037	0	0.004	99.80
Nugget Zone	Bulk	WRS 1572 B	S	76.207	23.274	0.01	0	0	99.49
Nugget Zone	Bulk	WRS 1572 B	T	77.053	22.809	0.002	0	0.006	99.87
Nugget Zone	Bulk	WRS 1572 B	U	74.349	25.852	0.011	0	0	100.21
Nugget Zone	Bulk	WRS 1572 B	V	71.222	27.308	0	46.533	0	145.06
Nugget Zone	Bulk	WRS 1572 B	W	72.004	28.267	0.022	0.096	0	100.39
Nugget Zone	Bulk	WRS 1572 B	X	76.758	22.803	0.007	0	0.038	99.61
Nugget Zone	Bulk	WRS 1572 C	A	74.576	25.152	0	0	0	99.73
Nugget Zone	Bulk	WRS 1572 C	B	76.099	22.866	0.01	0	0.013	98.99
Nugget Zone	Bulk	WRS 1572 C	C	74.013	25.909	0	0	0.013	99.94
Nugget Zone	Bulk	WRS 1572 C	D	77.023	22.251	0.001	0.125	0.019	99.42
Nugget Zone	Bulk	WRS 1572 C	E	76.273	22.866	0	0.037	0.01	99.19
Nugget Zone	Bulk	WRS 1572 C	F	74.762	25.018	0.015	0	0.016	99.81
Nugget Zone	Bulk	WRS 1572 C	G1	76.305	22.541	0.007	0	0.006	98.86
Nugget Zone	Bulk	WRS 1572 C	G2	79.411	19.054	0.009	0.269	0	98.74
Nugget Zone	Bulk	WRS 1572 C	H						
Nugget Zone	Bulk	WRS 1572 C	I	75.725	23.26	0	0	0	98.99
Nugget Zone	Bulk	WRS 1572 C	J	78.567	20.767	0	0	0	99.33

Occurrence	Sample Type	Block and ID	Grain ID	Wt.% (Au)	Wt.% (Ag)	Wt.% (Fe)	Wt. % (Hg)	Wt.% (Cu)	Probe Total
Nugget Zone	Bulk	WRS 1572 C	K	73.322	25.748	0.01	0	0	99.08
Nugget Zone	Bulk	WRS 1572 C	L	76.342	22.692	0.017	0	0.023	99.07
Nugget Zone	Bulk	WRS 1572 C	M	73.29	25.579	0	0.014	0.011	98.89
Nugget Zone	Bulk	WRS 1572 C	N	80.268	18.693	0.051	0	0	99.01
Nugget Zone	Bulk	WRS 1572 C	O	75.687	23.056	0.005	0	0	98.75
Lone Star	Bulk	WRS 1572 C	A	81.661	17.928	0.008	0	0	99.60
Lone Star	Bulk	WRS 1572 C	B	72.777	26.309	0.028	0	0	99.11
Lone Star	Bulk	WRS 1572 C	C	84.686	14.386	0.019	0	0.02	99.11
Lone Star	Bulk	WRS 1572 C	D	83.86	14.405	0.034	0	0.02	98.32
Lone Star	Bulk	WRS 1572 C	E	82.959	16.214	0	0	0.004	99.18
Lone Star	Bulk	WRS 1572 C	F	81.602	17.316	0	0	0.004	98.92
Lone Star	Bulk	WRS 1572 C	G	83.075	15.986	0	0	0.031	99.09
Lone Star	Bulk	WRS 1572 C	H	83.073	15.858	0.007	0	0.011	98.95
Lone Star	Bulk	WRS 1572 C	I	83.775	15.78	0.025	0	0.016	99.60
Lone Star	Bulk	WRS 1572 C	J	82.785	15.635	0	0	0.002	98.42
Lone Star	Bulk	WRS 1572 C	K	85.58	13.377	0.005	0	0.018	98.98
Lone Star	Bulk	WRS 1572 C	L	76.287	22.732	0.008	0	0.001	99.03
Lone Star	Bulk	WRS 1572 C	M	77.053	22.482	0.013	0.01	0.012	99.57
Lone Star	Bulk	WRS 1572 C	N	83.456	15.949	0.022	0	0	99.43
Dysle Zone	Bulk	WRS 1572 C	F	73.083	25.341	0.007	0	0	98.43
Dysle Zone	Bulk	WRS 1572 C	G	66.163	33.787	0.003	0	0	99.95
Dysle Zone	Bulk	WRS 1572 C	H	71.836	27.145	0	0.299	0.002	99.28
Dysle Zone	Bulk	WRS 1572 C	I	71.601	28.264	0.005	0.205	0	100.08
Dysle Zone	Bulk	WRS 1572 C	J	72.085	27.62	0.028	0.002	0.013	99.75
Dysle Zone	Bulk	WRS 1572 C	K	75.367	24.491	0	0	0	99.86
Dysle Zone	Bulk	WRS 1572 C	L	74.97	24.891	0	0	0	99.86
Dysle Zone	Bulk	WRS 1572 C	M	70.997	28.186	0	0	0	99.18
Dysle Zone	Bulk	WRS 1572 C	N	70.449	29.297	0.038	0	0	99.78
Dysle Zone	Bulk	WRS 1572 C	O	72.873	26.632	0.013	0.272	0	99.79
Dysle Zone	Bulk	WRS 1572 C	P	69.326	29.469	0.022	0.061	0	98.88
Dysle Zone	Bulk	WRS 1572 C	Q	73.239	25.699	0.017	0	0.016	98.97
Dysle Zone	Bulk	WRS 1572 C	R	70.226	29.548	0.017	0	0	99.79
Dysle Zone	Bulk	WRS 1572 C	S	71.566	28.088	0	0	0	99.65
Dysle Zone	Bulk	WRS 1572 C	T	71.075	28.571	0.013	0	0	99.66

Occurrence	Sample Type	Block and ID	Grain ID	Wt.% (Au)	Wt.% (Ag)	Wt.% (Fe)	Wt. % (Hg)	Wt.% (Cu)	Probe Total
Dysle Zone	Bulk	WRS 1572 C	U	67.036	32.965	0.011	0	0.005	100.02
Dysle Zone	Bulk	WRS 1572 C	V	72.72	26.12	0.024	0.024	0.032	98.92
Dysle Zone	Bulk	WRS 1572 C	W	62.707	36.608	0	0.267	0	99.58
Dysle Zone	Bulk	WRS 1572 C	X	73.694	25.501	0.031	0	0	99.23
Dysle Zone	Bulk	WRS 1572 C	Y	69.706	29.379	0.017	0.181	0	99.28
Dysle Zone	Bulk	WRS 1572 C	Z	73.17	27.144	0	0	0	100.31
Dysle Zone	Bulk	WRS 1572 C	A1	74.961	24.751	0.025	0	0	99.74
Dysle Zone	Bulk	WRS 1572 C	B1	72.102	27.165	0.011	0	0	99.28
Violet Mine	Bulk	WRS 1463 B	A	66.987	31.405	0.005	1.907	0	100.30
Violet Mine	Bulk	WRS 1463 B	B	74.378	25.058	0.014	1.251	0	100.70
Violet Mine	Bulk	WRS 1463 B	C	78.356	21.37	0.006	1.309	0.002	101.04
Violet Mine	Bulk	WRS 1463 B	D	81.271	19.161	0.014	0.64	0.012	101.10
Violet Mine	Bulk	WRS 1463 B	E	66.462	31.828	0	2.137	0	100.43
Violet Mine	Bulk	WRS 1463 B	F	72.725	26.555	0.012	1.71	0	101.00
Violet Mine	Bulk	WRS 1463 B	G	69.275	30.612	0	0.356	0	100.24
Violet Mine	Bulk	WRS 1463 B	H	69.746	30.166	0	0.828	0	100.74
Violet Mine	Bulk	WRS 1463 B	I	66.306	32.798	0.004	0.685	0	99.79
Violet Mine	Bulk	WRS 1463 B	J	66.573	33.491	0.003	0.314	0	100.38
Violet Mine	Bulk	WRS 1463 B	K						
Violet Mine	Bulk	WRS 1463 B	L	68.538	31.041	0	1.483	0	101.06
Violet Mine	Bulk	WRS 1463 B	M	81.467	18.664	0.02	0.591	0.02	100.76
Violet Mine	Bulk	WRS 1463 B	N	81.294	18.828	0.019	0.726	0.013	100.88
Buckland Zone	In situ			75.2479	25.0246		0.137114833	-0.00058617	100.13
Buckland Zone	In situ			79.33978	20.48981941		0.062468471	0.015517235	99.783
Buckland Zone	In situ			72.91476	25.23381667		0.013868972	0.00251975	98.165
Buckland Zone	In situ			68.96139	31.26586791		0.073616112	0.005072336	100.16
Buckland Zone	In situ			81.58764	18.07800769		0.094703769	0.013667423	99.585
Buckland Zone	In situ			79.71817	20.69213333		0.098746533	0.016572667	100.33
Buckland Zone	In situ			76.48741	23.75958788		0.120577879	0.015191727	100.14
Buckland Zone	In situ			72.64126	27.77045374		0.116506656	0.015934859	100.54
Drilling	In situ			83.81874	16.11343529		0.105931059	0.019162118	99.845
Drilling	In situ			73.45479	26.40923036		0.106796685	0.006739708	99.764
Drilling	In situ			77.3974	22.90512542		0.140807373	0.006725966	100.17
Nugget Zone	In situ			73.39215	26.2354		0.04585515	0.01417685	99.688

Occurrence	Sample Type	Block and ID	Grain ID	Wt.% (Au)	Wt.% (Ag)	Wt.% (Fe)	Wt. % (Hg)	Wt.% (Cu)	Probe Total
Nugget Zone	In situ			60.409	38.480612		0.06251008	0.0013984	98.954
Nugget Zone	In situ			74.24628	26.3206		0.036556167	0.002903167	100.53
Nugget Zone	In situ			81.77918	18.68216357		0.075233524	0.006780738	100.39
Nugget Zone	In situ			76.04008	24.28929231		0.035523203	0.009948253	100.34
Dysle Zone	In situ			71.76079	28.2073		0.199855	0.008119	100.18
Buckland Zone	Bulk	1665-B-109	354	76.24	23.79		0.00	0.00	100.03
Buckland Zone	Bulk	1665-B-110	355	76.65	22.95		0.00	0.00	99.60
Buckland Zone	Bulk	1665-B-111	356	78.83	21.22		0.00	0.00	100.05
Buckland Zone	Bulk	1665-B-112	357	79.19	20.62		0.08	0.00	99.89
Buckland Zone	Bulk	1665-B-113	358	77.47	21.36		0.00	0.01	98.83
Buckland Zone	Bulk	1665-B-114	359	78.32	21.89		0.00	0.02	100.24
Buckland Zone	Bulk	1665-B-115	360	82.83	17.61		0.00	0.01	100.45
Buckland Zone	Bulk	1665-B-116	361	75.55	24.33		0.02	0.02	99.92
Buckland Zone	Bulk	1665-B-117	362	79.12	20.88		0.00	0.01	100.01
Buckland Zone	Bulk	1665-B-118	363	73.66	25.43		0.03	0.03	99.15
Buckland Zone	Bulk	1665-B-119	364	75.09	24.33		0.00	0.03	99.45
Buckland Zone	Bulk	1665-B-120	365	81.80	18.72		0.03	0.02	100.57
Buckland Zone	Bulk	1665-B-121	366	63.42	17.26		0.06	0.00	80.75
Buckland Zone	Bulk	1665-B-122	367	76.03	23.63		0.00	0.02	99.68
Buckland Zone	Bulk	1665-B-123	368	78.57	21.40		0.00	0.01	99.98
Buckland Zone	Bulk	1665-B-124	369	76.37	23.08		0.00	0.01	99.46
Buckland Zone	Bulk	1665-B-125	370	78.99	20.09		0.00	0.00	99.08
Buckland Zone	Bulk	1665-B-126	371	81.66	18.25		0.00	0.00	99.92
Buckland Zone	Bulk	1665-B-127	372	70.03	28.70		0.00	0.01	98.73
Buckland Zone	Bulk	1665-B-128	373	80.38	18.02		0.01	0.01	98.42
Buckland Zone	Bulk	1665-B-129	374	79.59	19.28		0.00	0.00	98.87
Buckland Zone	Bulk	1665-B-130	375	76.85	23.11		0.03	0.01	99.99
Buckland Zone	Bulk	1665-B-131	376	78.60	21.24		0.00	0.00	99.84
Buckland Zone	Bulk	1665-B-132	377	61.97	36.49		0.85	0.00	99.31
Buckland Zone	Bulk	1665-B-133	378	78.06	21.09		0.00	0.02	99.17
Buckland Zone	Bulk	1665-B-134	379	74.53	24.97		0.00	0.00	99.51
Buckland Zone	Bulk	1665-B-135	380	85.31	15.76		0.00	0.04	101.11
Buckland Zone	Bulk	1665-B-136	381	79.35	20.49		0.03	0.00	99.87
Buckland Zone	Bulk	1665-B-137	382	80.05	19.76		0.00	0.01	99.82

Occurrence	Sample Type	Block and ID	Grain ID	Wt.% (Au)	Wt.% (Ag)	Wt.% (Fe)	Wt. % (Hg)	Wt.% (Cu)	Probe Total
Buckland Zone	Bulk	1665-D-29	30	70.59	28.82		0.00	0.00	99.41
Buckland Zone	Bulk	1665-D-30	31	77.47	21.76		0.08	0.00	99.31
Buckland Zone	Bulk	1665-D-31	32	73.72	25.91		0.00	0.02	99.65
Buckland Zone	Bulk	1665-D-32	33	74.52	23.88		0.00	0.02	98.43
Buckland Zone	Bulk	1665-D-33	34	71.97	26.89		0.00	0.00	98.86
Buckland Zone	Bulk	1665-D-34	35	76.30	22.90		0.03	0.03	99.26
Buckland Zone	Bulk	1665-D-35	36	80.99	18.74		0.00	0.03	99.76
Buckland Zone	Bulk	1665-D-36	37	76.17	22.09		0.00	0.02	98.27
Buckland Zone	Bulk	1665-D-37	38	67.08	32.43		0.01	0.00	99.51
Buckland Zone	Bulk	1665-D-38	39	83.07	15.72		0.03	0.04	98.87
Buckland Zone	Bulk	1665-D-39	40	82.37	16.73		0.00	0.05	99.15
Buckland Zone	Bulk	1665-D-41	42	83.16	15.40		0.00	0.00	98.57
Buckland Zone	Bulk	1665-D-42	43	72.32	27.11		0.00	0.00	99.43
Buckland Zone	Bulk	1665-D-43	44	69.98	29.33		0.00	0.01	99.32
Buckland Zone	Bulk	1665-D-44	45	72.98	26.87		0.00	0.02	99.88
Buckland Zone	Bulk	1665-D-45	46	78.04	22.46		0.00	0.00	100.50
Buckland Zone	Bulk	1665-D-46	47	66.67	32.77		0.13	0.02	99.59
Buckland Zone	Bulk	1665-D-47	48	69.38	29.74		0.00	0.00	99.12
Buckland Zone	Bulk	1665-D-48	49	83.25	15.98		0.00	0.03	99.26
Buckland Zone	Bulk	1665-D-49	50	64.46	33.82		0.02	0.02	98.32
Buckland Zone	Bulk	1665-D-50	51	76.34	23.50		0.04	0.02	99.89
Buckland Zone	Bulk	1665-D-51	52	80.90	18.67		0.00	0.04	99.60
Buckland Zone	Bulk	1665-D-52	53	70.55	28.82		0.00	0.03	99.40
Buckland Zone	Bulk	1665-D-53	54	75.45	25.23		0.00	0.00	100.69
Buckland Zone	Bulk	1665-D-54	55	82.38	17.50		0.01	0.02	99.92
Buckland Zone	Bulk	1665-D-55	56	82.83	16.52		0.00	0.01	99.37
Buckland Zone	Bulk	1665-D-56	57	76.42	22.76		0.18	0.01	99.36
Buckland Zone	Bulk	1665-D-57	58	75.06	24.95		0.00	0.00	100.01
Buckland Zone	Bulk	1665-D-58	59	73.18	25.33		0.00	0.00	98.51
Buckland Zone	Bulk	1665-D-59	60	67.27	32.00		0.00	0.03	99.30
Buckland Zone	Bulk	1665-D-60	61	70.44	29.21		0.00	0.01	99.67
Buckland Zone	Bulk	1665-D-61	62	70.48	28.82		0.07	0.01	99.37
Buckland Zone	Bulk	1665-D-62	63	71.94	27.83		0.04	0.00	99.80
Buckland Zone	Bulk	1665-D-63	64	69.28	29.62		0.00	0.02	98.92

Occurrence	Sample Type	Block and ID	Grain ID	Wt.% (Au)	Wt.% (Ag)	Wt.% (Fe)	Wt. % (Hg)	Wt.% (Cu)	Probe Total
Buckland Zone	Bulk	1665-D-64	65	76.98	22.10		0.00	0.02	99.10
Buckland Zone	Bulk	1665-D-65	66	83.53	15.90		0.00	0.01	99.44
Buckland Zone	Bulk	1665-D-66	67	71.33	27.82		0.08	0.00	99.22
Buckland Zone	Bulk	1665-D-67	68	79.51	20.10		0.00	0.00	99.61
Buckland Zone	Bulk	1665-D-68	69	70.82	28.16		0.00	0.02	99.00
Buckland Zone	Bulk	1665-D-69	70	66.80	32.41		0.00	0.00	99.21
Buckland Zone	Bulk	1665-D-70	71	68.20	30.48		0.03	0.02	98.72
Buckland Zone	Bulk	1665-D-71	72	76.13	23.69		0.00	0.01	99.82
Buckland Zone	Bulk	1665-D-72	73	73.77	25.52		0.01	0.00	99.30
Buckland Zone	Bulk	1665-D-73	74	76.03	22.95		0.00	0.02	99.00
Buckland Zone	Bulk	1665-D-74	75	76.52	22.89		0.00	0.00	99.41
Buckland Zone	Bulk	1665-D-75	76	80.06	19.68		0.00	0.00	99.74
Buckland Zone	Bulk	1665-D-76	77	79.03	20.82		0.08	0.02	99.95
Buckland Zone	Bulk	1665-D-77	78	62.26	36.36		0.73	0.00	99.35
Buckland Zone	Bulk	1665-D-78	79	78.85	20.01		0.00	0.00	98.86
Buckland Zone	Bulk	1665-D-79	80	73.21	26.38		0.00	0.00	99.59
Buckland Zone	Bulk	1665-D-80	81	83.81	16.73		0.00	0.03	100.57
Buckland Zone	Bulk	1665-D-81	82	82.27	17.08		0.00	0.01	99.35
Buckland Zone	Bulk	1665-D-82	83	78.33	21.44		0.08	0.00	99.85
Buckland Zone	Bulk	1665-D-83	84	80.06	19.53		0.03	0.02	99.63
Buckland Zone	Bulk	1665-D-84	85	80.52	17.96		0.00	0.00	98.48
Buckland Zone	Bulk	1665-D-85	86	70.39	28.45		0.00	0.00	98.83
Buckland Zone	Bulk	1665-D-86	87	77.33	22.78		0.00	0.02	100.12
Buckland Zone	Bulk	1665-D-87	88	76.50	21.88		0.00	0.01	98.39
Buckland Zone	Bulk	1665-D-88	89	76.95	22.65		0.00	0.02	99.62
Buckland Zone	Bulk	1665-D-89	90	80.41	19.79		0.00	0.00	100.21
Buckland Zone	Bulk	1665-D-90	91	61.98	36.27		0.71	0.00	98.95
Buckland Zone	Bulk	1665-D-91	92	79.62	19.78		0.02	0.00	99.42
Buckland Zone	Bulk	1665-D-92	93	81.13	19.47		0.00	0.00	100.60
Buckland Zone	Bulk	1665-D-93	94	79.35	20.74		0.00	0.04	100.12
Buckland Zone	Bulk	1665-D-94	95	80.28	19.46		0.00	0.01	99.74
Buckland Zone	Bulk	1665-D-95	96	78.15	22.00		0.00	0.03	100.18
Buckland Zone	Bulk	1665-D-96	97	82.36	17.61		0.13	0.02	100.12
Buckland Zone	Bulk	1665-D-97	98	79.78	19.13		0.00	0.00	98.91

Occurrence	Sample Type	Block and ID	Grain ID	Wt.% (Au)	Wt.% (Ag)	Wt.% (Fe)	Wt. % (Hg)	Wt.% (Cu)	Probe Total
Buckland Zone	Bulk	1665-D-98	99	70.18	29.21		0.00	0.04	99.43
Buckland Zone	Bulk	1665-D-99	100	76.57	23.77		0.00	0.01	100.35
Buckland Zone	Bulk	1665-D-100	101	79.75	20.70		0.00	0.01	100.46
Buckland Zone	Bulk	1665-D-102	103	76.59	22.71		0.00	0.02	99.33
Buckland Zone	Bulk	1665-D-103	104	80.81	18.59		0.00	0.00	99.40
Buckland Zone	Bulk	1665-D-104	105	77.28	22.88		0.04	0.00	100.20
Buckland Zone	Bulk	1665-D-105	106	81.93	17.99		0.00	0.03	99.96
Buckland Zone	Bulk	1665-D-106	107	76.62	23.26		0.00	0.01	99.89
Buckland Zone	Bulk	1665-D-107	108	78.29	21.32		0.00	0.01	99.62
Buckland Zone	Bulk	1665-D-108	109	74.49	24.89		0.02	0.02	99.41
Buckland Zone	Bulk	1665-D-109	110	81.03	19.04		0.00	0.02	100.09
Buckland Zone	Bulk	1665-D-110	111	79.41	20.11		0.00	0.00	99.52
Buckland Zone	Bulk	1665-D-111	112	79.04	20.61		0.00	0.00	99.64
Buckland Zone	Bulk	1665-D-112	113	82.27	17.21		0.00	0.00	99.49
Buckland Zone	Bulk	1665-D-113	114	77.92	22.54		0.07	0.02	100.54
Buckland Zone	Bulk	1665-D-114	115	69.34	29.69		0.00	0.01	99.03
Buckland Zone	Bulk	1665-D-115	116	75.32	24.81		0.00	0.01	100.15
Buckland Zone	Bulk	1665-D-116	117	74.68	24.63		0.00	0.03	99.35
Buckland Zone	Bulk	1665-D-117	118	74.81	24.07		0.09	0.00	98.97
Dysle Zone	Bulk	wrs 1572 8A		75.403	27.054	0	0	0	102.46
Dysle Zone	Bulk	wrs 1572 8B		70.927	29.853	0	0.617	0	101.4
Dysle Zone	Bulk	wrs 1572 8C		70.31	31.44	0.003	0	0	101.75
Dysle Zone	Bulk	wrs 1572 8D		74.531	27.493	0.005	0	0	102.03
Dysle Zone	Bulk	WRS 1572 B 8A		72.791	28.11	0.004	0	0	100.91
Dysle Zone	Bulk	WRS 1572 B 8B		78.571	21.853	0	0	0.008	100.43
Dysle Zone	Bulk	WRS 1572 B 8C		66.598	33.222	0	0	0	99.82
Dysle Zone	Bulk	WRS 1572 B 8D		67.821	32.762	0.01	0	0	100.59
Dysle Zone	Bulk	WRS 1572 B 8E		66.105	34.883	0.005	0.018	0	101.01
Dysle Zone	Bulk	WRS 1572 B 8F		70.148	29.209	0.024	0.012	0	99.393
Dysle Zone	Bulk	WRS 1572 B 8G		71.097	30.037	0.015	0.022	0.014	101.19
Dysle Zone	Bulk	WRS 1572 B 8H		75.079	24.98	0.02	0.305	0	100.38
Dysle Zone	Bulk	WRS 1572 C 4A		67.076	32.211	0.018	0	0.005	99.31
Dysle Zone	Bulk	WRS 1572 C 4B		69.754	29.474	0.019	0	0	99.247
Dysle Zone	Bulk	WRS 1572 C 4C		67.608	31.82	0.01	0	0	99.438

Occurrence	Sample Type	Block and ID	Grain ID	Wt.% (Au)	Wt.% (Ag)	Wt.% (Fe)	Wt. % (Hg)	Wt.% (Cu)	Probe Total
Dysle Zone	Bulk	WRS 1572 C 4D		72.366	27.38	0.019	0	0.023	99.788
Dysle Zone	Bulk	WRS 1572 C 4E		72.984	27.049	0.009	0	0	100.04
Dysle Zone	Bulk	WRS 1572 C 4F		73.083	25.341	0.007	0	0	98.431
Dysle Zone	Bulk	WRS 1572 C 4G		66.163	33.787	0.003	0	0	99.953
Dysle Zone	Bulk	WRS 1572 C 4H		71.836	27.145	0	0.299	0.002	99.282
Dysle Zone	Bulk	WRS 1572 C 4I		71.601	28.264	0.005	0.205	0	100.08
Dysle Zone	Bulk	WRS 1572 C 4J		72.085	27.62	0.028	0.002	0.013	99.748
Dysle Zone	Bulk	WRS 1572 C 4K		75.367	24.491	0	0	0	99.858
Dysle Zone	Bulk	WRS 1572 C 4L		74.97	24.891	0	0	0	99.861
Dysle Zone	Bulk	WRS 1572 C 4M		70.997	28.186	0	0	0	99.183
Dysle Zone	Bulk	WRS 1572 C 4N		70.449	29.297	0.038	0	0	99.784
Dysle Zone	Bulk	WRS 1572 C 4O		72.873	26.632	0.013	0.272	0	99.79
Dysle Zone	Bulk	WRS 1572 C P		69.326	29.469	0.022	0.061	0	98.878
Dysle Zone	Bulk	WRS 1572 C Q		73.239	25.699	0.017	0	0.016	98.971
Dysle Zone	Bulk	WRS 1572 C R		70.226	29.548	0.017	0	0	99.791
Dysle Zone	Bulk	WRS 1572 C S		71.566	28.088	0	0	0	99.654
Dysle Zone	Bulk	WRS 1572 C T		71.075	28.571	0.013	0	0	99.659
Dysle Zone	Bulk	WRS 1572 C U		67.036	32.965	0.011	0	0.005	100.02
Dysle Zone	Bulk	WRS 1572 C V		72.72	26.12	0.024	0.024	0.032	98.92
Dysle Zone	Bulk	WRS 1572 C W		62.707	36.608	0	0.267	0	99.582
Dysle Zone	Bulk	WRS 1572 C X		73.694	25.501	0.031	0	0	99.226
Dysle Zone	Bulk	WRS 1572 C Y		69.706	29.379	0.017	0.181	0	99.283
Dysle Zone	Bulk	WRS 1572 C Z		73.17	27.144	0	0	0	100.31
Dysle Zone	Bulk	WRS 1572 C A1		74.961	24.751	0.025	0	0	99.737
Dysle Zone	Bulk	WRS 1572 C B1		72.102	27.165	0.011	0	0	99.278
Dysle Zone	Bulk	WRS 1572 C C1		62.635	36.869	0.026	0.137	0	99.667
Dysle Zone	Bulk	WRS 1572 C C1 DARK		46.665	52.994	0.002	0.667	0.002	100.33
Dysle Zone	Bulk	WRS 1572 C D1		72.401	26.928	0	0.541	0.006	99.876
Dysle Zone	Bulk	WRS 1572 C E1		68.142	31.462	0.014	0	0	99.618
Dysle Zone	Bulk	WRS 1572 C f1		71.598	27.892	0.022	0	0.005	99.517
Dysle Zone	Bulk	WRS 1572 C G1		71.923	27.719	0.009	0	0	99.651
Dysle Zone	Bulk	WRS 1572 C H1		73.983	25.116	0.014	0	0	99.113
Dysle Zone	Bulk	WRS 1572 C I1		64.067	35.591	0	0.007	0.009	99.674

Occurrence	Sample Type	Block and ID	Grain ID	Wt.% (Au)	Wt.% (Ag)	Wt.% (Fe)	Wt. % (Hg)	Wt.% (Cu)	Probe Total
Dysle Zone	2013 Crushed Vein	RC40_9_1		69.7176	29.3825		0.117044	0.016851	99.234
Dysle Zone	2013 Crushed Vein	RC40_9_2		69.7706	29.7826		0.16786	0.002142	99.723
Dysle Zone	2013 Crushed Vein	RC40_9_3		73.3955	25.7633		0.181104	0.015145	99.355
Dysle Zone	2013 Crushed Vein	RC40_9_4		72.5854	26.6561		0.067173	0.022905	99.332
Dysle Zone	2013 Crushed Vein	RC40_9_5		71.5949	27.8675		0.120332	0.028786	99.612
Dysle Zone	2013 Crushed Vein	RC40_9_6		74.8537	24.5202		0.047679	0.016668	99.438
Dysle Zone	2013 Crushed Vein	RC40_9_7		73.3107	26.2485		0.103889	0.002814	99.666
Dysle Zone	2013 Crushed Vein	RC40_9_8		74.0743	25.6254		0.126441	0.024182	99.85
Dysle Zone	2013 Crushed Vein	RC40_9_9		71.301	28.2424		0.175995	0.023533	99.743
Dysle Zone	2013 Crushed Vein	RC41_8_1		74.515	24.9058		0.162581	0.019307	99.603
Dysle Zone	2013 Crushed Vein	RC41_8_2		70.5541	29.4375		0.132174	0.023354	100.15
Dysle Zone	2013 Crushed Vein	RC41_8_3		69.1025	30.4974		0.217989	0.007989	99.826
Dysle Zone	2013 Crushed Vein	RC41_8_4		73.1227	26.1266		0.096587	0.007758	99.354
Dysle Zone	2013 Crushed Vein	RC41_8_5		72.8569	26.9927		0.139592	0.021371	100.01
Dysle Zone	2013 Crushed Vein	RC41_8_6		73.3069	26.2786		0.066334	0.018555	99.67
Dysle Zone	2013 Crushed Vein	RC41_8_7		76.0982	24.0533		0.247621	0.009921	100.41
Dysle Zone	2013 Crushed Vein	RC41_8_8		69.3185	30.2845		0.121243	0.005679	99.73
Dysle Zone	2013 Crushed Vein	RC41_8_9		75.4336	24.9075		0.101138	0.023647	100.47
Dysle Zone	2013 Crushed Vein	RC44_8_1		73.3369	27.4871		0.204821	0.018591	101.05
Dysle Zone	2013 Crushed Vein	RC44_8_10		73.8625	26.7801		0.282217	0.005252	100.93
Dysle Zone	2013 Crushed Vein	RC44_8_11		74.0698	26.4951		0.234926	0.021153	100.82
Dysle Zone	2013 Crushed Vein	RC44_8_12		72.7366	28.1423		0.172198	0.002733	101.05
Dysle Zone	2013 Crushed Vein	RC44_8_13		70.9024	29.508		0.225612	0.00138	100.64
Dysle Zone	2013 Crushed Vein	RC44_8_2		75.9907	24.7955		0.087875	0.033081	100.91
Dysle Zone	2013 Crushed Vein	RC44_8_3		75.1993	25.104		0.221744	0.018118	100.54
Dysle Zone	2013 Crushed Vein	RC44_8_4		76.4326	24.1138		0.133066	0.008527	100.69
Dysle Zone	2013 Crushed Vein	RC44_8_5		71.2035	29.7108		0.06911	0.015129	101
Dysle Zone	2013 Crushed Vein	RC44_8_6		72.2129	28.5485		0.226301	0.02747	101.02
Dysle Zone	2013 Crushed Vein	RC44_8_7		75.7894	24.7346		0.240684	0.012575	100.78
Dysle Zone	2013 Crushed Vein	RC44_8_8		71.1396	29.2697		0.130105	0.0174	100.56
Dysle Zone	2013 Crushed Vein	RC44_8_9		69.2707	31.3163		0.164385	0.004341	100.76
Dysle Zone	2013 Crushed Vein	RC45_8_1		70.5311	29.8444		0.243994	0.016511	100.64
Dysle Zone	2013 Crushed Vein	RC45_8_2		70.6575	29.6549		0.312655	0.013218	100.64
Dysle Zone	2013 Crushed Vein	RC45_8_3		74.0633	26.1731		0.272351	0.016532	100.53

Occurrence	Sample Type	Block and ID	Grain ID	Wt.% (Au)	Wt.% (Ag)	Wt.% (Fe)	Wt. % (Hg)	Wt.% (Cu)	Probe Total
Dysle Zone	2013 Crushed Vein	RC45_8_4		72.6426	27.8034		0.184669	-0.0014	100.63
Dysle Zone	2013 Crushed Vein	RC45_8_5		68.8343	31.4265		0.217697	0.029804	100.51
Nugget Zone	2013 Crushed Vein	RC41_9a_1		82.2475	17.7775		0.129784	0.041166	100.2
Nugget Zone	2013 Crushed Vein	RC41_9a_10		83.15	16.5937		0.133772	0.032094	99.91
Nugget Zone	2013 Crushed Vein	RC41_9a_11		82.2329	17.6232		0.086534	0.025402	99.968
Nugget Zone	2013 Crushed Vein	RC41_9a_12		79.3615	20.3938		0.175812	0.022764	99.954
Nugget Zone	2013 Crushed Vein	RC41_9a_13		80.9409	18.988		0.133152	0.010752	100.07
Nugget Zone	2013 Crushed Vein	RC41_9a_14		78.4135	21.4474		0.092036	0.032342	99.985
Nugget Zone	2013 Crushed Vein	RC41_9a_15		69.874	29.9592		0.140196	0.000826	99.974
Nugget Zone	2013 Crushed Vein	RC41_9a_16		81.1737	18.6294		0.233491	0.028312	100.07
Nugget Zone	2013 Crushed Vein	RC41_9a_17		83.1532	16.6288		0.166223	0.008165	99.956
Nugget Zone	2013 Crushed Vein	RC41_9a_18		82.4911	17.3787		0.153564	0.014328	100.04
Nugget Zone	2013 Crushed Vein	RC41_9a_19		83.8089	16.1381		0.181774	0.005485	100.13
Nugget Zone	2013 Crushed Vein	RC41_9a_2		80.8602	19.0734		0.162166	0.025057	100.12
Nugget Zone	2013 Crushed Vein	RC41_9a_20		80.3769	19.4428		0.146843	0.015559	99.982
Nugget Zone	2013 Crushed Vein	RC41_9a_21		79.088	20.8661		0.151155	0.016796	100.12
Nugget Zone	2013 Crushed Vein	RC41_9a_22A		83.1072	16.6956		0.189633	0.017753	100.01
Nugget Zone	2013 Crushed Vein	RC41_9a_22B		83.2714	16.5595		0.172633	0.026287	100.03
Nugget Zone	2013 Crushed Vein	RC41_9a_23		82.1111	17.7596		0.110907	0.030426	100.01
Nugget Zone	2013 Crushed Vein	RC41_9a_24		81.7998	17.9726		0.167818	0.007191	99.947
Nugget Zone	2013 Crushed Vein	RC41_9a_25		81.6484	17.9529		0.150109	0.032929	99.784
Nugget Zone	2013 Crushed Vein	RC41_9a_3		83.2019	16.6691		0.207423	0.002148	100.08
Nugget Zone	2013 Crushed Vein	RC41_9a_4		69.7663	29.79		0.133818	0.009037	99.699
Nugget Zone	2013 Crushed Vein	RC41_9a_5		82.8581	17.4949		0.116863	0.024485	100.49
Nugget Zone	2013 Crushed Vein	RC41_9a_6		83.4124	16.7662		0.097405	0.025965	100.3
Nugget Zone	2013 Crushed Vein	RC41_9a_7		83.3069	16.8775		0.108344	0.013841	100.31
Nugget Zone	2013 Crushed Vein	RC41_9a_8		80.0942	19.6771		0.138287	0.031968	99.942
Nugget Zone	2013 Crushed Vein	RC41_9a_9		73.8613	25.9701		0.099296	0.028783	99.959
Nugget Zone	2013 Crushed Vein	RC41_9b_1		73.403	26.1439		0.190632	0.006682	99.744
Nugget Zone	2013 Crushed Vein	RC41_9b_10		77.2644	21.8124		0.12525	0.013389	99.215
Nugget Zone	2013 Crushed Vein	RC41_9b_2		77.5098	22.213		0.125097	0.016868	99.865
Nugget Zone	2013 Crushed Vein	RC41_9b_3		77.7535	21.8923		0.089009	0.008988	99.744
Nugget Zone	2013 Crushed Vein	RC41_9b_4		79.9181	19.9971		0.16003	0.019557	100.1
Nugget Zone	2013 Crushed Vein	RC41_9b_5		83.5273	16.465		0.199459	0.030054	100.22

Occurrence	Sample Type	Block and ID	Grain ID	Wt.% (Au)	Wt.% (Ag)	Wt.% (Fe)	Wt. % (Hg)	Wt.% (Cu)	Probe Total
Nugget Zone	2013 Crushed Vein	RC41_9b_6		74.3635	26.449		0.151741	0.016349	100.98
Nugget Zone	2013 Crushed Vein	RC41_9b_7		65.1874	33.9422		0.129834	0.020172	99.28
Nugget Zone	2013 Crushed Vein	RC41_9b_8		69.1311	30.9061		0.098814	0.020897	100.16
Nugget Zone	2013 Crushed Vein	RC41_9b_9		82.3261	17.9525		0.137249	0.015475	100.43
Nugget Zone	2013 Crushed Vein	RC43_5_1		69.7713	30.5204		0.136721	0.020504	100.45
Nugget Zone	2013 Crushed Vein	RC43_5_2		83.0684	16.7662		0.150443	0.017799	100
Nugget Zone	2013 Crushed Vein	RC43_5_3		81.8172	18.1386		0.166434	0.020455	100.14
Nugget Zone	2013 Crushed Vein	RC43_5_4		80.7354	17.9515		0.174525	0.017603	98.879
Nugget Zone	2013 Crushed Vein	RC43_5_5		81.4527	17.834		0.127284	0.021113	99.435
Nugget Zone	2013 Crushed Vein	RC43_5_6		82.6671	17.1178		0.213589	0.025399	100.02
Nugget Zone	2013 Crushed Vein	RC44_10_10		83.187	17.4453		0.247295	0.038653	100.92
Nugget Zone	2013 Crushed Vein	RC44_10_11		76.3522	24.6419		0.199902	0.019845	101.21
Nugget Zone	2013 Crushed Vein	RC44_10_12		80.4548	20.2086		0.097785	0.02449	100.79
Nugget Zone	2013 Crushed Vein	RC44_10_13		83.3325	17.2971		0.175906	0.019232	100.83
Nugget Zone	2013 Crushed Vein	RC44_10_14		83.7	17.2478		0.175994	0.010648	101.13
Nugget Zone	2013 Crushed Vein	RC44_10_15		83.8172	16.8565		0.161884	0.028501	100.86
Nugget Zone	2013 Crushed Vein	RC44_10_16		77.6589	22.9455		0.110154	0.013142	100.73
Nugget Zone	2013 Crushed Vein	RC44_10_17		82.0286	18.9892		0.197547	0.022631	101.24
Nugget Zone	2013 Crushed Vein	RC44_10_18		80.4581	20.4797		0.125643	0.026758	101.09
Nugget Zone	2013 Crushed Vein	RC44_10_19		82.76	18.1656		0.140858	0.035075	101.1
Nugget Zone	2013 Crushed Vein	RC44_10_2		82.1949	18.3723		0.19115	0.029078	100.79
Nugget Zone	2013 Crushed Vein	RC44_10_20		80.6545	20.0976		0.179441	0.021903	100.95
Nugget Zone	2013 Crushed Vein	RC44_10_21		84.3751	16.8001		0.139271	0.028558	101.34
Nugget Zone	2013 Crushed Vein	RC44_10_22		70.248	30.2372		0.161826	0.012514	100.66
Nugget Zone	2013 Crushed Vein	RC44_10_23		82.1984	18.0622		0.162791	0.0262	100.45
Nugget Zone	2013 Crushed Vein	RC44_10_24		83.9253	17.125		0.14425	0.020436	101.22
Nugget Zone	2013 Crushed Vein	RC44_10_3		80.3099	20.561		0.138004	0.029881	101.04
Nugget Zone	2013 Crushed Vein	RC44_10_4		83.1097	17.4293		0.127164	0.028155	100.69
Nugget Zone	2013 Crushed Vein	RC44_10_5		81.839	18.6893		0.098702	0.02775	100.66
Nugget Zone	2013 Crushed Vein	RC44_10_6		81.7211	18.7341		0.121238	0.023393	100.6
Nugget Zone	2013 Crushed Vein	RC44_10_7		69.8758	31.0272		0.078697	0.029279	101.01
Nugget Zone	2013 Crushed Vein	RC44_10_8		84.822	15.9163		0.230476	0.010314	100.98
Nugget Zone	2013 Crushed Vein	RC44_10_9		77.063	23.3254		0.189157	0.00565	100.58
Nugget Zone	2013 Crushed Vein	RC45_10a_1		0.216304	0.080016		0.008378	-0.00247	0.3022

Occurrence	Sample Type	Block and ID	Grain ID	Wt.% (Au)	Wt.% (Ag)	Wt.% (Fe)	Wt. % (Hg)	Wt.% (Cu)	Probe Total
Nugget Zone	2013 Crushed Vein	RC45_10a_10		80.0588	20.0657		0.195144	0.01276	100.33
Nugget Zone	2013 Crushed Vein	RC45_10a_11		80.4932	19.5219		0.155347	0.018137	100.19
Nugget Zone	2013 Crushed Vein	RC45_10a_12		79.6805	20.4878		0.164506	0.005061	100.34
Nugget Zone	2013 Crushed Vein	RC45_10a_13		82.5437	18.2506		0.09043	0.012971	100.9
Nugget Zone	2013 Crushed Vein	RC45_10a_14		83.2381	17.1077		0.206638	0.024657	100.58
Nugget Zone	2013 Crushed Vein	RC45_10a_15		77.8777	22.6735		0.191788	0.013033	100.76
Nugget Zone	2013 Crushed Vein	RC45_10a_16		81.5708	18.6057		0.152771	0.015809	100.35
Nugget Zone	2013 Crushed Vein	RC45_10a_17		84.0225	16.8189		0.128824	0.027905	101
Nugget Zone	2013 Crushed Vein	RC45_10a_18		72.6458	26.9846		0.06431	0.017042	99.712
Nugget Zone	2013 Crushed Vein	RC45_10a_19		82.9976	17.8684		0.115192	0.023272	101
Nugget Zone	2013 Crushed Vein	RC45_10a_2		73.6402	26.2181		0.123044	0.011723	99.993
Nugget Zone	2013 Crushed Vein	RC45_10a_20		80.3362	20.0855		0.148373	0.018346	100.59
Nugget Zone	2013 Crushed Vein	RC45_10a_21		71.974	28.6163		0.102641	0.011536	100.71
Nugget Zone	2013 Crushed Vein	RC45_10a_22		75.7782	24.2937		0.068944	0.007917	100.15
Nugget Zone	2013 Crushed Vein	RC45_10a_23		68.2395	32.1366		0.109556	0.019115	100.51
Nugget Zone	2013 Crushed Vein	RC45_10a_24		73.2262	27.1606		0.143422	0.027066	100.56
Nugget Zone	2013 Crushed Vein	RC45_10a_25		82.2224	18.933		0.134253	0.013407	101.3
Nugget Zone	2013 Crushed Vein	RC45_10a_26		82.4474	18.12		0.121908	0.0214	100.71
Nugget Zone	2013 Crushed Vein	RC45_10a_27		78.0394	22.9809		0.178721	0.017041	101.22
Nugget Zone	2013 Crushed Vein	RC45_10a_28		82.0314	18.3493		0.134631	0.030133	100.55
Nugget Zone	2013 Crushed Vein	RC45_10a_3		77.6388	22.7461		0.184393	0.021343	100.59
Nugget Zone	2013 Crushed Vein	RC45_10a_4		80.9744	19.3235		0.102289	0.035279	100.44
Nugget Zone	2013 Crushed Vein	RC45_10a_5		82.0058	18.2039		0.176754	0.026334	100.41
Nugget Zone	2013 Crushed Vein	RC45_10a_6		80.6768	19.6961		0.133275	0.022709	100.53
Nugget Zone	2013 Crushed Vein	RC45_10a_7		78.3337	21.9627		0.158137	0.019532	100.47
Nugget Zone	2013 Crushed Vein	RC45_10a_8		73.5713	26.8335		0.166209	0.01161	100.58
Nugget Zone	2013 Crushed Vein	RC45_10a_9		79.5762	20.9422		0.169031	0.018316	100.71
Nugget Zone	2013 Crushed Vein	RC45_10b_1		86.2342	14.3046		0.231952	0.012115	100.78
Nugget Zone	2013 Crushed Vein	RC45_10b_10		83.3294	17.0065		0.127699	0.025431	100.49
Nugget Zone	2013 Crushed Vein	RC45_10b_11		82.3262	18.1336		0.138052	0.0223	100.62
Nugget Zone	2013 Crushed Vein	RC45_10b_12		73.6442	26.7095		0.151431	0.014309	100.52
Nugget Zone	2013 Crushed Vein	RC45_10b_13		81.4544	18.737		0.16915	0.022591	100.38
Nugget Zone	2013 Crushed Vein	RC45_10b_14		69.5039	31.1358		0.111239	0.01092	100.76
Nugget Zone	2013 Crushed Vein	RC45_10b_15		81.5802	18.1794		0.121034	0.017018	99.898

Occurrence	Sample Type	Block and ID	Grain ID	Wt.% (Au)	Wt.% (Ag)	Wt.% (Fe)	Wt. % (Hg)	Wt.% (Cu)	Probe Total
Nugget Zone	2013 Crushed Vein	RC45_10b_16		83.0467	16.4319		0.12191	0.019277	99.62
Nugget Zone	2013 Crushed Vein	RC45_10b_17		83.2175	17.236		0.133463	0.014039	100.6
Nugget Zone	2013 Crushed Vein	RC45_10b_18		77.8523	22.4895		0.211659	0.035463	100.59
Nugget Zone	2013 Crushed Vein	RC45_10b_2		82.5611	17.7998		0.18019	0.037161	100.58
Nugget Zone	2013 Crushed Vein	RC45_10b_3		73.9714	25.2352		0.16946	0.009237	99.385
Nugget Zone	2013 Crushed Vein	RC45_10b_4		83.9862	16.2452		0.225222	0.019331	100.48
Nugget Zone	2013 Crushed Vein	RC45_10b_5		67.6987	32.1847		0.175846	0.019289	100.08
Nugget Zone	2013 Crushed Vein	RC45_10b_6		83.2196	17.2095		0.123695	0.026554	100.58
Nugget Zone	2013 Crushed Vein	RC45_10b_7		74.3382	25.636		0.134231	0.024886	100.13
Nugget Zone	2013 Crushed Vein	RC45_10b_8		79.1443	20.965		0.200787	0.008008	100.32
Nugget Zone	2013 Crushed Vein	RC45_10b_9		81.0877	18.5875		0.190661	0.014845	99.881
Nugget Zone	2013 Crushed Vein	RC45_10c_1		82.3274	18.0289		0.151999	0.057276	100.57
Nugget Zone	2013 Crushed Vein	RC45_10c_10		82.4304	18.0334		0.193211	0.025669	100.68
Nugget Zone	2013 Crushed Vein	RC45_10c_11		77.1212	23.6295		0.114021	0.014433	100.88
Nugget Zone	2013 Crushed Vein	RC45_10c_12		80.9485	19.6759		0.16962	0.020203	100.81
Nugget Zone	2013 Crushed Vein	RC45_10c_13		82.0307	18.925		0.257549	0.030416	101.24
Nugget Zone	2013 Crushed Vein	RC45_10c_2		69.6891	32.2975		0.06323	0.041146	102.09
Nugget Zone	2013 Crushed Vein	RC45_10c_3		83.8732	16.7564		0.150947	0.035027	100.82
Nugget Zone	2013 Crushed Vein	RC45_10c_4		78.8035	21.8646		0.186993	0.031356	100.89
Nugget Zone	2013 Crushed Vein	RC45_10c_5		78.7372	22.5981		0.123402	0.031753	101.49
Nugget Zone	2013 Crushed Vein	RC45_10c_6		69.2102	31.175		0.108219	0.051126	100.55
Nugget Zone	2013 Crushed Vein	RC45_10c_7		83.578	17.2544		0.193846	0.044714	101.07
Nugget Zone	2013 Crushed Vein	RC45_10c_8		74.0504	25.7053		0.154949	0.043864	99.955
Nugget Zone	2013 Crushed Vein	RC45_10c_9		73.1801	27.2538		0.057128	0.017221	100.51
Nugget Zone	2013 Crushed Vein	RC46_2a_1		69.4778	31.1348		0.097584	0.008931	100.72
Nugget Zone	2013 Crushed Vein	RC46_2a_10		63.8115	36.756		0.173806	0.025537	100.77
Nugget Zone	2013 Crushed Vein	RC46_2a_11		83.2119	16.5843		0.231294	0.020204	100.05
Nugget Zone	2013 Crushed Vein	RC46_2a_12		81.3368	19.3288		0.124543	0.022095	100.81
Nugget Zone	2013 Crushed Vein	RC46_2a_13		78.7216	21.1163		0.207346	0.022501	100.07
Nugget Zone	2013 Crushed Vein	RC46_2a_14		69.3478	31.2708		0.079487	0.01209	100.71
Nugget Zone	2013 Crushed Vein	RC46_2a_15		82.918	17.404		0.120901	0.02547	100.47
Nugget Zone	2013 Crushed Vein	RC46_2a_16		82.1669	18.1271		0.115002	0.020084	100.43
Nugget Zone	2013 Crushed Vein	RC46_2a_17		80.5922	19.6208		0.140261	0.028102	100.38
Nugget Zone	2013 Crushed Vein	RC46_2a_18		73.2194	27.3497		0.210773	0.010947	100.79

Occurrence	Sample Type	Block and ID	Grain ID	Wt.% (Au)	Wt.% (Ag)	Wt.% (Fe)	Wt. % (Hg)	Wt.% (Cu)	Probe Total
Nugget Zone	2013 Crushed Vein	RC46_2a_19		72.0895	28.1069		0.208791	0.018084	100.42
Nugget Zone	2013 Crushed Vein	RC46_2a_2		65.9808	33.738		0.086002	0.008682	99.813
Nugget Zone	2013 Crushed Vein	RC46_2a_20		73.1071	27.6327		0.165876	0.019399	100.93
Nugget Zone	2013 Crushed Vein	RC46_2a_21		75.6843	24.7016		0.156757	0.009146	100.55
Nugget Zone	2013 Crushed Vein	RC46_2a_22		83.769	17.3001		0.217144	0.02374	101.31
Nugget Zone	2013 Crushed Vein	RC46_2a_3		82.4373	17.7485		0.125566	0.026203	100.34
Nugget Zone	2013 Crushed Vein	RC46_2a_4		83.5001	16.7875		0.18074	0.03365	100.5
Nugget Zone	2013 Crushed Vein	RC46_2a_5		81.055	19.7007		0.196201	0.02365	100.98
Nugget Zone	2013 Crushed Vein	RC46_2a_6		78.9586	21.4822		0.166252	0.010896	100.62
Nugget Zone	2013 Crushed Vein	RC46_2a_7		68.6208	31.2748		0.073437	0.006028	99.975
Nugget Zone	2013 Crushed Vein	RC46_2a_8		75.0847	25.6044		0.085847	0.000115	100.78
Nugget Zone	2013 Crushed Vein	RC46_2a_9		73.6552	26.4323		0.133736	-0.00276	100.22
Nugget Zone	2013 Crushed Vein	RC46_2b_1		78.5401	21.5161		0.226959	0.001432	100.29
Nugget Zone	2013 Crushed Vein	RC46_2b_2		80.9884	18.9799		0.116086	0.017992	100.1
Nugget Zone	2013 Crushed Vein	RC46_2b_3		79.9952	20.5082		0.172562	0.030474	100.71
Nugget Zone	2013 Crushed Vein	RC46_2b_4		83.9072	18.5956		0.231954	0.034393	102.77
Nugget Zone	2013 Crushed Vein	RC46_2b_5		83.3661	17.0643		0.240061	0.018933	100.69
Nugget Zone	2013 Crushed Vein	RC46_2b_6		82.0387	20.576		0.179468	0.011746	102.81
Nugget Zone	2013 Crushed Vein	RC46_2b_7		80.0697	20.0177		0.188789	0.017716	100.29
Nugget Zone	2013 Crushed Vein	RC46_2c_1		83.6873	16.2679		0.1654	0.030231	100.15
Nugget Zone	2013 Crushed Vein	RC46_2c_10		83.4439	16.7796		0.090194	0.03304	100.35
Nugget Zone	2013 Crushed Vein	RC46_2c_11		83.8671	17.0164		0.162457	0.015596	101.06
Nugget Zone	2013 Crushed Vein	RC46_2c_12		76.5866	23.3961		0.166075	0.014634	100.16
Nugget Zone	2013 Crushed Vein	RC46_2c_13		68.3658	31.1022		0.184287	0.009476	99.662
Nugget Zone	2013 Crushed Vein	RC46_2c_13		74.4544	25.6172		0.125586	0.018845	100.22
Nugget Zone	2013 Crushed Vein	RC46_2c_14		72.1954	28.7112		0.216967	0.017903	101.14
Nugget Zone	2013 Crushed Vein	RC46_2c_15		82.9156	17.139		0.084008	0.016013	100.16
Nugget Zone	2013 Crushed Vein	RC46_2c_16		81.9981	18.4311		0.209288	0.012646	100.65
Nugget Zone	2013 Crushed Vein	RC46_2c_2		69.1133	30.5446		0.160122	0.007777	99.826
Nugget Zone	2013 Crushed Vein	RC46_2c_3		64.9441	35.6036		0.10254	0.007898	100.66
Nugget Zone	2013 Crushed Vein	RC46_2c_4		69.0707	31.6867		0.160198	0.021622	100.94
Nugget Zone	2013 Crushed Vein	RC46_2c_5		79.8042	20.5798		0.117384	0.018388	100.52
Nugget Zone	2013 Crushed Vein	RC46_2c_6		83.3795	16.6353		0.131413	0.012114	100.16
Nugget Zone	2013 Crushed Vein	RC46_2c_7		69.3817	31.3651		0.036754	0.010887	100.79

Occurrence	Sample Type	Block and ID	Grain ID	Wt.% (Au)	Wt.% (Ag)	Wt.% (Fe)	Wt. % (Hg)	Wt.% (Cu)	Probe Total	
Nugget Zone	2013 Crushed Vein	RC46_2c_8		83.7795	16.4969		0.155576	0.010634	100.44	
Nugget Zone	2013 Crushed Vein	RC46_2c_9		82.5894	17.7147		0.24907	0.005855	100.56	
Boulder Mine	Lode	2013 Crushed Vein	RC40_8_1A		83.4561	16.0117		0.087654	0.02388	99.579
Boulder Mine	Lode	2013 Crushed Vein	RC40_8_1B		83.6611	16.2041		0.135864	0.014667	100.02
Boulder Mine	Lode	2013 Crushed Vein	RC40_8_2		83.9421	15.8476		0.159622	0.006337	99.956
Boulder Mine	Lode	2013 Crushed Vein	RC41_7_1A		83.1873	17.0151		0.153158	0.028874	100.39
Boulder Mine	Lode	2013 Crushed Vein	RC41_7_2A		77.2124	22.4887		0.105512	0.023851	99.831
Boulder Mine	Lode	2013 Crushed Vein	RC41_7_2B		76.9332	21.7316		0.064184	0.03734	98.766
Boulder Mine	Lode	2013 Crushed Vein	RC44_7_1		84.1164	15.9673		0.112821	0.098026	100.3
Boulder Mine	Lode	2013 Crushed Vein	RC44_7_10		82.6725	17.7431		0.154202	0.030205	100.6
Boulder Mine	Lode	2013 Crushed Vein	RC44_7_11		84.3163	15.6086		0.212787	0.028535	100.17
Boulder Mine	Lode	2013 Crushed Vein	RC44_7_2		84.1693	16.5531		0.132448	0.035113	100.89
Boulder Mine	Lode	2013 Crushed Vein	RC44_7_3		83.4087	16.7023		0.049574	0.034123	100.2
Boulder Mine	Lode	2013 Crushed Vein	RC44_7_4		85.0282	15.4871		0.099621	0.034168	100.65
Boulder Mine	Lode	2013 Crushed Vein	RC44_7_5		83.2147	16.5123		0.056802	0.047622	99.831
Boulder Mine	Lode	2013 Crushed Vein	RC44_7_6		84.1509	16.0205		0.151581	0.016266	100.34
Boulder Mine	Lode	2013 Crushed Vein	RC44_7_7		83.7971	16.6386		0.152483	0.030242	100.62
Boulder Mine	Lode	2013 Crushed Vein	RC44_7_8		84.0184	16.5925		0.12033	0.063329	100.8

Occurrence	Sample Type	Block and ID	Grain ID	Wt.% (Au)	Wt.% (Ag)	Wt.% (Fe)	Wt. % (Hg)	Wt.% (Cu)	Probe Total	
Boulder Mine	Lode	2013 Crushed Vein	RC44_7_9		75.5656	24.45		0.169378	0.034012	100.22
Boulder Mine	Lode	2013 Crushed Vein	RC45_6_1		80.1376	20.2135		0.174024	0.016541	100.54
Boulder Mine	Lode	2013 Crushed Vein	RC45_6_2		82.4342	18.0904		0.186343	0.036163	100.75
Boulder Mine	Lode	2013 Crushed Vein	RC45_6_3		79.242	21.1726		0.115866	0.019201	100.55
Boulder Mine	Lode	2013 Crushed Vein	RC45_6_4		83.416	17.3876		0.175458	0.020309	101
Boulder Mine	Lode	2013 Crushed Vein	RC45_6_5		80.6687	19.8554		0.209992	0.015612	100.75
Boulder Mine	Lode	2013 Crushed Vein	RC45_6_6		83.6531	17.2642		0.158865	0.029431	101.11
Boulder Mine	Lode	2013 Crushed Vein	RC45_6_7		84.3667	16.2827		0.082943	0.031099	100.76
Violet Mine	Bulk	WRS 1463 B VIOLET 2A		66.987	31.405	0.005	1.907	0		100.3
Violet Mine	Bulk	WRS 1463 B VIOLET 2B		74.378	25.058	0.014	1.251	0		100.7
Violet Mine	Bulk	WRS 1463 B VIOLET 2C/1		78.356	21.37	0.006	1.309	0.002		101.04
Violet Mine	Bulk	WRS 1463 B VIOLET 2D		81.271	19.161	0.014	0.64	0.012		101.1
Violet Mine	Bulk	WRS 1463 B VIOLET 2E		66.462	31.828	0	2.137	0		100.43
Violet Mine	Bulk	WRS 1463 B VIOLET 2F		72.725	26.555	0.012	1.71	0		101
Violet Mine	Bulk	WRS 1463 B VIOLET 2G		69.275	30.612	0	0.356	0		100.24
Violet Mine	Bulk	WRS 1463 B VIOLET 2H		69.746	30.166	0	0.828	0		100.75
Violet Mine	Bulk	WRS 1463 B VIOLET 2I		66.306	32.798	0.004	0.685	0		99.793

Occurrence	Sample Type	Block and ID	Grain ID	Wt.% (Au)	Wt.% (Ag)	Wt.% (Fe)	Wt. % (Hg)	Wt.% (Cu)	Probe Total
Violet Mine	Bulk	WRS 1463 B VIOLET 2J		66.573	33.491	0.003	0.314	0	100.38
Violet Mine	Bulk	WRS 1463 B VIOLET 2L		68.538	31.041	0	1.483	0	101.06
Violet Mine	Bulk	WRS 1463 B VIOLET 2LDPR		36.21	54.35	0	9.067	0	99.627
Violet Mine	Bulk	WRS 1463 B VIOLET 2M		81.467	18.664	0.02	0.591	0.02	100.76
Violet Mine	Bulk	WRS 1463 B VIOLET 2N		81.294	18.828	0.019	0.726	0.013	100.88
Violet Mine	Bulk	WRS 1463 B VIOLET 2O C		74.876	24.392	0.024	1.375	0	100.68
Violet Mine	Bulk	WRS 1463 B VIOLET 2O D2		50.868	43.548	0	6.182	0	100.6
Violet Mine	Bulk	WRS 1463 B VIOLET 3A A		86.212	13.893	0.027	0.907	0.02	101.06
Violet Mine	Bulk	WRS 1463 B VIOLET 3A B		66.868	33.189	0.007	0.387	0	100.45
Violet Mine	Bulk	WRS 1463 B VIOLET 3A C		65.158	33.053	0	1.911	0	100.13
Violet Mine	Bulk	WRS 1463 B VIOLET 3A D		73.273	26.374	0.02	0.855	0	100.52
Violet Mine	Bulk	WRS 1463 B VIOLET 3A E		70.898	28.249	0	0.829	0	99.978
Violet Mine	Bulk	WRS 1463 B VIOLET 3A G		69.239	30.661	0.003	0.264	0	100.17
Violet Mine	Bulk	WRS 1463 B VIOLET 3A H		67.865	31.95	0	0.917	0	100.73
Violet Mine	Bulk	WRS 1463 B VIOLET 3A I		69.596	29.124	0.01	1.355	0	100.09
Violet Mine	Bulk	WRS 1463 B VIOLET 3A J		68.051	31.247	0	1.061	0	100.36
Violet Mine	Bulk	WRS 1463 B VIOLET 3A K		64.875	34.481	0	1.277	0	100.63

Occurrence	Sample Type	Block and ID	Grain ID	Wt.% (Au)	Wt.% (Ag)	Wt.% (Fe)	Wt. % (Hg)	Wt.% (Cu)	Probe Total
Violet Mine	Bulk	WRS 1463 B VIOLET 3A L		65.93	32.625	0	1.37	0	99.936
Violet Mine	Bulk	WRS 1463 B VIOLET 3A M		62.287	36.305	0.017	1.206	0	99.815
Violet Mine	Bulk	WRS 1463 B VIOLET 3A N		70.09	29.163	0.004	0.792	0	100.05
Violet Mine	Bulk	WRS 1463 B VIOLET 3A O		67.138	32.292	0	0.727	0	100.16
Violet Mine	Bulk	WRS 1463 B VIOLET 3A P		83.089	17.134	0.015	0.633	0.038	100.91
Violet Mine	Bulk	WRS 1463 B VIOLET 3A Q		65.104	33.91	0	1.27	0	100.29
Violet Mine	Bulk	WRS 1463 B VIOLET 3A R		65.809	33.369	0.005	0.742	0	99.925
Violet Mine	Bulk	WRS 1463 B VIOLET 3A SD2		52.45	42.326	0	4.275	0	99.051
Violet Mine	Bulk	WRS 1463 B VIOLET 3A S		69.99	27.67	0.005	0.635	0	98.3
Violet Mine	Bulk	WRS 1463 B VIOLET 3A T		73.125	25.923	0.004	0.564	0.009	99.625
Violet Mine	Bulk	WRS 1463 B VIOLET 3A U		79.874	20.108	0.023	0.663	0.031	100.7
Violet Mine	Bulk	WRS 1463 B VIOLET 3A UD2		64.162	35.508	0.041	1.262	0	100.97
Violet Mine	Bulk	WRS 1463 B VIOLET 3A V		64.595	34.988	0	0.591	0	100.17
Violet Mine	Bulk	WRS 1463 B VIOLET 3A WD		51.916	45.277	0	1.655	0	98.848
Violet Mine	Bulk	WRS 1463 B VIOLET 3A WL		79.02	19.935	0.027	0.343	0	99.325
Violet Mine	Bulk	WRS 1463 B VIOLET 3A X		80.046	18.173	0.017	1.079	0	99.315
Violet Mine	Bulk	WRS 1463 B VIOLET 3A Y		67.916	30.144	0.001	1.172	0	99.233

Occurrence	Sample Type	Block and ID	Grain ID	Wt.% (Au)	Wt.% (Ag)	Wt.% (Fe)	Wt. % (Hg)	Wt.% (Cu)	Probe Total
Violet Mine	Bulk	WRS 1463 B VIOLET 3A ZL		77.044	23.013	0.013	0.48	0	100.55
Violet Mine	Bulk	WRS 1463 B VIOLET 3A ZD		61.924	36.64	0.007	1.807	0	100.38
Violet Mine	Bulk	WRS 1463 B VIOLET3A A1C		56.557	40.017	0	2.973	0	99.547
Violet Mine	Bulk	WRS 1463 B VIOLET3A A1P		57.373	39.833	0.038	2.319	0	99.563
Violet Mine	Bulk	WRS 1463 B VIOLET3A B1PC		68.82	29.412	0	0.702	0	98.934
Violet Mine	Bulk	WRS 1463 B VIOLET3A B1D		45.176	50.904	0	2.813	0	98.893
Violet Mine	Bulk	WRS 1463 B VIOLET3A C1		78.541	19.615	0.02	0.782	0	98.958
Violet Mine	Bulk	WRS 1463 B VIOLET3A D1		74.58	24.634	0.019	1.154	0	100.39
Violet Mine	Bulk	WRS 1463 B VIOLET3A F1		69.647	30.076	0.006	0.639	0	100.37
Violet Mine	Bulk	WRS 1463 B VIOLET3A G1		63.86	34.656	0	1.313	0	99.829
Violet Mine	Bulk	WRS 1463 B VIOLET3A H1		79.816	18.474	0.027	1.27	0.012	99.599
Violet Mine	Bulk	WRS 1463 B VIOLET3A I1D		40.9	52.027	0.003	7.275	0	100.21
Violet Mine	Bulk	WRS 1463 B VIOLET3A I1L		70.201	30.023	0.045	0.342	0	100.61
Violet Mine	Bulk	WRS 1463 B VIOLET3B A		67.731	31.359	0.001	1.455	0	100.55
Violet Mine	Bulk	WRS 1463 B VIOLET3B C		79.13	19.237	0.025	1.136	0.023	99.551
Violet Mine	Bulk	WRS 1463 B VIOLET3B D		76.671	21.36	0.002	1.145	0.002	99.181
Violet Mine	Bulk	WRS 1463 B VIOLET3B E		65.901	31.899	0	1.453	0	99.253

Occurrence	Sample Type	Block and ID	Grain ID	Wt.% (Au)	Wt.% (Ag)	Wt.% (Fe)	Wt. % (Hg)	Wt.% (Cu)	Probe Total
Violet Mine	Bulk	WRS 1463 B VIOLET3B F		67.921	31.579	0	1.561	0	101.06
Violet Mine	Bulk	WRS 1463 B VIOLET3B G		68.702	29.793	0	1.255	0	99.75
Violet Mine	Bulk	WRS 1463 B VIOLET3B H		64.821	32.846	0	1.708	0	99.379
Violet Mine	Bulk	WRS 1463 B VIOLET3B I		71.888	25.871	0.002	1.064	0	98.825
Violet Mine	Bulk	WRS 1463 B VIOLET3B J		65.443	31.57	0	1.979	0	98.992
Violet Mine	Bulk	WRS 1463 B VIOLET3B K		66.907	31.67	0.003	1.5	0	100.08
Violet Mine	Bulk	WRS 1463 B VIOLET3B L		65.401	33.346	0	1.975	0	100.72
Violet Mine	Bulk	WRS 1463 B VIOLET3B M		70.444	27.835	0	1.215	0	99.494
Violet Mine	Bulk	WRS 1463 B VIOLET3B N		79.108	18.445	0.012	0.76	0	98.325
Violet Mine	Bulk	WRS 1463 B VIOLET3B O		81.072	18.701	0.058	0.391	0.016	100.24
Violet Mine	Bulk	WRS 1463 B VIOLET3B P		66.698	31.758	0.009	1.429	0	99.894
Violet Mine	Bulk	WRS 1463 B VIOLET3B Q		67.873	30.186	0.004	1.516	0	99.579
Violet Mine	Bulk	WRS 1463 B VIOLET3B R		65.678	31.752	0	1.394	0	98.824
Violet Mine	Bulk	WRS 1463 B VIOLET3B SL/1		66.347	31.153	0.003	1.146	0	98.649
Violet Mine	Bulk	WRS 1463 B VIOLET3B SL/2		67.164	31.219	0.006	1.31	0	99.699
Violet Mine	Bulk	WRS 1463 B VIOLET3B SD		46.264	47.521	0	5.646	0	99.431
Violet Mine	Bulk	WRS 1463 B VIOLET3B T		67.543	32.216	0	0.604	0	100.36

Occurrence	Sample Type	Block and ID	Grain ID	Wt.% (Au)	Wt.% (Ag)	Wt.% (Fe)	Wt. % (Hg)	Wt.% (Cu)	Probe Total
Violet Mine	Bulk	WRS 1463 B VIOLET3B U		67.927	29.923	0	0.636	0	98.486
Violet Mine	Bulk	WRS 1463 B VIOLET3B UL2		59.042	38.031	0	1.115	0	98.198
Violet Mine	Bulk	WRS 1463 B VIOLET3B UD2		60.472	36.611	0	2.116	0	99.199
Violet Mine	Bulk	WRS 1463 B VIOLET3B V		67.211	30.925	0.003	0.606	0	98.745
Violet Mine	Bulk	WRS 1463 B VIOLET3B W		69.23	29.738	0.007	1.053	0	100.03
Violet Mine	Bulk	WRS 1463 B VIOLET3B X		72.33	26.198	0.003	1.573	0	100.11
Violet Mine	Bulk	WRS 1463 B VIOLET3B XD		36.758	57.523	0	4.994	0	99.275
Violet Mine	Bulk	WRS 1463 B VIOLET3B Y		66.753	33.376	0	0.796	0	100.93
Violet Mine	Bulk	WRS 1463 B VIOLET3B Z		66.558	32.586	0	1.517	5.615	106.28
Violet Mine	Bulk	WRS 1463 B VIOLET3B A1		82.09	18.394	0.027	0.468	0.002	100.98
Violet Mine	Bulk	WRS 1463 B VIOLET3B B1		78.784	21.447	0.017	0.594	0.004	100.85
Violet Mine	Bulk	WRS 1463 B VIOLET3B C1		66.809	32.126	0	1.528	0	100.46
Violet Mine	Bulk	WRS 1463 B VIOLET3B D1		69.204	30.587	0	0.128	0	99.93
Violet Mine	Bulk	WRS 1463 B VIOLET3B E1C		66.436	33.022	0	0.44	0	99.902
Violet Mine	Bulk	WRS 1463 B VIOLET3B E1R		57.123	17.92	0.066	24.69	0.026	99.825
Violet Mine	Bulk	WRS 1463 B VIOLET3B F1		67.127	32.607	0	0.929	0	100.66
Violet Mine	Bulk	WRS 1463 B VIOLET3B G1		81.955	18.426	0.019	0.72	0.03	101.15

Occurrence	Sample Type	Block and ID	Grain ID	Wt.% (Au)	Wt.% (Ag)	Wt.% (Fe)	Wt. % (Hg)	Wt.% (Cu)	Probe Total
Violet Mine	Bulk	WRS 1463 B VIOLET3B G1D2		39.494	52.604	0.012	4.4	0	96.51
Violet Mine	Bulk	WRS 1463 B VIOLET3B H1		66.47	33.768	0.011	0.461	0	100.71
Violet Mine	Bulk	WRS 1463 B VIOLET3B I1		66.63	32.667	0.005	1.885	0	101.19
Violet Mine	Bulk	WRS 1463 B VIOLET3B J1		71.288	28.557	0.064	0.744	0	100.65
Violet Mine	Bulk	WRS 1463 B VIOLET3B K1		69.934	30.164	0.011	1.382	0	101.49
Violet Mine	Bulk	WRS 1463 B VIOLET3B L1		70.546	28.647	0	1.335	0	100.53
Violet Mine	Bulk	WRS 1463 B VIOLET3B M1P		74.028	25.97	0.015	1.348	0	101.36
Violet Mine	Bulk	WRS 1463 B VIOLET3B M1D		41.008	52.211	0	7.394	0	100.61
Violet Mine	Bulk	WRS 1463 B VIOLET3B N1		69.311	29.699	0.007	1.17	0	100.19
Violet Mine	Bulk	WRS 1463B VIOLET 4A		81.213	19.06	0.013	0.68	0.01	100.98
Violet Mine	Bulk	WRS 1463B VIOLET 4AD		42.573	51.088	0	7.084	0	100.75
Violet Mine	Bulk	WRS 1463B VIOLET 4B		81.82	18.729	0.019	0.841	0.01	101.42
Violet Mine	Bulk	WRS 1463B VIOLET 4C		79.794	20.457	0.011	1.477	0.012	101.75
Violet Mine	Bulk	WRS 1463B VIOLET 4D		80.407	19.957	0.014	1.372	0.014	101.76
Violet Mine	Bulk	WRS 1463B VIOLET 4E		79.938	20.409	0.023	1.332	0.017	101.72
Violet Mine	Bulk	WRS 1463B VIOLET 4ED		37.679	55.649	0.005	7.607	0	100.96
Violet Mine	Bulk	WRS 1463B VIOLET 4F		70.353	30.14	0.008	1.119	0	101.62

Occurrence	Sample Type	Block and ID	Grain ID	Wt.% (Au)	Wt.% (Ag)	Wt.% (Fe)	Wt. % (Hg)	Wt.% (Cu)	Probe Total
Violet Mine	Bulk	WRS 1463B VIOLET 4G		69.409	30.458	0.007	1.311	0	101.19
Violet Mine	Bulk	WRS 1463B VIOLET 4H		67.59	33.144	0	0.728	0	101.46
Violet Mine	Bulk	WRS 1463B VIOLET 4I		75.782	24.321	0.012	0.477	0.007	100.6
Violet Mine	Bulk	WRS 1463B VIOLET 4J		79.927	20.595	0.014	1.31	0.013	101.86
Violet Mine	Bulk	WRS 1463B VIOLET 4K		80.672	20.11	0.017	1.024	0.03	101.85
Violet Mine	Bulk	WRS 1463B VIOLET 4L		79.237	20.951	0.021	1.118	0.012	101.34
Violet Mine	Bulk	WRS 1463B VIOLET 4M		80.799	19.678	0.02	0.954	0.012	101.46
Violet Mine	Bulk	WRS 1463B VIOLET 4N		80.151	19.919	0.025	1.166	0.02	101.28
Violet Mine	Bulk	WRS 1463B VIOLET 4ND		55.148	41.818	0	3.341	0	100.31
Violet Mine	Bulk	WRS 1463B VIOLET 4O		80.938	19.567	0.015	1.156	0.021	101.7
Violet Mine	Bulk	WRS 1463B VIOLET 4OD		50.608	45.954	0	3.751	0	100.31
Violet Mine	Bulk	WRS 1463B VIOLET 4P		74.473	25.879	0.004	0.733	0	101.09
Violet Mine	Bulk	WRS 1463B VIOLET 4Q		80.855	19.936	0.015	1.19	0.017	102.01
Violet Mine	Bulk	WRS 1463B VIOLET 4R		80.955	19.472	0.019	0.83	0.015	101.29
Violet Mine	Bulk	WRS 1463B VIOLET 4S		80.269	20.411	0.013	1.11	0.013	101.82
Violet Mine	Bulk	WRS 1463B VIOLET 4T		80.571	19.428	0.013	1.06	0.014	101.09
Violet Mine	Bulk	WRS 1463B VIOLET 4U		81.47	19.267	0.025	0.911	0.032	101.71

Occurrence	Sample Type	Block and ID	Grain ID	Wt.% (Au)	Wt.% (Ag)	Wt.% (Fe)	Wt. % (Hg)	Wt.% (Cu)	Probe Total
Violet Mine	Bulk	WRS 1463B VIOLET 4V		81.77	19.181	0.022	0.83	0.005	101.81
Violet Mine	Bulk	WRS 1463B VIOLET 4W		78.256	22.209	0.005	0.393	0	100.86
Violet Mine	Bulk	WRS 1463B VIOLET 4X		81.675	19.125	0.019	0.829	0.029	101.68
Violet Mine	Bulk	WRS 1463B VIOLET 4Y		81.55	19.942	0.009	0.442	0.01	101.95
Violet Mine	Bulk	WRS 1463B VIOLET 4YD		55.742	41.28	0.014	3.782	0	100.82
Violet Mine	Bulk	WRS 1463B VIOLET 4Z		82.311	19.034	0.014	0.63	0.003	101.99
Violet Mine	Bulk	WRS 1463B VIOLET 4A1		79.611	20.417	0.011	1.782	0.021	101.84
Violet Mine	Bulk	WRS 1463B VIOLET 4B1		82.154	18.288	0.014	1.568	0.02	102.04
Violet Mine	Bulk	WRS 1463B VIOLET 4C1		83.036	17.928	0.014	1.003	0.024	102.01
Violet Mine	Bulk	WRS 1463B VIOLET 4D1		81.69	19.3	0.011	0.728	0.02	101.75
Violet Mine	Bulk	WRS 1463B VIOLET 4E1		82.17	18.894	0.029	0.821	0.015	101.93
Violet Mine	Bulk	WRS 1463B VIOLET 4F1		78.012	21.881	0.008	1.481	0.006	101.39
Violet Mine	Bulk	WRS 1463B VIOLET 4I1		67.105	32.266	0	0.944	0	100.32
Violet Mine	Bulk	WRS 1463B VIOLET 4H1		82.438	18.619	0.037	0.924	0.035	102.05
Violet Mine	Bulk	WRS 1463B VIOLET 4G1		86.342	15.479	0.014	0.541	0.027	102.4
Violet Mine	Bulk	WRS 1463B VIOLET 4J1		82.925	18.474	0.023	0.458	0.009	101.89
Violet Mine	Bulk	WRS 1463B VIOLET 4J1TR		49.545	47.56	0	3.629	0	100.73

Occurrence	Sample Type	Block and ID	Grain ID	Wt.% (Au)	Wt.% (Ag)	Wt.% (Fe)	Wt. % (Hg)	Wt.% (Cu)	Probe Total
Violet Mine	Bulk	WRS 1463B VIOLET 4K1		82.39	18.852	0.009	0.584	0.035	101.87
Violet Mine	Bulk	WRS 1463B VIOLET 4L1		80.27	20.193	0.016	1.126	0.006	101.61
Violet Mine	Bulk	WRS 1463B VIOLET 4M1		82.011	18.388	0.027	0.785	0.035	101.25
Violet Mine	Bulk	WRS 1463B VIOLET 4N1		81.872	19.082	0.015	0.896	0	101.87
Violet Mine	Bulk	WRS 1463B VIOLET 4P		79.933	20.503	0.018	1.258	0.022	101.73
Violet Mine	Bulk	WRS 1463B VIOLET 4PD		41.283	53.11	0	5.141	0	99.534
Violet Mine	Bulk	WRS 1463B VIOLET 4Q1/1		81.201	18.854	0.017	1.187	0.024	101.28
Violet Mine	Bulk	WRS 1463B VIOLET 4Q1/2		45.35	50.64	0	5.128	0	101.14
Violet Mine	Bulk	WRS 1463B VIOLET 4R1		80.607	18.977	0.023	1.634	0.008	101.25
Violet Mine	Bulk	WRS 1463B VIOLET 4S1		66.236	32.577	0	2.216	0	101.03
Violet Mine	Bulk	WRS 1463B VIOLET 4W1		78.82	20.489	0.02	1.857	0.011	101.2
Violet Mine	Bulk	WRS 1463B VIOLET 4X1		81.926	18.53	0.013	1.043	0.019	101.53

A.12 Table of samples and specimens

A summary of all samples and specimens prepared during this research. PB- polished block, PTS- polished thin section, DPW- double polished wafer, CL- cathodoluminescence, EDS- electron dispersive spectroscopy, LA- laser ablation, EPMA- electron probe micro analyser, XRF- X ray fluorescence, EBSD- electron backscatter diffraction.

Location	Sample Number	Grid Reference	Description	Specimens	Type	Analysis
Dysle	14D3	583931 7085562	Visible gold found in vug of quartz	MG23	PB	
	14D4	583931 7085562	Large euhedral galena in the centre of quartz	MG33	PB	CL, EDS, LA
	14D7	583944 7085554	Gold within oxidised pyrite proximal to the wallrock	MG21	PB	CL, EDS, EPMA
	14D8	583933 7085560		MG1	Chip	
	14D9	583912 7085573	Quartz vein cross cutting host rock. Small euhedral quartz	MG12	PTS	CL, EDS
				MG15	PTS	CL, EDS
15D01		Bladed quartz textures	MG60	DPW	CL, EDS	
Veronika	14VR6	586291 7098107		MG2	Chip	
	14VK1	583581 7086107	Quartz vein and host rock sample. Sulphidation at vein margin with milky quartz textures preserved	MG13	PTS	CL, EDS
Hunker Dome	14HD4	603113 7083294	Quartz and host rock which is oxidised. The wallrock is altered to limonite. The centre of the vein is filled with carbonate	MG3	PTS	EDS, XRF
	14HD8	602642 7084065		MG11	Chip	
Gay Gulch	14GG8	585243 7084142	Euhedral quartz grain	MG4	PTS	Pet
Violet	14V13	584644 7082095		MG5	Chip	
	14V12	584644 7082095	Pyrite rich part of a vein where pegmatite cross cuts quartz	MG36	PTS	
Upper Nugget	14UN6	584974 7085674	Sampled from in situ vein that cross cuts an earlier D3 metamorphic quartz vein	MG6	PTS	CL, EDS
	14UN3	584977 7085678	Large visible gold in quartz proximal to the wallrock	MG22	PB	CL, EDS, EPMA
	14UN11	584990 7085674		MG14	Chip	

Location	Sample Number	Grid Reference	Description	Specimens	Type	Analysis
			Sample displays well developed crenulation with multiple generations of quartz growth.	MG38	PTS	
	14UN8	585021 7085655	Gold in quartz but is a cluster of small particles	MG16	DPW	CL, EDS
				MG29	PB	RL, EDS, EPMA
	14UN13	584990 7085674	Large particle of gold on pyrite at edge of vein proximal to wallrock	MG17	DPW	CL, EDS
				MG27	PB	RL, EDS, EPMA
	14UN5	584974 7085674	Gold grain at wallrock margin which is pyrite rich	MG39	PTS	CL, EDS
	15UN01	584977 7085678	Bladed quartz texture	MG61b	DPW	CL, EDS
	OLT15_15	584798 7085578	Gold in pyrite found in quartz	MG53	PB	CL, EPMA, EDS, EBSD
				MG64	DPW	CL, EPMA,
Buckland Zone	14BZ10	585626 7084826	Large euhedral pyrite oxidised to limonite. Gold is within the pyrite and proximal to vein margin	MG18	DPW	
				MG28	PB	CL, EDS, EPMA, EBSD
	14BZ18	585624 7084837	Large piece of euhedral calcite	MG37	Chip	
	14BZ17	585624 7084837	Large gold grain at the wallrock contact. Margin of vein not sharp and rafts of rock can be found within quartz	MG26	PB	EDS, EPMA, EBSD
	BZ16	585624 7084819	Gold grain at vein margin within euhedral pyrite that is oxidised	MG20	PB	EDS, EPMA
	BZ7	585619 7084849	Fibrous quartz grain with gold hosted within euhedral pyrite	MG24	PB	CL, EDS, EPMA
	OLT15_024	585631 7084819	Gold in quartz	MG51	PB	EDS, EPMA, EBSD

Location	Sample Number	Grid Reference	Description	Specimens	Type	Analysis	
	OLT15_26	585623	7084823	Gold in quartz	MG50	PB	CL, RL, SEM, EPMA
	OLT15_27	585626	7084829	Gold is FREE and in quartz	MG54	PB	CL, EPMA, EDS
	OLT15_29	585970	7084736	Gold in pyrite in quartz	MG52	PB	CL, EPMA, EDS, EBSD
Lower Nugget	14LN7	584784	7085558	Small piece of visible gold on quartz proximal to the margin	MG25	PB	EDS, EPMA
	14LN6	584782	7085548	Sample of vein with milky quartz and large euhedral calcite in the centre	MG30	PTS	EDS, XRF
Eldorado Creek	14EC5	584957	7084270	Vein with 2 phases of quartz clearly observed. Later quartz in the centre is milky and is associated with pyrite	MG31	PTS	
	14EC1	585490	7083443	A sample of float which is composed of calcite, quartz and pyrite	MG32	PTS	
Boulder Lode	15LS01	587008	7086173	A large crystal of clear quartz found in pit	MG66	DPW	CL, EDS, FIA
Drill core	05LS09			Gold in core 36.76m-76.46m	MG55	PB	EDS, EPMA
	05LS16			Gold in core 73.15m	MG56	PB	EDS, EPMA, CL
	EC15_10			Gold in vein from core 25m	MG57	PB	CL, EPMA, EDS, EBSD
	05LS02			59.00-59.50M	MG7	PTS	EDS
				Gold in section	MG8	PTS	EDS, EPMA, XRF
					MG9	PTS	EDS
				Gold in section	MG10	PTS	EDS, EPMA, XRF

Location	Sample Number	Grid Reference	Description	Specimens	Type	Analysis
	05LS27		Depth of 69-70M 129,130	MG45	PTS	EDS, EPMA, XRF
			TS 131,132	MG46	PTS	EDS, EPMA,XRF, EBSD
	12LS03	587505 7085896	K186 Sulphide lense within schist	MG44	PTS	EDS

A.13 Trace element data from LA-ICP-MS

		Li7	Na23	Mg24	Al27	K39	Ca40	Ti47	Mn55	Fe56	Cu63	Zn66	As75	Sr88	Sn118	Sb121	Te125	Ba137	La139	Pb208	Bi209
Q1	Average	118.97	17.86	13.62	705.76	73.98	138.85	3.10	1.61	608.87	17.71	5.30	18.46	2.16	0.70	2.71	5.29	10.10	1.79	90.07	4.49
Q2	Average	22.27	24.65	12.57	193.31	101.21	6.82	1.85	0.59	18.92	1.48	2.49	0.85	0.82	0.08	1.93		7.17	9.46	172.03	1.56
Q3	Average	57.09	138.77	12.78	996.31	109.01	32.05	3.93	4.40	1808.24	7.12	6.83	2.14	3.07	0.16	5.93	5.02	18.12	9.84	107.61	42.75
Q1	Min	93.63	8.38	1.35	52.53	9.46	7.03	0.00	0.30	1.33	17.71	0.29	0.50	0.12	0.09	1.04	5.29	1.77	0.83	0.79	0.01
	Max	139.30	27.34	68.67	1743.15	258.29	552.08	18.50	5.45	4054.06	17.71	17.71	71.85	5.96	2.83	5.92	5.29	22.75	4.92	410.81	15.35
	Range	45.67	18.96	67.32	1690.62	248.83	545.05	18.50	5.15	4052.73	0.00	17.43	71.35	5.85	2.75	4.88	0.00	20.99	4.09	410.02	15.34
	St Dev	20.13	13.41	22.54	745.36	96.03	233.5	5.21	2.20	1519.48		7.37	35.5	2.47	1.20	1.69		7.70	1.56	135.54	6.05
Q2	Min	1.02	9.98	0.18	5.96	3.53	0.72	0.00	0.39	0.25	1.48	0.20	0.50	0.04	0.04	0.17	0.00	0.61	0.19	0.03	0.01
	Max	189.24	3321.66	83.01	2434.31	762.01	215.49	14.21	34.08	46406.3	36.27	32.76	10.27	13.31	0.57	16.09	16.79	157.92	28.81	3596.51	643.55
	Range	188.23	3311.68	82.83	2428.35	758.47	214.76	14.21	33.69	46406.12	34.79	32.56	9.776	13.27	0.52	15.91	16.79	157.31	28.62	3596.48	643.54
	St Dev	23.97	17.22	32.89	299.21	169.88	5.55	1.70	0.23	38.23		4.56	0.44	1.02	0.04	2.83		8.04	16.16	657.16	3.05
Q3	Min	2.73	3.26	0.49	72.43	4.20	1.16	0.00	0.35	0.20	1.30	0.10	0.30	0.08	0.05	0.53	0.97	1.40	0.03	0.02	0.01
	Max	189.24	3321.66	83.01	2434.31	762.01	215.49	14.21	34.08	46406.37	36.27	32.76	10.27	13.31	0.57	16.09	16.79	157.92	28.81	2492.96	643.55
	Range	186.51	3318.39	82.52	2361.88	757.81	214.32	14.21	33.73	46406.17	34.97	32.66	9.976	13.23	0.51	15.55	15.82	156.52	28.78	2492.94	643.55
	St Dev	48.50	562.46	20.38	602.97	161.42	41.51	2.64	7.39	7771.76	9.29	9.36	2.19	2.57	0.15	4.07	4.98	24.78	9.73	439.88	147.67

Table 11-3: Results of trace element content of quartz presented in parts per million for each generation of quartz.

A.14 Electron Microprobe Data from EPMA

Occurrence	Sample Type	Block and ID	Grain ID	Wt.% (Au)	Wt.% (Ag)	Wt.% (Fe)	Wt. % (Hg)	Wt.% (Cu)	Probe Total
Nugget Zone	Bulk	WRS 1665 D	A	70.59	28.82		0.00	0.00	99.41
Nugget Zone	Bulk	WRS 1665 D	B	77.47	21.76		0.08	0.00	99.31
Nugget Zone	Bulk	WRS 1665 D	C	73.72	25.91		0.00	0.02	99.65
Nugget Zone	Bulk	WRS 1665 D	D	74.52	23.88		0.00	0.02	98.43
Nugget Zone	Bulk	WRS 1665 D	E	71.97	26.89		0.00	0.00	98.86
Nugget Zone	Bulk	WRS 1665 D	F	76.30	22.90		0.03	0.03	99.26
Nugget Zone	Bulk	WRS 1665 D	G	80.99	18.74		0.00	0.03	99.76
Nugget Zone	Bulk	WRS 1665 D	H	76.17	22.09		0.00	0.02	98.27
Nugget Zone	Bulk	WRS 1665 D	I	67.08	32.43		0.01	0.00	99.51
Nugget Zone	Bulk	WRS 1665 D	J	83.07	15.72		0.03	0.04	98.87
Nugget Zone	Bulk	WRS 1665 D	K	82.37	16.73		0.00	0.05	99.15
Nugget Zone	Bulk	WRS 1665 D	L	83.16	15.40		0.00	0.00	98.57
Nugget Zone	Bulk	WRS 1665 D	M	72.32	27.11		0.00	0.00	99.43
Nugget Zone	Bulk	WRS 1665 D	N	69.98	29.33		0.00	0.01	99.32
Nugget Zone	Bulk	WRS 1665 D	O	72.98	26.87		0.00	0.02	99.88
Nugget Zone	Bulk	WRS 1665 D	P	78.04	22.46		0.00	0.00	100.50
Nugget Zone	Bulk	WRS 1665 D	Q	66.67	32.77		0.13	0.02	99.59
Nugget Zone	Bulk	WRS 1665 D	R	69.38	29.74		0.00	0.00	99.12
Nugget Zone	Bulk	WRS 1665 D	S	83.25	15.98		0.00	0.03	99.26
Nugget Zone	Bulk	WRS 1665 D	T	64.46	33.82		0.02	0.02	98.32
Nugget Zone	Bulk	WRS 1665 D	U	76.34	23.50		0.04	0.02	99.89
Nugget Zone	Bulk	WRS 1665 D	V	80.90	18.67		0.00	0.04	99.60
Nugget Zone	Bulk	WRS 1665 D	W	70.55	28.82		0.00	0.03	99.40
Nugget Zone	Bulk	WRS 1665 D	X	75.45	25.23		0.00	0.00	100.69
Nugget Zone	Bulk	WRS 1665 D	Y	82.38	17.50		0.01	0.02	99.92
Nugget Zone	Bulk	WRS 1665 D	Z	82.83	16.52		0.00	0.01	99.37
Nugget Zone	Bulk	WRS 1665 D	A1	76.42	22.76		0.18	0.01	99.36
Nugget Zone	Bulk	WRS 1665 D	B1	75.06	24.95		0.00	0.00	100.01
Nugget Zone	Bulk	WRS 1665 D	C1	73.18	25.33		0.00	0.00	98.51
Nugget Zone	Bulk	WRS 1665 D	D1	67.27	32.00		0.00	0.03	99.30
Nugget Zone	Bulk	WRS 1665 D	E1	70.44	29.21		0.00	0.01	99.67
Nugget Zone	Bulk	WRS 1665 D	F1	70.48	28.82		0.07	0.01	99.37

Occurrence	Sample Type	Block and ID	Grain ID	Wt.% (Au)	Wt.% (Ag)	Wt.% (Fe)	Wt. % (Hg)	Wt.% (Cu)	Probe Total
Nugget Zone	Bulk	WRS 1665 D	G1	71.94	27.83		0.04	0.00	99.80
Nugget Zone	Bulk	WRS 1665 D	H1	69.28	29.62		0.00	0.02	98.92
Nugget Zone	Bulk	WRS 1665 D	I1	76.98	22.10		0.00	0.02	99.10
Nugget Zone	Bulk	WRS 1665 D	J1	83.53	15.90		0.00	0.01	99.44
Nugget Zone	Bulk	WRS 1665 D	K1	71.33	27.82		0.08	0.00	99.22
Nugget Zone	Bulk	WRS 1665 D	L1	79.51	20.10		0.00	0.00	99.61
Nugget Zone	Bulk	WRS 1665 D	M1	70.82	28.16		0.00	0.02	99.00
Nugget Zone	Bulk	WRS 1665 D	N1	66.80	32.41		0.00	0.00	99.21
Nugget Zone	Bulk	WRS 1665 D	O1	68.20	30.48		0.03	0.02	98.72
Nugget Zone	Bulk	WRS 1665 D	P1	76.13	23.69		0.00	0.01	99.82
Nugget Zone	Bulk	WRS 1665 D	Q1	73.77	25.52		0.01	0.00	99.30
Nugget Zone	Bulk	WRS 1665 D	R1	76.03	22.95		0.00	0.02	99.00
Nugget Zone	Bulk	WRS 1665 D	S1	76.52	22.89		0.00	0.00	99.41
Nugget Zone	Bulk	WRS 1665 D	T1	80.06	19.68		0.00	0.00	99.74
Buckland Zone	Bulk	WRS 1665 D	A	82.52	17.20		0.06	0.00	99.78
Buckland Zone	Bulk	WRS 1665 D	B	77.91	21.57		0.00	0.00	99.48
Buckland Zone	Bulk	WRS 1665 D	C	72.14	27.19		0.04	0.02	99.39
Buckland Zone	Bulk	WRS 1665 D	D	79.57	20.02		0.00	0.00	99.59
Buckland Zone	Bulk	WRS 1665 D	E	71.57	28.73		0.00	0.00	100.30
Buckland Zone	Bulk	WRS 1665 D	F	77.84	21.45		0.00	0.03	99.32
Buckland Zone	Bulk	WRS 1665 D	G	81.74	18.15		0.00	0.03	99.93
Buckland Zone	Bulk	WRS 1665 D	H	80.75	19.05		0.00	0.02	99.81
Buckland Zone	Bulk	WRS 1665 D	I	76.18	22.64		0.00	0.00	98.81
Buckland Zone	Bulk	WRS 1665 D	J	82.48	17.65		0.00	0.02	100.15
Buckland Zone	Bulk	WRS 1665 D	K	83.26	16.31		0.02	0.00	99.59
Buckland Zone	Bulk	WRS 1665 D	L	80.47	19.10		0.00	0.00	99.58
Buckland Zone	Bulk	WRS 1665 D	M	82.39	17.19		0.00	0.06	99.64
Buckland Zone	Bulk	WRS 1665 D	N	80.90	18.74		0.00	0.00	99.63
Buckland Zone	Bulk	WRS 1665 D	O	82.24	16.54		0.00	0.00	98.78
Buckland Zone	Bulk	WRS 1665 D	P	77.85	21.25		0.00	0.01	99.10
Buckland Zone	Bulk	WRS 1665 D	Q	76.46	23.69		0.00	0.04	100.19
Buckland Zone	Bulk	WRS 1665 D	R	81.52	18.25		0.00	0.01	99.78
Buckland Zone	Bulk	WRS 1665 D	S	75.20	24.54		0.00	0.00	99.74
Buckland Zone	Bulk	WRS 1665 D	T	61.50	36.58		0.44	0.02	98.54

Occurrence	Sample Type	Block and ID	Grain ID	Wt.% (Au)	Wt.% (Ag)	Wt.% (Fe)	Wt. % (Hg)	Wt.% (Cu)	Probe Total
Buckland Zone	Bulk	WRS 1665 D	U	84.02	15.60		0.00	0.03	99.65
Buckland Zone	Bulk	WRS 1665 D	V	79.21	20.37		0.04	0.00	99.63
Buckland Zone	Bulk	WRS 1665 D	W	75.72	23.87		0.00	0.01	99.60
Buckland Zone	Bulk	WRS 1665 D	X	78.16	21.97		0.00	0.01	100.14
Buckland Zone	Bulk	WRS 1665 D	Y	79.29	20.08		0.00	0.03	99.39
Buckland Zone	Bulk	WRS 1665 D	Z	76.03	23.61		0.00	0.02	99.67
Buckland Zone	Bulk	WRS 1665 D	A1	78.75	21.51		0.00	0.01	100.27
Buckland Zone	Bulk	WRS 1665 D	B1	78.10	21.27		0.00	0.00	99.38
Buckland Zone	Bulk	WRS 1665 D	C1	79.03	20.82		0.08	0.02	99.95
Buckland Zone	Bulk	WRS 1665 D	D1	62.26	36.36		0.73	0.00	99.35
Buckland Zone	Bulk	WRS 1665 D	E1	78.85	20.01		0.00	0.00	98.86
Buckland Zone	Bulk	WRS 1665 D	F1	73.21	26.38		0.00	0.00	99.59
Buckland Zone	Bulk	WRS 1665 D	G1	83.81	16.73		0.00	0.03	100.57
Buckland Zone	Bulk	WRS 1665 D	H1	82.27	17.08		0.00	0.01	99.35
Buckland Zone	Bulk	WRS 1665 D	I1	78.33	21.44		0.08	0.00	99.85
Buckland Zone	Bulk	WRS 1665 D	J1	80.06	19.53		0.03	0.02	99.63
Buckland Zone	Bulk	WRS 1665 D	K1	80.52	17.96		0.00	0.00	98.48
Buckland Zone	Bulk	WRS 1665 D	L1	70.39	28.45		0.00	0.00	98.83
Buckland Zone	Bulk	WRS 1665 D	M1	77.33	22.78		0.00	0.02	100.12
Buckland Zone	Bulk	WRS 1665 D	N1	76.50	21.88		0.00	0.01	98.39
Buckland Zone	Bulk	WRS 1665 D	O1	76.95	22.65		0.00	0.02	99.62
Buckland Zone	Bulk	WRS 1665 D	P1	80.41	19.79		0.00	0.00	100.21
Buckland Zone	Bulk	WRS 1665 D	Q1	61.98	36.27		0.71	0.00	98.95
Buckland Zone	Bulk	WRS 1665 D	R1	79.62	19.78		0.02	0.00	99.42
Buckland Zone	Bulk	WRS 1665 D	S1	81.13	19.47		0.00	0.00	100.60
Buckland Zone	Bulk	WRS 1665 D	T1	79.35	20.74		0.00	0.04	100.12
Buckland Zone	Bulk	WRS 1665 D	U1	80.28	19.46		0.00	0.01	99.74
Buckland Zone	Bulk	WRS 1665 D	V1	78.15	22.00		0.00	0.03	100.18
Buckland Zone	Bulk	WRS 1665 D	W1	82.36	17.61		0.13	0.02	100.12
Buckland Zone	Bulk	WRS 1665 D	X1	79.78	19.13		0.00	0.00	98.91
Buckland Zone	Bulk	WRS 1665 D	Y1	70.18	29.21		0.00	0.04	99.43
Buckland Zone	Bulk	WRS 1665 D	Z1	76.57	23.77		0.00	0.01	100.35
Buckland Zone	Bulk	WRS 1665 D	A2	79.75	20.70		0.00	0.01	100.46
Buckland Zone	Bulk	WRS 1665 D	B2	76.59	22.71		0.00	0.02	99.33

Occurrence	Sample Type	Block and ID	Grain ID	Wt.% (Au)	Wt.% (Ag)	Wt.% (Fe)	Wt. % (Hg)	Wt.% (Cu)	Probe Total
Buckland Zone	Bulk	WRS 1665 D	C2	80.81	18.59		0.00	0.00	99.40
Buckland Zone	Bulk	WRS 1665 D	D2	77.28	22.88		0.04	0.00	100.20
Buckland Zone	Bulk	WRS 1665 D	E2	81.93	17.99		0.00	0.03	99.96
Buckland Zone	Bulk	WRS 1665 D	F2	76.62	23.26		0.00	0.01	99.89
Buckland Zone	Bulk	WRS 1665 D	G2	78.29	21.32		0.00	0.01	99.62
Buckland Zone	Bulk	WRS 1665 D	H2	74.49	24.89		0.02	0.02	99.41
Buckland Zone	Bulk	WRS 1665 D	I2	81.03	19.04		0.00	0.02	100.09
Buckland Zone	Bulk	WRS 1665 D	J2	79.41	20.11		0.00	0.00	99.52
Buckland Zone	Bulk	WRS 1665 D	K2	79.04	20.61		0.00	0.00	99.64
Buckland Zone	Bulk	WRS 1665 D	L2	82.27	17.21		0.00	0.00	99.49
Buckland Zone	Bulk	WRS 1665 D	M2	77.92	22.54		0.07	0.02	100.54
Buckland Zone	Bulk	WRS 1665 D	N2	69.34	29.69		0.00	0.01	99.03
Buckland Zone	Bulk	WRS 1665 D	O2	75.32	24.81		0.00	0.01	100.15
Nugget Zone	Bulk	WRS 1665 B	A	64.97	34.68		0.09	0.00	99.75
Nugget Zone	Bulk	WRS 1665 B	B	74.83	25.08		0.00	0.00	99.91
Nugget Zone	Bulk	WRS 1665 B	C	64.26	34.75		0.00	0.00	99.01
Nugget Zone	Bulk	WRS 1665 B	D	80.13	19.26		0.03	0.00	99.42
Nugget Zone	Bulk	WRS 1665 B	E	80.68	18.55		0.00	0.01	99.24
Nugget Zone	Bulk	WRS 1665 B	F	76.10	21.99		0.00	0.01	98.10
Nugget Zone	Bulk	WRS 1665 B	G	76.94	23.13		0.00	0.00	100.07
Nugget Zone	Bulk	WRS 1665 B	H	70.55	29.12		0.00	0.02	99.68
Nugget Zone	Bulk	WRS 1665 B	I	66.44	32.80		0.09	0.00	99.34
Nugget Zone	Bulk	WRS 1665 B	J	65.54	33.71		0.00	0.00	99.25
Nugget Zone	Bulk	WRS 1665 B	K	82.31	18.09		0.00	0.03	100.43
Nugget Zone	Bulk	WRS 1665 B	L	80.15	19.41		0.08	0.01	99.65
Nugget Zone	Bulk	WRS 1665 B	M	77.08	22.83		0.00	0.00	99.91
Nugget Zone	Bulk	WRS 1665 B	N	64.87	34.99		0.00	0.00	99.86
Nugget Zone	Bulk	WRS 1665 B	O	66.76	31.75		0.00	0.02	98.54
Nugget Zone	Bulk	WRS 1665 B	P	69.68	28.60		0.05	0.03	98.37
Nugget Zone	Bulk	WRS 1665 B	Q	70.02	30.19		0.00	0.00	100.21
Nugget Zone	Bulk	WRS 1665 B	R	66.34	33.80		0.06	0.00	100.21
Nugget Zone	Bulk	WRS 1665 B	S	76.22	23.07		0.00	0.00	99.29
Nugget Zone	Bulk	WRS 1665 B	T	83.15	16.20		0.02	0.01	99.39
Nugget Zone	Bulk	WRS 1665 B	U	83.86	15.40		0.00	0.01	99.27

Occurrence	Sample Type	Block and ID	Grain ID	Wt.% (Au)	Wt.% (Ag)	Wt.% (Fe)	Wt. % (Hg)	Wt.% (Cu)	Probe Total
Nugget Zone	Bulk	WRS 1665 B	V	73.26	26.26		0.02	0.02	99.55
Nugget Zone	Bulk	WRS 1665 B	W	78.51	20.90		0.00	0.03	99.44
Nugget Zone	Bulk	WRS 1665 B	X	77.48	22.23		0.00	0.00	99.71
Buckland Zone	Bulk	WRS 1665 B	A	76.24	23.79		0.00	0.00	100.03
Buckland Zone	Bulk	WRS 1665 B	B	76.65	22.95		0.00	0.00	99.60
Buckland Zone	Bulk	WRS 1665 B	C	78.83	21.22		0.00	0.00	100.05
Buckland Zone	Bulk	WRS 1665 B	D	79.19	20.62		0.08	0.00	99.89
Buckland Zone	Bulk	WRS 1665 B	E	77.47	21.36		0.00	0.01	98.83
Buckland Zone	Bulk	WRS 1665 B	F	78.32	21.89		0.00	0.02	100.24
Buckland Zone	Bulk	WRS 1665 B	G	82.83	17.61		0.00	0.01	100.45
Buckland Zone	Bulk	WRS 1665 B	H	75.55	24.33		0.02	0.02	99.92
Buckland Zone	Bulk	WRS 1665 B	I	79.12	20.88		0.00	0.01	100.01
Buckland Zone	Bulk	WRS 1665 B	J	73.66	25.43		0.03	0.03	99.15
Buckland Zone	Bulk	WRS 1665 B	K	75.09	24.33		0.00	0.03	99.45
Buckland Zone	Bulk	WRS 1665 B	L	81.80	18.72		0.03	0.02	100.57
Buckland Zone	Bulk	WRS 1665 B	M	63.42	17.26		0.06	0.00	80.75
Buckland Zone	Bulk	WRS 1665 B	N	76.03	23.63		0.00	0.02	99.68
Buckland Zone	Bulk	WRS 1665 B	O	78.57	21.40		0.00	0.01	99.98
Buckland Zone	Bulk	WRS 1665 B	P	76.37	23.08		0.00	0.01	99.46
Buckland Zone	Bulk	WRS 1665 B	Q	78.99	20.09		0.00	0.00	99.08
Buckland Zone	Bulk	WRS 1665 B	R	81.66	18.25		0.00	0.00	99.92
Buckland Zone	Bulk	WRS 1665 B	S	70.03	28.70		0.00	0.01	98.73
Buckland Zone	Bulk	WRS 1665 B	T	80.38	18.02		0.01	0.01	98.42
Buckland Zone	Bulk	WRS 1665 B	U	79.59	19.28		0.00	0.00	98.87
Buckland Zone	Bulk	WRS 1665 B	V	76.85	23.11		0.03	0.01	99.99
Buckland Zone	Bulk	WRS 1665 B	W	78.60	21.24		0.00	0.00	99.84
Buckland Zone	Bulk	WRS 1665 B	X	61.97	36.49		0.85	0.00	99.31
Buckland Zone	Bulk	WRS 1665 B	Y	78.06	21.09		0.00	0.02	99.17
Buckland Zone	Bulk	WRS 1665 B	Z	74.53	24.97		0.00	0.00	99.51
Buckland Zone	Bulk	WRS 1665 B	A1	85.31	15.76		0.00	0.04	101.11
Buckland Zone	Bulk	WRS 1665 B	B1	79.35	20.49		0.03	0.00	99.87
Buckland Zone	Bulk	WRS 1665 B	C1	80.05	19.76		0.00	0.01	99.82
Nugget Zone	Bulk	WRS 1572 B	A	76.792	23.86	0	0	0.006	100.66
Nugget Zone	Bulk	WRS 1572 B	B	76.492	24.965	0.009	0	0	101.47

Occurrence	Sample Type	Block and ID	Grain ID	Wt.% (Au)	Wt.% (Ag)	Wt.% (Fe)	Wt. % (Hg)	Wt.% (Cu)	Probe Total
Nugget Zone	Bulk	WRS 1572 B	C	74.264	26.807	0.011	0	0.001	101.08
Nugget Zone	Bulk	WRS 1572 B	D	77.375	23.876	0.004	0	0.031	101.29
Nugget Zone	Bulk	WRS 1572 B	E	74.23	27.47	0.037	0	0.004	101.74
Nugget Zone	Bulk	WRS 1572 B	F	76.061	24.34	0	0	0.017	100.42
Nugget Zone	Bulk	WRS 1572 B	G	79.237	20.151	0.001	0	0	99.39
Nugget Zone	Bulk	WRS 1572 B	H	76.657	23.639	0.018	0	0.007	100.32
Nugget Zone	Bulk	WRS 1572 B	I	74.256	26.143	0.027	0	0.005	100.43
Nugget Zone	Bulk	WRS 1572 B	J	77.981	22.708	0.015	0	0.012	100.72
Nugget Zone	Bulk	WRS 1572 B	K	80.073	19.965	0.02	0.027	0.002	100.09
Nugget Zone	Bulk	WRS 1572 B	L	77.165	23.074	0	0.152	0.004	100.40
Nugget Zone	Bulk	WRS 1572 B	M	76.537	23.514	0.015	0	0.005	100.07
Nugget Zone	Bulk	WRS 1572 B	N	78.561	21.357	0.055	0	0.011	99.98
Nugget Zone	Bulk	WRS 1572 B	O	76.456	22.809	0.001	0	0.013	99.28
Nugget Zone	Bulk	WRS 1572 B	P	77.395	22.865	0.015	0	0	100.28
Nugget Zone	Bulk	WRS 1572 B	Q	76.528	22.917	0	0	0.002	99.45
Nugget Zone	Bulk	WRS 1572 B	R	76.422	23.336	0.037	0	0.004	99.80
Nugget Zone	Bulk	WRS 1572 B	S	76.207	23.274	0.01	0	0	99.49
Nugget Zone	Bulk	WRS 1572 B	T	77.053	22.809	0.002	0	0.006	99.87
Nugget Zone	Bulk	WRS 1572 B	U	74.349	25.852	0.011	0	0	100.21
Nugget Zone	Bulk	WRS 1572 B	V	71.222	27.308	0	46.533	0	145.06
Nugget Zone	Bulk	WRS 1572 B	W	72.004	28.267	0.022	0.096	0	100.39
Nugget Zone	Bulk	WRS 1572 B	X	76.758	22.803	0.007	0	0.038	99.61
Nugget Zone	Bulk	WRS 1572 C	A	74.576	25.152	0	0	0	99.73
Nugget Zone	Bulk	WRS 1572 C	B	76.099	22.866	0.01	0	0.013	98.99
Nugget Zone	Bulk	WRS 1572 C	C	74.013	25.909	0	0	0.013	99.94
Nugget Zone	Bulk	WRS 1572 C	D	77.023	22.251	0.001	0.125	0.019	99.42
Nugget Zone	Bulk	WRS 1572 C	E	76.273	22.866	0	0.037	0.01	99.19
Nugget Zone	Bulk	WRS 1572 C	F	74.762	25.018	0.015	0	0.016	99.81
Nugget Zone	Bulk	WRS 1572 C	G1	76.305	22.541	0.007	0	0.006	98.86
Nugget Zone	Bulk	WRS 1572 C	G2	79.411	19.054	0.009	0.269	0	98.74
Nugget Zone	Bulk	WRS 1572 C	H						
Nugget Zone	Bulk	WRS 1572 C	I	75.725	23.26	0	0	0	98.99
Nugget Zone	Bulk	WRS 1572 C	J	78.567	20.767	0	0	0	99.33
Nugget Zone	Bulk	WRS 1572 C	K	73.322	25.748	0.01	0	0	99.08

Occurrence	Sample Type	Block and ID	Grain ID	Wt.% (Au)	Wt.% (Ag)	Wt.% (Fe)	Wt. % (Hg)	Wt.% (Cu)	Probe Total
Nugget Zone	Bulk	WRS 1572 C	L	76.342	22.692	0.017	0	0.023	99.07
Nugget Zone	Bulk	WRS 1572 C	M	73.29	25.579	0	0.014	0.011	98.89
Nugget Zone	Bulk	WRS 1572 C	N	80.268	18.693	0.051	0	0	99.01
Nugget Zone	Bulk	WRS 1572 C	O	75.687	23.056	0.005	0	0	98.75
Lone Star	Bulk	WRS 1572 C	A	81.661	17.928	0.008	0	0	99.60
Lone Star	Bulk	WRS 1572 C	B	72.777	26.309	0.028	0	0	99.11
Lone Star	Bulk	WRS 1572 C	C	84.686	14.386	0.019	0	0.02	99.11
Lone Star	Bulk	WRS 1572 C	D	83.86	14.405	0.034	0	0.02	98.32
Lone Star	Bulk	WRS 1572 C	E	82.959	16.214	0	0	0.004	99.18
Lone Star	Bulk	WRS 1572 C	F	81.602	17.316	0	0	0.004	98.92
Lone Star	Bulk	WRS 1572 C	G	83.075	15.986	0	0	0.031	99.09
Lone Star	Bulk	WRS 1572 C	H	83.073	15.858	0.007	0	0.011	98.95
Lone Star	Bulk	WRS 1572 C	I	83.775	15.78	0.025	0	0.016	99.60
Lone Star	Bulk	WRS 1572 C	J	82.785	15.635	0	0	0.002	98.42
Lone Star	Bulk	WRS 1572 C	K	85.58	13.377	0.005	0	0.018	98.98
Lone Star	Bulk	WRS 1572 C	L	76.287	22.732	0.008	0	0.001	99.03
Lone Star	Bulk	WRS 1572 C	M	77.053	22.482	0.013	0.01	0.012	99.57
Lone Star	Bulk	WRS 1572 C	N	83.456	15.949	0.022	0	0	99.43
Dysle Zone	Bulk	WRS 1572 C	F	73.083	25.341	0.007	0	0	98.43
Dysle Zone	Bulk	WRS 1572 C	G	66.163	33.787	0.003	0	0	99.95
Dysle Zone	Bulk	WRS 1572 C	H	71.836	27.145	0	0.299	0.002	99.28
Dysle Zone	Bulk	WRS 1572 C	I	71.601	28.264	0.005	0.205	0	100.08
Dysle Zone	Bulk	WRS 1572 C	J	72.085	27.62	0.028	0.002	0.013	99.75
Dysle Zone	Bulk	WRS 1572 C	K	75.367	24.491	0	0	0	99.86
Dysle Zone	Bulk	WRS 1572 C	L	74.97	24.891	0	0	0	99.86
Dysle Zone	Bulk	WRS 1572 C	M	70.997	28.186	0	0	0	99.18
Dysle Zone	Bulk	WRS 1572 C	N	70.449	29.297	0.038	0	0	99.78
Dysle Zone	Bulk	WRS 1572 C	O	72.873	26.632	0.013	0.272	0	99.79
Dysle Zone	Bulk	WRS 1572 C	P	69.326	29.469	0.022	0.061	0	98.88
Dysle Zone	Bulk	WRS 1572 C	Q	73.239	25.699	0.017	0	0.016	98.97
Dysle Zone	Bulk	WRS 1572 C	R	70.226	29.548	0.017	0	0	99.79
Dysle Zone	Bulk	WRS 1572 C	S	71.566	28.088	0	0	0	99.65
Dysle Zone	Bulk	WRS 1572 C	T	71.075	28.571	0.013	0	0	99.66
Dysle Zone	Bulk	WRS 1572 C	U	67.036	32.965	0.011	0	0.005	100.02

Occurrence	Sample Type	Block and ID	Grain ID	Wt.% (Au)	Wt.% (Ag)	Wt.% (Fe)	Wt. % (Hg)	Wt.% (Cu)	Probe Total
Dysle Zone	Bulk	WRS 1572 C	V	72.72	26.12	0.024	0.024	0.032	98.92
Dysle Zone	Bulk	WRS 1572 C	W	62.707	36.608	0	0.267	0	99.58
Dysle Zone	Bulk	WRS 1572 C	X	73.694	25.501	0.031	0	0	99.23
Dysle Zone	Bulk	WRS 1572 C	Y	69.706	29.379	0.017	0.181	0	99.28
Dysle Zone	Bulk	WRS 1572 C	Z	73.17	27.144	0	0	0	100.31
Dysle Zone	Bulk	WRS 1572 C	A1	74.961	24.751	0.025	0	0	99.74
Dysle Zone	Bulk	WRS 1572 C	B1	72.102	27.165	0.011	0	0	99.28
Violet Mine	Bulk	WRS 1463 B	A	66.987	31.405	0.005	1.907	0	100.30
Violet Mine	Bulk	WRS 1463 B	B	74.378	25.058	0.014	1.251	0	100.70
Violet Mine	Bulk	WRS 1463 B	C	78.356	21.37	0.006	1.309	0.002	101.04
Violet Mine	Bulk	WRS 1463 B	D	81.271	19.161	0.014	0.64	0.012	101.10
Violet Mine	Bulk	WRS 1463 B	E	66.462	31.828	0	2.137	0	100.43
Violet Mine	Bulk	WRS 1463 B	F	72.725	26.555	0.012	1.71	0	101.00
Violet Mine	Bulk	WRS 1463 B	G	69.275	30.612	0	0.356	0	100.24
Violet Mine	Bulk	WRS 1463 B	H	69.746	30.166	0	0.828	0	100.74
Violet Mine	Bulk	WRS 1463 B	I	66.306	32.798	0.004	0.685	0	99.79
Violet Mine	Bulk	WRS 1463 B	J	66.573	33.491	0.003	0.314	0	100.38
Violet Mine	Bulk	WRS 1463 B	K						
Violet Mine	Bulk	WRS 1463 B	L	68.538	31.041	0	1.483	0	101.06
Violet Mine	Bulk	WRS 1463 B	M	81.467	18.664	0.02	0.591	0.02	100.76
Violet Mine	Bulk	WRS 1463 B	N	81.294	18.828	0.019	0.726	0.013	100.88
Buckland Zone	In situ			75.2479	25.0246		0.137114833	-0.00058617	100.13
Buckland Zone	In situ			79.33978	20.48981941		0.062468471	0.015517235	99.783
Buckland Zone	In situ			72.91476	25.23381667		0.013868972	0.00251975	98.165
Buckland Zone	In situ			68.96139	31.26586791		0.073616112	0.005072336	100.16
Buckland Zone	In situ			81.58764	18.07800769		0.094703769	0.013667423	99.585
Buckland Zone	In situ			79.71817	20.69213333		0.098746533	0.016572667	100.33
Buckland Zone	In situ			76.48741	23.75958788		0.120577879	0.015191727	100.14
Buckland Zone	In situ			72.64126	27.77045374		0.116506656	0.015934859	100.54
Drilling	In situ			83.81874	16.11343529		0.105931059	0.019162118	99.845
Drilling	In situ			73.45479	26.40923036		0.106796685	0.006739708	99.764
Drilling	In situ			77.3974	22.90512542		0.140807373	0.006725966	100.17
Nugget Zone	In situ			73.39215	26.2354		0.04585515	0.01417685	99.688
Nugget Zone	In situ			60.409	38.480612		0.06251008	0.0013984	98.954

Occurrence	Sample Type	Block and ID	Grain ID	Wt.% (Au)	Wt.% (Ag)	Wt.% (Fe)	Wt. % (Hg)	Wt.% (Cu)	Probe Total
Nugget Zone	In situ			74.24628	26.3206		0.036556167	0.002903167	100.53
Nugget Zone	In situ			81.77918	18.68216357		0.075233524	0.006780738	100.39
Nugget Zone	In situ			76.04008	24.28929231		0.035523203	0.009948253	100.34
Dysle Zone	In situ			71.76079	28.2073		0.199855	0.008119	100.18
Buckland Zone	Bulk	1665-B-109	354	76.24	23.79		0.00	0.00	100.03
Buckland Zone	Bulk	1665-B-110	355	76.65	22.95		0.00	0.00	99.60
Buckland Zone	Bulk	1665-B-111	356	78.83	21.22		0.00	0.00	100.05
Buckland Zone	Bulk	1665-B-112	357	79.19	20.62		0.08	0.00	99.89
Buckland Zone	Bulk	1665-B-113	358	77.47	21.36		0.00	0.01	98.83
Buckland Zone	Bulk	1665-B-114	359	78.32	21.89		0.00	0.02	100.24
Buckland Zone	Bulk	1665-B-115	360	82.83	17.61		0.00	0.01	100.45
Buckland Zone	Bulk	1665-B-116	361	75.55	24.33		0.02	0.02	99.92
Buckland Zone	Bulk	1665-B-117	362	79.12	20.88		0.00	0.01	100.01
Buckland Zone	Bulk	1665-B-118	363	73.66	25.43		0.03	0.03	99.15
Buckland Zone	Bulk	1665-B-119	364	75.09	24.33		0.00	0.03	99.45
Buckland Zone	Bulk	1665-B-120	365	81.80	18.72		0.03	0.02	100.57
Buckland Zone	Bulk	1665-B-121	366	63.42	17.26		0.06	0.00	80.75
Buckland Zone	Bulk	1665-B-122	367	76.03	23.63		0.00	0.02	99.68
Buckland Zone	Bulk	1665-B-123	368	78.57	21.40		0.00	0.01	99.98
Buckland Zone	Bulk	1665-B-124	369	76.37	23.08		0.00	0.01	99.46
Buckland Zone	Bulk	1665-B-125	370	78.99	20.09		0.00	0.00	99.08
Buckland Zone	Bulk	1665-B-126	371	81.66	18.25		0.00	0.00	99.92
Buckland Zone	Bulk	1665-B-127	372	70.03	28.70		0.00	0.01	98.73
Buckland Zone	Bulk	1665-B-128	373	80.38	18.02		0.01	0.01	98.42
Buckland Zone	Bulk	1665-B-129	374	79.59	19.28		0.00	0.00	98.87
Buckland Zone	Bulk	1665-B-130	375	76.85	23.11		0.03	0.01	99.99
Buckland Zone	Bulk	1665-B-131	376	78.60	21.24		0.00	0.00	99.84
Buckland Zone	Bulk	1665-B-132	377	61.97	36.49		0.85	0.00	99.31
Buckland Zone	Bulk	1665-B-133	378	78.06	21.09		0.00	0.02	99.17
Buckland Zone	Bulk	1665-B-134	379	74.53	24.97		0.00	0.00	99.51
Buckland Zone	Bulk	1665-B-135	380	85.31	15.76		0.00	0.04	101.11
Buckland Zone	Bulk	1665-B-136	381	79.35	20.49		0.03	0.00	99.87
Buckland Zone	Bulk	1665-B-137	382	80.05	19.76		0.00	0.01	99.82
Buckland Zone	Bulk	1665-D-29	30	70.59	28.82		0.00	0.00	99.41

Occurrence	Sample Type	Block and ID	Grain ID	Wt.% (Au)	Wt.% (Ag)	Wt.% (Fe)	Wt. % (Hg)	Wt.% (Cu)	Probe Total
Buckland Zone	Bulk	1665-D-30	31	77.47	21.76		0.08	0.00	99.31
Buckland Zone	Bulk	1665-D-31	32	73.72	25.91		0.00	0.02	99.65
Buckland Zone	Bulk	1665-D-32	33	74.52	23.88		0.00	0.02	98.43
Buckland Zone	Bulk	1665-D-33	34	71.97	26.89		0.00	0.00	98.86
Buckland Zone	Bulk	1665-D-34	35	76.30	22.90		0.03	0.03	99.26
Buckland Zone	Bulk	1665-D-35	36	80.99	18.74		0.00	0.03	99.76
Buckland Zone	Bulk	1665-D-36	37	76.17	22.09		0.00	0.02	98.27
Buckland Zone	Bulk	1665-D-37	38	67.08	32.43		0.01	0.00	99.51
Buckland Zone	Bulk	1665-D-38	39	83.07	15.72		0.03	0.04	98.87
Buckland Zone	Bulk	1665-D-39	40	82.37	16.73		0.00	0.05	99.15
Buckland Zone	Bulk	1665-D-41	42	83.16	15.40		0.00	0.00	98.57
Buckland Zone	Bulk	1665-D-42	43	72.32	27.11		0.00	0.00	99.43
Buckland Zone	Bulk	1665-D-43	44	69.98	29.33		0.00	0.01	99.32
Buckland Zone	Bulk	1665-D-44	45	72.98	26.87		0.00	0.02	99.88
Buckland Zone	Bulk	1665-D-45	46	78.04	22.46		0.00	0.00	100.50
Buckland Zone	Bulk	1665-D-46	47	66.67	32.77		0.13	0.02	99.59
Buckland Zone	Bulk	1665-D-47	48	69.38	29.74		0.00	0.00	99.12
Buckland Zone	Bulk	1665-D-48	49	83.25	15.98		0.00	0.03	99.26
Buckland Zone	Bulk	1665-D-49	50	64.46	33.82		0.02	0.02	98.32
Buckland Zone	Bulk	1665-D-50	51	76.34	23.50		0.04	0.02	99.89
Buckland Zone	Bulk	1665-D-51	52	80.90	18.67		0.00	0.04	99.60
Buckland Zone	Bulk	1665-D-52	53	70.55	28.82		0.00	0.03	99.40
Buckland Zone	Bulk	1665-D-53	54	75.45	25.23		0.00	0.00	100.69
Buckland Zone	Bulk	1665-D-54	55	82.38	17.50		0.01	0.02	99.92
Buckland Zone	Bulk	1665-D-55	56	82.83	16.52		0.00	0.01	99.37
Buckland Zone	Bulk	1665-D-56	57	76.42	22.76		0.18	0.01	99.36
Buckland Zone	Bulk	1665-D-57	58	75.06	24.95		0.00	0.00	100.01
Buckland Zone	Bulk	1665-D-58	59	73.18	25.33		0.00	0.00	98.51
Buckland Zone	Bulk	1665-D-59	60	67.27	32.00		0.00	0.03	99.30
Buckland Zone	Bulk	1665-D-60	61	70.44	29.21		0.00	0.01	99.67
Buckland Zone	Bulk	1665-D-61	62	70.48	28.82		0.07	0.01	99.37
Buckland Zone	Bulk	1665-D-62	63	71.94	27.83		0.04	0.00	99.80
Buckland Zone	Bulk	1665-D-63	64	69.28	29.62		0.00	0.02	98.92
Buckland Zone	Bulk	1665-D-64	65	76.98	22.10		0.00	0.02	99.10

Occurrence	Sample Type	Block and ID	Grain ID	Wt.% (Au)	Wt.% (Ag)	Wt.% (Fe)	Wt. % (Hg)	Wt.% (Cu)	Probe Total
Buckland Zone	Bulk	1665-D-65	66	83.53	15.90		0.00	0.01	99.44
Buckland Zone	Bulk	1665-D-66	67	71.33	27.82		0.08	0.00	99.22
Buckland Zone	Bulk	1665-D-67	68	79.51	20.10		0.00	0.00	99.61
Buckland Zone	Bulk	1665-D-68	69	70.82	28.16		0.00	0.02	99.00
Buckland Zone	Bulk	1665-D-69	70	66.80	32.41		0.00	0.00	99.21
Buckland Zone	Bulk	1665-D-70	71	68.20	30.48		0.03	0.02	98.72
Buckland Zone	Bulk	1665-D-71	72	76.13	23.69		0.00	0.01	99.82
Buckland Zone	Bulk	1665-D-72	73	73.77	25.52		0.01	0.00	99.30
Buckland Zone	Bulk	1665-D-73	74	76.03	22.95		0.00	0.02	99.00
Buckland Zone	Bulk	1665-D-74	75	76.52	22.89		0.00	0.00	99.41
Buckland Zone	Bulk	1665-D-75	76	80.06	19.68		0.00	0.00	99.74
Buckland Zone	Bulk	1665-D-76	77	79.03	20.82		0.08	0.02	99.95
Buckland Zone	Bulk	1665-D-77	78	62.26	36.36		0.73	0.00	99.35
Buckland Zone	Bulk	1665-D-78	79	78.85	20.01		0.00	0.00	98.86
Buckland Zone	Bulk	1665-D-79	80	73.21	26.38		0.00	0.00	99.59
Buckland Zone	Bulk	1665-D-80	81	83.81	16.73		0.00	0.03	100.57
Buckland Zone	Bulk	1665-D-81	82	82.27	17.08		0.00	0.01	99.35
Buckland Zone	Bulk	1665-D-82	83	78.33	21.44		0.08	0.00	99.85
Buckland Zone	Bulk	1665-D-83	84	80.06	19.53		0.03	0.02	99.63
Buckland Zone	Bulk	1665-D-84	85	80.52	17.96		0.00	0.00	98.48
Buckland Zone	Bulk	1665-D-85	86	70.39	28.45		0.00	0.00	98.83
Buckland Zone	Bulk	1665-D-86	87	77.33	22.78		0.00	0.02	100.12
Buckland Zone	Bulk	1665-D-87	88	76.50	21.88		0.00	0.01	98.39
Buckland Zone	Bulk	1665-D-88	89	76.95	22.65		0.00	0.02	99.62
Buckland Zone	Bulk	1665-D-89	90	80.41	19.79		0.00	0.00	100.21
Buckland Zone	Bulk	1665-D-90	91	61.98	36.27		0.71	0.00	98.95
Buckland Zone	Bulk	1665-D-91	92	79.62	19.78		0.02	0.00	99.42
Buckland Zone	Bulk	1665-D-92	93	81.13	19.47		0.00	0.00	100.60
Buckland Zone	Bulk	1665-D-93	94	79.35	20.74		0.00	0.04	100.12
Buckland Zone	Bulk	1665-D-94	95	80.28	19.46		0.00	0.01	99.74
Buckland Zone	Bulk	1665-D-95	96	78.15	22.00		0.00	0.03	100.18
Buckland Zone	Bulk	1665-D-96	97	82.36	17.61		0.13	0.02	100.12
Buckland Zone	Bulk	1665-D-97	98	79.78	19.13		0.00	0.00	98.91
Buckland Zone	Bulk	1665-D-98	99	70.18	29.21		0.00	0.04	99.43

Occurrence	Sample Type	Block and ID	Grain ID	Wt.% (Au)	Wt.% (Ag)	Wt.% (Fe)	Wt. % (Hg)	Wt.% (Cu)	Probe Total
Buckland Zone	Bulk	1665-D-99	100	76.57	23.77		0.00	0.01	100.35
Buckland Zone	Bulk	1665-D-100	101	79.75	20.70		0.00	0.01	100.46
Buckland Zone	Bulk	1665-D-102	103	76.59	22.71		0.00	0.02	99.33
Buckland Zone	Bulk	1665-D-103	104	80.81	18.59		0.00	0.00	99.40
Buckland Zone	Bulk	1665-D-104	105	77.28	22.88		0.04	0.00	100.20
Buckland Zone	Bulk	1665-D-105	106	81.93	17.99		0.00	0.03	99.96
Buckland Zone	Bulk	1665-D-106	107	76.62	23.26		0.00	0.01	99.89
Buckland Zone	Bulk	1665-D-107	108	78.29	21.32		0.00	0.01	99.62
Buckland Zone	Bulk	1665-D-108	109	74.49	24.89		0.02	0.02	99.41
Buckland Zone	Bulk	1665-D-109	110	81.03	19.04		0.00	0.02	100.09
Buckland Zone	Bulk	1665-D-110	111	79.41	20.11		0.00	0.00	99.52
Buckland Zone	Bulk	1665-D-111	112	79.04	20.61		0.00	0.00	99.64
Buckland Zone	Bulk	1665-D-112	113	82.27	17.21		0.00	0.00	99.49
Buckland Zone	Bulk	1665-D-113	114	77.92	22.54		0.07	0.02	100.54
Buckland Zone	Bulk	1665-D-114	115	69.34	29.69		0.00	0.01	99.03
Buckland Zone	Bulk	1665-D-115	116	75.32	24.81		0.00	0.01	100.15
Buckland Zone	Bulk	1665-D-116	117	74.68	24.63		0.00	0.03	99.35
Buckland Zone	Bulk	1665-D-117	118	74.81	24.07		0.09	0.00	98.97
Dysle Zone	Bulk	wrs 1572 8A		75.403	27.054	0	0	0	102.46
Dysle Zone	Bulk	wrs 1572 8B		70.927	29.853	0	0.617	0	101.4
Dysle Zone	Bulk	wrs 1572 8C		70.31	31.44	0.003	0	0	101.75
Dysle Zone	Bulk	wrs 1572 8D		74.531	27.493	0.005	0	0	102.03
Dysle Zone	Bulk	WRS 1572 B 8A		72.791	28.11	0.004	0	0	100.91
Dysle Zone	Bulk	WRS 1572 B 8B		78.571	21.853	0	0	0.008	100.43
Dysle Zone	Bulk	WRS 1572 B 8C		66.598	33.222	0	0	0	99.82
Dysle Zone	Bulk	WRS 1572 B 8D		67.821	32.762	0.01	0	0	100.59
Dysle Zone	Bulk	WRS 1572 B 8E		66.105	34.883	0.005	0.018	0	101.01
Dysle Zone	Bulk	WRS 1572 B 8F		70.148	29.209	0.024	0.012	0	99.393
Dysle Zone	Bulk	WRS 1572 B 8G		71.097	30.037	0.015	0.022	0.014	101.19
Dysle Zone	Bulk	WRS 1572 B 8H		75.079	24.98	0.02	0.305	0	100.38
Dysle Zone	Bulk	WRS 1572 C 4A		67.076	32.211	0.018	0	0.005	99.31
Dysle Zone	Bulk	WRS 1572 C 4B		69.754	29.474	0.019	0	0	99.247
Dysle Zone	Bulk	WRS 1572 C 4C		67.608	31.82	0.01	0	0	99.438
Dysle Zone	Bulk	WRS 1572 C 4D		72.366	27.38	0.019	0	0.023	99.788

Occurrence	Sample Type	Block and ID	Grain ID	Wt.% (Au)	Wt.% (Ag)	Wt.% (Fe)	Wt. % (Hg)	Wt.% (Cu)	Probe Total
Dysle Zone	Bulk	WRS 1572 C 4E		72.984	27.049	0.009	0	0	100.04
Dysle Zone	Bulk	WRS 1572 C 4F		73.083	25.341	0.007	0	0	98.431
Dysle Zone	Bulk	WRS 1572 C 4G		66.163	33.787	0.003	0	0	99.953
Dysle Zone	Bulk	WRS 1572 C 4H		71.836	27.145	0	0.299	0.002	99.282
Dysle Zone	Bulk	WRS 1572 C 4I		71.601	28.264	0.005	0.205	0	100.08
Dysle Zone	Bulk	WRS 1572 C 4J		72.085	27.62	0.028	0.002	0.013	99.748
Dysle Zone	Bulk	WRS 1572 C 4K		75.367	24.491	0	0	0	99.858
Dysle Zone	Bulk	WRS 1572 C 4L		74.97	24.891	0	0	0	99.861
Dysle Zone	Bulk	WRS 1572 C 4M		70.997	28.186	0	0	0	99.183
Dysle Zone	Bulk	WRS 1572 C 4N		70.449	29.297	0.038	0	0	99.784
Dysle Zone	Bulk	WRS 1572 C 4O		72.873	26.632	0.013	0.272	0	99.79
Dysle Zone	Bulk	WRS 1572 C P		69.326	29.469	0.022	0.061	0	98.878
Dysle Zone	Bulk	WRS 1572 C Q		73.239	25.699	0.017	0	0.016	98.971
Dysle Zone	Bulk	WRS 1572 C R		70.226	29.548	0.017	0	0	99.791
Dysle Zone	Bulk	WRS 1572 C S		71.566	28.088	0	0	0	99.654
Dysle Zone	Bulk	WRS 1572 C T		71.075	28.571	0.013	0	0	99.659
Dysle Zone	Bulk	WRS 1572 C U		67.036	32.965	0.011	0	0.005	100.02
Dysle Zone	Bulk	WRS 1572 C V		72.72	26.12	0.024	0.024	0.032	98.92
Dysle Zone	Bulk	WRS 1572 C W		62.707	36.608	0	0.267	0	99.582
Dysle Zone	Bulk	WRS 1572 C X		73.694	25.501	0.031	0	0	99.226
Dysle Zone	Bulk	WRS 1572 C Y		69.706	29.379	0.017	0.181	0	99.283
Dysle Zone	Bulk	WRS 1572 C Z		73.17	27.144	0	0	0	100.31
Dysle Zone	Bulk	WRS 1572 C A1		74.961	24.751	0.025	0	0	99.737
Dysle Zone	Bulk	WRS 1572 C B1		72.102	27.165	0.011	0	0	99.278
Dysle Zone	Bulk	WRS 1572 C C1		62.635	36.869	0.026	0.137	0	99.667
Dysle Zone	Bulk	WRS 1572 C C1 DARK		46.665	52.994	0.002	0.667	0.002	100.33
Dysle Zone	Bulk	WRS 1572 C D1		72.401	26.928	0	0.541	0.006	99.876
Dysle Zone	Bulk	WRS 1572 C E1		68.142	31.462	0.014	0	0	99.618
Dysle Zone	Bulk	WRS 1572 C f1		71.598	27.892	0.022	0	0.005	99.517
Dysle Zone	Bulk	WRS 1572 C G1		71.923	27.719	0.009	0	0	99.651
Dysle Zone	Bulk	WRS 1572 C H1		73.983	25.116	0.014	0	0	99.113
Dysle Zone	Bulk	WRS 1572 C I1		64.067	35.591	0	0.007	0.009	99.674
Dysle Zone	2013 Crushed Vein	RC40_9_1		69.7176	29.3825		0.117044	0.016851	99.234

Occurrence	Sample Type	Block and ID	Grain ID	Wt.% (Au)	Wt.% (Ag)	Wt.% (Fe)	Wt. % (Hg)	Wt.% (Cu)	Probe Total
Dysle Zone	2013 Crushed Vein	RC40_9_2		69.7706	29.7826		0.16786	0.002142	99.723
Dysle Zone	2013 Crushed Vein	RC40_9_3		73.3955	25.7633		0.181104	0.015145	99.355
Dysle Zone	2013 Crushed Vein	RC40_9_4		72.5854	26.6561		0.067173	0.022905	99.332
Dysle Zone	2013 Crushed Vein	RC40_9_5		71.5949	27.8675		0.120332	0.028786	99.612
Dysle Zone	2013 Crushed Vein	RC40_9_6		74.8537	24.5202		0.047679	0.016668	99.438
Dysle Zone	2013 Crushed Vein	RC40_9_7		73.3107	26.2485		0.103889	0.002814	99.666
Dysle Zone	2013 Crushed Vein	RC40_9_8		74.0743	25.6254		0.126441	0.024182	99.85
Dysle Zone	2013 Crushed Vein	RC40_9_9		71.301	28.2424		0.175995	0.023533	99.743
Dysle Zone	2013 Crushed Vein	RC41_8_1		74.515	24.9058		0.162581	0.019307	99.603
Dysle Zone	2013 Crushed Vein	RC41_8_2		70.5541	29.4375		0.132174	0.023354	100.15
Dysle Zone	2013 Crushed Vein	RC41_8_3		69.1025	30.4974		0.217989	0.007989	99.826
Dysle Zone	2013 Crushed Vein	RC41_8_4		73.1227	26.1266		0.096587	0.007758	99.354
Dysle Zone	2013 Crushed Vein	RC41_8_5		72.8569	26.9927		0.139592	0.021371	100.01
Dysle Zone	2013 Crushed Vein	RC41_8_6		73.3069	26.2786		0.066334	0.018555	99.67
Dysle Zone	2013 Crushed Vein	RC41_8_7		76.0982	24.0533		0.247621	0.009921	100.41
Dysle Zone	2013 Crushed Vein	RC41_8_8		69.3185	30.2845		0.121243	0.005679	99.73
Dysle Zone	2013 Crushed Vein	RC41_8_9		75.4336	24.9075		0.101138	0.023647	100.47
Dysle Zone	2013 Crushed Vein	RC44_8_1		73.3369	27.4871		0.204821	0.018591	101.05
Dysle Zone	2013 Crushed Vein	RC44_8_10		73.8625	26.7801		0.282217	0.005252	100.93
Dysle Zone	2013 Crushed Vein	RC44_8_11		74.0698	26.4951		0.234926	0.021153	100.82
Dysle Zone	2013 Crushed Vein	RC44_8_12		72.7366	28.1423		0.172198	0.002733	101.05
Dysle Zone	2013 Crushed Vein	RC44_8_13		70.9024	29.508		0.225612	0.00138	100.64
Dysle Zone	2013 Crushed Vein	RC44_8_2		75.9907	24.7955		0.087875	0.033081	100.91
Dysle Zone	2013 Crushed Vein	RC44_8_3		75.1993	25.104		0.221744	0.018118	100.54
Dysle Zone	2013 Crushed Vein	RC44_8_4		76.4326	24.1138		0.133066	0.008527	100.69
Dysle Zone	2013 Crushed Vein	RC44_8_5		71.2035	29.7108		0.06911	0.015129	101
Dysle Zone	2013 Crushed Vein	RC44_8_6		72.2129	28.5485		0.226301	0.02747	101.02
Dysle Zone	2013 Crushed Vein	RC44_8_7		75.7894	24.7346		0.240684	0.012575	100.78
Dysle Zone	2013 Crushed Vein	RC44_8_8		71.1396	29.2697		0.130105	0.0174	100.56
Dysle Zone	2013 Crushed Vein	RC44_8_9		69.2707	31.3163		0.164385	0.004341	100.76
Dysle Zone	2013 Crushed Vein	RC45_8_1		70.5311	29.8444		0.243994	0.016511	100.64
Dysle Zone	2013 Crushed Vein	RC45_8_2		70.6575	29.6549		0.312655	0.013218	100.64
Dysle Zone	2013 Crushed Vein	RC45_8_3		74.0633	26.1731		0.272351	0.016532	100.53
Dysle Zone	2013 Crushed Vein	RC45_8_4		72.6426	27.8034		0.184669	-0.0014	100.63

Occurrence	Sample Type	Block and ID	Grain ID	Wt.% (Au)	Wt.% (Ag)	Wt.% (Fe)	Wt. % (Hg)	Wt.% (Cu)	Probe Total
Dysle Zone	2013 Crushed Vein	RC45_8_5		68.8343	31.4265		0.217697	0.029804	100.51
Nugget Zone	2013 Crushed Vein	RC41_9a_1		82.2475	17.7775		0.129784	0.041166	100.2
Nugget Zone	2013 Crushed Vein	RC41_9a_10		83.15	16.5937		0.133772	0.032094	99.91
Nugget Zone	2013 Crushed Vein	RC41_9a_11		82.2329	17.6232		0.086534	0.025402	99.968
Nugget Zone	2013 Crushed Vein	RC41_9a_12		79.3615	20.3938		0.175812	0.022764	99.954
Nugget Zone	2013 Crushed Vein	RC41_9a_13		80.9409	18.988		0.133152	0.010752	100.07
Nugget Zone	2013 Crushed Vein	RC41_9a_14		78.4135	21.4474		0.092036	0.032342	99.985
Nugget Zone	2013 Crushed Vein	RC41_9a_15		69.874	29.9592		0.140196	0.000826	99.974
Nugget Zone	2013 Crushed Vein	RC41_9a_16		81.1737	18.6294		0.233491	0.028312	100.07
Nugget Zone	2013 Crushed Vein	RC41_9a_17		83.1532	16.6288		0.166223	0.008165	99.956
Nugget Zone	2013 Crushed Vein	RC41_9a_18		82.4911	17.3787		0.153564	0.014328	100.04
Nugget Zone	2013 Crushed Vein	RC41_9a_19		83.8089	16.1381		0.181774	0.005485	100.13
Nugget Zone	2013 Crushed Vein	RC41_9a_2		80.8602	19.0734		0.162166	0.025057	100.12
Nugget Zone	2013 Crushed Vein	RC41_9a_20		80.3769	19.4428		0.146843	0.015559	99.982
Nugget Zone	2013 Crushed Vein	RC41_9a_21		79.088	20.8661		0.151155	0.016796	100.12
Nugget Zone	2013 Crushed Vein	RC41_9a_22A		83.1072	16.6956		0.189633	0.017753	100.01
Nugget Zone	2013 Crushed Vein	RC41_9a_22B		83.2714	16.5595		0.172633	0.026287	100.03
Nugget Zone	2013 Crushed Vein	RC41_9a_23		82.1111	17.7596		0.110907	0.030426	100.01
Nugget Zone	2013 Crushed Vein	RC41_9a_24		81.7998	17.9726		0.167818	0.007191	99.947
Nugget Zone	2013 Crushed Vein	RC41_9a_25		81.6484	17.9529		0.150109	0.032929	99.784
Nugget Zone	2013 Crushed Vein	RC41_9a_3		83.2019	16.6691		0.207423	0.002148	100.08
Nugget Zone	2013 Crushed Vein	RC41_9a_4		69.7663	29.79		0.133818	0.009037	99.699
Nugget Zone	2013 Crushed Vein	RC41_9a_5		82.8581	17.4949		0.116863	0.024485	100.49
Nugget Zone	2013 Crushed Vein	RC41_9a_6		83.4124	16.7662		0.097405	0.025965	100.3
Nugget Zone	2013 Crushed Vein	RC41_9a_7		83.3069	16.8775		0.108344	0.013841	100.31
Nugget Zone	2013 Crushed Vein	RC41_9a_8		80.0942	19.6771		0.138287	0.031968	99.942
Nugget Zone	2013 Crushed Vein	RC41_9a_9		73.8613	25.9701		0.099296	0.028783	99.959
Nugget Zone	2013 Crushed Vein	RC41_9b_1		73.403	26.1439		0.190632	0.006682	99.744
Nugget Zone	2013 Crushed Vein	RC41_9b_10		77.2644	21.8124		0.12525	0.013389	99.215
Nugget Zone	2013 Crushed Vein	RC41_9b_2		77.5098	22.213		0.125097	0.016868	99.865
Nugget Zone	2013 Crushed Vein	RC41_9b_3		77.7535	21.8923		0.089009	0.008988	99.744
Nugget Zone	2013 Crushed Vein	RC41_9b_4		79.9181	19.9971		0.16003	0.019557	100.1
Nugget Zone	2013 Crushed Vein	RC41_9b_5		83.5273	16.465		0.199459	0.030054	100.22
Nugget Zone	2013 Crushed Vein	RC41_9b_6		74.3635	26.449		0.151741	0.016349	100.98

Occurrence	Sample Type	Block and ID	Grain ID	Wt.% (Au)	Wt.% (Ag)	Wt.% (Fe)	Wt. % (Hg)	Wt.% (Cu)	Probe Total
Nugget Zone	2013 Crushed Vein	RC41_9b_7		65.1874	33.9422		0.129834	0.020172	99.28
Nugget Zone	2013 Crushed Vein	RC41_9b_8		69.1311	30.9061		0.098814	0.020897	100.16
Nugget Zone	2013 Crushed Vein	RC41_9b_9		82.3261	17.9525		0.137249	0.015475	100.43
Nugget Zone	2013 Crushed Vein	RC43_5_1		69.7713	30.5204		0.136721	0.020504	100.45
Nugget Zone	2013 Crushed Vein	RC43_5_2		83.0684	16.7662		0.150443	0.017799	100
Nugget Zone	2013 Crushed Vein	RC43_5_3		81.8172	18.1386		0.166434	0.020455	100.14
Nugget Zone	2013 Crushed Vein	RC43_5_4		80.7354	17.9515		0.174525	0.017603	98.879
Nugget Zone	2013 Crushed Vein	RC43_5_5		81.4527	17.834		0.127284	0.021113	99.435
Nugget Zone	2013 Crushed Vein	RC43_5_6		82.6671	17.1178		0.213589	0.025399	100.02
Nugget Zone	2013 Crushed Vein	RC44_10_10		83.187	17.4453		0.247295	0.038653	100.92
Nugget Zone	2013 Crushed Vein	RC44_10_11		76.3522	24.6419		0.199902	0.019845	101.21
Nugget Zone	2013 Crushed Vein	RC44_10_12		80.4548	20.2086		0.097785	0.02449	100.79
Nugget Zone	2013 Crushed Vein	RC44_10_13		83.3325	17.2971		0.175906	0.019232	100.83
Nugget Zone	2013 Crushed Vein	RC44_10_14		83.7	17.2478		0.175994	0.010648	101.13
Nugget Zone	2013 Crushed Vein	RC44_10_15		83.8172	16.8565		0.161884	0.028501	100.86
Nugget Zone	2013 Crushed Vein	RC44_10_16		77.6589	22.9455		0.110154	0.013142	100.73
Nugget Zone	2013 Crushed Vein	RC44_10_17		82.0286	18.9892		0.197547	0.022631	101.24
Nugget Zone	2013 Crushed Vein	RC44_10_18		80.4581	20.4797		0.125643	0.026758	101.09
Nugget Zone	2013 Crushed Vein	RC44_10_19		82.76	18.1656		0.140858	0.035075	101.1
Nugget Zone	2013 Crushed Vein	RC44_10_2		82.1949	18.3723		0.19115	0.029078	100.79
Nugget Zone	2013 Crushed Vein	RC44_10_20		80.6545	20.0976		0.179441	0.021903	100.95
Nugget Zone	2013 Crushed Vein	RC44_10_21		84.3751	16.8001		0.139271	0.028558	101.34
Nugget Zone	2013 Crushed Vein	RC44_10_22		70.248	30.2372		0.161826	0.012514	100.66
Nugget Zone	2013 Crushed Vein	RC44_10_23		82.1984	18.0622		0.162791	0.0262	100.45
Nugget Zone	2013 Crushed Vein	RC44_10_24		83.9253	17.125		0.14425	0.020436	101.22
Nugget Zone	2013 Crushed Vein	RC44_10_3		80.3099	20.561		0.138004	0.029881	101.04
Nugget Zone	2013 Crushed Vein	RC44_10_4		83.1097	17.4293		0.127164	0.028155	100.69
Nugget Zone	2013 Crushed Vein	RC44_10_5		81.839	18.6893		0.098702	0.02775	100.66
Nugget Zone	2013 Crushed Vein	RC44_10_6		81.7211	18.7341		0.121238	0.023393	100.6
Nugget Zone	2013 Crushed Vein	RC44_10_7		69.8758	31.0272		0.078697	0.029279	101.01
Nugget Zone	2013 Crushed Vein	RC44_10_8		84.822	15.9163		0.230476	0.010314	100.98
Nugget Zone	2013 Crushed Vein	RC44_10_9		77.063	23.3254		0.189157	0.00565	100.58
Nugget Zone	2013 Crushed Vein	RC45_10a_1		0.216304	0.080016		0.008378	-0.00247	0.3022
Nugget Zone	2013 Crushed Vein	RC45_10a_10		80.0588	20.0657		0.195144	0.01276	100.33

Occurrence	Sample Type	Block and ID	Grain ID	Wt.% (Au)	Wt.% (Ag)	Wt.% (Fe)	Wt. % (Hg)	Wt.% (Cu)	Probe Total
Nugget Zone	2013 Crushed Vein	RC45_10a_11		80.4932	19.5219		0.155347	0.018137	100.19
Nugget Zone	2013 Crushed Vein	RC45_10a_12		79.6805	20.4878		0.164506	0.005061	100.34
Nugget Zone	2013 Crushed Vein	RC45_10a_13		82.5437	18.2506		0.09043	0.012971	100.9
Nugget Zone	2013 Crushed Vein	RC45_10a_14		83.2381	17.1077		0.206638	0.024657	100.58
Nugget Zone	2013 Crushed Vein	RC45_10a_15		77.8777	22.6735		0.191788	0.013033	100.76
Nugget Zone	2013 Crushed Vein	RC45_10a_16		81.5708	18.6057		0.152771	0.015809	100.35
Nugget Zone	2013 Crushed Vein	RC45_10a_17		84.0225	16.8189		0.128824	0.027905	101
Nugget Zone	2013 Crushed Vein	RC45_10a_18		72.6458	26.9846		0.06431	0.017042	99.712
Nugget Zone	2013 Crushed Vein	RC45_10a_19		82.9976	17.8684		0.115192	0.023272	101
Nugget Zone	2013 Crushed Vein	RC45_10a_2		73.6402	26.2181		0.123044	0.011723	99.993
Nugget Zone	2013 Crushed Vein	RC45_10a_20		80.3362	20.0855		0.148373	0.018346	100.59
Nugget Zone	2013 Crushed Vein	RC45_10a_21		71.974	28.6163		0.102641	0.011536	100.71
Nugget Zone	2013 Crushed Vein	RC45_10a_22		75.7782	24.2937		0.068944	0.007917	100.15
Nugget Zone	2013 Crushed Vein	RC45_10a_23		68.2395	32.1366		0.109556	0.019115	100.51
Nugget Zone	2013 Crushed Vein	RC45_10a_24		73.2262	27.1606		0.143422	0.027066	100.56
Nugget Zone	2013 Crushed Vein	RC45_10a_25		82.2224	18.933		0.134253	0.013407	101.3
Nugget Zone	2013 Crushed Vein	RC45_10a_26		82.4474	18.12		0.121908	0.0214	100.71
Nugget Zone	2013 Crushed Vein	RC45_10a_27		78.0394	22.9809		0.178721	0.017041	101.22
Nugget Zone	2013 Crushed Vein	RC45_10a_28		82.0314	18.3493		0.134631	0.030133	100.55
Nugget Zone	2013 Crushed Vein	RC45_10a_3		77.6388	22.7461		0.184393	0.021343	100.59
Nugget Zone	2013 Crushed Vein	RC45_10a_4		80.9744	19.3235		0.102289	0.035279	100.44
Nugget Zone	2013 Crushed Vein	RC45_10a_5		82.0058	18.2039		0.176754	0.026334	100.41
Nugget Zone	2013 Crushed Vein	RC45_10a_6		80.6768	19.6961		0.133275	0.022709	100.53
Nugget Zone	2013 Crushed Vein	RC45_10a_7		78.3337	21.9627		0.158137	0.019532	100.47
Nugget Zone	2013 Crushed Vein	RC45_10a_8		73.5713	26.8335		0.166209	0.01161	100.58
Nugget Zone	2013 Crushed Vein	RC45_10a_9		79.5762	20.9422		0.169031	0.018316	100.71
Nugget Zone	2013 Crushed Vein	RC45_10b_1		86.2342	14.3046		0.231952	0.012115	100.78
Nugget Zone	2013 Crushed Vein	RC45_10b_10		83.3294	17.0065		0.127699	0.025431	100.49
Nugget Zone	2013 Crushed Vein	RC45_10b_11		82.3262	18.1336		0.138052	0.0223	100.62
Nugget Zone	2013 Crushed Vein	RC45_10b_12		73.6442	26.7095		0.151431	0.014309	100.52
Nugget Zone	2013 Crushed Vein	RC45_10b_13		81.4544	18.737		0.16915	0.022591	100.38
Nugget Zone	2013 Crushed Vein	RC45_10b_14		69.5039	31.1358		0.111239	0.01092	100.76
Nugget Zone	2013 Crushed Vein	RC45_10b_15		81.5802	18.1794		0.121034	0.017018	99.898
Nugget Zone	2013 Crushed Vein	RC45_10b_16		83.0467	16.4319		0.12191	0.019277	99.62

Occurrence	Sample Type	Block and ID	Grain ID	Wt.% (Au)	Wt.% (Ag)	Wt.% (Fe)	Wt. % (Hg)	Wt.% (Cu)	Probe Total
Nugget Zone	2013 Crushed Vein	RC45_10b_17		83.2175	17.236		0.133463	0.014039	100.6
Nugget Zone	2013 Crushed Vein	RC45_10b_18		77.8523	22.4895		0.211659	0.035463	100.59
Nugget Zone	2013 Crushed Vein	RC45_10b_2		82.5611	17.7998		0.18019	0.037161	100.58
Nugget Zone	2013 Crushed Vein	RC45_10b_3		73.9714	25.2352		0.16946	0.009237	99.385
Nugget Zone	2013 Crushed Vein	RC45_10b_4		83.9862	16.2452		0.225222	0.019331	100.48
Nugget Zone	2013 Crushed Vein	RC45_10b_5		67.6987	32.1847		0.175846	0.019289	100.08
Nugget Zone	2013 Crushed Vein	RC45_10b_6		83.2196	17.2095		0.123695	0.026554	100.58
Nugget Zone	2013 Crushed Vein	RC45_10b_7		74.3382	25.636		0.134231	0.024886	100.13
Nugget Zone	2013 Crushed Vein	RC45_10b_8		79.1443	20.965		0.200787	0.008008	100.32
Nugget Zone	2013 Crushed Vein	RC45_10b_9		81.0877	18.5875		0.190661	0.014845	99.881
Nugget Zone	2013 Crushed Vein	RC45_10c_1		82.3274	18.0289		0.151999	0.057276	100.57
Nugget Zone	2013 Crushed Vein	RC45_10c_10		82.4304	18.0334		0.193211	0.025669	100.68
Nugget Zone	2013 Crushed Vein	RC45_10c_11		77.1212	23.6295		0.114021	0.014433	100.88
Nugget Zone	2013 Crushed Vein	RC45_10c_12		80.9485	19.6759		0.16962	0.020203	100.81
Nugget Zone	2013 Crushed Vein	RC45_10c_13		82.0307	18.925		0.257549	0.030416	101.24
Nugget Zone	2013 Crushed Vein	RC45_10c_2		69.6891	32.2975		0.06323	0.041146	102.09
Nugget Zone	2013 Crushed Vein	RC45_10c_3		83.8732	16.7564		0.150947	0.035027	100.82
Nugget Zone	2013 Crushed Vein	RC45_10c_4		78.8035	21.8646		0.186993	0.031356	100.89
Nugget Zone	2013 Crushed Vein	RC45_10c_5		78.7372	22.5981		0.123402	0.031753	101.49
Nugget Zone	2013 Crushed Vein	RC45_10c_6		69.2102	31.175		0.108219	0.051126	100.55
Nugget Zone	2013 Crushed Vein	RC45_10c_7		83.578	17.2544		0.193846	0.044714	101.07
Nugget Zone	2013 Crushed Vein	RC45_10c_8		74.0504	25.7053		0.154949	0.043864	99.955
Nugget Zone	2013 Crushed Vein	RC45_10c_9		73.1801	27.2538		0.057128	0.017221	100.51
Nugget Zone	2013 Crushed Vein	RC46_2a_1		69.4778	31.1348		0.097584	0.008931	100.72
Nugget Zone	2013 Crushed Vein	RC46_2a_10		63.8115	36.756		0.173806	0.025537	100.77
Nugget Zone	2013 Crushed Vein	RC46_2a_11		83.2119	16.5843		0.231294	0.020204	100.05
Nugget Zone	2013 Crushed Vein	RC46_2a_12		81.3368	19.3288		0.124543	0.022095	100.81
Nugget Zone	2013 Crushed Vein	RC46_2a_13		78.7216	21.1163		0.207346	0.022501	100.07
Nugget Zone	2013 Crushed Vein	RC46_2a_14		69.3478	31.2708		0.079487	0.01209	100.71
Nugget Zone	2013 Crushed Vein	RC46_2a_15		82.918	17.404		0.120901	0.02547	100.47
Nugget Zone	2013 Crushed Vein	RC46_2a_16		82.1669	18.1271		0.115002	0.020084	100.43
Nugget Zone	2013 Crushed Vein	RC46_2a_17		80.5922	19.6208		0.140261	0.028102	100.38
Nugget Zone	2013 Crushed Vein	RC46_2a_18		73.2194	27.3497		0.210773	0.010947	100.79
Nugget Zone	2013 Crushed Vein	RC46_2a_19		72.0895	28.1069		0.208791	0.018084	100.42

Occurrence	Sample Type	Block and ID	Grain ID	Wt.% (Au)	Wt.% (Ag)	Wt.% (Fe)	Wt. % (Hg)	Wt.% (Cu)	Probe Total
Nugget Zone	2013 Crushed Vein	RC46_2a_2		65.9808	33.738		0.086002	0.008682	99.813
Nugget Zone	2013 Crushed Vein	RC46_2a_20		73.1071	27.6327		0.165876	0.019399	100.93
Nugget Zone	2013 Crushed Vein	RC46_2a_21		75.6843	24.7016		0.156757	0.009146	100.55
Nugget Zone	2013 Crushed Vein	RC46_2a_22		83.769	17.3001		0.217144	0.02374	101.31
Nugget Zone	2013 Crushed Vein	RC46_2a_3		82.4373	17.7485		0.125566	0.026203	100.34
Nugget Zone	2013 Crushed Vein	RC46_2a_4		83.5001	16.7875		0.18074	0.03365	100.5
Nugget Zone	2013 Crushed Vein	RC46_2a_5		81.055	19.7007		0.196201	0.02365	100.98
Nugget Zone	2013 Crushed Vein	RC46_2a_6		78.9586	21.4822		0.166252	0.010896	100.62
Nugget Zone	2013 Crushed Vein	RC46_2a_7		68.6208	31.2748		0.073437	0.006028	99.975
Nugget Zone	2013 Crushed Vein	RC46_2a_8		75.0847	25.6044		0.085847	0.000115	100.78
Nugget Zone	2013 Crushed Vein	RC46_2a_9		73.6552	26.4323		0.133736	-0.00276	100.22
Nugget Zone	2013 Crushed Vein	RC46_2b_1		78.5401	21.5161		0.226959	0.001432	100.29
Nugget Zone	2013 Crushed Vein	RC46_2b_2		80.9884	18.9799		0.116086	0.017992	100.1
Nugget Zone	2013 Crushed Vein	RC46_2b_3		79.9952	20.5082		0.172562	0.030474	100.71
Nugget Zone	2013 Crushed Vein	RC46_2b_4		83.9072	18.5956		0.231954	0.034393	102.77
Nugget Zone	2013 Crushed Vein	RC46_2b_5		83.3661	17.0643		0.240061	0.018933	100.69
Nugget Zone	2013 Crushed Vein	RC46_2b_6		82.0387	20.576		0.179468	0.011746	102.81
Nugget Zone	2013 Crushed Vein	RC46_2b_7		80.0697	20.0177		0.188789	0.017716	100.29
Nugget Zone	2013 Crushed Vein	RC46_2c_1		83.6873	16.2679		0.1654	0.030231	100.15
Nugget Zone	2013 Crushed Vein	RC46_2c_10		83.4439	16.7796		0.090194	0.03304	100.35
Nugget Zone	2013 Crushed Vein	RC46_2c_11		83.8671	17.0164		0.162457	0.015596	101.06
Nugget Zone	2013 Crushed Vein	RC46_2c_12		76.5866	23.3961		0.166075	0.014634	100.16
Nugget Zone	2013 Crushed Vein	RC46_2c_13		68.3658	31.1022		0.184287	0.009476	99.662
Nugget Zone	2013 Crushed Vein	RC46_2c_13		74.4544	25.6172		0.125586	0.018845	100.22
Nugget Zone	2013 Crushed Vein	RC46_2c_14		72.1954	28.7112		0.216967	0.017903	101.14
Nugget Zone	2013 Crushed Vein	RC46_2c_15		82.9156	17.139		0.084008	0.016013	100.16
Nugget Zone	2013 Crushed Vein	RC46_2c_16		81.9981	18.4311		0.209288	0.012646	100.65
Nugget Zone	2013 Crushed Vein	RC46_2c_2		69.1133	30.5446		0.160122	0.007777	99.826
Nugget Zone	2013 Crushed Vein	RC46_2c_3		64.9441	35.6036		0.10254	0.007898	100.66
Nugget Zone	2013 Crushed Vein	RC46_2c_4		69.0707	31.6867		0.160198	0.021622	100.94
Nugget Zone	2013 Crushed Vein	RC46_2c_5		79.8042	20.5798		0.117384	0.018388	100.52
Nugget Zone	2013 Crushed Vein	RC46_2c_6		83.3795	16.6353		0.131413	0.012114	100.16
Nugget Zone	2013 Crushed Vein	RC46_2c_7		69.3817	31.3651		0.036754	0.010887	100.79
Nugget Zone	2013 Crushed Vein	RC46_2c_8		83.7795	16.4969		0.155576	0.010634	100.44

Occurrence	Sample Type	Block and ID	Grain ID	Wt.% (Au)	Wt.% (Ag)	Wt.% (Fe)	Wt. % (Hg)	Wt.% (Cu)	Probe Total
Nugget Zone	2013 Crushed Vein	RC46_2c_9		82.5894	17.7147		0.24907	0.005855	100.56
Boulder Mine	Lode 2013 Crushed Vein	RC40_8_1A		83.4561	16.0117		0.087654	0.02388	99.579
Boulder Mine	Lode 2013 Crushed Vein	RC40_8_1B		83.6611	16.2041		0.135864	0.014667	100.02
Boulder Mine	Lode 2013 Crushed Vein	RC40_8_2		83.9421	15.8476		0.159622	0.006337	99.956
Boulder Mine	Lode 2013 Crushed Vein	RC41_7_1A		83.1873	17.0151		0.153158	0.028874	100.39
Boulder Mine	Lode 2013 Crushed Vein	RC41_7_2A		77.2124	22.4887		0.105512	0.023851	99.831
Boulder Mine	Lode 2013 Crushed Vein	RC41_7_2B		76.9332	21.7316		0.064184	0.03734	98.766
Boulder Mine	Lode 2013 Crushed Vein	RC44_7_1		84.1164	15.9673		0.112821	0.098026	100.3
Boulder Mine	Lode 2013 Crushed Vein	RC44_7_10		82.6725	17.7431		0.154202	0.030205	100.6
Boulder Mine	Lode 2013 Crushed Vein	RC44_7_11		84.3163	15.6086		0.212787	0.028535	100.17
Boulder Mine	Lode 2013 Crushed Vein	RC44_7_2		84.1693	16.5531		0.132448	0.035113	100.89
Boulder Mine	Lode 2013 Crushed Vein	RC44_7_3		83.4087	16.7023		0.049574	0.034123	100.2
Boulder Mine	Lode 2013 Crushed Vein	RC44_7_4		85.0282	15.4871		0.099621	0.034168	100.65
Boulder Mine	Lode 2013 Crushed Vein	RC44_7_5		83.2147	16.5123		0.056802	0.047622	99.831
Boulder Mine	Lode 2013 Crushed Vein	RC44_7_6		84.1509	16.0205		0.151581	0.016266	100.34
Boulder Mine	Lode 2013 Crushed Vein	RC44_7_7		83.7971	16.6386		0.152483	0.030242	100.62
Boulder Mine	Lode 2013 Crushed Vein	RC44_7_8		84.0184	16.5925		0.12033	0.063329	100.8
Boulder Mine	Lode 2013 Crushed Vein	RC44_7_9		75.5656	24.45		0.169378	0.034012	100.22

Occurrence	Sample Type	Block and ID	Grain ID	Wt.% (Au)	Wt.% (Ag)	Wt.% (Fe)	Wt. % (Hg)	Wt.% (Cu)	Probe Total	
Boulder Mine	Lode	2013 Crushed Vein	RC45_6_1		80.1376	20.2135		0.174024	0.016541	100.54
Boulder Mine	Lode	2013 Crushed Vein	RC45_6_2		82.4342	18.0904		0.186343	0.036163	100.75
Boulder Mine	Lode	2013 Crushed Vein	RC45_6_3		79.242	21.1726		0.115866	0.019201	100.55
Boulder Mine	Lode	2013 Crushed Vein	RC45_6_4		83.416	17.3876		0.175458	0.020309	101
Boulder Mine	Lode	2013 Crushed Vein	RC45_6_5		80.6687	19.8554		0.209992	0.015612	100.75
Boulder Mine	Lode	2013 Crushed Vein	RC45_6_6		83.6531	17.2642		0.158865	0.029431	101.11
Boulder Mine	Lode	2013 Crushed Vein	RC45_6_7		84.3667	16.2827		0.082943	0.031099	100.76
Violet Mine	Bulk	WRS 1463 B VIOLET 2A		66.987	31.405	0.005	1.907	0		100.3
Violet Mine	Bulk	WRS 1463 B VIOLET 2B		74.378	25.058	0.014	1.251	0		100.7
Violet Mine	Bulk	WRS 1463 B VIOLET 2C/1		78.356	21.37	0.006	1.309	0.002		101.04
Violet Mine	Bulk	WRS 1463 B VIOLET 2D		81.271	19.161	0.014	0.64	0.012		101.1
Violet Mine	Bulk	WRS 1463 B VIOLET 2E		66.462	31.828	0	2.137	0		100.43
Violet Mine	Bulk	WRS 1463 B VIOLET 2F		72.725	26.555	0.012	1.71	0		101
Violet Mine	Bulk	WRS 1463 B VIOLET 2G		69.275	30.612	0	0.356	0		100.24
Violet Mine	Bulk	WRS 1463 B VIOLET 2H		69.746	30.166	0	0.828	0		100.75
Violet Mine	Bulk	WRS 1463 B VIOLET 2I		66.306	32.798	0.004	0.685	0		99.793
Violet Mine	Bulk	WRS 1463 B VIOLET 2J		66.573	33.491	0.003	0.314	0		100.38

Occurrence	Sample Type	Block and ID	Grain ID	Wt.% (Au)	Wt.% (Ag)	Wt.% (Fe)	Wt. % (Hg)	Wt.% (Cu)	Probe Total
Violet Mine	Bulk	WRS 1463 B VIOLET 2L		68.538	31.041	0	1.483	0	101.06
Violet Mine	Bulk	WRS 1463 B VIOLET 2LDPR		36.21	54.35	0	9.067	0	99.627
Violet Mine	Bulk	WRS 1463 B VIOLET 2M		81.467	18.664	0.02	0.591	0.02	100.76
Violet Mine	Bulk	WRS 1463 B VIOLET 2N		81.294	18.828	0.019	0.726	0.013	100.88
Violet Mine	Bulk	WRS 1463 B VIOLET 2O C		74.876	24.392	0.024	1.375	0	100.68
Violet Mine	Bulk	WRS 1463 B VIOLET 2O D2		50.868	43.548	0	6.182	0	100.6
Violet Mine	Bulk	WRS 1463 B VIOLET 3A A		86.212	13.893	0.027	0.907	0.02	101.06
Violet Mine	Bulk	WRS 1463 B VIOLET 3A B		66.868	33.189	0.007	0.387	0	100.45
Violet Mine	Bulk	WRS 1463 B VIOLET 3A C		65.158	33.053	0	1.911	0	100.13
Violet Mine	Bulk	WRS 1463 B VIOLET 3A D		73.273	26.374	0.02	0.855	0	100.52
Violet Mine	Bulk	WRS 1463 B VIOLET 3A E		70.898	28.249	0	0.829	0	99.978
Violet Mine	Bulk	WRS 1463 B VIOLET 3A G		69.239	30.661	0.003	0.264	0	100.17
Violet Mine	Bulk	WRS 1463 B VIOLET 3A H		67.865	31.95	0	0.917	0	100.73
Violet Mine	Bulk	WRS 1463 B VIOLET 3A I		69.596	29.124	0.01	1.355	0	100.09
Violet Mine	Bulk	WRS 1463 B VIOLET 3A J		68.051	31.247	0	1.061	0	100.36
Violet Mine	Bulk	WRS 1463 B VIOLET 3A K		64.875	34.481	0	1.277	0	100.63
Violet Mine	Bulk	WRS 1463 B VIOLET 3A L		65.93	32.625	0	1.37	0	99.936

Occurrence	Sample Type	Block and ID	Grain ID	Wt.% (Au)	Wt.% (Ag)	Wt.% (Fe)	Wt. % (Hg)	Wt.% (Cu)	Probe Total
Violet Mine	Bulk	WRS 1463 B VIOLET 3A M		62.287	36.305	0.017	1.206	0	99.815
Violet Mine	Bulk	WRS 1463 B VIOLET 3A N		70.09	29.163	0.004	0.792	0	100.05
Violet Mine	Bulk	WRS 1463 B VIOLET 3A O		67.138	32.292	0	0.727	0	100.16
Violet Mine	Bulk	WRS 1463 B VIOLET 3A P		83.089	17.134	0.015	0.633	0.038	100.91
Violet Mine	Bulk	WRS 1463 B VIOLET 3A Q		65.104	33.91	0	1.27	0	100.29
Violet Mine	Bulk	WRS 1463 B VIOLET 3A R		65.809	33.369	0.005	0.742	0	99.925
Violet Mine	Bulk	WRS 1463 B VIOLET 3A SD2		52.45	42.326	0	4.275	0	99.051
Violet Mine	Bulk	WRS 1463 B VIOLET 3A S		69.99	27.67	0.005	0.635	0	98.3
Violet Mine	Bulk	WRS 1463 B VIOLET 3A T		73.125	25.923	0.004	0.564	0.009	99.625
Violet Mine	Bulk	WRS 1463 B VIOLET 3A U		79.874	20.108	0.023	0.663	0.031	100.7
Violet Mine	Bulk	WRS 1463 B VIOLET 3A UD2		64.162	35.508	0.041	1.262	0	100.97
Violet Mine	Bulk	WRS 1463 B VIOLET 3A V		64.595	34.988	0	0.591	0	100.17
Violet Mine	Bulk	WRS 1463 B VIOLET 3A WD		51.916	45.277	0	1.655	0	98.848
Violet Mine	Bulk	WRS 1463 B VIOLET 3A WL		79.02	19.935	0.027	0.343	0	99.325
Violet Mine	Bulk	WRS 1463 B VIOLET 3A X		80.046	18.173	0.017	1.079	0	99.315
Violet Mine	Bulk	WRS 1463 B VIOLET 3A Y		67.916	30.144	0.001	1.172	0	99.233
Violet Mine	Bulk	WRS 1463 B VIOLET 3A ZL		77.044	23.013	0.013	0.48	0	100.55

Occurrence	Sample Type	Block and ID	Grain ID	Wt.% (Au)	Wt.% (Ag)	Wt.% (Fe)	Wt. % (Hg)	Wt.% (Cu)	Probe Total
Violet Mine	Bulk	WRS 1463 B VIOLET 3A ZD		61.924	36.64	0.007	1.807	0	100.38
Violet Mine	Bulk	WRS 1463 B VIOLET3A A1C		56.557	40.017	0	2.973	0	99.547
Violet Mine	Bulk	WRS 1463 B VIOLET3A A1P		57.373	39.833	0.038	2.319	0	99.563
Violet Mine	Bulk	WRS 1463 B VIOLET3A B1PC		68.82	29.412	0	0.702	0	98.934
Violet Mine	Bulk	WRS 1463 B VIOLET3A B1D		45.176	50.904	0	2.813	0	98.893
Violet Mine	Bulk	WRS 1463 B VIOLET3A C1		78.541	19.615	0.02	0.782	0	98.958
Violet Mine	Bulk	WRS 1463 B VIOLET3A D1		74.58	24.634	0.019	1.154	0	100.39
Violet Mine	Bulk	WRS 1463 B VIOLET3A F1		69.647	30.076	0.006	0.639	0	100.37
Violet Mine	Bulk	WRS 1463 B VIOLET3A G1		63.86	34.656	0	1.313	0	99.829
Violet Mine	Bulk	WRS 1463 B VIOLET3A H1		79.816	18.474	0.027	1.27	0.012	99.599
Violet Mine	Bulk	WRS 1463 B VIOLET3A I1D		40.9	52.027	0.003	7.275	0	100.21
Violet Mine	Bulk	WRS 1463 B VIOLET3A I1L		70.201	30.023	0.045	0.342	0	100.61
Violet Mine	Bulk	WRS 1463 B VIOLET3B A		67.731	31.359	0.001	1.455	0	100.55
Violet Mine	Bulk	WRS 1463 B VIOLET3B C		79.13	19.237	0.025	1.136	0.023	99.551
Violet Mine	Bulk	WRS 1463 B VIOLET3B D		76.671	21.36	0.002	1.145	0.002	99.181
Violet Mine	Bulk	WRS 1463 B VIOLET3B E		65.901	31.899	0	1.453	0	99.253
Violet Mine	Bulk	WRS 1463 B VIOLET3B F		67.921	31.579	0	1.561	0	101.06

Occurrence	Sample Type	Block and ID	Grain ID	Wt.% (Au)	Wt.% (Ag)	Wt.% (Fe)	Wt. % (Hg)	Wt.% (Cu)	Probe Total
Violet Mine	Bulk	WRS 1463 B VIOLET3B G		68.702	29.793	0	1.255	0	99.75
Violet Mine	Bulk	WRS 1463 B VIOLET3B H		64.821	32.846	0	1.708	0	99.379
Violet Mine	Bulk	WRS 1463 B VIOLET3B I		71.888	25.871	0.002	1.064	0	98.825
Violet Mine	Bulk	WRS 1463 B VIOLET3B J		65.443	31.57	0	1.979	0	98.992
Violet Mine	Bulk	WRS 1463 B VIOLET3B K		66.907	31.67	0.003	1.5	0	100.08
Violet Mine	Bulk	WRS 1463 B VIOLET3B L		65.401	33.346	0	1.975	0	100.72
Violet Mine	Bulk	WRS 1463 B VIOLET3B M		70.444	27.835	0	1.215	0	99.494
Violet Mine	Bulk	WRS 1463 B VIOLET3B N		79.108	18.445	0.012	0.76	0	98.325
Violet Mine	Bulk	WRS 1463 B VIOLET3B O		81.072	18.701	0.058	0.391	0.016	100.24
Violet Mine	Bulk	WRS 1463 B VIOLET3B P		66.698	31.758	0.009	1.429	0	99.894
Violet Mine	Bulk	WRS 1463 B VIOLET3B Q		67.873	30.186	0.004	1.516	0	99.579
Violet Mine	Bulk	WRS 1463 B VIOLET3B R		65.678	31.752	0	1.394	0	98.824
Violet Mine	Bulk	WRS 1463 B VIOLET3B SL/1		66.347	31.153	0.003	1.146	0	98.649
Violet Mine	Bulk	WRS 1463 B VIOLET3B SL/2		67.164	31.219	0.006	1.31	0	99.699
Violet Mine	Bulk	WRS 1463 B VIOLET3B SD		46.264	47.521	0	5.646	0	99.431
Violet Mine	Bulk	WRS 1463 B VIOLET3B T		67.543	32.216	0	0.604	0	100.36
Violet Mine	Bulk	WRS 1463 B VIOLET3B U		67.927	29.923	0	0.636	0	98.486

Occurrence	Sample Type	Block and ID	Grain ID	Wt.% (Au)	Wt.% (Ag)	Wt.% (Fe)	Wt. % (Hg)	Wt.% (Cu)	Probe Total
Violet Mine	Bulk	WRS 1463 B VIOLET3B UL2		59.042	38.031	0	1.115	0	98.198
Violet Mine	Bulk	WRS 1463 B VIOLET3B UD2		60.472	36.611	0	2.116	0	99.199
Violet Mine	Bulk	WRS 1463 B VIOLET3B V		67.211	30.925	0.003	0.606	0	98.745
Violet Mine	Bulk	WRS 1463 B VIOLET3B W		69.23	29.738	0.007	1.053	0	100.03
Violet Mine	Bulk	WRS 1463 B VIOLET3B X		72.33	26.198	0.003	1.573	0	100.11
Violet Mine	Bulk	WRS 1463 B VIOLET3B XD		36.758	57.523	0	4.994	0	99.275
Violet Mine	Bulk	WRS 1463 B VIOLET3B Y		66.753	33.376	0	0.796	0	100.93
Violet Mine	Bulk	WRS 1463 B VIOLET3B Z		66.558	32.586	0	1.517	5.615	106.28
Violet Mine	Bulk	WRS 1463 B VIOLET3B A1		82.09	18.394	0.027	0.468	0.002	100.98
Violet Mine	Bulk	WRS 1463 B VIOLET3B B1		78.784	21.447	0.017	0.594	0.004	100.85
Violet Mine	Bulk	WRS 1463 B VIOLET3B C1		66.809	32.126	0	1.528	0	100.46
Violet Mine	Bulk	WRS 1463 B VIOLET3B D1		69.204	30.587	0	0.128	0	99.93
Violet Mine	Bulk	WRS 1463 B VIOLET3B E1C		66.436	33.022	0	0.44	0	99.902
Violet Mine	Bulk	WRS 1463 B VIOLET3B E1R		57.123	17.92	0.066	24.69	0.026	99.825
Violet Mine	Bulk	WRS 1463 B VIOLET3B F1		67.127	32.607	0	0.929	0	100.66
Violet Mine	Bulk	WRS 1463 B VIOLET3B G1		81.955	18.426	0.019	0.72	0.03	101.15
Violet Mine	Bulk	WRS 1463 B VIOLET3B G1D2		39.494	52.604	0.012	4.4	0	96.51

Occurrence	Sample Type	Block and ID	Grain ID	Wt.% (Au)	Wt.% (Ag)	Wt.% (Fe)	Wt. % (Hg)	Wt.% (Cu)	Probe Total
Violet Mine	Bulk	WRS 1463 B VIOLET3B H1		66.47	33.768	0.011	0.461	0	100.71
Violet Mine	Bulk	WRS 1463 B VIOLET3B I1		66.63	32.667	0.005	1.885	0	101.19
Violet Mine	Bulk	WRS 1463 B VIOLET3B J1		71.288	28.557	0.064	0.744	0	100.65
Violet Mine	Bulk	WRS 1463 B VIOLET3B K1		69.934	30.164	0.011	1.382	0	101.49
Violet Mine	Bulk	WRS 1463 B VIOLET3B L1		70.546	28.647	0	1.335	0	100.53
Violet Mine	Bulk	WRS 1463 B VIOLET3B M1P		74.028	25.97	0.015	1.348	0	101.36
Violet Mine	Bulk	WRS 1463 B VIOLET3B M1D		41.008	52.211	0	7.394	0	100.61
Violet Mine	Bulk	WRS 1463 B VIOLET3B N1		69.311	29.699	0.007	1.17	0	100.19
Violet Mine	Bulk	WRS 1463B VIOLET 4A		81.213	19.06	0.013	0.68	0.01	100.98
Violet Mine	Bulk	WRS 1463B VIOLET 4AD		42.573	51.088	0	7.084	0	100.75
Violet Mine	Bulk	WRS 1463B VIOLET 4B		81.82	18.729	0.019	0.841	0.01	101.42
Violet Mine	Bulk	WRS 1463B VIOLET 4C		79.794	20.457	0.011	1.477	0.012	101.75
Violet Mine	Bulk	WRS 1463B VIOLET 4D		80.407	19.957	0.014	1.372	0.014	101.76
Violet Mine	Bulk	WRS 1463B VIOLET 4E		79.938	20.409	0.023	1.332	0.017	101.72
Violet Mine	Bulk	WRS 1463B VIOLET 4ED		37.679	55.649	0.005	7.607	0	100.96
Violet Mine	Bulk	WRS 1463B VIOLET 4F		70.353	30.14	0.008	1.119	0	101.62
Violet Mine	Bulk	WRS 1463B VIOLET 4G		69.409	30.458	0.007	1.311	0	101.19

Occurrence	Sample Type	Block and ID	Grain ID	Wt.% (Au)	Wt.% (Ag)	Wt.% (Fe)	Wt. % (Hg)	Wt.% (Cu)	Probe Total
Violet Mine	Bulk	WRS 1463B VIOLET 4H		67.59	33.144	0	0.728	0	101.46
Violet Mine	Bulk	WRS 1463B VIOLET 4I		75.782	24.321	0.012	0.477	0.007	100.6
Violet Mine	Bulk	WRS 1463B VIOLET 4J		79.927	20.595	0.014	1.31	0.013	101.86
Violet Mine	Bulk	WRS 1463B VIOLET 4K		80.672	20.11	0.017	1.024	0.03	101.85
Violet Mine	Bulk	WRS 1463B VIOLET 4L		79.237	20.951	0.021	1.118	0.012	101.34
Violet Mine	Bulk	WRS 1463B VIOLET 4M		80.799	19.678	0.02	0.954	0.012	101.46
Violet Mine	Bulk	WRS 1463B VIOLET 4N		80.151	19.919	0.025	1.166	0.02	101.28
Violet Mine	Bulk	WRS 1463B VIOLET 4ND		55.148	41.818	0	3.341	0	100.31
Violet Mine	Bulk	WRS 1463B VIOLET 4O		80.938	19.567	0.015	1.156	0.021	101.7
Violet Mine	Bulk	WRS 1463B VIOLET 4OD		50.608	45.954	0	3.751	0	100.31
Violet Mine	Bulk	WRS 1463B VIOLET 4P		74.473	25.879	0.004	0.733	0	101.09
Violet Mine	Bulk	WRS 1463B VIOLET 4Q		80.855	19.936	0.015	1.19	0.017	102.01
Violet Mine	Bulk	WRS 1463B VIOLET 4R		80.955	19.472	0.019	0.83	0.015	101.29
Violet Mine	Bulk	WRS 1463B VIOLET 4S		80.269	20.411	0.013	1.11	0.013	101.82
Violet Mine	Bulk	WRS 1463B VIOLET 4T		80.571	19.428	0.013	1.06	0.014	101.09
Violet Mine	Bulk	WRS 1463B VIOLET 4U		81.47	19.267	0.025	0.911	0.032	101.71
Violet Mine	Bulk	WRS 1463B VIOLET 4V		81.77	19.181	0.022	0.83	0.005	101.81

Occurrence	Sample Type	Block and ID	Grain ID	Wt.% (Au)	Wt.% (Ag)	Wt.% (Fe)	Wt. % (Hg)	Wt.% (Cu)	Probe Total
Violet Mine	Bulk	WRS 1463B VIOLET 4W		78.256	22.209	0.005	0.393	0	100.86
Violet Mine	Bulk	WRS 1463B VIOLET 4X		81.675	19.125	0.019	0.829	0.029	101.68
Violet Mine	Bulk	WRS 1463B VIOLET 4Y		81.55	19.942	0.009	0.442	0.01	101.95
Violet Mine	Bulk	WRS 1463B VIOLET 4YD		55.742	41.28	0.014	3.782	0	100.82
Violet Mine	Bulk	WRS 1463B VIOLET 4Z		82.311	19.034	0.014	0.63	0.003	101.99
Violet Mine	Bulk	WRS 1463B VIOLET 4A1		79.611	20.417	0.011	1.782	0.021	101.84
Violet Mine	Bulk	WRS 1463B VIOLET 4B1		82.154	18.288	0.014	1.568	0.02	102.04
Violet Mine	Bulk	WRS 1463B VIOLET 4C1		83.036	17.928	0.014	1.003	0.024	102.01
Violet Mine	Bulk	WRS 1463B VIOLET 4D1		81.69	19.3	0.011	0.728	0.02	101.75
Violet Mine	Bulk	WRS 1463B VIOLET 4E1		82.17	18.894	0.029	0.821	0.015	101.93
Violet Mine	Bulk	WRS 1463B VIOLET 4F1		78.012	21.881	0.008	1.481	0.006	101.39
Violet Mine	Bulk	WRS 1463B VIOLET 4I1		67.105	32.266	0	0.944	0	100.32
Violet Mine	Bulk	WRS 1463B VIOLET 4H1		82.438	18.619	0.037	0.924	0.035	102.05
Violet Mine	Bulk	WRS 1463B VIOLET 4G1		86.342	15.479	0.014	0.541	0.027	102.4
Violet Mine	Bulk	WRS 1463B VIOLET 4J1		82.925	18.474	0.023	0.458	0.009	101.89
Violet Mine	Bulk	WRS 1463B VIOLET 4J1TR		49.545	47.56	0	3.629	0	100.73
Violet Mine	Bulk	WRS 1463B VIOLET 4K1		82.39	18.852	0.009	0.584	0.035	101.87

Occurrence	Sample Type	Block and ID	Grain ID	Wt.% (Au)	Wt.% (Ag)	Wt.% (Fe)	Wt. % (Hg)	Wt.% (Cu)	Probe Total
Violet Mine	Bulk	WRS 1463B VIOLET 4L1		80.27	20.193	0.016	1.126	0.006	101.61
Violet Mine	Bulk	WRS 1463B VIOLET 4M1		82.011	18.388	0.027	0.785	0.035	101.25
Violet Mine	Bulk	WRS 1463B VIOLET 4N1		81.872	19.082	0.015	0.896	0	101.87
Violet Mine	Bulk	WRS 1463B VIOLET 4P		79.933	20.503	0.018	1.258	0.022	101.73
Violet Mine	Bulk	WRS 1463B VIOLET 4PD		41.283	53.11	0	5.141	0	99.534
Violet Mine	Bulk	WRS 1463B VIOLET 4Q1/1		81.201	18.854	0.017	1.187	0.024	101.28
Violet Mine	Bulk	WRS 1463B VIOLET 4Q1/2		45.35	50.64	0	5.128	0	101.14
Violet Mine	Bulk	WRS 1463B VIOLET 4R1		80.607	18.977	0.023	1.634	0.008	101.25
Violet Mine	Bulk	WRS 1463B VIOLET 4S1		66.236	32.577	0	2.216	0	101.03
Violet Mine	Bulk	WRS 1463B VIOLET 4W1		78.82	20.489	0.02	1.857	0.011	101.2
Violet Mine	Bulk	WRS 1463B VIOLET 4X1		81.926	18.53	0.013	1.043	0.019	101.53